NASA/TM-20250002545

Progressive Damage and Failure Analysis Methods Applications for Aircraft Crashworthiness and Impact Energy Management

Mostafa Rassaian
Advanced Certification Technology, Boeing Research & Technology, Seattle, Washington

J. Michael Pereira
Glenn Research Center, Cleveland, Ohio

Alan Byar
Boeing Impact Simulation Group, Everett, Washington

Aswini Kona Ravi
National Institute for Aviation Research, Wichita, Kansas

Rudy Haluza
Pennsylvania State University, University Park, Pennsylvania

Daniel O. Adams
University of Utah, Salt Lake City, Utah

Reza Vaziri and Johannes Reiner
The University of British Columbia, Vancouver, Canada

Rajaneesh Anantharaju
GDTech, Ans, Belgium

Matthias Waimer and Thomas Feser
DLR German Aerospace Center, Stuttgart, Germany

Erin Blessing
University of Utah, Salt Lake City, Utah

Maria Pia Falaschetti and Francesco Rondina
University of Bologna, Forli (FC), Italy

Patrick de Luca and Sebastian Müller
ESI Group, Bagneux, France

Sharon Xiao
Michigan State University, East Lansing, Michigan

Juan Pedro Berro Ramirez
Altair Engineering Inc., Paris, France

Paolo Feraboli and Bonnie Wade
Advanced Composite Structures Laboratory, Seattle, Washington

Alastair Johnson
DLR German Aerospace Center, Stuttgart, Germany

Akhil Bhasin and Luis Gomez
National Institute for Aviation Research, Wichita, Kansas

April 2025

NASA STI Program Report Series

Since its founding, NASA has been dedicated to the advancement of aeronautics and space science. The NASA scientific and technical information (STI) program plays a key part in helping NASA maintain this important role.

The NASA STI program operates under the auspices of the Agency Chief Information Officer. It collects, organizes, provides for archiving, and disseminates NASA's STI. The NASA STI program provides access to the NTRS Registered and its public interface, the NASA Technical Reports Server, thus providing one of the largest collections of aeronautical and space science STI in the world. Results are published in both non-NASA channels and by NASA in the NASA STI Report Series, which includes the following report types:

- TECHNICAL PUBLICATION.
  Reports of completed research or a major significant phase of research that present the results of NASA programs and include extensive data or theoretical analysis. Includes compilations of significant scientific and technical data and information deemed to be of continuing reference value. NASA counterpart of peer-reviewed formal professional papers but has less stringent limitations on manuscript length and extent of graphic presentations.

- TECHNICAL MEMORANDUM.
  Scientific and technical findings that are preliminary or of specialized interest, e.g., quick release reports, working papers, and bibliographies that contain minimal annotation. Does not contain extensive analysis.

- CONTRACTOR REPORT.
  Scientific and technical findings by NASA-sponsored contractors and grantees.

- CONFERENCE PUBLICATION.
  Collected papers from scientific and technical conferences, symposia, seminars, or other meetings sponsored or cosponsored by NASA.

- SPECIAL PUBLICATION.
  Scientific, technical, or historical information from NASA programs, projects, and missions, often concerned with subjects having substantial public interest.

- TECHNICAL TRANSLATION.
  English-language translations of foreign scientific and technical material pertinent to NASA's mission.

Specialized services also include organizing and publishing research results, distributing specialized research announcements and feeds, providing information desk and personal search support, and enabling data exchange services.

For more information about the NASA STI program, see the following:

- Access the NASA STI program home page at http://www.sti.nasa.gov

NASA/TM-20250002545

Progressive Damage and Failure Analysis Methods Applications for Aircraft Crashworthiness and Impact Energy Management

Mostafa Rassaian
Advanced Certification Technology, Boeing Research & Technology, Seattle, Washington

J. Michael Pereira
Glenn Research Center, Cleveland, Ohio

Alan Byar
Boeing Impact Simulation Group, Everett, Washington

Aswini Kona Ravi
National Institute for Aviation Research, Wichita, Kansas

Rudy Haluza
Pennsylvania State University, University Park, Pennsylvania

Daniel O. Adams
University of Utah, Salt Lake City, Utah

Reza Vaziri and Johannes Reiner
The University of British Columbia, Vancouver, Canada

Rajaneesh Anantharaju
GDTech, Ans, Belgium

Matthias Waimer and Thomas Feser
DLR German Aerospace Center, Stuttgart, Germany

Erin Blessing
University of Utah, Salt Lake City, Utah

Maria Pia Falaschetti and Francesco Rondina
University of Bologna, Forli (FC), Italy

Patrick de Luca and Sebastian Müller
ESI Group, Bagneux, France

Sharon Xiao
Michigan State University, East Lansing, Michigan

Juan Pedro Berro Ramirez
Altair Engineering Inc., Paris, France

Paolo Feraboli and Bonnie Wade
Advanced Composite Structures Laboratory, Seattle, Washington

Alastair Johnson
DLR German Aerospace Center, Stuttgart, Germany

Akhil Bhasin and Luis Gomez
National Institute for Aviation Research, Wichita, Kansas

National Aeronautics and
Space Administration

Glenn Research Center
Cleveland, Ohio 44135

April 2025

Acknowledgments

The authors gratefully acknowledge Brian Justusson, Jenna Pang, Matthew Molitor, and Jeff Iqbal from the Boeing High Energy Dynamic Impact team for the NASA Advanced Composites Project; Mohammed H. Kabir of Boeing; Dalton Ostler of the University of Utah; and Andries Buitenhuis of Boom Aerospace for their invaluable contributions.

Special thanks to Larry Ilcewicz and Cindy Ashforth of the FAA for their critical feedback and thought-provoking questions, which greatly enhanced the quality of this report.

The authors would like to acknowledge support from the NASA Revolutionary Vertical Lift Technology Project for a portion of the research and publication of this report.

Finally, our appreciation goes to figure and layout artist Lorie Passe, illustrator Joshua Soderberg, and technical editor Sandra Mason, all of NASA Glenn's Publishing and Creative Services team, for their exceptional work in preparing this document.

This work was sponsored by the Advanced Air Vehicles Program at the NASA Glenn Research Center.

Level of Review: This material has been technically reviewed by technical management.

This report is available in electronic form at https://www.sti.nasa.gov/ and https://ntrs.nasa.gov/

NASA STI Program/Mail Stop 050
NASA Langley Research Center
Hampton, VA 23681-2199

Contents

Progressive Damage and Failure Analysis Methods Applications for Aircraft Crashworthiness and Impact Energy Management

Mostafa Rassaian*
Advanced Certification Technology
Boeing Research & Technology
Seattle, Washington 98124

J. Michael Pereira
National Aeronautics and Space Administration
Glenn Research Center
Cleveland, Ohio 44135

Alan Byar
Boeing Impact Simulation Group
Everett, Washington 98204

Aswini Kona Ravi
National Institute for Aviation Research
Wichita, Kansas 67260

Rudy Haluza
Pennsylvania State University
University Park, Pennsylvania 16802

Daniel O. Adams
University of Utah
Salt Lake City, Utah 84112

Reza Vaziri and Johannes Reiner†
The University of British Columbia
V6T 1Z4, Vancouver, Canada

Rajaneesh Anantharaju
GDTech
4432 Ans, Belgium

Matthias Waimer and Thomas Feser
DLR German Aerospace Center
70569, Stuttgart, Germany

Erin Blessing
University of Utah
Salt Lake City, Utah 84112

Maria Pia Falaschetti and Francesco Rondina
University of Bologna
47121, Forli (FC), Italy

Patrick de Luca and Sebastian Müller
ESI Group
92220, Bagneux, France

Sharon Xiao‡
Michigan State University
East Lansing, Michigan 48824

Juan Pedro Berro Ramirez
Altair Engineering Inc.
92184, Paris, France

Paolo Feraboli and Bonnie Wade
Advanced Composite Structures Laboratory
Seattle, Washington 98199

Alastair Johnson‡
DLR German Aerospace Center
70569, Stuttgart, Germany

Akhil Bhasin and Luis Gomez
National Institute for Aviation Research
Wichita, Kansas 67260

Summary

This report presents a range of analysis methods for performing progressive damage and failure analysis (PDFA) of composite structures with application to crashworthiness analyses and impact event simulation. The report reflects research efforts by the Composite Materials Handbook 17 (CMH–17)

*Currently retired. Contributions after 2019 were made through Rassaian LLC, Bellevue, Washington 98008.
†Now with Deakin University, Geelong, VIC, Australia 3220. Contributions after 2019 were made through Deakin.
‡Currently retired.

Crashworthiness Working Group toward advancing the state of the art in analysis methods and tools. As such, this report serves as a repository of various PDFA methods that users can apply to replicate benchmark problems, incorporating lessons learned to avoid repeating those same errors. Detailed modeling and testing guidelines, along with best practices as the means of compliance subject to regulatory requirements, are deferred to Revision H of CMH–17, Volume 3, Chapter 16, Crashworthiness and Energy Management. The objective of this report is to describe a selection of PDFA methods and show how they are applied in simulating component-level tests involving progressive failure and to present an overall approach for calibrating, evaluating, and validating these PDFA methods. The general intended application of PDFA in this case is aircraft crashworthiness, and therefore the tests are intended to represent aircraft structural features that could be used to manage energy for crashworthiness. Simulation results are compared with flat coupon and C-channel test data for multiple methods, and each of these methods is described in detail, including calibration and material characterization testing requirements. The multiple benefits in using PDFA include the ability to guide testing, reduce design risk, provide response data in support of certification, optimize design features, and perform detailed assessments of structural responses that are difficult to obtain through testing outputs. As with all finite element methods, use of PDFA requires testing for calibration and validation, and test requirements are presented in detail for a range of PDFA methods. Additionally, modeling guidance is provided on strengths, limitations, and recommended practices for several PDFA simulation methods.

1.0 Introduction

Progressive damage and failure analysis (PDFA) is used to represent progressive failure of composite structures under dynamic loading conditions. PDFA is used to show the resulting energy dissipation over time, the redistribution of loading as damage evolves, and changes in structural capability. PDFA methods are inherently linked with testing for calibration and validation, and this report provides details of specific test metrics used in calibration and validation processes.

Simulations with PDFA can be used to guide and select testing (“smarter testing”) and can also serve to reduce the risk of unacceptable test responses. Validated PDFA simulations can be used to perform analyses in lieu of physical testing that might be impractical. PDFA simulations can reduce the time needed to optimize designs, can generate data to support certification, and can provide additional insight into structural responses that would be difficult to assess with physical test instrumentation. PDFA simulation tools are continually evolving. Damage, deformation, and failure may be modeled in numerous ways, as discussed in References 1 and 2. In general, each PDFA simulation tool has strengths and limitations, and selection of a PDFA tool will depend on the modeling application and intended model use.

This report provides a snapshot of current modeling capabilities as of 2024, along with a means of assessing and validating updated or new simulation tools. The purpose of this report is to present composite material modeling and testing for simulating the crashworthiness of airframe structures. It outlines a framework for calibrating, evaluating, and validating PDFA methods while identifying strengths, weaknesses, best practices, and modeling guidelines. The goal is to promote the use of validated analyses supported by efficient testing, identifying best practices for safe composite design and helping prepare for dialogue with regulators to support certification. While the primary application is aircraft crashworthiness and impact, these PDFA methods may be applied to a broader range of dynamic events.

The work described in this report was performed under the Composite Materials Handbook 17 (CMH–17) Crashworthiness Working Group (CWG) through three stages of round-robin testing.

Conducted from 2008 to February 2024, this technical effort was led by the CWG, comprising researchers from universities, government laboratories, and industry, as represented by the authors. Various methods were employed to model damage, deformation, and failure, with guidance reflected in CMH–17, Volume 3, Chapter 16, Revision H (Ref. 3) and detailed modeling descriptions and strategies presented in this document.

1.1 Progressive Damage and Failure Modeling

Advanced failure theories for PDFA applications in dynamic loading of composite structures typically necessitate calibration using standard, repeatable tests. The NASA Advanced Composites Project (ACP) has established benchmark problems for high-energy dynamic impact (HEDI) scenarios at various length scales to evaluate material models and simulation methods. Results are set to be made available to the public in the near future.

Approaches for predicting failure of composites are currently still developing and evolving. While there are some commonalities in the input data used to exercise the selected material models for strength and stiffness properties, some models require unique input parameters obtained from specialized testing. (These model-specific material properties are discussed in Section 5.2.)

PDFA is beneficial for identifying critical tests to conduct across length scales with a consistent set of parameters. Accuracy of the analytical solutions is largely dependent on the choice of scales, relying on how closely mixed-mode delamination or damage during impact can be captured. Modeling considerations include mesh convergence, contact, multibody impact, material properties with strain-rate effects, interaction of failure modes, and solution time for simulating large-scale structures to impact events.

Simulation results that are validated and consistent are valuable to designers—and potentially to regulators—even when performed by different sources. Although specific details may vary depending on the PDFA application, the metric-driven building-block method ensures step-by-step validation to maintain accuracy, regardless of the team creating the model. This approach involves setting specific validation and calibration requirements before testing and includes steps for both calibration and higher level validation.

The use of PDFA methods in composite material modeling and testing plays a crucial role in enhancing the design and certification process. By guiding smarter testing and reducing risk, PDFA promotes the use of validated models for certification by analysis (CbA). This requires close attention to the calibration and validation processes, emphasizing the building-block approach and model validation and ensuring simulation repeatability and consistency.

Objectives of using virtual testing and PDFA during aircraft development and certification include the following:

(1) Provide guidance to designers concerning the expected behavior of the aircraft structure in a survivable crash event at an early stage of the project for evaluating different configurations.

(2) Determine the critical failure modes and where crushable elements should be used.

(3) Arrive at a predictable energy absorption determination that satisfies survivability requirements.

(4) Help determine the critical sections to be proposed for certification or validation drop testing with an increased chance of success.

1.2 Current State of the Art of Analysis Methods and Tools

In the last 15 years, significant progress has been made with modeling and simulation for crashworthiness. The underlying goal has been to expand the best modeling practices to the larger scale

structure representative of the aircraft fuselage lower lobe. In 2008, to address crash simulation in depth, the CMH–17 CWG launched a numerical round-robin exercise for a selection of components and coupons with the goal of assessing the predictive capability of commercially available finite element analysis methods for composite crash simulation, and to provide numerical best practices guidelines.

Round Robin 1 (RR–1) and RR–2 used LS–DYNA® (Livermore Software Technology Corp.[1]) material models and PAM–CRASH (ESI Group) to simulate the PDFA response. Eleven different publicly available analysis methods were evaluated for RR–3: LS-DYNA® MAT54, MAT58, MAT213, MAT219, MAT261, and MAT297; LS–DYNA® Modified Ladevèze; ABAQUS® Ladevèze–ABQ_DLR_UD; ABAQUS® CZone; ESI Virtual Performance Solution (VPS): Waas–Pineda (WP) Implementation; and Altair® RADIOSS®. The IM7/8552 unidirectional tape system used for NASA's ACP research work was selected for these crashworthiness studies. The overarching value of the predictive capability using modeling and simulation, or "virtual testing," during the design phase has been adopted by multiple original equipment manufacturers to help the design effort and reduce certification risk as an essential part of the overall aircraft design process; see Reference 4 for a B787 case study.

1.2.1 Metrics for Model Validation Assessment

The aim of this effort was to evaluate the effectiveness of each material model by comparing its results with test data. Simulation results from material models were evaluated through RR tests to generate comparative plots between test and analysis. The following parameters were used as validation metrics to determine success criteria. These success criteria were intended to guide ongoing testing and analysis efforts by the CWG group for energy dissipation in crush simulations and are not intended as regulatory requirements.

Global Response: Analyze the correlation of the model to the crush test load–displacement curve to meet the success criteria based on

- Initial slope: Initial slope in response from initial to peak load
- Initial peak load: Peak force response from the load-deflection curve
- Sustained crush load: Computed average crush load over steady-state response
- Specific energy absorption (SEA): Calculated in two ways to meet success criteria:
  - Stable SEA based on sustained crush load
  - Total SEA based on the total time from initial time

Local Response: Analyze the correlation of the model to test data based on damage parameters to establish success criteria.

- Ply-by-ply level damage: Damage at or near the site of impact versus nondestructive evaluation
- Mode of failure: Types of failure, such as transverse shearing, delamination, local buckling, splaying or lamina bending, and fragmentation

1.2.2 Success Criteria

The relative error (*RE*) is expressed as *RE* = (*computed quantity – measured quantity*)/*measured quantity*. The validation assessment or computational accuracy is based on the value of *RE* in percentage as follows:

- *RE* < 10 percent: Excellent

[1]Livermore Software Technology Corp. was acquired by Ansys, Inc., in 2019.

- *RE* = 10 to 19 percent: Good
- *RE* = 20 to 29 percent: Fair
- *RE* > 30 percent: Poor

Damage assessment criteria: The damage assessment in the model's local response compared to the test will be quantitatively based on

- Location of the failure zones
- Shape of the failure zones
- Size of the failure zones on a ply-by-ply and laminate basis

Interpreting crash simulation metrics: When comparing crash simulation data with test data, users should evaluate prediction errors appropriately. For example, consider the following scenarios:

- Acceleration is underpredicted: The lower predicted acceleration suggests the model might underestimate the forces on passengers, indicating a nonconservative aspect in occupant safety.
- Energy absorption is overpredicted: The model assumes the structure can absorb more energy, which is nonconservative.

Underpredicting displacement and energy absorption suggests conservatism, whereas underpredicting acceleration indicates nonconservatism. Users are responsible for assessing overall model conservatism.

1.3 Report Overview

This report summarizes the efforts conducted by the CMH–17 CWG to advance the use of PDFA methods for aircraft crashworthiness design.

Section 2.0 presents a typical application of PDFA for the case of aircraft crashworthiness. Section 3.0 presents RR–1 and RR–2 results for PDFA simulations of various channel sections. The channel sections are representative of potential designs for cargo floor support stanchions or other energy-absorbing structures in the lower fuselage. LS–DYNA® material models and PAM–CRASH were used to simulate PDFA response. These results are compared with test response, and key findings are presented.

Section 4.0 presents test and simulation results for RR–3. The focus of RR–3 was to expand the modeling best practices to the larger scale structure representative of the aircraft fuselage lower lobe relative to RR–1 and RR–2. For that purpose, the number of PDFA methods was increased from three to seven, the coupons included hard laminates as well as quasi-isotropic (QI) laminates, and the material system was changed from Toray® T700/2510 (Toray Industries, Inc.) (used in RR–1 and RR–2) to IM7/8552. The IM7/8552 unidirectional tape system was selected for this stage to take advantage of the ACP HEDI effort's shared goal in advancing predictive capabilities in impact dynamics. In RR–3, the selected test was crushing of flat-plate coupons with differing layups as well as C-channel coupons, and testing was used to generate a measure of SEA to compare with the analysis results.

Section 5.0 focuses on the experimental methods and data required for each of the analysis methods as presented in Sections 3.0 and 4.0. Section 5.0 describes the testing and simulation results used to calibrate and validate 11 different PDFA modeling methods. Because PDFA methods use differing approaches to simulate composite damage initiation and damage progression, these analysis methods have different data requirements for model calibration. For each analysis method, material modeling assumptions are summarized, including model-specific material property requirements. Section 5.0 also describes various test coupons that were used to calibrate PDFA models.

Nomenclature is provided in Appendix A. Appendix B provides supplementary information on crashworthiness testing and analysis methods, such as theoretical background, material cards, sample calculations, and detailed discussions. Appendix C provides supplementary information on nonstandard characterization tests for the ABQ_DLR_UD material model.

2.0 Aircraft Fuselage Modeling Considerations

A typical fuselage model used for crashworthiness simulations is shown in Figure 1. Overall fuselage-level response involves a series of components acting as a system. If floor-level acceleration response experienced by occupants is a metric of interest, then the skin, frames, stanchions, cargo, passenger floor stanchions, sidewall up to passenger floor, floor–frame connections, and floor stiffness should all be correctly represented. A front view of the model is seen in Figure 2, which shows the structures involved in the load path between ground impact and the passenger floor.

Figure 3 shows the crushing response of the lower lobe during impact. Energy dissipation from stanchion crushing plays a key role in managing impact energy, and additional energy is dissipated by the skin panels and frames. The load can then be transferred to the passenger floor by LD3 (lower deck type 3) cargo containers or by loose luggage, depending on the configuration and container design. The passenger stanchions will provide a clear load path to the passenger floor, and passenger stanchion design could also be evaluated as part of the overall crashworthiness response and energy mitigation. The frames also provide a load path to the passenger floor, and details of the floor design and floor-to-frame joint will influence the acceleration response for the floor and seat attachment points. Figure 4 shows a typical energy balance evolving between kinetic energy from the initial drop impact and energy dissipated through crushing and material failure. Overall total energy will increase slightly during impact due to the continued effect of gravity.

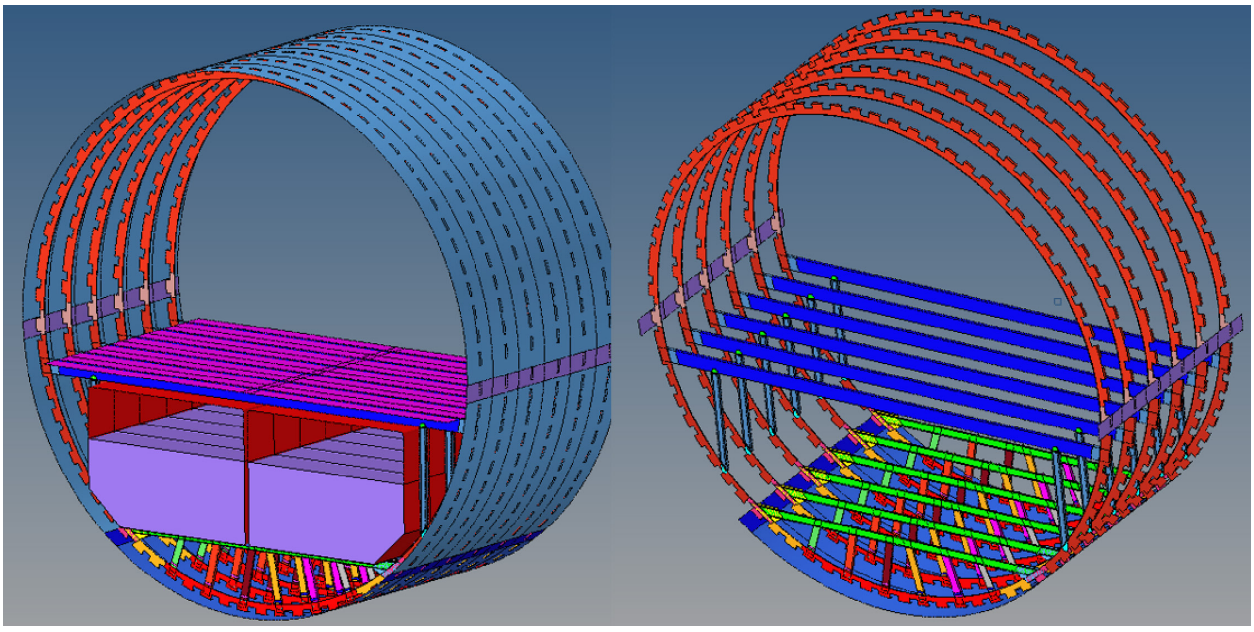

Figure 1.—Fuselage section model; occupants and stowage bins represented by mass elements.

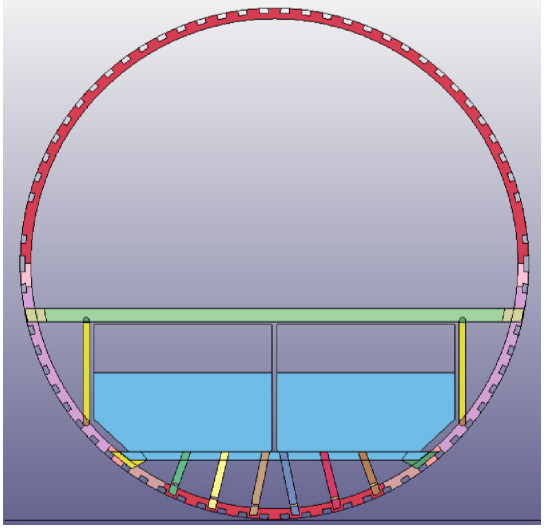

Figure 2.—Front view of fuselage section; occupants and stowage bins represented by distributed mass elements.

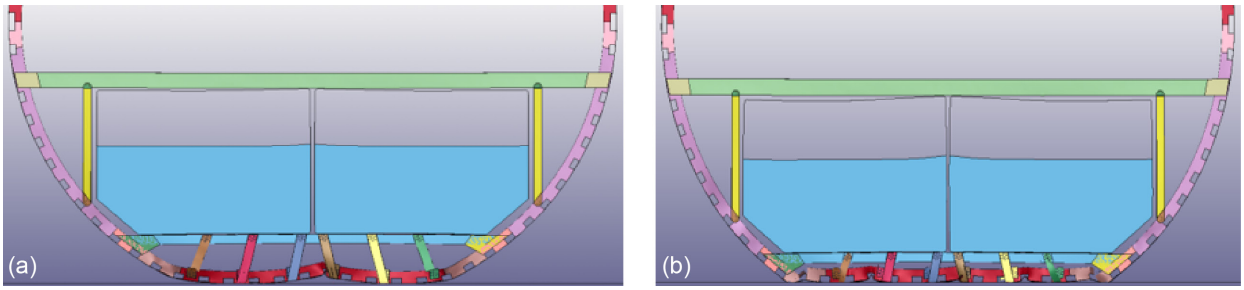

Figure 3.—Crushing of lower lobe during impact. (a) 30 ms after initial contact at 30 ft/s. (b) 60 ms after initial contact at 30 ft/s.

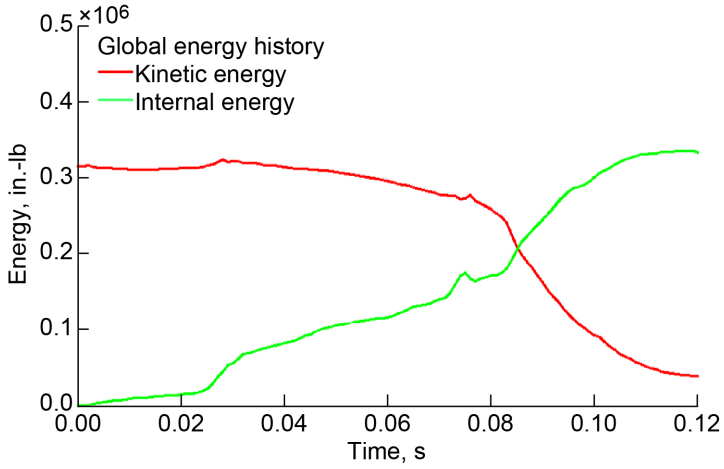

Figure 4.—Energy balance between kinetic energy from initial impact and energy dissipated by crushing.

The stiffness of underfloor structures may significantly influence the floor-level response, which is illustrated by previously conducted drop tests using a 737 fuselage section. Reference 5 provides detailed 737 fuselage drop-test results and simulation. Two different underfloor cargo types were tested: (1) loose

luggage restrained by a net and (2) a conformal fuel cell. The fuel cell is a relatively stiff structure and is effectively rigid in comparison with the surrounding structure, which leads to a significantly higher acceleration pulse experienced by occupants. These test configurations and posttest images are seen in Figure 5 and Figure 6. The effect on acceleration response is seen in Figure 7, which shows that the stiffer stucture (Figure 7(a)) reaches zero velocity (peak crush prior to rebound) earlier than the more compliant structure with luggage (Figure 7(b)). The floor-level acceleration results experienced by occupants will therefore be significantly higher with stiffer cargo, such as a conformal fuel cell.

Future developments in crashworthiness simulation include extending the fuselage section models to include a full aircraft fuselage, as shown in Figure 8 and Figure 9 (Ref. 6). Use of a full aircraft model allows for combined loading in x (longitudinal) and y (vertical) directions and allows for a more complete representation of other crashworthiness responses, such as strength of fuselage sections. This could also be used as a basis for evaluation of ditching crashworthiness.

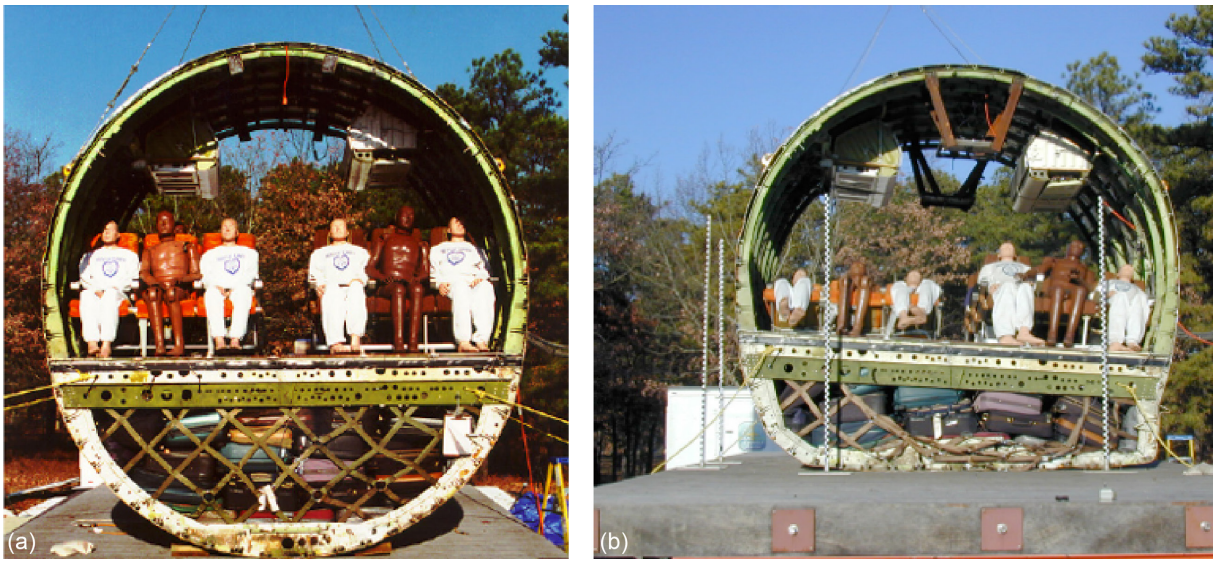

Figure 5.—Drop test of 737 fuselage section with underfloor luggage. (a) Test configuration. (b) After impact.

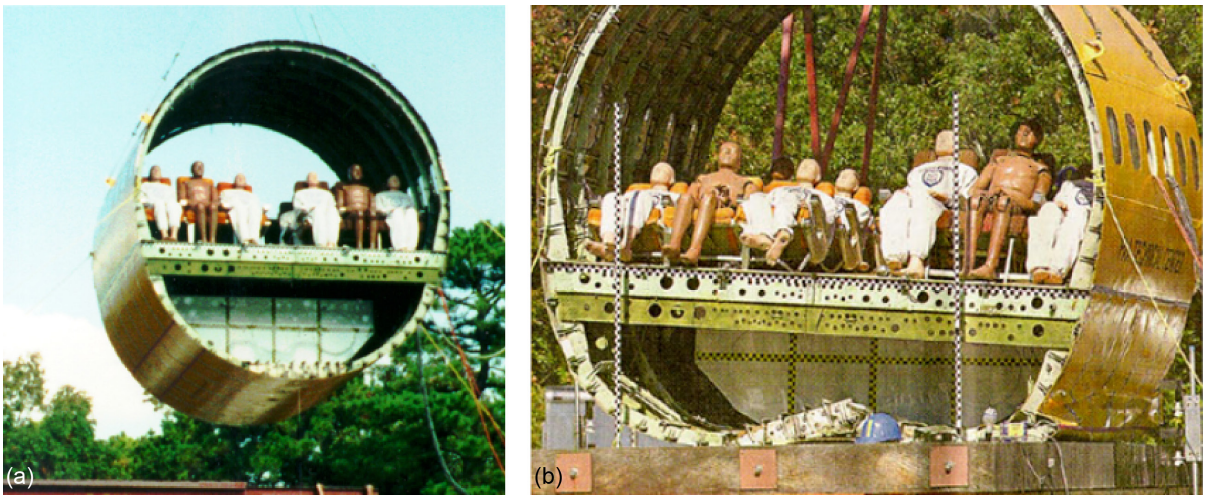

Figure 6.—Drop test of 737 fuselage section with conformal fuel cell. (a) Test configuration. (b) After impact.

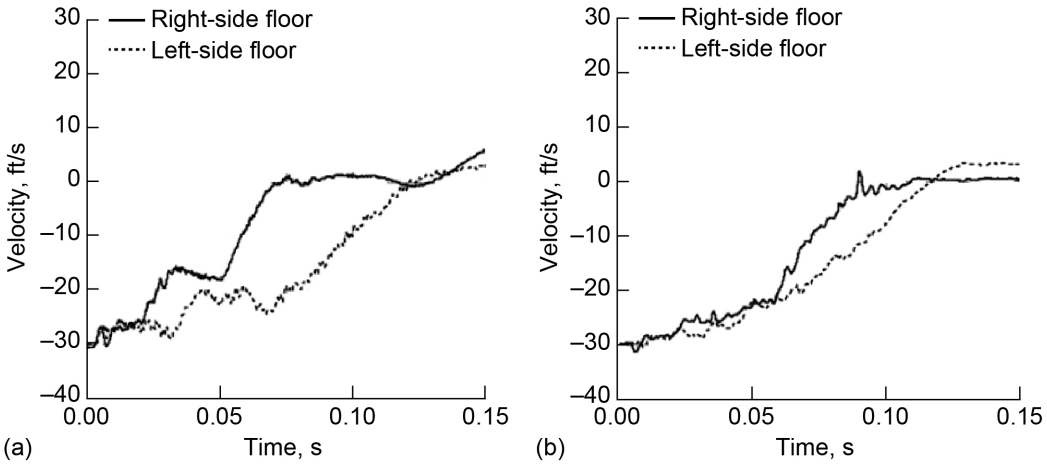

Figure 7.—Comparison of velocity–time history for two underfloor cargo types in 737 impact. (a) Conformal fuel cell. (b) Luggage restrained by net.

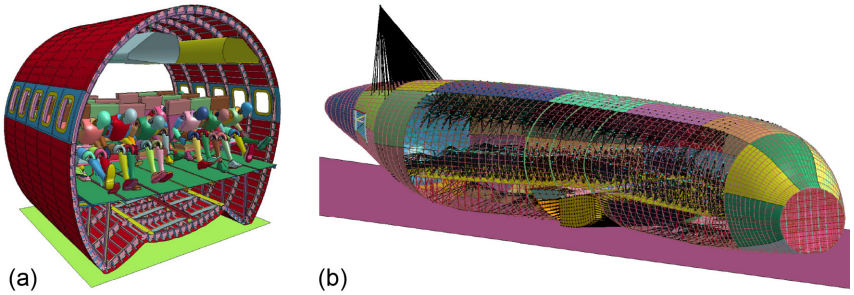

Figure 8.—Crashworthiness simulation models (courtesy of DLR German Aerospace Center). (a) Typical fuselage section (vertical drop). (b) Full aircraft fuselage model (combined xz impact).

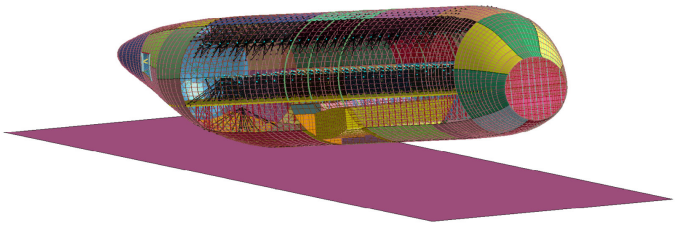

Figure 9.—Full fuselage at 5° initial angled impact condition (courtesy of DLR).

The crashworthiness response of the lower lobe contributes significantly to energy dissipation during impact and has a significant effect on the subsequent loads transferred to the passenger floor and seats. Figure 10 shows progressive crushing of stanchions below the cargo floor, illustrating the sequence of failure triggering and subsequent crushing. As noted elsewhere, the design of stanchions to optimize energy dissipation is a key consideration for crashworthiness. Figure 11 shows the full fuselage section; again, crushing in the lower lobe is seen to be a significant variable in overall impact response of the fuselage section.

Figure 12 shows a closer angled view of the stanchions in the lower lobe during crushing. After triggering failure, crushing occurs when the free end of the stanchion contacts the skin panels. Ideally, progressive failure will occur, but in large-scale physical tests, some random variations in crushing would be expected. For example, not all stanchions will crush with 100-percent effectiveness; some stanchions may catch or buckle against the frame or may partially fragment instead of crushing continuously. These

factors are accounted for in full-scale simulations but may not be adequately represented in tests using a single stanchion under well-controlled ideal impact conditions. Based on full-scale simulations, reasonable C-channel stanchion designs are seen to dissipate approximately one-third of the overall impact energy, as seen in Figure 13. The exact degree of energy dissipation will depend on the stanchion design features and layups.

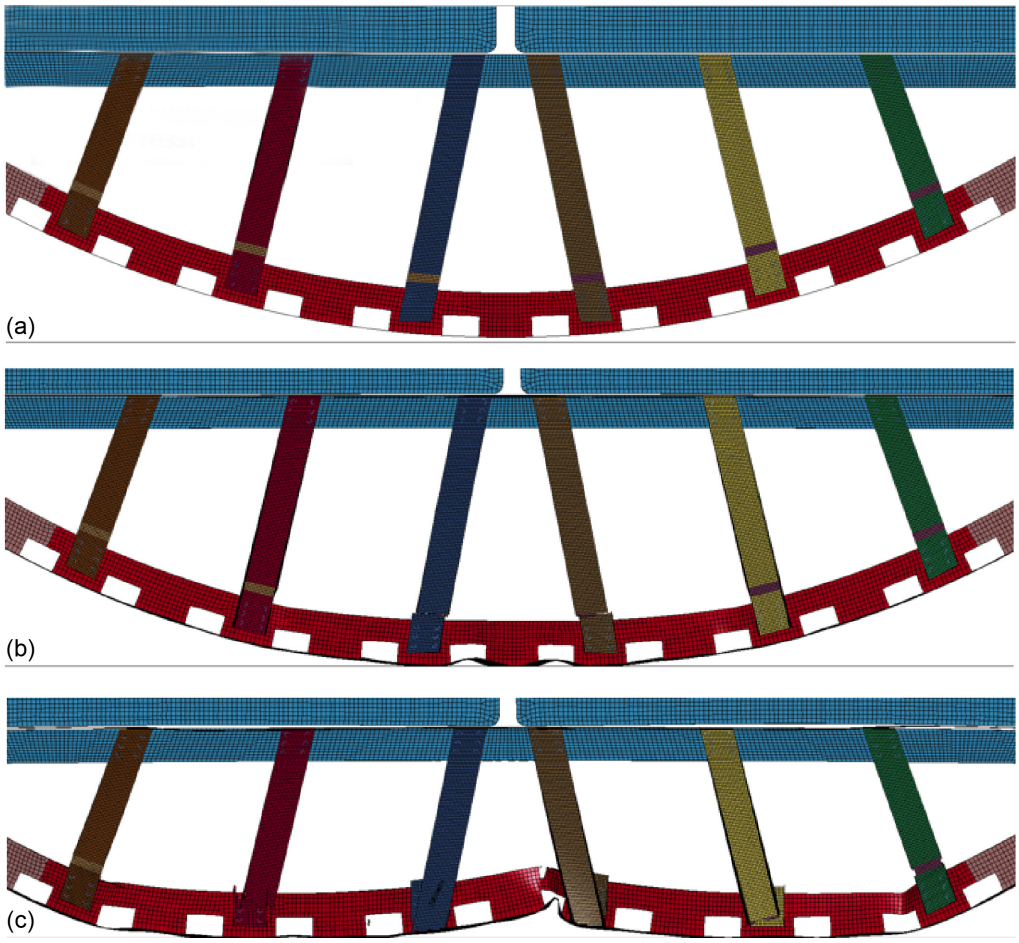

Figure 10.—Failure initiation and crush of lower-lobe cargo stanchions and lower frame sections. (a) Failure triggering. (b) and (c) Progressive crushing.

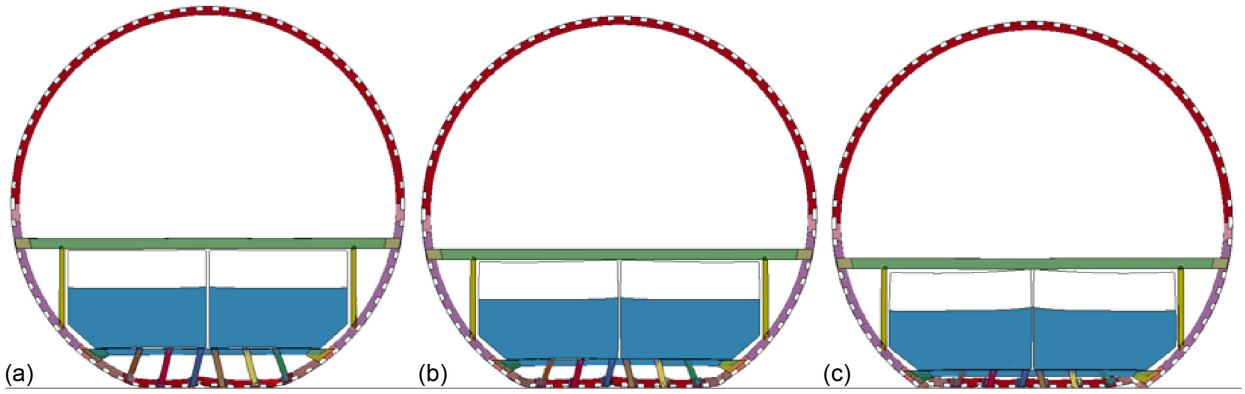

Figure 11.—Response of lower lobe during full-scale impact simulation. (a) Time = 0.025 ms. (b) Time = 0.050 ms. (c) Time = 0.075 ms.

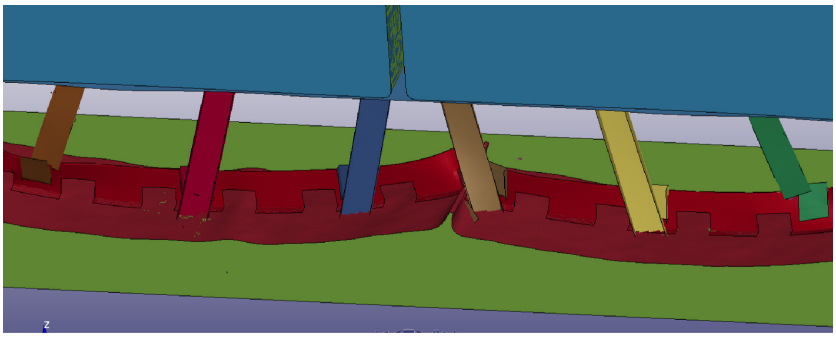

Figure 12.—Typical cargo stanchion crushing against skin after initiation.

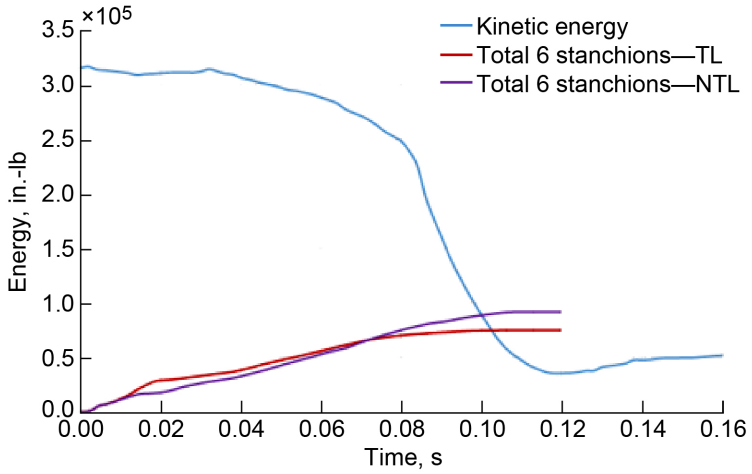

Figure 13.—Energy dissipation by cargo stanchion. Traditional laminate, TL; nontraditional laminate, NTL.

3.0 Numerical Round Robin 1 and 2: Results and Discussion

In RR–1 and RR–2, two material models, MAT54 and MAT58 in LS–DYNA®, were evaluated along with PAM–CRASH (ESI Group) for crush simulation of composite energy absorbers. The objective was to assess the predictive capabilities of these models for crush energy absorption. The simulations were compared with experimental results by comparing values of energy absorbed (EA), SEA, and load–displacement behavior. Here and throughout the report, units of measure are typically given as originally reported.

3.1 LS–DYNA® MAT54 Crush Model

This section describes the numerical models developed at the University of Washington using the LS–DYNA® MAT54 material model for crush simulation of composite energy absorbers defined in CMH–17 CWG RR–1 and RR–2. Crush simulation results are presented for the sinusoid specimen (RR–1) and for the small and large angle, small and large C-channel, and square tube specimens (RR–2). An in-depth parametric study of the MAT54 input parameters revealed that these crush models have a critical sensitivity to the MAT54 SOFT parameter, a crush-front damage knockdown factor. This parameter must be adjusted for each crush geometry to successfully match experimental data while all other parameters remain constant. The correct SOFT value cannot be determined without experimental data, and as such, the LS–DYNA® MAT54 crush simulations were empirically based, not predictive.

The MAT54 progressive failure material model works with shell elements to model orthotropic materials such as unidirectional tape composite laminates. In the elastic region, basic orthotropic stress–strain relations from Hashin (Ref. 7) were used. Prior to erosion, plies and elements failed in one of four modes defined by the stress-based Chang–Chang failure criteria (Refs. 8 and 9). Failure modes are defined in terms of "fiber" and "matrix," which corresponds to the 0° and 90° directions of a unidirectional lamina, not to the constituents. Tension and compression failure is defined for both modes. Detailed discussion of the MAT54 constitutive material models is presented in Appendix B along with MAT54 material cards showing input parameters.

3.1.1 Finite Element Model Description

The composite crush specimens in the CMH–17 crashworthiness exercise used the Toray® T700/2510 carbon fiber/epoxy plain weave fabric prepreg material system with a $[0/90]_{4S}$ layup and an average cured thickness of 0.073 in. (1.85 mm). A 45° single chamfer at the crush front acted as a trigger for crush initiation. This trigger was modeled by reducing the thickness of the first row of elements at the crush front. For each different specimen geometry, the trigger thickness was adjusted to capture the correct initial peak load by using a linear relationship between the required trigger thickness reduction and the property reduction of damaged crush-front elements as determined by the SOFT parameter. This process will be shown in Section 3.1.3.

The composite laminate was modeled using 0.1- by 0.1-in. (2.5- by 2.5-mm) fully integrated linear shell elements with eight integration points through the thickness to simulate the eight-ply laminate. Each ply was given the material properties of the fabric material system and defined to be oriented in the 0-direction. A damping coefficient of 0.05 was used for the composite part. The loading plate was modeled as a single-shell element perpendicular to the crush front with a rigid steel material model. The built-in LS–DYNA® contact model *RIGID_NODES_TO_RIGID_BODY was used to define the contact behavior between the loading plate and the composite crush specimen. This is a standard penalty formulation contact that requires input of a load–penetration (LP) curve to define the reaction normal forces applied to nodes at the contact interface. Each modeled specimen was kept at rest by constraining all degrees of freedom (DOFs) on the bottom row of nodes opposite the crush trigger. Each node of the loading plate was constrained in all DOFs except in the axial translation direction of the crush. A full description of the modeling contact and boundary conditions is given in Section B.2.2 and B.2.3.

3.1.1.1 Mesh Size and Sensitivity

Because explicit FE analysis tools are known to be particularly mesh sensitive, the RR–1 sinusoid specimen was modeled using different mesh sizes. Increasing the mesh size from 0.1 in. (2.54 mm) to 0.2 in. (5.08 mm) presented problems, as the linear shell element cannot bend through the thickness to capture the curvature of the sinusoidal geometry. Furthermore, stable crush behavior was not achieved due to the large spacing between elements. Using a smaller mesh size, 0.05 in. (1.27 mm), it was possible to achieve acceptable SEA and crush behavior results; however, the contact LP curve had to be modified to do so. The simulation using the 0.05-in. mesh took over 4.5 times longer to complete. To save computational cost and avoid trial-and-error modification of the LP curves, only the baseline mesh size was used for the RR–2 crush simulations.

The simulations were run using the LS–DYNA® 971 R5.1.1 double-precision solver on a 2.27-GHz dual quad-core 64-bit computer. The average simulation time for displacing 1.45 in. (36.8 mm) of the sinusoidal (RR–1) crush specimen was 288 s (4:48 min). As is common practice with crash simulation, a low-pass digital filter (SAE 600 Hz) was applied to the load–displacement data during postprocessing.

3.1.2 Description of Crush Test Coupons

The six coupon geometries simulated are shown in Figure 14 to Figure 16. Figure 14 shows the modeled coupon shapes. Figure 15 defines the cross-sectional geometry of the first five coupons as defined by the CWG, including section lengths and radii. Figure 16 shows the cross-sectional geometry of the sinusoid coupon, which is based on repeated semicircular sections with short end-tabs.

The material used was Toray® T700/2510. The properties established for use in all simulations are defined in Section B.2.3 (Table B.4).

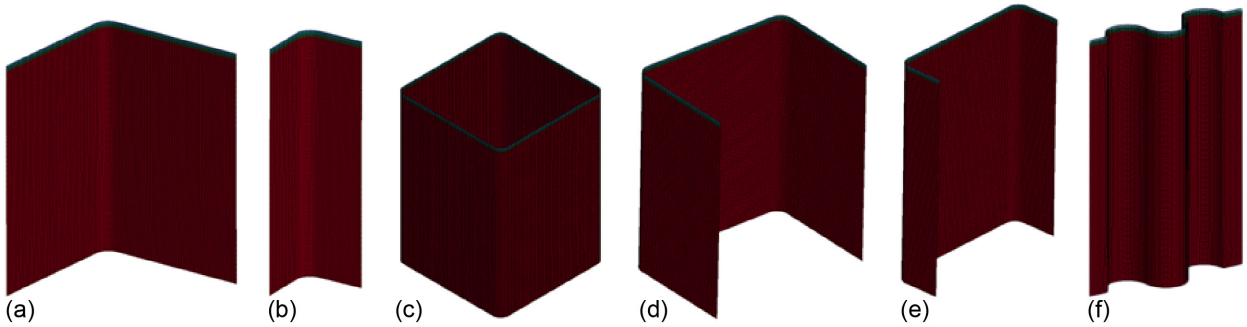

Figure 14.—Models of coupons used in testing. (a) Large angle. (b) Small angle. (c) Square tube. (d) Large C-channel. (e) Small C-channel. (f) Sinusoid.

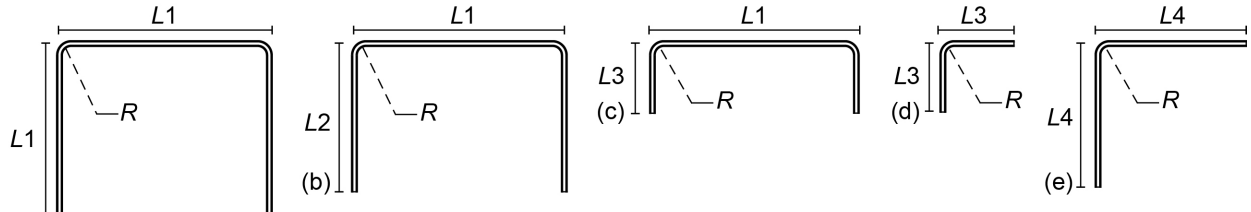

Parameter	Value
*L*1	2.500 in. (63.5 mm)
*L*2	1.750 in. (44.5 mm)
*L*3	0.750 in. (19.0 mm)
*L*4	2.000 in. (50.8 mm)
R	0.175 in. (4.45 mm)
t	0.065 in. (1.65 mm)

Figure 15.—Cross-sectional views of tube, angle, and C-channel coupon geometries and dimensions. (a) Square tube. (b) Large C-channel. (c) Small C-channel. (d) Small angle. (e) Large angle.

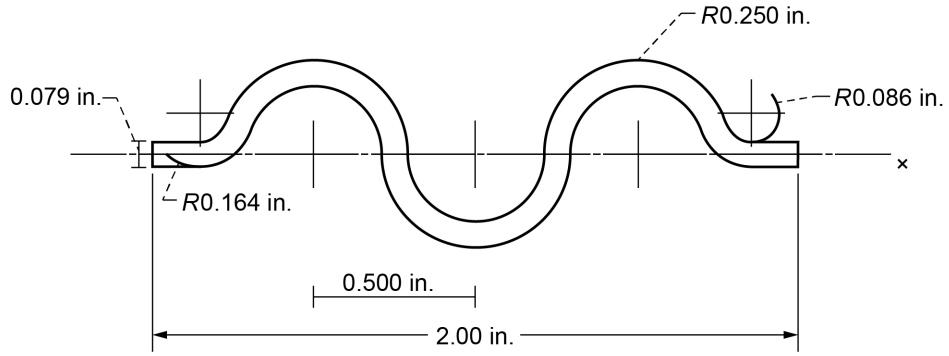

Figure 16.—Cross-sectional view of sinusoid coupon geometry and dimensions.

3.1.3 Crush Simulation Results

Simulation results for the RR–1 sinusoid crush specimen and the RR–2 tubular crush specimens are given in Sections 3.1.3.1 and 3.1.3.2, respectively.

3.1.3.1 Round Robin 1: Sinusoid Crush Specimen

Given the measured material properties of the T700/2510 material system, very few changes were made to produce a working LS–DYNA® crush simulation that matched the sinusoid crush experiment well. To improve stability and prevent premature element deletion, the transverse failure strain, DFAILM, was increased from its measured material value of 0.014 to 0.038 in./in. Adjustments of the MAT54 SOFT parameter directly affected the average crush load of the simulation, and changing the thickness of the trigger elements altered the initial peak load. Both of these parameters were adjusted such that the simulation data matched that of the experiment.

The simulated crush progression of the sinusoid crush specimen is shown in Figure 17. In MAT54, elements are removed from the simulation after achieving a maximum strain value; therefore, the physical crush morphology of the simulation is of little interest. The unfiltered and filtered simulated load–displacement data for the sinusoid crush specimen is shown in Figure 18. Figure 19 compares force–displacement results between the filtered crush simulation and the experiment.

The initial delay in the simulated load is caused by the contact LP curve, which was chosen to be conservative (non-stiff) to provide maximum stability at the contact interface. This delay is also noted in the EA, and more prominently in the SEA trends, shown in Figure 20 and Figure 21, respectively. The final EA and Total SEA values, however, match that of the experiment. Although this delay is undesirable, the conservative LP curve was found to be necessary to maintain the stability of some crush structures.

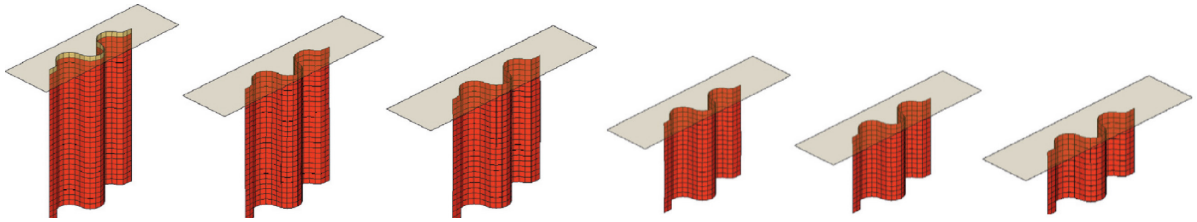

Figure 17.—Simulated crush morphology of sinusoid specimen.

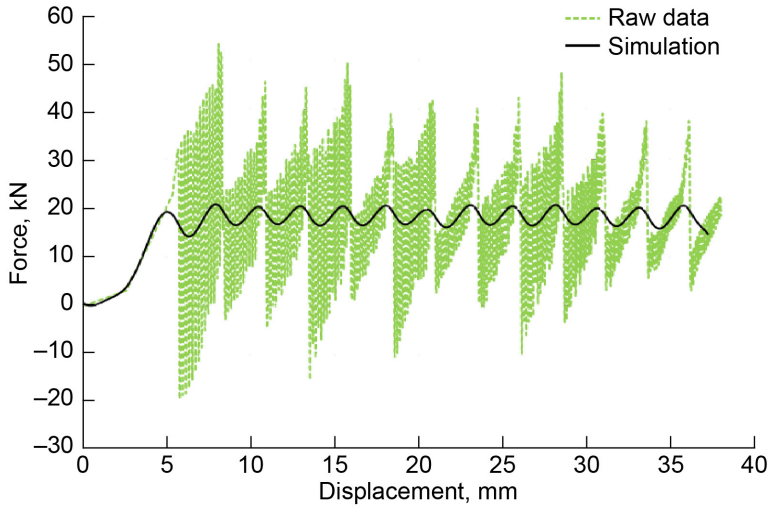

Figure 18.—Raw and filtered force–displacement data from sinusoid crush simulation.

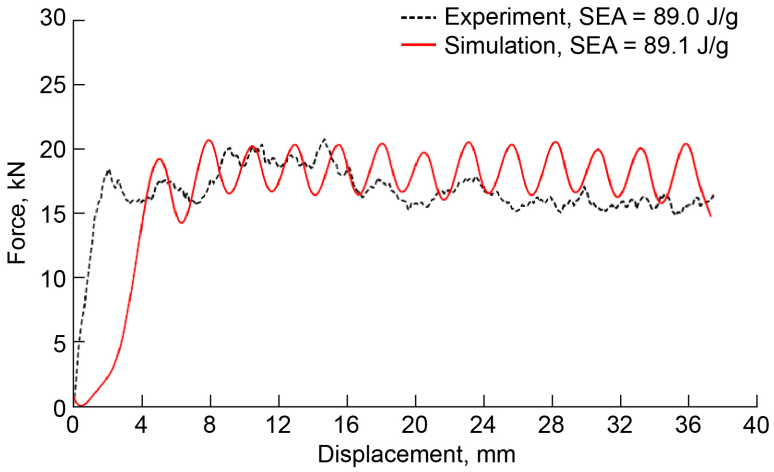

Figure 19.—Simulated and experimental force–displacement results for sinusoid crush specimen.

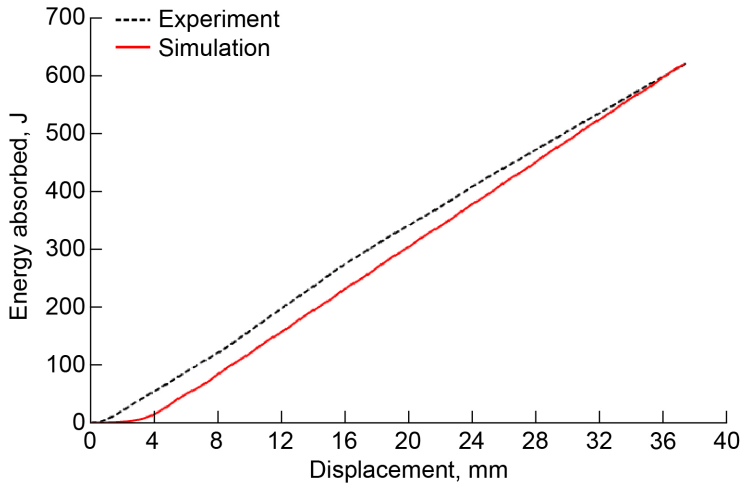

Figure 20.—Simulated and experimental energy absorption results for sinusoid crush specimen.

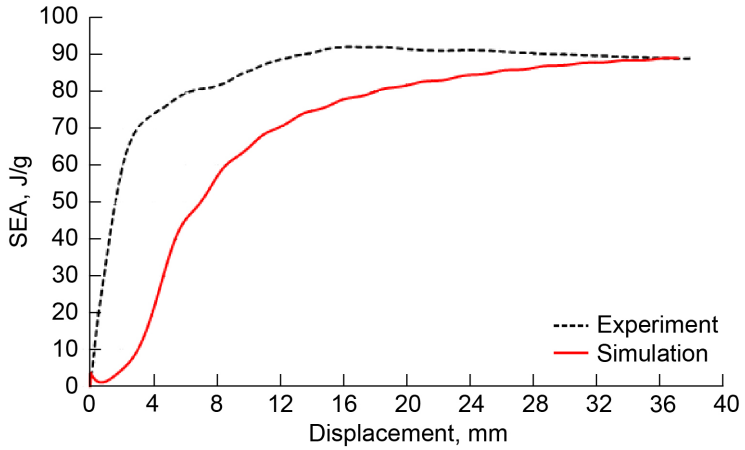

Figure 21.—Simulated and experimental SEA results for sinusoid crush specimen.

3.1.3.2 Round Robin 2: Tubular Crush Specimens

To model the other crush geometries, only the SOFT parameter and the crush trigger thickness were varied and calibrated to match the experimental results. All other MAT54 and LS–DYNA® parameters were kept constant throughout the six RR–2 crush specimen simulations.

Crush morphology images, load–displacement curves, and SEA values are given for the square tube in Figure 22 for a typical result and for the remaining four RR–2 crush simulations in Section B.2.4 (Figure B.7 to Figure B.10). Stability was observed in all simulations. The final Total SEA results from the six RR crush geometries are given in Table 1. The SOFT parameter and trigger thickness, which were the only parameters changed between the six crush geometry simulations, are also given in Table 1.

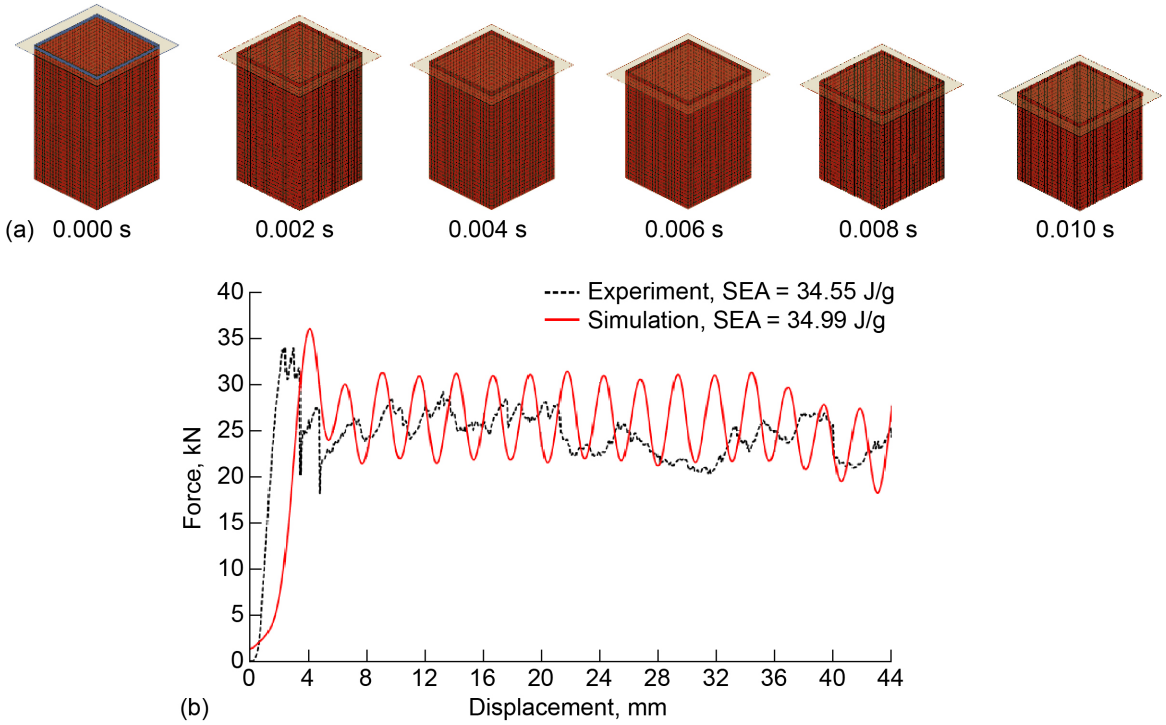

Figure 22.—RR–2 results for square tube crush specimen. (a) Crush morphology images. (b) Simulated and experimental force–displacement results.

TABLE 1.—FINAL EA, TOTAL SEA, AND ERROR RESULTS WITH CHANGED PARAMETER VALUES FROM RR–1 AND RR–2 CRUSH SIMULATIONS

Specimen	EA, J		SEA, J/g		SEA, % error	SOFT	t_{trig}, in.
	Exp.	Sim.	Exp.	Sim.			
Sinusoid	617.5	612.6	88.96	88.16	–0.9	0.600	0.050
Square tube	778.9	780.0	30.83	30.87	0.1	0.085	0.010
Large C-channel	643.0	566.5	28.93	27.69	–4.3	0.210	0.020
Small C-channel	607.0	608.1	44.49	44.18	–0.7	0.235	0.025
Large angle	487.9	478.7	33.71	32.84	2.6	0.210	0.020
Small angle	192.4	180.5	62.11	58.29	–6.2	0.310	0.030

3.1.4 Simulation Success Criteria

As noted in Sections 1.2.1 and 1.2.2, four success criteria have been defined by the CMH–17 CWG to describe specific aspects of the resulting load–displacement crush curve: initial peak load, initial slope, sustained crush load, and the resulting Total SEA. These criteria were used to evaluate the success of the LS–DYNA® MAT54 model in simulating the crush experiment by calculating the error of the analysis value relative to the value measured by the crush experiment. Relative error values within 10 percent rate the criteria as having excellent correlation with the experiment; within 20 percent is good, within 30 percent is fair, and above 30 percent is considered poor. The experimentally measured and simulated values for the four success criteria are given in Table 2 along with the relative error values.

The relative error of the initial peak load, sustained crush load, and Total SEA for all of the RR–1 and RR–2 geometries were each less than 10 percent, corresponding to excellent correlation with the experiment. In particular, the relative error of the calculated Total SEA was less than 2 percent for all cases, because SEA was used as the metric by which the MAT54 SOFT parameter was calibrated such that the simulation matched the experiment well. The relative error of the initial slope, however, was very high, resulting in a poor correlation between simulation and experiment for this success criterion. This is a consequence of applying the SAE 600 Hz filter to the analysis data, which causes an artificial non-zero initial load, as well as the contact definition between the loading plate and the MAT54 elements, which greatly influences the initial slope and initial peak load. The relative errors of the four success criteria are plotted in Figure 23 for each crush geometry. The ranking of the model correlation to the experiment, as given by the four success criteria, is also shown in this plot.

TABLE 2.—SUCCESS CRITERIA RESULT FOR LS–DYNA® MAT54 CRUSH MODEL

Specimen	Experiment/ simulation	Initial slope, kN/mm	Error, %	Initial peak load, kN	Error, %	Sustained crush load, kN	Error %	SEA, J/g	Error, %
Sinusoid	Experiment	10.40	–60	18.43	4	16.90	8	89.0	0.1
	Simulation	4.20		19.21		18.31		89.1	
Square tube	Experiment	19.60	–55	34.05	6	24.48	8	34.6	1.3
	Simulation	8.84		36.04		26.34		35.0	
Large C-channel	Experiment	12.31	–62	18.78	–6	12.57	–6	28.9	–2.1
	Simulation	4.63		17.63		11.78		28.3	
Small C-channel	Experiment	5.83	–36	14.61	1	10.53	–2	43.0	–1.0
	Simulation	3.76		14.76		10.27		42.5	
Large angle	Experiment	12.44	–69	14.42	3	9.95	5	33.7	1.8
	Simulation	3.86		14.86		10.43		34.3	
Small angle	Experiment	2.36	–39	5.82	6	4.75	4	62.1	0.5
	Simulation	1.43		6.19		4.94		62.4	
Overall grade		Poor		Excellent		Excellent		Excellent	

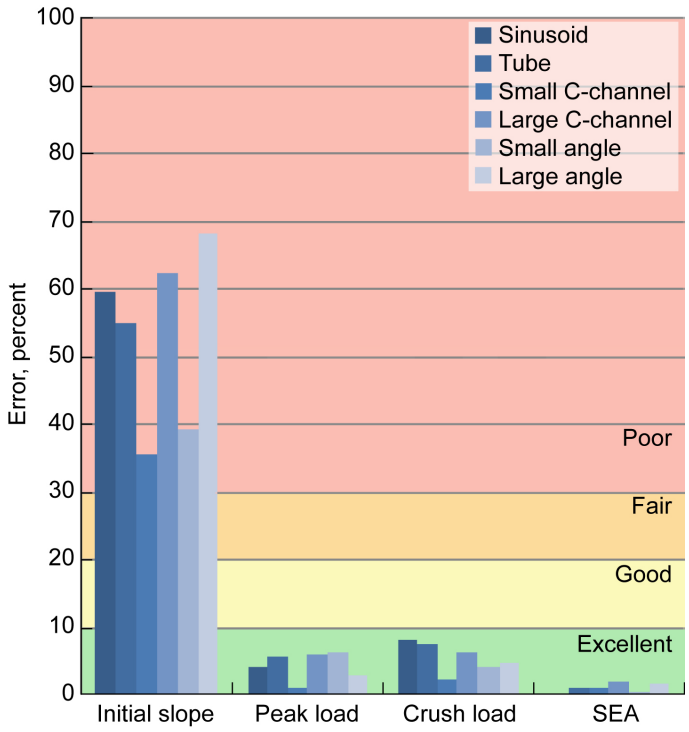

Figure 23.—Relative error of simulation versus experiment for four success criteria and their rankings.

3.1.5 Key Findings and Lessons Learned

The simulations of the six RR specimens revealed the sensitivity of the crush model to the MAT54 SOFT parameter, trigger element thickness, and contact LP curve. Additionally, a parametric study of all MAT54 input parameters revealed the sensitivity of the crush model to the fiber compressive strength, XC, and the fiber compressive failure strain, DFAILC, while all other parameters produced insignificant changes.

3.1.5.1 MAT54 SOFT Parameter

The SOFT parameter is the most critical and influential parameter in the MAT54 material model for crush simulation. By itself, it was capable of dictating whether a simulation was stable or unstable, and it also could shift the average crush load above or below the baseline value by more than 20 percent. The results from changing the SOFT parameter on the RR–1 sinusoid are shown in Figure 24. Increasing SOFT to 0.8 meant that the material ahead of the crush front maintained 80 percent of its strength during crush; this was too stiff, and the model buckled globally, as shown in Figure 24. Decreasing SOFT to 0.3 maintained 30 percent of the crush material strength, which dropped the crush load significantly as elements failed at lower loads. The Total SEA of the lowered SOFT simulation was 40 percent less than that of the baseline simulation.

For each crush geometry, it was necessary to calibrate the SOFT parameter until the numerical results matched the experimental results, meaning the MAT54 material model cannot predict crush behavior without experimental data. Furthermore, calibration of a crush simulation is geometry dependent such that the same material card cannot be used for two different geometries without changing the SOFT parameter.

Plotting the average experimental SEA of each crush geometry versus the calibrated SOFT value reveals a linear trend, shown in Figure 25. This figure includes two alternative sinusoidal crush geometries that were not part of the RR exercise. The linear trend indicates that as the SEA of a crush

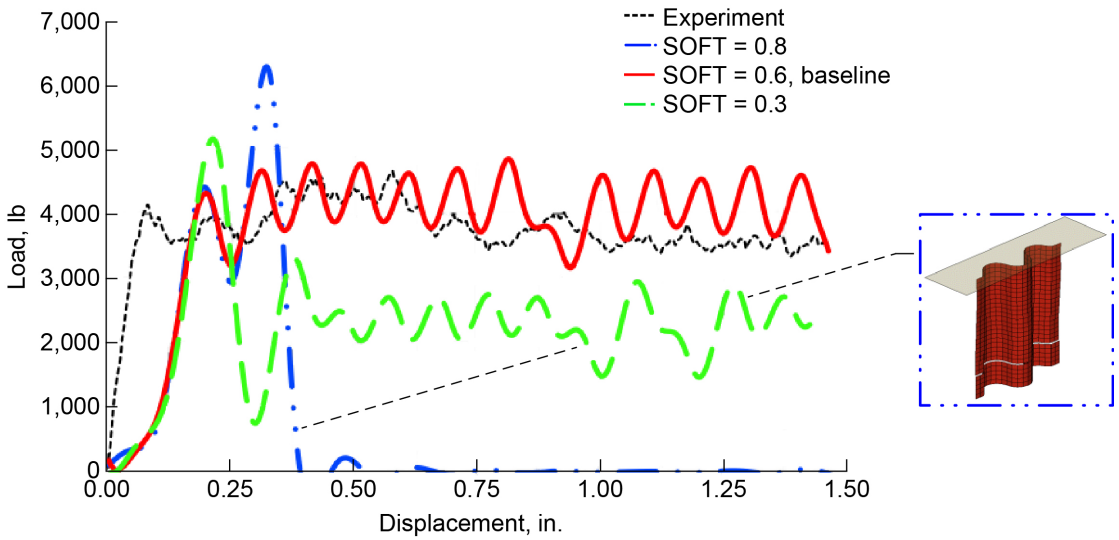

Figure 24.—Load–displacement results from changing SOFT parameter on RR–1 specimen.

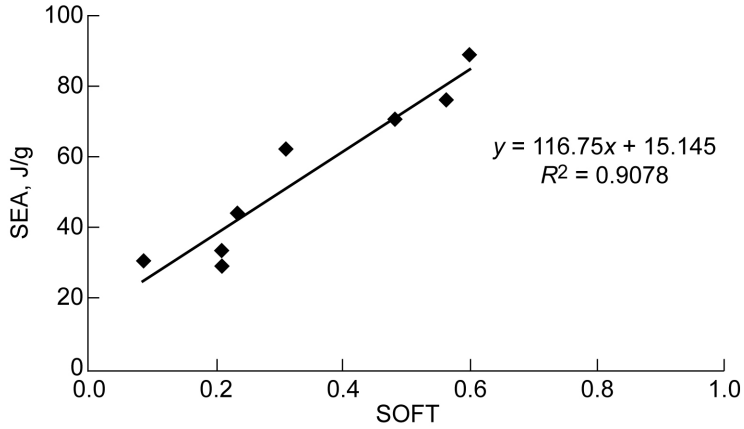

Figure 25.—Linear relationship between SOFT and SEA.

specimen increases, so does the strength of the damaged elements (as determined by the SOFT parameter). The linear trend can be used to approximate a value for SOFT; however, trial-and-error adjustments have to be made to find the precise SOFT value that best matches the experimental data.

3.1.5.2 Crush Trigger Element Thickness

The thickness of the trigger elements directly influences the value of the initial peak load such that the thickness must be changed to better match experimental data for each crush geometry. The trigger thickness that yields the best results can be determined by the calibrated SOFT parameter. It is important to note that the SOFT parameter does not apply a property reduction to the trigger elements; they form the initial row of elements and are therefore never behind the crush front. By reducing the thickness of the trigger elements, the amount of load these elements can sustain before failing is lowered, as if the SOFT parameter had applied a damaging effect. Plotting the percent thickness reduction of the trigger elements versus the calibrated SOFT value reveals a linear trend, shown in Figure 26, which can be used to determine the appropriate trigger thickness. Figure 26 shows that reducing trigger thickness by the value given by the percentage of SOFT damage reduction plus 7 percent produces the best results.

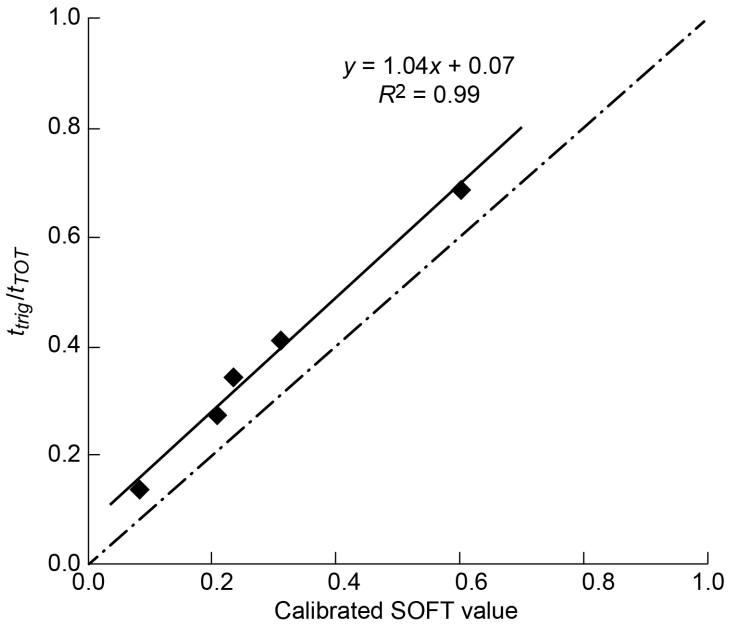

Figure 26.—Linear trend of trigger element thickness reduction (t_{trig}/t_{TOT}) with SOFT parameter.

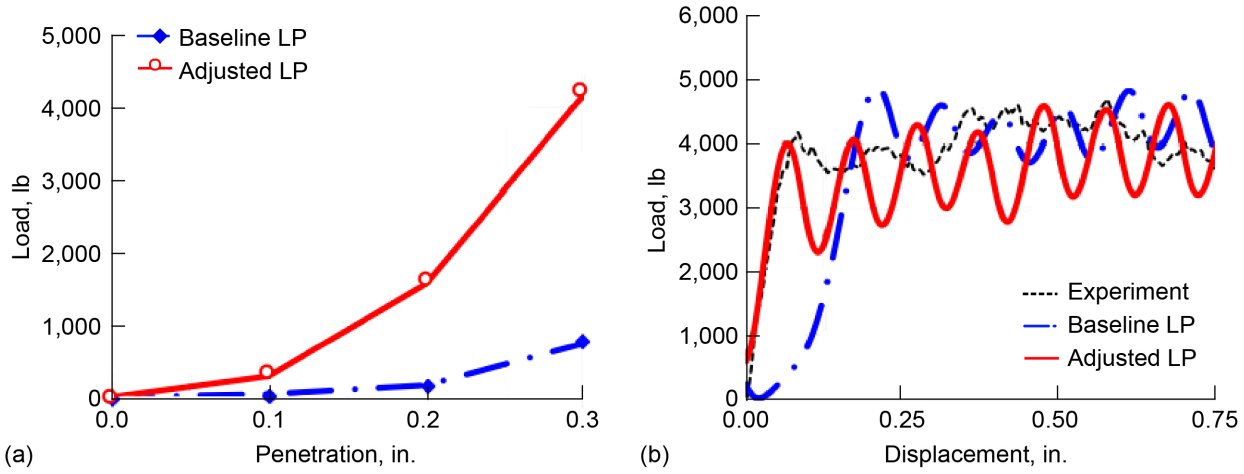

Figure 27.—Load–penetration (LP) and load–displacement curves for RR–1 sinusoid crush specimen. (a) Baseline and adjusted LP curves. (b) Initial slope results.

3.1.5.3 Contact Load–Penetration Curve

The LP curve is a piecewise linear curve in the contact definition that greatly influences the initial slope and overall stability of the crush simulations. The baseline curve chosen for the crush simulations is a low-energy curve with low reaction forces imposed at the contact interface. This causes the initial slope to be inaccurate, as load is applied on the trigger elements much more gradually than observed in the experimental data. It is possible to obtain better results for each of the six geometries by changing the stiffness of the LP curve. The high-SEA, stable-crush geometries can absorb a more aggressive load ramp. An example of this is shown for the case of the RR–1 sinusoid crush specimen. The LP curves implemented for the baseline and adjusted simulations are shown in Figure 27 along with the resulting crush load–displacement curves. This adjusted LP curve input works well for the RR–1 sinusoid crush simulation; however, it yields unstable buckling when used as an input for the RR–2 crush specimens.

Although it is possible to tailor each LP curve for each simulation to obtain results that better match the initial peak load of the experimental data, predicting the best LP curve prior to comparison against test data is not possible. For this reason, a conservative LP curve that works for all geometries, namely, the baseline LP, was used in the RR exercises.

3.1.5.4 MAT54 Fiber Compression Parameters

Varying the MAT54 fiber compression strength, XC, and failure strain, DFAILC, significantly altered the SEA value and load–displacement curve. Sensitivity studies for these parameters were conducted on the RR–1 sinusoidal specimen.

Changing XC produced stable results until an upper limit of 130 ksi, with larger values shifting the load–displacement curve to higher loads, as shown in Figure 28. The Total SEA at this upper limit had increased by 15 percent above the baseline simulation. Beyond 130 ksi, the simulation experienced global buckling. Variations of DFAILC also produced shifted load–displacement curves to a stable lower limit of –0.011, as shown in Figure 29. Higher values of DFAILC increased the crush load, causing a SEA increase of 30 percent from the baseline simulation using a DFAILC value of –0.05, and values lower than –0.011 caused global buckling.

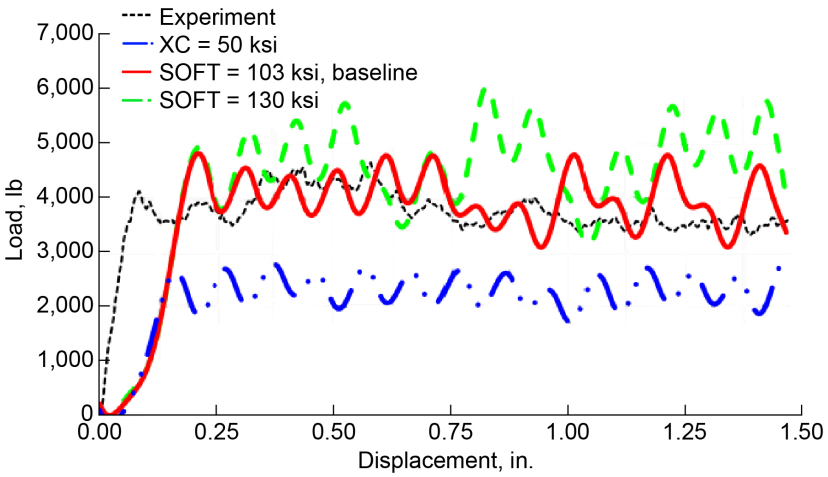

Figure 28.—Sensitivity study results on MAT54 XC parameter.

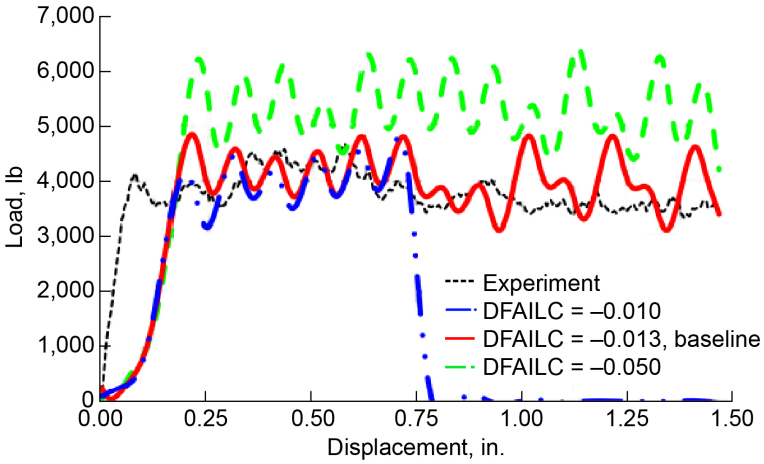

Figure 29.—Sensitivity study results on MAT54 DFAILC parameter.

3.2 LS–DYNA® MAT58 Crush Model

LS–DYNA® was used to perform simulations of coupon crush response with six different coupons. The simulations employed shell elements with MAT58 and established a single set of material and progressive failure parameters that show reasonable response for all coupons. A comparison of simulation and test data for all coupons shows generally excellent to good correlation, with the exception of the initial load–displacement slope. This discrepancy is likely due to (1) a lack of sufficient detail in modeling the trigger zone of the test article and (2) the sensitivity of results to small variations in the initial displacement needed to trigger crush. Overall, however, the results show that this simulation approach accurately predicts SEA and is reasonable for use in predicting crush response at the coupon level. Section 3.2.1 presents a description of the simulation approach, both a summary and detailed comparisons of test and simulation results. Key material parameters influencing crush response are also noted. (A complete list of MAT58 material card parameters used in all simulations is provided in Table B.5 in Section B.3.1.) MAT58 employs several parameters relating to progressive failure, as will be noted in the following section.

3.2.1 Description of Simulation

All test coupons described in Section 3.1.2 were modeled with shell elements, and the platen that forces crushing failure was modeled with solid elements. The platen was represented as elastic, using typical properties for steel. Contact between the platen and each coupon was defined as *CONTACT_ERODING_SINGLE_SURFACE with all parts included. A contact friction coefficient of 0.3 was used for both static and dynamic friction, and default values were used for all contact options. The crush pulse was performed using enforced displacement of the platen. The crush speed was artificially increased for use with the explicit solver and was set to 3.81 m/s. Figure 30 shows the platen with coupon boundary conditions. The shell elements were modeled as type 16, which is a fully integrated element formulation. Hourglass type 8 with a value of 0.1 was used for these elements.

The simulation used two rows of trigger elements with reduced thickness to approximately represent the physical trigger. The first trigger section was 2 plies thick, and the second trigger section was 4 plies thick. As soon as a trigger element was deleted, the SOFT parameter was applied to adjacent elements. (SOFT is the crush-front parameter that specifies the reduction in element strength when an adjacent element has been eroded.) The rows of trigger elements are seen in Figure 31. The response of these trigger elements early in the simulation is shown in Figure 32, where multiple elements have been deleted. The element length was 0.508 mm (0.002 in.), so that each trigger section was 1.016 mm (0.04 in.) high, for a combined trigger zone height of 2.032 mm (0.08 in.).

The MAT58 parameters used in all simulations are provided in Section B.3.1 (Table B.5). The SLIM factors were adjusted to reduce strength by 80 percent after initial tensile failure, and to reduce strength by 20 percent after initial compressive failure. Final element erosion is set by ERODS, which is the strain at which the element is deleted. The SOFT and ERODS parameters were initially based on previous crush simulation experience with a different material system and were then adjusted to provide a best fit with the current test data. The same parameters were used in all six simulations presented in this study.

Figure 33 illustrates the effect of the SLIM factors on residual strength after initial failure. The element will carry a reduced stress until it reaches the failure strain specified by ERODS, at which point the element is deleted.

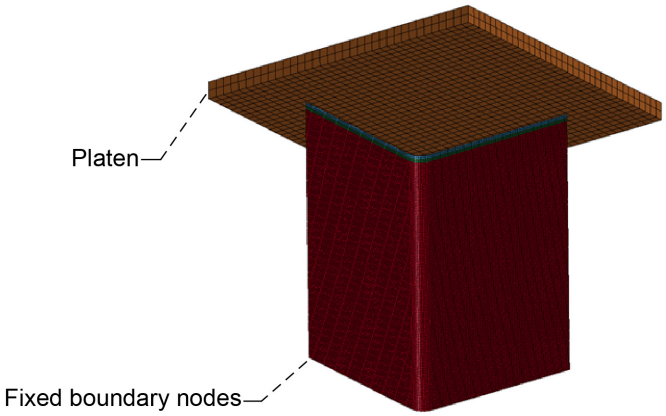

Figure 30.—Typical simulation approach with platen and fixed nodes.

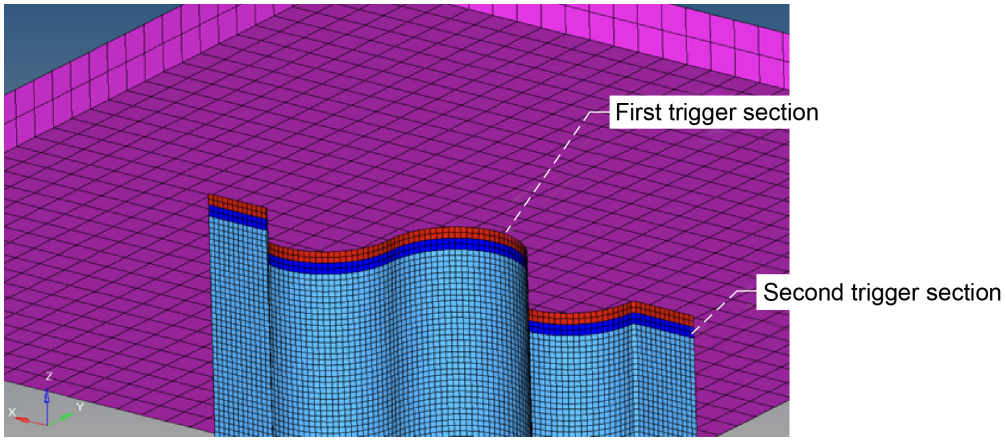

Figure 31.—Simulation of trigger with two sections of reduced thicknesses.

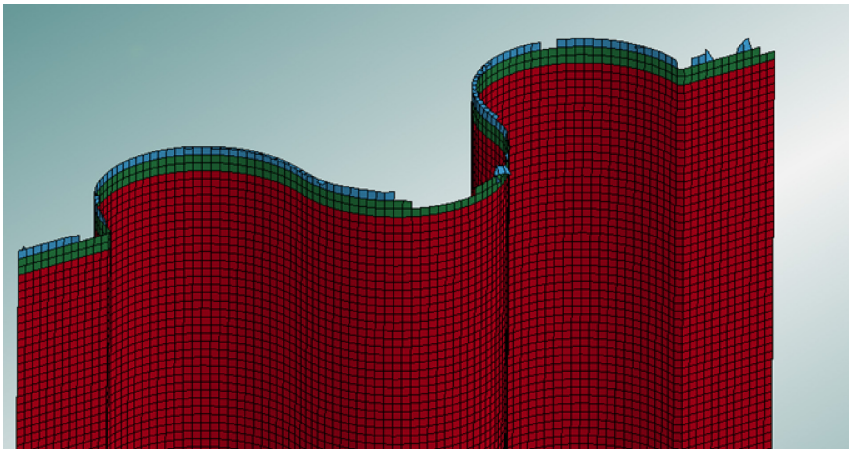

Figure 32.—Initial crush of trigger elements in reduced-thickness sections with SOFT parameter applied.

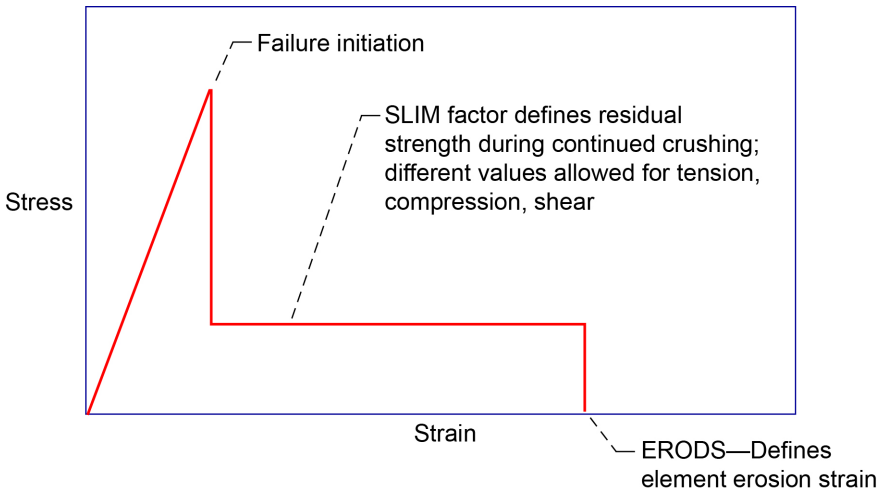

Figure 33.—General approach to progressive damage simulation with MAT58.

TABLE 3.—COMPARISON OF TEST AND ANALYSIS FOR ENERGY ABSORPTION

	Simulation EA, kJ	Test EA, kJ	Simulation energy/weight, J/g	Test energy/weight, J/g	Percentage difference
Large C-channel	625.8	643.0	28.15	28.93	2.7
Small C-channel	527.3	607.0	38.65	44.49	13.1
Large angle	533.4	487.9	36.85	33.71	9.3
Small angle	186.8	192.4	60.30	62.11	2.9
Square tube	1,090.8	1,219.7	27.57	30.83	10.6
Sinusoid	554.5	617.5	79.88	88.96	10.2

3.2.2 Summary of Test and Simulation Results for All Coupons

Results for the six simulations are presented in comparison with test data. The initial comparison was focused on predicting energy absorption, which is a function of crush load and displacement. Results in Table 3 show that all simulation results are within 15 percent of test values for Total SEA. A rough overall estimate of the simulation response may be made by taking an average of the six percentage error values, which leads to an overall average error of 8.1 percent. In general, the simulation results compare well with test values for energy absorption.

One possible use of crush simulations would be to evaluate and rank the effectiveness of competing design configurations with respect to SEA. Table 4 shows how the six coupon configurations would be ranked by test and by simulation. The rankings are identical for the first four coupons, whereas the last two coupons are reversed. The final two coupons, however, both have low SEA and are very similar in value in both simulation and test. The comparison of ranking ability in Table 4 shows that the simulation may be effectively used to rank composite coupons with respect to SEA from high to low, and to compare relative performance.

Four specific success criteria of initial peak load, initial slope, sustained crush load, and SEA, with their ranking, were established by the CWG to evaluate the overall effectiveness of each simulation methodology. The results for all four success criteria categories for all six simulations are presented in Table 5.

Table 6 summarizes the overall results by category and ranking, showing that of the 24 rankings (6 coupons with 4 categories each), 10 are excellent, 7 are good, 1 is fair, and 6 are poor. All of the poor rankings occur with respect to the initial slope, which will be discussed in the next section.

TABLE 4.—COMPARISON OF TEST AND ANALYSIS
RANKING OF COUPONS BASED ON SEA

	Simulation ranking	Simulation energy/weight, J/g	Test ranking	Test energy/weight, J/g
1	Sinusoid	79.88	Sinusoid	88.96
2	Small angle	60.30	Small angle	62.11
3	Small C-channel	38.65	Small C-channel	44.49
4	Large angle	36.85	Large angle	33.71
5	Large C-channel	28.15	Square tube	30.83
6	Square tube	27.57	Large C-channel	28.93

TABLE 5.—COMPARISON OF TEST AND ANALYSIS BASED ON CWG SUCCESS CRITERIA

Configuration	Parameter	Test value	Simulation value	Percent difference	Assessment
Sinusoid	Initial peak, kN	17.90	18.03	0.7	Excellent
	Initial slope, kN/mm	9.42	5.31	43.6	Poor
	Sustained crush load, kN	16.50	14.38	12.8	Good
	SEA, J/g	88.96	79.88	10.2	Good
Small angle	Initial peak, kN	5.62	5.83	3.7	Excellent
	Initial slope, kN/mm	2.04	4.78	134.3	Poor
	Sustained crush load, kN	4.61	4.46	3.3	Excellent
	SEA, J/g	62.11	60.30	2.9	Excellent
Small C-channel	Initial peak, kN	14.61	10.37	29.0	Fair
	Initial slope, kN/mm	5.31	9.33	75.7	Poor
	Sustained crush load, kN	10.36	8.90	14.1	Good
	SEA, J/g	44.49	38.65	13.1	Good
Large angle	Initial peak, kN	14.42	15.48	7.4	Excellent
	Initial slope, kN/mm	8.74	5.07	42.0	Poor
	Sustained crush load, kN	9.81	10.43	6.3	Excellent
	SEA, J/g	33.71	36.85	9.3	Excellent
Square tube	Initial peak, kN	34.05	30.55	10.3	Good
	Initial slope, kN/mm	14.61	6.54	55.2	Poor
	Sustained crush load, kN	24.36	21.80	10.5	Good
	SEA, J/g	30.83	27.57	10.6	Good
Large C-channel	Initial peak, kN	18.78	18.24	2.9	Excellent
	Initial slope, kN/mm	14.44	19.00	31.6	Poor
	Sustained crush load, kN	12.43	11.95	3.9	Excellent
	SEA, J/g	28.93	28.15	2.7	Excellent

TABLE 6.—RESULTS OF SIMULATION USING SUCCESS
CRITERIA SHOWN BY EVALUATION CATEGORY

	Excellent	Good	Fair	Poor
Initial peak	4	1	1	--
Initial slope	--	--	--	6
Average crush	3	3	--	--
Specific energy	3	3	--	--

3.2.3 Comparison of Experiment and Simulation Results

Simulation and test results for the large-channel specimen are shown as a typical response in Figure 34, Figure 35, and Figure 36. Results comparisons for the remaining five coupons are provided in Section B.3.2. Each comparison plots force–displacement history, showing the reaction loads during crushing, and energy absorption as a function of displacement. For each of the coupons, these two plots clearly indicate where the simulation compares well with the test response and where deviations occur. In addition, an image of each coupon during crushing shows a typical response state. Generally, the simulations show fairly uniform element deletion as crushing progresses, though there are regions where element deletion shows a notched crush front. Figure 34 shows a typical crushing failure pattern at 23 mm of crush.

Figure 34.—Typical crushing failure pattern at 23 mm of crush.

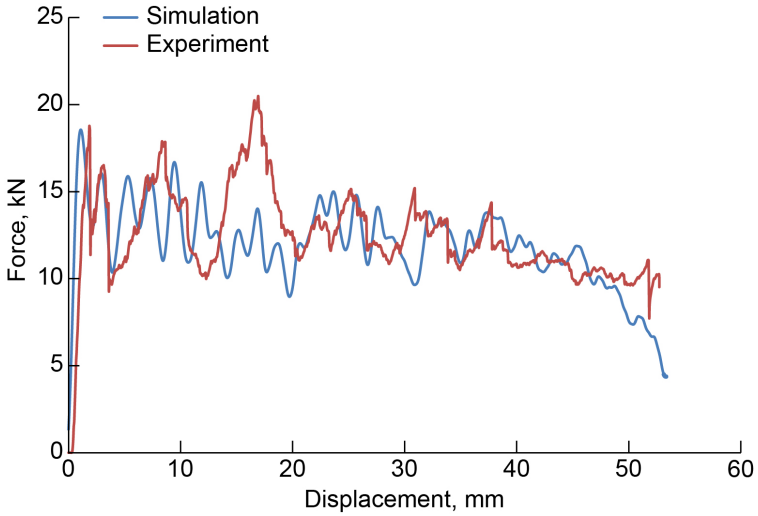

Figure 35.—Comparison of test and simulation reaction force during large C-channel crushing.

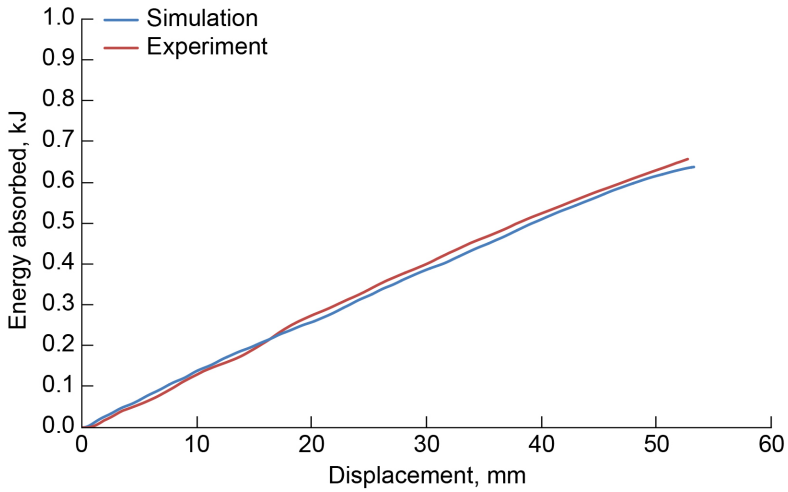

Figure 36.—Comparison of test and simulation energy absorption during large C-channel crushing.

3.2.4 LS–DYNA® MAT58 Simulation Results and Best Practices

Overall, the MAT58 simulation results provide a reasonable representation of the reaction force during crushing and the EA for each coupon.

Crushing of six different carbon composite coupon-level geometries was successfully modeled using LS–DYNA® with the MAT54 material model. Crush simulations are critically sensitive to the MAT54 crush-front damage parameter, SOFT, and this parameter can be used to calibrate the numeric results such that they match experimental data. Simulations are also sensitive to the thickness of the crush trigger elements; however, the appropriate thickness can be determined from the calibrated SOFT value. The LP curve of the contact is also influential on the initial peak load and crush stability. A conservative low-energy curve can be used to assure stable results at the cost of a delayed initial peak load in the simulation. The MAT54 crush model is not predictive; the SOFT parameter must be recalibrated against experimental data for each crush geometry.

MAT58 provides material parameters for residual strength after failure initiation and allows elements to carry a reduced load before final failure and element deletion. This is similar to the behavior observed during physical testing, where the onset of failure was followed by progressive failure and crushing rather than instantaneous failure.

Parameters within MAT58 that may influence results are the SLIM factors, which specify the residual strength, and the ERODS parameter, which specifies the final failure strain for element deletion. Also, the SOFT parameter may influence crush response, as it determines the reduction of strength for crash-front elements that occurs during progressive crushing failure.

The four success criteria identified by the CWG show that the simulation approach with MAT58 performs well in representing average crush forces, peak loads, and energy absorption during the overall crush event. However, the initial slope of the simulations did not compare well with the test data. As a rough means of evaluation, the average error for slope for the six coupons was 64 percent.

There are likely two reasons for this discrepancy in simulated and tested values for initial slope. First, the trigger region was approximated with several rows of elements intended for deletion early in the crush event. This early deletion then serves to invoke the SOFT parameter in elements beneath the trigger rows. This early deletion, however, may lead to a slight delay in simulating the rapid rise in load that occurs with the initial slope. The second point follows from this, in that the initial slope occurs over a very limited displacement distance. If the test shows the initial slope to occur over 2 mm, for example, then a 1-mm

delay in simulating the onset of the initial slope will immediately lead to a 50 percent error, even if the peak is identical. This can be seen in several cases, where the initial slope of the simulation appears similar to the experiment but is actually in significant variance. In contrast, the average error for all six initial peak loads between simulation and experiment was 9 percent, which falls overall in the “excellent” category.

These results show that MAT58 may be used successfully to simulate crushing of composite coupons in order to predict overall reaction loads and energy absorption. A set of MAT58 values and parameters was presented for use with Toray® T700/2510, and similar values could be used for other similar material systems. This simulation approach could then be used to evaluate energy absorption of other coupon geometries or of larger assemblies under impact or crush conditions.

Detailed results are included in Section B.3.2.

3.3 PAM–CRASH Model

This section describes numerical models developed at the DLR (Deutsches Zentrum für Luft- und Raumfahrt) German Aerospace Center with the commercial explicit FE code PAM–CRASH (Ref. 10) for fine-scale crush simulation of composite absorber elements, as defined in Section 3.1.2. Results are presented for the sinusoid specimen (RR–1) and for the small C-channel, corner section, and square tube specimens (RR–2). Novel stacked-shell models were developed that combine mesoscale ply damage models with cohesive interfaces to model delamination at the crush front. Materials parameters were obtained from the standard ply dataset on the Toray® T700/2510 material provided by CMH–17 to the CWG and supplemented by DLR tests to characterize ply shear nonlinearity. The same materials dataset was used for simulating the four specimens by adapting the numerical trigger used to the failure mode. Satisfactory agreement was obtained with measured steady crush forces and energy absorbed.

3.3.1 Features of PAM–CRASH Section Crush Model

The PAM–CRASH simulations used a mesoscale composite model in which the composite laminate was modeled by layered shell elements. The shells were composed of composite plies assumed to be homogeneous orthotropic elastic or elastic–plastic damaging materials whose properties are degraded by microcracking prior to ultimate failure. The mesoscale FE models were extended to include stacked-shell elements for the composite laminate connected through cohesive interfaces to model possible delaminations, as described by Johnson (Ref. 11), for modeling impact failure. This can be described as a 2.5-dimensional (2.5D) FE model, where the stacked-shell technique allows a composite laminate to split into plies or sublaminates when the cohesive interface fails, and delamination occurs. The ply properties assigned were based on the Ladevèze (Ref. 12) ply damage model for unidirectional composites with shear plasticity, which was extended to fabric plies by Johnson et al. (Ref. 13).

Failure in the ply is controlled by fiber failure strains in tension or compression, or by reaching ply shear failure as determined by the shear damage energy at failure. The cohesive interface is controlled by an interface traction-displacement law such that interface contact is broken when the interface energy dissipated reaches the mixed-mode delamination energy criteria. This contact interface is an efficient way of modeling delamination, with the advantage that the critical integration time step is relatively large since it depends on the area size of the shell elements and not on the interply thickness. The formulation of the composite ply fabric model and the cohesive interfaces for delamination as used in PAM–CRASH is provided in Section B.4.

The PAM–CRASH model uses a bilinear four-node quadrilateral isoparametric Belytschko–Tsay shell element with uniform reduced integration in bending and shear. A Mindlin–Reissner shell formulation is used to model a composite laminate made up of plies. The multilayered shell properties, ply layup, and ply type are defined in MAT131, with composite elastic and damage properties assigned to

the plies that have additional materials cards. Several composite ply types are available in PAM–CRASH. For the composite fabric plies used here, the global fabric ply damage model was defined as PLY 7 (see Section B.4 for details).

Ply elastic material properties were obtained from tension and compression coupon test data available in the CMH–17 database. In addition, cyclic loading shear tests were conducted at the DLR on the Toray® T700/2510 material. From these tests, a shear elastic damage evolution equation was determined, and an inelastic shear plasticity law obtained, for additional PLY 7 parameters, as discussed in Reference 13. The cohesive interface used is a node-segment or segment-segment penalty contact (TIED interface) whose properties are defined in MAT303. The main interface data required for MAT303 in the Pickett model (Ref. 14) are fracture toughnesses G_{Ic} and G_{IIc} together with through-thickness tensile, shear moduli, and crack initiation stresses (see Section B.4 for details). This interface model represents an initially elastic interface that is progressively degraded after reaching a maximum failure stress, where the delamination fracture energy is fully absorbed at separation.

FE model.—The composite sections in the RR exercise were carbon fabric/epoxy laminates composed of eight plies of Toray® T700/2510 with a $[0/90/0/90]_S$ configuration and an average cured laminate thickness of 1.65 mm. After some initial parameter studies, they were modeled by four stacked shells connected by three cohesive TIED interfaces. Mesh refinement studies led to use of four-node shell elements with a mesh size of 1 mm.

Numerical triggers.—Numerical triggers were developed to accurately represent the initiation and propagation of a numerically stable crushing process as observed from visual inspection of crushed specimens. The numerical trigger concept was first introduced to initiate stable crushing in DLR half-tube segment specimens, as described in Reference 15. It was used to initiate a central delamination crack, which led to a splaying failure with a debris wedge. The numerical triggers utilized in the section models are discussed with the numerical results in Section 3.3.2.

Element elimination method (EEM).—As the shell elements distort due to the degradation of the ply properties, implementation of an EEM at ultimate failure was necessary to prevent numerical instability. The equivalent strain criterion was the EEM selected to eliminate the shell elements when they had reached a prescribed equivalent shear strain value after damage had propagated in all the plies in each shell element.

Contact, boundary conditions, and datasets.—Contact algorithms were used to ensure that during the simulation, undesired penetration between the geometric boundaries during deformation is provided. Detailed discussions on contact algorithms, in addition to boundary conditions, are provided in Section B.4. PAM–CRASH provides datasets for global fabric PLY 7 and cohesive interface models (MAT303) for the Toray® T700/2510 fabric carbon/epoxy prepreg material system. PAM–CRASH parameters required for the MAT131, PLY 7, and MAT303 materials models are listed in Section B.4.3 (Table B.6). MAT131 data consist of only the number of plies, ply layup, and ply type, with no ply or interface data. The damage and failure parameters required for PLY 7 and MAT303 are also summarized in Section B.4.3.

Computation.—The numerical simulations were carried out with the PAM–CRASH 2G Solver Version 2009.0 with single precision. On average, each numerical simulation for a crushing distance of 38 mm took approximately 4.85 central processing unit (CPU) hours. The CPU was a Linux® (Linus Torvalds) Beowulf system with a distributed memory parallel (DMP) parallelization of two nodes, where each node was equipped with an AMD Opteron™ 250 (Advanced Micro Devices, Inc.) operated at 2.4 GHz. Preprocessing and postprocessing were prepared in Visual-Crash for PAM Version 4.0.

3.3.2 PAM–CRASH Simulation Results for Sinusoid Crush Specimen

The computational methods developed were first validated with test data on the sinusoid crush specimen (this will be evident from Figure 39, which compares test and analysis for crush force versus crush displacement curves). In addition, Table 7 summarizes test specimen responses in SEA performances and peak and average forces from both experimental and numerical crush tests. In this specimen, the curved segments are very stable against buckling and behave very similarly to the DLR segment specimens (Ref. 15), which fail by a central delamination crack that is initiated at the chamfer and then opened and driven along the specimen by a central debris wedge. The numerical trigger shown in Figure 37 first offsets the nodes of the two central stacked shells at the loading platen, causing a central delamination crack to initiate. Next, a rigid element called a separation wedge mimics the behavior of the debris wedge seen in crush tests, causing the crack to propagate along the specimen. In addition to separating the lamina bundles, the separation wedge causes bending of the lamina bundles about a radius of curvature, inducing hoop stresses in the lamina bundles, which in turn lead to axial cracks and frond formation. To control the extent of separation, and hence the length of the central delamination crack, the contact distances and friction between the shells of the test specimen and the separation wedge may be varied.

Figure 38 shows a typical computed crush sequence for the sinusoid specimen. The crushing sequence images in Figure 38(a) show the initiation of the failure process by the crushing down of the trigger portion, followed by the steady crushing process seen in Figure 38(b). It is seen that numerical simulation was efficient in initiating the observed failure mode and provided a numerically stable crushing process qualitatively very similar to observed crush behavior. A comparison of the numerical and experimental crush force versus the crush displacement of the sinusoid specimen is presented in Figure 39. This shows good agreement. The test and simulated curves consist of four main phases: (1) initial crush load increase to a peak value, (2) rapid crush load drop as the trigger is initiated, (3) crush load saturation (measured from the crush load drop to the first crush load peak in the steady-state crushing phase), and (4) steady-state crushing.

Detailed discussion of test and analysis comparisons for the C-channel and for the remaining crush specimen sections is provided in Section B.4.

TABLE 7.—CRUSH PERFORMANCE COMPARISON OF ELEMENTS

	Sinusoid			Small angle			C-channel			Square tube		
	Exp.	Num.	Rel. error, %	Exp.	Num.	Rel. error, %	Exp.	Num.	Rel. error, %	Exp.	Num.	Rel. error, %
Initial peak load, P_0, kN	20.93	23.88	14.1	6.40	6.47	1.0	14.61	15.62	6.9	34.05	40.31	18.4
Initial slope, kN/mm	11.58	7.53	–34.9	3.18	3.83	20.2	6.52	8.88	36.1	22.30	14.43	–35.3
[a]Crush load, P_{crush}, k	15.06	15.19	0.8	4.65	4.27	–8.1	9.73	10.18	4.6	24.34	25.18	3.4
[a]SEA, kJ/kg	84.37	82.68	–2.0	59.59	57.16	–4.1	44.31	45.25	2.1	30.78	30.17	–2.0
[a]Crush efficiency	0.72	0.64	–11.6	0.73	0.66	–9.1	0.67	0.65	–2.2	0.71	0.62	–12.6
[a]EA, kJ	0.57	0.58	0.9	0.17	0.16	–6.8	0.37	0.39	4.7	0.93	0.96	3.5
Excellent Rel. error ±10%	Good Rel. error ± 10 to 19%			Fair Rel. error ± 20 to 29%			Poor ±30% and higher					

[a]For 38-mm crush length.

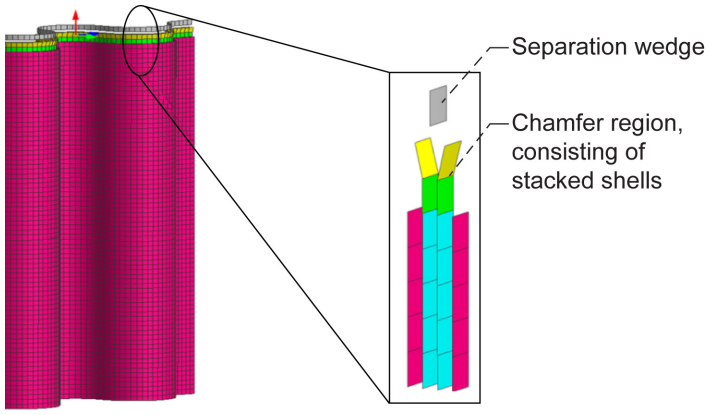

Figure 37.—Trigger mechanism of sinusoid specimen numerical model.

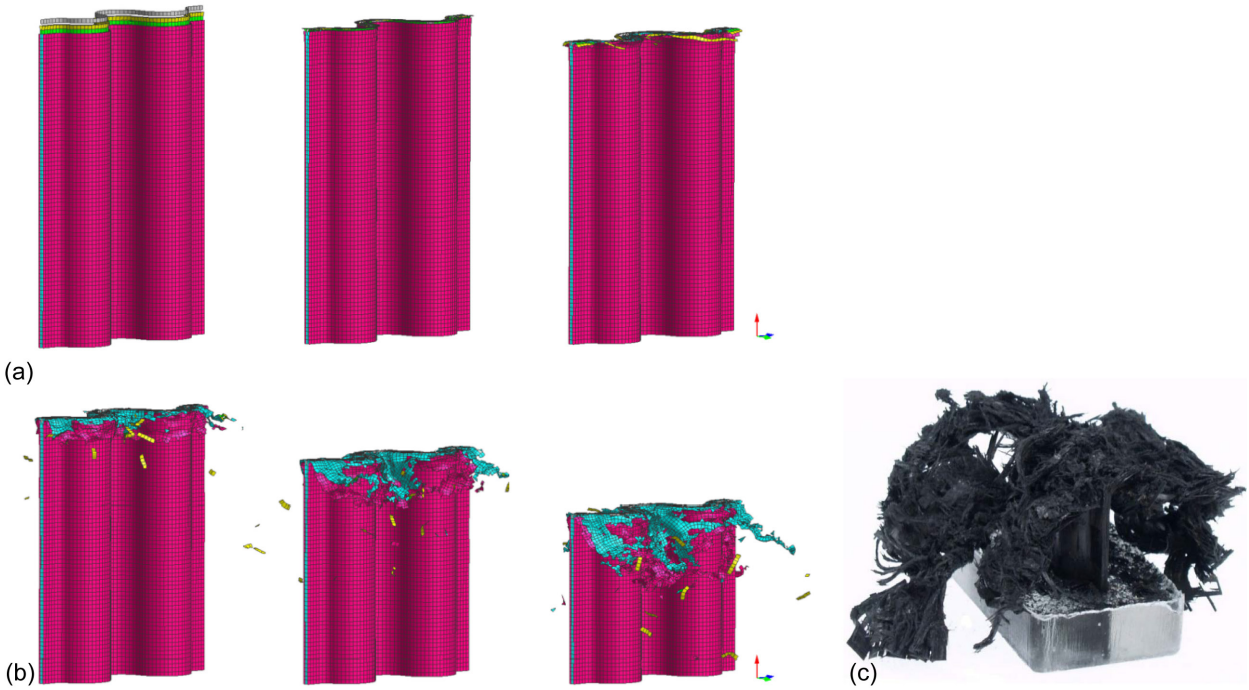

Figure 38.—Sequence of corrugated plate specimen numerical crushing process. (a) Initiation of failure process. (b) Steady crushing progress. (c) Observed crush behavior.

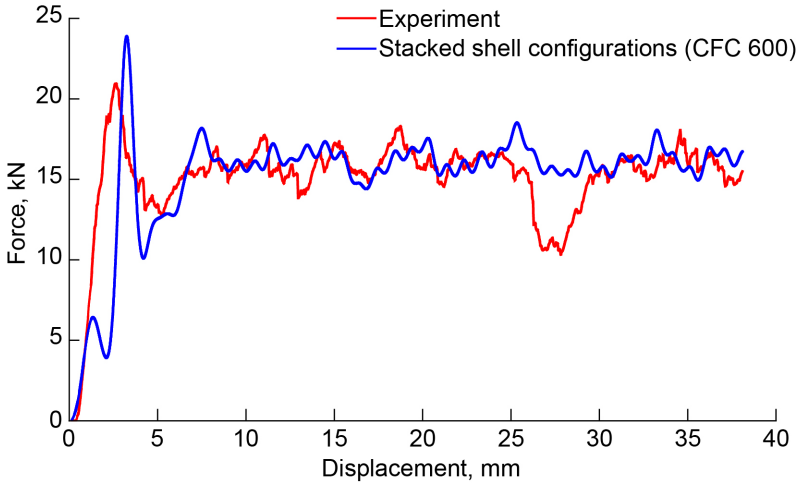

Figure 39.—Numerical and experimental crush force versus crush displacement for sinusoid specimen; experimental results filtered with CFC 600 (channel frequency class 600) filter.

3.3.3 Assessment of PAM–CRASH Results With Respect to Success Criteria

EA, SEA, and crush efficiency were chosen to measure the energy absorption performances of the specimens. EA represents the total area under the crush load–displacement curve for the crushing process, chosen to be 38-mm crush length here. The SEA is the EA divided by the mass of the 38-mm-long section crushed down. Crush efficiency is the ratio of the average crush force to the peak crush force. The average crush force was calculated by dividing the EA by the total crush distance. A crush efficiency value close to 1 is desired, as this would minimize the imparting of large forces onto the overall structure during the crushing process. Table 7 summarizes these energy absorption performances in addition to the peak and average forces calculated from both experimental and numerical crush tests. A reasonable quantitative correlation between experimental and numerical results is observed, with a tendency for the numerical results to overestimate slightly for most profiles. In the case of the small angle, computed average crush force and EA were below the test data. Computational accuracy is excellent or good except for the initial slope, where only fair and poor correlation with experimental results was achieved. This poor prediction quality for the initial slope can be attributed to the computation method's use of an explicit solver and an increased loading platen velocity. Resulting oscillations and the application of channel frequency class (CFC) 600 filtering affect the initial slope in numerical force–crush distance curves.

Figure 40 presents a bar chart comparing experimental and numerical Total SEA results for each of the specimens. This figure is valuable, as it provides direct information for design of composite absorbers and the efficiency of the crush mode developed. It shows that the corrugated section has SEA values 2.8 times higher than those of the square tube and about twice as high as those of the C-channel. This indicates that the steady crushing initiated by the chamfer trigger in the corrugated plate with the splaying crush process is by far the most efficient energy absorption mechanism in the four sections tested. This is due to the delamination failure energy absorbed in the splaying mode, a result not observed in the box section, which failed by local buckling plus bending failure. Of the two open sections, the small angle absorbed energy by corner fracture, which was more efficient than buckling but still below the splay crushing energy.

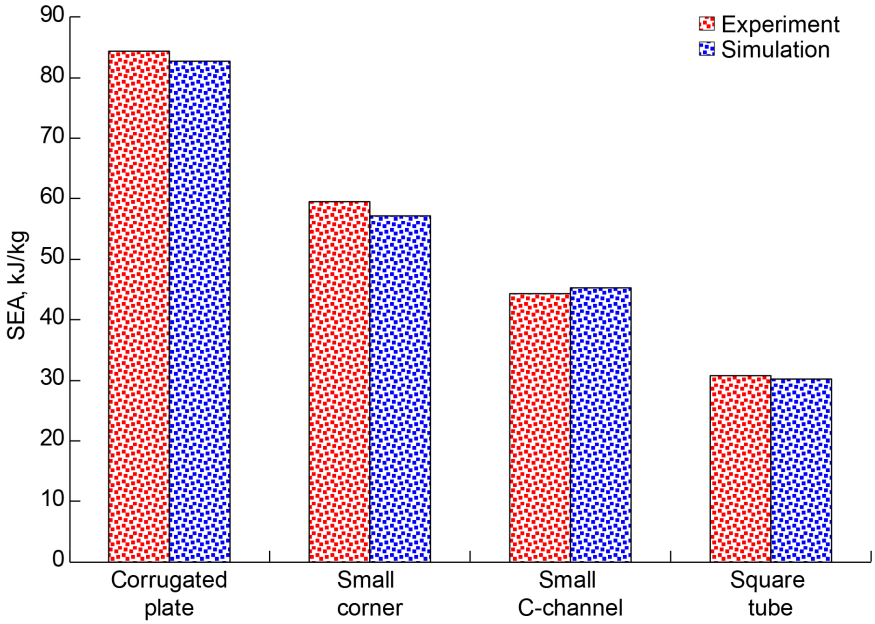

Figure 40.—Comparison of measured and predicted SEA.

The DLR contribution to the Round Robin phase was presented in this section with a methodology for modeling crashworthy structures successfully implemented in RR–1 and RR–2. This philosophy consists of utilizing basic mechanical properties of the composite material derived from standard tests on coupon specimens, the modeling of delamination in the numerical model through the use of cohesive interface elements, and the inclusion of varied novel numerical triggers that depend on the crush behavior to initiate and propagate a numerically stable crush failure mode. The outcome of this crush modeling as presented here provided numerical results with good qualitative and quantitative correlation with experimental results. Further validation of this methodology is needed for other failure modes observed in composite structures in addition to the numerical modeling of the structures under dynamic loading conditions.

4.0 Round Robin 3 Material Models

The objective of RR–3 was to evaluate the effectiveness and robustness of the 11 selected progressive damage models, detailed in Sections 4.1 to 4.11, by using a common, predefined target structure and common material, fabrication, specimen geometry, and dataset. Flat coupon data served as the basis for model calibration, with the expectation of performing pretest predictions for the C-channel crush coupon. This effort was to focus on a small-scale structural element level and transition to large-scale structures. Deliverables for each investigation included the following:

- Simulation details and modeling approach
- Force–displacement curve and SEA curve
- Sequential figures of failure morphology
- Successes and shortcomings
- Best practices and modeling strategies

It is crucial to note that in several methods from RR–3, the impactor mass for the C-channel crush test was incorrectly assumed to match that of the flat coupon. (See Table 21 for the actual values.) Consequently, the affected methods are limited to demonstrating modeling approaches for simulating the C-channel's energy absorption or analytically comparing the crush energy behavior of the two geometries at a given impact energy level. As a result, the numerical predictions from these methods do not allow for direct test–analysis correlation and are not compared to the C-channel test data in this report. To ensure clarity, a footnote to this effect appears in this report where these methods are discussed.

Despite limitations, these methods still provide a valuable foundation for users to effectively apply PDFA methods. It is worth noting that three methods—LS-DYNA® MAT213, ABAQUS® CZone, and ESI VPS: Waas-Pineda implementation—used the correct platen mass, and their C-channel test–analysis correlations are valid. The impacted models will be updated in future efforts to enable accurate test–analysis correlation.

4.1 LS–DYNA® MAT54

This section provides an overview of the crush simulations of composite energy absorbers conducted at the National Institute for Aviation Research (NIAR). Flat coupon and C-channel sections were the composite energy absorbers numerically evaluated. Analysis results for crush behavior of flat coupons were calibrated with their test data; this calibrated material model was then used to conduct simulation of C-channel test articles, which included a simplifying assumption of a drop-weight mass identical to that of the flat coupon for modeling crush energy absorption.[2] Section B.5 shows simulation results for the two hard laminates that were also evaluated for flat coupons. The analysis work presented here was performed using material model *MAT_ENHANCED_COMPOSITE_DAMAGE, also known as MAT54 (Ref. 16). This section also discusses the modeling capabilities, material model limitations, and best practices identified when using LS–DYNA® MAT54. Theoretical background is presented in Section B.5.

LS–DYNA® MAT54 offers strength reduction parameters to degrade the pristine strengths of a ply postfailure. Reduction factors FBRT, YCFAC, and SOFT were considered in this model and are defined as follows:

- FBRT—Percentage of the pristine fiber tensile strength existent after failure has occurred in compressive matrix mode
- YCFAC—Reduction factor for compressive fiber strength after matrix compressive failure
- SOFT—Softening reduction factor for material strength in crash-front elements that are direct neighbors of the eroded elements

The SOFT parameter was found to be greatly influential in crush behavior (Ref. 17).

FBRT, YCFAC, and SOFT are numerical parameters that cannot be measured from experiments and hence are calibrated using numerical analysis. They vary based on specimen geometry and loading condition and thus must be determined through trial and error (Refs. 16 and 18). As part of the RR–3 numerical analysis task, SOFT, FBRT, and YCFAC were calibrated to and match the flat coupon experimental results. Detailed results appear in Section B.5.

The parameters used to define a fully populated material card can be broadly classified as constitutive properties (such as strength parameters), erosion parameters, modeling parameters, and material axes definition (Ref. 16). The strength and element erosion parameters are presented in Section 5.3.5. Section B.5 provides the fully populated MAT54 material card.

[2]See Table 21 for listing of impact loading conditions for flat coupon and C-channel crush tests.

4.1.1 Flat Coupon Crush Simulations and Test and Analysis Correlation

As part of the RR–3 simulation task, the crush characteristics of the flat coupon were evaluated. The numerical models were developed based on the specimen geometry, loading conditions, and other test setup details described in Section 5.6.1. Figure 41 illustrates the FE model setup, which was based on the flat coupon test setup. All the components were generated using shell elements. The composite laminate was defined as a single-shell layer and the ply orientations were defined using LS–DYNA® *PART_COMPOSITE (Ref. 19). The initial and boundary conditions of the model were represented by the top row of nodes in the specimen that were assigned the impact velocity using *INITIAL_VELOCITY and *PRESCRIBED_MOTION (Ref. 19).

The top 20 mm of the specimen was constrained in translational DOFs (x and y) to simulate the resin-embedded section of the specimen. The impact plate of 96.8 lb and the support plates were constrained in all DOFs. The contact definitions in the model were as follows: LS–DYNA® *ERODING_SURFACE_TO_SURFACE with a friction coefficient of 0.2 between the specimen and the impact plate, and *AUTOMATIC_SURFACE_TO_SURFACE with a friction coefficient of 0.01 between specimen and the support plates (Ref. 19).

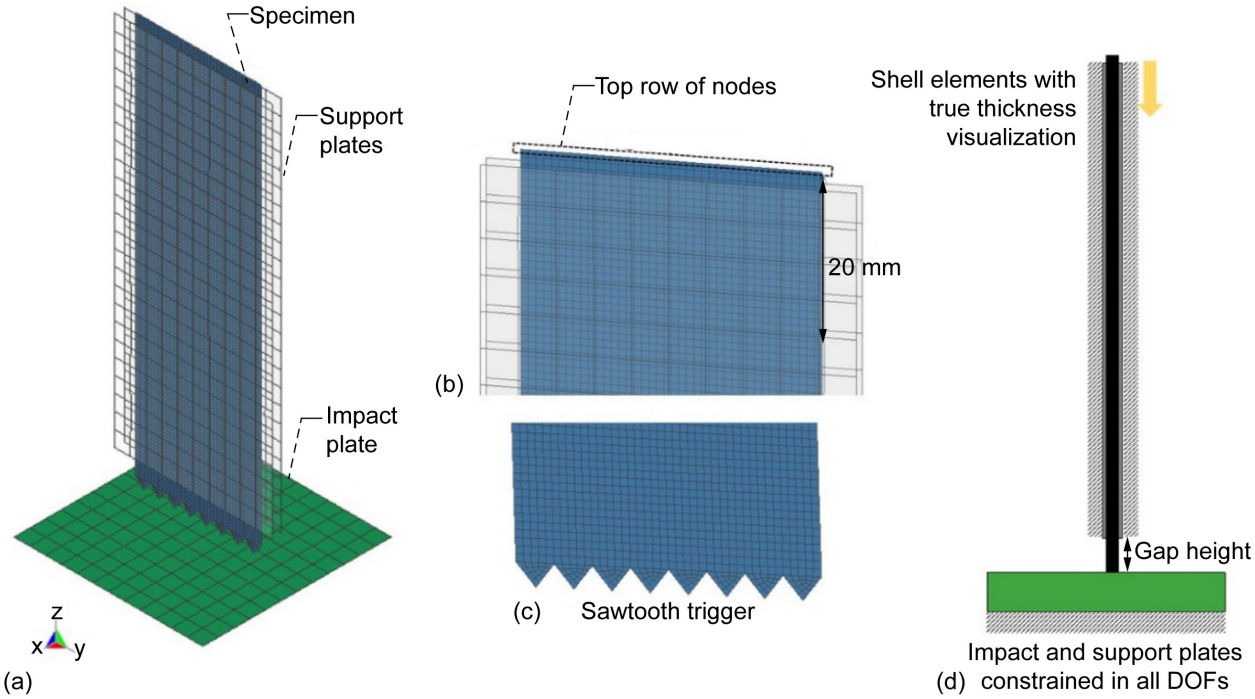

Figure 41.—Numerical model of NIAR MAT54 flat coupon crush model. (a) Specimen and support plates. (b) Model detail; degrees of freedom fixed in x and y direction, initial velocity assigned in z direction. (c) Sawtooth trigger. (d) Side view.

The specimen was modeled using LS–DYNA® MAT54, and the support plates were modeled as rigid bodies using LS–DYNA® MAT20 (Ref. 16). Two different flat coupon hard laminates were evaluated as defined in the test matrix: stacking sequence $[90_2/0_2/\pm45/0_2]_S$, referred to in this report as "HL01," and stacking sequence $[90/45/0_2/90/-45/0_2]_S$, referred to in this report as "HL02" (see Section 5.6.1).

Figure 42 presents sequential images illustrating the stable crush progression of the flat coupon numerical analysis. Figure 43 presents a force–displacement data comparison between test and analysis for the two hard laminates. Stable crush was observed in both cases, but the simulations predicted lower initial peak forces than the test data.

The crashworthiness parameters evaluated for test and analysis correlation were mean crush force (P_{crush}) and SEA. SEA was computed for two different displacement ranges: Stable SEA (10 to 30 mm) and Total SEA (0 to 30 mm). Figure 44 and Figure 45 illustrate the Stable and Total SEA comparisons between test and numerical analysis for the two hard laminates.

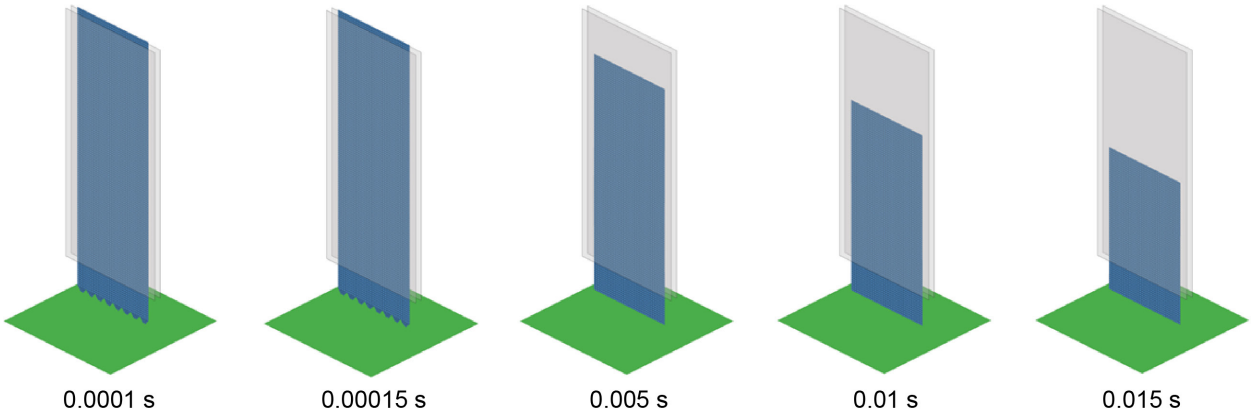

Figure 42.—Crush progression of laminate HL01 $[90_2/0_2/\pm45/0_2]_S$ using MAT54.

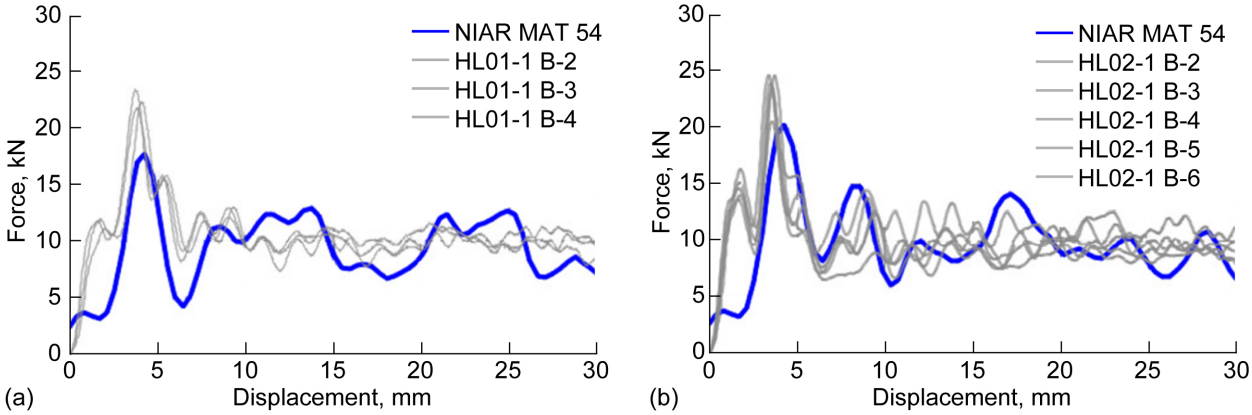

Figure 43.—Comparison of experiment and simulation force–displacement results for two flat coupon laminates. (a) HL01 $[90_2/0_2/\pm45/0_2]_S$. (b) HL02 $[90/45/0_2/90/-45/0_2]_S$.

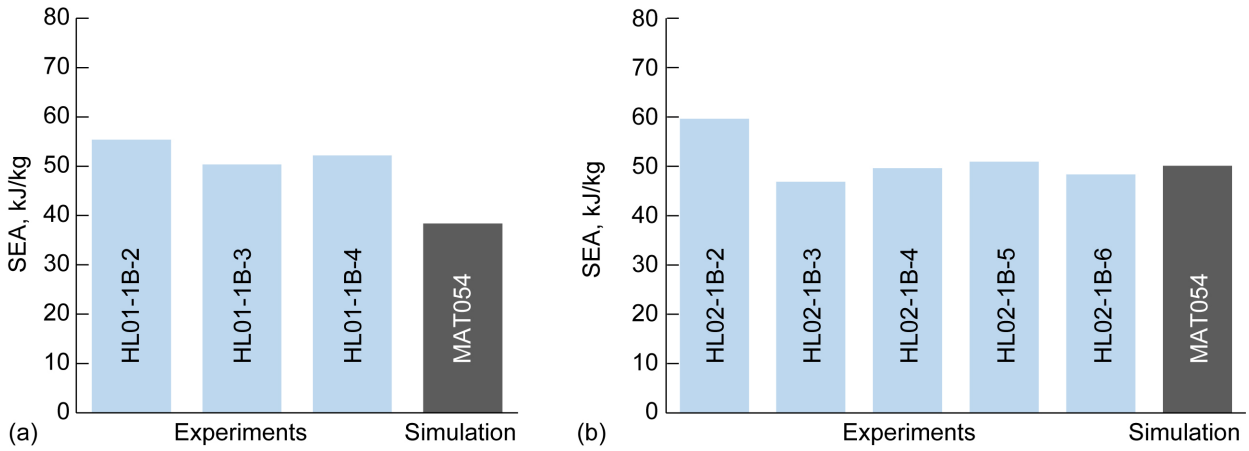

Figure 44.—Comparison of experiment and simulation Stable SEA (10 to 30 mm) for two flat coupon laminate configurations using MAT54. (a) HL01 $[90_2/0_2/\pm45/0_2]_S$. (b) HL02 $[90/45/0_2/90/-45/0_2]_S$.

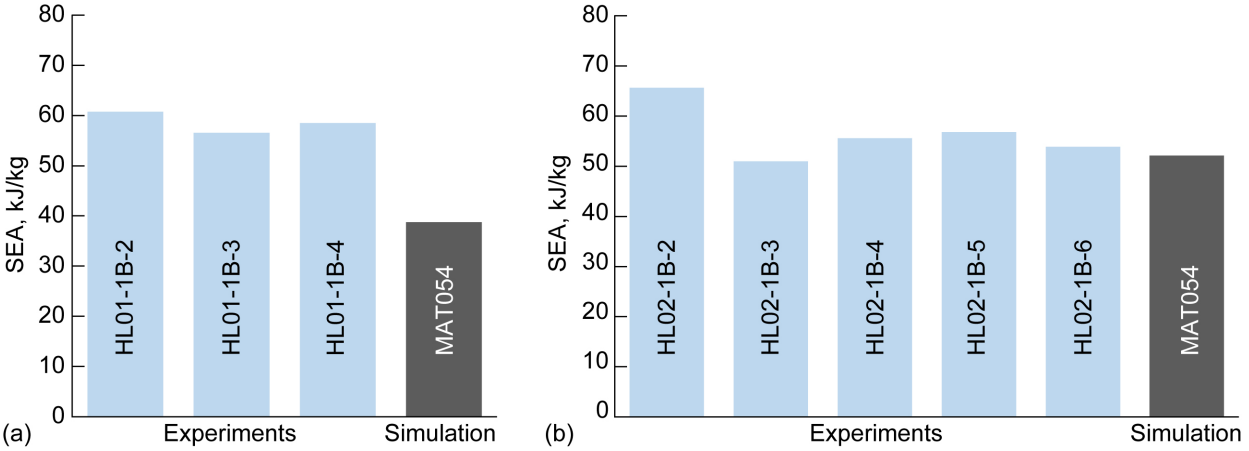

Figure 45.—Comparison of experiment and simulation Total SEA (0 to 30 mm) for two flat coupon laminate configurations using MAT54. (a) HL01 $[90_2/0_2/\pm45/0_2]_S$. (b) HL02 $[90/45/0_2/90/-45/0_2]_S$.

4.1.2 C-Channel Numerical Model Description

This section discusses the C-channel numerical model developed according to the test setup defined in Section 5.6.2. The test specimen was modeled using shell elements where each ply was defined as a discrete integration point. The epoxy base was modeled using solid elements. A fine mesh was used in an attempt to achieve stable crushing. The mesh size for the specimen was maintained at 0.726 mm, as shown in Figure 46. The drop-test impactor plate was assumed to be identical to the flat coupon platen mass[3] of 96.8 lb to be able to analytically compare the crush energy absorption behavior of the two different test specimens' geometry for a given impact energy level. In future efforts, the platen mass of the C-channel model will be updated to match that of the drop test or sled test to conduct test and analysis correlation.

[3]See Table 21 for listing of experimental platen mass values for flat coupon and C-channel crush tests.

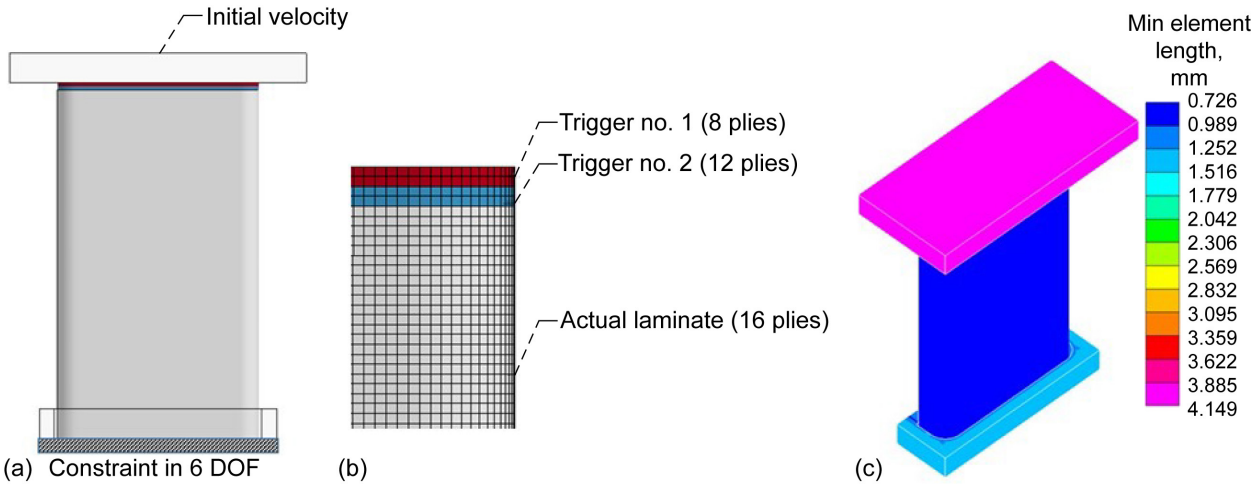

Figure 46.—Numerical model description of NIAR MAT54 C-channel specimen. (a) Model setup. (b) Trigger and laminate elements. (c) Isometric view of model.

The C-channel base plate and the bottom row of nodes of the stanchion were constrained in all DOFs. The impactor was assigned an initial impact velocity along the stanchion length. The contact definitions between the base plate and the stanchion in the model were *AUTOMATIC_ONE-WAY_SURFACE_TO_SURFACE_TIEBREAK with option 1 (Ref. 19) and *ERODING_SURFACE_TO_SURFACE between the impact plate and the stanchion. The crush trigger in the actual specimen was accounted for in analysis by reducing the thickness of the first two rows of elements in the specimen. The crush trigger definition is greatly influential in attaining stable crush and is generally determined through a trial-and-error approach based on the experimental data.

Stanchion crush behavior was evaluated for two different hard laminate stacking sequences, $[90_2/0_2/\pm45/0_2]_S$ (HL01) and $[90/45/0_2/90/-45/0_2]_S$ (HL02), using LS–DYNA® MAT54 at an initial impact velocity of 150 in./s (3.81 m/s) and 300 in./s (7.62 m/s). The calibrated material model from the flat coupon simulations was used for this simulation work. The numerical analysis results are presented in Section B.5.

4.1.3 LS–DYNA® MAT54 Capabilities, Limitations, and Best Practices

This section presents the modeling capabilities and limitations of LS–DYNA® MAT54, including best practices as they pertain to utilization of this material model for crush simulation of the flat crush coupon and C-channel composite test articles considered here.

Modeling capabilities:

- MAT54 is an orthotropic material model that requires minimal input parameters typically based on tensile, compressive, and shear experiments. Due to its relatively simple input definition, it is computationally efficient, especially for large-scale applications (Ref. 18).
- It has the capability to predict individual ply failure using through-thickness integration points for shell elements. The failure model is based on four failure modes: tensile fiber mode, compressive fiber mode, tensile matrix mode, and compressive matrix mode.

Modeling limitations:

- MAT54 requires experimental data to calibrate modeling parameters to simulate the crush characteristics observed in tests (Refs. 17 and 18).
- It is a semi-empirical material model with parameters that are not physics-based, that is, they cannot be measured from experiments and hence are calibrated using numerical analysis. They vary based on the specimen geometry and loading condition and thus must be determined through trial-and-error approach.
- Delamination effects are not physically accounted for when using this material for crashworthiness analysis because they typically have one shell element through the thickness of a part.
- Inability to simulate failure modes such as fiber crush and intralaminar dominated failure modes.

Modeling strategies and best practices:

- MAT54 is typically used for shell elements and is applicable to unidirectional layups. Failure criteria are defined for both tension and compression and for fiber and matrix. Ply angles in the layup are defined at integration points, and each ply can fail individually; element stiffness reduces as plies fail. The element is removed once all plies fail.
- MAT54 does require test and analysis correlation for parameters such as SOFT, to capture damage progression accurately for each application.
- Physically modeling delamination with MAT54 is unnecessary as long as the strain energy absorbed by the coupon matches between test and simulation.
- The crush front mechanism is activated with the SOFT parameter in MAT54. This reduces failure properties adjacent to failed elements and encourages crushing to proceed after the initial failure.

4.2 LS–DYNA® MAT58

This section describes the use of LS–DYNA® *MAT_LAMINATED_COMPOSITE_FABRIC (MAT58) for composite crush and crashworthiness simulations.

4.2.1 MAT58 Capabilities and Limitations

LS–DYNA® MAT58 is used for composite crush and crashworthiness simulations intended to use with either unidirectional tape or fabric composites and allows for either ply-by-ply modeling of laminates, or for modeling using smeared laminate properties. For all of the following discussion, it is assumed that individual plies are represented with the ply-level material properties for IM7/8552. This section assumes use of shell elements, with plies defined individually in either *SECTION_SHELL cards or using *PART_COMPOSITE. However, this continuum material model may now be applied to both solid and shell elements.

MAT58 provides several user-defined parameters for simulating progressive crushing and damage evolution with residual strength and ultimate element erosion. This approach can approximate overall expected physical energy dissipation even without explicitly modeling all of the complex failure mechanisms that occur. However, this continuum method does not provide for convenient crack growth simulations since crack growth requires full element deletion. MAT58 does allow for overall damage degradation prior to element deletion, and provides simulation of post-damage initiation residual strength, which is physically reasonable under many progressive damage conditions.

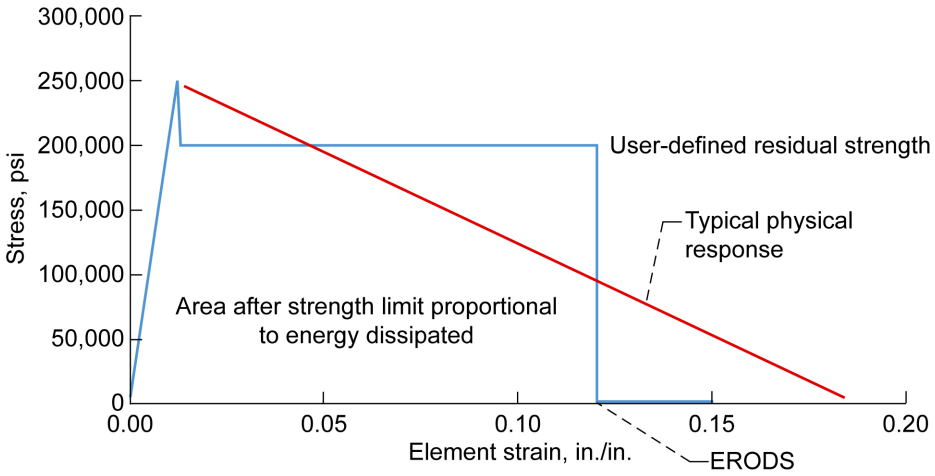

Figure 47.—Typical element response for compression with specified residual strength.

Subsequent to damage initiation and prior to element erosion, damage is accumulated, and energy is dissipated as the damaged element continues to strain. Thus, the combination of residual strength, which is specified with SLIM parameters, and final erosion strain, specified by ERODS, serve to define the element energy absorption prior to deletion. With these factors, plus the SOFT parameter, which simulates the crush-front effect, it is possible to calibrate the energy dissipation to within reasonable physical limits. This is possible even without considering delamination, intraply splitting, and other 3D damage effects. The ability to simulate a calibrated level of energy absorption using shell elements is a major advantage of this material model and allows for modeling of larger scale structures.

As shown in Figure 47, the stress level falls after damage initiation and remains at a user-defined value. This reduction factor is specified as a percentage of the damage initiation load. Prior to damage initiation, response is elastic. When strain progresses to the limit defined by ERODS, the element is deleted, and no further energy dissipation occurs. Thus SLIM, in this case SLIMC1, along with ERODS will influence the load distribution through the part and will affect energy dissipation.

Figure 47 illustrates compression in the fiber x-direction, but similar parameters are also used to specify residual strength for fiber tension, y-direction compression, y-direction tension, and in-plane shear. From Figure 47, it can be seen that energy dissipation can be calibrated to provide a reasonable response over a range of loading and crush conditions.

In general, MAT58 has a number of important advantages, making it well suited for larger scale crashworthiness simulations:

- Is ideal for representing large regions of structure subjected to high dynamic loading conditions.
- Multiple parts may be readily connected with spotweld beam fasteners (e.g., to connect frames and stanchions).
- Can be calibrated to accurately represent energy dissipation for structural elements, such as stanchions, webs, and frames.
- Material properties and parameters are only calibrated once, after which they are applied to multiple different layups and thicknesses.
- Can represent edge-on crushing, buckling, and fragmentation.
- Update to this material model allows its use for solid elements, which provides for convenient subscale modeling without changing material types.
- Update to this material model allows for strain-rate effects to be included, both for strength and modulus.

There are also some disadvantages inherent with this material model:

- Is not an ideal method for simulating crack growth, as element size becomes a critical variable.
- Requires multivariable optimization to initially calibrate input parameters. Key parameters include
    - Residual strength after initial strength limit is exceeded
    - Element strain erosion limits
    - Crash-front effects, simulated by reducing strength of elements adjacent to damage
    - Strain-rate effects for both strength and modulus in tension, compression, and shear

The required calibration should be performed over a range of strain rates to take advantage of the available strain-rate effect curves in this material model. Although it is possible to calibrate these parameters to match exactly with any given test, a better approach is to establish a set of parameters that provides reasonable results over the full range of expected geometries and loading conditions.

4.2.2 MAT58 Parameters and Key Options for Calibration

Important parameters requiring calibration include the following:

- SLIMT1, SLIMC1, SLIMT2, SLIMC2, and SLIMS for residual strength for different failure modes (tension, compression, and shear) and for both x- and y-directions
- ERODS—Effective element strain that determines limit for element erosion
- SOFT—Determines reduction in strength for elements adjacent to the progressive crush front (requires TSIZE value)

In addition to the usual elastic material properties and strength properties, calibration of MAT58 is required for the parameters shown in Section B.6.1 (Figure B.40 and Figure B.41), with further discussions in Section B.6. This includes additional parameters that have more recently been included as updates to the material model.

Strain-rate curves are not required and are not defined in the current models used in simulating coupon or part-crushing response. However, use of these calibration curves would be highly advantageous in simulating differing crush responses over the velocity range from quasistatic to higher impact velocities, such as the 30 ft/s (360 in./s) used in some Federal Aviation Administration (FAA) drop tests.

4.2.3 MAT58 Validation With Flat Coupon Test Data

Validation of MAT58 for crush simulations is based primarily on a comparison of overall energy dissipation during the crush event shown in this section. While these validations are important, it is also important to realize that design features in actual structures will vary from the ideal coupons and that the angles for crushing and loading directions will vary significantly. This means that the simulation should not be overly focused on replicating a narrow band of impact conditions such as are found in a single coupon test. Rather, the simulation should be calibrated to apply to a range of loading conditions and geometries.

Ideally, testing of actual stanchions, double stanchions, or other more complex parts and assemblies will provide final validation of the material model.

This section presents test and simulation results for flat-plate coupon tests that have been previously performed and documented. Figure 48 shows the model used to simulate the coupon crush events, which is based on test geometry, and Figure 49 shows initial crushing of the trigger region. The flat coupon

crush simulations were performed with MAT58 using an impact mass of 43.9 kg (96.8 lbf).[4] The trigger region successfully initiates crushing with an irregular sawtooth contact shape and leads to progressive crushing for the flat coupon, which is supported by guide plates. The distance between the guide plate and the crush plate is defined as the "gap."

Figure 50 provides an image of the mesh density for the coupon. It also shows the element erosion after 1.0 in. of crushing, roughly midway in the total crush zone used in testing to determine SEA.

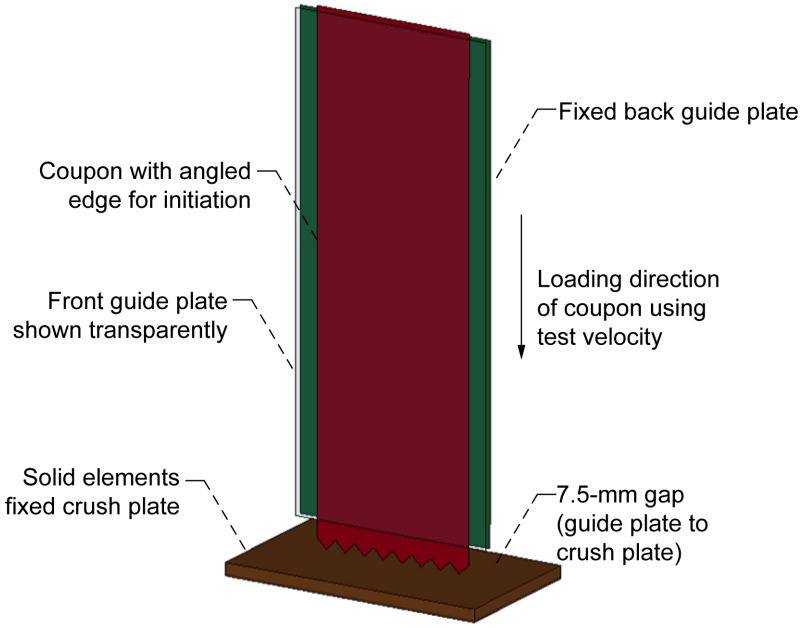

Figure 48.—Flat coupon crush simulation model, based on test geometry.

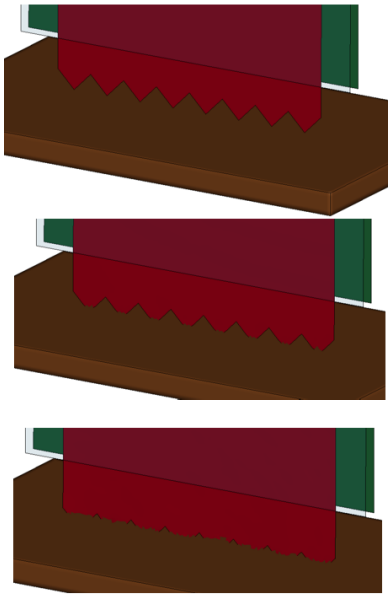

Figure 49.—Initial crush of trigger region for flat coupon.

[4]The correct platen mass of 44.0 kg was used in the MAT58 flat specimen simulations; see Table 21 for reference to experimental platen mass values.

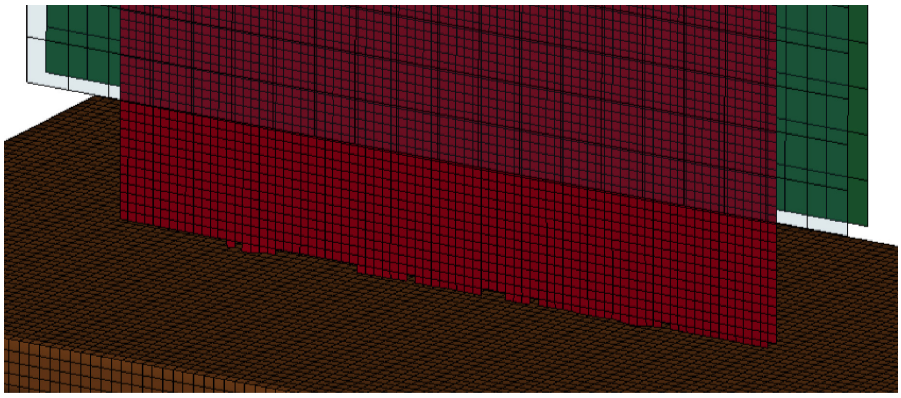

Figure 50.—Typical crush response after 1.0 in. of crushing.

Results for three different layups are reported in this section. The layups and gap distances are as follows:

1. Quasi-isotropic, QI01: $[90/\pm45/0]_{2S}$, gap = 8.6 mm
2. Hard laminate, HL01: $[90_2/0_2/\pm45/0_2]_S$, gap = 14.5 mm
3. Hard laminate, HL02: $[90/45/0_2/90/-45/0_2]_S$, gap = 12.0 mm

The gap between the guide plate vertical supports and the base plate differs for various tested layups. This gap can influence the test response. In the simulations, the gap distance was adjusted to match the reported gap distance in the experiments. A comparison of test and MAT58 simulation for the quasi-isotropic layup is shown in Figure 51. The comparison of test and analysis correlations for all three layups is shown in Section B.6.2 (Figure B.42, Figure B.43, and Figure B.44). Each figure reports both force–displacement history and cumulative energy absorbed during crushing in comparison with repeated test results.

Figure 52 shows a comparison of trends for the simulation with the three laminates tested. The simulation correctly shows the trend of increasing energy absorption between the quasi-isotropic laminate and the two hard laminates. This provides a useful method of assessing the energy absorption capabilities of differing laminates.

Overall, the simulation with MAT58 shows SEA values that are, in general, reasonable, as seen in Table 8.

The quasi-isotropic layup simulation shows a noticeably lower prediction for SEA, whereas the hard laminates show good comparisons. This could be due in part to differences in response due to varying gaps. This discrepancy between test and simulation could be mitigated by adjusting SOFT or by lowering the residual strength factors, currently set at 80 percent for compression. An effort was made, however, to limit changes to material parameters as much as possible, in comparison to parameters used in previous channel and sine-wave section crush simulations, which were already validated with flat coupon and element crush tests. Also, the simulation parameters were selected to approximate an allowable energy-absorbing response. Additional component-level tests will show if the current material parameters are adequate for part-level and assembly-level crashworthiness simulations.

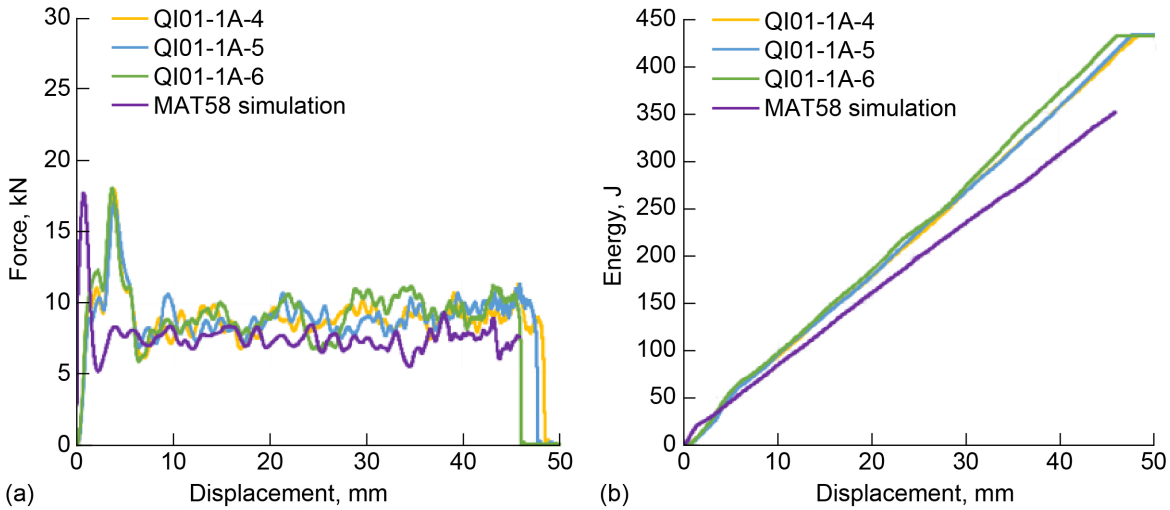

Figure 51.—Comparison of experiment and MAT58 simulation for quasi-isotropic layup. (a) Force–displacement curves. (b) Energy absorbed versus displacement.

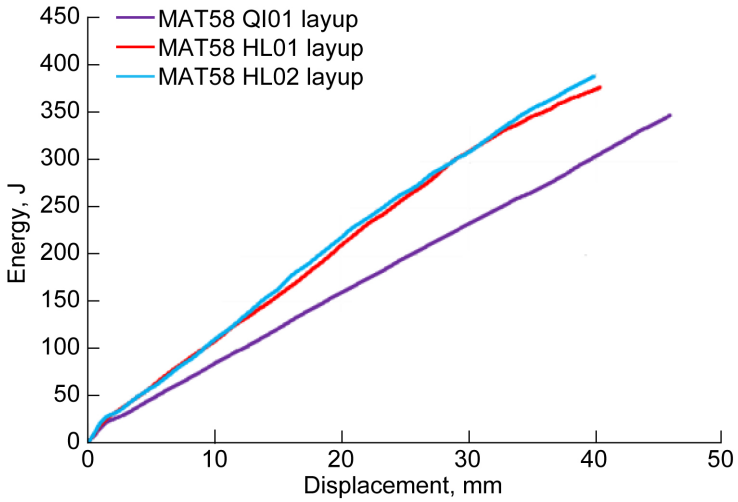

Figure 52.—Comparison of energy absorption trends from MAT58 simulation with three laminates.

TABLE 8.—COMPARISON OF STABLE SEA FROM TEST AND MAT58 SIMULATIONS

Coupon layup	Experiment average Stable SEA, kJ/kg	MAT58 Stable SEA, kJ/kg
QI01	46.11	39.80
HL01	53.59	54.02
HL02	54.34	53.36

4.2.4 MAT58 Recommended Simulation Practices and Methods

The comparison of test and simulation results for flat-plate coupons in the previous section provides partial validation of this material model. Final validation of this simulation method will occur at the part or small-assembly (e.g., a double stanchion assembly) level.

For future C-channel section simulations, it is important to include the base section, which provides support to the channel during crush. Previous experience has shown that these boundary conditions, which have some degree of elasticity, will generally provide for a more stable crush response during simulation.

Other features that can influence results are the angle of impact, contact friction, global mass damping, contact damping, and element formulation. Contact damping was not used in the previous simulations, but in some cases the use of damping may increase the stability of the part at the point of impact.

SLIM factors for compression are generally set relatively high (e.g., 0.7 to 0.9) based on the assumption that compressive response remains relatively stable even after initial failure. Tensile SLIM factors, in contrast, are generally set relatively low (e.g., 0.1 to 0.3) based on the assumption that tensile failure will likely lead to physical discontinuities and loss of load path for that ply.

The mesh using MAT58 does not require specific alignment, but ERODS may need to be increased as an adjustment for large element sizes. At low ERODS, premature erosion of a large element will lead to significant discontinuity in loading, and the adjacent elements may begin to unload in a physically unreasonable manner. In typical physical crush conditions, loading is continuous, even as the structure fails progressively. Thus, ERODS should be set high enough to largely maintain load continuity during progressive failure, though perfect continuity of loading is not generally possible. Some degree of loading oscillation is expected, both for test and simulation.

4.3 LS–DYNA® MAT213

MAT213 is an orthotropic macroscopic three-dimensional (3D) material model designed to simulate the impact response of composites that has been implemented in the commercial transient dynamic FE code LS–DYNA®. MAT213 was developed by an FAA/NASA-led consortium including collaborators from Arizona State University, George Mason University, Ohio State University, and ANSYS-Livermore Software Technology Corp. MAT213 has shown promising predictive capability for out-of-plane penetration impacts on flat, unidirectional-tape composite specimens.

A key goal in the development of MAT213 was to create a framework where the material model is primarily characterized through well-defined coupon-level tests. The advantage of this approach is to develop a model with enhanced predictive capabilities and less reliance on correlation to structural-level impact, crash, or crush tests. In addition, the model includes the capability of simulating tension–compression asymmetry, strain-rate effects, temperature effects, and stochastic variation of material properties.

The material model is a combined deformation/plasticity, damage, and failure model suitable for use with both solid and thin shell elements. The deformation/plasticity portion of the model utilizes an orthotropic yield function and flow rule. A key feature of the material model is that the evolution of the deformation response is computed based on tabulated stress–strain curves in the various coordinate directions that are input based on experimental data. The damage model employs a semicoupled formulation in which applied plastic strains in one coordinate direction can lead to stiffness reductions in multiple coordinate directions. The evolution of the damage is also based on tabulated input from a series of load–unload tests, as described in Section 5.2.3. A tabulated failure model has also been implemented in which a failure surface is represented by tabulated single-valued functions. While not explicitly part of MAT213, when using the model, interlaminar failure is modeled using either tiebreak contacts or cohesive elements.

Additional features have been added to the original deformation model. Strain-rate effects have been incorporated by allowing users to define different stress–strain curves at various strain rates (Ref. 20). Similarly, users may also define different stress–strain curves at various temperatures. The local

temperature rises that can occur during a dynamic event due to adiabatic heating can be accounted for through the use of a Taylor–Quinney effect (Ref. 21), which accounts for the effect of the local temperature increases (Ref. 22). Additionally, stochastic variation is now included, which allows users to vary input properties with user-defined probabilistic criteria (Ref. 22). While these features are incorporated into MAT213, users can selectively enable features of interest for a given simulation; only some of these features were included in the succeeding crush simulations. A full description of the deformation, damage, and failure model is discussed in detail in Section B.7.

4.3.1 MAT213 Capabilities and Limitations

Modeling Capabilities.—MAT213 is distinguished from similar orthotropic material models by the functionality available to the user, including nonlinear stress–strain behavior, shell and solid elements, tension–compression asymmetry, strain-rate effects, temperature effects, and stochastic variation of material properties. Additionally, MAT213 was designed with the intention of facilitating more predictive simulations; thus, the requisite user inputs can be determined using coupon data generated without prior knowledge of the structural-level response. The damage and failure models implemented in MAT213 also allow customizable modulus degradation, postpeak softening, and element erosion.

Modeling Limitations.—MAT213 has been shown to be effective for simulating out-of-plane penetration impact of composite laminates (Refs. 20, 22, and 23). However, its capability of simulating in-plane dynamic crushing of composites is still a primary objective of ongoing research efforts. Additionally, there is less documentation for overcoming preprocessing errors and troubleshooting unexpected results compared with similar, well-established models. Thus, new users can expect to spend time reviewing the material model theory, becoming familiar with the unique tabular user-defined inputs of MAT213, and troubleshooting errors. The volume of data necessary to perform even basic models in MAT213 is large compared with other composite impact models because entire stress–strain curves are required inputs. Due to the required yield surface convex correction, loading conditions offset from the principal material directions of the carbon-fiber-reinforced polymer (CFRP) may lead to higher error.

4.3.2 Flat Crush Coupon Modeling Approach

FE Model and Boundary Conditions for Flat Crush Coupon Specimen.—The CFRP flat coupon crush model was designed using the geometry and layup of the flat coupon specimens tested experimentally. The geometry of the specimen is defined in Section 5.6.1. Although two layups were tested for the flat crush coupon experimentally, only the $[90_2/0_2/\pm45/0_2]_S$ layup (HL01) has been simulated at the time of this writing. The specimen support plates that inhibit specimen buckling and a rectangular plate representing the ground were incorporated in the model as rigid (MAT20), fully integrated (ELFORM = 2) solid elements.

The support plate nodes and ground nodes were constrained in all three coordinate directions. Additionally, as opposed to applying displacement boundary conditions to nodes on the specimen, an impactor mass was modeled using rigid (MAT20), fully integrated (ELFORM = 2) solid elements. The thickness of the impactor mass was adjusted to be slightly less than the gap between the support plates but more than the thickness of the specimen. An initial downward velocity of 168 in./s was applied to the impactor mass, and displacement in lateral directions was constrained. The density of the simulated impactor was adjusted to ensure it had the same weight as the experiment impactor (96.8 lbf).[5] Figure 53 shows the model parts at the beginning of the simulation.

[5]The correct platen mass of 96.8 lbf was used in the MAT213 flat specimen simulations; see Table 21 for reference to experimental platen mass values.

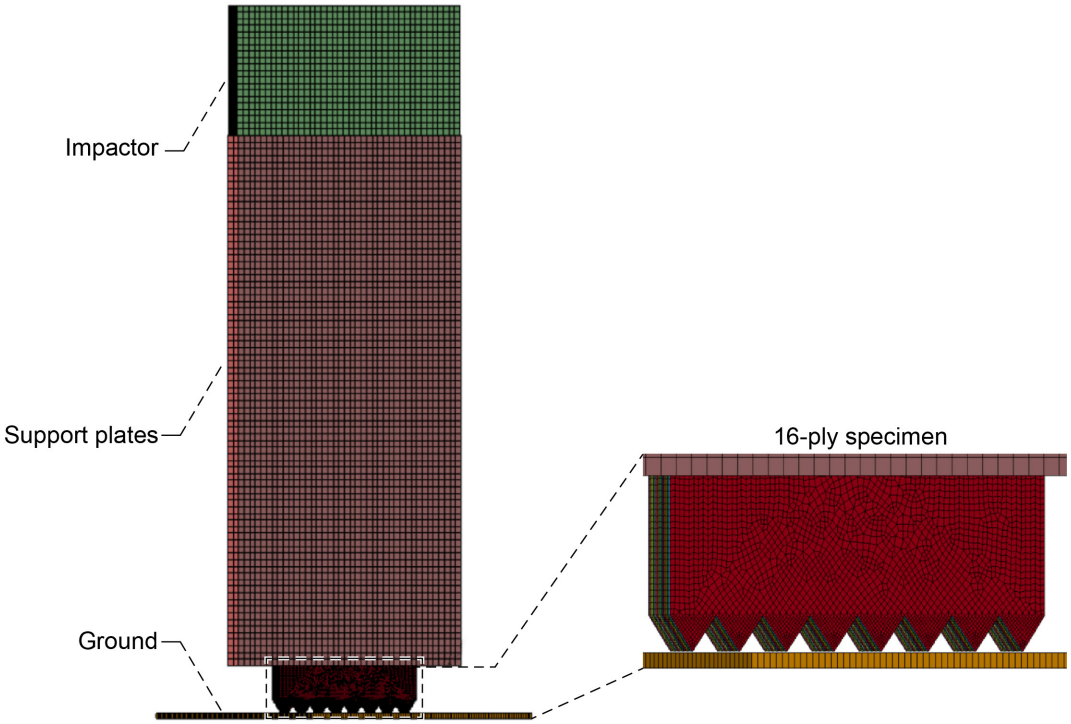

Figure 53.—Flat-plate crush model setup at start of simulation.

The composite laminate was modeled with 16 layers of shell elements, with each layer representing one ply of the laminate. Each ply was modeled using fully integrated linear shell elements (ELFORM = 16) with two integration points through the thickness. Because the flat-plate crush specimen had the same thickness throughout its entire volume, a thickness of 0.007158 in. was defined for all shell elements. As shown in Figure 54, the majority of the flat-plate specimen had a nominal element size of 0.002 by 0.002 in. The trigger region had a finer mesh, with a nominal element size of 0.001 by 0.001 in. The trigger mesh was refined because preliminary models showed non-ramp-like loading with a coarser mesh.

The mesh was generated using the AutoMesher in LS–PrePost® (Livermore Software Technology Corp.), and the trigger mesh was manually refined using the split tool in LS–PrePost®. Some nodes on the left and right side of the mesh that were initially co-linear were manually offset in the vertical direction to create a zigzag pattern, which was found to help promote stable crushing. Similarly, nodes of different plies through the thickness were offset relative to other plies (i.e., the vertical coordinates of nodes in ply 1 were different than the vertical coordinates of nodes in ply 2, ply 3, etc.).

Flat Crush Coupon Material Model.—Four MAT213 material cards were used to define the four ply orientations: 0°, 45°, −45°, and 90°. Each of the four material cards contained the same parameters except for the AOPT parameters, which define the material orientation with respect to the global coordinate system (AOPT = 2). A Rayleigh damping coefficient (*DAMPING_PART_STIFFNESS) of 0.05 was applied to all shell plies, which was shown to stabilize single-element models in preliminary MAT213 studies. MAT213 material card parameters are described in detail in Section B.7.

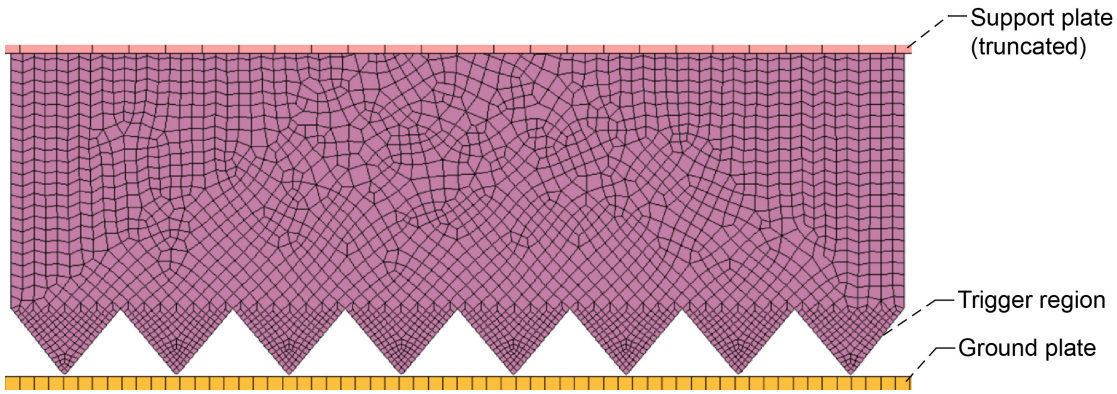

Figure 54.—Mesh of simulated flat-plate crush specimen with finer elements in trigger region.

Contacts and Delamination Modeling.—Several contact cards were used to properly define the contacts between the various parts of the flat-plate crush model. An *AUTOMATIC_NODES_TO_SURFACE contact was defined between the impactor elements and the part set that included all the specimen elements. Two *AUTOMATIC_SURFACE_TO_SURFACE contacts were defined between the specimen support plates the part set that included all the specimen elements. An *ERODING_NODES_TO_SURFACE contact was defined between the part set that included all the specimen elements and the ground. Additionally, an *ERODING_SINGLE_SURFACE contact was defined for the part set that included all the specimen elements to prevent interply penetration after delamination occurred. In each of these five contacts, the coefficient of static friction was defined as 0.5 and the coefficient of kinetic friction was defined as 0.4, following guidance from Reference 24. Also, for all five contact definitions, pinball-segment-based contact (SOFT = 2) was used with SBOPT = 5 and DEPTH = 23.

Delamination was modeled using 15 *AUTOMATIC_SURFACE_TO_SURFACE tiebreak contacts between each pair of side-by-side ply pairs. Segment sets were defined for each ply, and the tiebreak contacts were applied to the segment sets. Option 11 was used in the tiebreak contact definitions for bilinear traction–separation law. The peak tractions (NFLS = 1,425; SFLS = 22,500), energy release rates (ERATEN = 1.85; ERATES = 4.44), and initial stiffnesses (CT2CN = 228.58; CN = 562,600) were based on experimentally measured data from Arizona State University tests conducted on unidirectional IM7/8552 and data from a NASA/Boeing collaboration (Ref. 25). Penalty formulation (SOFT = 0) was used for the tiebreak contacts with default values.

Computation.—The MAT213 flat-plate crush simulations were run using LS–DYNA® developer version MPP (massively parallel processing) R13 using double precision and 140 processors. The simulation runtime was 62 h, which corresponded to a total simulation time of 12 ms and a crush displacement of 1.45 in. For comparison, the same model run with MAT58 instead of MAT213 was about 4 times faster.

4.3.3 Flat Crush Coupon Simulation Results: Calibration of Flat-Plate Specimen Model Using Laminate $[90_2/0_2/\pm45/0_2]_S$ (HL01)

A flat-plate specimen model was calibrated using laminate $[90_2/0_2/\pm45/0_2]_S$ (HL01). One representative experimentally measured force–displacement curve is shown in Figure 55 along with the simulated force–displacement curve (and two filtered versions of the simulation results). The simulated force is the contact force between the specimen and ground. The simulated contact force is recorded at a rate of 1×10^6 Hz (one data point per μs). The displacement is the vertical displacement of one of the nodes along the top of the specimen and is recorded at a rate of 1,000 Hz. Two low-pass Butterworth

filters were applied to the simulated force data to remove noise in the force data and to compare different filtering cutoff frequencies (8,000 and 2,500 Hz). A platen mass of 43.9 kg was used for the flat coupon simulations, which corresponds with the experimental platen mass listed in Table 21.

In general, the raw data curve and the two filtered curves have comparable initial slopes in the region from zero load to the peak force and stable crushing force (the force in the plateau region well after the peak force). The curve filtered with a cutoff frequency of 2,500 Hz best matches the experimental data, and a fast Fourier transform (FFT) analysis of the experimental force data shows that there is little contribution from frequencies above 2,100 Hz. Force–time curves for the experiment, unfiltered simulation, and filtered simulation (2,500 Hz cutoff) are shown in Figure 56. The filtered force–time curve is about 10 percent lower than the experimental result; however, only about 60 percent of the test was simulated. The simulation was manually terminated prematurely to conserve computational resources. The last 40 percent of the test (time-wise) accounts for only 12 percent of the crush displacement because of the low velocity of the impactor at the end of the test.

The unfiltered model data are plotted along with a filtered curve that used a low-pass Butterworth filter with a cutoff frequency of 2,500 Hz. One of the three experimentally measured curves is also plotted for comparison. The curve is shown over the timespan of the simulation (Figure 56(a)) and over the timespan of the entire experimental test (Figure 56(b)).

The simulated impactor displacement–time curve and corresponding experimentally measured curve are shown in Figure 57. Similar to the force–time history, the simulated and experimentally measured data are comparable up to the point of simulation termination.

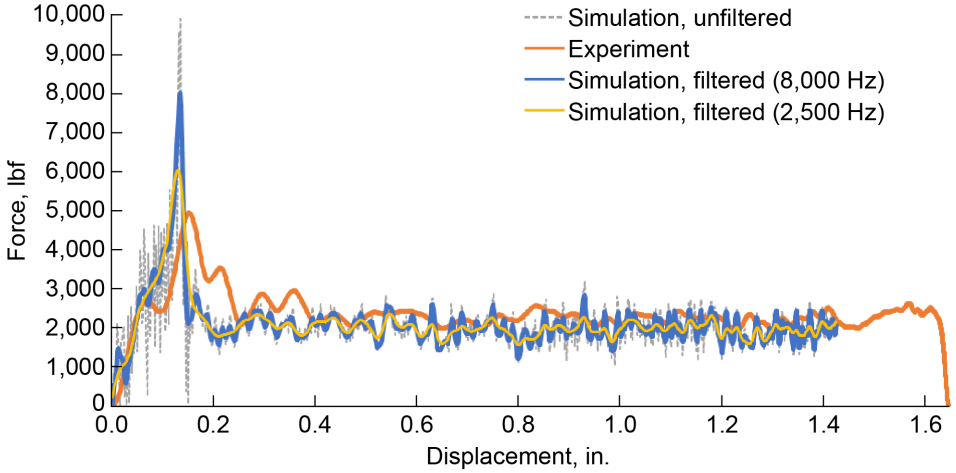

Figure 55.—Force–displacement curves for MAT213 flat-plate crush simulation of $[90_2/0_2/\pm45/0_2]_S$ laminate (HL01).

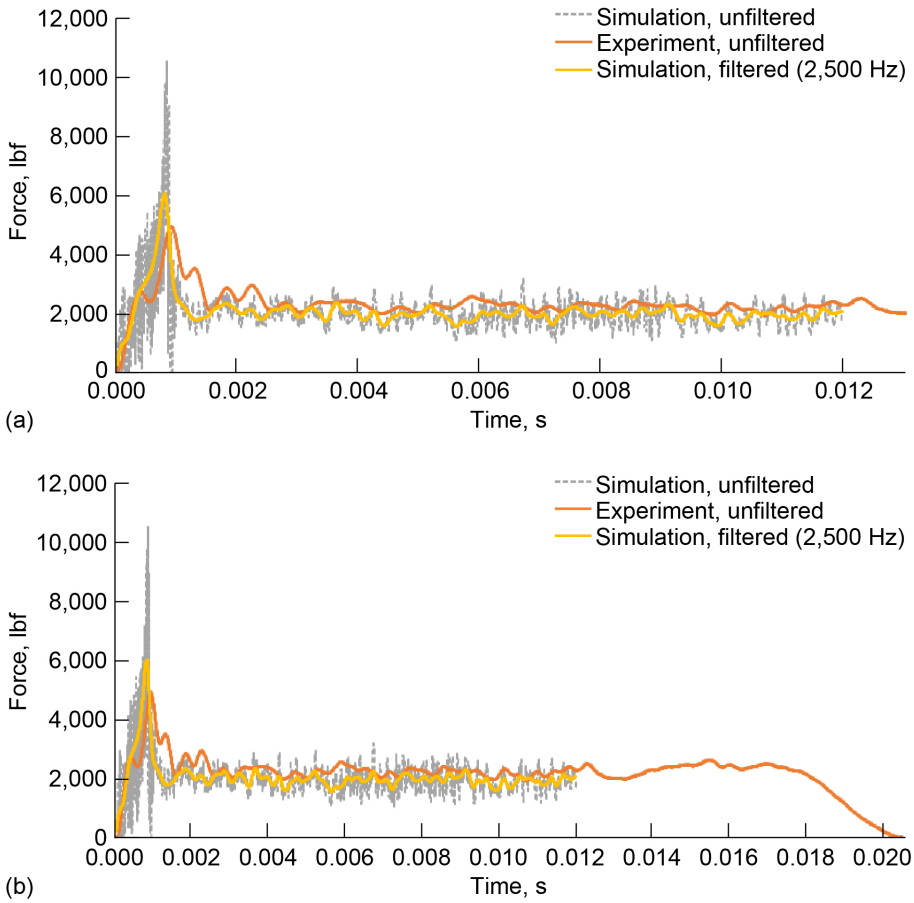

Figure 56.—Force–time curves for MAT213 flat-plate crush simulation of laminate $[90_2/0_2/\pm45/0_2]_S$ (HL01). (a) Simulation timespan. (b) Full experiment timespan.

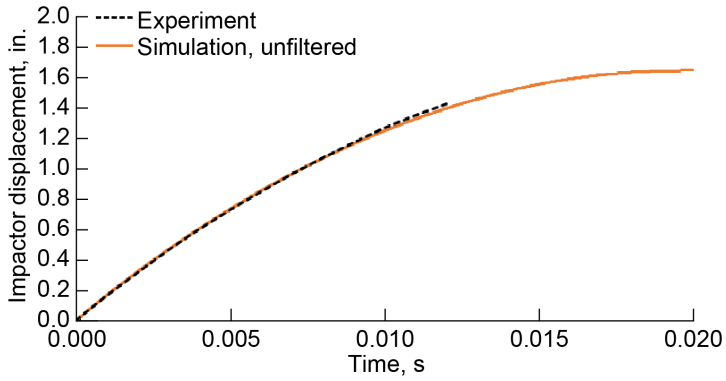

Figure 57.—Impactor displacement–time curve for MAT213 flat-plate crush simulation of laminate $[90_2/0_2/\pm45/0_2]_S$ (HL01) compared with experimentally measured curve.

Integrating the force–displacement curves of the experimental data and simulation data gives the cumulative energy absorption curves shown in Figure 58. The curves generally overlap during the crushing of the trigger; however, the force in the region near the peak force of the model is slightly higher than that of the experiment, which leads to more energy absorbed in the model at around 0.15 in. of crush displacement. After the peak force, the stable crushing force of the model is slightly lower than that of the

experiment, which explains the lesser slope of the model in the linear part of the absorption curve that corresponds to the stable crushing region.

The SEA is calculated using Equation (1), where P is the crushing force, δ is the crush displacement, and μ_L is the mass per unit length of the specimen.

$$SEA = \frac{\int_{\delta_i}^{\delta_f} P \, d\delta}{\mu_L \delta_f} \tag{1}$$

The initial crush displacement, δ_i, is 0—that is, Total SEA is calculated from zero load onward as opposed to only considering the stable crushing regime. The final crush displacement, δ_f, is the last recorded displacement for the simulation and is the crush displacement corresponding to complete unloading of the specimen in the experimental data. Using this methodology, the SEA of the three experimentally tested specimens and the model are shown in Figure 59. The mean SEA of the experimental specimens was 56.8 J/g and the SEA of the model was 50.1. The lower SEA of the model is related to its lower stable crushing force as compared with the experimental data. The change in SEA relative to the δ_f is illustrated in Figure 60.

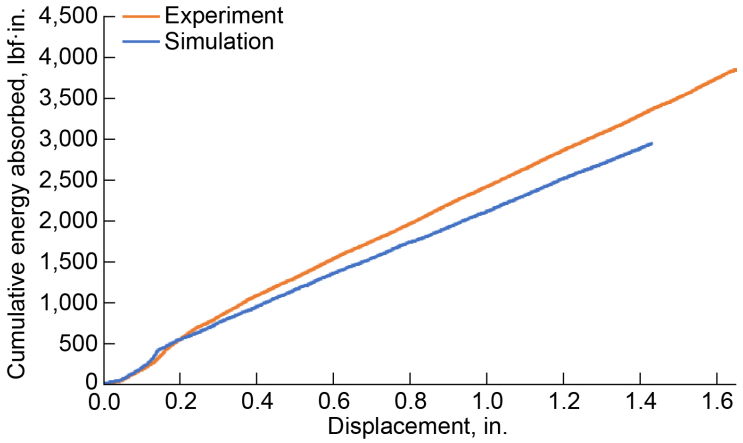

Figure 58.—Cumulative energy absorbed versus crush displacement curve for MAT213 flat-plate crush simulation of laminate $[90_2/0_2/\pm45/0_2]_S$ (HL01) compared with experimentally measured curve.

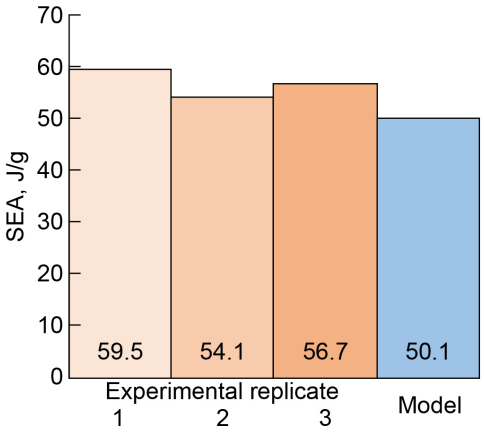

Figure 59.—Comparison of SEA values measured for three experimental replicate specimens with simulated SEA.

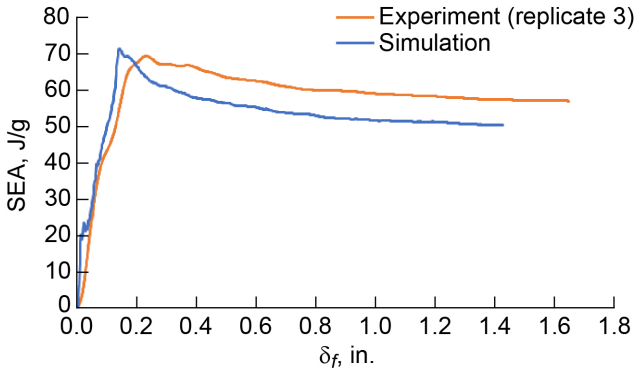

Figure 60.—SEA calculated at various final crush displacement δ_f values using experimental and model datasets.

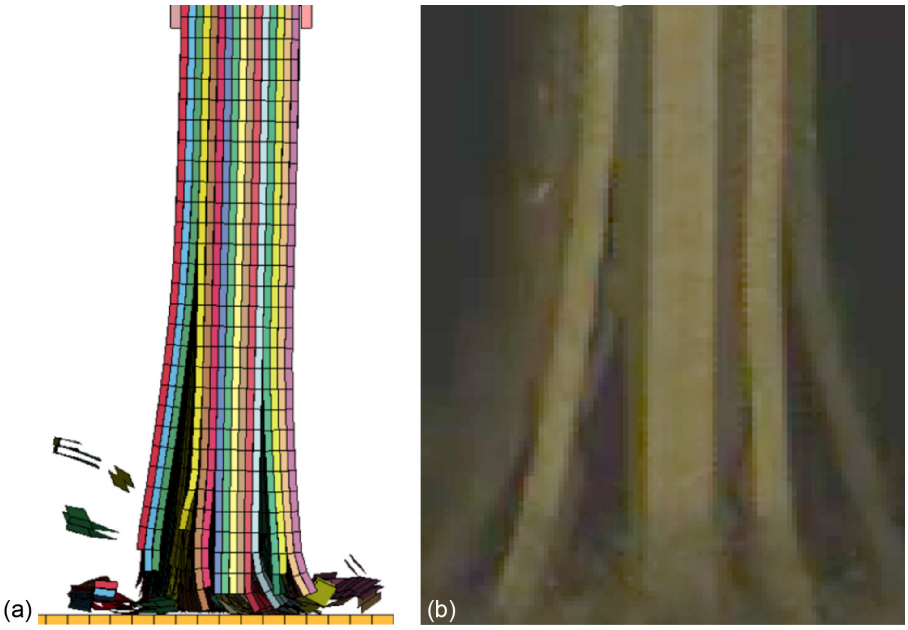

Figure 61.—Edge-on view of flat-plate crush test simulation. (a) Simulation with shell element thicknesses artificially shown (via postprocessing). (b) Frame from high-speed test video.

A comparison of the simulated failure mode is shown next to a frame from the experiment high-speed video in Figure 61. Both simulation and experiment show delamination cracks, splaying of outer-layer plies, and crushing of inner-layer plies.

Using the energies recorded in the simulation, the contribution of each energy absorption mechanism can be calculated and compared, as shown in Figure 62. The internal energy represents the elastic and plastic strain energy in elements that have not been eroded. Eroded internal energy is the energy removed from the model when an element of the specimen is eroded, and friction energy is energy loss due to friction between contacts. The contribution to frictional energy loss of each contact surface that had significant friction is plotted in Figure 63. The surface contributions include the sum of the friction between the 15 adjacent ply pairs (“interply”), the sum of the friction between the outer plies and the specimen support plates (“support plates”), and the friction between the specimen and the ground (“ground”).

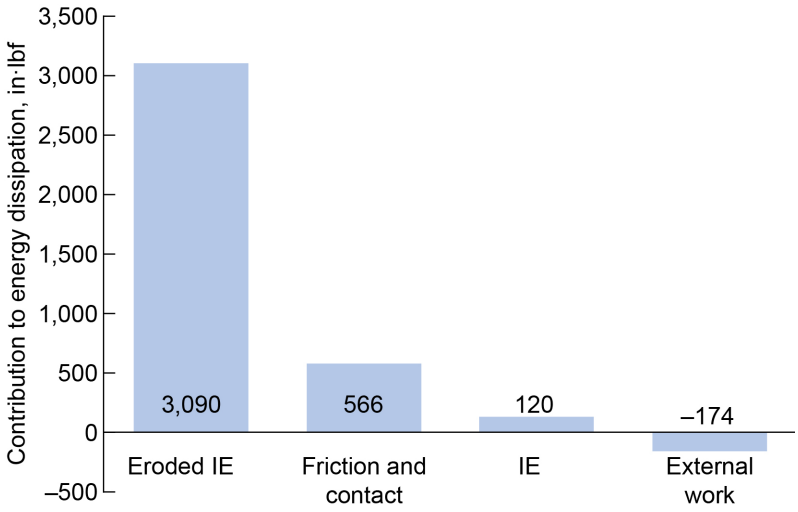

Figure 62.—Contribution of internal energy (IE), eroded IE, and friction in simulation at final crush displacement δ_f; external work due to gravity included for comparison.

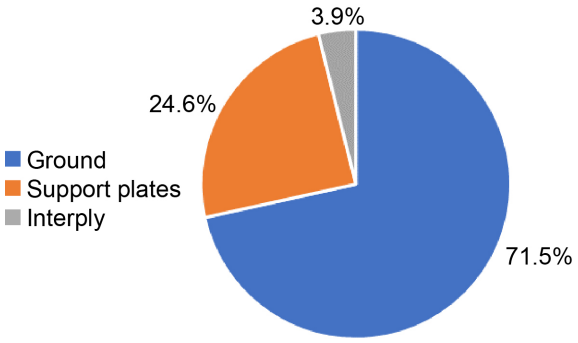

Figure 63.—Contribution of contact surfaces to total friction energy.

In the simulation, the majority of energy absorption is due to element erosion, although friction and internal energy are non-negligible. While there is moving debris (disconnected elements that have not eroded) in the simulation, the mass of these elements is low compared with the rest of the model, which results in negligible kinetic energy contributions to energy dissipation. External work is related to the work done by gravity and is negative in comparison of energy dissipation mechanisms because gravity adds energy to the system.

A second simulation of the flat-plate specimen was performed using HL02; detailed results are reported in Section B.7.5. This simulation was considered predictive because the same model was used as the calibration case except that the stacking sequence of the plies was altered.

4.3.4 Drop Tower Simulation of C-Channel Specimen Using Laminate HL01

A model of the drop tower experiment performed with C-channel specimens was created based on the test conditions as shown in Figure 64, and a portion of the mesh is shown in Figure 65. Similar to the calibrated flat-plate specimen models, the C-channel model has 16 individual shell-element layers to represent the plies. A bevel-shaped crush trigger was applied to the model using a ply-drop approach. All

nodes in the bottom 0.5 in. of the specimen are fixed to represent the region of the specimen potted in epoxy for experiments. An *ERODING_NODES_TO_SURFACE contact was defined between the impactor and the C-channel, and an *ERODING_ SINGLE_ SURFACE contact was defined between each of the adjacent ply pairs. The tiebreak contacts were the same as those used in the calibrated flat-plate simulation; however, IGNORE = 1 was used in *CONTROL_CONTACT to ignore initial penetrations caused by the use of stacked-shell elements in a curved geometry. A platen mass of 113 kg was used for the C-channel simulation with an impactor velocity of 7.6 m/s, and a platen mass of 144 kg was used for the C-channel simulation with an impactor velocity of 3.8 m/s; these values correspond with the experimental platen mass and velocity pairings listed in Table 21.[6]

The simulated force–displacement curve of the C-channel simulation is shown in Section B.7.6 (Figure B.52). Visualizations of the failure mode of the C-channel simulations are shown in Figure 66. The edges of the simulated specimen failed similarly to the flat-plate specimens. In the middle of the C-channel cross section, there was significant delamination occurring that did not occur in the legs or the corners. Thus, there was a tearing action in the simulated C-channel specimen where the delamination of the middle region meets the corner.

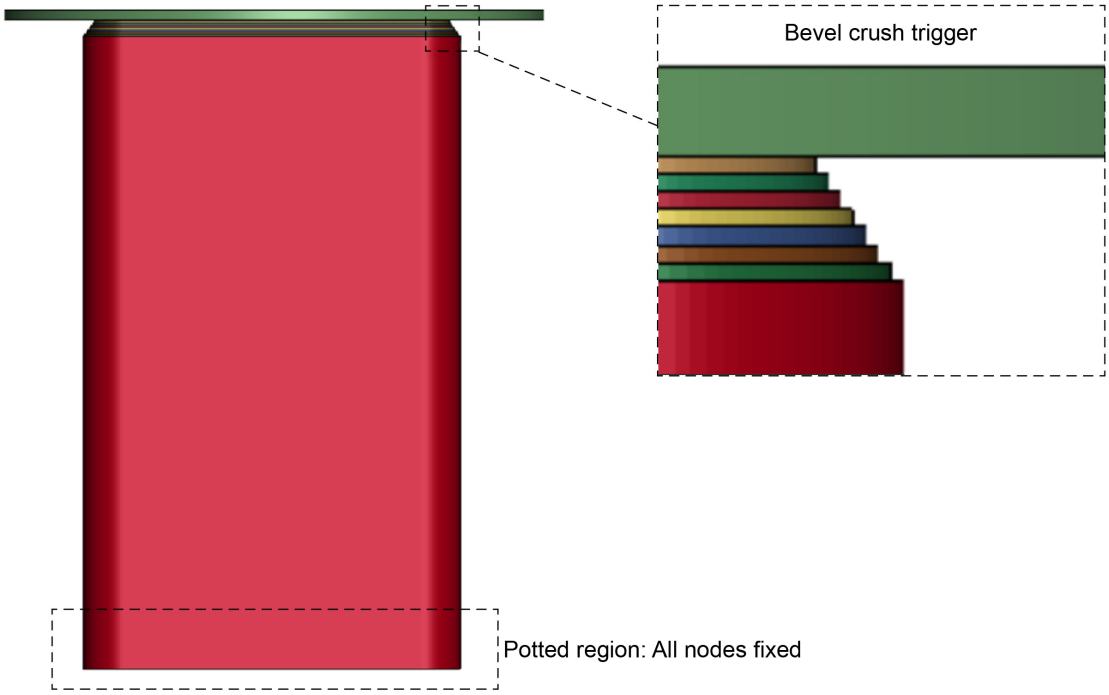

Figure 64.—Model of C-channel simulation including solid-element impactor and C-channel specimen modeled with 16 individual shell-element plies.

[6]The correct platen mass and velocity pairings were used in the MAT213 C-channel specimen simulations; see Table 21 for reference to experimental platen mass and velocity values.

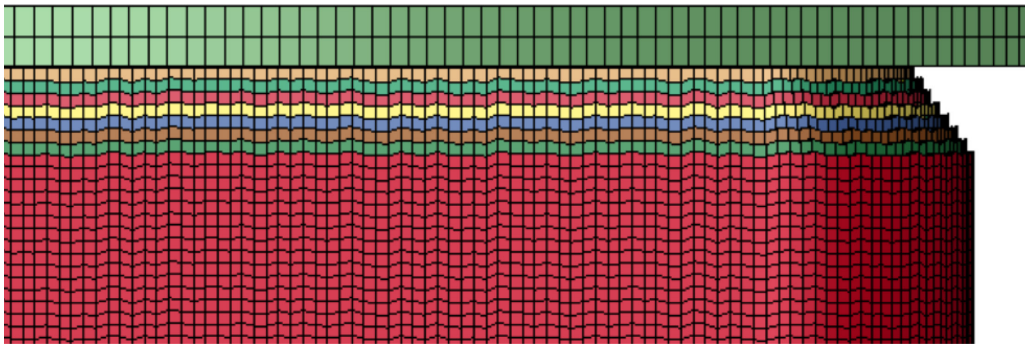

Figure 65.—Mesh of C-channel simulation and impactor.

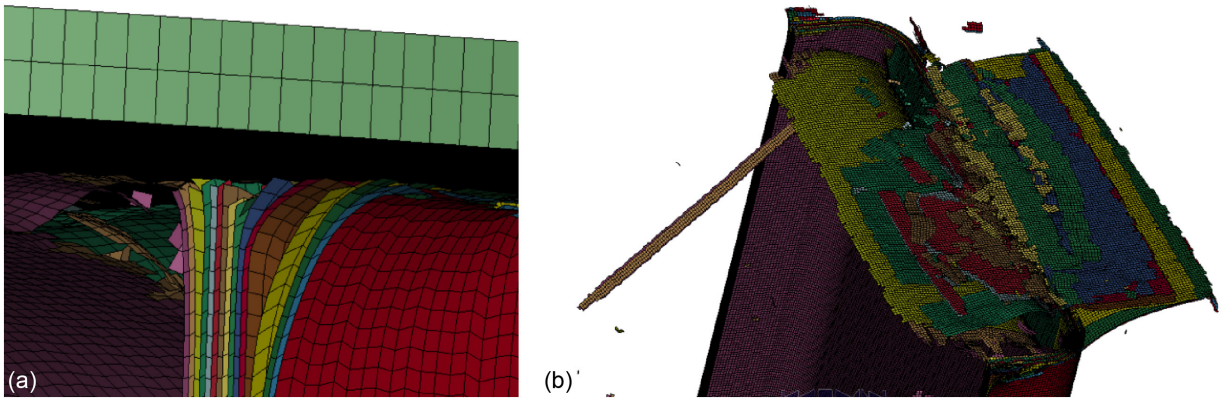

Figure 66.—Visualizations of failure mode in C-channel drop tower simulations. (a) Closeup of specimen edge. (b) Angled view of specimen top (with impactor hidden).

4.3.5 Lessons Learned From Troubleshooting and Calibration

Several iterations of preliminary models were performed before a successful model was produced. Thus, several lessons were learned that could be reported for future modeling efforts when utilizing MAT213 for crush simulations. It is highly recommended that single-element studies be conducted using the desired MAT213 card and corresponding input curves before attempting any multi-element model. In initial attempts at creating the full-scale flat-plate crush model, it was found that verifying and troubleshooting the model parameters (e.g., contact definitions, boundary conditions, mesh size, mesh pattern, AOPT material orientation parameters, damage and failure/erosion parameters, and data outputs) was more efficient in MAT58, which has less computational cost than MAT213. Additionally, initial models showed that setting postpeak stress plateaus at 10 percent of the peak stress in all five principal material directions sometimes led to unexpected behavior in multi-element models. For crush models, use of postpeak plateaus at ≥80 percent of the peak stress in compression material-law curves is recommended.

A few observations made in MAT58 and MAT213 suggest that these recommendations may apply to other material models. Models with element edges parallel to the ground tended to splay or delaminate at forces lower than those measured experimentally. Editing the mesh to have element sides not parallel to the ground tended to improve the agreement of model results with experimental results, especially considering initial stiffness, delamination and splaying, and stable crush force. Furthermore, ensuring that rows of nodes were not perfectly aligned (i.e., offsetting adjacent nodes to be at different vertical coordinates) tended to alleviate the load–unload behavior commonly observed in FE composite crush models and generally produced results closer to the experimental data as compared to models with aligned element rows. Lastly,

erosion strain is an important parameter that requires calibration. Preliminary models showed that, to best match the experimental crush force data, the optimal erosion strain should vary with element size.

Modeling delamination correctly was paramount to producing a successful crush model that relied on individual shell plies (as opposed to one shell element through the thickness). Initially, the bilinear traction–separation laws in modes I and II were not fully defined by the data in the literature; only the area under the bilinear curves (fracture toughness G_{Ic} and G_{IIc}) was measured. With the addition of measured traction–separation curves using a methodology developed in Reference 25, the tiebreak contacts better matched the behavior of the experiment while also ensuring the crushing force was accurate.

4.4 LS–DYNA® MAT219

This section presents the continuum damage model CODAM2, MAT219 in LS–DYNA®, developed by the University of British Columbia (UBC) Composites Research Network, and includes application of this model to various test cases in order to assess its predictive capabilities for the crush performance of fiber-reinforced composite structures within RR–3. The underlying building-block methodology has been developed in a research collaboration with DLR, the German Aerospace Center (Refs. 26 to 30). DLR's analysis results are presented in Section 4.8.

This section provides an outline of a simulation methodology to study progressive crushing of composite structures; this methodology includes use of intermediate coupon-level fracture tests to calibrate damage parameters. The modeling capabilities and limitations identified in the scope of the RR–3 analyses are also discussed in this section.

A short description of the CODAM2 composite damage model that is implemented as the built-in material card MAT219 in LS–DYNA® is provided in Section B.7.6.

4.4.1 Input Data and Assumptions

The material elastic and strength properties, or input data, used in the RR–3 analyses were based on the material model-specific parameters for state-of-the-art progressive damage models as presented in Section 5.2.3 (Table 16). The effective tensile and compressive fiber fracture energies (or damage saturation strains) at the ply level were back-calculated (calibrated) using simulations of over-height compact tension (OCT) and compact compression (CC) tests, respectively, carried out on quasi-isotropic laminated specimens as described in the following sections. A description of these tests and experimental data generated from them for the European IM7/8552 material system (with fiber areal density of 134 g/m^2) is provided in Reference 3.

4.4.2 Simulation Methodology

The building-block methodology to predict progressive crushing of composite structures is shown in Figure 67. In addition to the three commonly used levels (coupon, subcomponent, and component), a purely virtual level is also considered whereby the material response is assessed and calibrated at the ply scale and the laminate scale in tension and compression, respectively.

In particular, single-element simulations at the ply level were used to verify the implemented material model. Single-element laminate simulations were performed to assess the macroscopic behavior predicted by the ply-based material model. Simulations of progressive fracture tests were then correlated with corresponding experimental data to calibrate the effective ply-level fiber fracture energies. Such methodology enables the true prediction of the structural response of fiber-reinforced composites at the subcomponent level given that all numerical parameters are thoroughly determined and verified in previous assessments at lower levels.

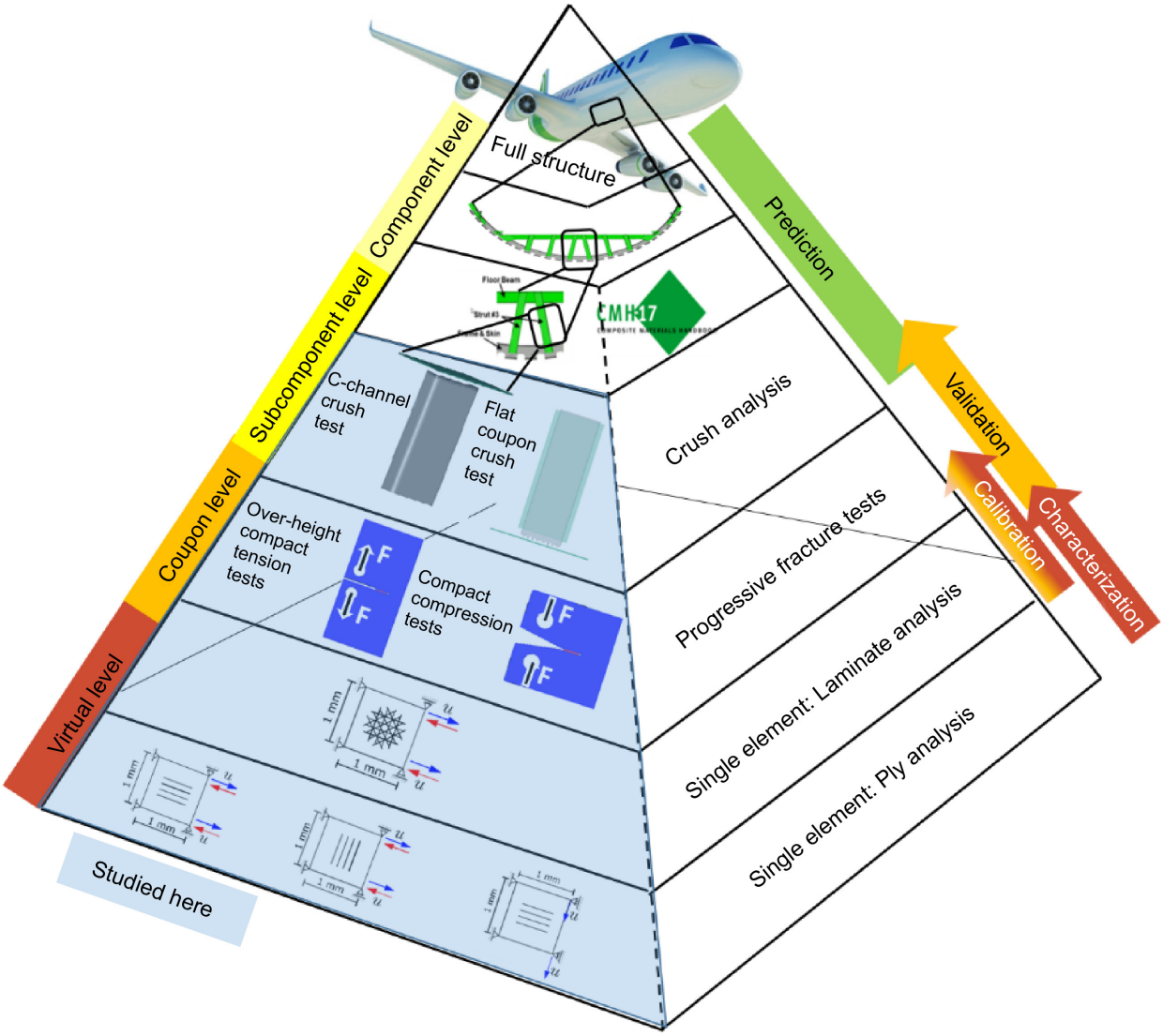

Figure 67.—Modified building-block approach used to predict progressive crushing of composite structures using MAT219 material model. Blue shading indicates levels studied in RR–3.

In the presented study, the focus is on the progressive crush behavior of flat coupon and C-channel composite structures. Results obtained from flat coupon simulations are compared with experimental data. Simulation results for the crushing of C-channel composite structures (presented in Section B.7.6) are considered to be pretest predictions as part of the RR–3 analysis exercise. Note that the composite laminate is discretized using one single-shell element layer through the thickness at all levels of the building block. This efficient modeling technique enables the simulation of large-scale structures at the subcomponent level and beyond.

4.4.3 Model Verification Using Single-Element Simulations

Verification of the principal behavior and implementation of the material model is considered on the virtual level of the building block. Simulations of single-element models with unidirectional plies represent the material behavior in the two principal material directions. Figure 68 presents stress–strain

curves obtained from single-element simulations under uniaxial strain conditions in tensile, compressive, and shear loadings, respectively. The tensile/compressive behavior in the fiber direction (0°) is shown in Figure 68(a), illustrating that CODAM2 (MAT219) incorporates linear softening behavior governed by damage initiation and saturation strains as outlined in Section B.8.1 (Eq. (B.30)).

The area under each stress–strain curve represents the fiber fracture energies; these will be further discussed at the coupon level. Matrix behavior under transverse (90°) tensile and compressive loading is shown in Figure 68(b). Here, it is assumed that the matrix material behaves linear elastically followed by instantaneous (brittle) failure. Unidirectional ply behavior under shear loading is shown in Figure 68(c). The built-in material card MAT219 considers linear elastic behavior in shear; however, it is well known that CFRP materials show nonlinear shear behavior due to the evolution of microscopic damage and plastic effects emanating from the constitutive behavior of the polymeric matrix.

To understand how these unidirectional properties translate into the structural response of the laminate, a single-element study of a quasi-isotropic ($[0/45/90/–45]_S$) laminate layup is considered under both tensile and compressive loadings. Figure 69 shows the stress–strain response at the laminate level obtained from the MAT219 input data at the ply level in single-element simulations under uniaxial strain conditions. The fracture energy of the laminate, G_f, is determined as the area under each stress–strain curve in tensile and compressive load cases, respectively. Considering the building-block approach shown in Figure 67, these fracture energies will be compared with values obtained from physical and virtual fracture tests at the coupon level.

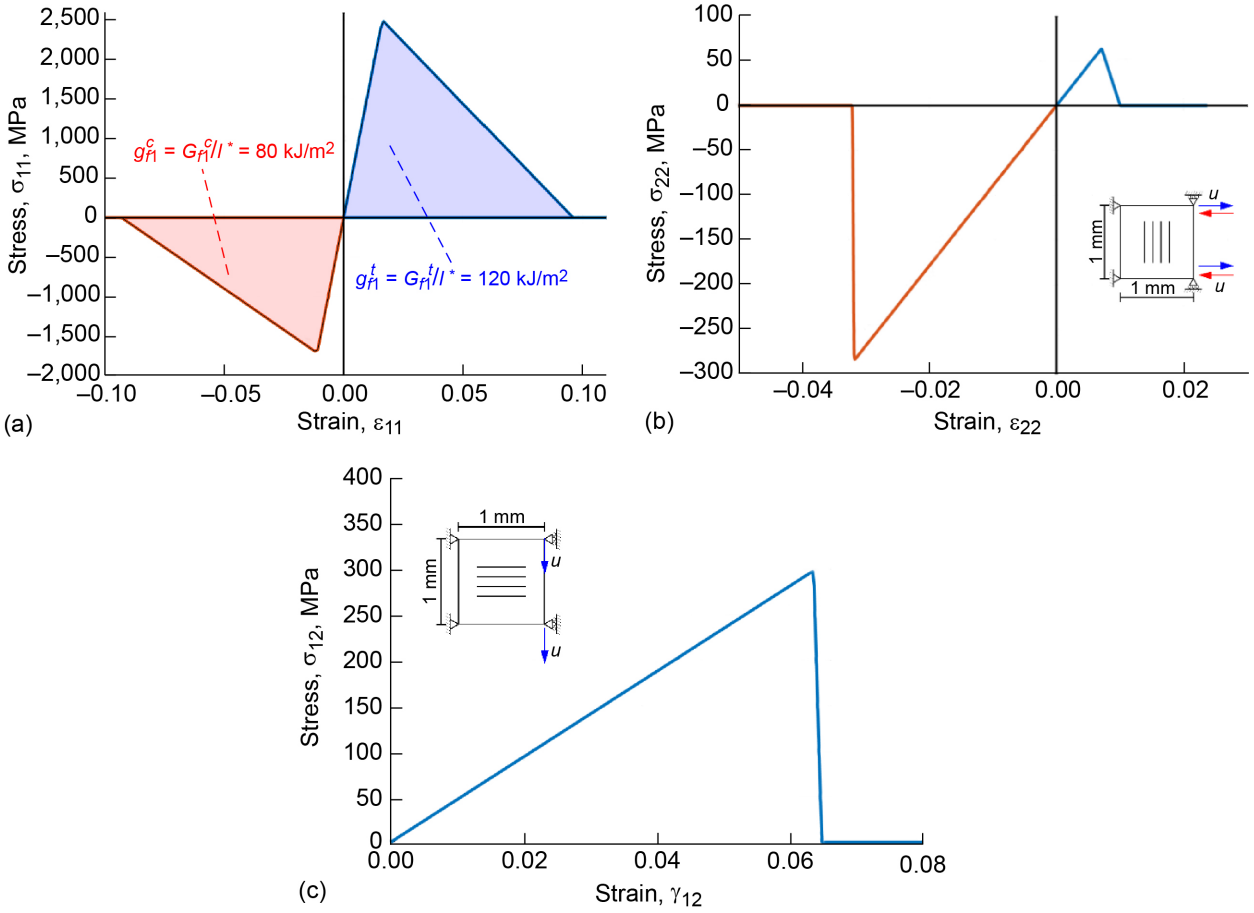

Figure 68.—Stress–strain curves of single-element simulations under uniaxial strain conditions for (a) longitudinal (0°) tensile and compressive loading, (b) transverse (90°) tensile and compressive loading, and (c) shear loading.

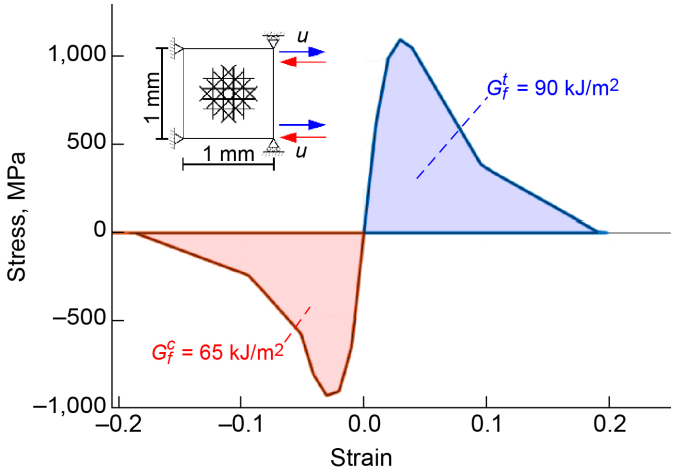

Figure 69.—Stress–strain curves of single-element simulations representing quasi-isotropic $[0/45/90/–45]_S$ laminate under uniaxial tensile and compressive strain.

The results obtained from the single-element simulations provide a fundamental understanding and illustration of the underlying material model MAT219 in LS–DYNA®. These results further show the stress–strain response of a quasi-isotropic laminate in tension and compression on the basis of ply-based input data. These findings will be useful to discuss capabilities and limitations of the material model when applied to higher levels of the building block.

4.4.4 Simulation of Progressive Fracture Tests

Coupon-level tests of the building-block approach consist of progressive fracture tests of quasi-isotropic $[90/45/0/–45]_{4S}$ IM7/8552 laminates in tension and compression, respectively. Based on experimental data, these tests are used for calibration of the input data for the longitudinal (fiber) fracture energy, G_{f1}. This assumes that these tests lead to stable progression of fiber-dominated damage modes, and hence G_{f1} values will govern the structural response. Thereby, the tensile fiber fracture energy G_{f1}^t is calibrated using OCT test results, whereas the compressive fiber fracture energy G_{f1}^c is extracted from CC tests.

The tests were previously performed at UBC; results are presented in Reference 31. These experimental tests used the European version of IM7/8552 with an areal density of 134 g/m^2, as compared with the U.S. version's 190 g/m^2, which was considered at higher levels of the building block in flat coupon and C-channel crush specimens.

The laminate fracture energies at the coupon level (as determined in Section B.7.6) can be directly compared with the values obtained from the single-element study at the virtual level of the building block, shown in Figure 69. Table 9 summarizes the results for the two simulation strategies. It can be seen that both simulation types lead to similar predictions of the laminate fracture energy, with a maximum difference of 11 percent in tension and 18 percent in compression. The higher discrepancy in compression can be attributed to the difference in unloading behavior between simulation and experiments.

Overall, the results imply that single elements can be evaluated to calibrate fiber fracture energies. In contrast to the simulations of the progressive fracture tests, these models are simple to set up at very low computational cost. It should also be noted that the postpeak force level from CODAM2 simulations is slightly lower than values obtained from experimental data in the CC tests.

TABLE 9.—COMPARISON OF LAMINATE FRACTURE ENERGIES IN SINGLE-ELEMENT STUDY (FIGURE 69) AND FRACTURE TESTS (FIGURE B.53)

	Single element study, kJ/m^2	Fracture tests, kJ/m^2	Difference, %
Tension	90	102	11
Compression	65	53	18

The calibrated ply-based fiber fracture energies are used in the subcomponent level of the building-block approach, which considers crushing of flat coupon samples (presented in Section 4.4.5) and C-channel specimens (presented in Section B.8.3).

4.4.5 Simulation of Progressive Axial Crushing of Flat Coupons

The first test considered at the subcomponent level of the building block is the investigation of flat CFRP coupon samples under axial crushing. As illustrated in Figure 70, the top row of elements of the composite specimen is subjected to a prescribed velocity $v = 4$ m/s. Two rigid support plates guide the vertical movement of the flat coupon CFRP plate before it impacts a rigid plate. In addition, a resin-embedded clamping in the upper 20 mm of the flat coupon specimen is applied by constraining the lateral, translational DOFs (y, z). The mass of the impactor was not considered in the crush simulation of the flat coupon, as the analysis was performed quasistatically, requiring only a constant velocity be specified as a boundary condition.

A sawtooth trigger at the impacted end of the flat coupon specimen helps to achieve the simulation of stable progressive crushing. Friction between the specimen and the impact plate was modeled with a friction coefficient of $\mu_F = 0.2$, whereas the contact of the flat coupon specimen and the support plates was assumed to be frictionless. Based on related mesh type studies carried out by DLR and presented in Section 4.8, a skewed mesh type was selected for the flat coupon model with 10° inclination angle of the element edges. The characteristic length of the elements is $l^* = 1.0$ mm. As described earlier, the composite plate is modeled using a single-shell element through the thickness. A detailed mesh sensitivity analysis can be found in Reference 32.

Existing experimental data presented in Section 5.6.1 is used to assess the capability of CODAM2 to simulate progressive crushing. Experiments included numerous quasi-isotropic and hard laminates with varying layup sequences and various gap heights. Compared with quasi-isotropic laminates, hard laminates contain more plies in the 0° direction to enhance energy absorption capabilities by fracturing the fibers. The continuum modeling technique is insensitive to the layup sequence. For comparison of force–displacement response, one set of experimental data will be considered for each laminate configuration.

Figure 71 shows the experimental force–displacement response of two laminates made from IM7/8552: one quasi-isotropic laminate with stacking sequence $[90/\pm45/0]_{2S}$ (QI01) and one hard laminate with stacking sequence $[90_2/0_2/\pm45/0_2]_S$ (HL01). Figure 71 compares these datasets with unfiltered numerical results obtained from CODAM2 simulations where contact forces were evaluated at the impact plate. It can be seen that CODAM2 predicts slightly lower force values as compared with the experimental data. This is consistent with previously investigated fracture tests at the coupon level, where simulations of CC tests yielded lower force values as compared with experimental measurements.

The Total and Stable SEA were calculated according to Equations (1) and (3), respectively. (See Ref. 33 for a full description of Total and Stable SEA.) Stable SEA values were determined for the crush displacement range from 10 to 30 mm, which is in the range of stable steady-state crushing. Table 10 summarizes these quantities, including the calculation of the crush efficiency, which is defined as the ratio of the average crush force to peak crush force. In addition to Stable SEA (10 to 30 mm displacement), Total SEA (0 to 30 mm displacement) was evaluated.

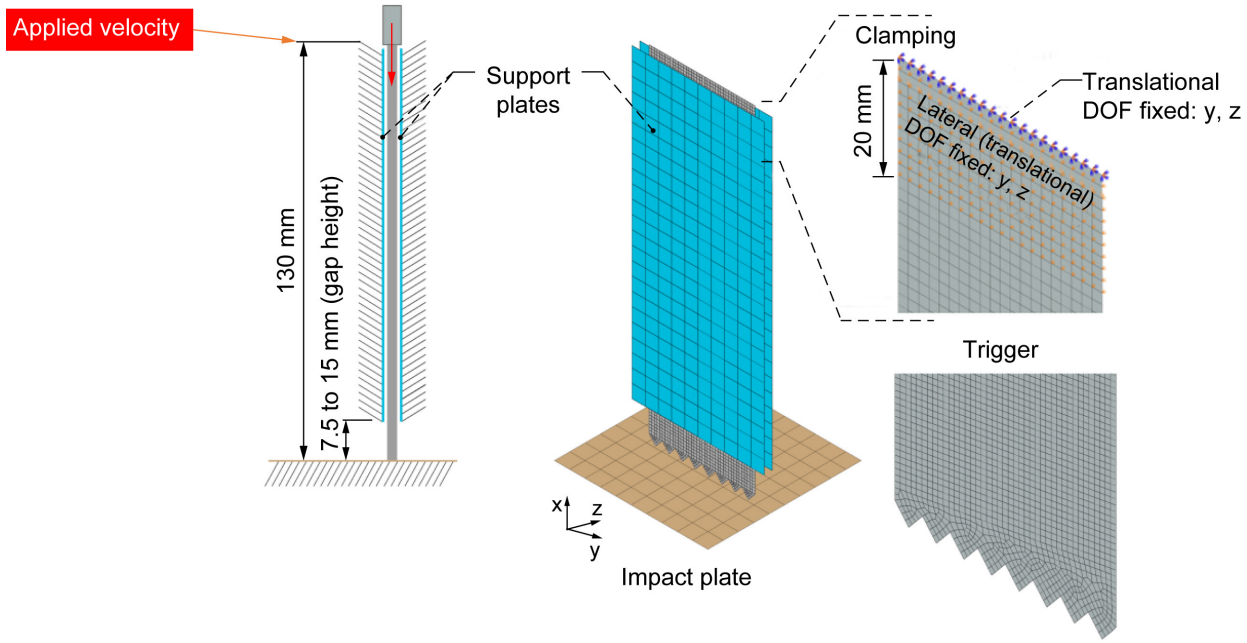

Figure 70.—Finite element model for simulation of flat coupon specimen crushing.

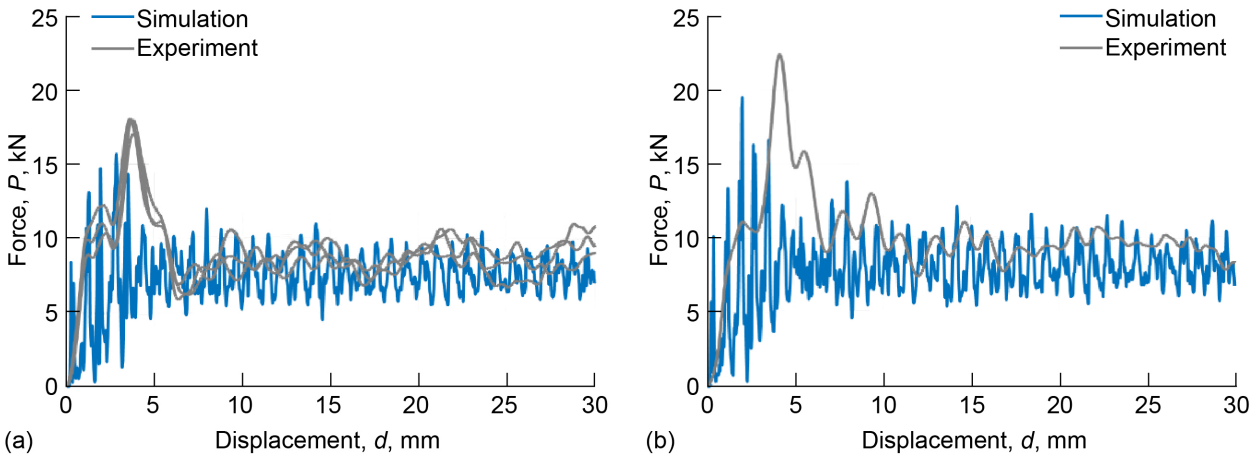

Figure 71.—Prediction of flat coupon crushing response compared with experimentally measured force–displacement data for composite laminates. (a) Quasi-isotropic laminate $[90/\pm45/0]_{2S}$ (QI01). (b) Hard laminate $[90_2/0_2/\pm45/0_2]_S$ (HL01).

TABLE 10.—SUMMARY OF PREDICTIONS OF FLAT COUPON CRUSHING

	Quasi-isotropic laminates		Hard laminates	
	Simulation	Experiment	Simulation	Experiment
Peak crush force, kN, unfiltered	15.7	17.7	19.4	22.4
Average crush force, kN (10 mm ≤ d ≤ 30 mm)	7.6	8.7	8.2	9.4
Stable SEA, kJ/kg (10 mm ≤ d ≤ 30 mm)	41.4	46.1	44.3	51.8
Total SEA, kJ/kg (0 mm ≤ d ≤ 30 mm)	39.9	49.7	42.7	57.6
Crush efficiency	0.48	0.49	0.42	0.42

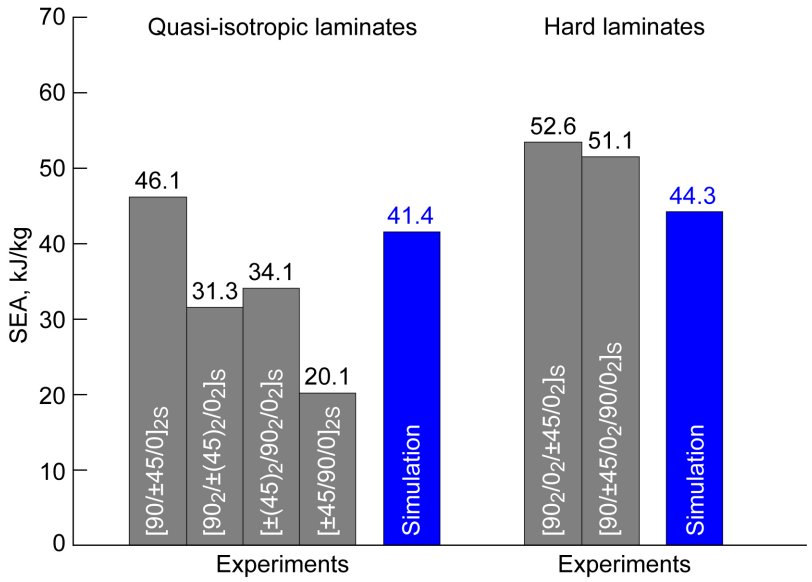

Figure 72.—Prediction of Stable SEA in flat coupon crush tests compared with experimental results.

Considering the insensitivity of the current continuum model to the layup sequence, Figure 72 compares the predicted Stable SEA values to the complete range of experimentally tested quasi-isotropic and hard laminates. It can be seen that the predicted Stable SEA value of 41.4 kJ/kg for quasi-isotropic laminates lies well within the measured range of experimental data (20.1 to 46.6 kJ/kg). Compared with these quasi-isotropic laminates, the simulation of a hard laminate leads to a higher predicted Stable SEA value of 44.3 kJ/kg. Experimental results of the hard laminates show higher Stable SEA values at around 51.0 kJ/kg. It can be concluded that CODAM2 is able to predict the overall crush response of IM7/8552 CFRP laminates. However, the effect of enhancing energy absorption capabilities through hard laminates is less pronounced as compared with the experimental data. Therefore, CODAM2 can be considered to provide conservative predictions of the crush response of hard laminates.

4.4.6 Simulation of Progressive Crushing: C-Channel

As part of the RR–3 exercise, the analysis teams were tasked to predict the C-channel crush response for two different hard laminates. Due to the current CODAM2 model's insensitivity to layup sequence, simulation results representative of the complete class of hard laminates are presented. C-channel crushing is another test at the subcomponent level of the building-block approach. In contrast to the pure compressive nature of the damage progression in the flat coupon specimen, crushing of the C-channel configuration can trigger tearing mechanisms in the corner (curved) region that is initiated by tensile circumferential (hoop) stresses that reach critical values.

The crushing of C-channel specimens was simulated both quasistatically and dynamically using two different initial velocities of 3.81 m/s (150 in./s) and 7.62 m/s (300 in./s) assigned to a drop mass of 49.3 kg (96.8 lb).[7] The following quantities were determined from the analysis:

- Crush distance
- Peak crush force
- Average crush force
- SEA
- Crush force efficiency

Figure 73 illustrates the modeling approach for the C-channel structure. In the quasistatic load case, a prescribed constant velocity of 3.81 m/s (150 in./s) is applied to the rigid impact plate, whereas velocities of 3.81 m/s (150 in./s) and 7.62 m/s (300 in./s) were applied in the two dynamic load cases as initial conditions. A chamfer trigger consisting of elements with gradually increasing shell thickness is used to initiate stable progressive crushing. Clamping at the bottom of the C-channel is represented by fully constrained translational DOFs. To be consistent with previous flat coupon simulations, a skewed mesh with 10° inclination angle of quadrilateral elements with approximate element size of 1 by 1 mm is applied. It should be noted that the built-in CODAM2 material model does not consider strain-rate effects. Results of C-channel pretest simulations are presented in Section B.7.6.

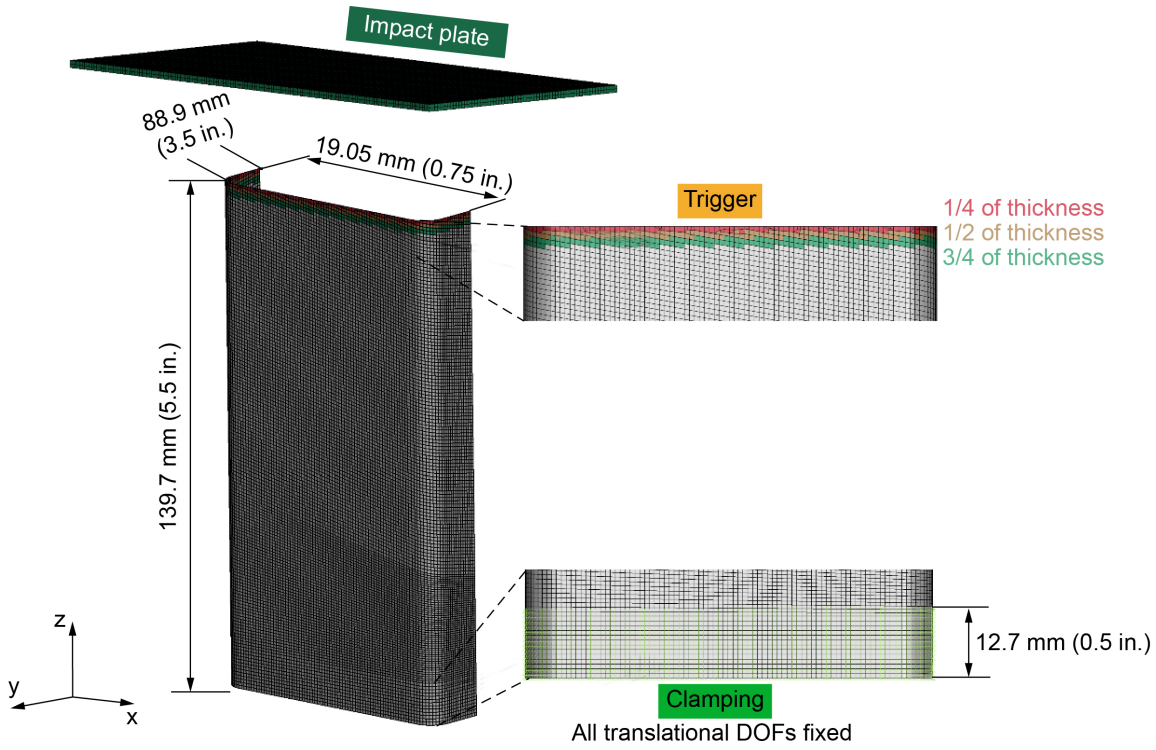

Figure 73.—FE model for simulation of progressive crushing of C-channel structures.

[7]As noted in Section 4.0, impactor mass for the C-channel crush test was incorrectly assumed to match that of the flat coupon; see Table 21 for correct values.

4.4.7 MAT219 Capabilities, Limitations, and Best Practices

The presented simulation methodology followed a modified building-block approach ranging from the virtual level (single-element simulations) to the subcomponent level, including simulation of C-channel structures subjected to crushing.

This section presents the modeling capabilities and limitations of LS–DYNA® MAT219 (CODAM2), including best practices as they pertain to utilization of this material model for crush simulation of the flat-panel and C-channel composite structures considered here.

Modeling capabilities:

- The CODAM2 material model strikes an appropriate balance of accuracy, efficiency, and ease of calibration to make it practical for use in design and analysis of large-scale composite structures.
- As evidenced by predicted fracture energy values in OCT and CC tests, the sublaminate-based CODAM2 material model captures the overall progressive damage response of the laminate in both tension and compression modes, including the ply interactions using a single-shell element discretization through the thickness. This results in considerable efficiencies both in terms of model setup and computational effort.

Modeling limitations:

- CODAM2 does not account for permanent deformation (plastic effects) resulting in linear unloading to the origin. This leads to lower energy evaluations ($\Delta W - \Delta U$) and hence lower fracture energies as compared with experiments where the force–displacement response exhibits nonlinear unloading.
- The presented sublaminate-based continuum modeling approach is only valid for the particular laminate for which the fracture energies have been calibrated. As such, it cannot be extrapolated to variants of the laminate with different layup sequences.
- The built-in LS–DYNA® MAT219 implementation of CODAM2 material model does not consider strain-rate effects.
- MAT219 is able to approximately predict the crush response. However, as is the case with all progressive continuum damage mechanics (CDM) models, CODAM2 is not able to represent crush mechanisms involving fragmentation and pulverization of fibers. Discrete, particle-based numerical methods might be better suited to capture these failure mechanisms.

Modeling strategies and best practices:

- Perform single-element laminate simulations to assess the macroscopic behavior predicted by the ply-based material model. In comparison with the simulations of the progressive fracture tests, these models are simple to set up at very low computational cost.
- Discretize the composite laminate using one single-shell element layer through the thickness at all levels of the building block. This efficient modeling technique enables the simulation of large-scale structures at the subcomponent level and beyond.
- The simulations of OCT and CC tests ensure reasonable calibration of fiber fracture energies as input into the CODAM2 material model to analyze the structural response of composite laminates subjected to tension and compression, respectively.
- For the development of numerical methods, joint research work between different teams using various material models and FE codes was found to be a valuable strategy. This practice provides

better objectivity of the numerical results and enables the identification of material-model-specific or FE-code-specific effects that otherwise could not be identified. This finding is an outcome of the research collaboration between DLR and UBC.

4.5 LS–DYNA® MAT261

This section describes the use of LS–DYNA® *MAT_LAMINATED_FRACTURE_DAIMLER_PINHO (MAT261) for composite crush and crashworthiness simulations. The flat coupon crush simulations were performed with MAT261, using an impact mass of 43.9 kg (96.8 lbf).[8] These simulations used exactly the same mesh and loading conditions as the MAT58 simulations presented in Section 4.2. The only change was in the material card used for the composite flat coupon (shown in Figure B.55 in Section B.9).

Figure 74 to Figure 76 compare MAT261 simulation and test data as reported in the comparisons with MAT58. MAT261 for force and energy responses consistently follow the lower range of test responses.

Table 11 summarizes the Stable SEA values obtained for both test and simulation, including for comparison the MAT58 simulation results shown previously. For both simulations, the trend of increasing SEA is correctly captured for the harder laminates. MAT58 shows lower than expected SEA for the quasi-isotropic layup, and MAT261 shows lower than expected SEA for laminate configuration HL02. The MAT261 response, even for HL02, is still within the range of test scatter, as it follows the low end of the test response.

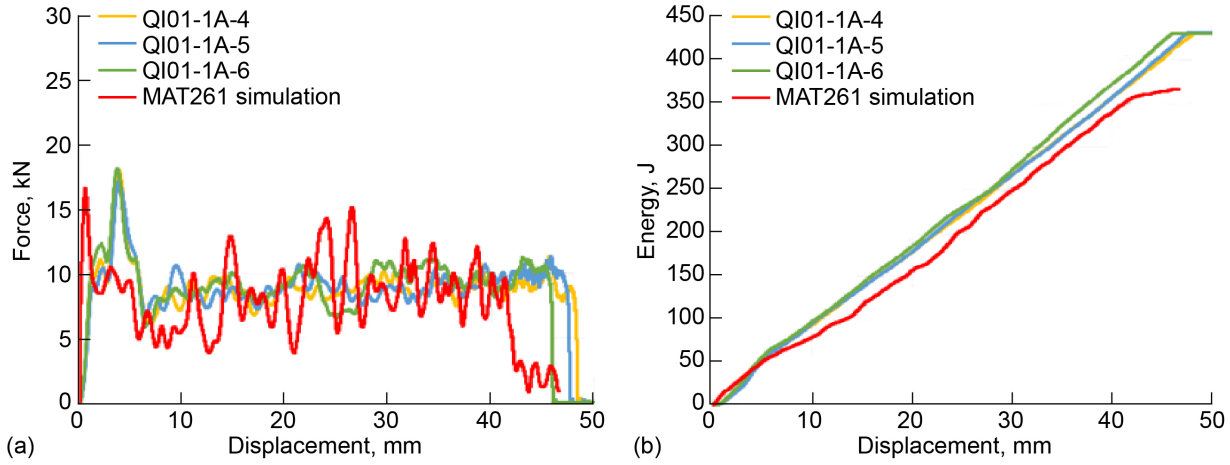

Figure 74.—Comparison of quasi-isotropic layup test data with MAT261 simulation. (a) Force response. (b) Energy response.

[8]See Table 21 for listing of impact loading conditions for flat coupon and C-channel crush tests.

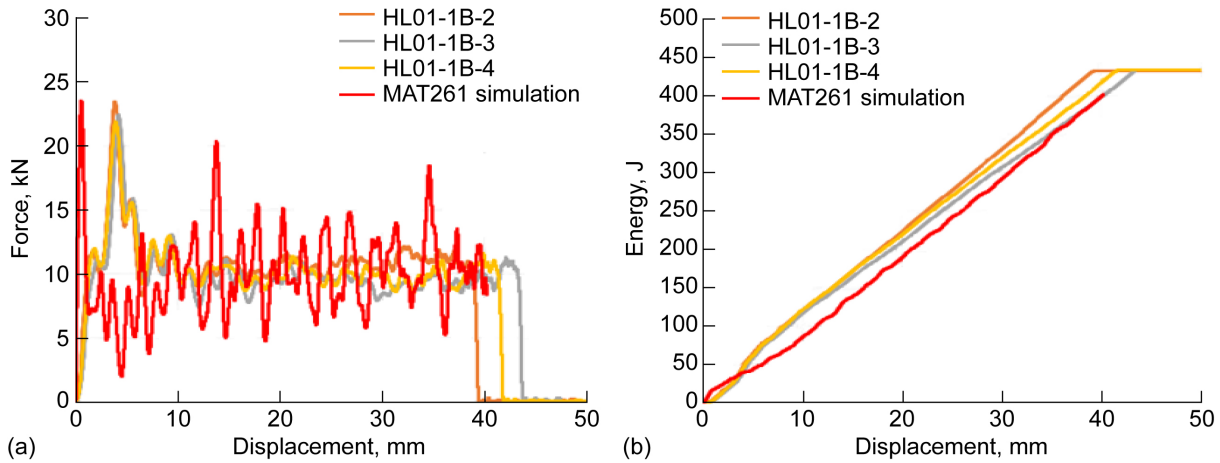

Figure 75.—Comparison of flat crush coupon test data and MAT261 simulation for hard laminate HL01. (a) Force response. (b) Energy response.

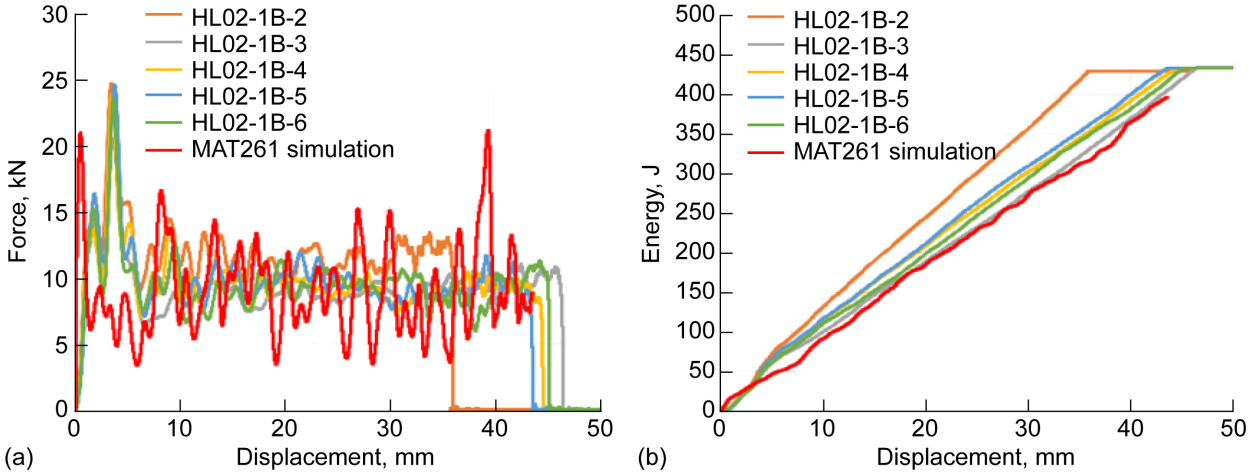

Figure 76.—Comparison of test data and MAT261 simulation for hard laminate HL02. (a) Force response. (b) Energy response.

TABLE 11.—COMPARISON OF STABLE SEA FOR TEST AND MAT58 AND MAT261 SIMULATIONS

Coupon layup	Stable SEA, kJ/kg		
	Experiment	MAT58	MAT261
QI01	46.11	39.80	45.25
HL01	53.59	54.02	54.55
HL02	54.34	53.36	48.56

For MAT261, the fragmentation response changes with the layup, and differences in SEA from simulation are therefore expected with differing layups. As previously noted, differences in gap relative to mesh density can also influence responses in the simulation. Both simulations use a single-shell element with ply angles defined at integration points through the thickness. Another variable in these simulations is the number of integration points that must fail in order for the element to be eroded. For MAT261, this is set at 70 percent, but increasing this value could also increase the overall SEA response.

A comparison of simulation responses for MAT58 and MAT261 is shown in Figure 77 for the quasi-isotropic coupon. The simulation responses are similar, although MAT261 in this case more closely matches the test response. The two responses diverge later in the crush stroke, due likely to the changing load response in MAT261 as fragmentation progresses and as fragments interact with the progressive crushing response. Also, crush velocity decreases as the simulation progresses, and this effect may influence results later in the crush response.

Figure 78 shows a qualitative comparison of failure morphology between MAT58 and MAT261. MAT58 shows progressive element erosion, based on ERODS and the crash-front softening parameter. The erosion strain limit allows for load continuity to the extent possible as element erosion proceeds. With MAT261, element erosion is combined with bending and fragmentation. This may appear more physically accurate, but it also results in greater fluctuation of load response during crushing.

Overall, the values used in simulation for MAT261 appear reasonable for use with shell elements, although there is still room for further optimization.

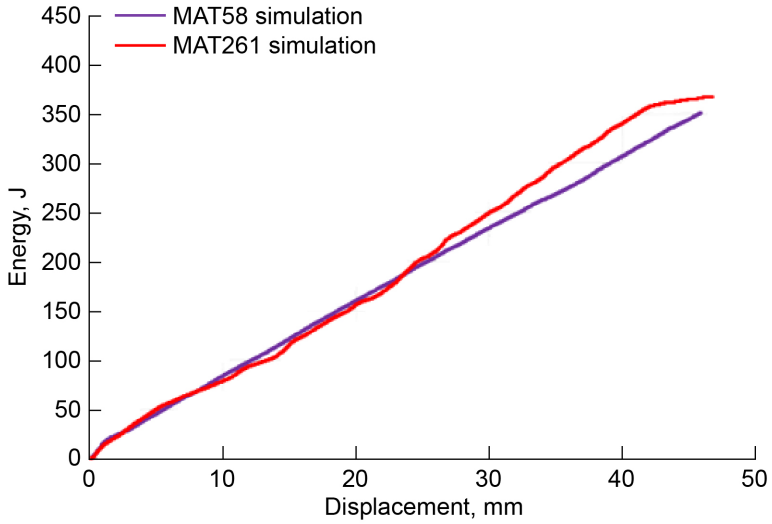

Figure 77.—Comparison of quasi-isotropic simulation response in MAT58 and MAT261.

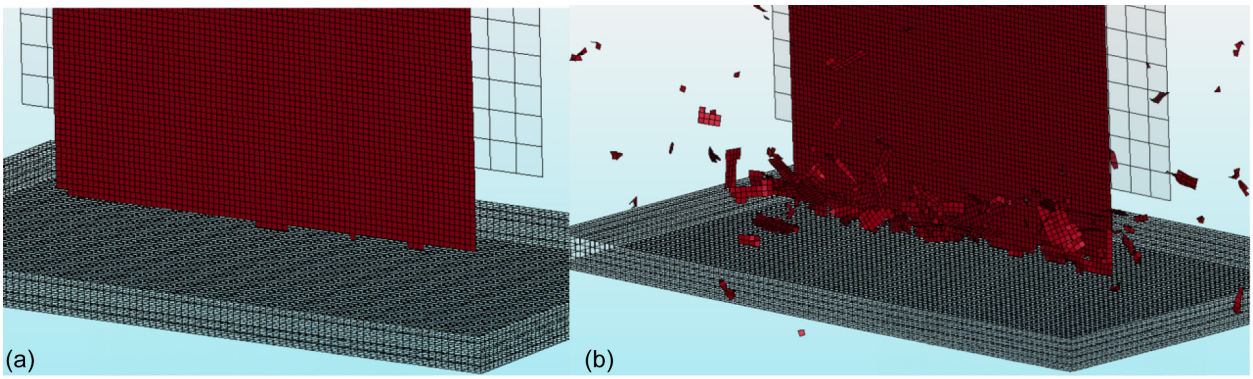

Figure 78.—Comparison of simulation failure morphology in MAT58 and MAT261. (a) M58 showing erosion only. (b) M261 showing fragmentation and erosion.

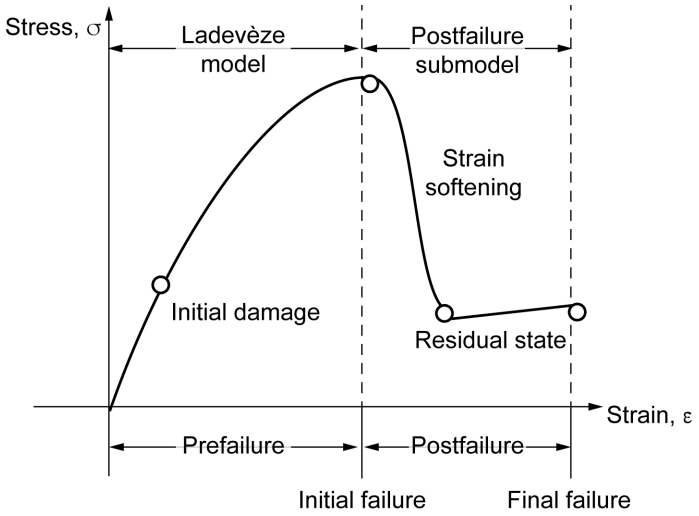

Figure 79.—Stress–strain diagram of MAT297.

4.6 LS–DYNA® MAT297

This section describes the MAT297 composite material model for crashworthiness simulations. MAT297 is based on an enhanced continuum damage mechanics (ECDM) model for composite materials (Ref. 34) and is available for shell element only.

MAT297 has a total of 48 material parameters. These parameters can be divided into three groups:

1. Mechanical properties, including elastic constants and strength—16 parameters
2. Parameters that are common in composite models for crash simulation—19 parameters
3. Parameters for the prefailure submodel (i.e., the Ladevèze model)—13 parameters

These three groups of parameters are summarized in Section B.10 (Table B.11 to Table B.13). Input values for the IM7/8552 unidirectional composite, such as the material-model-specific elastic and strength parameters, are presented in Section 5.2.3 (Table 16). These inputs were verified using single-element simulations for tension, compression, and shear cases.

The ECDM model consists of a prefailure submodel, based on the modified Ladevèze model, and a postfailure submodel. As shown in Figure 79, the two submodels describe the stress–strain behavior before and after the stress reaches the strength value. The switch between the two models occurs when the strain reaches the peak stress value. Computationally, at small strain, the simulation follows the modified Ladevèze model. When strain reaches the value corresponding to the strength, it follows the postfailure submodel.

The Ladevèze model (Ref. 12) relates the damage variable d with damage force Y; detailed discussions are presented in Section B.10.2.

4.6.1 Finite Element Model Description of Flat Coupon and C-Channel Crush Test

As mentioned previously, MAT297 is available for shell element only. Shell elements are efficient in modeling the thin-walled structures. However, FE models with shells are not suitable to represent the load cases with large in-plane compression. A slight perturbation in the out-of-plane direction of any node may result in a sudden out-of-plane movement, leading to inconsistent results and even instability. To overcome the instability, a shell–beam (SB) element method has been developed (Ref. 35). As shown in Figure 80, the SB element is composed of two shell elements and four beam elements connected by shared nodes. The cross section and the beam element properties are determined such that the stress–

strain response of the element in the through-thickness direction is equal to the measured through-thickness tensile properties.

The laminate for the flat coupon and C-channel structures were modeled with four layers of shell elements. These four layers are arranged into two layers of SB elements, as shown in Figure 81. The interface between the two SB layers was modeled with a *SURFACE_TO_SURFACE_TIEBREAK contact.

The FE models for flat coupons and C-channel crush simulations are shown in Figure 82. The mesh size for the composite part is about 2 mm. A finer mesh is used in the tip area. The impact platen is modeled with two layers: a solid layer modeled as rigid and a shell layer modeled as steel. For flat coupon simulations, the platen is fully constrained, and a constant velocity is prescribed at the bottom nodes of the coupon. For C-channel simulations, the nodes at the bottom row are constrained in x, y, and z displacements, and an initial velocity or a constant velocity is prescribed for the rigid part. The platen weight of 44 kg (96.8 lb) was assumed in both the flat and C-channel crush simulations.[9] The friction coefficient is assumed to be 0.22 at the platen/composite interface and 0.3 for all other contacts.

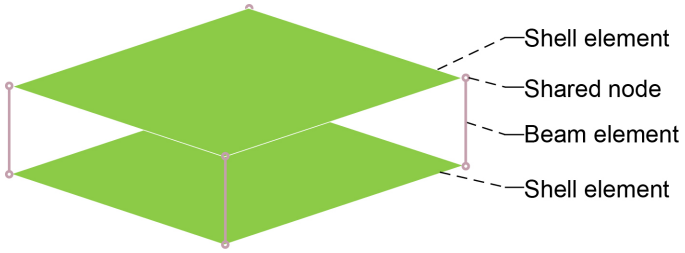

Figure 80.—Schematic of shell–beam element.

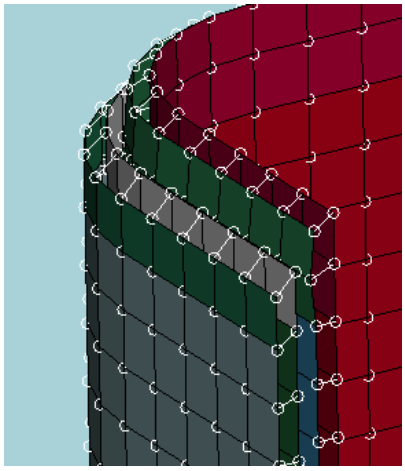

Figure 81.—Laminate modeled with four layers of shells arranged in two shell–beam layers.

[9]As noted in Section 4.0, impactor mass for the C-channel crush test was incorrectly assumed to match that of the flat coupon; see Table 21 for correct values.

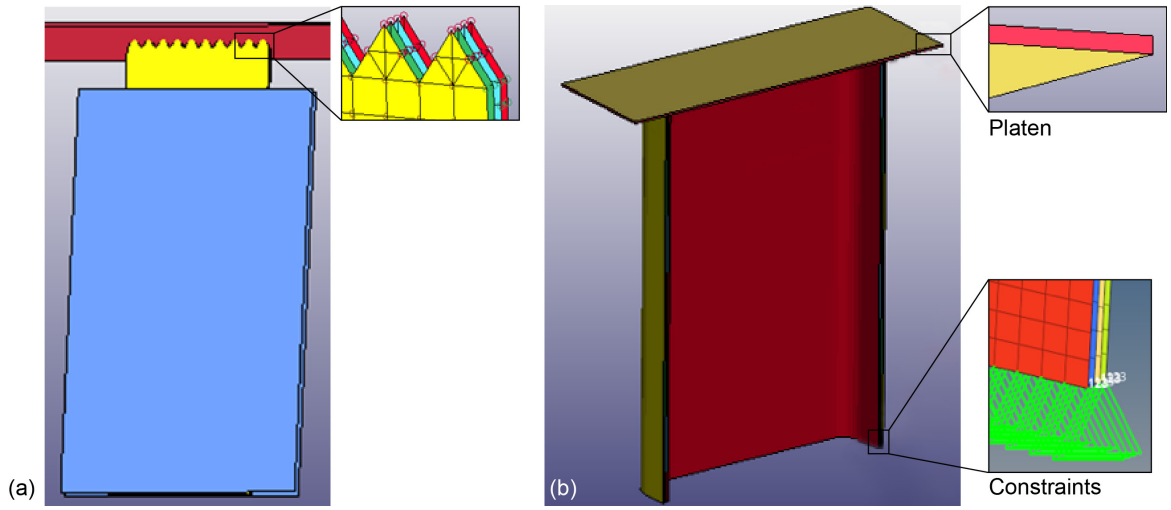

Figure 82.—FE models for crush simulations. (a) Flat coupon simulation. (b) C-channel simulation.

TABLE 12.—SUMMARY OF FLAT COUPON SIMULATIONS

	$[90/\pm45/0]_{2S}$	$[90_2/(\pm45)_2/0_2]_S$	$[(\pm45)_2/90_2/0_2]_S$	$[\pm45/90/0]2_S$
Impact velocity, m/s	4.3	4.3	4.3	3.48
Gap, mm	8.6	15	15	7.5
Crush distance, mm	30	30	30	30
Peak force, kN	39.3	33	29.6	42
Mean crush force, kN	9.13	5.7	7.6	10.2
Total SEA, kJ/kg	53.6	42.9	44.9	59.5
Mean crush force, kN	9.4	6.4	7.6	10.1
Stable SEA, kJ/kg	50.1	34.2	40.5	53.6
Experimental SEA, stable, kJ/kg, and standard deviation	46.6, 0.6	31.3, 6.8	32.0, 6.3	20.1, 6.6
Error of SEA prediction, percent	7.51	9.27	26.56	166.67

4.6.2 Flat Coupon Simulation Results

The simulation results for the flat coupons are summarized in Table 12. The force–displacement curves are shown in Figure 83. The force–displacement data were filtered with an SAE 3000 filter. The flat coupon simulation results were compared with the experimental data. For the flat coupon tests, the Total SEA values initially were calculated for the entire crushed length, and the mean crush force was estimated for the crush distance after the peak force. However, the experimental SEA values (also referred to as "Stable SEA") were computed for a crush distance between 10 and 30 mm. Therefore, the simulation results for SEA and mean crush force were recalculated and are reported in Table 12. In general, simulations overpredicted the peak values, the mean crush force, and SEA values. For SEA prediction, the errors were 7.5 and 9.3 percent for the two laminates with a 90° layer at the outer surface. For the two laminates with a 45° layer at the outer surface, the errors were 26.6 and 166.7 percent.

The C-channel has a laminate layup of $[90_2/0_2/\pm45/0_2]_S$ (HL01). It was simulated for three cases: a constant velocity $v = 150$ in./s, an initial velocity $v_0 = 150$ in./s, and $v_0 = 300$ in./s. The results are summarized in Table 13. The C-channel force–displacement responses are discussed in Section B.10.3.

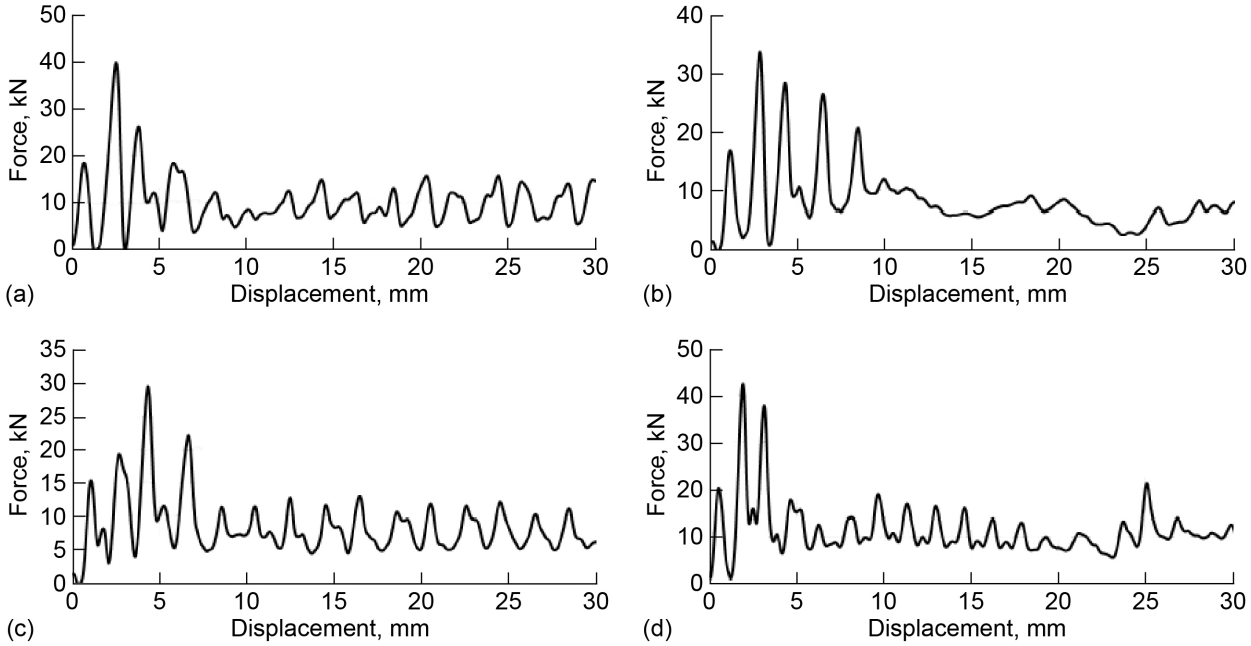

Figure 83.—Force–displacement curves for flat coupon crush from simulations with four different laminates filtered with SAE 3000. (a) Laminate $[90/\pm45/0]_{2S}$. (b) Laminate $[90_2/(\pm45)_2/0_2]_S$. (c) Laminate $[(\pm45)_2/90_2/0_2]_S$. (d) Laminate $[(\pm45)/90/0]_{2S}$.

TABLE 13.—SUMMARY OF C-CHANNEL SIMULATIONS

Impact velocity	Peak force, kN	Crush distance, mm	Crush force, kN	Stable SEA, kJ/kg
v = 150 in./s (3.81 m/s)	38.1	30	22.3	95.2
v_0 = 150 in./s (3.81 m/s)	41.3	7.7	-----	----
v_0 = 300 in./s (7.62 m/s)	39.5	29.5	19.5	83.2

4.6.3 MAT297 Modeling Capabilities, Limitations, and Best Practices

Modeling Capabilities.—MAT297 is designed for use in large-structure crashworthiness simulations, such as full-vehicle crashes. Modeling composite laminates with shell elements is computationally efficient. The shell-beam (SB) element method improves the stability of thin-walled structures under axial impact loads.

Modeling Limitation.—Like other material models for shells, MAT297 cannot consider the damage in the through-thickness direction within the material model. To model delamination, multilayered shells with cohesive zone elements or tiebreak contact at their interface have to be employed. The current work used tiebreak contact. The tiebreak parameters were determined based on previous experience and trial and error. Another weakness of MAT297 is that it does not consider mesh-size irregularity.

Modeling Best Practices.—FE models can influence and even alter the results of crush simulations. For example, the FE representation of the platen was found to influence the results. The current method is not necessarily the best practice for truthfully representing the experimental scenario. In the flat coupon model, initially a friction coefficient was assigned between the support plate and the specimen. As a result, the support plate restricted the free motion of the specimen. The amount of space between the support plate and the specimen is another factor that can lead to significantly different outcomes. If space is too tight, the specimen's free motion is restricted; if it is too loose, global buckling of the specimen cannot be prevented.

4.7 LS–DYNA® Modified Ladevèze

This section describes the numerical methodology used by the analysis team of GDTech Engineering in collaboration with University of Liège, Belgium, for RR–3. A self-supported flat crush coupon test was used as the basis for model validation to deploy simulation of a C-channel test article. Self-supported crush specimens are discussed in Section 3.1.2 for RR–1 and RR–2 and in Section 5.6.1 for RR–3. This section presents a discussion to understand the predictability of the modified mesomodel in modeling the axial crushing of the composite laminates using the Modified Ladevèze modeling approach. It also provides modeling strategies and best practices to accurately conduct the crushing behavior of composites and aid in the development of high-fidelity FE models to minimize the need for testing campaigns.

4.7.1 Modified Ladevèze Material Model Description

The present study uses a modified Ladevèze mesomodel (Ref. 12) as documented by Rajaneesh and Bruyneel (Ref. 36), implemented in LS–DYNA® commercial software. The mesomodel accounts for (1) fiber tensile/compressive failure, (2) matrix tensile failure, and (3) matrix shear failure. Fiber is assumed to have a brittle failure. The current model accounts for inelasticity resulting from matrix plasticity and damage. Plasticity is accounted for via a power-law hardening. Two damage variables govern the behavior of the ply in the matrix direction: matrix transverse tensile damage (d_{22}) and ply shear damage (d_{12}); d_{22} is assumed to be a scalar multiple of d_{12}. The modified mesomodel accounts for mesh size (l^*) and ply fracture toughnesses in fiber tension (Γ_{11+}), fiber compression (Γ_{11-}), matrix tension (Γ_{22+}, Γ_{33+}), matrix transverse out-of-plane shear (Γ_{23}), and matrix longitudinal shear (Γ_{13}, Γ_{23}) modes. Fracture toughness is accounted for by using equivalent matrix stress–strain space, as shown in Figure 84.

Typical properties of the mesomodel for the ply are taken from Abissett et al. (Ref. 37). Fiber-dominated values under tension (Γ_{11+}) and compression (Γ_{11-}) are more difficult to obtain. Compact tension or compact compression (CT or CC) specimens were commonly adopted following Pinho et al. (Ref. 38). Based on different studies available in the literature (Ref. 39), 100 kJ/m^2 is used for Γ_{11+} in the current study. A limited number of studies are available in the literature to measure Γ_{11-} of carbon fiber composites using CC specimens. Catalanotti et al. (Ref. 40), using one CC specimen made of IM7/8552 composite, measured Γ_{11-} as 47.5 kJ/m^2. A value of 50 kJ/m^2 is used for Γ_{11-} in the current research. Matrix fracture toughness values are taken from Camanho et al. (Ref. 41).

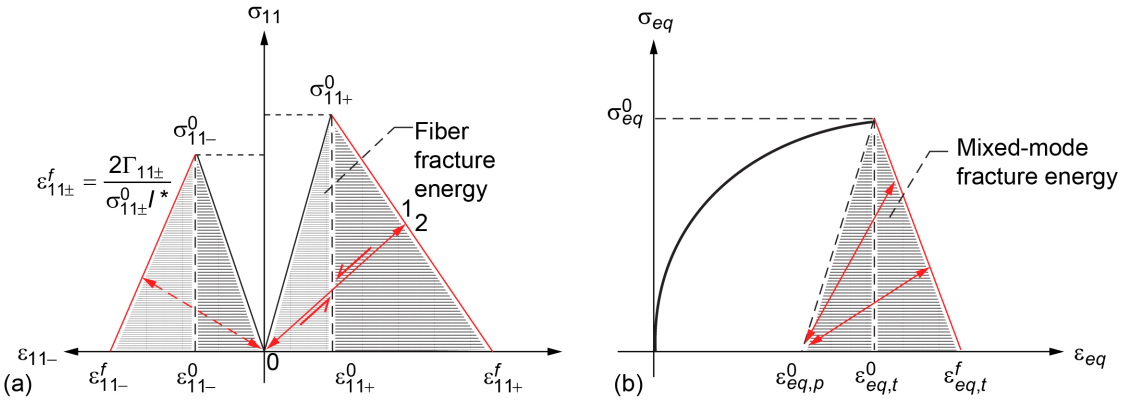

Figure 84.—Description of modified Ladevèze mesomodel. (a) Fiber-dominated responses. (b) Matrix-dominated responses.

In comparison with other Ladevèze-based advanced damage models, such as the original Ladevèze model (Ref. 12) and ABQ_DLR_UD (Ref. 30, also presented in Section 4.8), the present model differs in several ways. The modified mesomodel (Ref. 37)

- Does not rely on the numerical delay damage constants, as is the case in the original Ladevèze model.
- Is based on a 3D stress state, whereas the ABQ_DLR_UD model is based on a 2D stress state.
- Accounts for fiber and matrix fracture toughness properties, whereas the ABQ_DLR_UD model accounts for fiber fracture toughness properties only.
- Should be used with solid elements, whereas ABQ_DLR_UD is applicable to shell elements.
- Is implemented in LS–DYNA®, whereas ABQ_DLR_UD is implemented in ABAQUS® (Dassault Systemes Simulia Corp.).

Damage and failure attributes of the modified Ladevèze material model are discussed further in Section B.11.

4.7.2 Numerical Model Description

All the simulations were conducted in commercial FE solver LS–DYNA®. Interaction between the laminate and rigid bodies is simulated by defining an eroding single-surface contact. A coefficient of friction of 0.1 is used between the rigid bodies and the laminate, whereas a coefficient of 0.4 is assumed between delaminated plies. Each ply is modeled using one element per ply in thickness direction. A flat coupon test configuration is considered as shown in Figure 85. Flat crush coupon ply and interface material properties, layup definition, specimen dimensions, and test conditions are presented in Section 5.6.1.

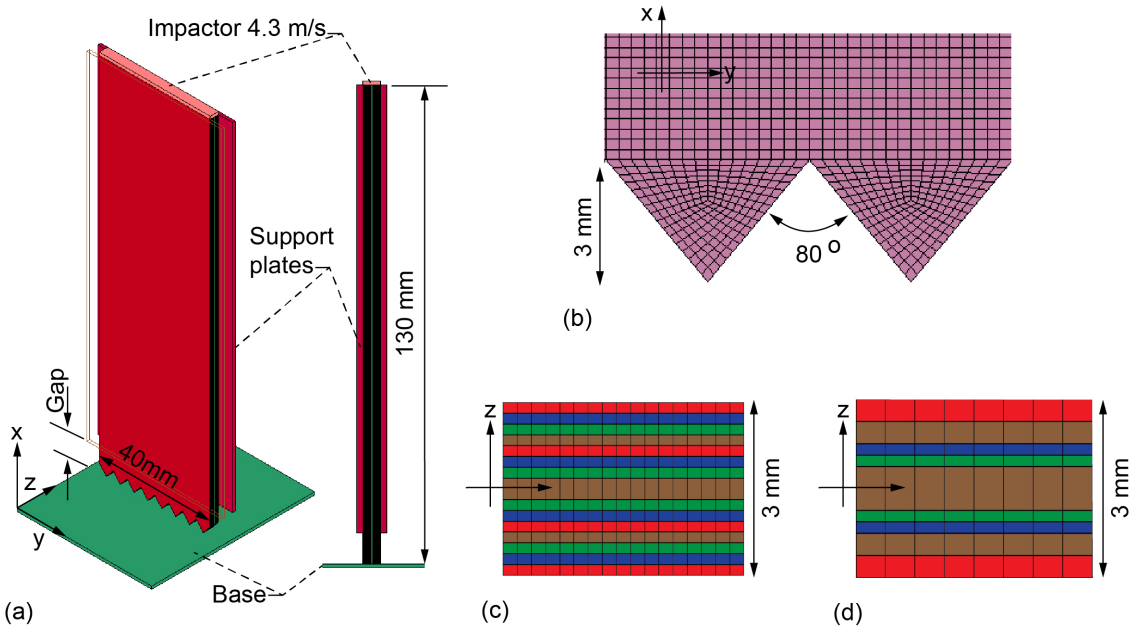

Figure 85.—(a) Finite element model. (b) In-plane mesh. (c) Through-thickness mesh of QI01 $[90/\pm45/0]_{2S}$. (d) Through-thickness mesh of HL01 $[90_2/0_2/\pm45/0_2]_S$.

A sawtooth trigger is used for flat coupons and a chamfer trigger is used for the C-channel coupons. A nominal in-plane mesh size of 0.5 by 0.5 mm is used for plies and interfaces. Acceptability of the simulations is verified following AWG guidelines (Ref. 42), including permissible energy ratio limits, ratio of artificial hourglass energy to total energy, ratio of sliding interface energy to total energy, and ratio of damping energy to total energy. Comparison of tests and FE prediction is demonstrated in terms of peak load, SEA, and load–displacement curves for flat coupon. The accuracy of the material models based on smeared crack formulation can be improved using material-aligned mesh (mesh along the fiber direction), as proposed by Garijo et al. (Ref. 43). For practical reasons, however, material-aligned mesh was not adopted in the present work.

4.7.3 Flat Crush Coupon Test Predictions

As discussed in Section 5.6.1, two layups were considered in the present study: QI01, with stacking sequence $[90/\pm45/0]_{2S}$, and HL01, with stacking sequence $[90_2/0_2/\pm45/0_2]_S$. The drop weight mass was 43.9 kg[10] with an initial velocity of 4.3 m/s. Gaps of 8.6 mm (QI01) and 14.5 mm (HL01) were used. Each specimen had a nominal width of 40 mm and a nominal thickness of 3 mm. A density of 1,570 kg/m^3 was used.

Figure 86 compares load–displacement and velocity–time responses for these FE models and tests. A Butterworth filter with 600-Hz frequency was used to filter the noise from the response curves. The FE models are able to closely follow the deceleration of the impactor. Figure 87 compares experimental and predicted SEA for the QI01 and HL01 laminates. Two types of SEA measures were considered: Total SEA and Stable SEA. Total SEA was calculated between 0 and 30 mm crush displacements. Stable SEA was calculated within a 10- to 30-mm crush displacement range to emphasize the stable crushing capacity of the CFRP material excluding crush-trigger effects.

Failure modes predicted by these FE models are shown in Figure 88. The QI01 laminate showed a splaying with limited crushing, whereas the HL01 laminate failed primarily by fragmentation.

4.7.4 Modified Ladevèze Modeling Capabilities, Limitations, and Best Practices

Key capabilities of the proposed modified mesomodel include the ability to predict fiber tensile failure, fiber compressive failure, matrix tensile failure, and matrix in-plane shear failure while accounting for inelasticity resulting from the matrix material's plasticity and damage. In addition, all the material model parameters can be directly evaluated from physical tests, making it a completely physically based model.

The present model has several limitations, including absence of ply failure under in-plane transverse compression and fiber kinking under compression in the fiber direction. The current version of the modified mesomodel can only be used with solid and thick-shell elements at present, so the associated computational cost to analyze subcomponents is relatively high. The practical feasibility of using this material model for component levels can be addressed by extending the material model for thin-shell elements; such efforts are underway. Maximum FE size is governed by matrix model fracture energies, thus increasing the computational cost.

[10]As noted in Section 4.0, the flat coupon impactor mass matches Table 21, whereas the C-channel simulation is deferred for future publications.

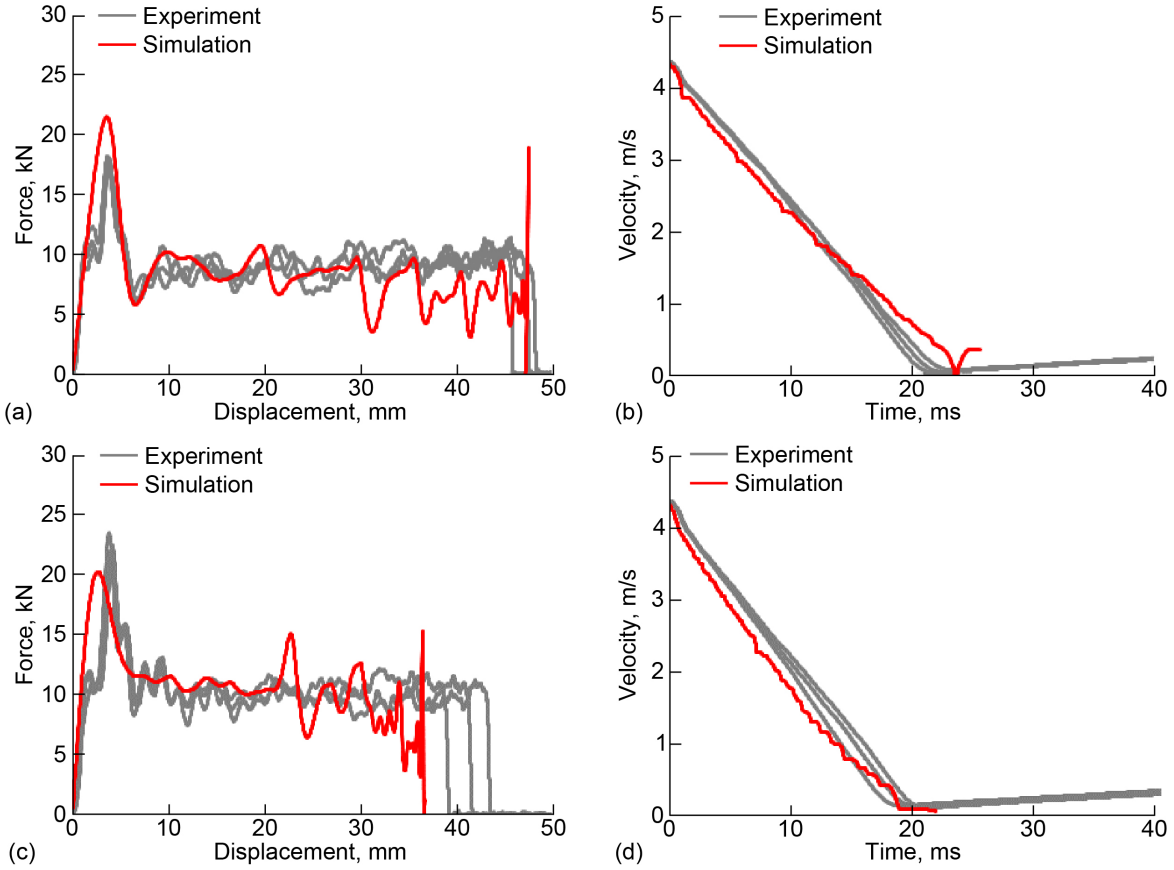

Figure 86.—Comparison of force–displacement and velocity–time responses from finite element predictions and tests. (a) Force–displacement curve for QI01. (b) Velocity–time curve for QI01. (c) Force–displacement curve for HL01. (d) Velocity–time curve for HL01.

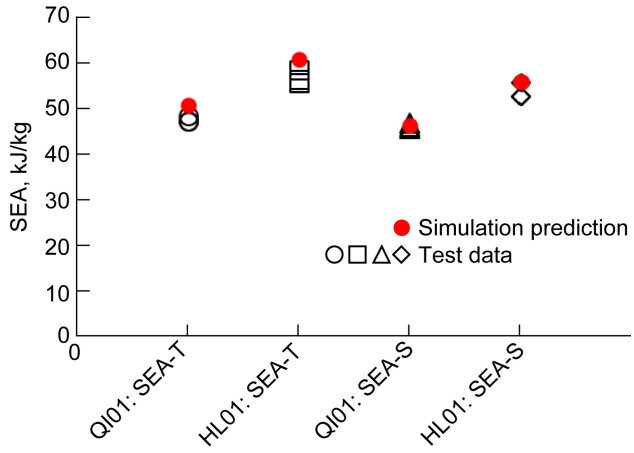

Figure 87.—Comparison of SEA predictions and test data for Total SEA (SEA-T) and Stable SEA (SEA-S) for QI01 and HL01 laminates.

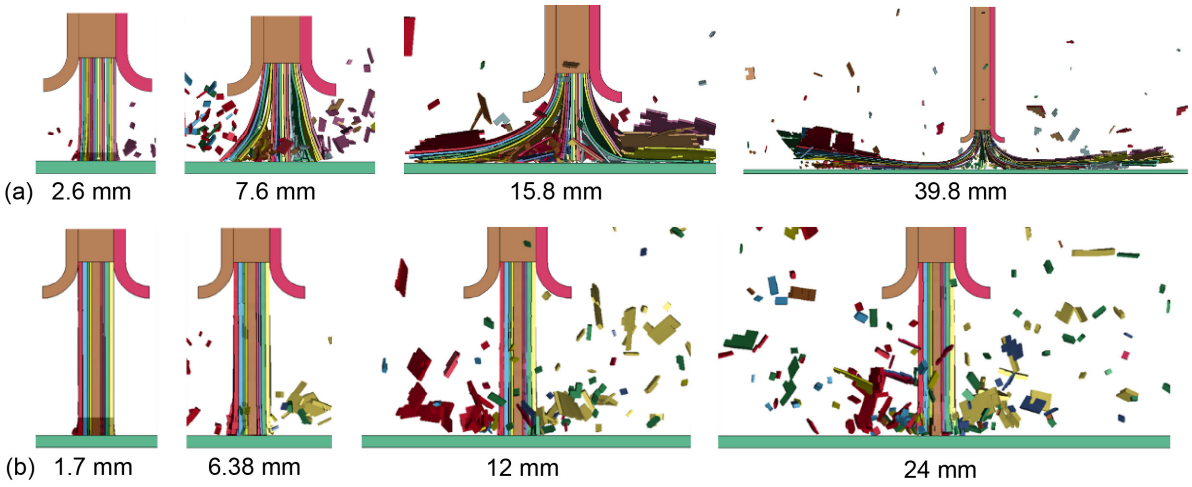

Figure 88.—Predicted failure modes. (a) QI01 laminate. (b) HL01 laminate.

Best practices in adopting this material model are worth noting. Accurate representation of the damage law under matrix-dominated loads is essential. Reducing the default maximum damage value helps to minimize artificial hourglass energy and avoids error termination due to negative element volume. FE size should be decided based on the matrix fracture energy.

4.8 ABAQUS® Ladevèze: ABQ_DLR_UD

This section describes the numerical methodology used by the DLR analysis team for RR–3. The work presented here has been developed in a research collaboration with UBC (Refs. 26 to 30). In this collaboration, material modeling and discretization techniques were jointly investigated while UBC and DLR used their own different material models and different finite element codes. With that, modeling recommendations could be derived independent from material model and finite element code specifics. Results from the UBC analysis team are presented in Section 4.4. This section contains a short description of the DLR user material model, which is partly based on the Ladevèze theory; a description of the simulation methodology used for the prediction of progressive crushing; and limitations and capabilities identified in the scope of the RR–3 analyses.

4.8.1 Material Model Description

The DLR material model ABQ_DLR_UD is implemented as vectorized user material (VUMAT) in ABAQUS®/Explicit. ABQ_DLR_UD is a mesoscale, plane-stress ply damage model in the framework of CDM that captures the intralaminar damage and failure in unidirectional fiber-reinforced polymers. Stiffness degradation and energy dissipated during the damaging process are captured by damage variables and damage evolution laws. The material model is based on a lamina-level modeling approach for stiffness and strength and uses intralaminar fracture toughness test data for damage propagation in the fiber direction as well as cyclic coupon test data for plasticity and damage propagation in the transverse and shear direction.

The elementary ply is assumed to be homogeneous and orthotropic and is represented by its two basic constituents: fiber and matrix. Fiber damage is based on fracture mechanics where tensile and compressive loading is assumed to be linear elastic until a maximum stress criterion is reached and damage initiates. A detailed material model description is provided in Section B.12.

4.8.2 Model Input Data and Assumptions

The elastic and strength material input data used in the RR–3 analyses are presented in Section 5.2.2 (Table 15). The model-specific parameters for the Ladevèze formulations were experimentally characterized for the considered material system (IM7/8552, 190 g/m^2) as outlined in Section 5.2.3 (Table 16) and presented in Section 5.2.5 and Appendix C. The tensile and compressive fiber fracture energies were calibrated using OCT and CC tests, respectively, as described in the following sections.

4.8.3 Simulation Methodology for Model Verification and Validation

The simulation methodology to predict progressive crushing of unidirectional (UD) composite structures followed a building-block approach, as shown in Figure 89.

Single-element simulations were used to verify the implemented material model theory. Single laminate element simulations were performed to verify the macroscale behavior predicted by the mesoscale material model. Fracture mechanic tests were used for calibration of fiber fracture energies with experimental results. On this level, the material input data were frozen and fixed input data were used for the subsequent predictions of progressive crushing without further calibration. The next building-block level (progressive crushing) contained a numerical study of discretization options and provided modeling guidelines for simulation of progressive crushing. The modeling approach was applied, and predictions were compared with experimental results of flat coupon crush tests performed at the University of Utah. Finally, the validated modeling approach based on flat crush coupon was used for performing the simulation of C-channel crushing, which are presented in Section B.12.

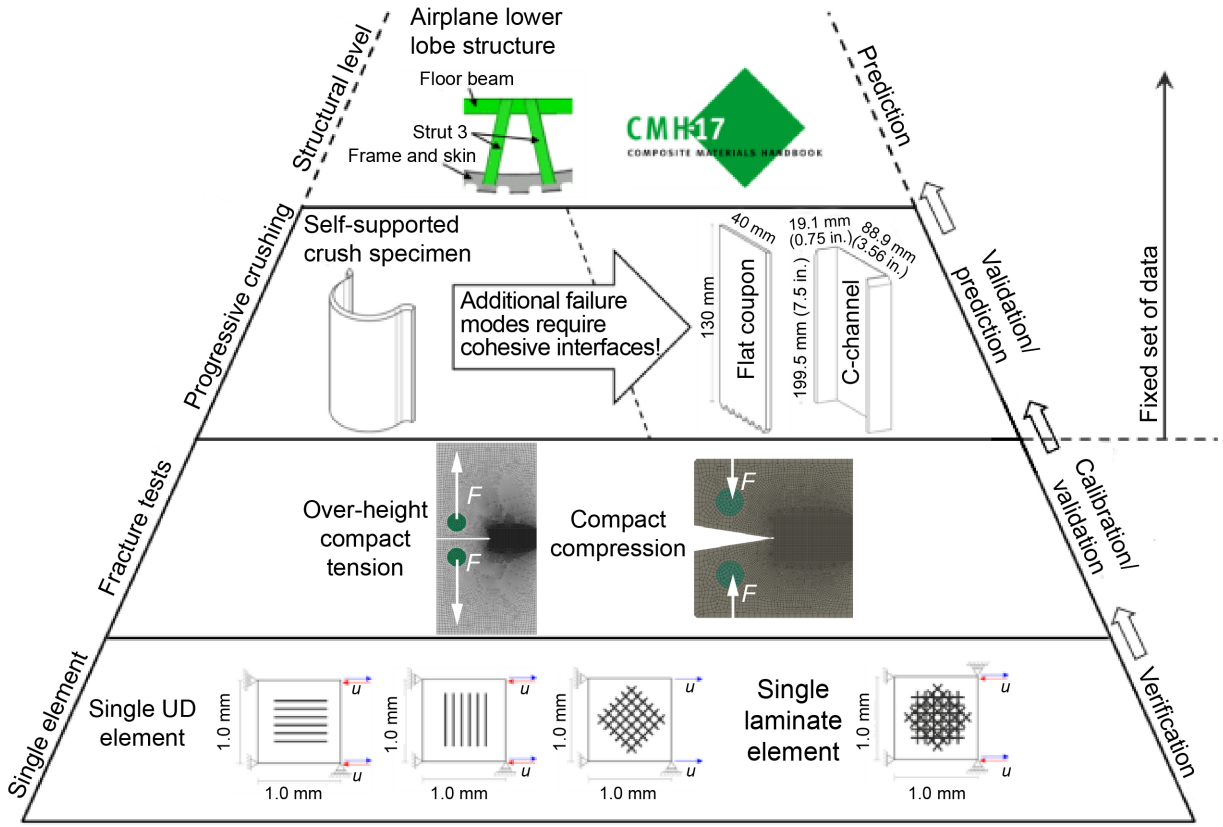

Figure 89.—Building-block approach used to predict progressive crushing of UD composite structures.

4.8.4 Single-Element Simulation for Model Verification

Verification of the material model is considered on the first level of the building block. Simulations of single-element models with unidirectional plies represent the material behavior of the two basic constituents, fiber and matrix. Figure 90 presents stress–strain characteristics of single-element simulations under uniaxial stress.

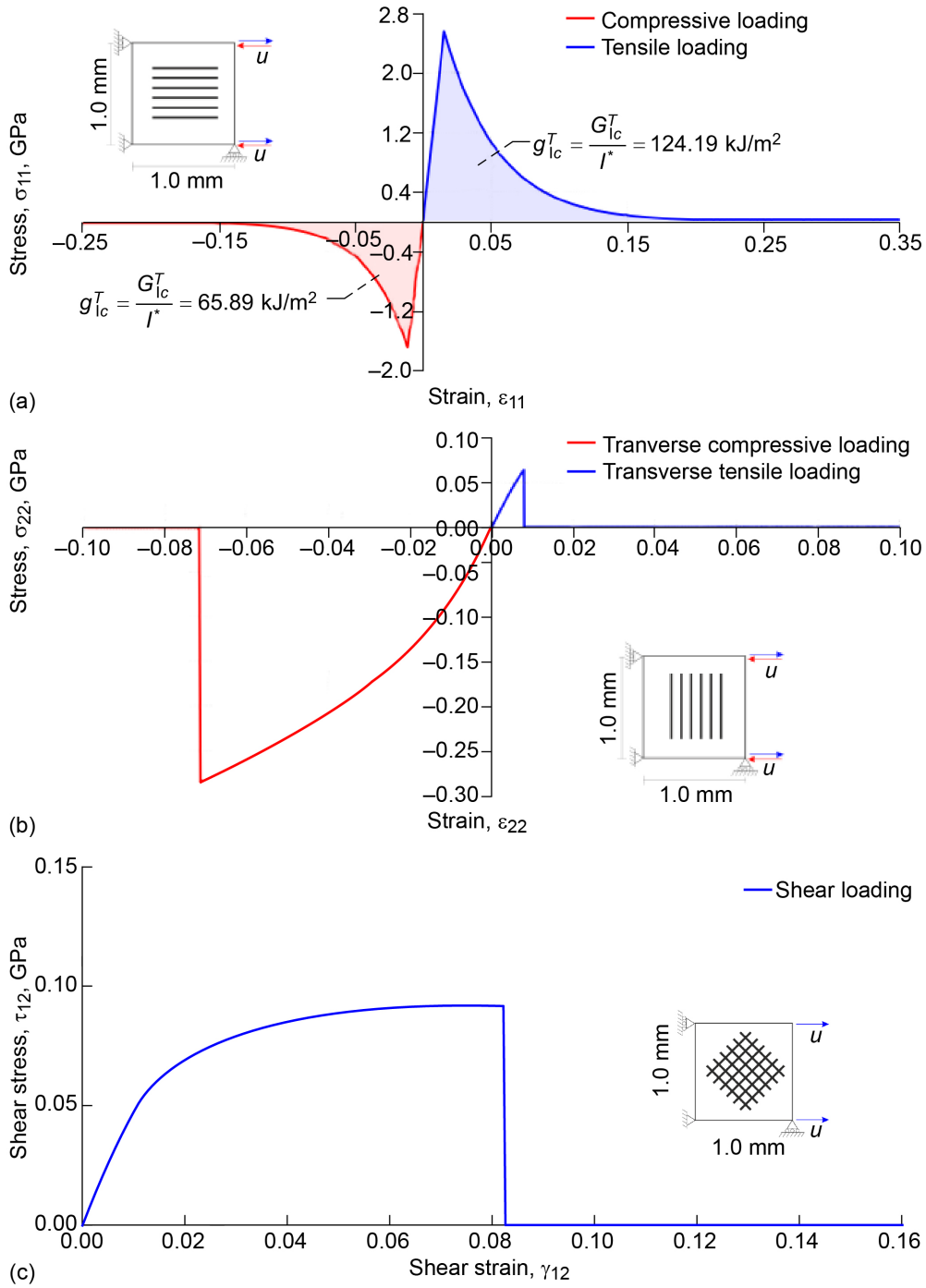

Figure 90.—Stress–strain characteristics of single-element simulations. (a) Longitudinal compressive and tensile loading. (b) Transverse compressive and tensile loading. (c) Shear loading.

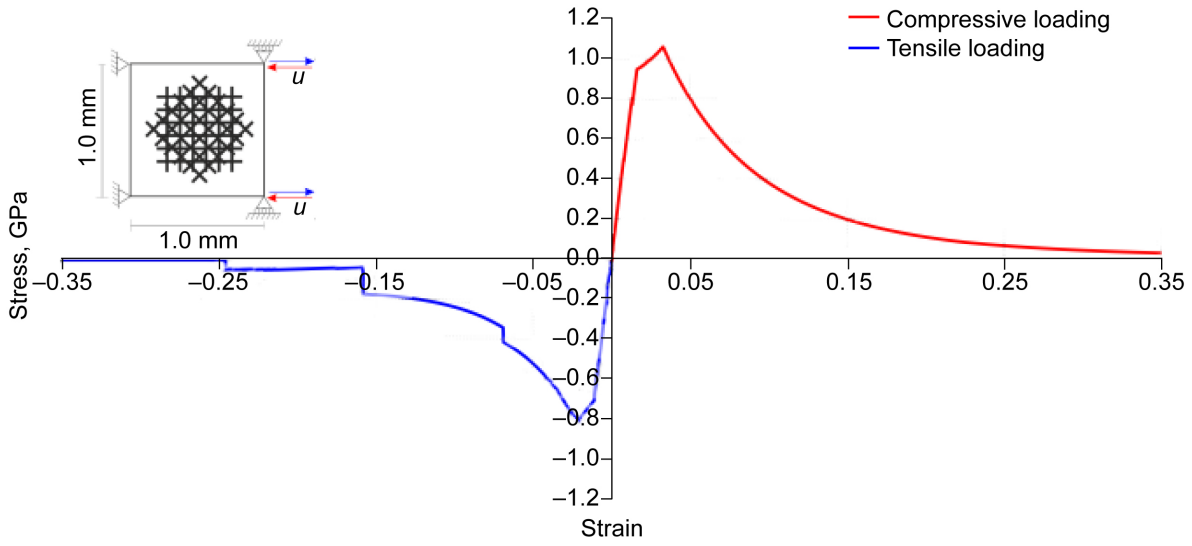

Figure 91.—Stress–strain characteristics of single-element simulation representing quasi-isotropic laminate under uniaxial compressive and tensile strain.

The tensile and compressive behavior in the fiber direction is shown in Figure 90(a) with an exponential damage evolution, as defined in Section B.12.1 (Eq. (B.47)). The area under the stress–strain curve represents the fiber fracture energies. Matrix behavior under transverse tensile and compressive loading is shown in Figure 90(b). Nonlinearity in the stress–strain characteristics under transverse compressive loading is given by plasticity after exceeding the yield stress. Matrix behavior under shear loading is shown in Figure 90(c). The nonlinear shear behavior is given due to both shear damage and plasticity.

Verification of the mesoscale material model on the macroscale laminate level is considered on single-element simulations of a quasi-isotropic laminate under both tensile and compressive loading. In Figure 91, the response at the macroscale laminate level predicted by the mesoscale material model on ply level is shown under uniaxial strain. At this level, comparison can be made with macroscale (laminate-based) material models. The fracture energy of the laminate is determined as the area under the stress–strain curve under tensile and compressive loading.

4.8.5 Simulation of Fracture Mechanic Tests

The building-block level fracture tests were used to calibrate the fiber fracture energies (input data) based on experiments. Tensile fiber fracture energies are calibrated using OCT test results and compressive fiber fracture energies with CC test results. The tests were previously performed at the University of British Columbia (UBC) (Ref. 31). These experimental tests used the European version of IM7/8552 with an areal density of 134 g/m^2, compared to the U.S. version of IM7/8552 (190 g/m^2) considered for the flat coupon and C-channel crush specimens. It is assumed that the influence of the material version on the fiber fracture energies is negligible. The dimensions and numerical models of OCT and CC specimens are shown in Figure 92. The force versus pin opening displacement curves of OCT and CC simulations are shown in Figure 93 and compared with the test results from Reference 31.

From this, the laminate fracture energies are calculated in Equation (2) as

$$G_f = \frac{\Delta W - \Delta U}{t \Delta a} \tag{2}$$

where W is total dissipated energy, U is elastic strain energy, and t is laminate thickness (here, $t = 4$ mm). The fiber fracture energies, as simulation input data, have been calibrated with these experimental results and were determined as $G_{f1}^{t} = 120$ kJ/m^2 and $G_{f1}^{c} = 60$ kJ/m^2 for the simulation of crushing. At this level of the building block, the material parameters were fixed and used for the subsequent simulation of crushing.

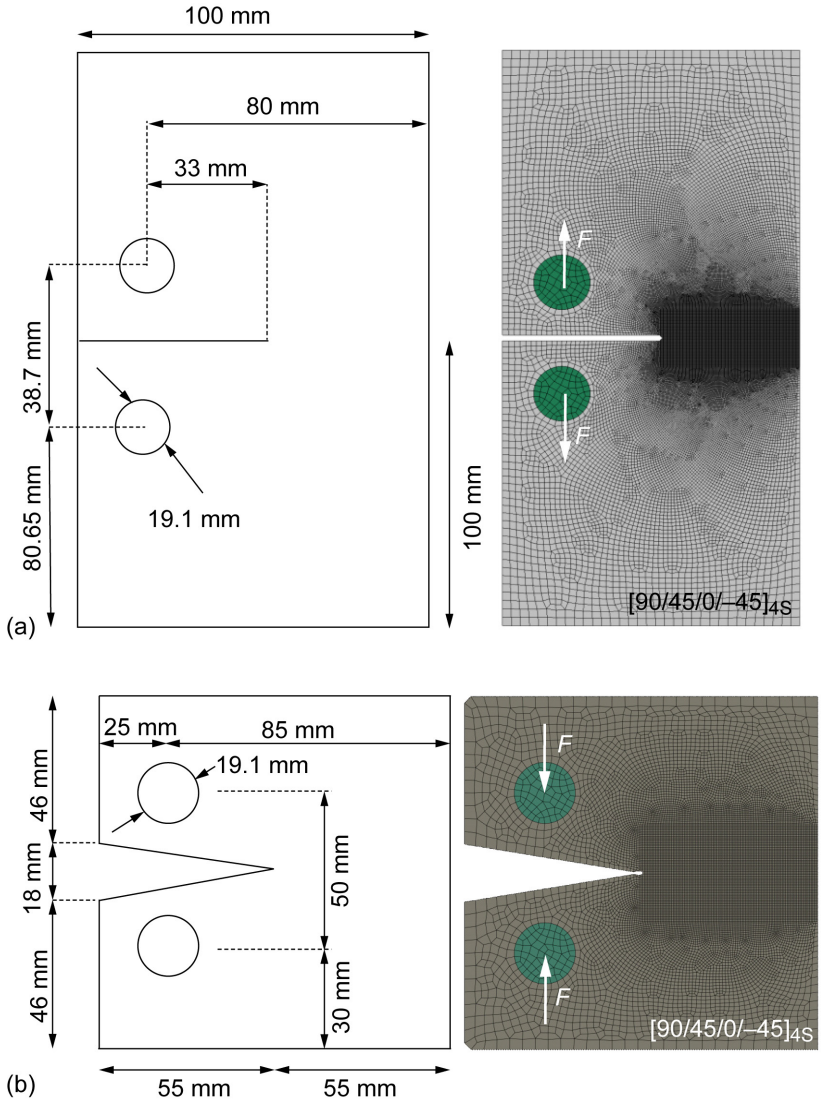

Figure 92.—Fracture mechanic test dimensions and numerical models.
(a) Dimensions and simulation model for over-height compact tension test.
(b) Dimensions and simulation model for compact compression test.

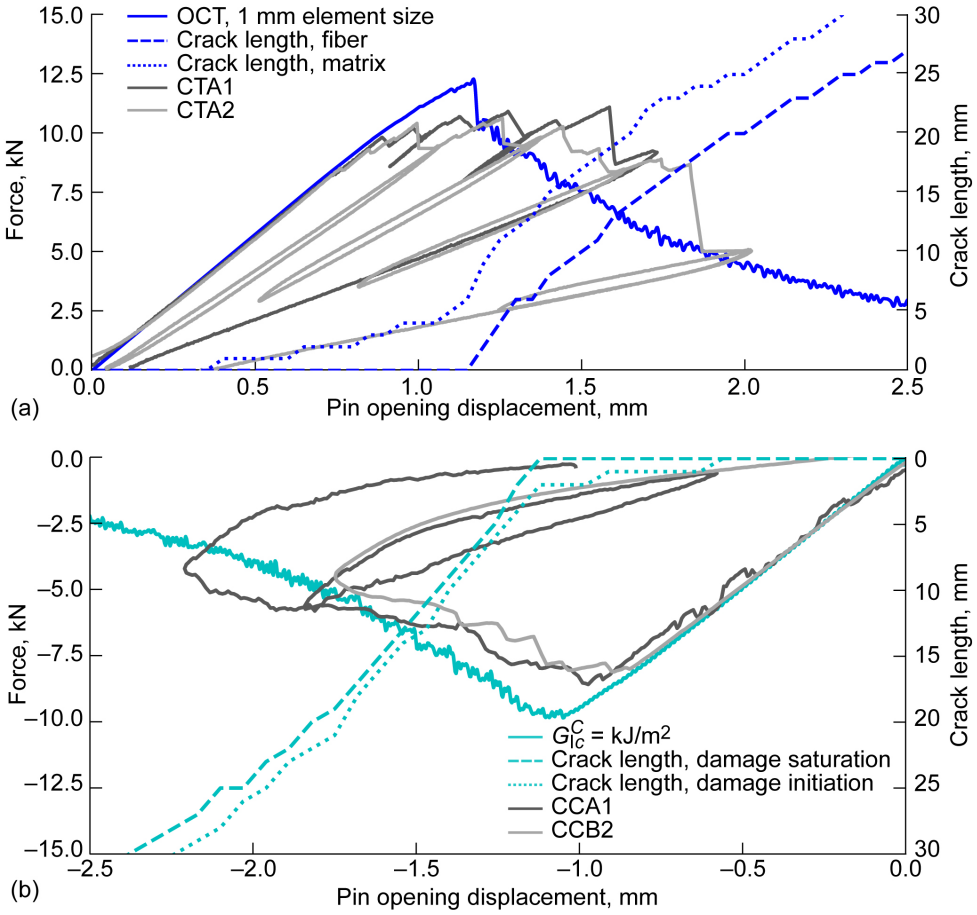

Figure 93.—Comparison of force versus pin-opening displacement test data and simulations for fracture mechanics tests. (a) Compact tension (CT) tests. (b) Compact compression (CC) tests; displacement scaled.

4.8.6 Simulation of Progressive Crushing: Self-Supported Crush Segment and Discretization Study

At the building-block level of progressive crushing, a numerical study on a self-supported, omega-shaped crush segment (the so-called DLR segment) was carried out first. Self-supported crush specimens had been previously discussed, tested, and simulated in the scope of RR–1 and RR–2 (see Section 3.0). The self-supported crush segment has been used in the past in various studies (Refs. 44 to 46) and proved suitable for investigation of composite materials. The transient–dynamic crush behavior of the self-supported DLR segment was previously identified as mainly intralaminar fragmentation. Due to the intralaminar-dominated failure mode, this segment was identified as a helpful intermediate step between the building-block level of fracture mechanic tests and the simulation of progressive crushing of flat coupon and C-channel specimens, which provide a more complex crush response, including fragmentation, splaying and, to some extent, tearing. Self-supported crush segments were also identified as suitable for comparison of numerical damage models, modeling approaches, and FE solvers, as the test boundary conditions are simple and allow precise representation in the numerical models.

The numerical study carried out on the self-supported segment considered discretization options, investigating in detail the FE mesh and element size dependency. Figure 94 shows the numerical models. Three mesh types and three element sizes were investigated. A structured mesh (Figure 94(a)), a skewed mesh with 10° inclined element edges (Figure 94(b)), and an unstructured mesh (Figure 94(c)) were

investigated, and elements with characteristic lengths of 0.5, 1.0, and 2.0 mm were considered. The influence of mesh type is shown in Figure 94 based on the 1.0-mm element size. With a structured mesh (Figure 94(a)), the simulation results show the well-known force–displacement characteristics driven by significant force spikes. Simultaneous failure and element deletion of entire element rows leads to force drops and subsequent unrealistic high force spikes when the next undamaged element row gets in contact with the impact plate. In this way, the force spikes reach force levels that are significantly higher than the failure initiation force of the triggered specimen. As a consequence, in the simulation, the excessive force spikes led to catastrophic failure of the specimen. In contrast, the skewed and unstructured meshes (Figure 94(b) and (c)) provided continuous damage, failure, and erosion of elements in the crush zone.

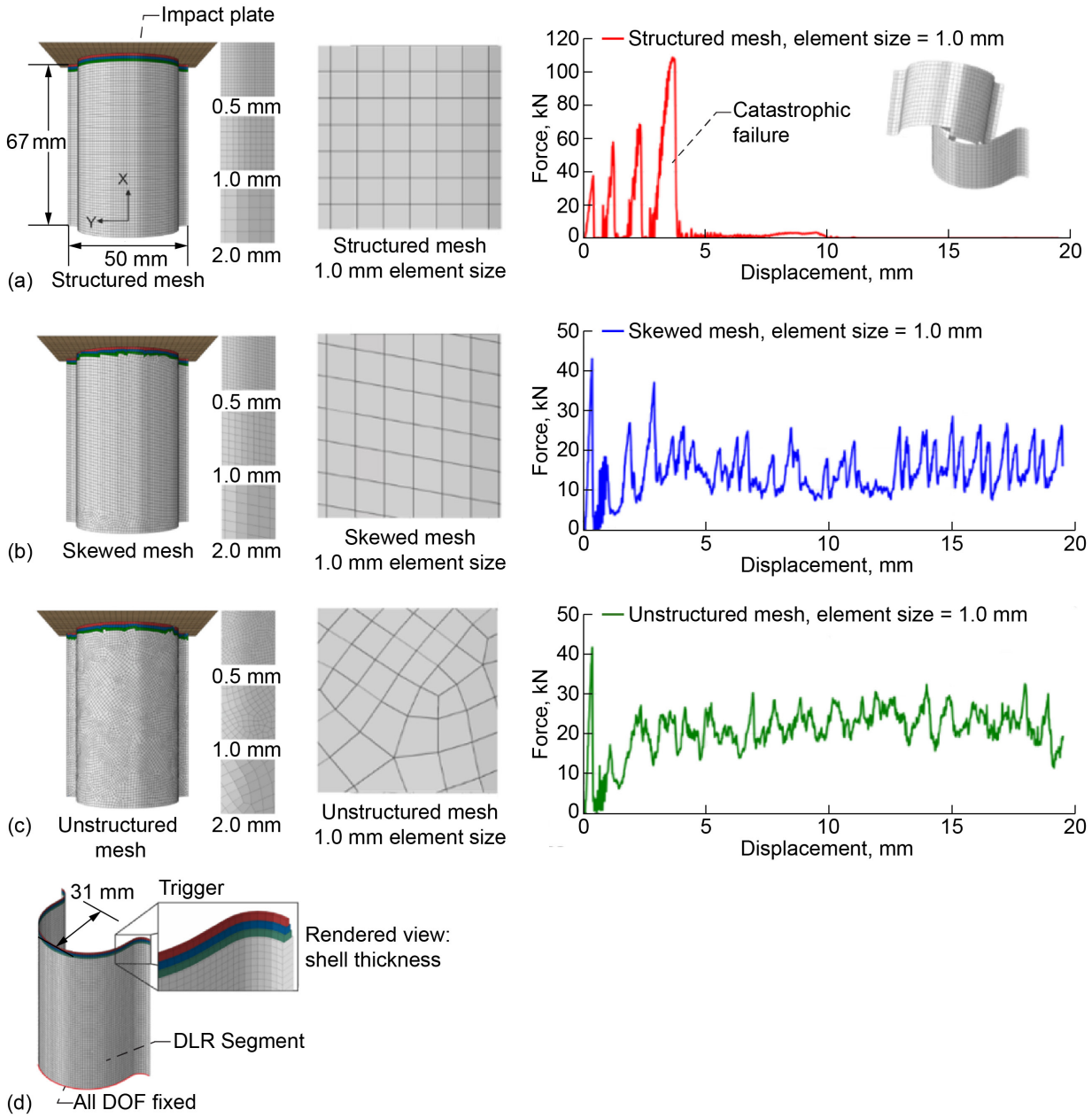

Figure 94.—Self-supported crush segment numerical models with simulation results showing influence of mesh type; v = 2 m/s. (a) Structured mesh. (b) Skewed mesh. (c) Unstructured mesh. (d) View of model showing trigger.

This mesh dependency study clarified the significant influence of model discretization on the simulation of progressive crushing. Based on these findings, skewed mesh elements were used for the numerical modelings of flat coupon and C-channel crushing.

4.8.7 Simulation of Progressive Crushing: Flat Coupon Crush Test

Up to this building-block level, a mesoscale single-shell layer approach was used in which the composite laminate is discretized through thickness by one single-shell element layer. Each ply of the composite laminate is represented by one or multiple integration points through the thickness of the shell element (a ply-based modeling approach). In contrast to the self-supported crush specimen previously simulated, flat coupons generally tend to locally buckle when subjected to crush loading. As a consequence, the crush-zone failure phenomena are no longer driven solely by intralaminar failure modes but also by interlaminar failures in terms of large delamination, and this needs to be considered in the simulations.

To reliably capture this complex crush failure mode, an extended mesoscale approach, the so-called stacked-shell approach, was used in which the composite laminate is discretized through thickness by a stack of multiple shell element layers representing the individual plies. Cohesive elements or cohesive contact are modeled between the individual shell element layers and enable the separation of the shell layers, thus representing interlaminar failure. In this applied modeling approach, fragmentation as an intralaminar-dominated failure mode was represented by the shell-element-implemented material model ABQ_DLR_UD, whereas splaying as a major interlaminar failure mode was modeled using cohesive elements with a bilinear traction–separation behavior.

The interlaminar material parameters were taken from literature and are outlined in Reference 3. Figure 95 illustrates the flat coupon simulation models and compares the single-shell and stacked-shell modeling approaches. Both approaches were considered to identify their capabilities and limitations. The boundary conditions in the numerical models were derived from the test setup, including the support plates as well as the clamping in the upper 20 mm of the flat coupon specimen. The gap height in the experimental tests was selected dependent on the layup of the flat coupon specimen and was modeled in accordance with the experimental tests in a range of 7.5 to 15 mm. A sawtooth trigger at the impacted end of the flat coupon specimen was implemented in the model. Friction between the specimen and the impact plate was modeled with a friction coefficient of $\mu_F = 0.2$. Self-contact of the specimen was modeled with $\mu_F = 0.4$, whereas the contact of the flat coupon specimen and the support plates was assumed to be frictionless. The support and impact plates were modeled as rigid bodies.

Instead of modeling the drop mass from the experiments, loading was modeled by a constant velocity boundary condition ($v = 4$ m/s) applied to a set of nodes containing the uppermost nodes of the flat coupon specimen, whereas the remaining translational and rotational DOFs were fixed. The resin-embedded clamping in the test setup was modeled by fixing the lateral, translational DOFs (y, z) of all nodes within 20 mm from the top of the flat coupon. For the stacked-shell modeling approach, the clamping boundary condition was applied only to the nodes on the surface of the specimen. The skewed-mesh element type was selected for the flat coupon model with 10° inclination angle of the element edges. The characteristic length of the elements is $l^* = 1.0$ mm. In the single-shell model, the intralaminar plies were modeled by a single layer of conventional four-node shell elements (element type S4R). The laminate thickness was modeled via section properties in the model definition. In the stacked-shell model, identical mesh types and element sizes were used for the intralaminar shell layers and cohesive layers. However, eight-node continuum shell elements were used here. The thickness of the cohesive elements was selected as $t_{COH} = 0.01$ mm.

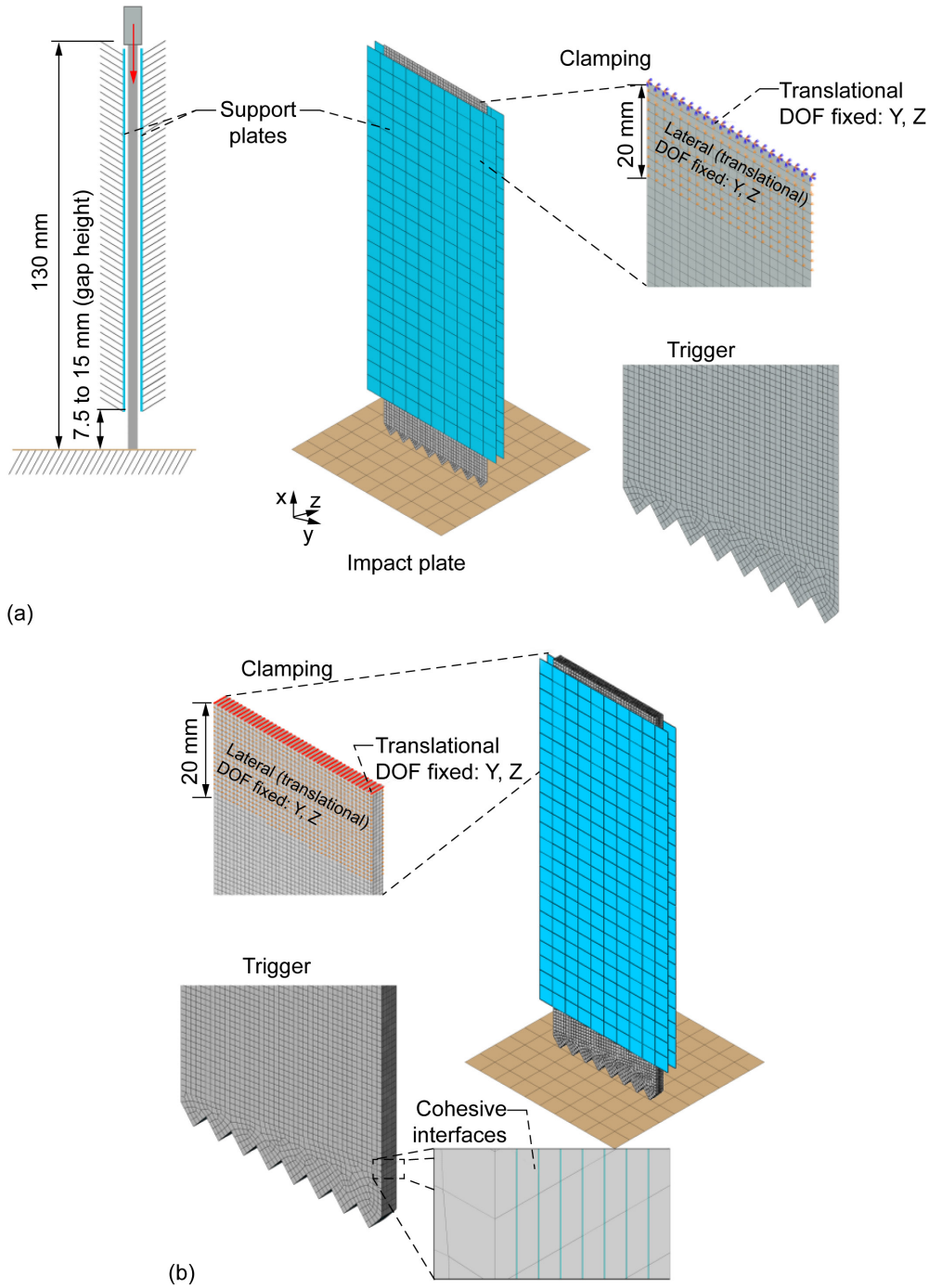

Figure 95.—Numerical model of flat coupon crush tests. Degree of freedom, DOF. (a) Single-shell model. (b) Stacked-shell model.

The results of the single-shell model are presented in Figure 96. Contact force versus displacement of the impact plate for the quasi-isotropic layup QI01 with stacking sequence $[90/\pm45/0]_{2S}$ and a gap height of 8.6 mm is shown. Figure 96 presents the results of the single-shell model simulation as well as the experimental results obtained from the University of Utah. Unfiltered and filtered numerical results using a Butterworth low-pass filter with 20-kHz cutoff frequency are shown. The presented experimental results

are unfiltered. Comparison of the experimental and numerical results was quantitatively performed based on the mean crush force P_{crush} and the Stable SEA, defined in Equation (3) as

$$\text{Stable SEA} = \frac{P_{crush}}{\rho A} \tag{3}$$

(See also Section 4.3.2, Eq. (1), and Chapter 16 of Ref. 3 for further discussion of SEA.) Where ρ is the density of the material and A the cross-sectional area of the flat coupon specimen, P_{crush} and Stable SEA were determined for the displacement range of 10 to 30 mm, which is in the range of steady-state crushing. Comparison of the force–displacement characteristics shows that the single-shell simulation predicts a higher steady-state crush force level as compared with the experimental results. The mean crush force of the simulation is $P_{crush,sim}$ = 15.2 kN, nearly twice as high as the average mean crush force of the three experimental results, which is P_{crush} = 8.7 kN. The same tendency is seen for Stable SEA, where the simulated Stable SEA of 91.2 kJ/kg is twice as high as the average experimental result of 46.1 kJ/kg. The reason for this discrepancy could be identified in the single-shell modeling approach.

This model is able to capture the pure fragmentation failure mode, whereas ply interface failure, such as splaying, cannot be captured. Splaying as a low-energy failure mode has significant influence on the crush response and furthermore depends on the laminate layup. In the flat coupon crush experiments of different quasi-isotropic laminates as well as nonisotropic hard laminates, it has been shown that different layups result in different crushing behavior, with varying extent of splaying. Depending on the ratio of fragmentation and splaying failure, the SEA of the layups varies. Because the single-shell model is not able to predict splaying, the SEA is generally overpredicted. (This can be seen in Figure 99 in the force–displacement characteristics of different quasi-isotropic and hard laminates.) For all layups, the single-shell model prediction provided higher Stable SEA as obtained in the experiments. As a result, the single-shell modeling approach, which is not capable of representing splaying, generally tends to overpredict Stable SEA and was not able to predict the influence of different layups on the Stable SEA.

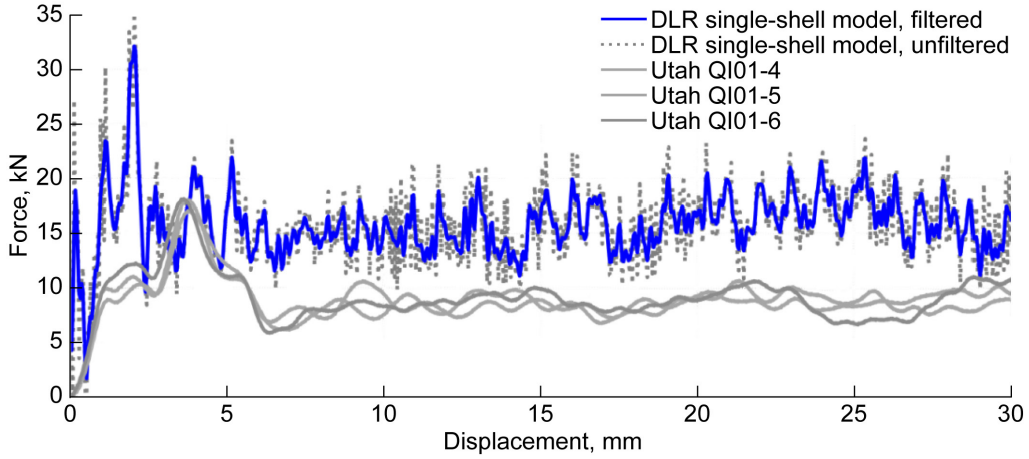

Figure 96.—Force–displacement characteristics of flat coupon simulation for laminate QI01 $[90/\pm45/0]_{2S}$ using single-shell model.

The results of the stacked-shell model are shown in Figure 97. In this model, cohesive interfaces were implemented, enabling the simulation of interlaminar failure such as splaying. Comparing the force–displacement characteristics shows good correlation between the stacked-shell simulation and the experimental results in terms of the steady-state force level. The mean crush force of the stacked-shell simulation between 10- and 30-mm crush displacement is P_{crush} = 7.2 kN (vs. the experimental result of 8.7 kN). This results in a simulated Stable SEA of 43.9 kJ/kg (vs. the experimental result of 46.1 kJ/kg).

Moving from the single-shell to the stacked-shell modeling approach, no further calibration of the intralaminar model was performed. Only the cohesive interface model was additionally implemented into the model, with cohesive material input data taken directly from the literature without further calibration. The cohesive material input data is outlined in Section 5.3.5 (Table 20). Figure 98 highlights the stacked-shell modeling capability to represent splaying and exemplarily compares the crush failure mode with the experiment for a hard laminate with layup $[90_2/0_2/\pm 45/0_2]_S$ (HL01). For both experiment and simulation, splaying of the outer layers can be seen, whereas the inner layers fail in fragmentation. The extent of splaying and depth of delamination failure may change with a calibrated interface model. However, this demonstrates the model's capability to capture both relevant failure modes, fragmentation and splaying, which absorb the majority of energy under progressive crushing.

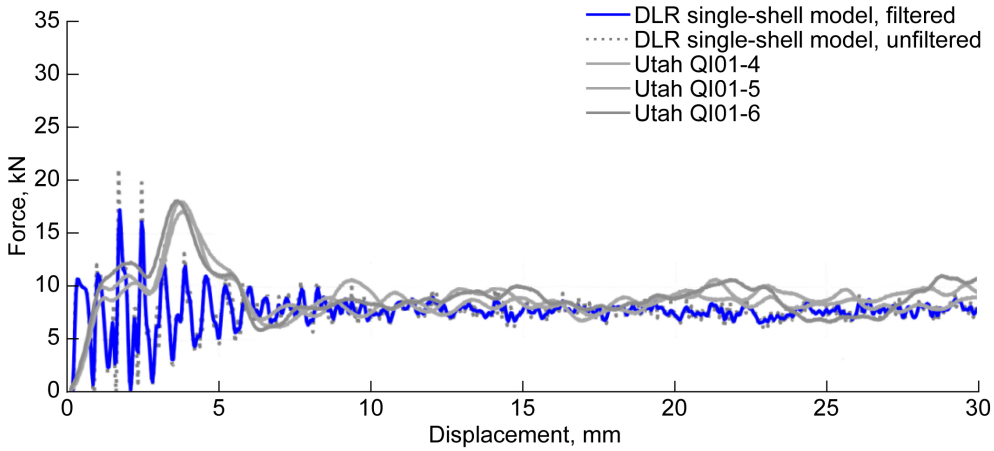

Figure 97.—Force–displacement characteristics of flat coupon simulation of laminate QI01 $[90/\pm45/0]_{2S}$ using stacked-shell model.

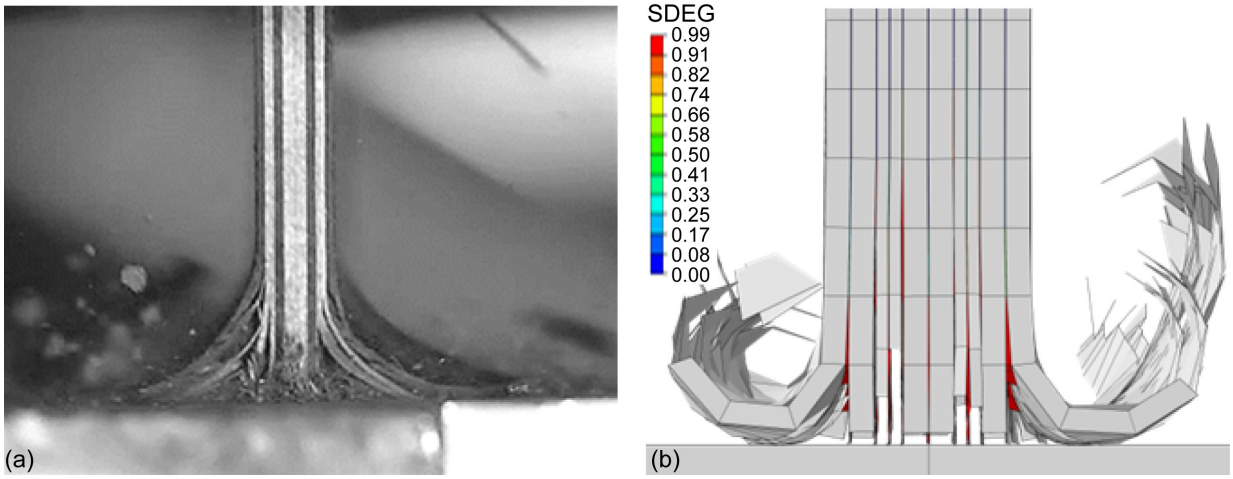

Figure 98.—Side view of flat coupon crush test and simulation with stacked-shell model for HL01 $[90_2/0_2/\pm45/0_2]_S$. (a) High-speed images from test. (b) Contour plot of simulation.

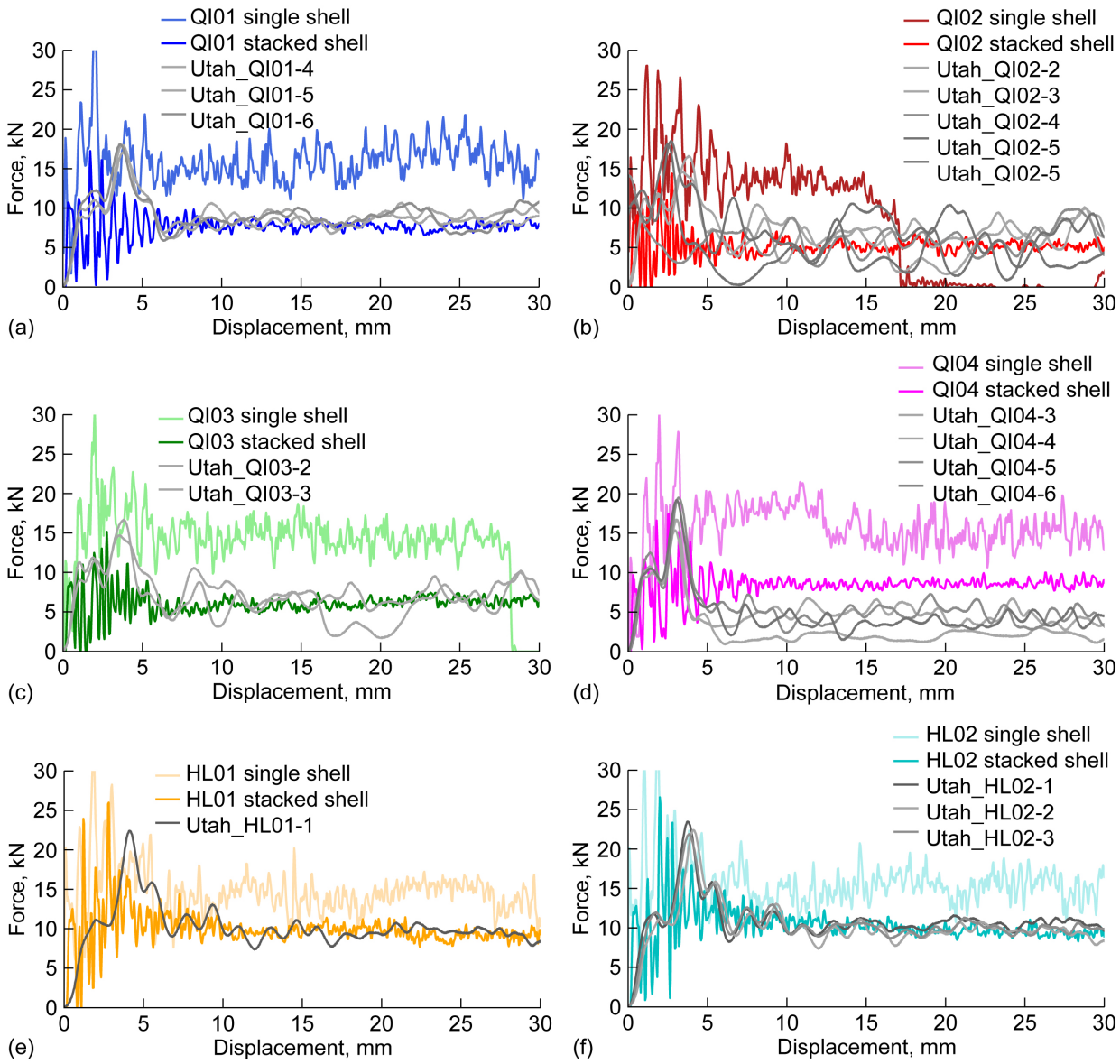

Figure 99.—Force–displacement curves for QI and HL simulations using both single-shell and stacked-shell models versus experimental results. (a) QI01, $[90/\pm45/0]_{2S}$, gap height 8.6 mm. (b) QI02, $[90_2/(\pm45)_2/0_2]_S$, gap height 15.0 mm. (c) QI03, $[(\pm45)_2/90_2/0_2]_S$, gap height 15.0 mm. (d) QI04, $[\pm45/90/0]_{2S}$, gap height 7.5 mm. (e) HL01, $[90_2/0_2/\pm45/0_2]_S$, gap height 14.5 mm. (f) HL02, $[90/\pm45/0_2/90/-45/0_2]_S$, gap height 12.0 mm.

Due to its capability of modeling the splaying failure mode, the stacked-shell model is also capable of predicting the influence of different layups. This is shown in Figure 99, where the force–displacement characteristics show good correlation with the experimental results for the quasi-isotropic and hard laminates. The test and analysis correlation for variant QI04 shows an outlier, but the reasons are unclear.

Figure 100 quantitatively compares the Stable SEA values of both single-shell and stacked-shell simulations with the experimental results. The same tendency is shown: the influence of different layups is reasonably predicted by the stacked-shell simulations due to the capability to model both dominant crushing modes, fragmentation, and splaying. The single-shell modeling approach was not able to predict the Stable SEA and the influence of the layups. In addition to the Stable SEA (10 to 30 mm displacement), Total SEA (0 to 30 mm displacement) is presented in this figure.

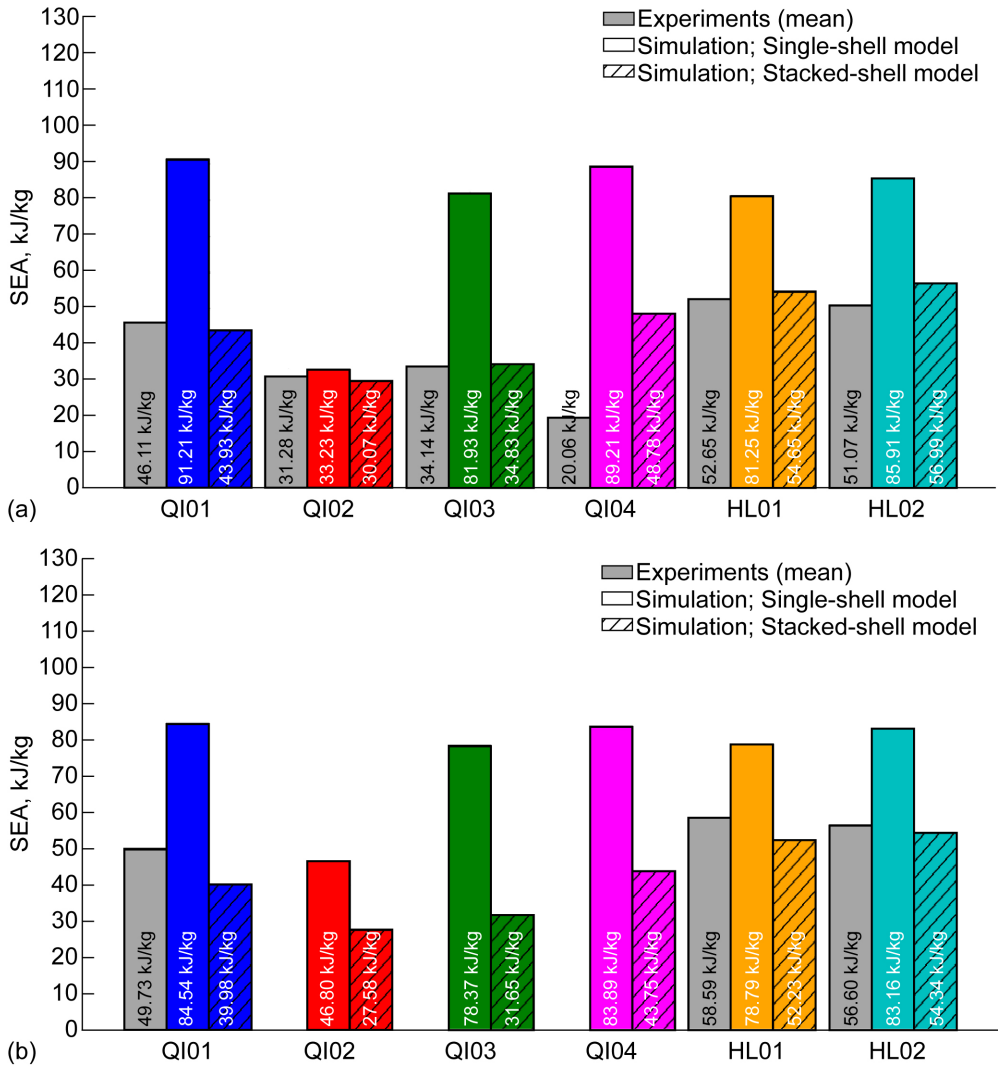

Figure 100.—SEA values for QI and HL simulations using both single-shell and stacked-shell models versus experimental results. (a) Stable SEA (10 to 30 mm). (b) Total SEA (0 to 30 mm).

Based on the outcomes of the flat coupon crush predictions, the conclusion was made that model capability of representing ply interface failure is essential, although further complexity in the simulation model may lead to a significant increase of resources in terms of simulation times and effort for the modeling setup. For this reason, the stacked-shell modeling approach was chosen for the modeling C-channel crushing.

4.8.8 Simulation of Progressive Crushing: C-Channel Crush Test Analysis

The analysis teams were tasked to simulate the C-channel crush response for two different hard laminates selected from the set of layups previously tested with the flat crush coupons:

- HL01 with stacking sequence $[90_2/0_2/\pm45/0_2]_S$
- HL02 with stacking sequence $[90/45/0_2/90/-45/0_2]_S$

C-channel specimens were tested quasistatically, as well as in drop tests with different initial velocities of 3.81 m/s (150 in./s) and 7.62 m/s (300 in./s) using a drop mass of 39.92 kg (88 lb).[11] Accordingly, a drop mass of 39.92 kg was applied in the simulations. The following properties were identified as responses in the numerical models:

- Crush distance
- Peak crush force
- Average crush force
- Stable SEA
- Crush force efficiency

Figure 101 shows the numerical model of the C-channel segment used for the stacked-shell modeling approach.

As a typical response of the C-channel crush test, Figure 102 shows the contour plots of matrix damage at two states for hard laminate HL01, directly after reaching the peak force and at crush displacements of 14.7 mm (Figure 102(a) and 14.5 mm (Figure 102(b)). The simulation results for different loading conditions are presented with detailed discussion in Section B.12.

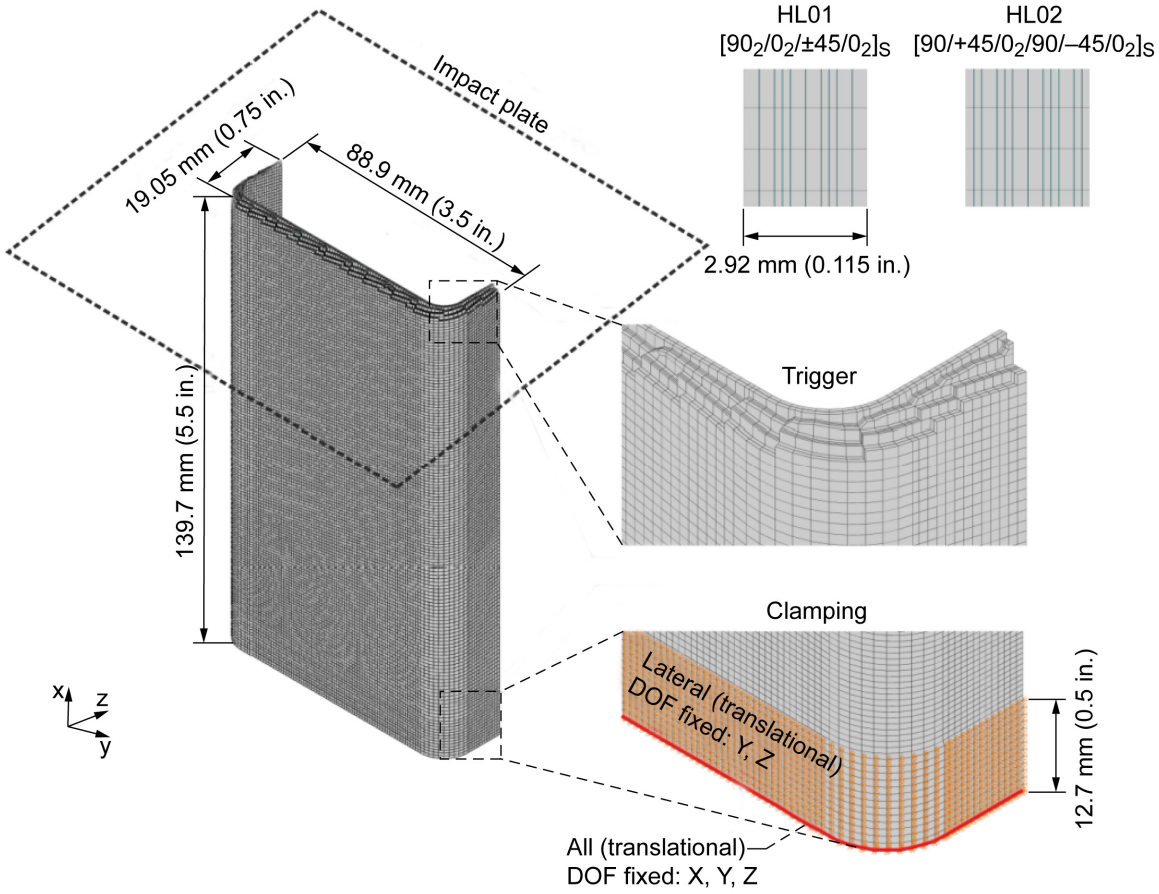

Figure 101.—Numerical model of C-channel segment used for simulation (stacked-shell model).

[11]As noted in Section 4.0, impactor mass for the C-channel crush test was incorrectly assumed to match that of the flat coupon; see Table 21 for correct values.

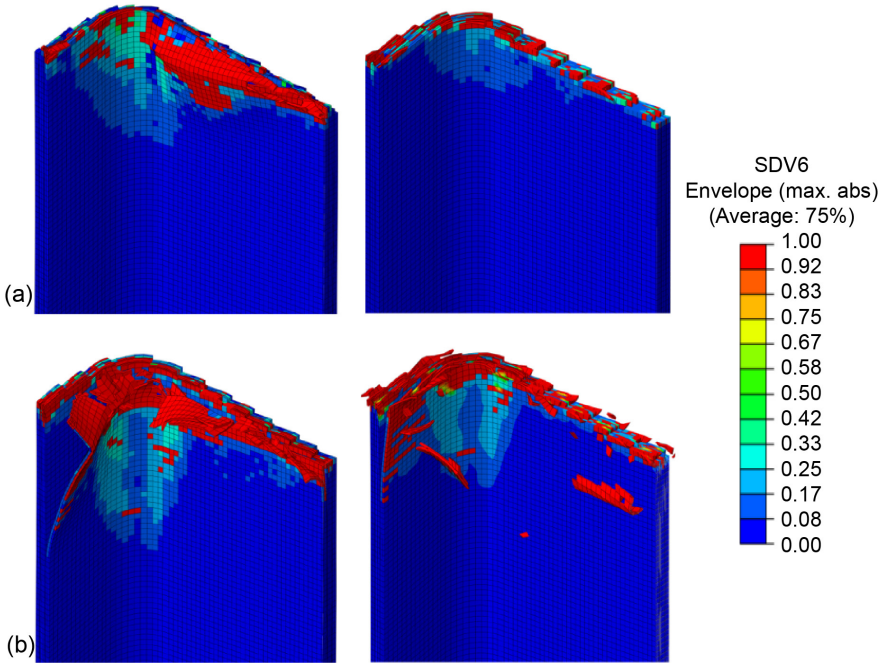

Figure 102.—C-channel HL01 $[90_2/0_2/\pm45/0_2]_S$ crush simulations. SDV6 is ABAQUS® solution-dependent variable 6, matrix damage. Envelope plot of all plies showing absolute maximum value (max. abs). (a) Impact velocity 3.81 m/s; directly after reaching peak force at 1.9 mm (left) and at crush displacement of 14.7 mm (right). (b) Impact velocity 7.62 m/s; directly after reaching peak force at 1.9 mm (left) and at crush displacement of 14.5 mm (right).

4.8.9 ABAQUS® Ladevèze: ABQ_DLR_UD Modeling Best Practices

The presented numerical methodology employed a building-block approach from single-element simulations to C-channel crushing predictions. Based on the performed work, the following modeling best practices can be identified:

- Simulations of a single-laminate element were identified as a basic level for comparison of different material models as well as FE codes. General tendencies valid for the entire building block could already be identified at this level.
- Calibration of the fiber fracture energies was successfully performed based on intralaminar fracture mechanic tests. Experimental results of OCT and CC tests were used to calibrate the tensile and compressive fiber fracture energies, respectively. With the calibration of fiber fracture energies, the material input dataset was fixed, and further calibration on higher building-block levels was not performed.
- At the building-block level of progressive crushing, self-supported crush segments were identified as ideal specimens for the validation of numerical methods, as test boundary conditions are simple allowing precise representation in the numerical models, and the crush failure is dominated by intralaminar fragmentation.
- A mesh dependency study can be crucial in identifying proper discretization for simulation of progressive crushing. Use of a skewed mesh element was identified as a best practice in obtaining smooth force characteristic without unrealistic and mesh-dependent force spikes.
- Use of a single-shell versus stacked-shell modeling approach needs to be considered depending on the individual application case. The single-shell model capability showed major limitations and only pure fragmentation failure could be captured, which resulted in an overprediction of the crush

force and Stable SEA when splaying occurs in the experiment. As splaying strongly depends on the layup, the single-shell modeling approach is not able to identify the influence of different layups. In contrast, the stacked-shell modeling approach was able to capture fragmentation and splaying. This results in good test and analysis correlation of the crush force and Stable SEA for different layups. However, a significant increase in cost and effort required to build up the simulation model must be considered in the decision between a single-shell and stacked-shell modeling approach.

- As splaying is expected to be a dominant failure mode for C-channel crushing, the simulations were performed based on stacked-shell models.
- For development of numerical methods, joint research work by different teams using different approaches and FE codes was identified as a very helpful and valuable strategy. This practice provides better objectivity and enables the identification of model- or FE-code-specific effects which would otherwise have been difficult or impossible to identify. This finding is an outcome of the research collaboration between DLR and UBC.

4.9 ABAQUS® CZone

This section describes the prediction of a crush event using the CZone methodology. CZone predictions were completed by the University of Utah in collaboration with Engenuity Ltd. The objective of these predictions was to use CZone to accurately predict Total SEA of a composite in crush while simultaneously monitoring for failure away from the crush front.

4.9.1 Material Model Description

CZone is an ABAQUS®/Explicit add-on created by Engenuity Ltd. that is designed to predict the crush behavior of polymer matrix composite structures. Composite crush structures are designed to absorb large amounts of energy through controlled, progressive failure. Modeling the crush process at the lamina (ply) level requires a broad understanding of the failure mechanisms of composite laminates during crushing. This ply-level approach is both complex and computationally expensive. In contrast, CZone provides an engineering approach to predicting the crush behavior of composites structures that focuses on use of the laminate crush stress as an input property to the analysis. This laminate crush stress, measured using flat coupon crush tests, inherently controls the energy absorption due to crushing of the specific composite laminate. CZone does not microscopically predict the failure mechanisms at the crush front.

To accurately predict the behavior of a composite crush structure, FE simulations must be able to predict failures occurring both at the crush front and in the backup structure that is not part of the crush progression. CZone works in conjunction with ABAQUS®/Explicit to perform these analyses: CZone is used to predict crush events at defined crush fronts within the structures while ABAQUS®/Explicit is used to predict all failures occurring away from the crush front. CZone requires inputting the laminate crush stress as an input property. Additional required input properties include those used to define strain-rate effects, damping effects, cyclic shear behavior, and fracture response.

4.9.2 Model Input and Assumptions

Due to CZone's engineering approach, a VUMAT subroutine must be extensively defined. Accurate material characterization is crucial for CZone models to accurately predict a crush event. CZone utilizes the laminate crush stress as a material property to characterize the stress that produces material crushing. Additionally, all of the stiffness properties of the IM7/8552 carbon/epoxy composite material were defined as shown in Section 5.2.2 (Table 15). However, due to the strain-rate dependency of certain mechanical properties and specific CZone requirements, additional material properties were needed to monitor failure in the backup structure using ABAQUS®/Explicit. It should be noted that once the

material properties are determined from coupon-level tests, they do not need to be tuned to adjust for the different geometry, size, or boundary conditions of the crush structure.

Laminate Crush Stress.—The crush stress of a laminate is determined using flat coupon crush tests. To measure the crush response of a laminate, the test coupons must be free to crush but must be constrained against buckling. A suitable flat coupon crush test fixture, developed at the University of Utah, is shown in Figure 103. Because crush behavior can be geometry dependent, crush values for both the flat regions and curved regions of a structure are measured through the use of unsupported and pin-supported delamination-suppressed flat coupon tests. The flat and curved regions of the structure in the model are identified so that the appropriate crush stresses are assigned to the appropriate regions. Engenuity Ltd. suggests that the curved crush stress is to be applied to a region that extends one laminate thickness beyond the actual region with curvature.

The CZone code assumes that the laminate stacking sequence exhibits stable crush, meaning there is minimal crush-stress variation during coupon crush tests. A laminate that exhibits low stability (large crush stress variations) should not be used with the CZone code, because the laminate crush stress implemented in the VUMAT subroutine is an average crush stress.

In addition to measuring overall laminate crush stress, the individual lamina (ply) crush stress associated with all of the ply orientations within the laminate can be determined using a procedure developed by Engenuity Ltd. The crush stress can therefore be input into CZone either as an overall laminate crush stress or as individual ply crush stresses. Defining the crush stress at the ply level allows CZone to predict crushing for more complex geometries and loadings that produce more complex stress distributions in the composite laminate.

Dynamic Strength Properties.—To monitor the structure for failure away from the crush front, some dynamic strength properties of the composite material must be input. The required input properties include both the dynamic compression and dynamic shear response of the particular composite laminate. These dynamic tests were performed at Engenuity Ltd. using IM7/8552 carbon/epoxy panels fabricated at the University of Utah.

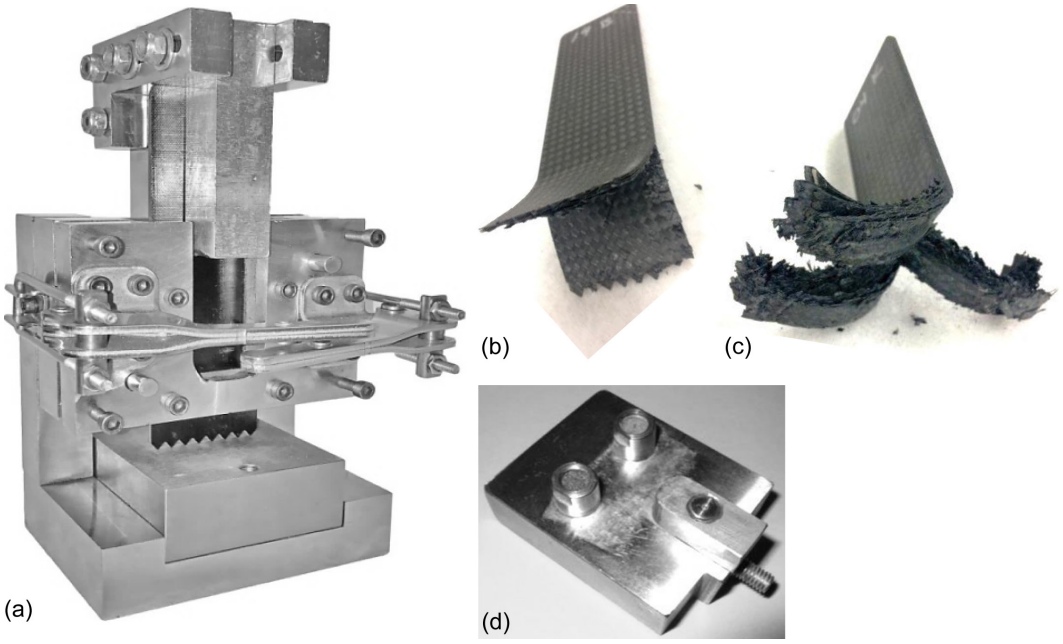

Figure 103.—University of Utah flat coupon crush test fixture and specimens. (a) Test fixture. (b) Flat free-supported specimen. (c) Pin-supported specimen. (d) Pin supports.

Damping Properties.—When analyzing the dynamic response of a structure, characterization of the material's damping properties is required. These damping properties control the structural vibrations, the dissipation of energy, and the stress–strain response of the material. Such damping reduces the magnitude of stress wave oscillations produced in a structure during dynamic loading, which can lead to failure in the backup structure. Section B.13.1 (Table B.16) provides IM7/8552 damping properties based on DMA testing; see Reference 47.

Shear Degradation Properties.—Cyclic shear tests were performed to define the nonlinear shear stress versus shear strain response of the IM7/8552 carbon/epoxy material. The methodology used and parameters determined are discussed in Reference 47. The results and values implemented into the CZone material card are presented in Section B.13.2 (Table B.17).

Fracture Properties.—Predicting failures in a composite structure away from the crush front requires characterizing the fracture behavior of the composite material. Once a failure is initiated, the fracture behavior of a laminate will dictate subsequent failures and crush behavior. Therefore, fracture energy release rate (FERR) values are required to predict how the composite laminate will fail at the crush trigger and in the backup structure. The test methodologies for characterizing FERR for IM7/8552 used in the CZone analyses are discussed in Section B.12, and FERR testing results are presented (Table B.18); see also Reference 47.

Friction must be defined for implementation at the interface between the impact mass and the crush structure. The friction coefficient was defined as 0.2 for all simulations. This value was recommended by Engenuity Ltd. due to their previous experience with composite crush simulations (Ref. 47).

CZone Crush Interaction.—A resistive force is calculated and distributed to the nodes of the elements. The resistive force is calculated as

$$F = \sigma A \tag{4}$$

where σ is the crush stress of the ply and A is the cross-sectional area. The cross-sectional area is defined as

$$A = t * w \tag{5}$$

where t is the thickness of the shell element and w is the width of the element at the interaction, as shown in Figure 104. During the interaction, the element is allowed to pass through the rigid surface with which it is in contact. However, the element is not deleted until the entire element has passed through the rigid surface. Using this methodology, there are no force spikes due to element deletion, and thus the force results do not require filtering.

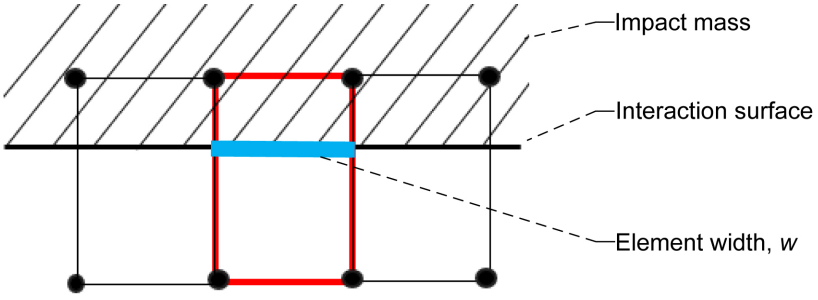

Figure 104.—CZone crush interaction.

4.9.3 Simulation of Progressive Crushing

Flat Coupon Model Description.—To simulate a crush event within ABAQUS®/Explicit, two different components must be modeled: the crush structure and the impacting mass. For this effort, the crush structure was modeled as a 3D deformable shell structure, and the 44-kg impact mass was modeled as a 3D discrete rigid shell.[12] The composite layup feature in ABAQUS® was used to define the stacking sequence of the two hard laminates, and the flat and curved surfaces of the crush front were identified.

Meshing.—The unsupported and pin-supported flat coupon tests were used as the basis to validate the CZone simulations. The aforementioned crush stress and additional input properties were implemented through a VUMAT subroutine. The crush structure was meshed on the part using S4R elements. When using CZone, the elements cannot exceed a critical length (Ref. 47). This critical length L_{crit} is defined as

$$L_{crit} = \frac{2G_f E}{(X U_{\max})^2} \tag{6}$$

where G_f is the FERR, E is the stiffness, X is the static strength, and $U_{\max}$ is an uplift factor. The uplift factor is defined as

$$U_{\max} = \frac{X_d}{X} \tag{7}$$

where X_d is the dynamic strength. The critical length is calculated for 0° tension, 90° tension, 0° compression, and 90° compression. The smallest calculated critical length is taken as the largest permissible element length. For this simulation, the largest critical length was 0.04 in. (2.54 cm) Therefore, the CZone analysis could utilize any element length up to 0.04 in.

Crush Stress Definition at Interaction.—Once the laminate and/or ply crush stresses are determined, they are applied to the elements of the FE model through a general contact approach, as described in Section 4.9.2. The crush stresses can also be applied to the interaction surface through a surface contact approach.

4.9.4 Simulation of Progressive Crushing: Flat Coupon Predictions Using CZone

Figure 105 and Figure 106 compare the CMH–17 flat coupon crush test results with the CZone simulations for the unsupported and pin-supported coupons, respectively. Note that for the selected $[90/45/0_2/90/–45/0_2]_S$ laminate (HL02), the experimental crush stress values from both the unconstrained and pin-constrained crush tests were similar. The experimental results show a large initial peak force with a subsequent oscillating crush force. In contrast, the CZone simulations do not show an elevated, initial peak force but rather a constant crush force.

Due to CZone's modeling approach, the differences between the experimental test results and the CZone simulation results were expected. As previously described, CZone calculates a crush force using the defined crush stress. The crush force is then divided out equally to the element's nodes. Therefore, oscillating forces are not expected at the contact interface during crushing. If desired, the oscillations the material experiences can be monitored away from the contact interface using an integrated output section assignment. Furthermore, when calculating the crush stress from the crush tests using CZone, the peak force is not included in calculated crush stress, as this peak force does not affect the energy absorption of

[12]The correct platen mass of 44.0 kg was used in the CZone flat specimen simulations; see Table 21 for reference to experimental platen mass values.

the structure. However, this peak force can produce failure in the backup structure if crush initiators, or triggers, are not properly implemented. Therefore, crush triggers should be designed into composite structures to mitigate the initial peak force.

To validate the CZone predictions, a comparison of average crush stress between flat coupon crush tests and CZone simulations is presented in Section B.13.

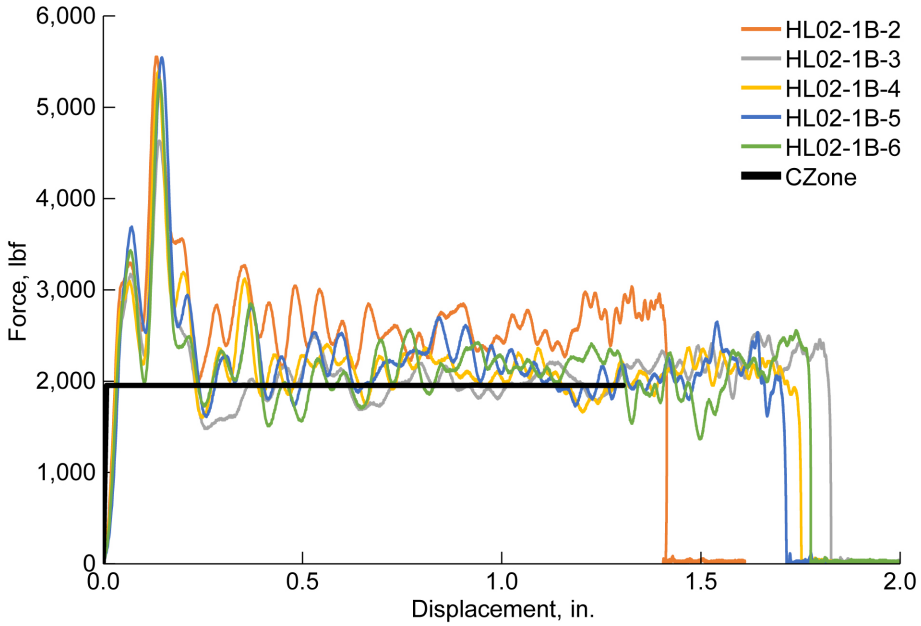

Figure 105.—Unsupported flat coupon crush test force–displacement results for CZone simulation versus experiments.

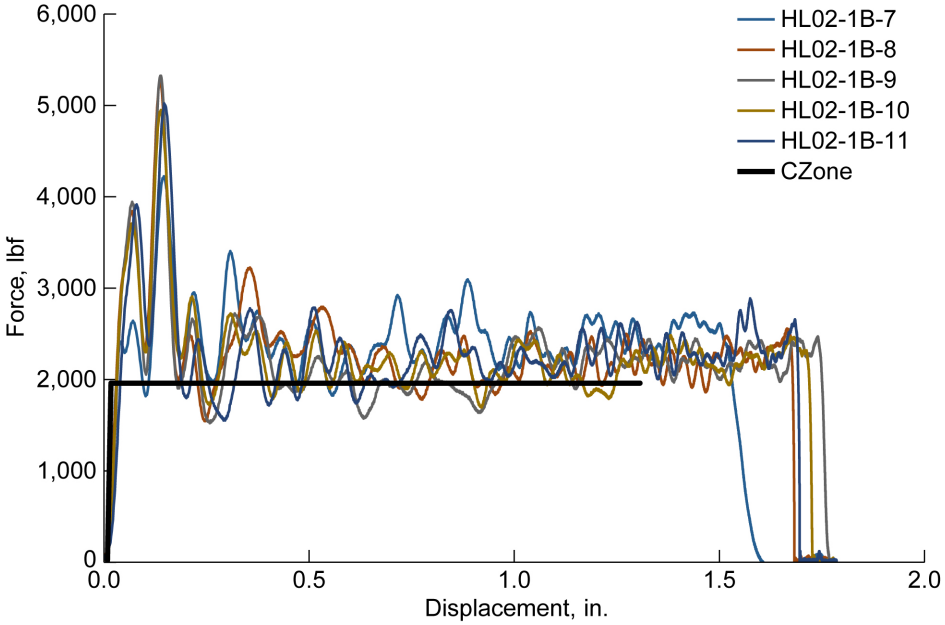

Figure 106.—Pin-supported flat coupon crush test force–displacement results for CZone simulation versus experiments.

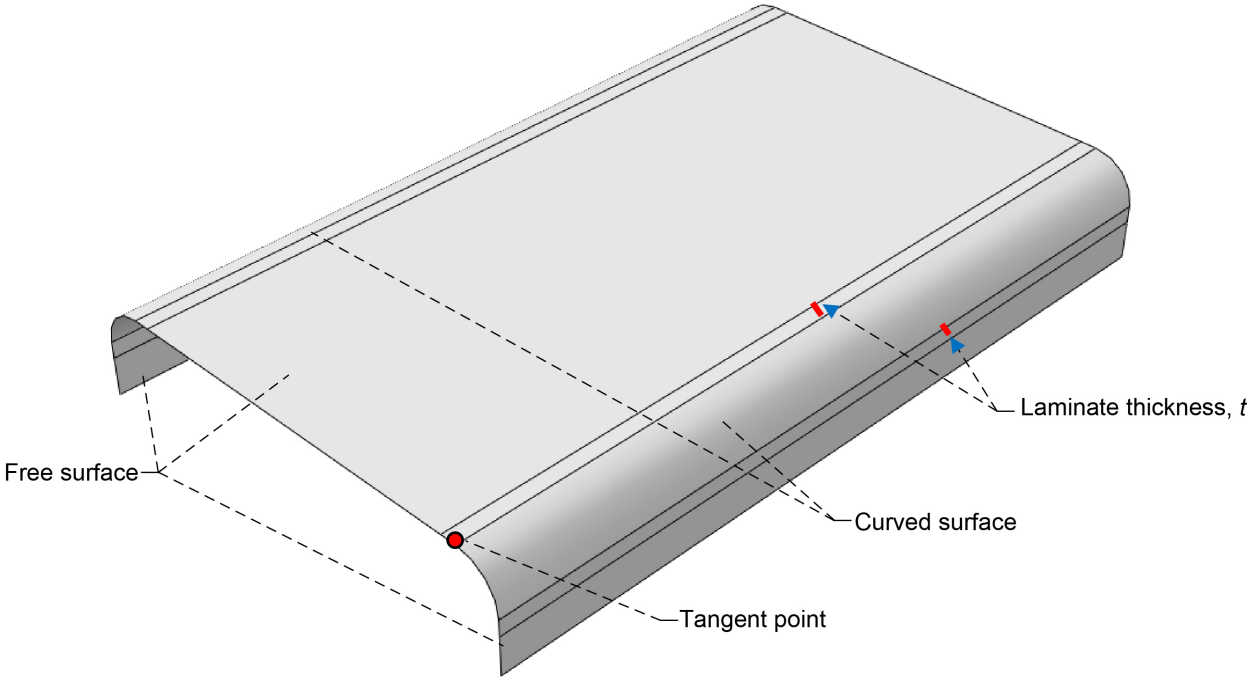

Figure 107.—CZone-defined field variables for free and curved crush stresses.

4.9.5 Simulation of Progressive Crushing: C-Channel Using CZone

The same modeling approach used for the flat coupons was used to model the C-channel specimens according to the test setup defined in Section 5.6.2. Field variables were defined at the free and curved regions to assign the various crush stress values obtained from the flat coupon tests. To define the field variables, the C-channel was partitioned into flat and curved regions, as shown in Figure 107. The curved regions extended one laminate thickness past the tangent point of the curved surface (Ref. 47). The crush structure was modeled as a 3D deformable shell structure, and the impact mass was modeled as a 3D discrete rigid shell. The composite layup feature in ABAQUS® was used to define the stacking sequence of the two hard laminates, and the flat and curved surfaces of the crush front were identified.

Two drop test impacting masses[13] and drop heights were used for the C-channel specimen simulations, closely matching the values used in C-channel specimen testing. In Loading Condition 1, a 144-kg impact mass was dropped from a height of 0.74 m, resulting in an initial velocity of 3.8 m/s. In Loading Condition 2, a 113-kg impact mass was dropped from a height of 2.94 m, resulting in an initial velocity of 7.6 m/s.

Results of the C-channel crush simulation using CZone are shown in Section B.13.4 (Figure B.65). The CZone-predicted crush force is constant over the duration of the crush event with a magnitude of 25.8 kN (5,800 lbf). The average crush stress values input to CZone were obtained from the flat coupon crush tests and applied at the contact interaction. The use of this average crush stress input property results in the prediction of a constant crush force, as discussed previously. For this effort, the initial peak force was not calculated in the C-channel crush prediction; if a predicted peak force is desired, the crush initiator can be explicitly modeled, and an additional field variable can be assigned. It should also be noted that the crush force would not remain constant if the C-channel cross-sectional geometry were to

[13]The correct platen mass and velocity pairings were used in the CZone C-channel specimen simulations; see Table 21 for reference to experimental platen mass and velocity values.

change. Unless explicitly defined by a field variable, the CZone code applies an average crush force to the element's nodes at the interaction. This crush force remains constant because the cross-sectional geometry is constant, and failure occurs near the crush front. This constant crush force accounts for the lack of fluctuations in the load–displacement curve.

Unlike other numerical methods, CZone does not predict how the onset of failure occurs (i.e., fiber buckling, fiber pullout, fiber breakage, and matrix cracking). Additionally, the peak force measured experimentally will vary with respect to the overall geometry of the crush initiator as well as the stiffness of the impacting mass. Therefore, the peak force is not included in the simulation. If required, the peak force can be replicated by using a field variable to define a different initial stress at the interaction surface.

It is understood that the analyses of both the flat coupon and the C-channel specimen predict progressive crushing without any catastrophic failure in the backup structure. However, crush analyses need to be capable of predicting catastrophic failure elsewhere in the model. CZone is unique in being able to predict the SEA associated with a robust crush model while also being able to monitor for catastrophic failure throughout the entire model. Furthermore, relatively little tuning is required to simulate more robust models.

4.9.6 CZone Modeling Capabilities, Limitations, and Best Practices

This section presents the modeling capabilities and limitations of CZone, including best practices based on crush simulation of flat crush coupons and C-channel composite test articles.

4.9.6.1 CZone Capabilities

- Because CZone is an engineering approach, there is no need to model lamina-level crush failure mechanisms. CZone offers a relatively simple and computationally efficient approach for modeling the crush behavior of a composite structure.
- The CZone code works simultaneously with the ABAQUS®/Explicit solver. This allows CZone to monitor crush while the structural analysis proceeds with ABAQUS®/Explicit.
- By not deleting elements until they pass through the impacting mass, CZone avoids severe force oscillations due to element deletion. The resulting forces transmitted to the structure allow for the analysis of failure in the backup structure without the use of filtering.
- Because CZone applies an average crush stress, the data computed from the simulation do not need to be filtered.

4.9.6.2 CZone Limitations

- Additional crush testing at the flat coupon level is required to characterize the laminate crush stress, a required input property for CZone.
- The regions for crush stress application must be manually defined in the curved and flat regions of the mesh.
- Due to an average crush stress being input, the crush simulation does not predict the experimentally observed force fluctuations during the crush progression.
- CZone does not predict how the onset of failure occurs (i.e., fiber buckling, fiber pullout, fiber breakage, and matrix cracking).

CZone's ability to handle robust models, as well as its user-friendliness, make it ideal for many numerical crush predictions to capture the SEA and crush force of a structure.

4.10 ESI Virtual Performance Solution (VPS, Formerly Known as PAM–CRASH): Waas–Pineda Implementation

This section describes the numerical models developed by the University of Bologna in conjunction with ESI Group software company using their commercial software Virtual Performance Solution (VPS) version 2020.0 (Ref. 48), formerly PAM–CRASH. (PAM–CRASH software was used in 2013 by DLR during RR–1; see Section 3.3). Later revisions of the software included new modeling and solution capabilities, including the most recent Waas–Pineda (WP) numerical model (Ref. 49) for progressive damage of unidirectional and fabric-reinforced composites.

The following sections include a description of this recently implemented model, strategies for consistent and efficient simulation, material card calibration technique and procedure, modeling capabilities, and current limitations. Finally, results are shown for the flat coupon, and the C-channel geometry, representative of an aircraft subfloor stanchion (further discussed in Section 5.6), is described. C-channel pretest prediction results are shown in Section B.14.4.

4.10.1 Waas–Pineda Numerical Model Description

The WP model is a progressive damage and failure model developed for fiber-reinforced composite/laminate materials. The original development of the material model is found in Reference 49, and its application to tensile tests on notched laminates is presented in Reference 50. The implementation of the model in VPS maintains the orthotropic elasticity with compression microbuckling and matrix plasticity formulation of Ladevèze and combines it with the nonlocal approach to include discontinuities (cracks) in the continuum.

The separation of virtual crack faces is computed using a cohesive formulation, which overcomes stress localization and guarantees energy consistency independent of mesh size. An implementation of the model to simulate composite crushing is shown in References 51 and 52. The model distinguishes three states of material response, as represented in Figure 108:

- Continuum state
- Cohesive state
- Post-damage state

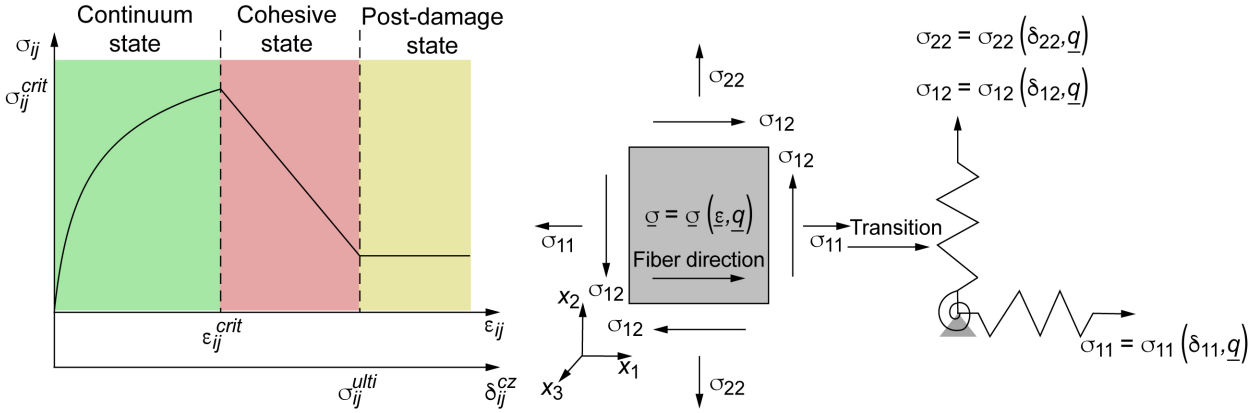

Figure 108.—Schematic representation of Waas–Pineda model states. (a) Material response states. (b) Transition method from continuum to cohesive state. Symbols defined in Nomenclature, Appendix A.

Conceptually, these three states represent, respectively, the elastic–plastic region, the internal material cracking, and the residual stress after complete degradation. The continuum state is obtained from the traditional classical laminate orthotropy theory and includes the nonlinearity of matrix transverse–shear plasticity of the original Ladevèze continuum damage model (Ref. 12), in particular, the plasticity model, defined as a plastic hardening function $R(\varepsilon_p) = \beta\varepsilon_p^m$. With the yield stress R_0, the elastic domain is the region defined by $f = \sqrt{\tau_{12}^2 + \alpha^2\sigma_{22}^2} - R(p) - R_0$ where the coupling parameter α^2 is the additional parameter for shear–transverse coupling. Material parameters are therefore R_0, β, m, and α^2. A detailed description of the WP damage model is presented in Section B.14.

4.10.2 Modeling Strategies

Mesoscale modeling.—The high-fidelity simulation of a crush event using explicit solution techniques is mostly limited to coupons of small physical dimensions. The detailed definition of the complex physical microscale phenomena occurring during the compressive crushing of composites requires expensive computational infrastructures and onerous solution times. Instead, for real industrial applications, a simplified approach representing the physical phenomena at the mesoscale is required, allowing for discretization of the FE model at the ~10^0-mm scale, which allows for explicit time integration steps on the order of ~10^{-8} s and is ultimately compatible with crush event durations of ~10^{-2} to 10^{-1} s. Therefore, mesoscale models must offer a tradeoff between the fidelity of the physical phenomena to be captured and the complexity of the model to be simulated. For this application, the numerical model of the crushing coupon was made of ply-level stacked-shell elements interconnected by beams representing the damaging ply interfaces.

To further reduce computational effort and to improve the stability of the solution, a lumped-plies approach was implemented in the flat coupons simulations: groups of aligned plies were lumped together and modeled as a single entity. This decision was supported by experimental evidence, as groups of aligned plies are rarely observed to delaminate internally; instead, it is the fiber orientation mismatch between adjacent plies that promotes delamination and splaying during crush events. This way, a laminate is modeled with a smaller number of stacked shells than the total number of plies, reducing the computational cost of the simulation while still retaining the critical interlaminar damage where it is expected to occur. The locations likely for interlaminar damage were found to be the 0/90, 0/+45, and 0/–45 interfaces, while the +45/–45 interlaminar failure was included in the in-plane shear damage model.

With this technique, the hard laminates under investigation, composed of 16 plies, were modeled using only 7 stacked shells and 6 interfaces for the $[90_2/0_2/\pm45/0_2]_S$ laminate, and 11 stacked shells and 10 interfaces for the $[90/45/0_2/90/-45/0_2]_S$ laminate, for a significant reduction of solver time.

For the C-channel simulations, considering the complex and entangled material failure modes, the whole stacking sequences were modeled using 16 shells and 15 cohesive interfaces.

In both models, only the modes of damage observed in experiments were activated. The central block of 0 plies was only allowed to degrade due to fiber compression, thus avoiding undesirable instability or collapse due to weak matrix-dominated modes.

Interlaminar interaction.—Interface damage was introduced with traditional bilinear cohesive formulation available using the MAT303 TIED element (Ref. 13), which is described in Section 3.3.1 (RR–1). The material card, defined in Section B.14, consisted of physical quantities that can be obtained from test data and numerical parameters that need further calibration.

In particular, a comparison between stacked-shell and single-shell models was carried out to verify the consistency of the results with experimental tests under in-plane dominated load. These simulations were subsequently used to calibrate the numerical parameters of the material card and test the stability of

the cohesive model. This activity was carried out by simulating open-hole tension and compression with different laminates and OCT and CC properties and comparing numerical results with test data (as found in References 31 and 53.

Mesh strategy.—By default, most FE pre-processors tend to generate uniformly structured meshes aligned with the principal axes and geometrical features of the parts. When simulating the compressive crushing of simple coupons and elements, the choice of structured mesh will lead to highly oscillating loads, caused by the combined effect of the contact and element-erosion algorithms. Additionally, wave propagation phenomena captured by explicit solvers will be significantly amplified, leading to undesired behavior and unstable damage. To overcome these issues, it is good practice to model the crushing part with an unstructured or skewed mesh. Here, both flat coupon and C-channel models are modeled using a mesh with 1-mm side length and one axis tilted 15° with respect to the crushing wall plane.

Contact algorithm.—In the flat coupon analysis, three contact pairs were identified. The sliding interaction between the coupon and the side walls was activated to prevent undesired buckling of the coupon, with no friction assumed to adversely influence the crush load response. The crushing of the specimen against the fixed rigid floor was governed by the symmetric contact algorithm type 33 (node-to-segment contact search) with a Coulomb friction coefficient of 0.2 based on past experience. Finally, a self-contact among the stacked shells composing the coupon laminate was implemented to avoid interpenetration between the stacked shells of the coupon. The latter was activated locally only after breakage of the interlaminar link (e.g., after ply delamination), as the TIED beam elements already prevent the penetration between adjacent plies when subjected to compressive forces. For this contact pair, the friction coefficient was set to 0.4.

The C-channel models required only two contact pairs, namely the self-contact between the stacked shells of the specimen and the symmetric contact between the specimen and the rigid wall. The same parameters used in former simulations were kept, including friction.

Boundary conditions.—In the flat coupon models, the top region of the laminate was collected into a rigid-body multipoint constraint, with its master node limited to move with the imposed velocity of 4 mm/s in the vertical direction according to the test data (Section 5.6.1). Both the sliding walls and the floor were modeled as rigid bodies and fixed in all DOFs.

In the C-channel models, the base of the specimen was constrained in all DOFs and the 0.5-in. epoxy pot was simulated by constraining the displacement of the nodes in the lower region in the lateral direction. The impact weight was modeled as a rigid body with an imposed mass and an imposed initial velocity in the vertical direction, while all other DOFs were constrained. The mass and velocity values for both flat and C-channel coupon crush testing are listed in Section 4.10.5.

The boundary conditions for each model are illustrated in Figure 109.

Time scaling and element erosion.—To prevent catastrophic failure due to high-velocity load application, an upper limit on the damage rate increase was introduced: the minimum number of solution cycles for damage to increase from 0 to 1 was set to NMIN = 1,000. Additionally, to maintain objectivity across multiple simulations, the time integration step was fixed to 1×10^{-5} ms, such that the rate of damage accumulation became $\dot{D}_{ij} = 100\ \mathrm{ms}^{-1}$. This can be interpreted as a viscous effect of the material.

Internal damage variables and element strain were checked to activate element erosion. This parameter is also responsible for the stability of the simulation, as highly deformed elements following the erosion criterion will cause the run to halt due to convergence issues.

Finally, for element erosion, the ply should be in post-damage state (as defined in Figure 108), and the equivalent shear strain must be higher than the threshold level EPSIslim = 0.15. The equivalent shear strain is the square root of the second invariant of strain tensor, or $\varepsilon_{sLim} = \sqrt{Tr(3/2\ \varepsilon_D : \varepsilon_D)}$, where ε_D is the deviatoric strain.

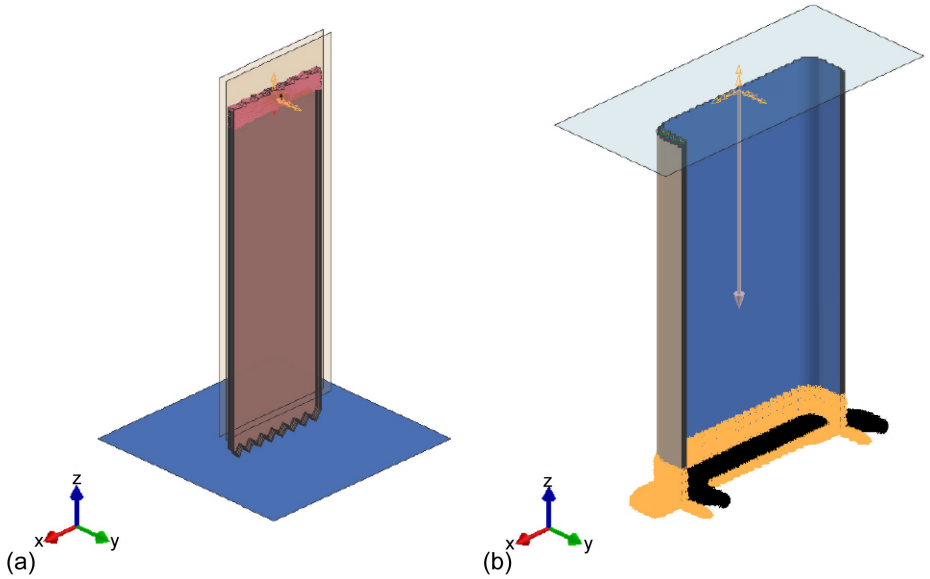

Figure 109.—Representation of boundary conditions. (a) Flat coupon model. (b) C-channel model.

Dataset derivation for the IM7/8552 unidirectional material.—The material cards for the models were defined by MAT131, PLY 1, and MAT303. MAT131 was used to define the number of layers per shell stack, the layup, and ply layer type, while ply interface data were defined in the MAT303 card, including different part numbers used in the model. Even when one single ply is modeled as a shell using MAT131, at least five layers must be created to accurately capture membrane bending, as each layer represents one integration point through the thickness.

Ply data.—The material data for the IM7/8552 unidirectional ply were defined in the PLY 1 card, and the WP damage model was activated by selecting IFAILTYP = 11 directly in the card. With this setup, the dataset can be divided into three categories:

- Orthotropic elastic properties
- Failure initiation envelope
- Damage fracture energies

The first two groups of inputs derive directly from standard coupon tests where elastic moduli and strengths are measured. The third group includes the five modal fracture energies, one mixed-mode coupling parameter, and the post-damage stress level. The ply material properties are presented in Section B.14.2 (Table B.19) with the software material card (Figure B.66).

Note that it is not possible to introduce rate-sensitive damage inputs. In fact, the full material card can be derived from quasistatic tests; modification to work under dynamic loading conditions is therefore advisable.

4.10.3 Technical Challenges

As stated previously, calibration of interlaminar damage requires at least two additional parameters that cannot be found from direct fracture modes characterization testing. Namely, the interface stiffness (computed from the thickness parameter hcont and the modes I and II elastic moduli E_0 and G_0 and the maximum initiation and propagation stresses SIGMAst, GAMMAst, SIGMApr, and GAMMApr. In the literature, several authors tried to add physical meaning to these parameters, but ultimately, in a dynamic

application such as crush simulation, one must necessarily resort to numerical trial-and-error procedures. Furthermore, no acknowledged procedure is yet available to test delamination toughness under dynamic loading; in fact, all material properties used here derive from quasistatic testing.

The interlaminar damage can additionally influence in-plane response in geometries that introduce stress concentrations such as notches and holes. This effect is particularly evident at interfaces between plies at different orientations, as out-of-plane shear stresses are only transmitted through cohesive interface elements.

For this reason, internal numerical calibrations have been carried out on National Center for Advanced Materials Performance (NCAMP) tests: open-hole tension and open-hole compression were simulated using single-shell and stacked-shell methods, and both the PLY 1 and MAT303 card were calibrated until an agreement with experimental strength was achieved.

Finally, because of the high degree of orthotropy of the unidirectional ply, it is often difficult to maintain numerical stability under dynamic loading. Using the standard strength and fracture energy values from quasistatic testing will often cause instability of the damaging part due to pressure waves exceeding the matrix strength. This phenomenon can lead to catastrophic collapse when the wave propagation is further amplified by the intermittent contact during element erosion, which ultimately leads to further premature element damage and elimination.

This is considered a numerical artifact, as the element erosion effectively removes material from the simulation that is still present in the experiments in the form of debris; the phenomenon is compensated for by increasing the initial failure stress beyond the pressure wave, ensuring that the simulation is stable, and no unexpected damage is observed outside of the crushing zone.

4.10.4 Capabilities and Limitations

The WP damage model was introduced in the 2017 release of VPS for unidirectional plies and was then improved in 2019 to work with fabric material. It allows the definition of fracture energies to control the progressive damage accumulation and energy dissipation for five distinct modes of damage, allowing for a concise set of material inputs applicable to a broad range of loading conditions. The transition from a continuum to a cohesive formulation effectively avoids stress localization, and therefore mesh sensitivity issues are greatly reduced. At increasing strain level, the material enters the post-damage state separately for each damage mode, until the threshold defined by the external damage parameter D_{max} is triggered. This scalar is defined uniquely for all damage modes; therefore, the post-damage stress level cannot be fine tuned on a mode-based criterion.

For example, in this activity, the post-damage state was idealized to represent the frictional effects following complete material degradation, but the model could not distinguish the post-damage state stress level between compressive (where friction is induced) and tensile loading (where no friction is involved). Similarly, the element erosion criterion was defined using the equivalent shear strain EPSIslim defined earlier. This limitation does not allow a flexible definition of the later stage of damage. Additionally, using the equivalent shear strain does not allow one to impose a prescribed energy to failure for each damage mode, as the elimination involves the full strain tensor. To partially overcome this, plies can be functionalized by activating only the necessary modes of damage, according to experimental observation. For example, the central block of [0] plies, observed to fail in compression, was not allowed to damage due to matrix traction and shear.

4.10.5 VPS Simulation Results

This section presents the simulation results for the flat coupon and C-channel specimens using a representative C-channel test setup.

The flat coupons were simulated with 43.9 kg mass for drop impact plate imposing a constant crush velocity of 4 m/s, whereas the C-channel was simulated under three load-rate conditions[14]:

1. 144 kg mass for drop impact plate with 3.81 m/s (150 in./s) initial velocity
2. 113 kg mass for drop impact plate with 7.62 m/s (300 in./s) initial velocity
3. Imposed 4 m/s velocity

Both geometries were simulated with the two hard laminate stacking sequences, hereafter defined as HL01: $[90_2/0_2/\pm45/0_2]_S$ and HL02: $[90/45/0_2/90/-45/0_2]_S$. Gravitational acceleration was not included in the simulations due to its negligible effect.

4.10.5.1 Flat Crush Coupon

The flat coupon geometry (discussed in Section 5.6.1) was built with stacked shells using the lumped-plies method. HL01 consisted of seven shell meshes, lumped together by two plies consisting of the central $[0]_4$ block as well as the [+45/–45] group. HL02 was composed of 11 stacked shells; only the $[0]_N$ subsets were lumped together. In both cases, 4 m/s constant velocity was simulated.

The trigger region replicated the experimental setup, and the mesh was modeled in order to reduce the use of triangular elements, which are not compatible with the WP damage model. Figure 110 and Figure 111 provide a detail of the mesh transition from the trigger region to the skewed mesh, with 15° misalignment from the main specimen axes. Figure 111, moreover, shows the detail of the splaying of lateral plies after 8 mm displacement.

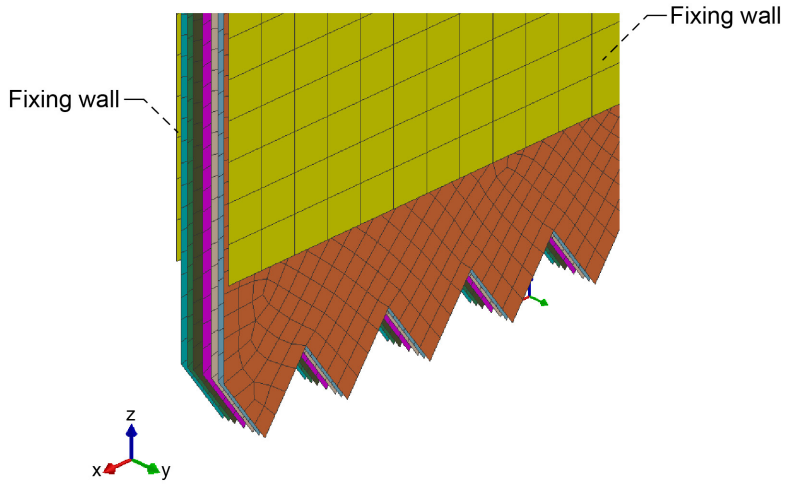

Figure 110.—Detail of sawtooth trigger for HL01 highlighting unstructured mesh. Yellow parts front and back are fixed sliding walls; floor not shown.

[14]Drop mass values in the models reflect the flat coupon and C-channel impact tests defined in Table 21 of Section 4.0.

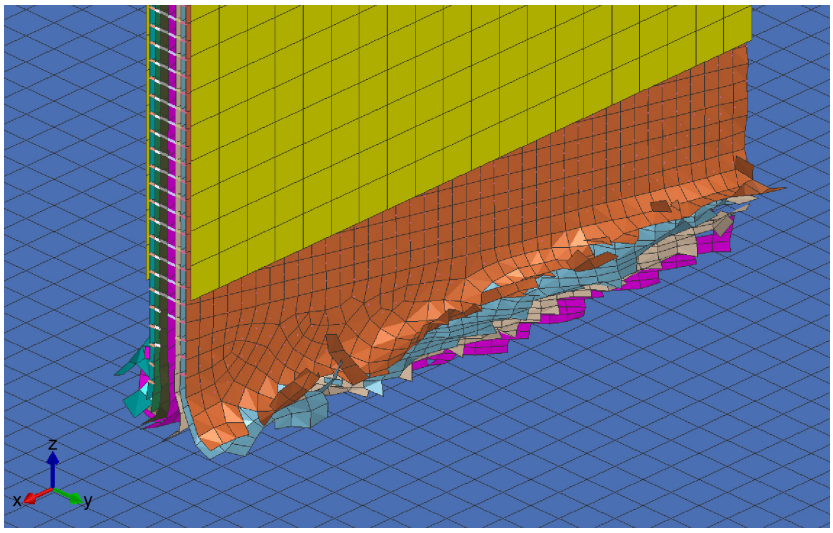

Figure 111.—HL01 detail: Splaying of lateral plies after 8 mm displacement; mesh transition from unstructured to 15° skewed.

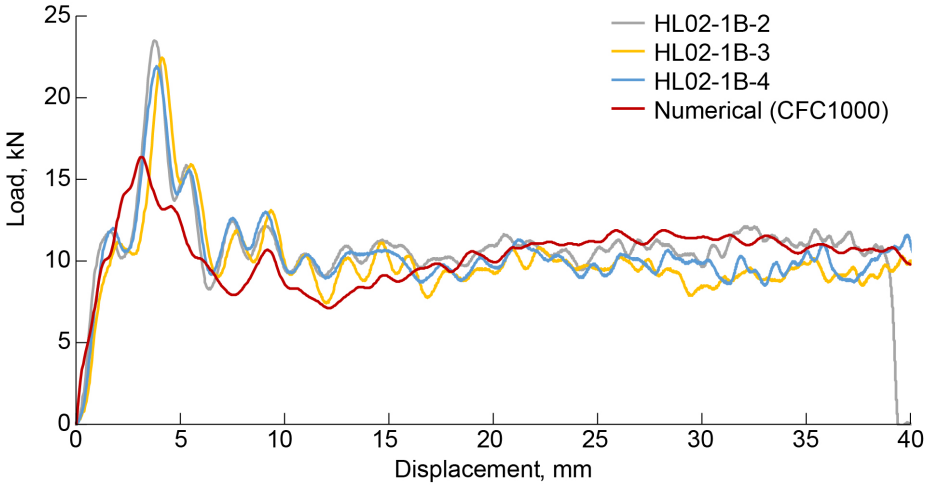

Figure 112.—Load–displacement curves for flat specimen HL02 for experiment versus numerical (CFC1000-filtered) simulation.

In Figure 112 and Figure 113, the load–displacement curves are shown for both laminates: after a transient region involving the crushing of the sawtooth trigger, the load reached a minimum close to 10 mm and then stabilized from 20 mm onward once the skewed mesh was completely developed. Both coupons showed splaying of the outer plies and compressive failure of the central subset of 0 plies. The numerical SEA was then calculated, as defined in Equation (1): the crush energy was the area below the load–displacement curve, the density used for the calculation was $\rho = 1.58\times10^{-6}$ kg/mm^3, and the coupon cross section A = 116 mm^2. Two ranges were used for calculation: 0 to 30 mm for Total SEA and 10 to 30 mm for Stable SEA. For a simulated time of 10 ms, the models containing 40,000 elements required a 2-h runtime using 24 parallel solver units.

As shown in the graph of Figure 114, the numerical SEA was within or close to experimental scatter, and a steady-state condition was entered from around 20 mm of displacement. In this region, the load oscillated between 7.8 and 14.4 kN for HL01, with a weighted average of 11.0 kN, and between 8.3 and 15.1 kN for HL02, 11.0 kN on average.

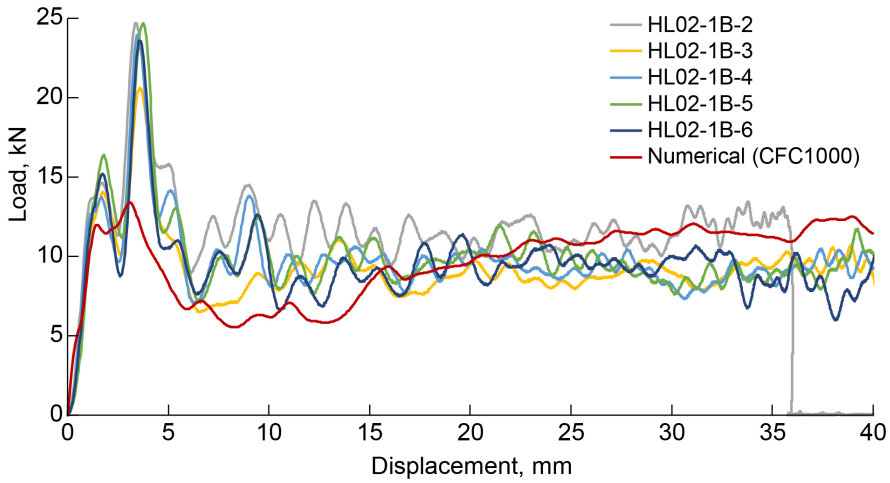

Figure 113.—Load–displacement curves for flat specimen HL02 for experiment and numerical (CFC1000-filtered) simulation.

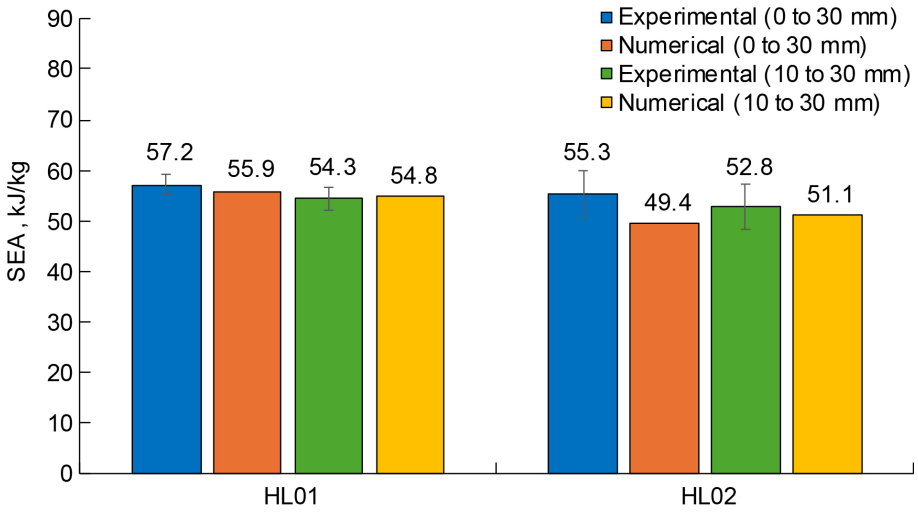

Figure 114.—Comparison of flat coupon simulation numerical SEA and experiment results (including scatter).

4.10.5.2 C-Channel Simulations

The C-channel geometry (discussed in Section 5.6.2) was constructed using 16 shells, each representing a single ply of the laminate stacking sequence. The chamfered trigger of the experimental setup was realized by eliminating excess elements in the model without altering the mesh size or pattern; therefore, the first contact between the specimen and the crushing wall happened in a limited region, as can be seen in Figure 115. Both HL01 $[90_2/0_2/\pm45/0_2]_S$ and HL02 $[90/45/0_2/90/-45/0_2]_S$ were simulated.

The simulations assumed a mass of 144 kg and 113 kg for the drop-test impactor plate, with initial velocities of 3.8 m/s and 7.6 m/s, respectively.[15] The impactor wall was modeled as a rigid body for the simulations with a constant velocity of 4 m/s. Regardless of the initial conditions, the simulations were

[15] The mass values in the models reflect the flat coupon and C-channel impact tests defined in Table 21 of Section 4.0.

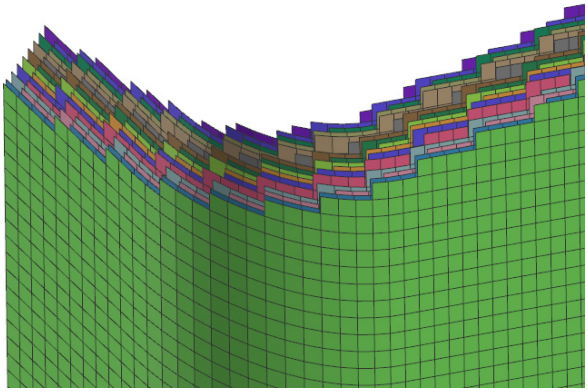

Figure 115.—Detail of trigger realized for C-channel specimens.

halted after the drop mass reached 40 mm of displacement. The numerical values of SEA were calculated thus: the crush energy was the area below the load–displacement curve, the density used for the calculation was $\rho = 1.58\times10^{-6}$ kg/mm^3, and the coupon cross section $A = 332$ mm^2. As with previous results, displacement ranges used for calculation were 0 to 30 mm and 10 to 30 mm.

The simulations were stopped after either 40 mm of displacement or 10 ms of simulated time. The models containing 265,000 elements required between 6- and 12-h runtimes using 24 parallel solver units.

C-channel simulation results are shown in Section B.14.4 (Figure B.68 to Figure B.71). The summary of numerical simulation results for C-channel geometry is also provided in Section B.14.4 (Table B.21).

4.10.6 Waas–Pineda Modeling Best Practices

The simulation of composite dynamic crushing events poses several challenges. The complex interaction of multiple failure modes requires the implementation of a comprehensive building-block approach to validate the numerical model against experiments of increasing complexity. In addition, the explicit solver VPS offers the possibility to tune several numerical parameters to guarantee convergence and stability of the solution under a wide range of load conditions. If not handled carefully, however, these parameters can affect the results significantly. The suggested workflow for efficient calibration process, adopted in this activity, is described hereafter.

First, the basic elastic mechanical properties and strength values are taken from standard quasistatic testing of simple laminates to directly populate the material cards. Second, the fracture toughness values found by interlaminar and intralaminar fracture tests are introduced to the model using the available test data. Next, post-damage threshold and element erosion limits are calibrated iteratively by reproducing the notched fracture tests until a good match is found between experiments and simulations.

It is necessary to guarantee the stability of the cohesive model under crush loading by evaluating its behavior under in-plane loading conditions. This is achieved by directly comparing single-shell and stacked-shell numerical models of notched samples.

At this stage, since all material quantities are derived from quasistatic tests, no dynamic effects have been introduced. These are left for the last stage of the building block. Therefore, the calibration of the model against the flat coupon crush tests is performed under dynamic loading conditions. The goal of this calibration stage is to determine the numerical solver parameters (max. damage rate, time integration steps, etc.) while maintaining other input unchanged.

It is important that these elementary crush tests for intermediate calibrations are carried out at a velocity close to the final application of interest, as viscous effects, calibrated at a specific rate, might not work

properly if the crushing speed differs by the orders of magnitude. For these reasons, a numerical model that has been validated for crushing applications will only be applicable to a limited range of loading rates.

It must be noted that, due to the particular damage formulation of the WP model, the simulation results for crush are necessarily dependent on the mesh structure. In order to reduce the load oscillations and minimize unwanted dynamic spurious effects, the mesh must be constructed in a way that allows a gradual erosion of the elements close to the loading plate. This can be obtained with either unstructured or skewed mesh.

Finally, for a successful crush prediction, it is important to identify from experimental observations the predominant failure modes in the laminates and implement only the relevant damage mechanisms in the numerical model. In fact, a significant improvement in the numerical outputs has been achieved by lumping together groups of plies that do not typically show interlaminar failure and preventing undesirable matrix damage in load-bearing 0 plies.

4.11 Altair® RADIOSS®

This section describes the numerical methodology used by the Altair Engineering analysis team for RR–3. This section contains a short description of LAW25, the Altair® RADIOSS® (Altair Engineering Inc.) material law (CRASURV (crash survivability) formulation) (Ref. 54); a description of the simulation methodology for prediction of progressive crushing for flat coupon analyses; and C-channel crushing simulations. It also outlines the best practices, limitations, and capabilities identified within the scope of the RR–3 analyses.

4.11.1 Material Model Description

The orthotropic composite material law proposed in RADIOSS® software is LAW25 (Ref. 54), based on a visco-elasto-plastic modeling of composites' nonlinear and strain-rate-dependent behaviors. This material law is already implemented in the commercial FE code Altair® RADIOSS®. The plastic flow threshold $F(\sigma)$ uses a Tsai–Wu formulation (Ref. 55). Detailed discussion of constitutive material laws, stress–strain relationships, strain-rate effects, and the damage and failure employed in this material model is presented in Section B.15.

4.11.2 Model Input Data and Assumptions

The elastic and strength material input data used in the RR–3 analyses were taken from the material model-specific parameters presented in Section 5.2.3 (Table 16). The LAW25 parameters were experimentally characterized for the considered material system IM7/8552 (190 g/m^2) as outlined in Section 5.2.2 (Table 15). The nonstandard characterization tests for ABQ_DLR_UD material models such as shear damage, plasticity parameters, transverse damage, and coupling parameters are discussed in Appendix C.

4.11.3 Simulation Methodology for Model Verification and Validation

The simulation methodology to predict progressive crushing of composite structures followed a building-block approach, starting with a single-element test followed by flat coupon and C-channel crushing.

Single-element simulations were used to identify material law parameters at the mesoscale (ply) level, making it possible to set up the composite behavior in fiber, transverse, and shear directions. On this level, the material input data were frozen and fixed input data were used for subsequent predictions of progressive crushing without further calibration. The next step consisted of applying this material law to intermediate structures to validate and/or adjust some crushing parameters. The proposed single-shell modeling approach was applied, and predictions were validated with experimental results of flat coupon

crush tests performed at the University of Utah. Finally, the validated modeling approach was used for performing the simulation of C-channel crushing.

4.11.4 Single-Element Simulation for Model Verification

Initial verification of the material model was done at the single-element level. Strength and stiffness values were used to define elastic material behavior. G_{Ic} was used in compression (64.8 kJ/m^2) to determine the fracture behavior after maximum stress. A small plateau was added after the maximum stress to avoid oscillatory behavior during crushing. The single-element simulation results are provided in Section B.15.2.

4.11.5 Simulation of Progressive Crushing: Predictions of Flat Coupon Crush Test

Flat coupon tests were simulated to evaluate the behavior of the CRASURV material model during crushing. Full integrated elements (BATOZ formulation) were used in this model. The boundary conditions in the numerical models were consistent with the test setup. Support plates were modeled and considered rigid with respect to the coupon. The gap between the support plates and the impact surface was modeled in a range of 7.5 to 15 mm.

To promote the onset of stable crushing, a sawtooth trigger was modeled. Friction between the specimen and the impact plate was modeled with a friction coefficient of $\mu_F = 0.2$ as well as automatic contact. No friction was considered between support plates and coupon. The support plates and the impact plate with mass of 44 kg (96.8 lb)[16] were modeled as rigid bodies, shown in Figure 116. Loading was modeled by a constant velocity boundary condition ($v = 4$ m/s) applied to a set of nodes containing the uppermost nodes of the flat coupon specimen, whereas the remaining translational and rotational DOFs were fixed.

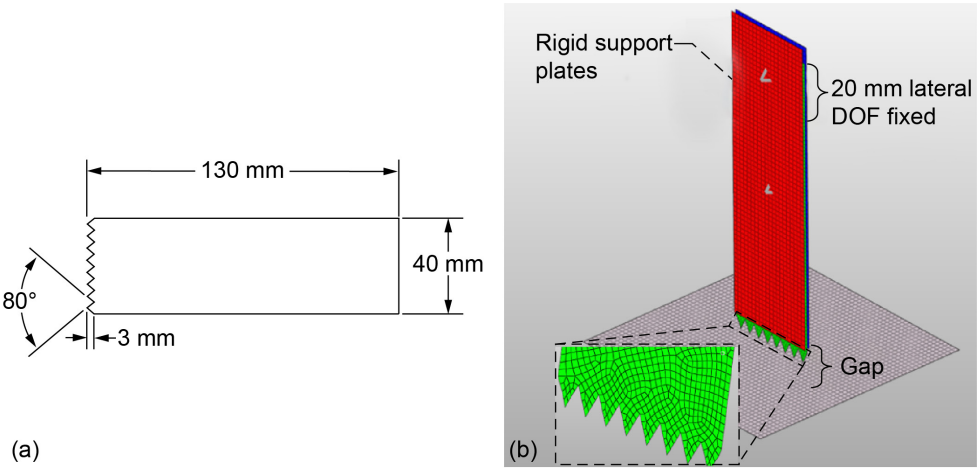

Figure 116.—Numerical model of flat coupon crush tests using single shell. (a) Specimen dimensions. (b) Model setup.

[16]The correct platen mass of 44.0 kg was used in the RADIOSS® flat specimen simulations; see Table 21 for reference to experimental platen mass values.

The simulation results of the single-shell model are presented in Section B.15.3 (Figure B.77). The contact force versus displacement of the impact plate for the sequence $[90/\pm45/0]_{2S}$ and a gap height of 8.6 mm is shown. Section B.14.3 (Figure B.78) presents the results of the single-shell model simulation as well as the experimental results obtained from the University of Utah. Unfiltered and filtered numerical results using an SAE filter with a cutoff frequency of 10 kHz are shown.

A comparison of experimental and numerical results was computed using the mean crush force P_{crush}, and SEA was determined following Equation (1). Stable SEA was determined for the displacement range of 10 to 30 mm, the range where a steady-state crushing occurred. Comparison of simulation's force–displacement characteristics with University of Utah experimental results showed that the single-shell simulation predicted both a higher steady-state crush force level and a higher force peak. The simulation's steady crush force (83.41 kJ/m_2) was almost twice that of the experiment (46.58 kJ/m_2). The difference between these overestimations can be explained by the single-shell approach.

The single-shell model can consider intraply damage modes (matrix cracking, fiber rupture, and microcracking) but it is not able to predict and model phenomena such as massive delamination and ply splaying. Those phenomena are layup dependent and can explain the lower values for Stable SEA. For all layups, the single-shell model prediction provided higher SEA than was obtained in the experiments, and the differences between layups were not significant (except for the hard laminate). As a result, the single-shell modeling approach, which is not capable of representing splaying, generally tends to overpredict SEA and is not able to predict the influence of different layups on the SEA.

Figure 117 quantitatively compares the SEA values for all single-shell simulations with the experimental results. Again, the single-shell modeling approach was not able to predict the SEA and the influence of the layups. Detailed results of flat coupon crush testing are discussed in Section B.15.3.

Two laminates were modeled using a more detailed approach. Each ply was modeled using orthotropic thick-shell elements (/PROP/TYPE21), and interfaces were represented by cohesive elements using the elastoplastic material law /SNCONNECT. The interface followed a bilinear material law calibrated using G_{Ic} and G_{IIc}. Figure 118 shows force–displacement curves for two different laminates: a QI laminate and a hard laminate.

The thick-shell cohesive model captured the peak force (both in time and value) and average crushing force well for both laminates. This confirms that a thick-shell model can represent ply splaying and delamination that drives the crushing behavior. However, these types of models are harder to build and computationally expensive.

Based on the outcomes of the flat coupon crush predictions, SEA was systematically overestimated by single-shell models. This can be explained by the lack of delamination on the single-shell model. However, the increase in SEA of the hard laminate relative to the QI laminate was captured by the law even though delamination was not modeled explicitly. Delamination appears to be a first-order factor to predict crushing force on this model. However, a solid or thick-shell model with a cohesive model is not practical in full structure simulation, which was the main objective of this exercise.

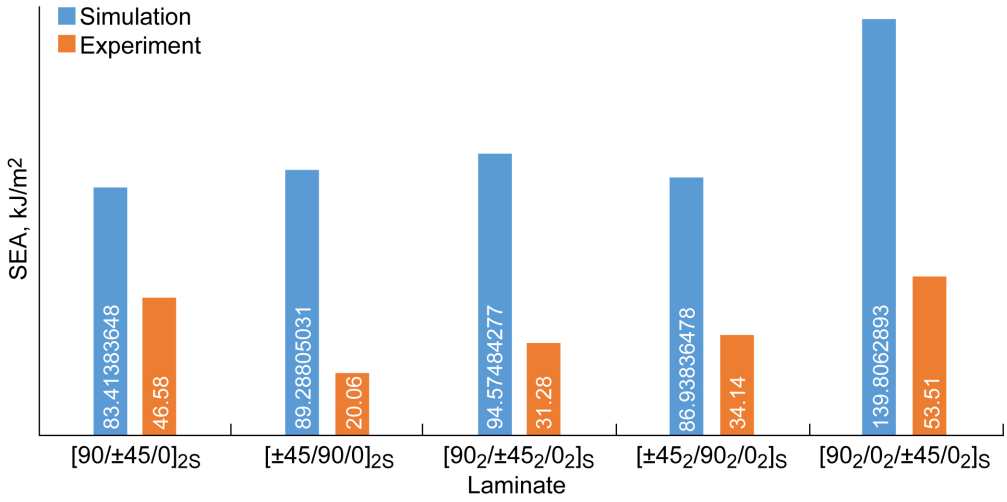

Figure 117.—Prediction of flat coupon crushing using single shell; SEA of simulations compared with experimental results.

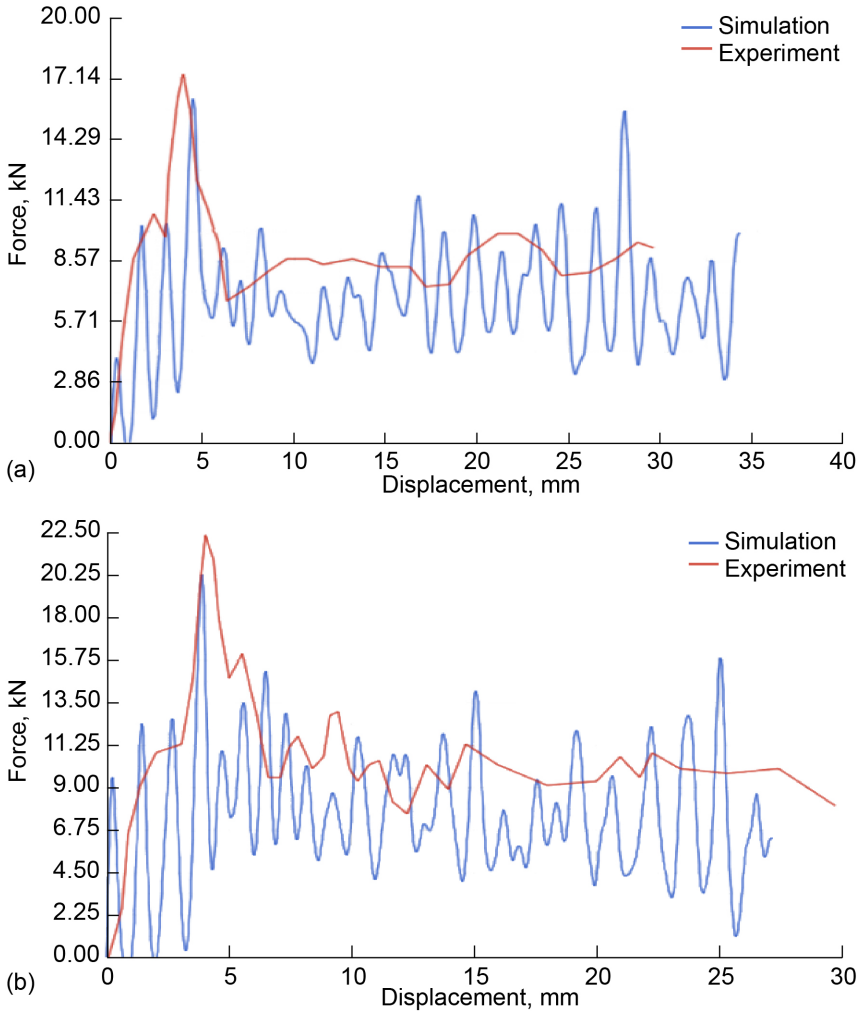

Figure 118.—Prediction of flat coupon crushing using thick-shell and cohesive approach. (a) QI laminate. (b) Hard laminate.

4.11.6 Progressive Crushing Simulation of C-Channel

The analysis teams were tasked to predict the C-channel crush response for two hard laminates from the set of layups previously tested with the flat crush coupons:

1. HL01 with stacking sequence $[90_2/0_2/\pm45/0_2]_S$
2. HL02 with stacking sequence $[90/45/0_2/90/-45/0_2]_S$

The friction coefficients between the impactor and C-channel were the same as those used in the flat coupon simulations. The trigger was modeled by a 45° dropoff, built using different sets of elements to represent each ply in the single-shell model.

The C-channel specimens were tested quasistatically as well as in drop tests with initial velocities of 3.81 m/s (150 in./s) and 7.62 m/s (300 in./s). The drop mass of 44 kg (96.8 lb) was assumed in the C-channel numerical model.[17] The following parameters were defined as response outputs in the simulations:

- Crush distance
- Peak crush force
- Average crush force
- SEA
- Crush force efficiency

The numerical model used for the C-channel simulation is shown in Figure 119.

The results of the C-channel crush simulations for both hard laminates are provided in Section B.15.

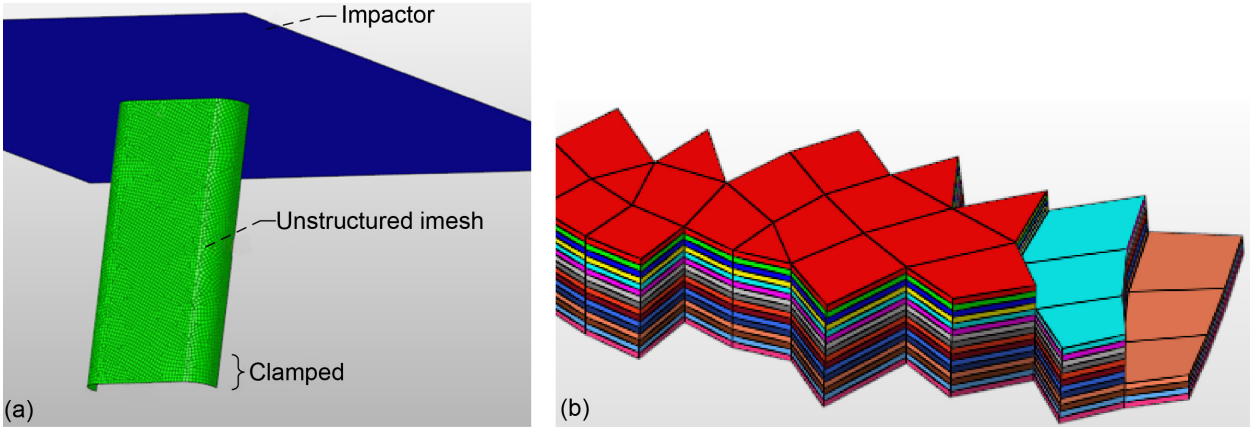

Figure 119.—Numerical model of C-channel segment (stacked-shell model). (a) Full model. (b) Unstructured mesh schematic.

[17]As noted in Section 4.0, impactor mass for the C-channel crush test was incorrectly assumed to match that of the flat coupon; see Table 21 for correct values.

4.11.7 RADIOSS® LAW25 CRASURV Modeling Best Practices

The presented numerical methodology followed a building-block approach ranging from single-element simulation up to the pretest predictions for C-channel crushing. From the work performed, the following modeling best practices can be drawn:

- Single-element simulations were used to identify the material parameters. Post-rupture parameters were set up using energy release rate.
- Mesh size and shape have a strong influence on crush stability. Misoriented or nonstructured meshes were able to capture progressive crushing. In C-channel crushing, boundary conditions and contact frictions can also have a strong influence on the final results.
- In this study, flat coupons were used as a validation test, but they can also be used to modify post-rupture parameters $\varepsilon_{ic}^{1}, \varepsilon_{ic}^{2}$, and σ_{ires} in order to better represent laminate behavior. This can be done by inverse calibration.

A major limitation of the single-shell model (as-built) was its inability to capture massive delamination (mostly on external plies) and associated stiffness loss. Mesoscale models, with an explicit modeling of plies and interfaces, can solve this limitation, but they are not suitable for global crash models.

5.0 Test Data Requirements for Impact Model Validation

High-fidelity analysis methods known as progressive damage failure analysis (PDFA) methods, capable of reliably predicting the onset and progression of damage in composite materials, were developed for the NASA-sponsored high-energy dynamic impact (HEDI) event simulation. The generated test data from the subsequent building-block model validation process, though performed for high-velocity impact threats, are equally applicable to developing a wide range of impact models, including crashworthiness simulations. These PDFA models are validated through a building-block approach, starting at the coupon level and culminating in component-level testing and analysis. As part of the overall effort, material characterization testing was performed to bridge gaps between existing experimental data and the material property inputs required to predict ballistic impact behavior at the component level. The test activities were designed to capture the effects of a wide variety of impact variables, including impact velocity, projectile type, laminate thickness, fiber architecture, and material constituents.

The ultimate goal of the HEDI effort was to develop accurate predictive methods for high-energy impact events with application to a variety of structures, configurations, and design parameters. The effort started with simulation of simple flat-panel tests and progressed to include configured panels (fastener, stringer, and frame), curvature, and scale. The building-block approach for the HEDI task, shown in Figure 120, incorporates increased complexity moving upward in the diagram.

The first level of the building block contains coupon testing that provides input to the material models:

1. Split Hopkinson pressure bar (SHPB) testing, as discussed in Section 5.4 for strain-rate material models
2. Quasistatic punch shear test (QS–PST), as discussed in Section 5.2.3.2
3. End-notch flexure (ENF) testing, as discussed in Section 5.3.3
4. Double cantilever beam (DCB) testing, as discussed in Section 5.3.2
5. Depth of penetration (DOP) testing, as discussed in Section 5.2.3.3
6. Fracture toughness testing, summarized in Sections 5.3.1 and 5.3.5

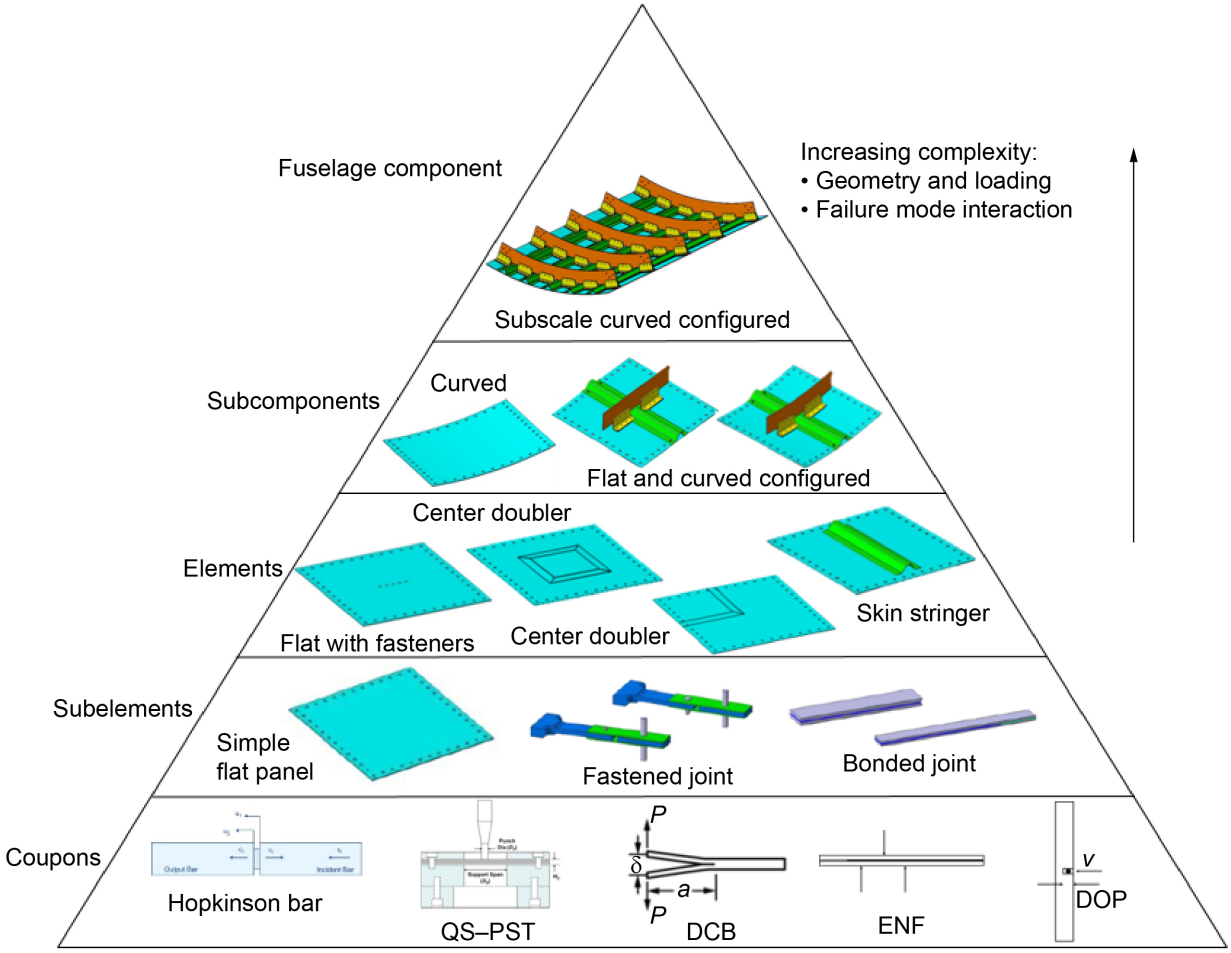

Figure 120.—High-energy dynamic impact (HEDI) material model verification and validation building block. Quasistatic punch shear test, QS–PST; double cantilever beam, DCB; end-notch flexure, ENF; depth of penetration, DOP.

The second level of the building block includes three major features of the elements and subcomponents tested in the HEDI effort. These features are as follows:

1. A quasi-isotropic laminated flat panel that is representative of the skin used on test articles further up the building block. The test article was subjected to HEDI loading to measure the penetration threshold velocity, or ballistic limit, as well as deformation and damage.
2. A bonded joint to better understand the disbonding behavior under modes I and II loading. This helps to better inform the requirements for test articles that include a cobonded stringer. The high-rate bonded joint testing is discussed in Section 5.4.
3. A bolted joint to better understand the high loading rate behavior of a substructure attached to the test articles (e.g., a shear tie mechanically fastened to the skin). High-load-rate testing of fastener joints is discussed in Section 5.5.

The third level of the building block includes the combination of the aforementioned features. These articles include the following:

1. Flat panel with fasteners: A skin with seven fasteners in a row. For the HEDI effort, this test article was used to examine how the fasteners arrest damage.
2. Flat panel with a doubler: An interleaved doubler was placed either in the middle or the corner of the panel and impacted at the panel center. This test article was used to examine how far the doubler needs to be extended past a threat zone and how effective the ramp is in dissipating the energy.
3. Skin stringer: A hat stringer was cobonded to the skin and subjected to impact loading on the outer mold line (OML). This test article was used to examine how a cobonded stringer flange may disbond under impact loading.

The building block then adds complexity at the next level, in which curved geometry, stringers, frames, and shear ties are used to build a structure. The final test article is a fully configured panel that includes five stringers and five frames. Ballistic limit, deformation, damage, and failure were documented for all of the test articles. High-fidelity validation data were developed across each length scale for the selected PDFA methods validation.

In the impact testing, high-speed photogrammetric techniques and 3D digital image correlation (DIC) were utilized to obtain high-fidelity data required to characterize and validate the models. The test articles were supported on four load cells to measure the reaction forces at the supports. These data were used to assess the global model response. Test articles of interest were subjected to further nondestructive and destructive evaluation. Samples were ultrasonically scanned and imaged with computed tomography to determine the ply-by-ply damage states.

At each building-block stage, simulations with the selected methods were used to inform test article design details (including holding fixtures) and set the impact energy range for the next stage. Early and ongoing use of simulation helped to reduce testing cost and ensure relevance to in-service experience for aircraft structures.

5.1 High-Energy Dynamic Impact (HEDI) Coupon Characterization Testing

This section presents the HEDI technology content developed in NASA's ACP that was identified for transition to CMH–17 pertinent to impact event predictive capabilities validated by smart testing. This technology enables a reduction in the time required to develop and certify new aircraft structures that utilize advanced composite materials (Ref. 56). As part of this effort, high-fidelity analysis methods capable of reliably predicting the onset and progression of damage in composite materials were evaluated under HEDI events (Ref. 57).

The composite material system selected for this exercise was IM7/8552 unidirectional tape, and the analysis methods evaluated were commercially available PDFA methods: LS–DYNA® MAT162, MAT261, MAT213, and Peridynamics (Ref. 58). Detailed information regarding Peridynamics can be found in Reference 59. Testing conducted for MAT213 that was investigated by NASA is presented in Section 5.2.3.3. Following the building-block approach, coupon-level and subcomponent-level experiments were used to generate the experimental data required for validation of these material models.

The ACP IM7/8552 coupon test data generated for the HEDI effort were highly valuable to the CMH–17 CWG for developing crash simulations of energy-absorbing structures. The numerical task group used the coupon test data to populate selected material cards to evaluate the effectiveness and robustness of progressive damage models using a common, predefined target structure. Toray® T700/2510 material was used to support subelement-level crush modeling in RR–1 and RR–2. The simulations were based on numerical models MAT54, MAT58, and PAM–CRASH using the commercial explicit FE tool LS–DYNA®. Detailed results of these efforts, including modeling strategies, best practices, and success criteria, are well documented in Section 3.0.

The current focus of the CMH–17 CWG is to expand the modeling best practices to the larger scale structure representative of an aircraft fuselage lower lobe. Eleven different methods were employed for RR–3: LS–DYNA® MAT54, MAT58, MAT213, MAT219, MAT261, and MAT297; LS–DYNA® modified Ladevèze; ABAQUS® Ladevèze ABQ_DLR_UD; ABAQUS® CZone; ESI VPS, Waas–Pineda (WP) implementation; and Altair® RADIOSS®. See Section 4.0 for details. The IM7/8552 unidirectional tape system was selected for this stage of the CMH–17 crashworthiness studies to take advantage of work conducted under the NASA ACP HEDI effort in advancing predictive capabilities in impact dynamics. The following sections summarize the experiments conducted by various groups to generate the data necessary for the material models.

5.2 Tests Required To Generate Experimental Data To Populate Material Cards

The CWG worked together to identify the necessary material model input properties, looking for commonality between analysis methods. As commonality was established, the next step was to identify the appropriate experiments to obtain the necessary material properties. Table 14 presents the test matrix developed to cover test requirements for all the analysis methods.

5.2.1 HEDI Material Characterization Experiments

Three different sources were considered for the experimental data: the NASA ACP HEDI effort, NCAMP's test report on Hexply® (Hexcel Corporation) 8552 (Ref. 53), and a Hexply® 8552 product data sheet (Ref. 60). However, this section refers to the IM7/8552 material characterization experiments conducted for the HEDI effort due to the thorough documentation and data traceability. Detailed information regarding the test setup, results, and other details can be found in the coupon testing report (Ref. 25). In general, the required tests were either standard or nonstandard depending on whether or not a test method was available. Generally, standard test methods for coupon-level experiments were recommended from American Society for Testing and Materials (ASTM) (or similar) standards. Additionally, some of the material models required calibration of erosion and plasticity type parameters that needed nonstandard subelement-level testing. The following section presents the sources and details regarding coupon-level experiments required for effective definition of material models.

TABLE 14.—DESCRIPTION OF REQUIRED TESTS TO GENERATE EXPERIMENTAL DATA TO POPULATE MATERIAL MODELS

No.	Test standard	Description
1	ASTM D3039, SRM 4	0° tension
2	ASTM D3039, SRM 4	90° tension
3	ASTM D3518, SRM 7	In-plane shear properties, ±45° tension loading
4	ASTM D3410, SRM 1R	Compressive properties, shear loading
5	Nonstandard	Quasistatic punch shear test
6	Nonstandard	Edge-on crush test
7	ASTM D6484	Open-hole compression (OHC)
8	Nonstandard	Off-axis compression
9	ASTM D3039, SRM 4	Through-the-thickness tension
10	ASTM D5766	Open-hole tension (OHT)
11	Nonstandard	Hopkinson bar
12	Nonstandard	Compact compression (CC)
13	Nonstandard	Compact tension (CT)
14	Nonstandard	Four-point bending
15	ASTM D3800	Density test
16	ASTM D695	90° compression
17	Nonstandard	Ballistic impact
18	ASTM D5528	Double cantilever beam (DCB)
19	ASTM D7905	End notch flexure (ENF)
20	Nonstandard	Unnotched compression (UNC) with delamination
21	Cyclic shear test	Cyclic test on $[\pm 45]_{4S}$ laminate (Ladevèze)
22	Cyclic ±67.5° test	Cyclic test on $[\pm 67.5]_{4S}$ laminate (Ladevèze)
23	ASTM D6671	Mixed-mode bending test
24	ASTM D5379	Iosipescu shear test
25	Nonstandard	[45/–45] under axial tension Load–unload or cyclic test to determine plasticity parameters
26	Flat coupon crush test	Flat coupon crush stress
27	ASTM D5379 or D7078	In 90° direction Load–displacement response is required

5.2.2 Coupon-Level Experiments

This section presents and compares the coupon-level IM7/8552 unitape material properties obtained from primary sources such as NCAMP, NASA's HEDI effort, and Hexcel's Hexply® 8552 product data sheet. It also highlights the finalized input chosen from these three sources for the material models used by the numerical task group in the RR–3 exercise. Table 15 summarizes this information and provides additional notes. It is important to note that the experiments conducted by NCAMP and NASA's HEDI effort were based on the IM7/8552 U.S version, whereas the Hexcel data sheet was based on the European version. The primary difference between the U.S. and European versions is the areal weight, which is defined as the weight of the fiber per unit area (width × length). The areal weight of IM7/8552 in the U.S. version is 190 gsm; in the European version, it is 134 gsm.

TABLE 15.—SUMMARY OF IM7/8552 MATERIAL CHARACTERIZATION FOR STIFFNESS AND STRENGTH PROPERTIES (REFS. 53, 60, AND 25)

Property	Source[a]			Method	Additional notes	CWG-selected material property
	NCAMP	NASA ACC HEDI	Hexcel data sheet			
Fiber direction stiffness—tension, E_1^t, Msi	22.99 22.42* (11.99 measured with $[0/90]_{NS}$)	24.98* (13.36 measured with $[0/90]_{NS}$)	23.8	NCAMP and NASA: ASTM D3039	*Backout factor (BF) = 1.87 (based on Hexcel data)	22.42 (NCAMP)
Axial failure stress—tension, F_1^{tu}, ksi	362.7* 320.5** (171.38 measured with $[0/90]_{NS}$)	368.7*** 394.3**** (197.17 measured with $[0/90]_{NS}$)	395	NCAMP: *ASTM D3039 [0] **ASTM D3039 $[0/90]_S$ (BF applied) NASA: ASTM D3039 Using $[0/90]_{NS}$	***BF = 1.87 (based on Hexcel data) ****BF = 2.0 (not per CMH–17 guidelines)	362.7 (NCAMP)
Maximum tensile strain—axial direction, ε_1^{tu}, %	---	1.42 (measured with $[0/90]_{NS}$)	1.62	NCAMP and NASA: ASTM D3039	Ultimate strain	1.62 (NCAMP) With BF = 1.87
Major Poisson's ratio—tension, ν_{12}^t	0.316	---	0.316	NCAMP: ASTM D3039	---	0.316 (NCAMP)
Transverse stiffness, E_2^{tu}, Msi	1.30 (1,000 to 3,000 microstrain)	1.29 (2,000 to 5,000 microstrain)	1.70	NCAMP and NASA: ASTM D3039	---	1.30 (NCAMP)
Transverse failure stress—tension, F_2^{tu}, ksi	9.29	13.64	9.3	NCAMP and NASA: ASTM D3039	---	9.29 (NCAMP)
Maximum tensile strain—transverse direction, ε_2^{tu}, %	---	1.13	---	NASA: ASTM D3039	---	1.13 (NASA)
Axial failure stress—compression, F_1^{cu}, ksi	248.6* (94.51 measured with $0/90_2$ laminate)	192.2	245	NCAMP: ASTM D6641 NASA: ASTM 6484 without hole	*BF = 2.63 (based on Hexcel data)	248.6 (NCAMP)
Maximum compressive strain—axial direction, ε_1^{cu}, %	---	0.87	---	---	Compressive strength divided by tensile modulus	1.11 (NASA)
Major Poisson's ratio—compression, ν_{12}^c	0.356	---	0.356	NCAMP: ASTM D6641	---	0.356 (NCAMP)
Young's modulus—transverse direction (compression), E_2^c, Msi	1.41	1.45	------	NCAMP and NASA: ASTM D6641	---	1.41 (NCAMP)
Transverse failure stress—compression, F_2^{cu}, ksi	41.44	41.59	44.2	NCAMP and NASA: ASTM D6641	---	41.44 (NCAMP)
Minor Poisson's ratio—compression, ν_{21}^c	0.024	---	0.026*	NCAMP: ASTM D6641	*Use of reciprocity relationship, Hexcel data (E_1, E_2, ν_{12})	0.024 (NCAMP)
In-plane shear modulus, G_{12}, Msi	0.68	0.66	---	NCAMP and NASA: ASTM D3518	---	0.68 (NCAMP)
In-plane shear strength at 0.2% strain, $F_{12}^{0.2\%strain}$, ksi	7.76	---	---	NCAMP: ASTM D3518	---	7.76 (NCAMP)
In-plane shear strength at 5% strain, $F_{12}^{5\%\ strain}$, ksi	13.22	12.25	---	NCAMP and NASA: ASTM D3518	---	13.22 (NCAMP)
Through-the-thickness failure stress, F_3^{max}, ksi (interlaminar tensile strength)	11.04	---	---	---	NIAR data from ASTM D6416 (curved beam flexure)	11.04 (NIAR)
Out-of-plane shear modulus, G_{13}, Msi	---	---	---	Penn State University (Penn State)	Testing completed	Penn State
Out-of-plane shear strength, F_{13}, ksi	---	---	---	Penn State	Testing completed	Penn State
Out-of-plane shear modulus, G_{23}, Msi	---	---	---	Penn State	Testing completed	Penn State
Out-of-plane shear strength, F_{23}, ksi	---	---	---	Penn State	Testing completed	Penn State

[a]Asterisks correspond to information provided in Method and Additional notes columns.

Based on the data presented here, significant differences in results between these two versions were not observed; however, this was not investigated in detail. Apart from the data comparison, another purpose of compiling this information was to reduce additional testing by identifying and choosing the data required for the material models from previously conducted experiments. The CWG finalized material properties primarily using data from NCAMP, as these were derived from extensive testing. When NCAMP data were unavailable, the team used information from NASA's HEDI effort and the Hexcel product data sheet.

These tests were primarily conducted based on ASTM standards and included experiments under tensile, compressive, and shear states for material characterization. Backout factor (BF) was used to calculate stiffness and strength values measured from axial tensile and compressive tests. BFs are used when a test specimen has a cross-ply layup instead of the conventional unidirectional layup.

5.2.3 Model-Specific Parameters Characterized by Testing

The strength, stiffness, and strain properties compiled and finalized based on different sources were then assigned to the different analysis methods. As presented in Table 16, the numerical analysis task group consisted of 11 analysis teams, with each team employing a different material model to define the IM7/8552 composite material system. The input required by each material model varied primarily based on the failure criteria and the level of fidelity. However, the strength and stiffness properties were common for all the analysis methods. The material models shown in Table 16 include both commercially available and user-defined material models. The table also shows test type and standard for each material property and notes whether the property was directly measured from the test or numerical modeling parameter or obtained from open literature. The numbers under each material model aid in describing the test conducted to measure these properties.

The majority of the material properties required for these models were derived from material characterization based on coupon test data, as outlined in Table 15. These tests were conducted at the lamina level. However, certain material models required additional test data from more complex experiments. These data were obtained either through new experiments or from the open literature.

The following subsections and associated appendixes describe the experiments conducted to obtain specific data necessary to enhance the material models. The tests were designed based on material-model-specific parameters for the progressive damage models described in Table 16. These experiments were conducted at the laminate level, ranging from coupon-level to subcomponent-level systems, to account for strain-rate dependency, erosion calibration, and postpeak softening parameters. Material characterization testing for specific models is discussed in Sections 5.2.3 and 5.2.4.

As a summary, continuum damage models in Table 16 often utilize 90° load-deflection tests (test no. 27 in Table 14) to parameterize transverse tensile matrix damage behavior and out-of-plane stiffness for accurate composite impact responses. These tests are crucial for simulating progressive failure, crashworthiness, and impact energy absorption in laminated composites. They provide data for damage initiation criteria (e.g., Hashin) and progression models, including fracture energy for transverse cracking, and are frequently used for interlaminar fracture characterization, such as mode I (tensile opening) fracture toughness in cohesive elements.

TABLE 16.—STANDARDS AND NONSTANDARD TESTS IN SUPPORT OF MATERIAL MODELS WITH MATERIAL PROPERTY INPUT AT LAMINATE, FIBER, AND MATRIX LEVELS
[Numbers below each material model refer to tests described in Table 14.]

(a) Laminate-level properties

Required input, data available	Required input, testing possible but assumptions available	Required input, testing required	Not required

Property	Value	LS–DYNA® MAT54	LS–DYNA® MAT58	LS–DYNA® MAT219 CODAM2	LS–DYNA® MAT261	Modified Ladevèze	ABAQUS® Ladevèze	ABAQUS® CZone	VPS: Waas–Pineda	Altair® RADIOSS®	LS–DYNA® MAT213	Non-standard?
Fiber direction stiffness	154.58 GPa	1	1	1	1	1	1	1	1	1	[a]1	
Transverse stiffness	8.96 GPa	2	2	2	2	2	2	2	2	2	[a]2	
Poisson's ratio	0.316	1,2	1,2	1,2	1,2	1,2	1,2	1,2	1,2	1,2	1,2	
Shear modulus	4.69 GPa	3	3	3	3	3	3	3	3	3	[b]24	
Axial peak stress (tension)	2,500.7 MPa	1	1	1	1	1	1	1	1	1	[a]1	
Axial peak stress (compression)	1,714.03 MPa	4	4	4	4	4	4	4	4	4	[a]4	
Transverse peak stress	64.05 MPa	2	2	2	2	2	2	2	2	2	[a]2	
Transverse peak stress (compression)	285.71 MPa	4	4	4	4	4	4	4	4	4	[a]4	
Longitudinal shear strength	Test data available, MPa	5			5					5	[b]24	
In-plane shear yield stress	53.5 MPa	3	3	3	3	3	3	3	3	3	[b]24	
In-plane shear damage and plasticity parameters (Tests performed at DLR according to condition 21)	Y_{120} = 0.168 MPa$^{1/2}$ Y_{12c} = 3.48 MPa$^{1/2}$ R_0 = 32.5 MPa β = 680 MPa μ = 0.45			24,25		21	21		21	3	21	Yes
Crush stress	Test data available, MPa							26				Yes
Residual tension strength, axial direction	20%	1/nonphysical parameter	7,10							7,10	1/nonphysical parameter	
Residual compression strength, axial direction	80%	4/nonphysical parameter	7,10							7,10	4/nonphysical parameter	

TABLE 16.—STANDARDS AND NONSTANDARD TESTS IN SUPPORT OF MATERIAL MODELS WITH MATERIAL PROPERTY INPUT AT LAMINATE, FIBER, AND MATRIX LEVELS
[Numbers below each material model refer to tests described in Table 14.]

(a) Laminate-level properties

Required input, data available	Required input, testing possible but assumptions available	Required input, testing required	Not required

Property	Value	LS–DYNA® MAT54	LS–DYNA® MAT58	LS–DYNA® MAT219 CODAM2	LS–DYNA® MAT261	Modified Ladevèze	ABAQUS® Ladevèze	ABAQUS® CZone	VPS: Waas–Pineda	Altair® RADIOSS®	LS–DYNA® MAT213	Non-standard?
Residual tension strength, transverse direction	20%	2/nonphysical parameter	7,10							7,10	2/nonphysical parameter	
Residual compression strength, transverse direction	80%	4/nonphysical parameter	7,10							7,10	4/nonphysical parameter	
Residual shear strength	50%	3/nonphysical parameter	3,6							3,6	3/nonphysical parameter	
ERODS – maximum effective strain for element failure	0.13	Nonphysical parameter	6							6	6	Yes
Maximum tensile strain, axial direction	0.0162 mm/mm	1	1							1		
Maximum compressive strain, axial direction	–0.0111 mm/mm	4	7			4		2		7		
Maximum tensile strain, transverse direction	0.0128 mm/mm	2	2							2		
Maximum compressive strain, transverse direction	0.0293 mm/mm	4	7							7		
Element erosion limit for axial strain	Numerical, model dependent			1/literature			Nonphysical parameter					
Element erosion limit for transverse strain	Numerical, model dependent			2/literature			Nonphysical parameter					
Element erosion limit for shear strain	Numerical, model dependent			3/literature			Nonphysical parameter					
Parameters for transverse matrix damage (Tests performed at DLR according to condition 22)	Y_{20} = 0.094 MPa$^{1/2}$ Y_{2c} = 4.05 MPa$^{1/2}$ b = 0.465 α = 0.75						27					Yes
Delamination critical length	mm			Nonphysical parameter								Yes

TABLE 16.—STANDARDS AND NONSTANDARD TESTS IN SUPPORT OF MATERIAL MODELS WITH MATERIAL PROPERTY INPUT AT LAMINATE, FIBER, AND MATRIX LEVELS
[Numbers below each material model refer to tests described in Table 14.]

(a) Laminate-level properties

Required input, data available	Required input, testing possible but assumptions available	Required input, testing required	Not required

Property	Value	LS–DYNA® MAT54	LS–DYNA® MAT58	LS–DYNA® MAT219 CODAM2	LS–DYNA® MAT261	Modified Ladevèze	ABAQUS® Ladevèze	ABAQUS® CZone	VPS: Waas–Pineda	Altair® RADIOSS®	LS–DYNA® MAT213	Non-standard?
Strain-rate parameters fiber compression	Literature data for EU version (134 gsm) available (Ref. 60)						11/literature			11/ literature		Yes
Strain-rate parameters transverse compression	Literature data for EU version (134 gsm) available (Ref. 60)						11/literature			11/ literature		Yes
Strain-rate parameters in-plane shear	Literature data for EU version (134 gsm) available (Ref. 60)						11/literature			11/ literature		Yes
Softening reduction factor for elements in crush front	-	Nonphysical parameter	6		6					6		Yes
Density	1.55×10^{-9} tonne/mm^3											

[a]See Reference 61 [Haluza, R. T.: Measurement and Explicit Finite Element Modeling of Dynamic Crush Behavior of Carbon Fiber Reinforced Polymer Composites. Ph.D. Dissertation, The Pennsylvania State University, 2022] for sources of tabular material property data used for MAT213 models.
[b]V-notch shear testing was used to generate tabular shear property data for MAT213. See Reference 61 for further details on material properties used for the MAT213 models.

TABLE 16.—STANDARDS AND NONSTANDARD TESTS IN SUPPORT OF MATERIAL MODELS WITH MATERIAL PROPERTY INPUT AT LAMINATE, FIBER, AND MATRIX LEVELS
[Numbers below each material model refer to tests described in Table 14.]

(b) Fiber-level properties

Required input, data available	Required input, testing possible but assumptions available	Required input, testing required	Not required

Property	Material property	LS–DYNA® MAT54	LS–DYNA® MAT58	LS–DYNA® CODAM2	LS–DYNA® MAT261	Modified Ladevèze	ABAQUS® Ladevèze	ABAQUS® CZone	VPS: Waas–Pineda	Altair® RADIOSS®	LS–DYNA® MAT213	Non standard?
Mode I fracture toughness of fiber (tension)	[a]kJ/m^2			13	13	13	13		13			Yes
Mode I fracture toughness of fiber (compression)	[a]kJ/m2			12	12	12	12		12			Yes

[a]Fracture toughness and strain energy release rates are defined in Section 4.4.1.

TABLE 16.—STANDARDS AND NONSTANDARD TESTS IN SUPPORT OF MATERIAL MODELS WITH MATERIAL PROPERTY INPUT AT LAMINATE, FIBER, AND MATRIX LEVELS
[Numbers below each material model refer to tests described in Table 14.]

(c) Matrix-level properties

Required input, data available	Required input, testing possible but assumptions available	Required input, testing required	Not required

Property	Material property	LS–DYNA® MAT54	LS–DYNA® MAT58	LS–DYNA® CODAM2	LS–DYNA® MAT261	Modified Ladevèze	ABAQUS® Ladevèze	ABAQUS® CZone	VPS: Waas–Pineda	Altair® RADIOSS®	LS–DYNA® MAT213	Non standard?
Matrix shear strength	-											
Fracture angle in pure transverse compression	Test data available, deg.				8							
Failure strain	-		2									
Failure strain (compression, matrix)	-											
Failure strain (shear, matrix)	-		3									
Mode I fracture toughness of matrix	0.277 kJ/m^2 (Literature data)			18	14,18	18	18		18	18		
Mode II and III fracture toughness of matrix	0.788 kJ/m^2 (Literature data)			19	19	19	19		19	19		
Mixed-mode fracture toughness of matrix	0.33 kJ/m^2			23			23		23			

5.2.3.1 Low-Velocity Impact Testing for MAT162

Low-velocity impact tests were conducted on two types of laminated specimens fabricated using IM7/8552 unitape material and smoothed particle Galerkin (SPG) 196–PW/8552 fabric material. The primary intent of this activity was to use the data to calibrate the postpeak softening parameters for LS–DYNA® MAT162. Two types of quasi-isotropic test laminates (16 plies and 32 plies) were fabricated using the aforementioned material systems. Test laminates with nominal dimensions of 4 by 6 in. were held between two custom-built picture-frame fixture plates that provided a simply supported edge boundary condition along a rectangular boundary measuring 3.5 by 5.5 in., as illustrated in Figure 121.

The boundary conditions deviated from the ASTM D7136 standard (Ref. 62), which recommends point clamp supports, as these are difficult to simulate. Other impact test methods are described in References 63 to 65. An Instron® Dynatup (Illinois Tool Works Inc.) instrumented impact testing machine was used to conduct the impact tests using a 0.5-in.-diameter steel tup. The fabric laminates were tested with 0° direction either parallel to the long edge (configuration A) or the short edge (configuration B). All unitape laminates were tested in configuration A only. Impact energy levels between 100 and 500 in·lb were employed to achieve impact damage states ranging from permanent dents to puncture of laminates. DIC was employed to measure the strain fields on the back side of the laminate during impact. The image correlation data were used to extract the strain rates experienced by the laminates as well as the onset and propagation of failure. The impact-tested laminates were subjected to nondestructive damage inspection, which included the measurement of residual dent depth.

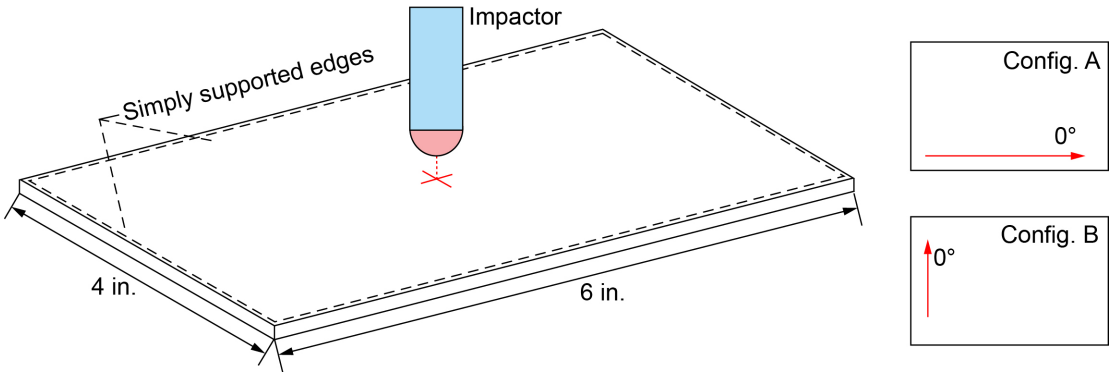

Figure 121.—Low-velocity impact test configuration.

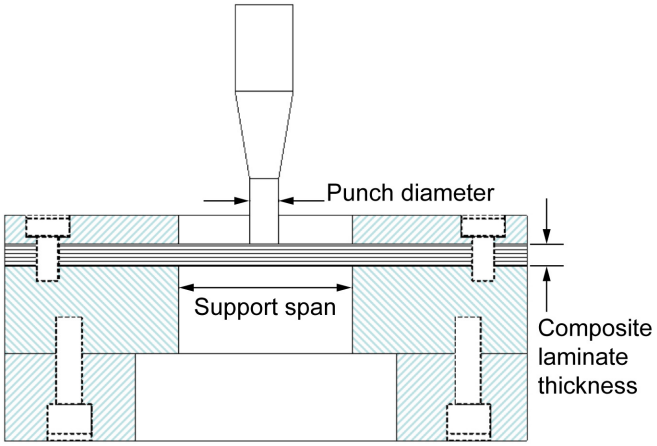

Figure 122.—Quasistatic punch shear test schematic.

5.2.3.2 Punch Shear Testing

The quasistatic punch shear test (QS–PST) (Refs. 66 and 67) is required to calibrate the postpeak response, or softening curves, for a composite damage material model. Reduction in modulus ϖ is defined by the function given in Equation (8), where m is a material parameter that determines softening behavior and r is the ratio of strain to yield strain. The derivation of this expression is described in Reference 66. There are four such material parameters in general, and the values for these are determined indirectly, based on correlating simulation response with test data. Values for m are determined in large part through punch shear tests, where the values are optimized to match punch shear test data for various test configurations.

$$\varpi = 1 - e^{\left(\frac{1-r^m}{m}\right)} \tag{8}$$

Although the QS–PST is conducted through quasistatic testing, that is, at low loading rate, it is integral to material characterization testing for PFDA for impact, hence relevant to discuss in this section. The QS–PST is shown in Figure 122. Further discussion of punch shear testing can be found in Reference 33.

5.2.3.3 Depth of Penetration Testing for Element Erosion Modeling for MAT162

The goal of the depth of penetration (DOP) test is to determine how deep an impacting projectile penetrates into a thick composite as a function of impact velocity. As the velocity is increased, so does the DOP. At some defined velocity, the material in front of the projectile approaches a hydrostatic state of stress and the DOP is limited. Penetration depth is frequently used to calibrate element erosion and crushing. As noted previously, the punch shear test can be modified to provide complete support of the coupon and provides a crushing load–displacement curve for use in calibrating out-of-plane crush response. In such a case, element erosion may also occur, depending on depth of punch penetration. Like punch shear testing, the DOP is integral to material characterization testing for PFDA for impact.

Figure 123.—Test specimen support fixture for measuring dent depth and extent of impact damage.

Dent depth is also found through testing, similar to barely visible impact damage (BVID) impacts, where residual dent depth is measured after impact. A typical impact coupon is shown in Figure 123. The impact results in an out-of-plane dent without full penetration. The dent depth can be used to calibrate crush or element erosion parameters to allow the simulation to show dent depth similar to that seen in the test. Impact may also result in both minor dent depth and delamination. In such cases, calibration of element erosion can be performed based on observed dent depth and diameter of surface damage. The element erosion due to through-thickness crushing measured through DOP supports continuum damage models, including LS–DYNA® MAT162. Further discussion of DOP testing can be found in Reference 33.

5.2.4 Material Characterization Testing for MAT213

MAT213 is an orthotropic plasticity-based material model in LS–DYNA®, a transient dynamic FE software package. MAT213 is designed to contain three submodels: deformation, damage, and failure (Ref. 68). The deformation model dictates the relationship between strain and stress before damage and failure occur. As opposed to traditional FE material models that require pointwise properties (e.g., elastic moduli), the deformation model of MAT213 utilizes full stress–strain curves in the various coordinate directions that are stored as tabulated data. Two element types can be used with MAT213: 3D solid elements and shell elements. Table 17 gives the material characterization tests necessary to provide the required input for the MAT213 deformation model, the ASTM standards utilized, and whether that test is required for solid or shell elements (Refs. 22, 68, and 69). Note that as described by Khaled (Ref. 68), variations on the standard ASTM tests have been developed for several of the tests, such as the shear tests, to provide optimum input data for MAT213. The ASTM standards listed (Refs. 70 to 73) provide the baseline procedures for obtaining the required data.

The damage model features optional parameters to allow for the loss of stiffness prior to failure and postpeak stress degradation (Refs. 22, 68, and 69). As described in the cited references, a tabulated approach is also used for the material input for the damage model, where damage parameters in the various coordinate directions are defined as a function of the corresponding total strain. Multiple failure models are available in MAT213, including the well-known Tsai–Wu and Puck models, along with a new generalized tabulated failure criterion (GTFC), which is a stress- or strain-based criterion in which the geometric failure surface is converted into a single valued function and defined in MAT213 in a tabulated fashion. More details on the GTFC model can be found in Reference 22.

TABLE 17.—REQUIRED TESTING FOR MAT213 DEFORMATION MODEL AND INTERLAMINAR ELEMENTS

Characterization test ([a]direction or plane)	ASTM standard	Required for MAT213 solid elements?	Required for MAT213 shell elements?
Tension (1)	D3039 (Ref. 70)	Yes	Yes
Tension (2)	D3039	Yes	Yes
Tension (3)	D7291 (Ref. 71)	Yes	No
Compression (1)	D3410 (Ref. 72)	Yes	Yes
Compression (2)	D3410	Yes	Yes
Compression (3)	D7291	Yes	No
Shear (1–2)	D5379 (Ref. 73)	Yes	Yes
Shear (1–3)	D5379	Yes	No
Shear (2–3)	D5379	Yes	No
Compression (45° offset in 1–2 plane)	D7291 (Ref. 71)	Yes	Yes
Compression (45° offset in 1–3 plane)	D7291	Yes	No
Compression (45° offset in 2–3 plane)	D7291	Yes	No

[a] Direction 1 is in-plane parallel to fibers, 2 is in-plane perpendicular to fibers, and 3 is orthogonal to lamina plane.

5.2.4.1 Test Methods

To measure the properties and stress–strain curves required for MAT213 in an optimal manner, several specimen geometries were modified from the ASTM standard geometry as described in Reference 66. For longitudinal and transverse tension tests, dog-bone specimens were used in place of straight-sided coupons due to failure near the grips in prior testing. ASTM D7291 compression specimens were converted to cubic specimens for ease of manufacturing. ASTM D7291 was also utilized in three-direction tension tests, but a rectanguloid geometry was chosen with dimensions dictated by the size of the panel. The selection of the ASTM standard test methods and motivation for modifying the aforementioned standards is given in Reference 69. Suitable modifications to specimen geometries may be required should the material not be a unidirectional material.

DIC was used to measure the strain in all of the characterization tests. DIC is valuable to MAT213 models because the full-field strain data allow for a broad range of posttest analysis techniques, enable strain measurement in multiple directions, and provide a comparison to coupon-level models to verify MAT213 inputs.

5.2.4.2 Test Results Discussion

At the time of this writing, testing was still in progress; thus, the data for the characterization tests described above are not yet available. For the presented modeling efforts, input curves were derived from characterization test results reported by Reference 25. These values will be used until detailed characterization tests are performed.

The 1–3 and 2–3 shear tests were conducted at Pennsylvania State University, and the tabulated stress strain data were successfully recorded. Reference 74 describes the results in further detail and provides the tabulated data in an appendix.

5.2.5 Cyclic Testing To Determine Matrix Damage and Plasticity Parameters for ABAQUS®/Explicit ABQ_DLR_UD

The purpose of this test series was to identify material input parameters for the ABQ_DLR_UD ply model developed by DLR, which is used as a user-material model in ABAQUS®/Explicit (VUMAT). This

test series concerned the identification of the matrix damage and plasticity parameters based on the formulations by Ladevèze and LeDantec (Ref. 12). These test methodologies are discussed in Reference 33.

The test procedure is explained in detail by Ladevèze and LeDantec (Ref. 12) as well as by O'Higgins et al. (Ref. 75). Tests on $[\pm 45]_{4S}$ laminates were carried out to determine shear damage and plasticity input parameters. Tests on $[\pm 67.5]_{4S}$ laminates were used to determine the shear–transverse damage coupling parameter, transverse damage input parameters, and the shear–transverse plasticity coupling parameter. Experimental data presented in this section is related to the material system IM7/8552 (U.S. version: 190 gsm).

5.2.5.1 Testing Details and Results

The geometry of the test specimens is based on guidelines given in ASTM D3039 (Ref. 70) and ASTM D3518 (Ref. 76), with nominal dimensions 260 by 25 by 3 mm. The testing procedure is based on the methods outlined by Ladevèze and LeDantec (Ref. 12). One specimen of each layup was subjected to quasistatic monotonous loading up to failure, and five specimens of each layup were subjected to quasistatic cyclic loading with force control, transferring to displacement control for the later cycles. The amplitude of force was increased with each load/unload cycle, whereas the displacement was constant.

Cyclic tensile tests on the specimens with $[\pm 45]_{4S}$ layup were used to identify shear damage growth and plasticity parameters: initial shear damage threshold parameter Y_{120}, shear damage evolution parameter Y_{12c}, shear damage failure threshold Y_{12s}, yield stress R_0, plastic hardening law coefficient β, and plastic hardening law exponent μ. Shear damage is characterized by the reduction of the shear modulus G_{12} with each loading/unloading cycle. Plasticity is characterized by the increase of the total plastic strain with each loading/unloading cycle.

Cyclic tensile tests on the specimens with $[\pm 67.5]_{4S}$ layups were used to identify the transverse damage master curves and shear–transverse damage and plasticity coupling parameters: transverse damage initiation threshold Y_{20}, transverse damage failure threshold Y_{2s}, transverse damage evolution parameter Y_{2c}, shear–transverse damage coupling parameter b, and shear–transverse plasticity coupling parameter α^2. The one specimen of each layup that was tested under quasistatic monotonous tensile loading up to failure was used to determine the shear-stress-to-shear-strain and transverse-stress-to-transverse-strain master curves from which the maximum strains and load/unload points were derived.

All testing was performed at the DLR Institute of Structures and Design in Stuttgart, Germany. All testing was carried out on a ZwickRoell 1494 500-kN universal electromechanical testing machine. A 500-kN auxiliary load cell was used. The loading speed of each test was 0.033 mm/s, which includes both the loading and unloading cycles. All tests were performed at room temperature and in dry conditions.

The delivered plates with the $[\pm 45]_{4S}$ and $[\pm 67.5]_{4S}$ layups and dimensions of 12 by 12 in. (about 30.5 by 30.5 mm) were manufactured at the University of Utah and handed over to DLR. The plates were ultrasonically scanned prior to cutting and showed good uniformity. The specimens were cut using a diamond saw. Each test specimen was instrumented with one biaxial strain gauge rosette (FCA-6-11-1L) that was placed in the center of the specimen. Strain readings were taken from these strain gauges at a frequency of 10 Hz. The instrumented specimens are shown in Figure 124. Additionally, observable markers were painted on the specimen for strain measurement with an optical extensometer, and specimen surfaces were painted with a speckle pattern for strain field analysis. However, only the strain gauge data were used for material characterization. Figure 125(a) and Figure 125(b) show the markers and speckle patterns of one exemplary specimen. No tabs were mounted on the specimens; instead, sandpaper strips were used.

Damage of the specimens initiated for all tests outside of the clamping region, as exemplarily shown in Figure 125(b) and Figure 126(b). Five repeats were carried out for each layup. The gauge length in between the clamping was chosen to be larger than 150 mm (specifically, 154.2 mm) for all tests.

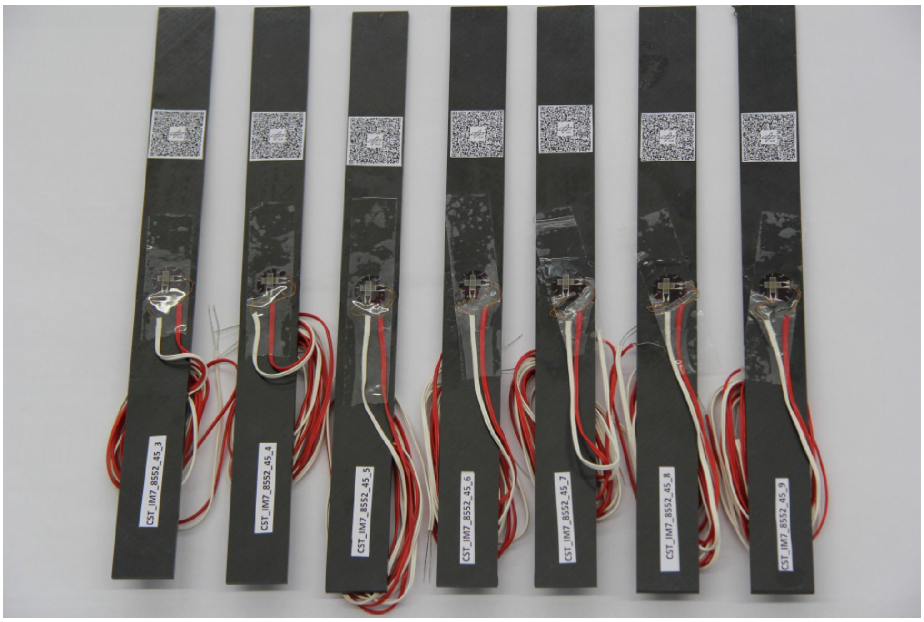

Figure 124.—Instrumented specimens of $[\pm 45]_{4S}$ test series, including one spare.

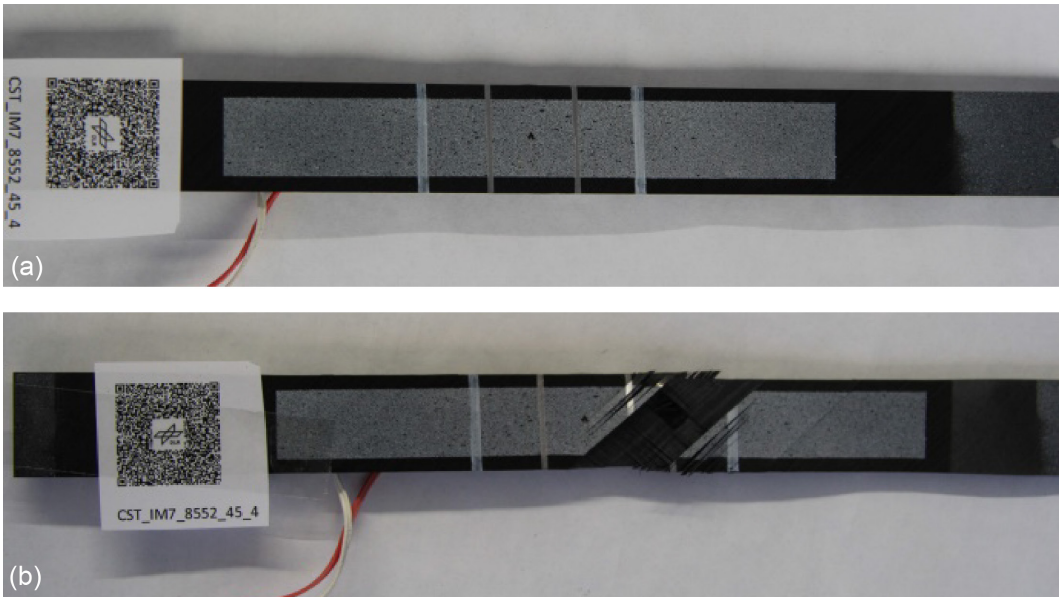

Figure 125.—Specimen of $[\pm 45]_{4S}$ test series with speckle pattern and markers for optical extensometer. (a) Prior to testing. (b) After testing.

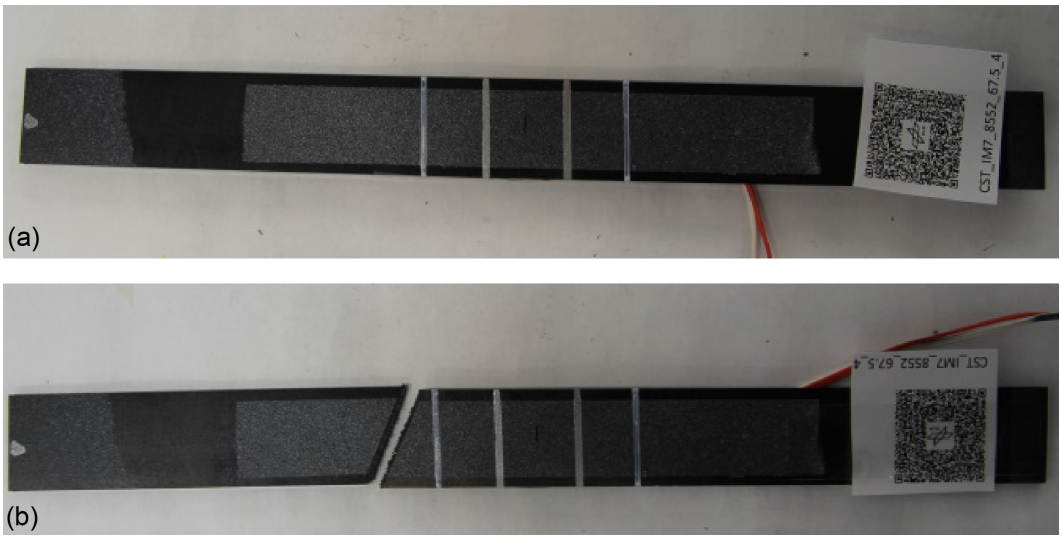

Figure 126.—Specimen of $[\pm 67.5]_{4S}$ test series with spackle pattern and markers for optical extensometer. (a) Prior to testing. (b) After testing.

5.2.5.2 Shear Damage and Plasticity Parameters ($[\pm 45]_{4S}$ Tests)

The $[\pm 45]_{4S}$ tests were used to determine the shear damage and plasticity parameters. The specimens were cyclically loaded and unloaded in a combination of force and piston displacement control with increased force amplitude. Details of the loading/unloading cycles are listed in Section C.1 (Table C.1).

5.2.5.3 Cyclic Tensile Test and Shear Damage Material Characterization Summary

The $[\pm 67.5]_{4S}$ tests were used to determine transverse damage parameters and the shear–transverse damage and plasticity coupling parameters. The specimens were cyclically loaded and unloaded in force control with increased force amplitude for the loading cycles. Details are listed in Section C.1.2 (Table C.3).

Tests were carried out to determine material input parameters for material model ABQ_DLR_UD, which was developed at DLR and is used as a user material (VUMAT) in the explicit FE code ABAQUS®/ Explicit. The determined material parameters are used for modeling the matrix behavior of material system IM7/8552 (U.S. version). The material behavior under transverse tension and shear and the modeling of plasticity are based on the formulations by Ladevèze and LeDantec (Ref. 11).

Cyclic tensile tests on the specimens with $[\pm 45]_{4S}$ layup were used to identify shear damage growth and plasticity parameters: initial shear damage threshold parameter Y_{120}, shear damage evolution parameter Y_{12c}, shear damage failure threshold Y_{12s}, yield stress R_0, plastic hardening law coefficient β, and plastic hardening law exponent μ.

Cyclic tensile tests on the specimens with $[\pm 67.5]_{4S}$ layup were used to identify the transverse damage master curves and shear–transverse damage and plasticity coupling parameters: transverse damage initiation threshold Y_{20}, transverse damage failure threshold Y_{2S}, transverse damage evolution parameter Y_{2c}, shear–transverse damage coupling parameter b, and shear–transverse plasticity coupling parameter α^2.

Five repeats for each test group were performed, and the results showed good repeatability for all results. The requested plates with $[\pm 45]_{4S}$ and $[\pm 67.5]_{4S}$ layups fabricated from IM7/8552 were provided courtesy of the University of Utah.

5.3 Required Fiber-Level and Matrix-Level Input Properties

This section summarizes the experiments conducted to characterize material properties at fiber and matrix level. These properties were necessary for enhanced definition of certain material models shown in Table 16. These are high-fidelity, state-of-the-art progressive damage material models that employ failure based on fracture toughness criteria. Specifically, these properties add another layer of fidelity to the material model that would help in better simulating the evolution and propagation of complex damage modes. To characterize the discrete fiber and matrix damage evolution, interlaminar fracture toughness tests such as mode I, mode II, and mode III experiments were considered. NASA's HEDI effort had previously conducted experiments to capture delamination criteria and ply-to-ply interfacial interaction using tiebreak contacts (based on cohesive zone modeling). However, the material models evaluated by UBC and DLR required additional parameters that were measured from additional in-house experiments and open literature.

Table 18 presents the required fiber-level and matrix-level material properties as identified to support seven analysis material models. The tests were conducted at two different test sites, UBC and DLR; the material properties were shared across the numerical analysis task group.

TABLE 18.—SUMMARY OF TEST DATA SOURCES FOR FIBER- AND MATRIX-LEVEL MATERIAL PROPERTY INPUT

Analysis group	Material property	Test no.[a]	Test site/literature data available
LS-DYNA®: MAT219	In-plane shear damage and plasticity parameters	24	UBC
		25	DLR
	Mode I fracture toughness of fiber (tension)	13	Literature data
	Mode I fracture toughness of fiber (compression)	12	Literature data
	Mode I fracture toughness of matrix	18	Literature data
	Mode II and III fracture toughness of matrix	19	Literature data
	Mixed-mode fracture toughness of matrix	23	Literature data
LS-DYNA®: ABAQUS® LADEVÈZE ABQ_DLR_UD	In-plane shear damage and plasticity parameters	21	DLR
	Parameters for transverse fiber damage (fabric) or matrix damage (tape)	22	DLR
	Mode I fracture toughness of fiber (tension)	13	Literature data
	Mode I fracture toughness of fiber (compression)	12	Literature data
ESI VPS: Waas–Pineda implementation	In-plane shear damage and plasticity parameters	21	DLR
	Mode I fracture toughness of fiber (tension)	13	Literature data
	Mode I fracture toughness of fiber (compression)	12	Literature data
Altair® RADIOSS®	Mode I fracture toughness of matrix	18	Literature data
	Mode II and III fracture toughness of matrix	19	Literature data

[a]Numbers refer to tests described in Table 14.

5.3.1 Fracture Toughness and Strain Energy Release Rates Literature Survey

The DLR conducted a literature survey to determine interlaminar fracture toughness parameters that complement HEDI test data and, in certain cases, compared with HEDI where test data was available. The results of this survey as presented in this section were used in progressive damage predictive models. It is important to note that the open literature data are primarily based on the European IM7/8552 material (134 gsm), whereas the HEDI studies used the U.S. version of IM7/8552 (190 gsm) (see Section 4.2.1 for further discussion).

Camanho et al. (Ref. 41) used a continuum damage model to predict strength and size effects in notched carbon/epoxy laminates. The material used was Hexcel Hexply® IM7/8552 carbon/epoxy with a nominal ply thickness of 0.131 mm. To measure the fracture toughness values, double cantilever beam (DCB) testing was performed in accordance with standard ASTM D5528–01 and four-point bend ENF (4ENF) testing was performed in accordance with Reference 77. The measured fracture toughness values were as follows:

- IM7/8552 fracture toughness in mode I: G_{Ic} = 0.277±0.0246 kJ/m^2 ≅ 1.581 in·lb/in^2
- IM7/8552 fracture toughness in mode II: G_{IIc} = 0.788±0.0803 kJ/m^2 ≅ 4.494 in·lb/in^2

This shows that G_{Ic}, as determined by Camanho et al. (Ref. 41), was lower compared with HEDI test data, whereas G_{IIc} was approximately equal for both tests.

Schön et al. performed an extensive numerical and experimental investigation on the fracture mechanical properties of DCB (Ref. 78) and ENF (Ref. 79) specimens in accordance with European Structural Integrity Society (ESIS) standards (Ref. 80). Static and cyclic properties were studied for various interfaces (0°/0°, 45°/45°, and 90°/90°) for several materials, including IM7/8552, with a nominal ply thickness of 0.13 mm. For analysis of the test results, Schön et al. used Berry's method (Refs. 80 and 81) to estimate the energy release rates. Berry's method plots compliance versus crack length on a log-log plot (Ref. 78). The slope of this plot n can be used to calculate G_{Ic} as

$$G_{Ic} = \frac{nP\delta}{2wa} \tag{9}$$

where P is the applied load, δ is the crack-opening displacement at the point of the applied load, w is the width of the specimen, and a is the crack length. For IM7/8552, G_{Ic} was calculated for the 0°/0° interfaces as follows:

0°/0° interface: G_{Ic} = 0.22±0.01 kJ/m^2 ≅ 1.257 in·lb/in^2

For the 45°/45° and 90°/90° interfaces, damage initiation occurred at G_{Ic} values similar to those for the 0°/0° interface (Ref. 78).

Mode II fracture toughness was determined using ENF specimens (Ref. 11). The results for mode II fracture toughness G_{IIc} for 0°/0°, 90°/90°, and 45°/45° interfaces are presented in a bar diagram in Reference 79. From this, the following values can be derived:

0°/0° interface: G_{IIc} ~ 0.63 kJ/m^2 ≅ 3.597 in·lb/in^2

90°/90° interface: G_{IIc} ~ 0.87 kJ/m^2 ≅ 4.97 in·lb/in^2

45°/45° interface: G_{IIc} ~ 1.3 kJ/m^2 ≅ 7.423 in·lb/in^2

However, Andersons and König (Ref. 82) state in their review paper that for the tests reported in Reference 79, the delamination cracks did not follow the intended interfaces for off-axis interfaces. Therefore, the values reported in Reference 79 relate to complex interlaminar and intralaminar failure events rather than mode II delamination along a given interface (Ref. 82).

From the data reported by Schön et al. (Ref. 79), G_{Ic} was lower compared to the HEDI test data. G_{IIc} was lower for the 0°/0° interface, whereas for the 90°/90° and 45°/45° interfaces, G_{IIc} was higher compared to the HEDI test data.

Hiley (Ref. 83) performed mode I, mode II, and mixed-mode delamination tests between plies of different orientation (0°/0°, 0°/45°, 0°/90°) on IM7/8552 specimens. Mode I and mode II critical strain energy release rates G_{Ic} and G_{IIc} were determined using DCB and ENF tests in accordance with Reference 80. Mixed-mode tests were performed using the fixed-ratio mixed-mode (FRMM) test method in accordance with Reference 84.

The mode I fracture toughness G_{Ic} was calculated as

$$G_{Ic} = \frac{3P\delta}{2w(a+\Delta)}\frac{F}{N} \tag{10}$$

where P is the applied load, δ is the crack-opening displacement, w is the width of the specimen, a is the crack length, and Δ is a correction factor for the crack length. Corrections for large displacements F and end-block effects N were also included but showed negligible effects (Ref. 83). G_{Ic} was calculated for different interfaces for IM7/8552 as follows:

0°/0° interface: $G_{Ic} = 0.208$ kJ/m^2 ≅ 1.188 in·lb/in^2

0°/45° interface: $G_{Ic} = 0.181$ kJ/m^2 ≅ 1.03 in·lb/in^2

The mode II fracture toughness G_{IIc} was determined in accordance with Reference 83:

$$G_{IIc} = \frac{9a^2 3P^2\delta}{2w(2L^3+3a^3)} \tag{11}$$

where L is the half span width. The reported values for the 0°/45° and 0°/90° interfaces (values for the 0°/0° interfaces were not reported) were as follows:

0°/45° interface: $G_{IIc} = 0.941$ kJ/m^2 ≅ 5.373 in·lb/in^2

0°/90° interface: $G_{IIc} = 0.727$ kJ/m^2 ≅ 4.151 in·lb/in^2

Compared to the HEDI test data, the mode I fracture toughness G_{Ic} was significantly lower, whereas the mode II fracture toughness G_{IIc} was higher for 0°/45° interfaces and slightly lower for 0°/90° interfaces.

Hansen and Martin (Ref. 85) performed DCB, 4ENF, and mixed-mode bending (MMB) tests on IM7/8552 under both quasistatic and fatigue loading. The mode I fracture toughness was determined using DCB tests in accordance with ASTM D5528 (Ref. 81). The mode I fracture toughness was determined as

$$G_{Ic} = 0.208 \pm 0.0085 \text{ kJ/m}^2 \cong 1.18 \text{ in·lb/in}^2 \tag{12}$$

Mode II fracture toughness was determined using 4ENF tests performed on a standard four-point bend fixture (Ref. 85). The mode II fracture toughness was determined as

$$G_{IIc} = 1.334 \pm 0.293 \text{ kJ/m}^2 \cong 7.617 \text{ in·lb/in}^2 \tag{13}$$

The MMB tests were performed on a test fixture suggested by a draft ASTM MMB standard. The fracture toughness under MMB G_c was determined for ratios $G_{II}/G_{tot} = 0.33$ and $G_{II}/G_{tot} = 0.66$. The reported values are

$G_{II}/G_{tot} = 0.33$: $G_c = 0.298 \pm 0.042 \text{ kJ/m}^2 \cong 1.702 \text{ in·lb/in}^2$

$G_{II}/G_{tot} = 0.66$: $G_c = 0.374 \pm 0.109 \text{ kJ/m}^2 \cong 1.702 \text{ in·lb/in}^2$

Compared to the HEDI test data, G_{Ic} was lower but was the same as reported for 0°/0° interfaces reported in Reference 83. The value of G_{IIc} was significantly higher than the HEDI test data but was the same as the value reported for 45°/45° interfaces in Reference 79.

5.3.2 Double Cantilevered Beam Testing for Mode I Using ASTM D5528

For DCB testing, the crack tip location is estimated from the start and end positions of the stroke. Strain energy release rate testing was performed to provide G_{Ic}, which is required for interlaminar cohesive zone or tiebreak elements. G_{Ic} is calculated using Equation (14), where P_i is the load measured at time step i, L_i is the initial length of the beam, a_f is the difference between the final and initial crack length, and w is the beam width (Ref. 25). See Reference 33 for details of DCB test methods using ASTM5528 and International Standards Organization (ISO) 15024.

$$G_{Ic} = \frac{\sum_{i=1}^{n} (P_{i+1} - P_i) L_i}{a_f w} \tag{14}$$

Figure 127 shows the load displacement response for the fabric and tape coupons. The results are consistent between samples. The fabric curve shows a less stable propagation than the tape because of the plane over which the fracture front occurs. The undulation of the warp and weft fibers adds complexity to the crack plane; however, the propagation is stable enough to determine a strain energy release rate. The IM7/8552 fracture toughness in mode I was determined to be 1.85±0.07 in·lb/in^2, and the SPG 196–PW/8552 was determined to be 4.22±0.25 in·lb/in^2. This value is slightly lower than the value reported by Thorsson et al. (2.196 in·lb/in^2) for the same material system (Ref. 63).

Images of the failed samples for the IM7/8552 and SPG 196–PW/8552 material systems can be seen in Reference 25.

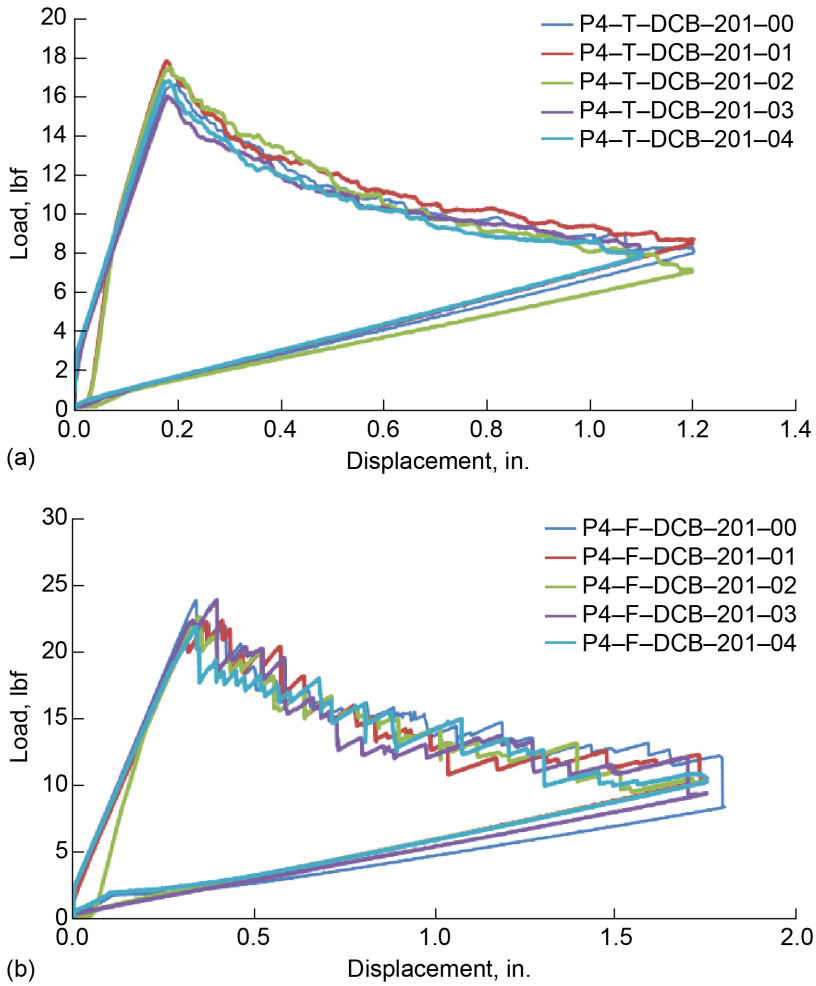

Figure 127.—Load–displacement response for double cantilever beam (DCB) tests for two material systems. (a) IM7/8552 tape (T). (b) SPG 196–PW/8552 fabric (F).

5.3.3 End-Notch Flexure Testing for Mode II ASTM D5045

ENF test methods are discussed in Reference 33 using an ASTM test standard. Following ASTM D7905, the HEDI effort conducted ENF testing as reported in Reference 25. According to that report, test samples were cured with a 3-in. polytetrafluoroethylene (PTFE) insert placed at the interface between the 16th and 17th ply to serve as a precrack in the panel. The cross-sectional area was measured from the coupon after sample preparation. The test configuration is shown in Figure 128.

The sample was loaded in displacement control at a loading rate of 0.002 in./s. The crack was monitored using a microscope and the location of the crack was noted. Prior to testing, the compliance of the fixture was determined by loading the fixture with an elastic bar. Based on this compliance, the critical load was established. This load was not exceeded for testing, as the data becomes unreliable. The crack propagation was monitored throughout the test until the critical load was reached.

The crack tip location was measured using a microscope at predetermined intervals during the test. As shown in Equation (15), G_{IIc} was calculated using the same parameters used for G_{Ic} (Ref. 25).

$$G_{IIc} = \frac{\sum_{i=1}^{n} (P_{i+1} - P_i) L_i}{a_f w} \tag{15}$$

Figure 129 shows the load-deflection response for the fabric and tape coupons. Results were consistent between samples. The IM7/8552 fracture toughness in mode II was determined to be 4.44±0.36 in·lb/in^2; for SPG 196–PW/8552, it was determined to be 12.86±0.51 in·lb/in^2.

Images of the failed samples for the IM7/8552 and SPG 196–PW/8552 material systems are provided in Reference 25.

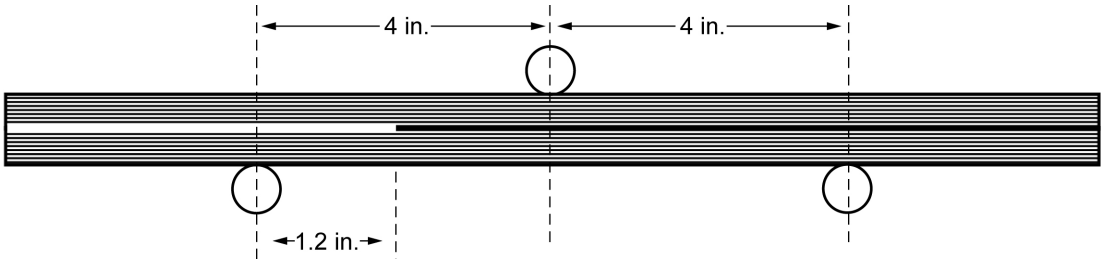

Figure 128.—Test configuration for end-notch flexure testing.

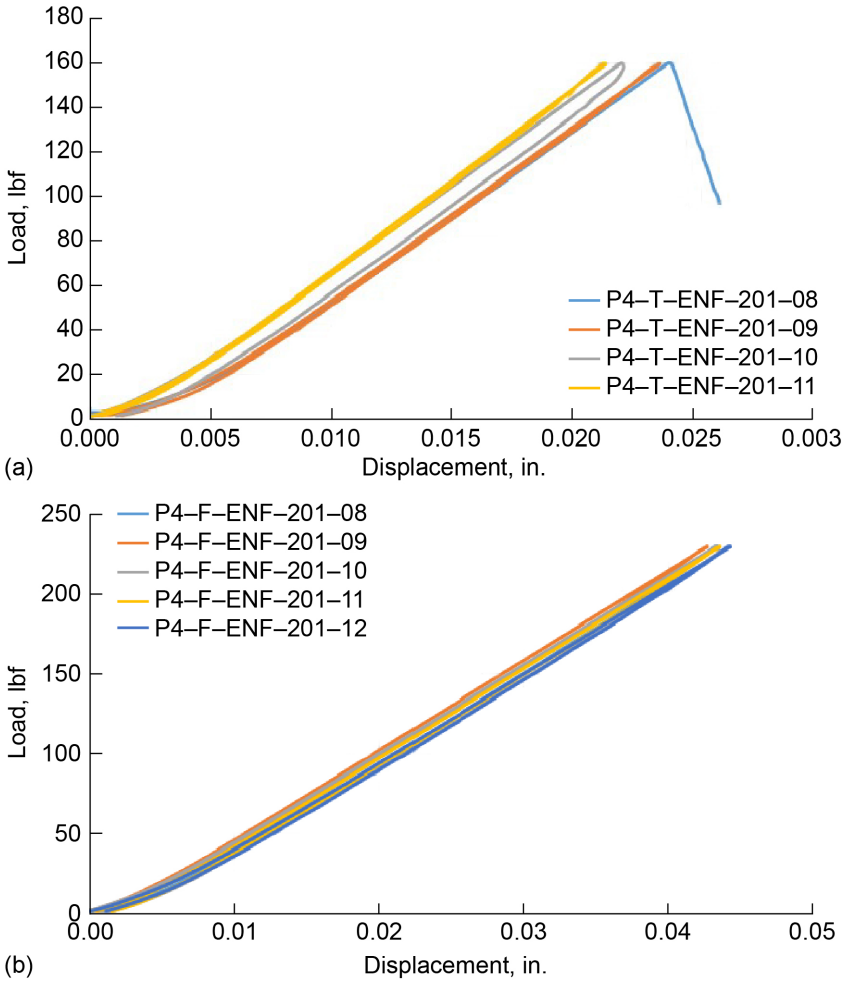

Figure 129.—Load–displacement response for ENF tests. (a) IM7/8552 tape (T). (b) SPG 196–PW/8552 fabric (F).

5.3.4 Mixed-Mode Bending Testing

MMB test methods are discussed in Reference 33. Following ASTM test standard D6671, the HEDI effort conducted MMB testing as reported in Reference 25. According to this report, test samples were cured with a 3-in. PTFE insert placed at the interface between the 16th and 17th ply to serve as a precrack in the panel. Samples were extracted from the bulk panel using a diamond-coated wet saw and were inspected to be free of delamination. The cross-sectional area was measured from the coupon after sample preparation. Piano hinges were bonded to the samples with FM® (Cytec Technology Corp.) 300–2 adhesive, using a 250 °F cure for 90 min. Testing was performed on an MTS Systems Corp. electromechanical load frame with a load capacity of 1,000 lbf. The displacement was measured using a laser extensometer (Figure 130). The crack tip was monitored using a digital camera with 70× optical zoom.

Testing was performed over three targeted mixed-mode ratios: 25, 50, and 75 percent, as shown in Figure 131. In general, at least three replicates were performed, except in the event of hinge failure, in which case additional specimens were tested. Hinge failure was observed only in the 75 percent mixed-mode ratio tests for the tape and fabric. The fracture toughness values are shown in Table 19.

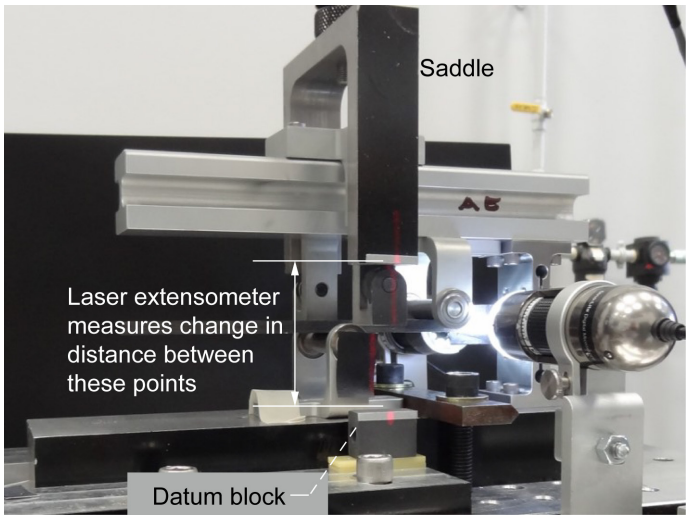

Figure 130.—Laser extensometer setup for mixed-mode bending tests.

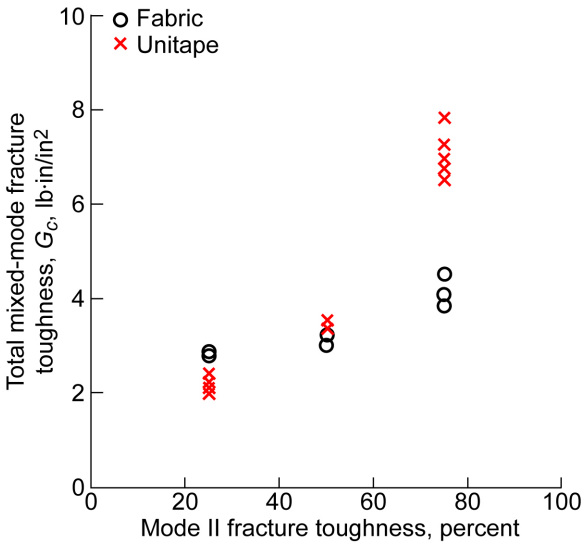

Figure 131.—Mixed-mode fracture toughness.

TABLE 19.—MEASURED FRACTURE TOUGHNESS VALUES FOR MIXED-MODE BENDING

Percent, mode II	Average fracture toughness, G_c, lb·in./in. (%CV)	
	Fabric	Tape
25	2.85 (1.3)	2.24 (6.0)
50	3.04 (2.7)	3.49 (2.2)
75	4.07 (6.0)	7.05 (7.6)

5.3.5 Fracture Toughness Testing for Material Models

IM7/8852 is widely used, and results for fracture toughness in mode I, mode II, and MMB have been published. Mode I fracture toughness is determined using DCB tests, and most of the reported tests' procedures followed ESIS (Ref. 80) and ASTM standards (Refs. 81 and 86). The results of mode I fracture toughness G_{Ic} published in the literature for tests following ESIS/ASTM standards are lower compared with the fracture toughness reported for the HEDI testing, which followed a Boeing-preferred test standard. For mode II fracture toughness G_{IIc}, the values reported in the literature show a strong dependency on the fiber orientation of the interfaces.

Based on the large range of fracture toughness values reported in the literature, the literature data will be used as the basis for ongoing CMH–17 material models for crash modeling efforts. Table 20 provides the fracture toughness values that will be used in progressive damage analysis models. The parameters presented in Table 20 were defined based on information from Table 15 in Section 5.2.2.

TABLE 20.—SUMMARY OF INTERLAMINAR FRACTURE TOUGHNESS PARAMETERS OF MATRIX FOR IM7/8552

Modes I and II	
Mode I fracture toughness, G_{Ic}, kJ/m^2	0.277
Mode II fracture toughness, G_{IIc}, kJ/m^2	0.787
IM7/8552 interfaces	
0°/0°	
Mode I fracture toughness, G_{Ic}, kJ/m^2	0.22
Mode II fracture toughness, G_{IIc}, kJ/m^2	0.63
0°/45°	
Mode I fracture toughness, G_{Ic}, kJ/m^2	0.22
Mode II fracture toughness, G_{IIc}, kJ/m^2	0.94
0°/90°	
Mode I fracture toughness, G_{Ic}, kJ/m^2	0.22
Mode II fracture toughness, G_{IIc}, kJ/m^2	0.73
45°/–45°	
Mode I fracture toughness, G_{Ic}, kJ/m^2	0.22
Mode II fracture toughness, G_{IIc}, kJ/m^2	1.30
Mixed-mode bending	
Mixed-mode ratio, G_{II}/G_{tot}	0.33
Fracture toughness, G_c, kJ/m^2	0.298
Mixed-mode ratio, G_{II}/G_{tot}	0.66
Fracture toughness, G_c, kJ/m^2	0.374

5.4 High Load Rate Bonded Joint Test

The experiments described in this section characterize the interlaminar fracture toughness of bonded composite joints at high loading rates within the range of 8 to 15 m/s. This test method has also been briefly discussed in Chapter 7 of Reference 33. Due to the challenges associated with high loading rate testing, there is a lack of standard test methods to evaluate interlaminar fracture behavior. Therefore, extensive research was conducted through literature review and pretest numerical analysis to overcome these challenges and design the test setup. The designed test setup was a modified split Hopkinson pressure bar (SHPB) comprising a striker bar and incident bar with a wedge to load the specimen under mode I conditions. The test specimen included an adhesively bonded composite laminate with a precrack and a notch for the incident bar wedge. Numerical analysis of the same was carried out using LS–DYNA® software, and the ply-level composite laminate was modeled using LS–DYNA® MAT162. Testing was conducted at the University of South Carolina (USC) in collaboration with The Boeing Company and NIAR. This section summarizes the detailed test setup and results presented in Reference 87.

The composite laminates were fabricated from IM7/8552 unidirectional tape with a nominal ply thickness of 0.183 mm (0.0072 in.) and were then cobonded using FM® 309–2 epoxy-based film adhesive. The overall dimensions of the composite specimen were 127 by 25.4 mm (5 by 1 in.) with a total thickness of 6.35 mm (0.25 in.). The length of the adhesive layer was 114.3 mm (4.5 in.) and the thickness was 0.152 mm (0.006 in.). A precrack of length 10 mm (0.4 in.) was induced in the specimen ahead of the adhesive during the fabrication process using a PTFE insert. The incident bar was 6 ft in length and 1 in. in diameter and was manufactured from an aluminum bar. The tip of the incident bar was designed with a wedge angle of 60° to slide into the groove on the specimen. More details of the test setup are given in Reference 87.

The incident bar was mounted with two strain gauges to measure the incident and reflected strain signals in the bar. Impactor velocity was measured using a two-laser-diode/receiver assembly placed at the impact end, and the load response was measured using the 5,000-lb-capacity load cell mounted at the end of the specimen by means of an adapter. For the dynamic experiments, high-speed imaging was conducted using Hyper Vision HPV–X2 video cameras from Shimadzu Scientific Instruments. A Navitar® (Navitar, Inc.) high-magnification, long-distance microscope was attached to the high-speed camera to obtain local deformations at the crack tip on test specimens. To capture the crack propagation and understand whether the crack simultaneously initiates and grows across the width of the sample, two cameras were used, one on each side of the test specimen (Ref. 87).

The microstructural crack-tip evolution under quasistatic and dynamic loading conditions can be seen in Reference 87. The images captured for the quasistatic experiments show crack initiation at 1.6 kN. The crack propagated through the adhesive, causing cohesive failure, followed by deflection to the composite–adhesive interface, resulting in interface failure. The high plastic deformations of the adhesive were observed to cause significant whitening of the epoxy. The two quasistatic experiments conducted had crack initiation consistently at the same load. The crack initiation for the dynamic experiments was observed to occur at 0.477, 0.437, and 0.421 kN for impact velocities 8.24, 10.2, and 14.6 m/s, respectively. However, the microstructural crack evolution in these tests was observed to be similar to that of the quasistatic experiments. This included initiation of crack growth in the adhesive layer, followed with a jump to the composite–adhesive interface. Note that the crack propagation in these tests did not occur entirely in the adhesive or the interface but rather was a combination of cohesive and interface failure. Failure modes were consistent throughout the tests.

5.5 High Load Rate Testing of Fastener Joints

This section discusses in detail the experiments conducted on composite fastener joints to evaluate their bearing behavior. This test method is also briefly discussed in Chapter 7 of Reference 33. The objective of fastener joints testing is to document the results from a set of experiments that were used to validate the selected PDFA methods, namely, MAT162 and MAT261. These subelement tests are high-rate tests that are representative of loading rates seen in a high-energy dynamic impact event that will be used to evaluate the behavior and failure of fastener joints under dynamic loading conditions compared to quasistatic loading conditions. Ultimately, this data will help developing fastener modeling methodologies in large-scale structures. Testing was conducted at NIAR in collaboration with The Boeing Company. These tests were performed with laminates of IM7/8552 unidirectional tape, a material system representative of those used in fuselage structures, and two different joint types: pins and Hi-Lok® (Hi-Shear Corp.) bolted fasteners (Ref. 88). This report contains summarized details of the experimentation and test results from the Fastener Joints Test Report (Ref. 89).

5.5.1 Test Article Description

The test article consisted of two carbon-fiber-reinforced laminates made of IM7/8552 unidirectional tape, each eight plies thick with a $[45/90/–45/0]_S$ stacking sequence. Test articles were assembled using two CFRP laminates and a 17–4PH steel spacer by means of epoxy paste adhesive (Figure 132). Uniaxial strain gauges were bonded to the inner surfaces of the specimens prior to assembly.

The titanium (Ti-6Al-4V) pins used in pin joint test articles have a nominal length of 0.6 in. and a nominal diameter of 0.25 in. The titanium fasteners have a nominal diameter of 0.25 in. Washers were included between the bolted fasteners (head and collar sides) and the laminates in order to remove the gap.

Figure 132.—Test article assembly for joint testing. (a) CRFP laminates and spacer. (b) Titanium pin. (c) Bolted fastener.

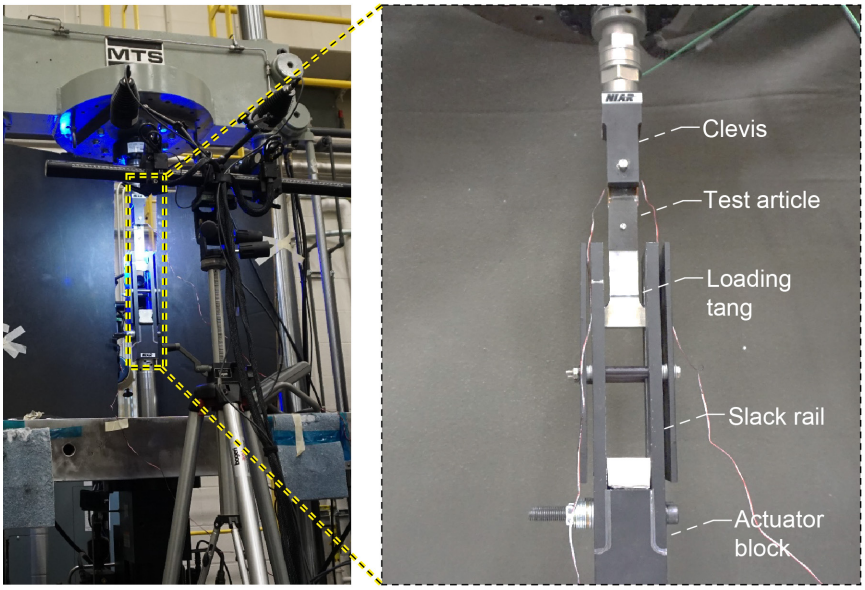

Figure 133.—Test fixture and load frame.

5.5.2 Test Setup

A servohydraulic MTS Systems 10-kip load frame was used for both the quasistatic and dynamic tests. The load frame was equipped with a hydraulic actuator with a maximum stroke of 15 in. and a load capacity of 10 kip. The test fixture's purpose was to induce tensile loading of the bearing joint by means of a loading tang pulled by the slack inducer. The overall design of the test fixture allowed the actuator to reach the targeted high-speed stroke rates before engaging in the test article. The test fixture and the load frame are shown in Figure 133.

DIC was performed to analyze the distribution and progression of strains, highlighting hot spots and damage regions around the pin/fastener joint. For the dynamic tests, two pairs of high-speed cameras were focused on the front and back of the CFRP laminates; for the quasistatic tests, two ARAMIS systems were used.

5.5.3 Pin Joint Test Results Summary

Pin joints mimic bolted fastener joints without clamp-up loads, and DIC results for pin joints provide additional information on strain fields around the fastener hole that could not be acquired from the fastener joints due to the fastener head and washer. With initiation of bearing failure in pin joint tests, surface plies (45°) split and delaminated, which resulted in debris accumulation and subsequent bending of the laminates, as shown in Figure 134. This debris accumulation and laminate separation caused the pin to disengage from the laminates and also affected the results obtained from DIC.

Results of pin joint testing conducted under quasistatic loading are shown in Figure 135, including strain data obtained from the strain gauges on the inner surfaces of the laminates, force response from the load cell, and pin displacement and velocity from DIC. Beyond initial peak, which corresponds to bearing failure, strain gauge readings tended to increase with loading, but the load signals tended to decay and reduce to zero. The load eccentricity and debris accumulation between the faying surfaces of the laminate and the loading tang produced bending deformation of the laminates, which eventually led to pin disengagement. After disengagement of the pin, the accumulated debris, along with the pin, acted as a wedge and bent the laminates by contact. This explains the nonzero strain gauge readings even though the load cell reading had completely dissipated.

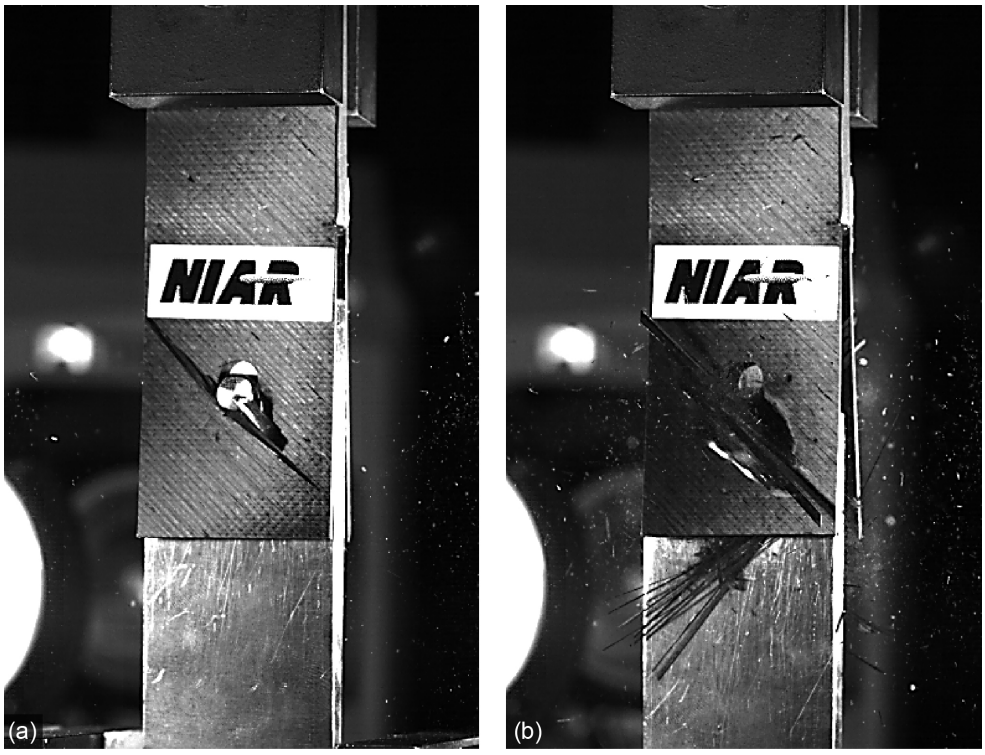

Figure 134.—Results of pin joint testing conducted at 100 in./s. (a) Surface ply splitting. (b) Bending of laminates due to debris buildup and pin disengagement.

DIC was used to measure displacement and strain fields on the outer surfaces of the test article's two CFRP laminates. Reference dots on the pin ends were used to measure the pin displacement and velocity. The reference dots cannot be tracked once the pin disengages from the hole and goes underneath the CFRP laminates. Figure 135(d) shows the initiation of the pin displacement (time = 0), the first visible damage, and the pin displacement equal to 10 percent of the hole diameter.

Figure 136 illustrates results of the pin joint testing conducted at 500 in./s. The force signals exhibited oscillatory behavior at dynamic stroke rates, which may not necessarily be a good indicator of the force experienced by the joints under dynamic loading. In this case, the strain data from the strain gauges mounted on the inner surfaces of the laminates provide a better understanding of joint performance at different dynamic stroke rates. Similar trends were observed in experiments conducted at 100 in./s and 300 in./s. Similar to the quasistatic tests, the pin disengaged from the laminates due to debris buildup and further pushed the laminates, causing them to bend, which corresponded to the increase in strain as seen in the plots. Details of the tests conducted at 100 in./s and 300 in./s and the strain field results from DIC can be found in Reference 90.

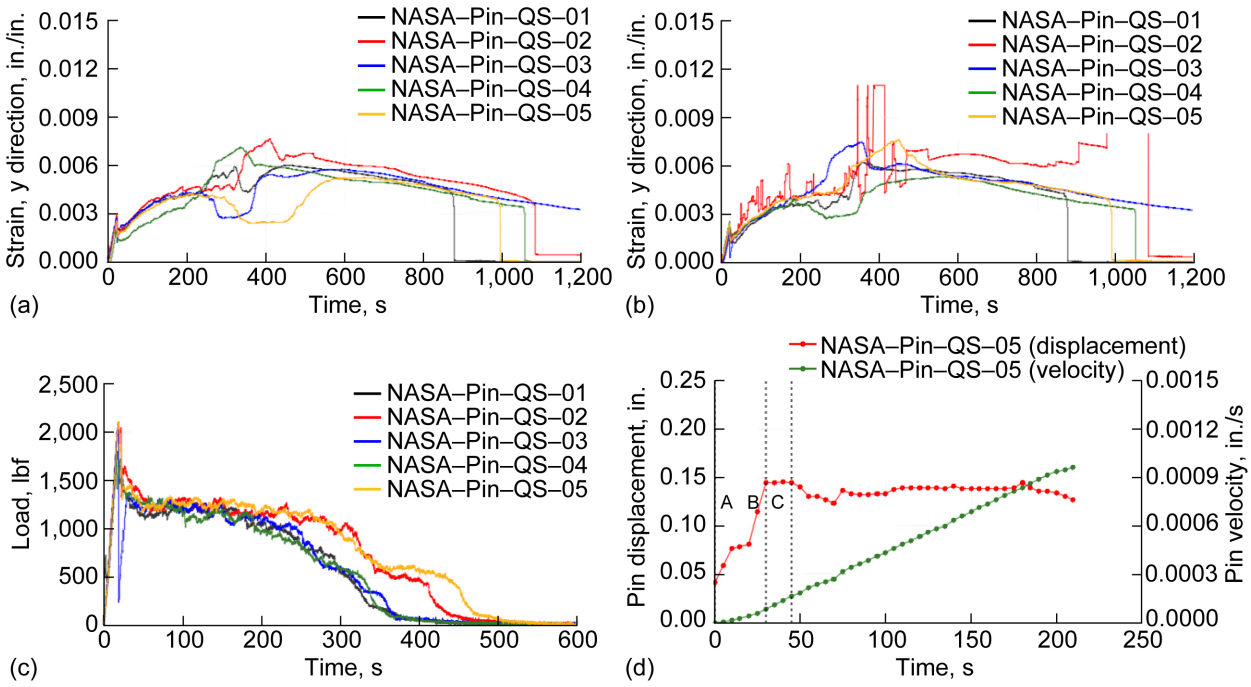

Figure 135.—Results of pin joint testing conducted at quasistatic test speed. (a) Strain gauge data from front laminate. (b) Strain gauge data from back laminate. (c) Force response from load cell. (d) Pin displacement and velocity from DIC; initiation of displacement (A, time = zero), first visible damage (B), and pin displacement equal to 10 percent of hole diameter (C).

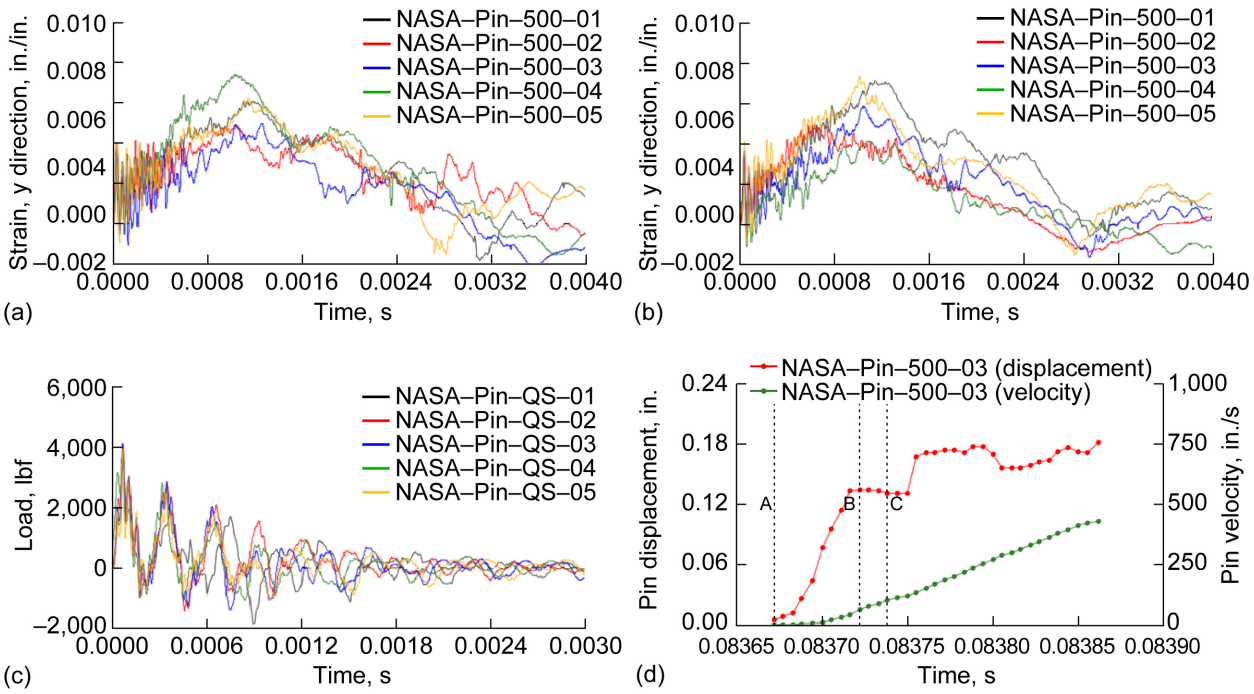

Figure 136.—Results of pin joint testing conducted at 500 in./s. (a) Strain gauge data from front laminate. (b) Strain gauge data from back laminate. (c) Force response from load cell. (d) Pin displacement and velocity from DIC; initiation of displacement (A), first visible damage (B), and pin displacement equal to 10 percent of hole diameter (C).

5.5.4 Bolted Fastener Joint Test Summary

Due to the fastening of bolted fasteners and washers to the test article, laminate separation was alleviated as compared with the pin joints. However, composite fragment accumulation between laminates and washers caused laminate bending with eventual plastic deformation of washers, as shown in Figure 137. At times, surface ply splitting (45°) initiated transverse crack propagation across the laminates, which caused large pieces of ply separation.

Figure 138 illustrates results of the bolted fastener joint testing conducted under quasistatic loading, including strain data obtained from the strain gauges on the inner surfaces of the laminates, force response from the load cell, fastener head displacement, and velocity from DIC. In contrast to the pin joint tests, significant laminate bending did not occur subsequent to bearing failure, which resulted in a drop in strain levels. Peak strain and load levels in fastener joints were significantly higher than in the pin joints due to the induced clamp-up forces and the constraint effects provided by the washers. Attaching the fasteners and washers to the laminates constrained laminate separation. Figure 138(d) shows the initiation of the pin displacement, the first visible damage, and the pin displacement equal to 10 percent of the hole diameter.

Figure 137.—Results of bolted fastener joint testing conducted at 100 in./s. (a) Surface ply splitting. (b) Bending of washers due to debris accumulation and failed composite fragments.

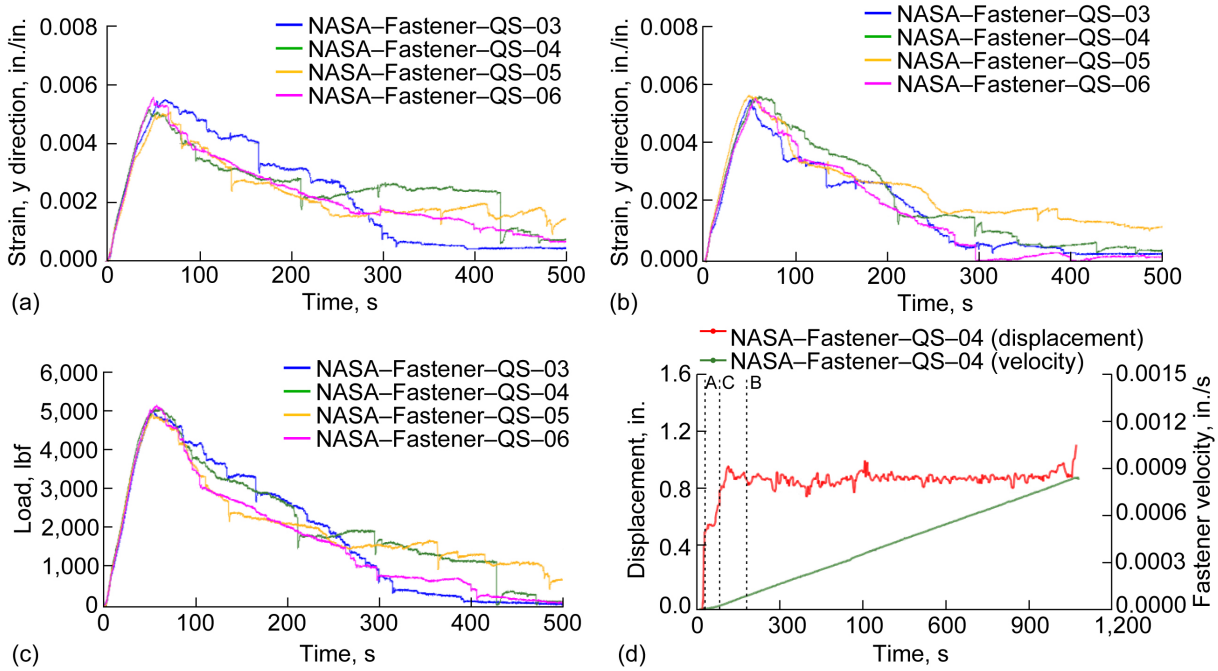

Figure 138.—Results of bolted fastener joint testing conducted at quasistatic test speed. (a) Strain gauge data from head side. (b) Strain gauge data from collar side. (c) Force response from load cell. (d) Bolted fastener displacement and velocity from DIC; initiation of displacement (A), first visible damage (B), and pin displacement equal to 10 percent of hole diameter (C).

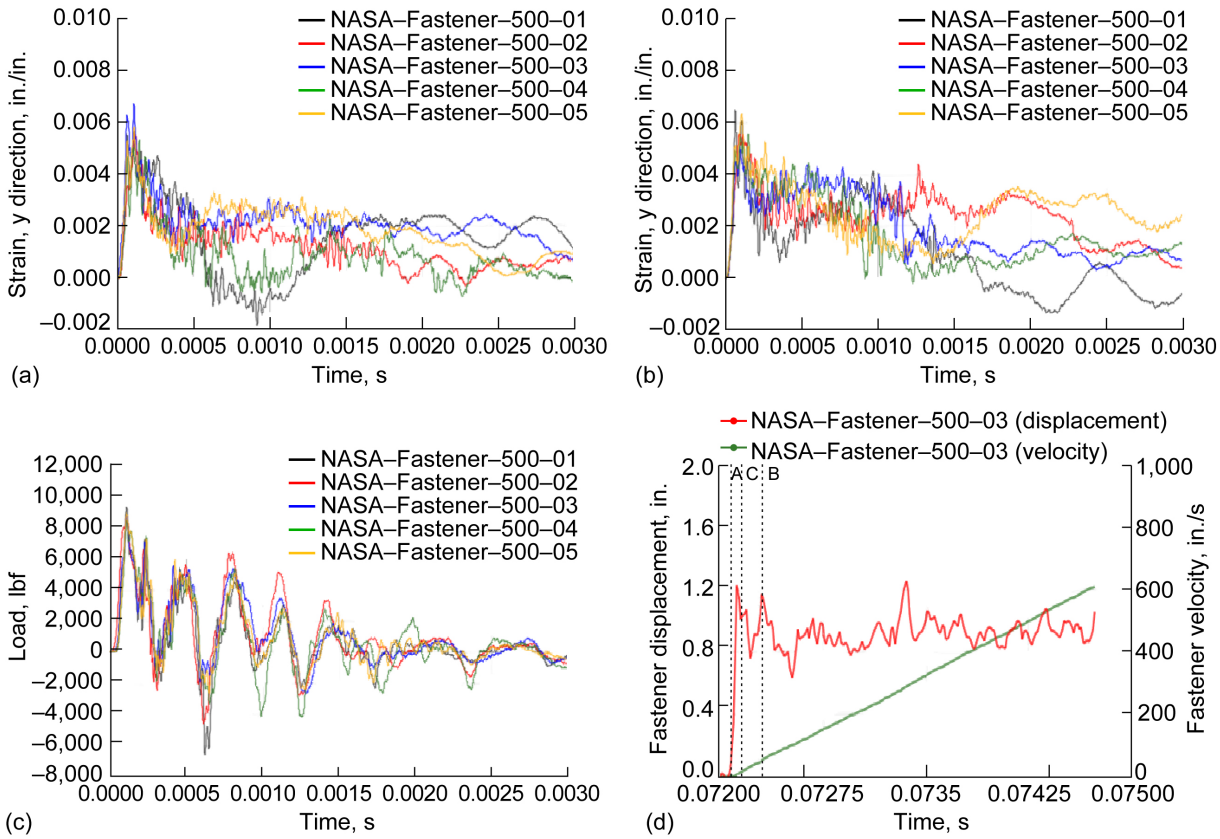

Figure 139.—Results of bolted fastener joint testing conducted at 500 in./s. (a) Strain gauge data from head side. (b) Strain gauge data from collar side. (c) Force response from load cell. (d) Bolted fastener displacement and velocity from DIC; initiation of displacement (A), first visible damage (B), and pin displacement equal to 10 percent of hole diameter (C).

Figure 139 illustrates the bolted fastener joint results from testing conducted at 500 in./s. The force signals exhibit oscillatory behavior at dynamic stroke rates which may not necessarily be a good indicator of the force experienced by the joints under dynamic loading. In this case, the strain data from the strain gauges mounted on the inner surfaces of the laminates provide a better understanding of the joint performance at different dynamic stroke rates. The strain levels post-bearing failure initiation tend to decrease progressively with minimal oscillations in the strain signal. Details of the tests conducted at 100 in./s, 300 in./s and strain field results from DIC could be found in the fastener joints test report specifically released to CMH–17 CWG (Ref. 90).

5.5.5 Strain Rates Comparison

In an effort to quantify the strain rates associated with each test, an average strain rate was computed using a linear fit to the initial portion of the strain versus time curves up to the onset of bearing failure. The average strain rates for both pin and fastener joint test articles tested at different speeds are summarized in Figure 140(a). The remote strain rates for the pin joint approached 200 s^{-1} at the maximum test speed, and strain rates for the fastener joint were close to 130 s^{-1}. The radial strains underneath the pin, as close as possible to the bottom edge of the hole (0.161 in. below), were evaluated for the pin joint type. The averaged peak radial strain rates in the bearing-dominated region of the specimens were much higher (2,500 s^{-1}) compared to the remote strain rate (≈200 s^{-1}) as presented in Figure 140(b). This information is not available for the fastener joint test articles, as the washer covers the region of interest around the hole.

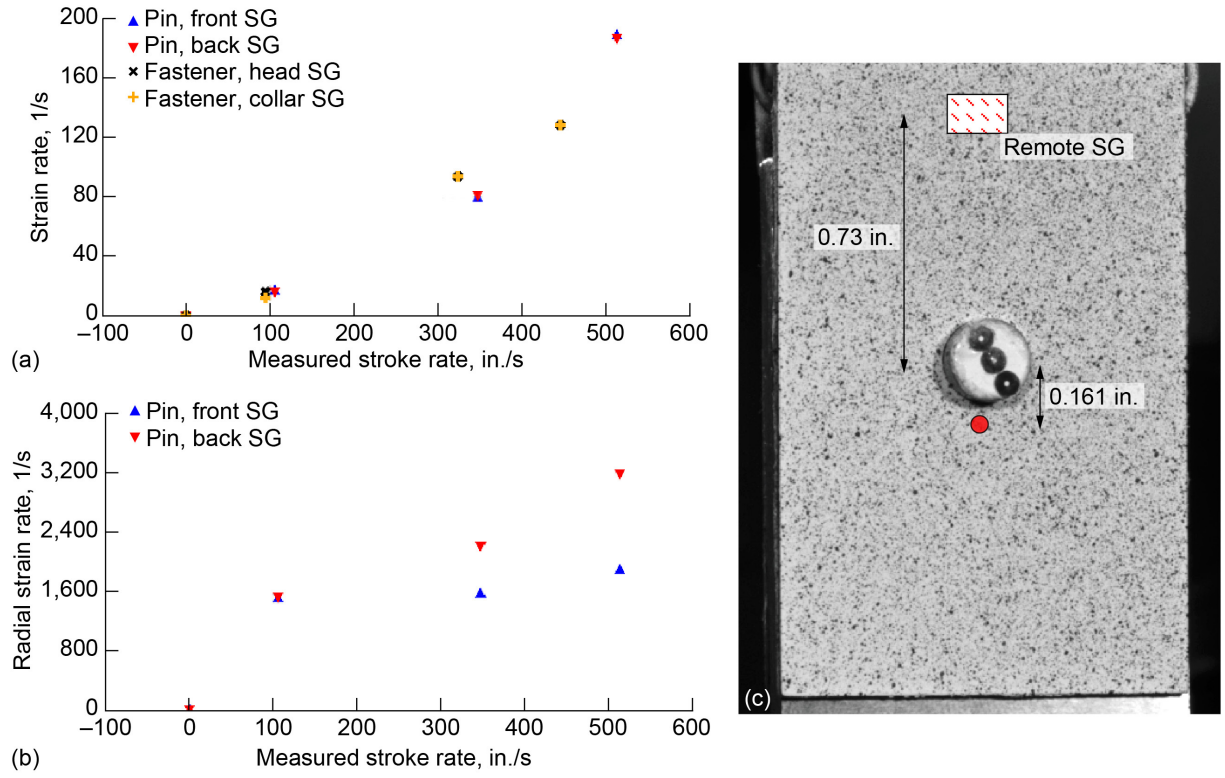

Figure 140.—Pin and fastener joint tests; strain gauge, SG. (a) Remote strain rate versus measured stroke rate. (b) Radial strain rate at bearing region versus measured stroke rate. (c) Test setup showing location of strain measurements.

TABLE 21.—TEST MATRIX FOR CALIBRATION CASE (FLAT-PLATE CRUSH TESTS) AND C-CHANNEL CRUSH TEST CASES USING DROP TOWER AND CRASH SLED

Case	Drop tower	Crash sled
Flat-plate test case	$M_{impactor}$ = 43.9 kg (96.8 lbf)	NA
C-channel test case 1	$M_{impactor}$ = 113 kg (249 lbf) $v_{impactor}$ = 7.6 m/s (17 mph)	$M_{impactor}$ = 113 kg (249 lbf) $v_{impactor}$ = 7.6 m/s (17 mph) $M_{stopper}$ = 320 kg (705 lbf)
C-channel test case 2	$M_{impactor}$ = 144 kg (317 lbf) $v_{impactor}$ = 3.8 m/s (8.5 mph)	$M_{impactor}$ = 144 kg (317 lbf) $v_{mpactor}$ = 3.8 m/s (8.5 mph) $M_{stopper}$ = 320 kg (705 lbf)

5.6 Crush Testing for Crashworthiness Model Validation

Crush experiments were performed in multiple stages. Initially, flat-plate specimens were crushed using a drop tower with the intention of providing modelers with an initial set of experimental force deflection data and impactor velocity data. Two hard laminate layups were tested: $[90_2/0_2/\pm45/0_2]_S$ (HL01) and $[90/45/0_2/90/-45/0_2]_S$ (HL02). In the second stage, C-channel specimens (consisting of the same hard laminate layups as the flat-plate specimens) were tested under two test cases (i.e., pairs of impactor masses and initial impactor velocities). The experimental results for the C-channel specimens were withheld from modeling teams until an initial, blind prediction was produced for each test case. C-channel specimens were also tested using a horizontal crash sled with a movable boundary. The crash sled utilized the same impactor masses and impactor velocities as the drop tower tests; however, the kinematics of the movable boundary could also be considered for comparison to the simulations. Table 21 lists a summary of the impactor conditions for each test.

5.6.1 Flat Coupon Crush Testing

Crush experiments were performed with flat-plate specimens as a preliminary calibration step toward model validation. A complete description of the flat-plate specimen manufacturing procedures and crush testing is available at Reference 91.

Two 16-ply hard laminates—$[90_2/0_2/\pm45/0_2]_S$ (HL01) and $[90/45/0_2/90/-45/0_2]_S$ (HL02)—were selected for crush testing based on results from an initial trial of several layups. The laminates are denoted as "hard" because of the predominance of 0° plies relative to other ply directions (i.e., 50 percent 0°, 25 percent ±45°, and 25 percent 90°). The specimens were manufactured using 190 g/m^2 unidirectional IM7/8552 plies stacked in a well-and-plunger mold. Up to 12 specimens were cut from each molded panel. As shown in Figure 141, the specimens had nominal dimensions of 130 by 40 by 2.98 mm with a 3-mm-long sawtooth-shaped crush trigger cut from the bottom of the specimens using a waterjet.

The University of Utah Composites Laboratory conducted the flat-plate drop tower experiments. Beneath the base plate holding the specimen, a Kistler® (Kistler Holding AG) 9371B load cell (range of ±120 kN) measured force during the experiment at a sampling rate of 109 kHz. The acceleration of the impactor during crushing was calculated using the load-cell force data and the known mass of the impactor (43.9 kg), and the velocity and displacement of the impactor were calculated using numerical integration.

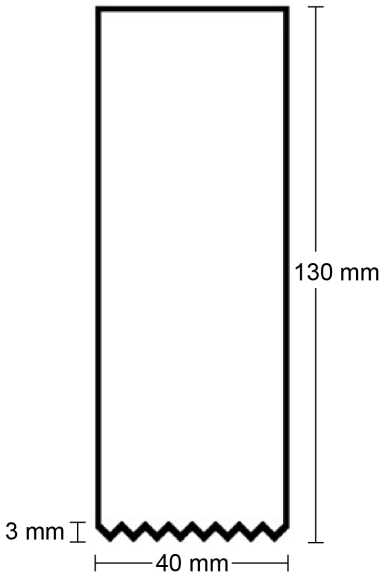

Figure 141.—Flat-plate specimen dimensions; nominal thickness 2.98 mm.

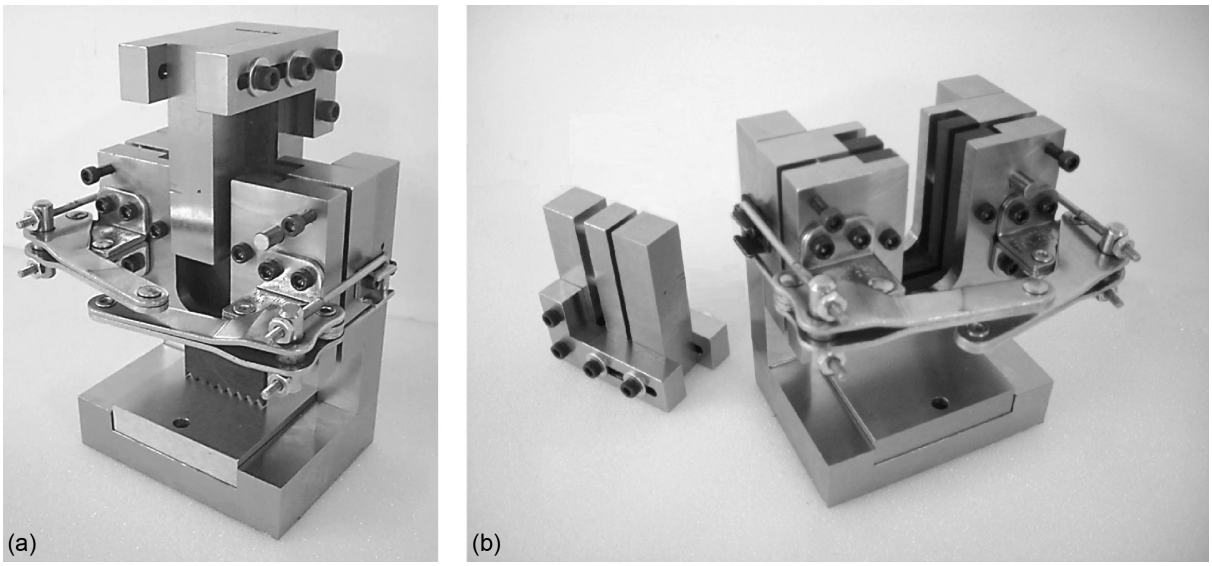

Figure 142.—Flat-plate specimen test fixture. (a) Assembled. (b) Partially disassembled showing upper component (left, inverted) and lower component (right). (Ref. 90; used with permission.)

A crush test fixture developed at the University of Utah (Ref. 91) was used to inhibit buckling and promote stable crushing of the flat-plate specimens. The fixture design is shown in Figure 142. The top of the specimen was secured in the top part of the fixture, and the assembly was inserted into the bottom part (right side of Figure 142(b)), which has an adjustable clearance between the buckling-inhibiting support plates. The top part of the fixture was wider than the 40-mm width of the specimen, so the entire cross-sectional area of the top of the specimen was in contact with the fixture. The surfaces of the bottom part of the fixture that were in contact with the specimen were faced with Delrin® acetal homopolymer (Delrin USA LLC) to minimize friction. During drop tower testing, the fixture sits atop the base plate of the tower, the falling impactor contacts the top part of the fixture, and specimen crushing initiates at the bottom of the fixture. High-speed video captures the edge-on view of the crushing.

5.6.2 Single-Stanchion Test

Crush experiments were performed with C-channel specimens for comparison with predictive models generated using calibrated input parameters (determined from simulating the flat-plate specimen experiments). The C-channel specimens had the same two 16-ply hard laminates as the flat-plate specimens.

5.6.2.1 Drop Tower Tests

The C-channel specimens for the drop tower tests were manufactured at the University of Utah using 190 g/m^2 unidirectional IM7/8552 plies stacked on a male mold and utilized an autoclave-pressurized vacuum bagging process for consolidation. More details regarding manufacturing of the C-channel specimens are provided in Reference 92. The cross-sectional dimensions of the C-channel specimens are shown in Figure 143. A 45° bevel-shaped crush trigger was cut on each specimen with a nominal length of 3.2 mm, with the longer side of the bevel on the inner side of the C-channel. The nominal specimen length was 152.4 mm.

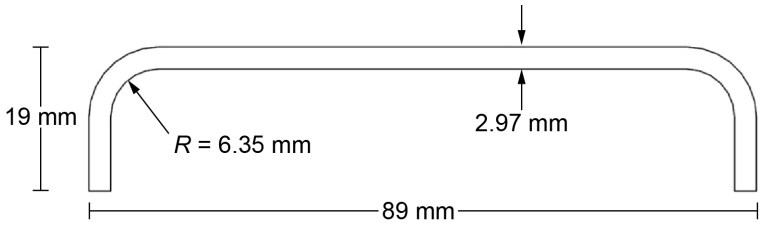

Figure 143.—C-channel specimen cross-sectional dimensions. Radius, *R*.

The University of Utah Composites Laboratory also performed the C-channel drop tower experiments. A Kistler® 9371B load cell (range of ±120 kN) measured force during the experiment at a sampling rate of 200 kHz. As with the flat-plate crush tests, the acceleration of the impactor during crushing was calculated using the load-cell force data and the known mass of the impactor, and the velocity and displacement of the impactor were calculated using numerical integration. Two combinations of impactor mass and initial impactor velocity (113 kg at 7.6 m/s and 144 kg at 3.8 m/s) were selected for testing.

The bottom 12.7 mm of the C-channel specimens were potted in epoxy, and the potted region was attached to the base plate of the drop tower rig. Unlike the flat-plate crush tests, where the crush trigger was on the bottom of the specimen, the crush trigger of the C-channels was on the top of the specimen and contacted the impactor directly. The impactor face that contacted the specimen was circular with a diameter of 127 mm. Above the potted region, the C-channel specimens were unsupported (i.e., no support plates or other fixtures were used).

5.6.2.2 Crash Sled Tests

The C-channel specimens for the crash sled tests were manufactured separately from the C-channels used for the drop tower experiments, but they also used 190 g/m^2 unidirectional IM7/8552 plies stacked on a male mold and utilized an autoclave-pressurized vacuum bagging process for consolidation. The same specimen dimensions were used for the crash sled C-channel tests, and the same crush trigger was applied. The drop tower and sled test methods are presented in Reference 33. A full description of the crash sled design, associated instrumentation, and data reduction methodology is available in Reference 93.

In summary, an impactor mass is accelerated by a pneumatic-actuated ram. Before impact, the ram and impactor mass separate. Following separation, the impactor mass collides with the specimen, which is supported by a second, movable stopper mass that is initially at rest. Figure 144 illustrates the impact event where the impactor (M_1) crushes the specimen against the support plate (M_{pl}), which is bolted to the support mass (M_2). Table 22 lists the instrumentation of the crash sled; each mass has its own accelerometer. There are three force sensors between the support plate and stopper mass, and a top-view, high-speed camera records photogrammetry measurements. Energy absorption is calculated using the accelerometer- and force-sensor-measured datasets to calculate crush force, and the photogrammetry data provides crush displacement. Absorbed energy is also calculated from the change in kinetic energy of the system using photogrammetry measurements of velocity. The specimen plate contains a cutout of the cross section of the C-channel specimens, and two-part epoxy is applied to the cutout to hold the specimen in place during testing. A summary of the test conditions for the three crush tests is shown in Table 23.

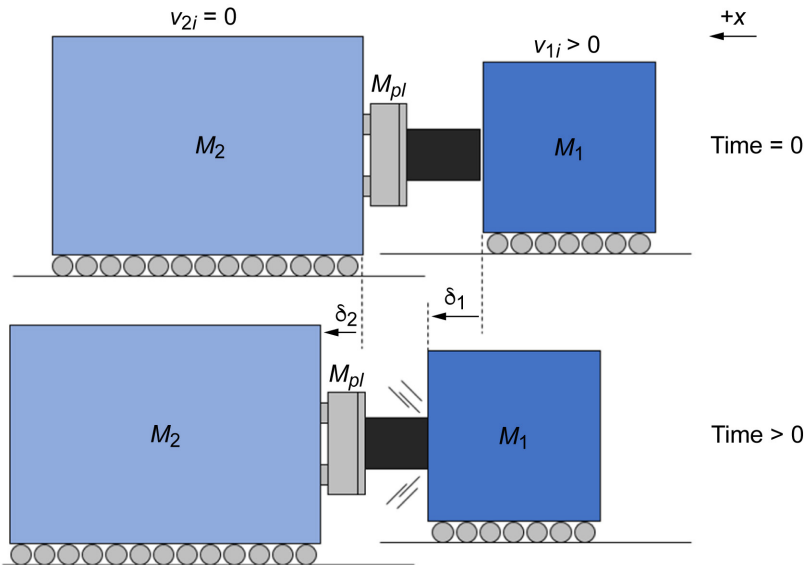

Figure 144.—Sled masses at instant before (time = 0) and after (time > 0) impact. Impactor, M_1; support mass, M_2; support plate mass, M_{pl}.

TABLE 22.—INSTRUMENTATION FOR CRASH SLED EXPERIMENTS

Equipment	Make and model	Record rate	Range
Force sensor (×3)	PCB[a] 203B/FCS–5	1.25 MHz	89 kN
M_1 accelerometer	PCB[a] ICP 350C04	1.25 MHz	5,000 g
M_2 accelerometer	PCB[a] ICP 353B14	1.25 MHz	1,000 g
High-speed camera	Photron[b] Fastcam SA–Z	70,000 fps	NA

[a]PCB Piezotronics (Depew, New York).
[b]Photron (Tokyo, Japan).

TABLE 23.—SUMMARY OF TEST CONDITIONS FOR CALIBRATION (FLAT PLATE), DROP TOWER, AND CRASH SLED TESTS

Test parameters	Calibration case (Flat-plate specimens)	Drop tower (C-channels)	Crash sled (C-channels)
Specimen characteristics			
Nominal length, mm	130	152.4	152.4
Nominal thickness, mm	2.98	2.98	2.98
Nominal corner thickness, mm	NA	3.09	3.2
Nominal specimen mass, g	23.7	80.2	80.7
Crush trigger			
Trigger shape	Sawtooth	45° bevel	45° bevel
Trigger length, mm	3	3.2	3.2
Impactor			
Impactor mass, kg	43.9	113 or 144	113 or 144
Impactor initial velocity, m/s	4.3	7.6 or 3.8	7.6 or 3.8
Movable stopper mass, kg	NA	NA	319 kg
Other test conditions			
Trigger first contacts?	Fixture base	Circular impactor plate	Rectangular stopper mass
Buckling support plates?	Yes	No	No

5.6.3 Double-Stanchion Test

Future testing of actual stanchions, double stanchions, or other more complex parts and assemblies will provide final validation of the material models following the building-block modeling approach discussed in Section 4.0.

6.0 Conclusions and Future Work

Several examples of progressive damage and failure analysis (PDFA) methods have been presented as applied to coupons and sample components to determine load histories and evaluate energy dissipation from accumulated damage and failure. Each of these PDFA methods requires testing for calibration and validation, and successful applications of validated PDFA simulations were presented.

Based on the simulations presented, several points should be noted.

1. Selection of a PDFA method will depend on the length and time scale of the dynamic simulation as well as the intended model use. It will also depend on the overall goal of the simulation, such as comparative engineering studies or data generation to support certification. Therefore, no single PDFA method can be recommended. Additionally, as this report has demonstrated, multiple methods may be used to generate acceptable response outputs for any given physical event.
2. Validation of each method is critical and should include specific validation criteria as well as an understanding of the design and analysis space over which the method may be applied. Calibrated parameters are also required for each method based on coupon or component testing, and each PDFA method may have somewhat differing calibration and validation requirements.
3. Mesh size should be compatible with the selected PDFA method, and validation should be consistent with the intended mesh discretization. Mesh regularization may be available for some material models, which can provide a range of acceptable mesh sizing in a simulation.
4. Mesh orientation should be compatible with the selected PDFA method and also with the intended model application. Depending on the event and structure of interest, preferred meshing may be irregularly aligned, nonaligned, fully aligned with fibers, or simple uniform mesh.
5. Mesh orientation may also be influenced by the manner in which delaminations or individual ply failure are represented, and any traction–separation response that is used in the simulation should also be validated with similar mesh.
6. Several methods highly recommend the use of single-element models to ensure that the material response is as expected and that loading, damage, and unloading (if applicable) followed the intended response parameters. This is in addition to the lower level material testing that is part of the building-block process.
7. This report provides guidance on both validating and evaluating multiple PDFA methods, and use of the validation and evaluation metrics provided here can guide selection of a PDFA method.
8. Several PDFA methods show correlation of results within 10 percent of test on selected metrics, and as such, several current PDFA methods may be suitable for use in modeling and simulation of crashworthiness response of composite structures.

To address future needs for crashworthiness PDFA, several key areas are under consideration. Extending material characterization and modeling capabilities is essential to meet the evolving requirements of the Composite Material Handbook 17 (CMH–17), while modeling guidelines should be substantiated using high-fidelity analysis, testing correlation, and a building-block approach to enhance best practices based on success criteria. Utilizing both C-channel test data from the University of Utah

drop tower and sled test data from the NASA Glenn Research Center will enable more rigorous model validation. This will also potentially allow for extending these simulation methods to higher levels of the building block, such as stanchion assembly design. A library of benchmark problems should be established to streamline the verification and validation process for crashworthiness modeling. Furthermore, it is important to evaluate Material Science Corporation's MAT162 progressive composite damage model using CMH–17 crush test data to enhance the guidelines and advance current crush modeling capabilities. The MAT162 assessment findings will be provided in future updates of CMH–17, Chapter 16.

Appendix A.—Nomenclature

A.1 Acronyms

2.5D	2.5-dimensional
3D	three-dimensional
4ENF	four-point-bending end-notch flexure
ACP	Advanced Composites Project
AMD	Advanced Micro Devices
ASTM	American Society for Testing and Materials
BF	backout factor
BVID	barely visible impact damage
CbA	certification by analysis
CC	compact compression
CDM	continuum damage mechanics
CFC	channel frequency class
CFRP	carbon-fiber-reinforced polymer
CMH–17	Composite Materials Handbook 17
CODAM2	continuum damage model 2
CPU	central processing unit
CRASURV	crash survivability design
CT	compact tension
CW	crashworthiness
CWG	Crashworthiness Working Group
DCB	double cantilever beam
DIC	digital image correlation
DLR	Deutsches Zentrum für Luft- und Raumfahrt (German Aerospace Center)
DMA	dynamic mechanical analysis
DMP	distributed memory parallel
DOF	degree of freedom
DOP	depth of penetration
EA	energy absorbed
ECDM	enhanced continuum damage mechanics
EEM	element elimination method
ENF	end-notch flexure
ESIS	European Structural Integrity Society
FAA	Federal Aviation Administration
FE	finite element
FERR	fracture energy release rate
FFT	fast Fourier transform
FRMM	fixed-ratio mixed-mode
FRP	fiber-reinforced polymer
GTFC	generalized tabulated failure criterion

HEDI	high-energy dynamic impact
HL01, HL02	hard laminate 1, hard laminate 2
IE	internal energy
IM	intermediate modulus
ISO	International Organization for Standardization
KE	kinetic energy
LD3	lower deck type 3
LP	load–penetration
MAT	material model
MMB	mixed-mode bending
MPP	massively parallel processing
NCAMP	National Center for Advanced Materials Performance
NIAR	National Institute for Aviation Research
NTL	nontraditional laminate
OCT	over-height compact tension
OHC	open-hole compression
OHT	open-hole tension
OML	outer mold line
PDFA	progressive damage and failure analysis
PTFE	polytetrafluoroethylene
QI	quasi-isotropic
QS	quasistatic
QSPS	quasistatic punch shear
QS–PST	quasistatic punch shear test
RR	Round Robin
SACMA	Suppliers of Advanced Composite Materials Association
SB	shell–beam
SDV6	solution-dependent variable 6
SEA	specific energy absorption
SG	strain gauge
SHPB	split Hopkinson pressure bar
SPG	smoothed particle Galerkin
TL	traditional laminate
UBC	University of British Columbia
UD	unidirectional
USC	University of South Carolina
VPS	Virtual Performance Solution
VUMAT	vectorized user material
WG	working group
WP	Waas–Pineda

A.2 Symbols

A	area
A_i	area under accumulated plastic strain curve at interval i
$\mathbf{A}$	in-plane secant stiffness
a	crack length
a_f	difference between final and initial crack length
B	constitutive material constant (scalar value)
b	(1) shear–transverse damage coupling parameter (2) plastic hardening parameter (3) ply shear plasticity model parameter
b_i^c	plastic hardening parameter in direction i (compression)
b_i^t	plastic hardening parameter in direction i (tension)
C_{ij}	stiffness matrix
c	global strain-rate coefficient for plastic work criteria
D	damage
D_{max}	external damage parameter
$\dot{D}_{ij}$	damage accumulation rate
d	(1) displacement (2) damage parameter
d_1^c	damage parameter cutoff (compression)
d_1^t	damage parameter cutoff (tension)
d_f	damage at peak load
d_I	interface damage
d_{max}	maximum displacement
E	stiffness
E_0	(1) mode I elastic modulus (2) matrix Young's modulus (through thickness)
e_c	compressive failure indicator in fiber direction
e_d	compressive failure indicator transverse to fibers
e_f	tensile failure indicator in fiber direction
e_m	tensile failure indicator transverse to fibers
F	(1) strength (2) failure stress
F_i, F_{ij}	(1) fiber damage threshold (2) coefficients of Tsai–Wu-based yield function of the deformation model
$F(\sigma)$	plastic flow threshold
f	(1) quadratic yield function (2) elastic domain function
G	(1) shear modulus (2) fracture energy

G_0	(1) mode II elastic modulus (2) matrix shear modulus (in-plane)
G_{I}, G_{II}	strain energy release rate for fracture modes I and II
G_{Ic}, G_{IIc}	critical strain energy release rate, or fracture toughness, for modes I and II loading
G_c	average fracture toughness
G_{cm}	mixed-mode transverse fracture energy
G_f	(1) fracture energy, laminate fracture energy (2) fracture energy release rate
g	fracture energy density
H_{ij}	flow rule coefficients
h	nonassociative flow rule function
K_{ij}	cohesive stiffness coefficients
k	layer
L	(1) length (2) half span width
l^*	characteristic element length
l_f, l_m	element length along two main axes of orthotropy
M_1	impactor
M_2	support mass
M_{ij}	diagonal damage terms
M_{impactor}	impactor mass
M_{pl}	support plate
m	(1) material parameter that determines softening behavior (2) ply shear plasticity model parameter
n	plastic hardening exponent
n_i^c	plastic hardening exponent in direction i (compression)
n_i^t	plastic hardening exponent in direction i (tension)
P	force or applied load
P_0	peak load
P_{crush}	crush force
p	effective plastic strain
$\tilde{p}$	accumulated plastic strain
$\mathbf{Q}_k$	effective in-plane secant stiffness matrix describing constitutive behavior of each layer k
$\underline{\boldsymbol{q}}$	vector representing all internal state variables, including damage state and maximum deformation
R	radius
R^2	coefficient of determination
R_0	plasticity yield stress
R_i	plasticity development law parameter (B.80)
R_α	stiffness reduction factors R_1 and R_2
RE	relative error

$R(p)$	hardening law
r	ratio of strain to yield strain, $\varepsilon/\varepsilon_y$
S_c	transverse or axial shear strength
SEA	specific energy absorption
sym	symmetric matrix
$\mathbf{T}$	transformation matrix
t	thickness
t_{COH}	thickness of cohesive elements
t_{TOT}	total thickness
t_{trig}	trigger element thickness
U	strain energy
U_{max}	uplift factor
u	displacement
v	velocity
v_0	initial velocity
v_{1i}	initial velocity of mass 1
v_{2i}	initial velocity of mass 2
v_{impactor}	impactor velocity
W	(1) work (2) total dissipated energy
W_p	global plastic work
w	width
X	static strength
X_c	(1) compressive strength in fiber direction (2) compressive failure initiation stress in X direction
X_d	dynamic strength
X_s	shear failure strength
X_t	(1) tensile strength in fiber direction (2) tensile failure initiation stress in X direction
Y	damage force
Y_0	experimentally determined material parameter in MAT297
Y^c_{11C}	damage evolution curve slope (compression)
Y^t_{11C}	damage evolution curve slope
Y^c_{11R}	upper critical damage energy threshold (compression)
Y^t_{11R}	upper critical damage energy threshold (tension)
Y^c_{110C}	lower critical damage energy threshold (compression)
Y^t_{110C}	lower critical damage energy threshold (tension)
Y_{12}	energy release rate function
Y_{12C}, Y_{12c}	damage evolution curve slope parameter (shear)
Y_{12i}	shear damage function

Y_{12R}	upper critical damage energy threshold (shear)
Y_{12s}	shear damage failure threshold parameter
Y_{120}	(1) initial shear damage threshold parameter
	(2) lower critical damage energy threshold (shear)
Y_2	energy release rate function
Y_{2c}	transverse damage evolution parameter
Y_{2i}	transverse damage function
Y_{2s}	transverse damage failure threshold parameter
Y_{20}	transverse damage threshold parameter
Y_c	(1) compressive strength transverse to fibers
	(2) compressive failure initiation stress in Y direction
	(3) experimentally determined material parameters in MAT297
$Y_{EQ,I}$	equivalent thermodynamic force
Y_t	(1) tensile strength transverse to fibers
	(2) tensile failure initiation stress in Y direction
$\underline{Y}$	damage evolution variable
$\underline{Y}_2$	damage evolution variable
$\underline{Y}_i$	damage evolution law
Z	failure initiation stress in Z direction
α	material-dependent parameter (varies by model formation)
α^2	shear–transverse plasticity coupling parameter
β	(1) plastic hardening law coefficient
	(2) material parameter
	(3) scaling factor
β_1	strain hardening parameter
Γ	ply fracture toughness
γ_{12}	engineering shear strain
$\gamma_{12,el}$	elastic part of total strain
γ_{12i}	shear strain for the i^{th} load cycle
$\gamma_{12,pl}$	plastic strain
γ_{prop}	interface maximum failure stress (in-plane shear)
δ	displacement
δ_0	initial displacement
δ_f	final displacement
δ_i	initial crush displacement
δ_{ij}^{cz}	crack tip opening displacement
δ_m	matrix crack opening
ε	strain
ε_{11+}^0	onset of failure in fiber tension
ε_{11-}^0	onset of failure in fiber compression

$\varepsilon_{11\pm}^{0}$	onset of failure in fiber tension/compression
ε_{11+}^{f}	final failure strains in fiber tension
ε_{11-}^{f}	final failure strains in fiber compression
$\varepsilon_{11\pm}^{f}$	final failure strains in fiber tension/compression
ε_{12}^{p} , ε_{22}^{p}	strains when failure criterion is satisfied
ε_{D}	deviatoric strain
ε_{eq}	equivalent strain variable
$\varepsilon_{eq,p}^{0}$	equivalent plastic strain at failure onset
$\varepsilon_{eq,t}^{0}$	equivalent total strain at failure onset
$\varepsilon_{eq,t}^{f}$	equivalent total strain to failure
ε_{f}	strain at peak load
ε_{fi}	element deletion strain
$\varepsilon_{i\_\text{reversible}}$	reversible strain
$\varepsilon_{i\_\text{total}}$	total strain
ε_{ic}^{1} , ε_{ic}^{2}	post-rupture parameters
ε_{ij}^{crit}	critical strain for transition to cohesive state
ε_{Li}	longitudinal strain
ε_{mi}	strain at maximum damage
ε_{p}, ε^{p}	plastic strain
ε^{s}	damage saturation strain
ε_{sLim}	equivalent shear strain
$\varepsilon_{Ti,}$ ε_{ti}	damage initiation strain
$\dot{\varepsilon}_{0}$	reference strain rate
$\dot{\varepsilon}_{j}$	strain rate
$\dot{\varepsilon}_{j}^{EL}$	elastic strain rate
$\dot{\varepsilon}_{j}^{PL}$	plastic strain rate
η	Benzeggagh–Kenane exponent for mixed-mode formulation
λ	scalar plastic multiplier
$\dot{\lambda}$	effective plastic strain rate
μ	plastic hardening law exponent
μ_{F}	friction coefficient
μ_{L}	mass per unit length
ν_{12}	major Poisson’s ratio
ν_{21}	minor Poisson’s ratio
ν_{31}	minor Poisson’s ratio
ρ	density

σ	stress
σ_1	σ_{11}, longitudinal normal stress (fiber direction)
σ_1^C	yield stress in 1-coordinate direction (compression)
σ_1^T	yield stress in 1-coordinate direction (tension)
σ_{11+}^0	onset of failure in fiber tension
σ_{11-}^0	onset of failure in fiber compression
$\sigma_{11\pm}^0$	onset of failure in fiber tension/compression
σ_2	σ_{22}, transverse normal stress (perpendicular to fiber direction)
σ_2^C	yield stress in 2-coordinate direction (compression)
σ_2^T	yield stress in 2-coordinate direction (tension)
σ_3	σ_{33}, out-of-plane normal stress (through-thickness direction)
σ_3^C	yield stress in 3-coordinate direction (compression)
σ_3^T	yield stress in 3-coordinate direction (tension)
σ_4	σ_{12}, in-plane shear stress in fiber/transverse plane
σ_5	σ_{23}, transverse shear stress (transverse/through-thickness plane)
σ_6	σ_{13}, out-of-plane shear stress in the fiber/through-thickness plane
σ_{eq}	equivalent stress variable
σ_{ij}	stress in *i,j* direction
σ_{ij}^{crit}	critical stress for transition to cohesive state
σ_{ires}	residual stress after softening
σ_{Li}	shear stress at load/unload point
σ_{OA45y}^{i-j}	yield stress measured from 45° off-axis (OA) test in the *i–j* plane
σ_{prop}	interface maximum failure stress (through thickness)
σ_{rti}	softening parameter in tension in direction *i*
$\tilde{\sigma}_{22}$	effective transverse stress
τ	stress
τ_{12i}	peak shear stress of i^{th} cycle
$\tilde{\tau}_{12}$	effective shear stress
ω_a	damage variable for longitudinal (1) and transverse (2) direction
ϖ	reduction in modulus

A.2.1 Subscripts

0	initial or undamaged
1, 11	longitudinal or fiber direction
12, 21	in-plane direction
13, 31	out-of-plane direction
2, 22	transverse direction
I, II, III	modes I, II, and III

C	compression
COH	cohesive
c	compression
crit	critical
D	deviatoric
eff	effective
el	elastic value
EQ, eq	equivalent
f	(1) final
	(2) at peak load
I	interface
i	(1) initial
	(2) index of load cycle
	(3) time step
ij	coefficients; can be equal to 1, 2, or 3, representing plane on which property is calculated
k	layer variable
L	longitudinal
max	maximum
N	number of plies
OA	off axis
p	plastic
PL	plasticity
pl	support plate
ply	ply
S	symmetric
s	shear
sim	simulation
T, t	tension
T/C	tension/compression
TOT	total
trig	trigger element
y	yield
α	variable for longitudinal and transverse directions

A.2.2 Superscripts

0	initial
C, c	compression
crit	critical
EL	elastic
eq	equivalent
f	final
I	interface
i	initiation

m	strain-hardening parameter
max	maximum
n	plastic hardening exponent
PL	plastic
pl	support plate
s	shear
T, t	tension
T/*C*	tension/compression
u, ulti	ultimate
μ	plastic hardening law exponent

Appendix B.—Supplementary Analysis Information

This section presents further background information on the crashworthiness analysis methods discussed in this report. Supplementary information on the supporting tests for material characterization and model validation is presented in Appendix C.

B.1 SEA Calculation Using Flat Coupon Crush Test Data

A typical test configuration for composite flat-plate coupon crushing is shown in Figure B.1. In this case, guide plates are used to prevent out-of-plane motion and to ensure stable crushing. Other boundary configurations have also been tested in which pins provide support for the composite coupon.

The definitions for calculating Stable SEA and Total SEA are introduced in Equations (1) and (3). The QI01 flat crush coupon test data used here as a typical example is reported in displacement increments of approximately 0.03 to 0.04 mm depending on the impactor velocity, and these data are sufficiently refined to allow for accurate numerical integration by incrementally calculating the area under the curve. Load–displacement data for flat coupon crush testing is shown in Figure B.2. After integrating over the displacement, the energy absorbed during crushing is shown in Figure B.3.

Figure B.3 also notes the energy values at 10 and 30 mm of crush. Stable SEA is calculated by determining the net energy between points A and B and dividing by the mass of the coupon for a 20-mm section. The mass calculation considers the measured width, which is constant at 40 mm in this case, and also accounts for the measured thickness of the test specimen, since thickness can vary slightly from coupon to coupon.

For all of the sample data presented here, the exact measured thickness of each individual coupon was used in determining the mass of the crushed region. In this case, with a measured thickness of 2.99 mm, the mass of a 20-mm section is 0.0037657 kg. The weight of the full 30-mm section, accounting for the sawtooth cut for crush initiation, is 0.005409 kg.

Thus, the sample calculations for Stable SEA and Total SEA based on the QI01 flat crush coupon test are as follows:

- $Stable\ SEA = \dfrac{(0.26717\ \text{kJ} - 0.09349\ \text{kJ})}{0.0037657\ \text{kg}} = 46.12\ \text{kJ/kg}$
- $Total\ SEA = \dfrac{0.26717\ \text{kJ}}{0.005409\ \text{kg}} = 49.39\ \text{kJ/kg}$

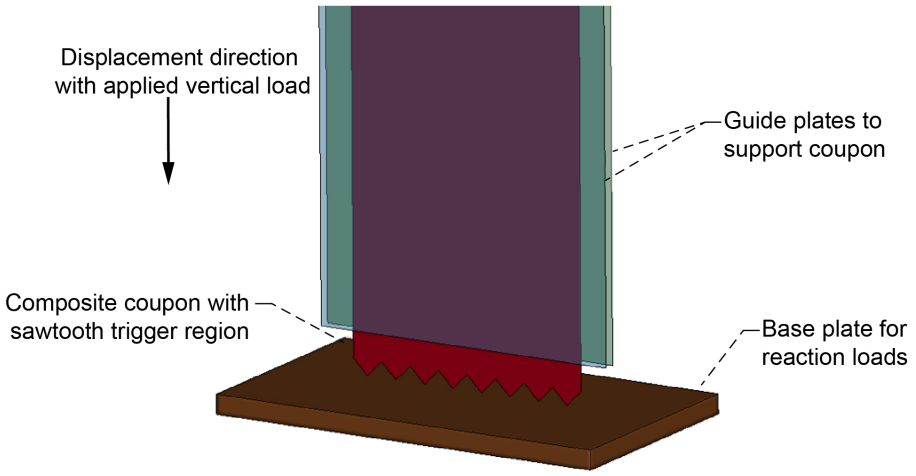

Figure B.1.—Typical flat coupon crush test configuration.

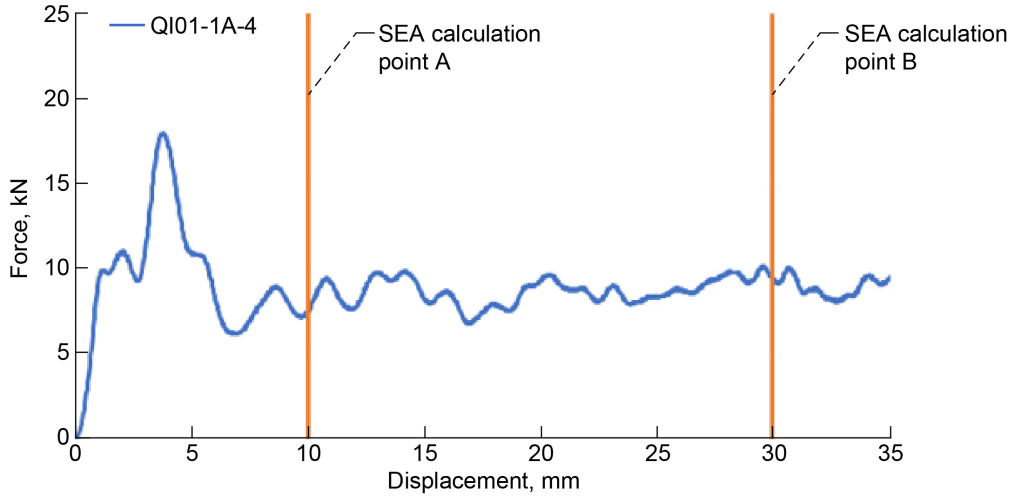

Figure B.2.—Force–displacement history for QI01 coupon crush test.

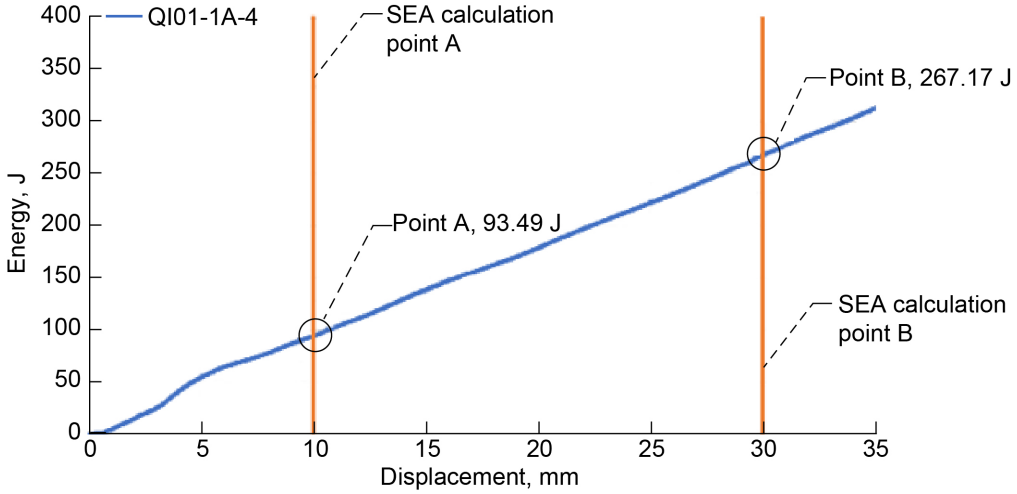

Figure B.3.—Energy–displacement from integrating force for QI01 coupon crush test.

Total SEA for crush tests is always higher than Stable SEA because of the higher peak crush initiation load. This is also seen in the initial slope of the energy plot, which is higher than the slope for the stable crush zone.

The following figures and table summarize the results from flat coupon crush testing. Figure B.4 shows the load–displacement and energy plots for a medium layup, $[90/\pm45/0]_{2S}$ (QI01), where the test was repeated three times. Figure B.5 shows the load and energy plots for a hard laminate, $[90_2/0_2/\pm45/0_2]_S$ (HL01), and two different boundary supports. Figure B.6 shows the load and energy plots for a different hard laminate, $[90/45/0_2/90/-45/0_2]_S$ (HL02), and two boundary supports reported from tests. Table B.1 shows a summary of Stable and Total SEA derived from test data and notes the laminates tested and the boundary conditions. As previously noted, Total SEA is always higher than Stable SEA, frequently on the order of 10 percent higher.

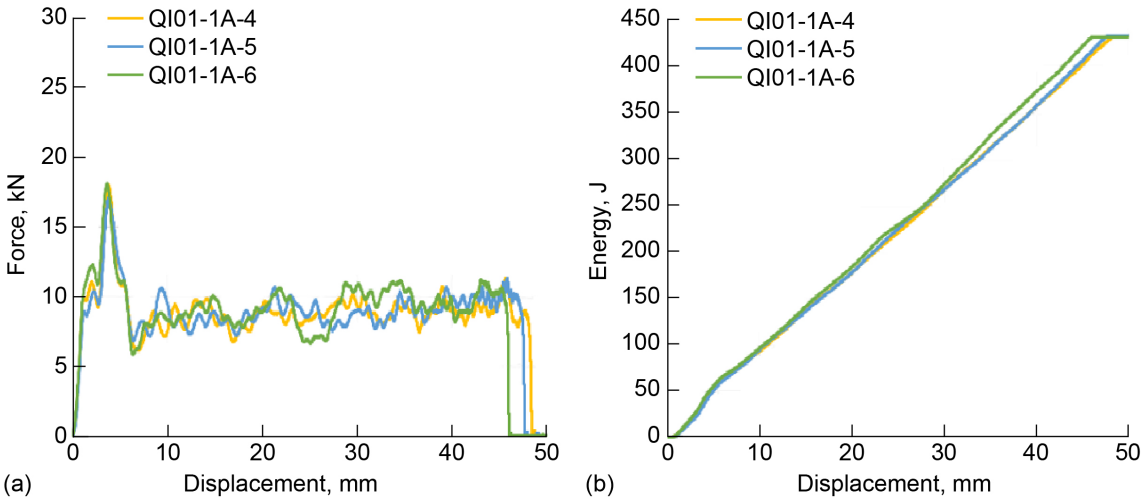

Figure B.4.—Force–displacement history and resulting energy–displacement from medium laminate (QI01).

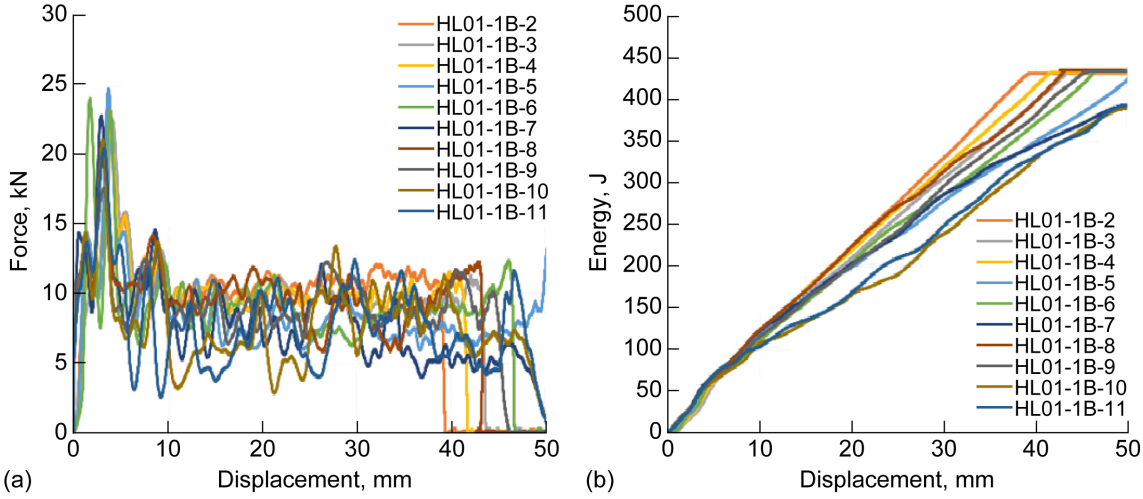

Figure B.5.—Force–displacement history and resulting energy–displacement for laminate $[90_2/0_2/\pm45/0_2]_S$ (HL01).

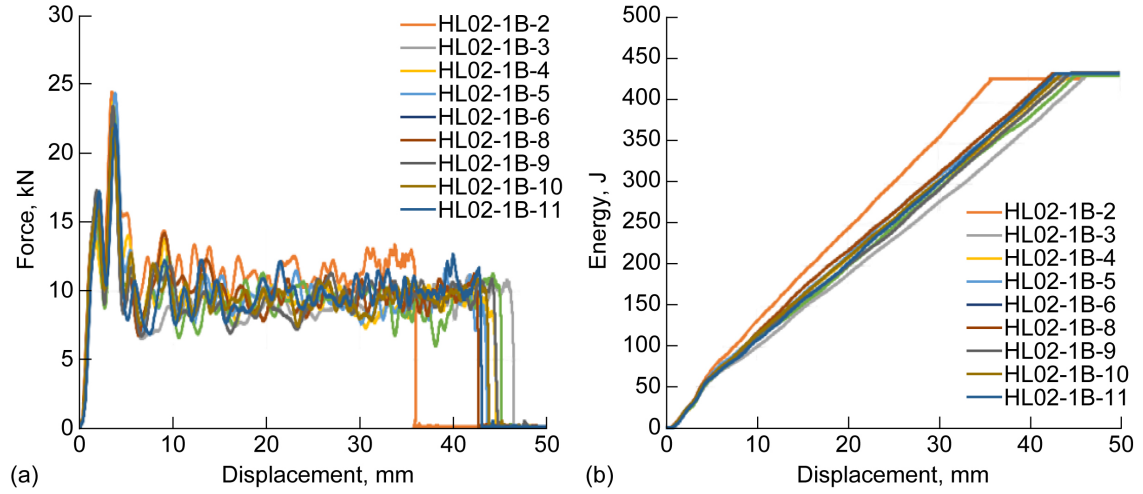

Figure B.6.—Force–displacement history and resulting energy–displacement for laminate $[90/45/0_2/90/-45/0_2]_S$ (HL02).

TABLE B.1.—SUMMARY OF STABLE AND TOTAL SEA DERIVED FROM TEST DATA

Test configuration	Layup	Specimen ID	Stable SEA, 10 to 30 mm, kJ/kg	Total SEA, 0 to 30 mm, kJ/kg
Gap 8.6 mm	$[90/\pm45/0]_{2S}$	Q101-1A-4	46.12	49.39
		Q101-1A-5	45.55	49.39
		Q101-1A-6	46.66	50.41
Gap 14.5 mm	$[90_2/0_2/\pm45/0_2]_S$	HL01-1B-2	55.38	60.73
		HL01-1B-3	50.38	56.55
		HL01-1B-4	52.18	58.50
Pin supported	$[90_2/0_2/\pm45/0_2]_S$	HL01-1B-5	42.24	51.52
		HL01-1B-6	46.61	52.80
		HL01-1B-7	43.79	53.01
		HL01-1B-8	50.24	57.55
		HL01-1B-9	47.88	54.50
		HL01-1B-10	35.25	44.36
		HL01-1B-11	38.87	46.12
Gap 12 mm	$[90/45/0_2/90/-45/0_2]_S$	HL02-1B-2	59.59	65.64
		HL02-1B-3	46.87	50.99
		HL02-1B-4	49.60	55.62
		HL02-1B-5	50.93	56.83
		HL02-1B-6	48.34	53.90
Pin supported	$[90/45/0_2/90/-45/0_2]_S$	HL02-1B-8	51.21	56.99
		HL02-1B-9	47.59	53.97
		HL02-1B-10	50.26	56.38
		HL02-1B-11	51.23	55.61

B.2 LS–DYNA® MAT54 Material Model in Round Robin 1 and 2

This section provides additional information about the simulations discussed in Section 3.1. The MAT54 material model is a progressive failure model designed for shell elements to model orthotropic materials such as unidirectional tape composite laminates. In the elastic region, basic orthotropic stress–strain relations from Hashin (Ref. 7) are used, with the option of including a higher order shear term using the parameter α.

$$\varepsilon_1 = \frac{1}{E_1}(\sigma_1 - \nu_{12}\sigma_2) \tag{B.1}$$

$$\varepsilon_2 = \frac{1}{E_2}(\sigma_2 - \nu_{21}\sigma_1) \tag{B.2}$$

$$2\varepsilon_{12} = \frac{1}{G_{12}}\tau_{12} + \alpha\tau_{12}^3 \tag{B.3}$$

Prior to erosion, plies and elements fail in one of four modes defined by the stress-based Chang–Chang failure criteria (Refs. 8 and 9). Failure modes are defined in terms of “fiber” and “matrix,” which corresponds to the 0° and 90° directions of a unidirectional lamina, not to the constituents. Tension and compression failure is defined for both modes as shown in Equations (B.4) to (B.7), where e_f and e_c

indicate tensile and compressive failure in the fiber direction, e_m and e_d indicate tensile and compressive failure transverse to the fibers, X_t and X_c are tensile and compressive strength in the fiber direction, Y_t and Y_c are tensile and compressive strength transverse to the fibers, and S_c denotes transverse and axial shear strength.

Fiber (axial):

Tension, $\sigma_{11} > 0$:

$$e_f^2 = \left(\frac{\sigma_{11}}{X_t}\right)^2 + \beta\left(\frac{\sigma_{12}}{S_c}\right)^2 - 1 \begin{cases} \geq 0 \text{ failed} \\ \leq 0 \text{ elastic} \end{cases} \tag{B.4}$$

Compression, $\sigma_{11} < 0$:

$$e_c^2 = \left(\frac{\sigma_{11}}{X_c}\right)^2 - 1 \begin{cases} \geq 0 \text{ failed} \\ \leq 0 \text{ elastic} \end{cases} \tag{B.5}$$

Matrix (transverse):

Tension, $\sigma_{22} > 0$:

$$e_m^2 = \left(\frac{\sigma_{22}}{Y_t}\right)^2 + \left(\frac{\sigma_{12}}{S_c}\right)^2 - 1 \begin{cases} \geq 0 \text{ failed} \\ \leq 0 \text{ elastic} \end{cases} \tag{B.6}$$

Compression, $\sigma_{22} < 0$:

$$e_d^2 = \left(\frac{\sigma_{22}}{2S_c}\right)^2 + \left[\left(\frac{Y_c}{2S_c}\right)^2 - 1\right]\frac{\sigma_{22}}{Y_c} + \left(\frac{\sigma_{12}}{S_c}\right) - 1 \begin{cases} \geq 0 \text{ failed} \\ \leq 0 \text{ elastic} \end{cases} \tag{B.7}$$

These failures cause an immediate and total loss of stiffness, resulting in an elastic–perfectly plastic response of the material. Property degradation following failure varies for each of the four failure modes:

Fiber tension: $E_1 = E_2 = G_{12} = \nu_{12} = \nu_{21} = 0$

Fiber compression: $E_1 = \nu_{12} = \nu_{21} = 0$

Matrix tension: $E_2 = G_{12} = \nu_{21} = 0$ (B.8)

Matrix compression: $E_2 = G_{12} = \nu_{12} = \nu_{21} = 0$, XT = XT·FBRT, XC = YC·YCFAC

Elements are not deleted if all of their plies have failed according to Equation (B.8). Element erosion (deletion) is determined by the violation of maximum strain parameters, which can cause element deletion regardless of the damage state of the element.

B.2.1 LS–DYNA® MAT54 Input Parameters

The baseline MAT54 material input card that models the T700–2510 material is shown in Table B.2, with each of its parameters categorized into seven groups. The constitutive properties, material strengths, and deletion parameters can all be measured from standard tension, compression, and shear tests of the material system. The element deletion parameters are maximum strain limits, where DFAILM defines both the tensile and compressive transverse strain limits, and DFAILT and DFAILC are the tensile and

compressive failure strains in the axial direction. The shear weighing factors and damage factors cannot be measured from experiment and must be calibrated for a given material system. The only parameter of these five found to be influential in crush simulations was the SOFT. This is a crash-front damage parameter which reduces the material strengths in elements immediately following those at the crash-front, which is determined by the tool given the element orientations and loading conditions. This parameter does not have a baseline value, as it must be adjusted for each crush simulation. The remaining parameters shown in Table B.2 define the local coordinate system relative to the global coordinate system. Input parameters for MAT54 material cards are defined in Table B.3.

TABLE B.2.—BASELINE MAT54 MATERIAL CARD PROPERTY VALUES

MID	RO	EA	EB	EC	PRBA	PRCA[a]	PRCB[a]
1	1.50×10^{-4}	8.11×10^{6}	7.89×10^{6}	1×10^{6}	0.043	0.0	0.0
GAB	GBC[a]	GCA[a]	KF[a]	AOPT			
6.09×10^{5}	6.09×10^{5}	6.09×10^{5}	0.0	0.0			
XP	YP	ZP	A1	A2	A3	MANGLE	
0.0	0.0	0.0	0.0	0.0	0.0	0.0	
V1	V2	V3	D1	D2	D3	DFAILM	DFAILS
0.0	0.0	0.0	0.0	0.0	0.0	0.024	0.03
TFAIL	ALPH	SOFT	FBRT	YCFAC	DFAILT	DFAILC	EFS
1.1530×10^{-9}	0.3	[0,1][b]	0.95	1.2	0.0164	–0.013	0.0
XC	XT	YC	YT	SC	CRIT	BETA	
103000	132000	102000	112000	19000	54	0.5	
1. Constitutive properties: RO, EA, EB, EC, PRBA, PRCA, PRCB, GAB, GBC, GCA, KF							
2. Local material axes: AOPT, XP, YP, ZP, A1–A3, MANGLE, V1–V3, D1–D3							
3. Shear weighing factors: ALPH, BETA							
4. Delete parameters: DFAILM, DFAILS, TFAIL, DFAILT, DFAILC, EFS							
5. Damage factors: SOFT, FBRT, YCFAC							
6. Material strengths: XC, XT, YC, YT, SC							
7. Failure criteria selection: CRIT							

[a]Inactive parameter in MAT54.

[b]Range of possible values for the SOFT parameter.

TABLE B.3.—MAT54 INPUT PARAMETERS

Parameter	Description	Type	Measurement
RO	Mass per unit volume	Experimental	Density test
EA	Axial Young's modulus	Experimental	0° tension test
EB	Transverse Young's modulus	Experimental	90° tension test
EC	Through-thickness Young's modulus	(Not active in MAT54)	
PRBA	Minor Poisson's ratio, ν_{21}	Experimental	0° tension test with biaxial strain measurement
PRCA	Minor Poisson's ratio, ν_{31}	(Not active in MAT54)	
PRCB	Major Poisson's ratio, ν_{12}	(Not active in MAT54)	
GAB	Shear modulus, G_{12}	Experimental	Shear test
GBC	Shear modulus, G_{23}	(Not active in MAT54)	
GCA	Shear modulus, G_{31}	(Not active in MAT54)	
KF	Bulk modulus	(Not active in MAT54)	
ALPH	Elastic shear stress nonlinear factor	Shear factor	None
BETA	Shear factor in tensile axial failure criteria	Shear factor	None
DFAILT	Axial tensile failure strain	Experimental	0° tension test
DFAILC	Axial compressive failure strain	Experimental	0° compression test
DFAILM	Transverse failure strain	Experimental	90° tension and compression tests
DFAILS	Shear failure strain	Experimental	Shear test
EFS	Effective failure strain	Optional	None
TFAIL	Time step failure value	Computational	Derived from numeric time step
FBRT	Axial tensile strength factor after two-direction failure	Damage factor	None
SOFT	Material strength factor after crushing failure	Damage factor	None
YCFAC	Axial compressive strength factor after two-direction failure	Damage factor	None
XT	Axial tensile strength	Experimental	0° tension test
XC	Axial compressive strength	Experimental	0° compression test
YT	Transverse tensile strength	Experimental	90° tension test
YC	Transverse compressive strength	Experimental	90° compression test
SC	Shear strength	Experimental	Shear test
CRIT	Specification of failure criterion	Computational	None necessary

TABLE B.4.—PROPERTIES FOR TORAY® T700/2510

Axial Young's modulus, E_1, GPa	55.9
Transverse Young's modulus, E_2, GPa	54.4
Tensile strength 1, MPa	911
Compressive strength 1, MPa	704
Tensile strength 2, MPa	770
Compressive strength 2, MPa	698
Minor Poisson's ratio	0.043
In-plane shear strength, MPa	132

The experimentally measured material properties of the T700/2510 were established by the CWG. The basic properties are given in Table B.4.

B.2.2 Contact Model

The built-in LS–DYNA® contact model *CONTACT_RIGID_NODES_TO_RIGID_BODY was used to define the contact behavior between the loading plate and the composite crush specimen. This is a standard penalty formulation contact that requires input of a load–penetration (LP) curve to define the reaction normal forces applied to nodes at the contact interface. The LP curve greatly influences the stability of the simulation runs. Using a conservative approach, a low-energy LP curve was implemented such that contact forces were initially low and increased gradually. While this causes a delay of the load increase at the onset of the simulation, which does not match the experimental results, a low-energy LP curve allows for greater numerical stability and versatility such that it could successfully be applied to all of the crush specimen geometries. More aggressive curves that introduced greater loads at contact were capable of producing a better curve fit with the experiment; however, they also caused instabilities in some of the crush simulations.

B.2.3 Boundary Conditions

Each modeled specimen was kept at rest by constraining all DOFs on the bottom row of nodes opposite the crush trigger. Each node of the loading plate was constrained in all DOFs except in the axial translation direction of the crush. A prescribed motion boundary condition was applied to the loading plate nodes to provide a constant crush velocity of 150 in./s (3.8 m/s). This is significantly higher than the experimental velocity in order to reduce computational cost. Since MAT54 does not have strain-rate sensitive parameters, and since the explicit time integration method is conditionally stable when the time step is sufficiently small, this velocity difference did not affect the numeric results. Crush simulations were investigated at various loading speeds to verify this.

B.2.4 LS–DYNA® MAT54 Crush Specimen Test and Analysis Results

Crush morphology images and load–displacement curves are given for the following four Round Robin 2 (RR–2) crush simulations: large C-channel (Figure B.7), small C-channel (Figure B.8), large angle (Figure B.9), and small angle (Figure B.10).

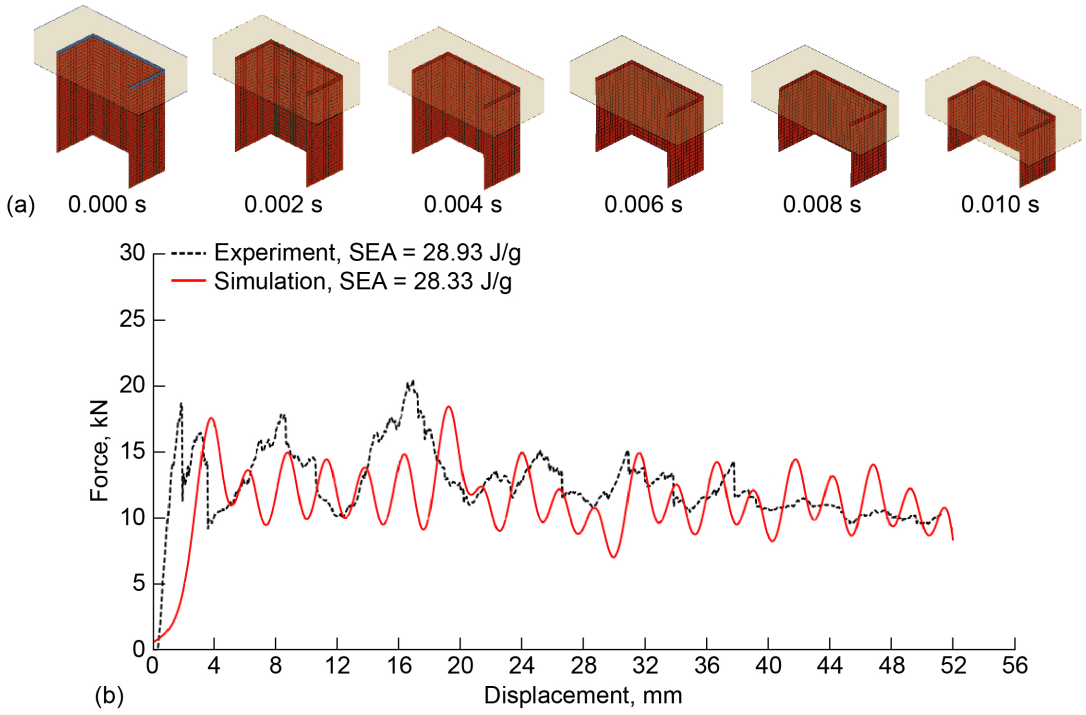

Figure B.7.—Simulation results for large C-channel crush specimen. (a) Crush progression. (b) Simulation versus experiment force–displacement curves.

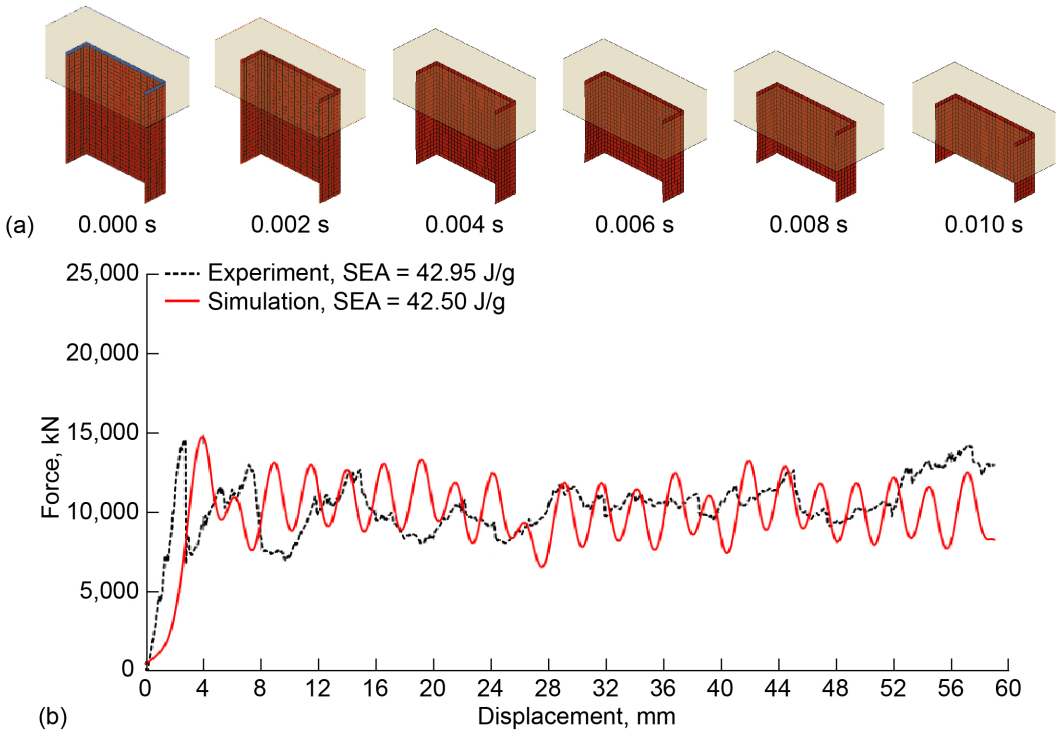

Figure B.8.—Simulation results for small C-channel crush specimen. (a) Crush progression. (b) Simulation versus experiment force–displacement curves.

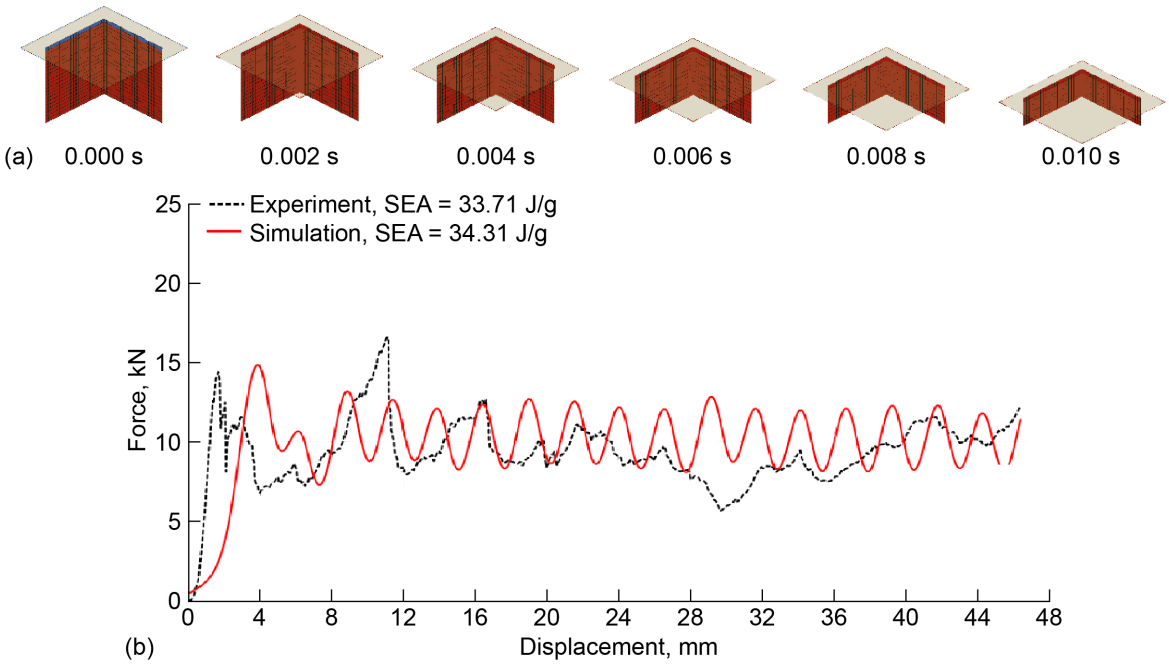

Figure B.9.—Simulation results for large angle crush specimen. (a) Crush progression. (b) Simulation versus experiment force–displacement curves.

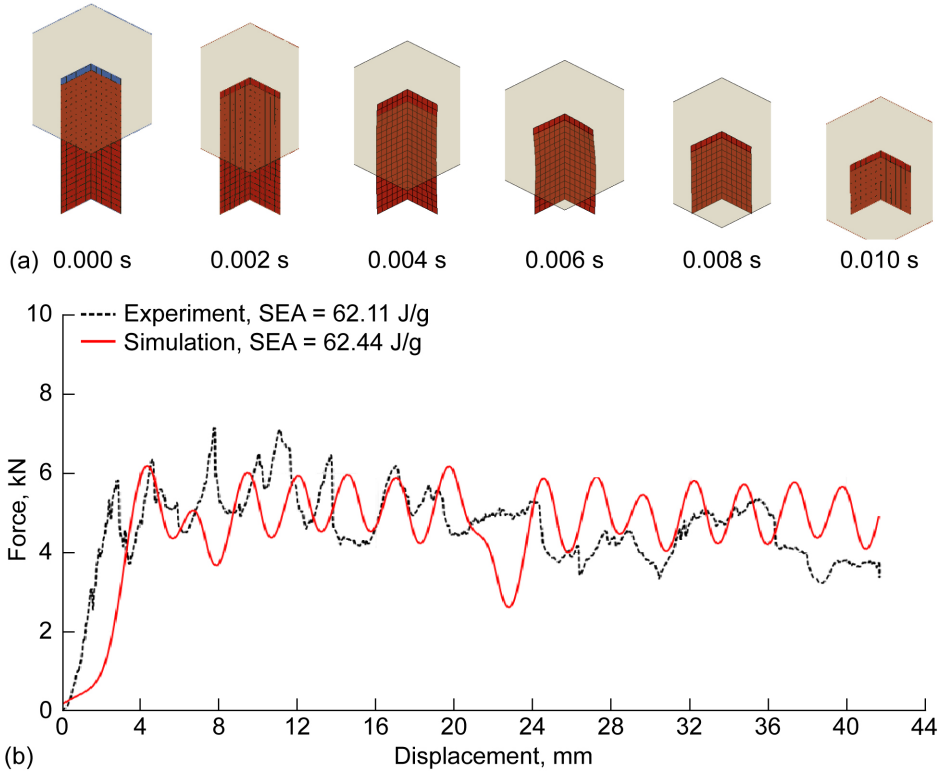

Figure B.10.—Simulation results for small angle crush specimen. (a) Crush progression. (b) Simulation versus experiment force–displacement curves.

B.3 LS–DYNA® MAT58 Material Model in Round Robin 1 and 2

This section provides additional information about the simulations discussed in Section 4.2.

B.3.1 LS–DYNA® MAT58 Parameters

Table B.5 gives the parameters used in the MAT58 material model for RR–1 and RR–2.

TABLE B.5.—PARAMETERS USED IN MAT58

Parameter	Value
Mass density, RO, g/cm^3	1.52
Young's modulus, longitudinal, EA, GPa	55.9
Young's modulus, transverse, EB, GPa	54.4
Young's modulus, normal, EC	Not used
Poisson's ratio in BA direction, PRBA	0.043
Stress point for shear stress strain curve, TAU1, MPa	124
Strain point for shear stress strain curve, GAMMA1	0.06
Shear modulus in AB direction, GAB, GPa	3.86
Shear modulus in BC direction, GBC, GPa	3.86
Shear modulus in CA direction, GCA, GPa	3.86
Fiber tension minimum stress limit factor, SLIMT1	0.2
Fiber compression minimum stress limit factor, SLIMC1	0.8
Matrix tension minimum stress limit factor, SLIMT2	0.2
Matrix compression minimum stress limit factor, SLIMC2	0.8
Shear stress minimum stress limit factor, SLIMS	0.5
Maximum effective strain for failure, ERODS	0.13
Reduction factor for strength in crush front, SOFT	0.3
Failure surface — faceted surface that includes fiber tension, compression, and shear, FS	–1
Transverse shear maximum damage, TSMD	0.9
Strain at longitudinal compressive strength, E11C	0.0124
Strain at longitudinal tension strength, E11T	0.0163
Strain at transverse compressive strength, E22C	0.0128
Strain at transverse tension strength, E22T	0.0142
Strain at shear strength in AB plane, GMS	0.075
Longitudinal compressive strength, XC, MPa	704
Longitudinal tensile strength, XT, MPa	911
Transverse compressive strength, YC, MPa	698
Transverse tensile strength, YT, MPa	770
Shear strength in AB plane, SC, MPa	132

B.3.2 Summary of Results of LS–DYNA® MAT58 Simulations

This section supplements the LS–DYNA® MAT58 simulation results provided in Section 4.2.4. Figure B.11 to Figure B.25 give typical crushing failure patterns and comparisons with experimental results for the small C-channel, small angle, large angle, square tube, and sinusoid specimens.

- *Small C-channel specimen*: Figure B.11 shows a typical crushing failure pattern for the small C-channel specimen. Simulation and experiment results are compared for reaction force in Figure B.12 and for energy absorption in Figure B.13.
- *Small angle specimen*: Figure B.14 shows a typical crushing failure pattern for the small angle specimen. Simulation and experiment results are compared for reaction force in Figure B.15 and for energy absorption in Figure B.16.
- *Large angle specimen*: A typical large angle crushing failure pattern is shown in Figure B.17, with simulation and experiment results compared for reaction force in Figure B.18 and for energy absorption in Figure B.19.
- *Square tube specimen*: A typical crushing failure pattern is shown for the square tube specimen in Figure B.20, with results compared for reaction force in Figure B.21 and for energy absorption in Figure B.22.
- *Sinusoid coupon:* Figure B.23 shows a typical crushing failure pattern for the sinusoid specimen, with experiment and simulation reaction force compared in Figure B.24 and energy absorption compared in Figure B.25.

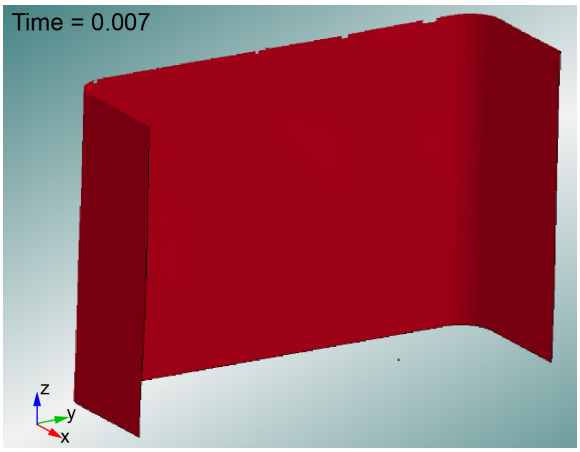

Figure B.11.—Typical crushing failure pattern at 27 mm of crush for small-channel specimen.

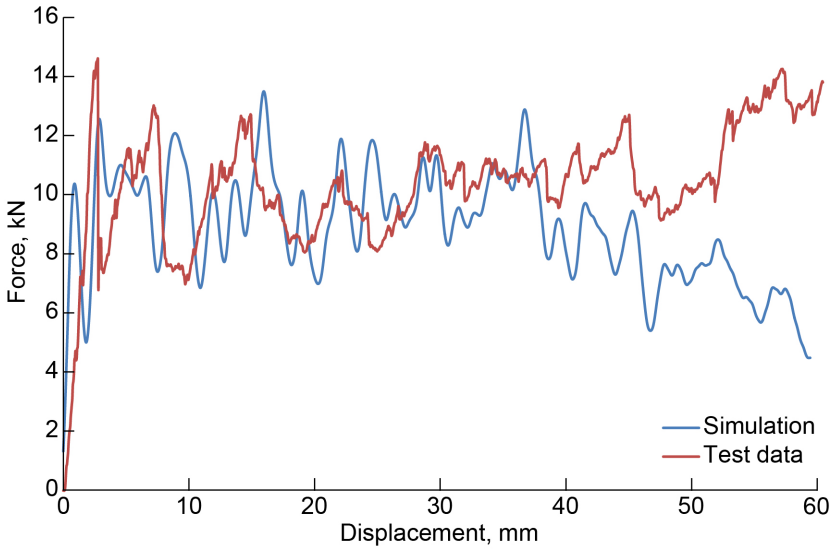

Figure B.12.—Comparison of small C-channel test and simulation reaction force during crushing.

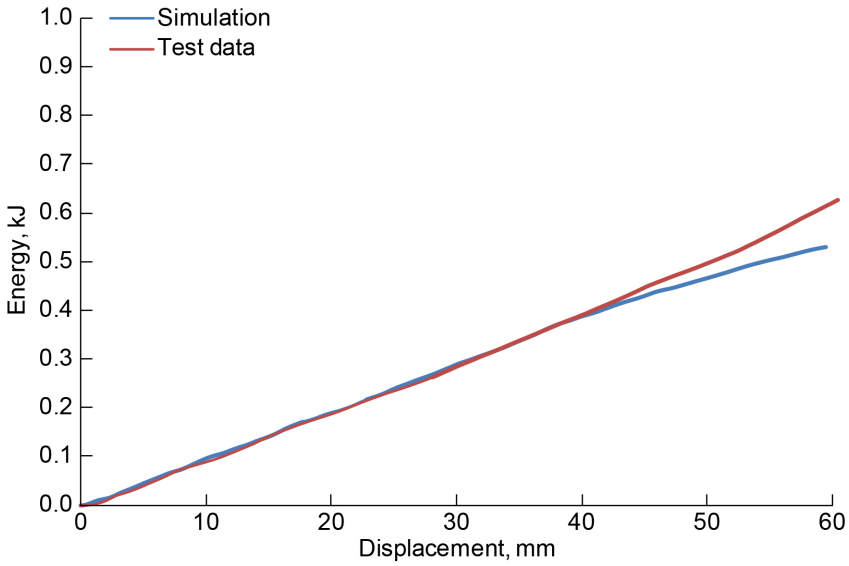

Figure B.13.—Comparison of small C-channel test and simulation energy absorption during crushing.

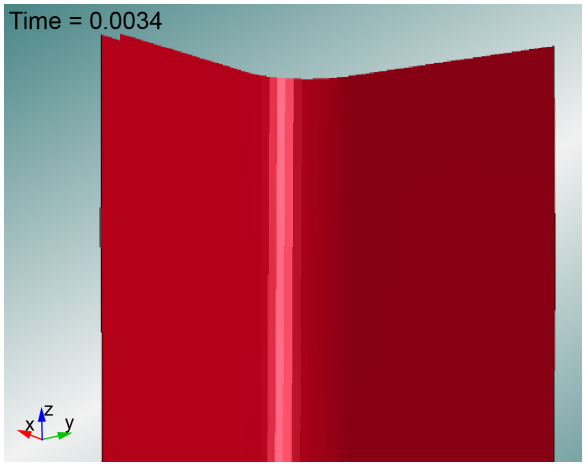

Figure B.14.—Typical crushing failure pattern at 13 mm of crush for small angle specimen.

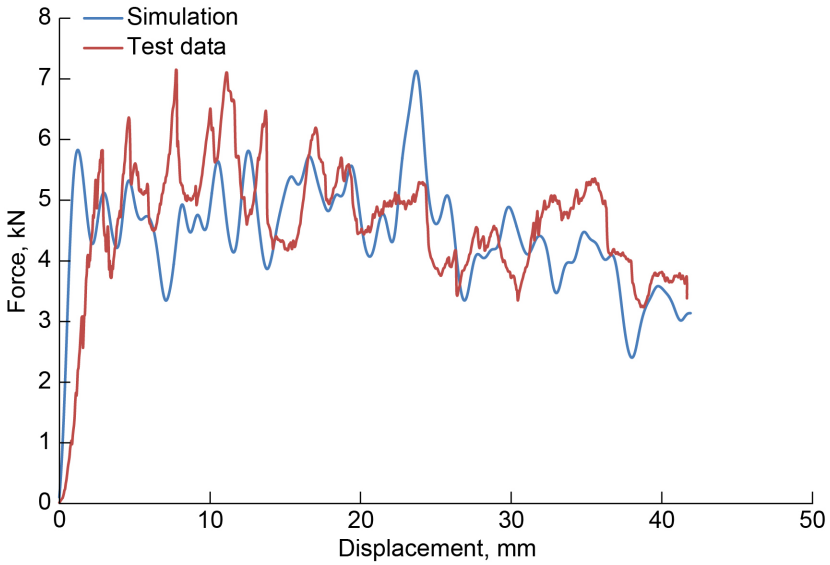

Figure B.15.—Comparison of small angle test and simulation reaction force during crushing.

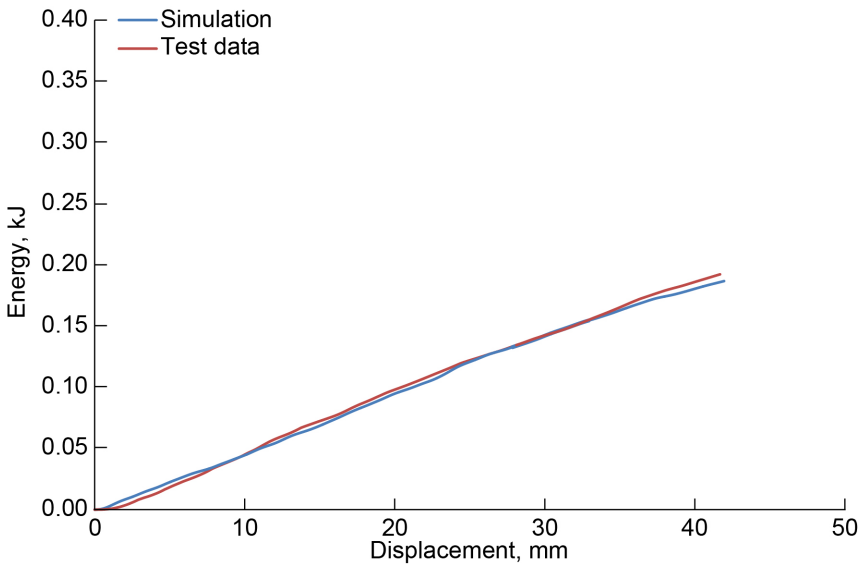

Figure B.16.—Comparison of small angle test and simulation energy absorption during crushing.

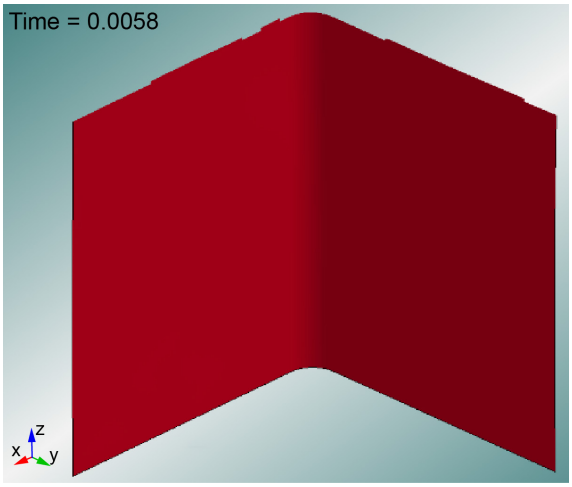

Figure B.17.—Typical crushing failure pattern at 22 mm of crush for large angle specimen.

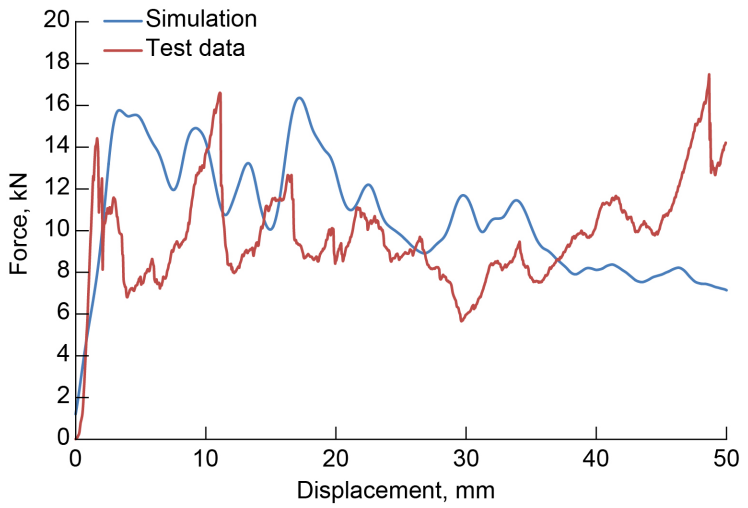

Figure B.18.—Comparison of large angle test and simulation reaction force during crushing.

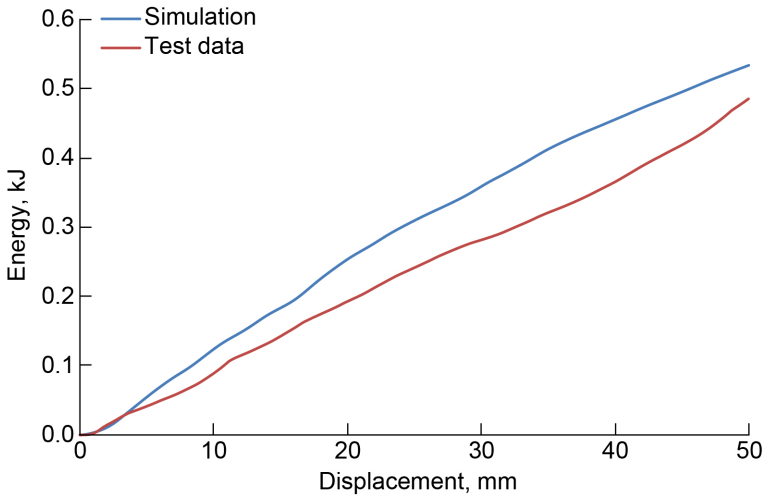

Figure B.19.—Comparison of large angle test and simulation energy absorption during crushing.

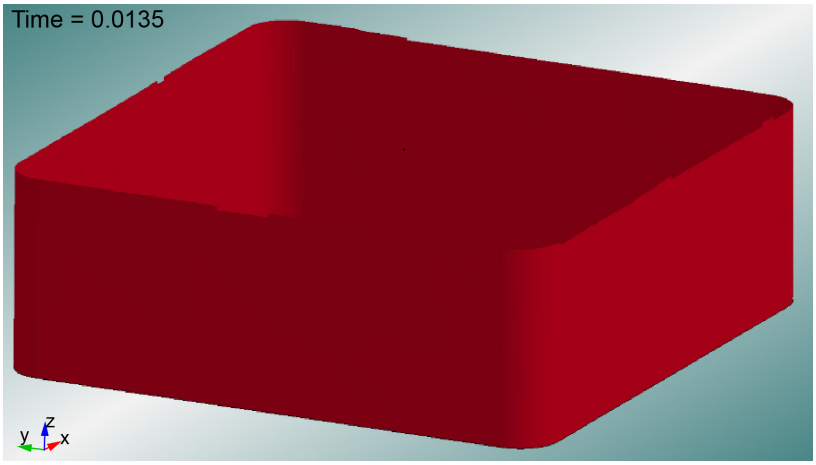

Figure B.20.—Typical crushing failure pattern at 50 mm of crush for square tube specimen.

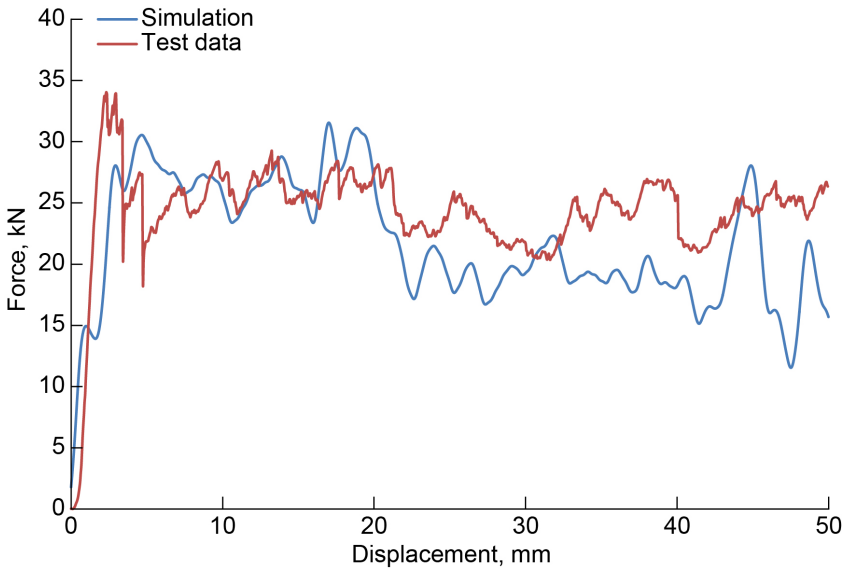

Figure B.21.—Comparison of square tube test and simulation reaction force during crushing.

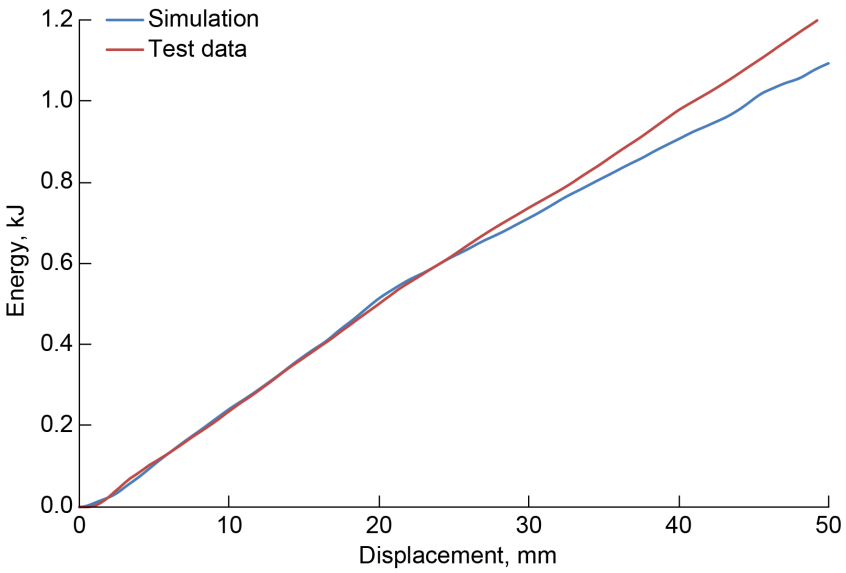

Figure B.22.—Comparison of square tube test and simulation energy absorption during crushing.

Figure B.23.—Typical crushing failure pattern at 13 mm of crush for sinusoid specimen.

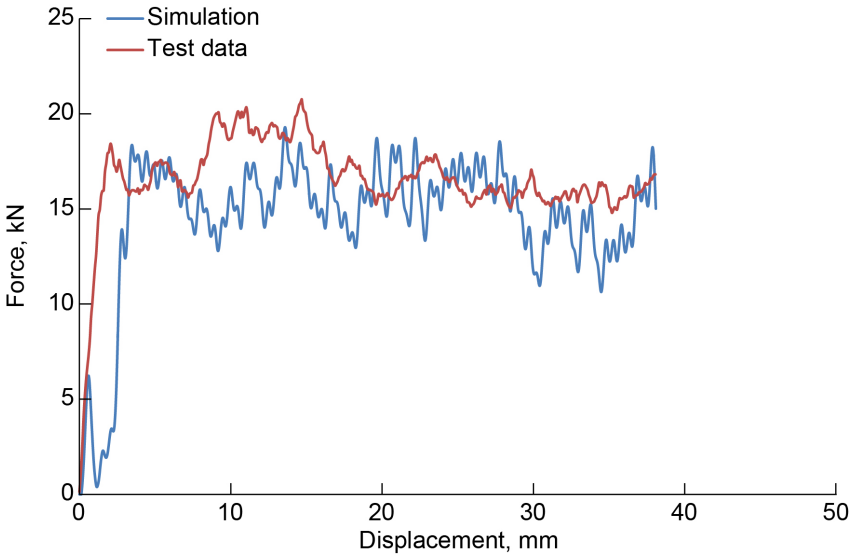

Figure B.24.—Comparison of sinusoid test and simulation reaction force during crushing.

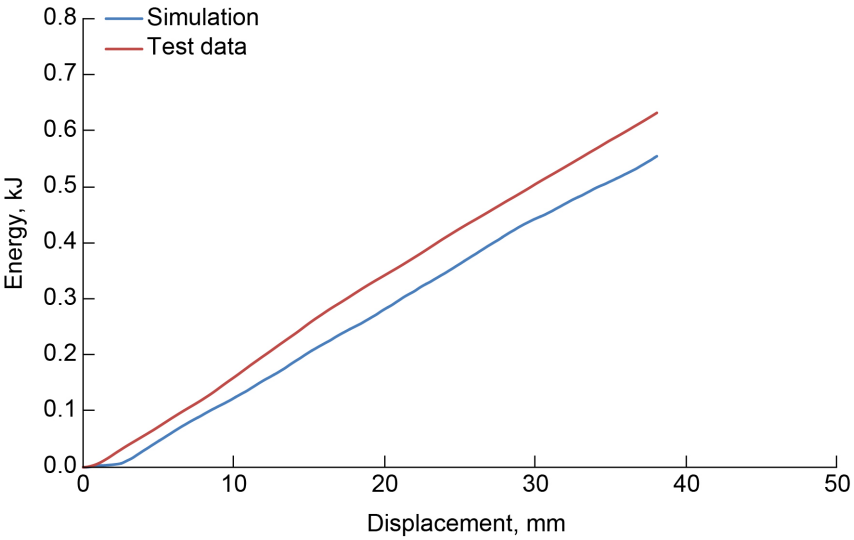

Figure B.25.—Comparison of sinusoid test and simulation energy absorption during crushing.

B.4 PAM–CRASH Material Model in Round Robin 1 and 2

This section provides additional information about the simulations discussed in Section 3.3.

B.4.1 Contact Algorithms

Contact algorithms were used to prevent undesired penetration between geometric boundaries during deformation. To represent the interaction of the metal loading platen with the specimen, a nonsymmetric node-segment contact with edge treatment was selected. A standard Coulomb friction model with a friction coefficient of 0.30 was used for this interaction. The same contact algorithm was employed for the interaction between the debris wedge and composite shells. In the numerical model with the bending wedge, a friction coefficient of 0 was implemented given that the role of the wedge here is to control the bending out of the stacked shells. To prevent the stacked shells from colliding and penetrating each other during the crushing process, a self-contact with edge treatment was introduced into the numerical simulation. Here, a friction coefficient of 0.60 was used for contact to represent the high friction between the delaminated plies, which cannot easily slide over each other due to fiber bridging.

B.4.2 Boundary Conditions

To represent the specimens potted in an epoxy resin to provide stability during the crush tests, the nodes on the base of the numerical model of the specimen were constrained in all DOFs. The loading platen and separation and bending wedges were modeled numerically as a single rigid body entity with displacement boundary conditions assigned to a single node (artificial node), which represents the center of gravity of this rigid body. This artificial node was constrained in all DOFs except in translation along the axial loading direction. This entity was assigned a constant velocity of 1 m/s. This does not correspond to the actual velocity in the test as the explicit time integration method is conditionally stable when the time step is sufficiently small and there are no rate-dependent materials models being used. A quasistatic test was then simulated with an increased loading platen velocity together with a scaling up of the mass density, which minimized the inertial effect. In this way, central processing unit (CPU) time was significantly reduced.

B.4.3 PAM–CRASH Datasets

PAM–CRASH provides datasets for global fabric PLY 7 and cohesive interface models (MAT303) for the Toray® T700/2510 fabric carbon/epoxy prepreg material system. The PAM–CRASH parameters required for the MAT131, PLY 7, and MAT303 materials models are listed in Table B.6. MAT131 data consist only of the number of plies, ply layup, and ply type, with no ply or interface data. The PAM damage and failure parameters required for PLY 7 and MAT303 are summarized in this section and in the PAM user manuals (Ref. 10).

The parameter values used for the RR–1 and RR–2 crash element simulations are listed in Table B.7. Data for tension and compression are given when measured, since the code allows different elastic and damage properties in tension and compression.

TABLE B.6.—MATERIALS PARAMETERS FOR PLY 7 AND MAT303

Variable	Property	Type	Measurement
PLY 7			
E_1^t	Axial Young's modulus (tension)	Experimental	0° tension test
E_2^t	Transverse Young's modulus (tension)	Experimental	90° tension test
E_1^c	Axial Young's modulus (compression)	Experimental	0° compression test
E_2^c	Transverse Young's modulus (compression)	Experimental	90° compression test
G_{12}	Shear modulus	Experimental	45° tension test
ν_{12}^t	Poisson's ratio (tension)	Experimental	0° tension test
ν_{12}^c	Poisson's ratio (compression)	Experimental	0° compression test
d_1^t	Damage parameter cutoff (tension)	Assumption	Observed from 0° tension test
d_1^c	Damage parameter cutoff (compression)	Assumption	Observed from 0° compression test
d_{12}	Damage parameter cutoff (shear)	Assumption	Observed from 45° tension test
Y_{11C}^t	Damage evolution curve slope (tension)	Experimental	0° tension test
Y_{11C}^c	Damage evolution curve slope (compression)	Experimental	0° compression test
Y_{12C}	Damage evolution curve slope (shear)	Experimental	45° cyclic tension test
Y_{110C}^t	Lower critical damage energy threshold (tension)	Experimental	0° tension test
Y_{110C}^c	Lower critical damage energy threshold (compression)	Experimental	0° compression test
Y_{11R}^t	Upper critical damage energy threshold (tension)	Experimental	0° tension test
Y_{11R}^c	Upper critical damage energy threshold (compression)	Experimental	0° compression test
Y_{120}	Lower critical damage energy threshold (shear)	Experimental	45° cyclic tension test
Y_{12R}	Upper critical damage energy threshold (shear)	Experimental	45° cyclic tension test
R_0	Yield stress	Experimental	45° cyclic tension test
β	Multiplier	Experimental	45° cyclic tension test
m	Power index	Experimental	45° cyclic tension test
MAT303			
E_0	Matrix Young's modulus (through thickness)	Experimental	Tension test
G_0	Matrix shear modulus (in-plane)	Experimental	Shear test
G_{Ic}	Critical strain energy release rate (mode I)	Experimental	Double cantilever beam (DCB)
G_{IIc}	Critical strain energy release rate (mode II)	Experimental	End-notched flexural (ENF) beam
σ_{prop}	Interface maximum failure stress (through thickness)	Calibrated	From DCB numerical simulation
γ_{prop}	Interface maximum failure stress (in-plane shear)	Calibrated	From ENF numerical simulation

TABLE B.7.—PAM–CRASH DATASETS FOR PLY 7 DAMAGE MODEL AND MAT303 COHESIVE INTERFACE

(a) Elastic constants, as provided in RR information and CMH–17 dataset

E_1^t, GPa	55.89
E_2^t, GPa	54.49
E_1^c, GPa	55.36
E_2^c, GPa	53.19
G_{12}, GPa	4.18
ν_{12}^t	0.042
ν_{12}^c	0.042

(b) Critical damage energy thresholds

Y_{110}^t, $GPa^{1/2}$	0.08618
Y_{110}^c, $GPa^{1/2}$	0.06657
Y_{11R}^t, $GPa^{1/2}$	0.08619
Y_{11R}^c, $GPa^{1/2}$	0.06658
Y_{120}, $GPa^{1/2}$	0.01076
Y_{12R}, $GPa^{1/2}$	0.05335

(c) Damage evolution curve slope parameters

Y_{11C}^t, $GPa^{1/2}$	0.08619
Y_{11C}^c, $GPa^{1/2}$	0.06658
Y_{12C}	3.86749

(d) Ply shear plasticity model parameters

R_0, GPa	0.0069
b, GPa	0.2632
m	0.2184

(e) Damage parameters cutoff values

d_1^t	0.900
d_1^c	0.500
d_{12}	0.650

(f) MAT303 cohesive interface properties

E_0, GPa	9.70
G_0, GPa	4.20
G_{IC}, J/mm^{-2}	0.00050
G_{IIC}, J/mm^{-2}	0.00157
σ_{prop}, MPa	4
γ_{prop}, MPa	40

B.4.4 Comparisons of PAM–CRASH Simulation Results With Coupon Test Data

In this section, simulation and test results are compared for C-channel, small-corner, and square tube specimens.

B.4.4.1 C-Channel Specimen (Small C-Channel)

The C-channel specimens had two unsupported side plates with free edges that started to bend outward and were not stiff enough to support the steady crushing seen in the corrugated specimens. Simulating this failure mode required a different numerical trigger to initiate plate bending rather than axial crushing. This consisted of a bending wedge (the gray shell element seen in Figure B.26), which initiated transverse outward bending of the stacked shells. This in turn caused axial tearing at the corner segments as the stacked shells impacted the loading platen and bent outward. To control the bending radius of the stacked shells and thus the axial tearing, the contact distances in the contact algorithm between the shells of the specimen and the bending wedge can be varied. Another feature of the numerical trigger was the offsetting of the nodes of the inner two stacked shells at the top of the specimen (the yellow shell elements in Figure B.26). To assist in the bending initiation of the inner stacked shells, the nodes were offset in the chamfer region upon contact from the bending wedge. Reduction in the number of stacked shells in the first and second row from the crush front was the final feature of this numerical trigger, which emulated the thin chamfer region.

The simulation sequence of the C-channel in Figure B.27 clearly shows laminate fracture at the corners caused by the outward bending of the three main plate elements in the section. This agrees very well with the photographs of the damaged specimens. Figure B.28 compares measured and simulated axial crush forces, which are in good agreement on the main features. Because the tearing failure mechanism absorbed less energy than steady axial crush, the steady crush load was significantly below that measured in the corrugated plate test.

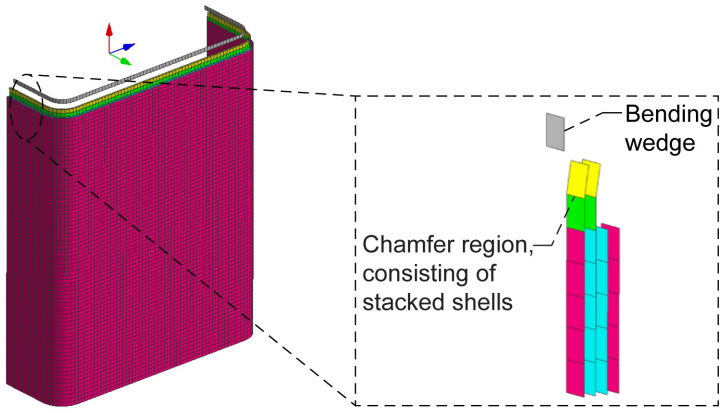

Figure B.26.—Trigger mechanism of C-channel specimen numerical model.

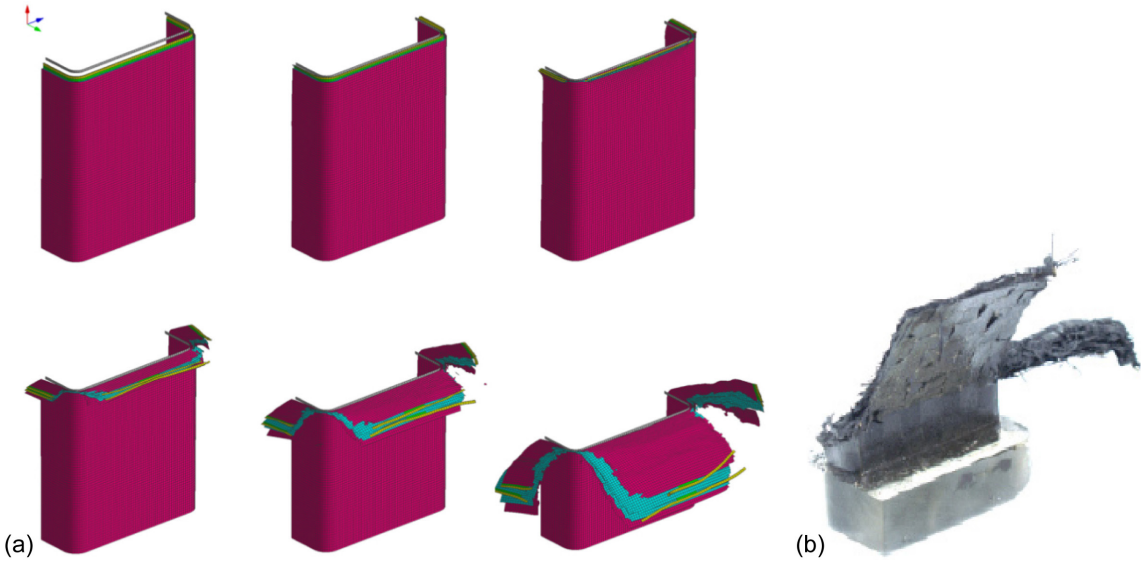

Figure B.27.—C-channel specimen crushing response. (a) Numerical model crushing process sequence. (b) Experimental result.

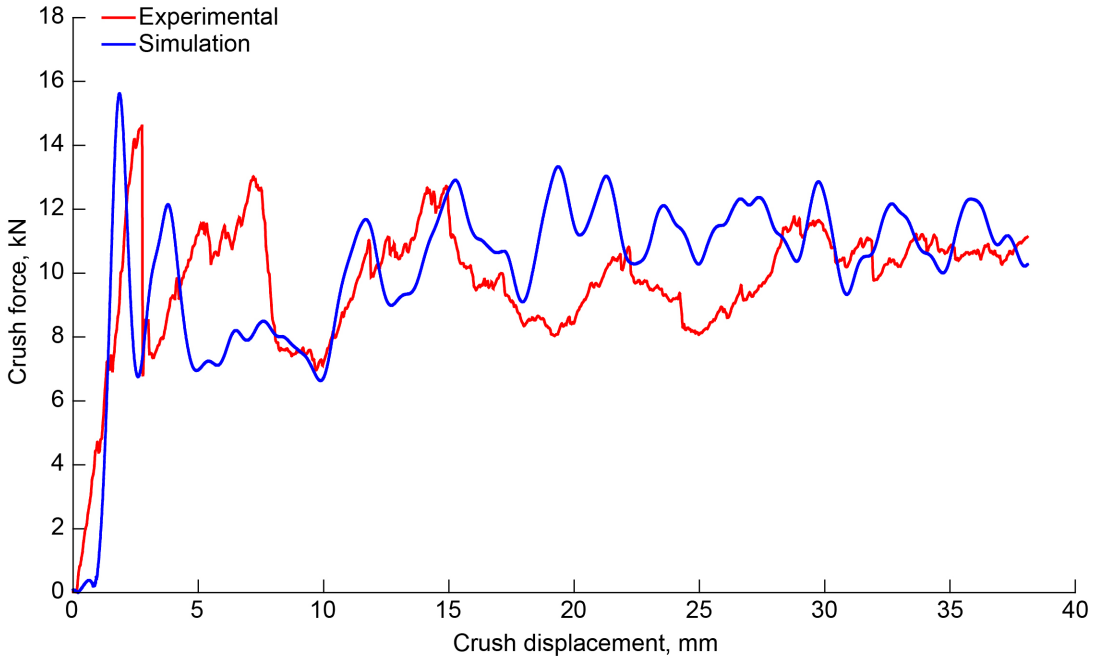

Figure B.28.—Force–displacement curves for C-channel crushing.

B.4.4.2 Tube Corner Section (Small Angle)

The small angle section is the corner subelement of the previous small C-channel specimen. The long edges were unsupported, so they were expected to splay out, and steady crushing was not anticipated. The bending trigger used with the C-channel specimen was thus applied to this section, as a similar failure mode was anticipated. Figure B.29 shows the FE model with a detail of the bending trigger. The simulation sequence of the small-angle channel in Figure B.30 shows laminate fracture at the corners caused by the outward bending of the three plate elements in the section. Again, this agrees very well with photographs of the damaged specimens (Figure B.30(b)). Figure B.31 compares measured and simulated axial crush forces, which are in good agreement on the main features. Because the tearing failure

mechanism absorbed less energy than steady axial crush, the steady crush load was significantly below that measured in the corrugated plate test.

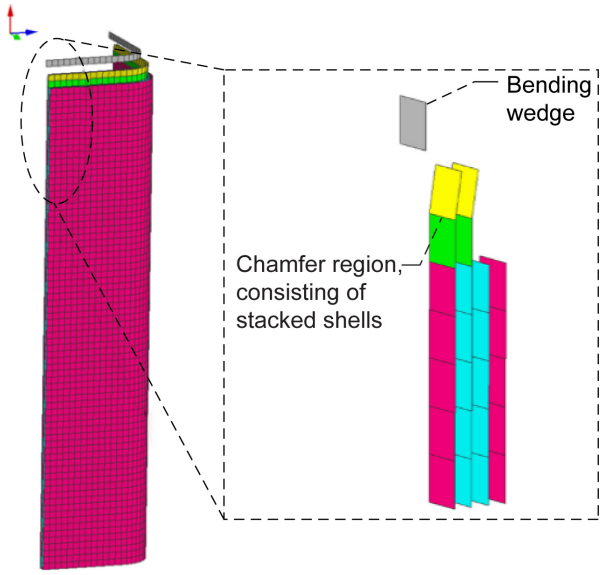

Figure B.29.—Small angle FE model with bending trigger detail.

Figure B.30.—Small angle specimen crushing response. (a) Numerical model crushing process sequence. (b) Experimental result.

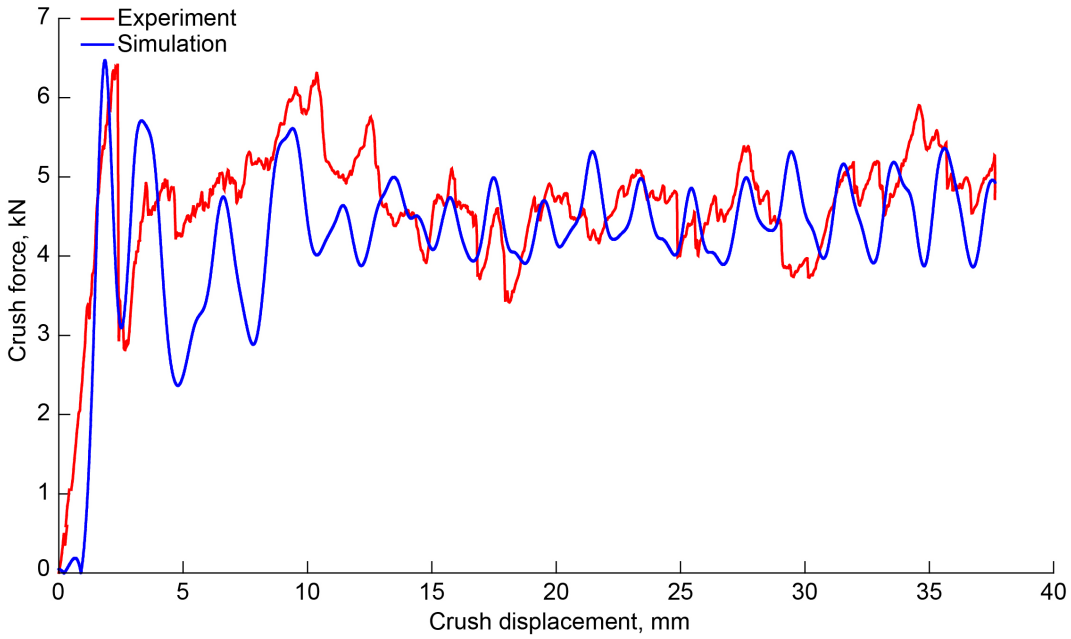

Figure B.31.—Force–displacement curves for small-corner specimen.

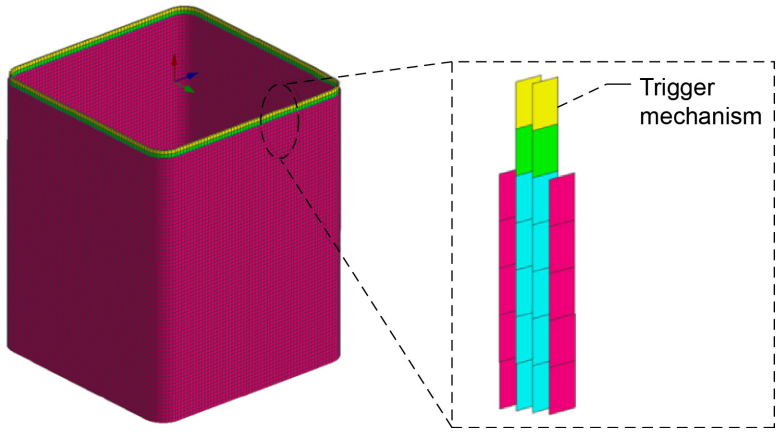

Figure B.32.—Trigger mechanism of square tube specimen numerical model.

B.4.4.3 Square Tube Specimen

In the square tube specimen, there was no free edge on the side plates to cause a bending and tearing failure mode. Furthermore, the width, or thickness, of the side plates was too high for initiation of an axial crush failure, with the result that failure was nearer to the local ring- or cell-buckling failure observed in thin-walled metal tubes. In this case, the numerical trigger consisted of the two reduced stacked shells to model the reduction in specimen thickness brought about by the chamfer (see Figure B.32). The trigger then has a neutral effect on the specimen, with no initiation of axial splaying or plate bending as in the previous specimens.

The numerical simulation of the square tube (Figure B.33) now predicts local bending at the trigger, which initiates ring or diamond buckles with small cell size. As rows of elements buckle and then fracture, a steady crushing response is produced, as observed in the tests. Crush force levels were similar between simulation and test, as seen in Figure B.34. Because of the buckling type failures, it is seen that the numerical force curve has global instabilities when compared with the more stable crushing curve seen in Figure 39 for the corrugated plate.

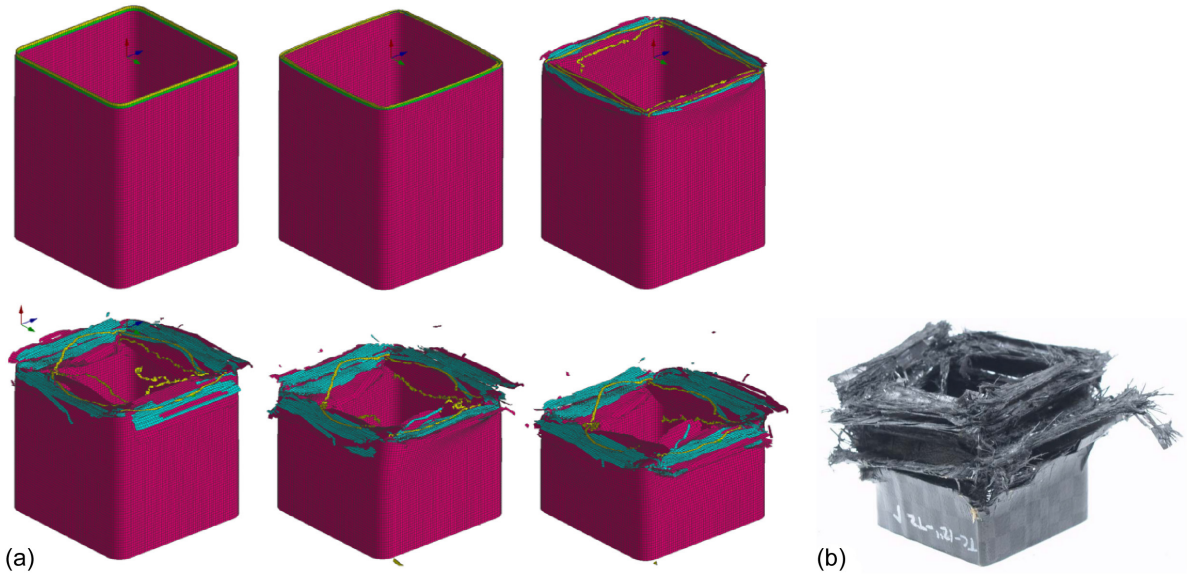

Figure B.33.—Square tube specimen crushing response. (a) Numerical model crushing process sequence. (b) Experimental result.

Figure B.34.—Force–displacement curves for square tube specimen.

B.5 LS–DYNA® MAT54 Material Model in Round Robin 3

This section provides additional information about the simulations discussed in Section 4.1.

B.5.1 Model Description

LS–DYNA® MAT54 is a progressive failure model used to model orthotropic materials such as composites. It offers Chang–Chang failure criteria to simulate ply-by-ply failure and property degradation (Ref. 16). In the elastic region, the material stress–strain behavior for axial, transverse, and shear directions is governed by Equations (B.9) to (B.11).

$$\varepsilon_{11} = \frac{1}{E_1}(\sigma_{11} - \nu_{12}\sigma_{22}) \tag{B.9}$$

$$\varepsilon_{22} = \frac{1}{E_2}(\sigma_{22} - \nu_{21}\sigma_{11}) \tag{B.10}$$

$$2\varepsilon_{12} = \frac{1}{G_{12}}\tau_{12} + \alpha\tau_{22}^3 \tag{B.11}$$

The material model uses ply-by-ply progressive failure criteria followed with element erosion once all the plies in the laminate have failed. Beyond the elastic region, the material model uses Chang–Chang failure criteria to determine the individual ply failure (through-thickness integration points for shell elements). The four failure modes considered are tensile fiber mode, compressive fiber mode, tensile matrix mode, and compressive matrix mode. Ply failure occurs when one of these four modes governed by Equations (B.12) to (B.15) is satisfied (Refs. 16, 18, and 94).

Fiber failure (axial direction):

Tension:
$$\sigma_{11} > 0 \Rightarrow e_f^2 = \left(\frac{\sigma_{11}}{X_t}\right)^2 + \beta\left(\frac{\sigma_{12}}{S_c}\right)^2 - 1, \begin{array}{l} e_f^2 \geq 0 \Rightarrow \text{failed} \\ e_f^2 < 0 \Rightarrow \text{elastic} \end{array} \tag{B.12}$$

Upon failure: $E_1 = E_2 = G_{12} = \nu_{21} = \nu_{12} = 0$

Compression:
$$\sigma_{11} < 0 \Rightarrow e_c^2 = \left(\frac{\sigma_{11}}{X_c}\right)^2 - 1, \begin{array}{l} e_m^2 \geq 0 \Rightarrow \text{failed} \\ e_m^2 < 0 \Rightarrow \text{elastic} \end{array} \tag{B.13}$$

Upon failure: $E_1 = \nu_{21} = \nu_{12} = 0$

Matrix failure (transverse direction):

Tension:
$$\sigma_{22} > 0 \Rightarrow e_m^2 = \left(\frac{\sigma_{22}}{Y_t}\right)^2 + \left(\frac{\sigma_{12}}{S_c}\right)^2 - 1, \begin{array}{l} e_m^2 \geq 0 \Rightarrow \text{failed} \\ e_m^2 < 0 \Rightarrow \text{elastic} \end{array} \tag{B.14}$$

Upon failure: $E_2 = \nu_{21} = 0 \Rightarrow G_{12} = 0$

Compression:
$$\sigma_{22} > 0 \Rightarrow e_d^2 = \left(\frac{\sigma_{22}}{2S_c}\right)^2 + \left[\left(\frac{Y_c}{2S_c}\right)^2 - 1\right]\frac{\sigma_{22}}{Y_c} + \left(\frac{\sigma_{12}}{S_c}\right)^2 - 1, \begin{array}{l} e_d^2 \geq 0 \Rightarrow \text{failed} \\ e_d^2 < 0 \Rightarrow \text{elastic} \end{array} \tag{B.15}$$

Upon failure: $E_2 = \nu_{21} = \nu_{12} = 0 \Rightarrow G_{12} = 0$

When one of these equations is satisfied, ply failure resulting in stiffness degradation occurs and prevents the failed ply from carrying stress any further. The stress value is not reduced to zero but rather results in an elastic–perfectly plastic material response. The failed ply stresses are therefore constant until deletion, as illustrated in Figure B.35. LS–DYNA® allows for monitoring of these failure modes through history variables. Four failure flags represent the four failure modes in tensile (fiber and matrix) and compressive (fiber and matrix) loading conditions (Refs. 18 and 94).

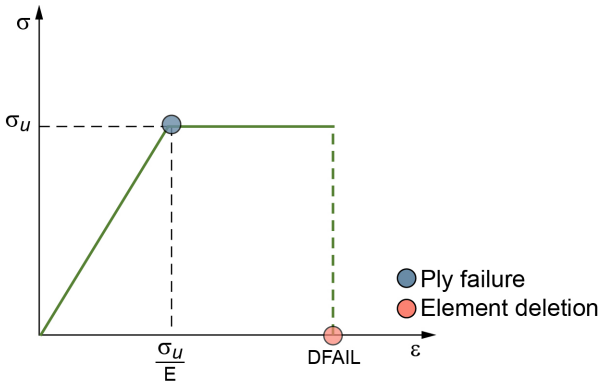

Figure B.35.—Stress–strain behavior and ply failure and deletion in MAT54.

These failure criteria determine the maximum stress limit resulting in ply-by-ply failure (through-thickness integration points) but do not govern the element deletion criteria. The deletion of elements is controlled by failure strain values in fiber tension (DFAILT), fiber compression (DFAILC), matrix direction (DFAILM), shear state (DFAILS), and effective failure strain (EFS). In the matrix direction, there is only one option to define failure strain value for both tensile and compressive states. EFS is a nonphysical strain parameter that is generally used when test data for the other four strain values are unavailable. In MAT54, when DFAIL parameters are defined (as in the present material model), element erosion occurs if (1) the fiber strain is greater than DFAILT or less than DFAILC, (2) the absolute value of matrix strain is greater than DFAILM, and (3) the absolute value of tensorial shear strain is greater than DFAILS. Element deletion occurs when all the plies (through-thickness integration points) fail and the DFAIL criteria are reached.

Equations (B.16) to (B.18) present the strength reduction criteria, where parameters with an asterisk represent the pristine strengths. Table B.8 represents LS–DYNA® MAT54 input parameters for the IM7/8552 composite material system.

$$XT = XT^* \times FBRT \tag{B.16}$$

$$XC = YC^* \times YCFAC \tag{B.17}$$

$$\{XT, XC, YT, YC\} = \{XT, XC, YT, YC\}^* \times SOFT \tag{B.18}$$

B.5.2 Description of Strength Reduction Parameters FBRT, YCFAC, and SOFT

FBRT is the percentage of pristine fiber tensile strength existent after failure has occurred in compressive matrix mode; it ranges between 0 and 1. YCFAC is the reduction factor for compressive fiber strength after matrix compressive failure. The SOFT parameter is a strength reduction factor and was observed to yield stable crush behavior in simulations (Refs. 18 and 94). It is a modeling parameter and ranges from 0 to 1. The default value is 1, which means that the crush-front elements retain their pristine strength when the neighboring elements are deleted. SOFT is only activated when the TFAIL parameter, time step size criteria for element deletion, is set to greater than zero.

TABLE B.8.—LS–DYNA® MAT54 INPUT DEFINITION
FOR IM7/8552 COMPOSITE MATERIAL SYSTEM

(a) *MAT_ENHANCED_COMPOSITE_DAMAGE (MAT54)

Parameter	Description	Value[a]
RO	Density	1.55×10^{-9}
EA	Axial Young's modulus	154,563.48
EB	Transverse Young's modulus	8,962.0
EC	Through-thickness Young's modulus	8,962.0
PRBA	Poisson's ratio, BA	0.024
PRCA	Poisson's ratio, CA	0.024
PRCB	Poisson's ratio, CB	0.4
GAB	Shear modulus, AB	4,688.0
GBC	Shear modulus, BC	4,688.0
GCA	Shear modulus, CA	4,688.0
DFAILM	Matrix failure erosion strain	0.0128
DFAILS	In-plane shear erosion strain	0.0375
DFAILT	Fiber tension erosion strain	0.0162
DFAILC	Fiber compression erosion strain	–0.0111
EFS	Effective strain erosion value	0
XC	Longitudinal compressive strength	1,713.85
XT	Longitudinal tensile strength	2,500.45
YC	Transverse compressive strength	285.69
YT	Transverse tensile strength	64.05
SC	Shear strength, AB	119.97
TFAIL	Time step size criteria for element deletion	3.20967×10^{-8}
SOFT	Crash-front elements reduction factor	0.3
FBRT	Softening of fiber tensile strength	0.9
YCFAC	Softening of compressive fiber strength	1.1

[a]Units are based on mm/second/tonne/Newton system.

(b) Modeling parameters

Parameter	Description
AOPT	Material axes
2WAY	Flag for two-way fiber action
TI	Flag for transversal isotropic
MANGLE	Material angle
CRIT	Failure criterion

(c) Other parameters

Parameter	Description
PFL	Percentage of layers failure to initiate crush front
ALPH	Shear stress
SOFT2	Orthogonal element reduction factor
TSMD	Transverse shear maximum damage
SLIMT1	Minimum stress limit after stress maximum, fiber tension
SLIMC1	Minimum stress limit after stress maximum, fiber tension
SLIMT2	Minimum stress limit after stress maximum, matrix tension
SLIMC2	Minimum stress limit after stress maximum, matrix compression
SLIMS	Minimum stress limit after stress maximum, shear

B.5.3 C-Channel Crush Simulation Results With Platen Mass of 96.8 lb

Figure B.36 to Figure B.38 present the crush progression kinematics of the stanchion. As the stanchion crush progressed, stable crush behavior was achieved. However, at times fragmentation was observed, where parts of the specimen broke away.

Figure B.38 and Figure B.39 present the force–displacement graphs of laminates HL01 and HL02. The force levels show stable crush beyond the initial peak load. To initiate crush behavior, two rows of trigger elements with reduced thickness were defined. Previous studies (Refs. 18 and 94) have shown that an appropriate trigger element thickness is required to accurately capture the initial peak force.

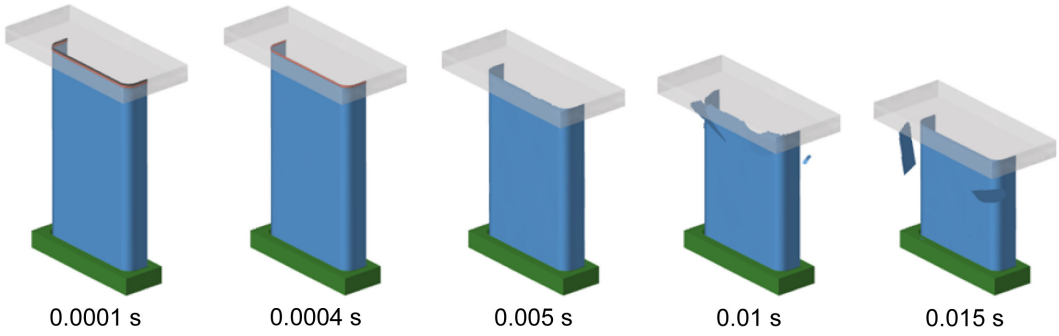

Figure B.36.—Crush progression in laminate HL01 $[90_2/0_2/\pm45/0_2]_S$ at impact velocity of 150 in./s using MAT54.

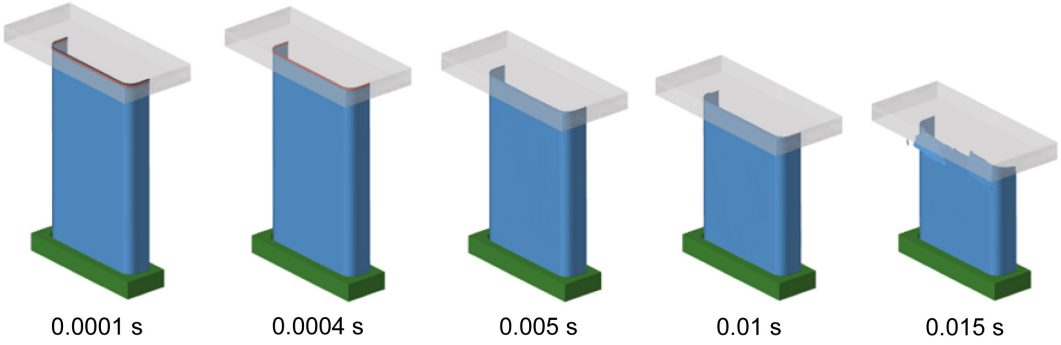

Figure B.37.—Crush progression in laminate HL02 $[90/45/0_2/90/-45/0_2]_S$ at impact velocity of 150 in./s using MAT54.

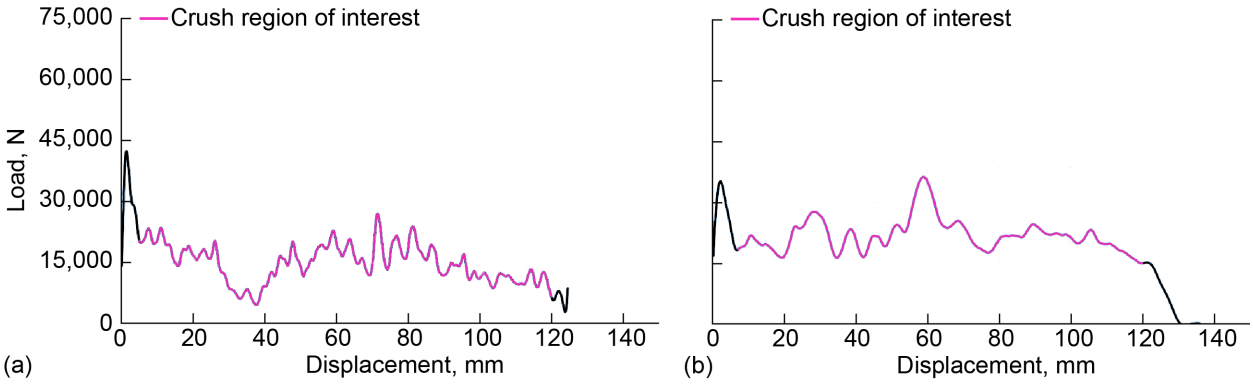

Figure B.38.—Load–displacement data simulation results for laminate HL01 $[90_2/0_2/\pm45/0_2]_S$ for two velocities using MAT54 filtered with SAE 600-Hz filter. (a) Impact velocity 150 in./s. (b) Impact velocity 300 in./s.

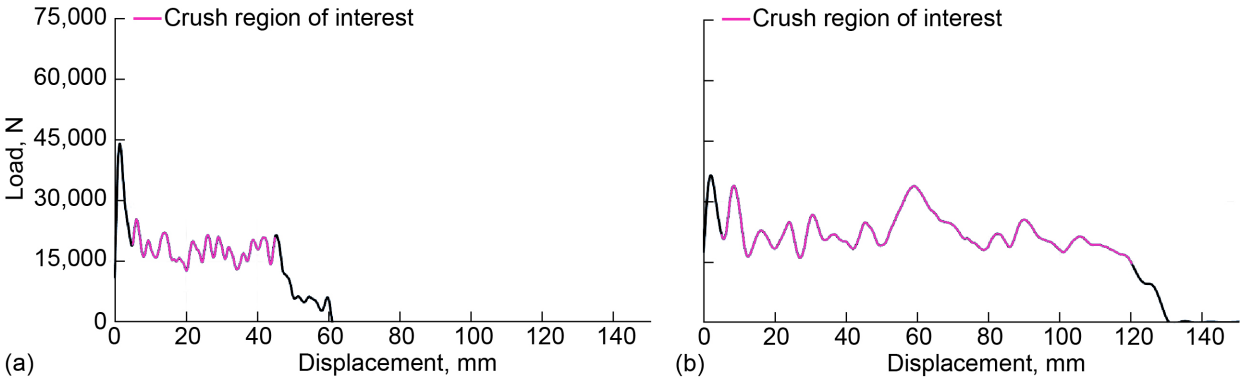

Figure B.39.—Load–displacement data simulation results for laminate HL02 $[90/45/0_2/90/-45/0_2]_S$ for two velocities using MAT54 filtered with SAE 600-Hz filter. (a) Impact velocity 150 in./s. (b) Impact velocity 300 in./s.

TABLE B.9.—PREDICTED CRASHWORTHINESS PARAMETERS OF C-CHANNEL LAMINATE CONFIGURATIONS USING MAT54

Parameter	Laminate HL01		Laminate HL02	
	150 in./s	300 in./s	150 in./s	150 in./s
Crush distance, mm	115	113	Crush distance, mm	115
Peak crush force, N	42,559.1	36,364.0	Peak crush force, N	42,559.1
Average crush force, N	15,071.0	21,954.4	Average crush force, N	15,071.0
SEA, kJ/kg	81.0	118.0	SEA, kJ/kg	81.0
Crush force efficiency	0.35	0.60	Crush force efficiency	0.35

Table B.9 presents the crashworthiness parameters evaluated for these C-channel crush test predictions with assumed platen mass of 96.8 lb.

B.6 LS–DYNA® MAT58 Material Model in Round Robin 3

This section provides additional information about the simulations discussed in Section 4.2.

B.6.1 MAT58 Parameters and Key Options for Calibration

In addition to the usual elastic material properties and strength properties, calibration of MAT58 is required for parameters shown in Figure B.40.

Figure B.41 shows additional parameters that have more recently been included as updates to the material model. These parameters include additional elastic and failure properties for additional material directions for solid elements. One very significant update is highlighted in red and allows for inclusion of curves to define strain-rate effects for both strength and modulus.

Strain-rate curves are not required and are not defined in the current models used in simulating coupon or part crushing response. However, use of these curves would be highly advantageous in simulating differing crush responses over the velocity range from quasistatic to higher impact velocities, such as the 30 ft/s (360 in./s) used in some Federal Aviation Administration (FAA) drop tests.

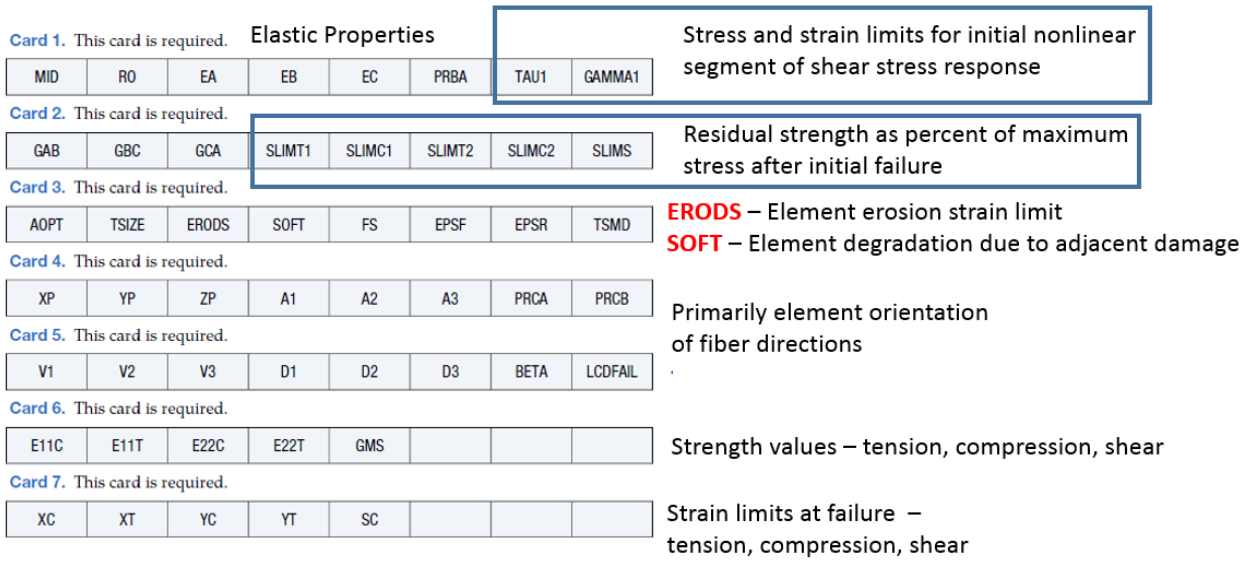

Figure B.40.—Required input parameters for shell elements in MAT58.

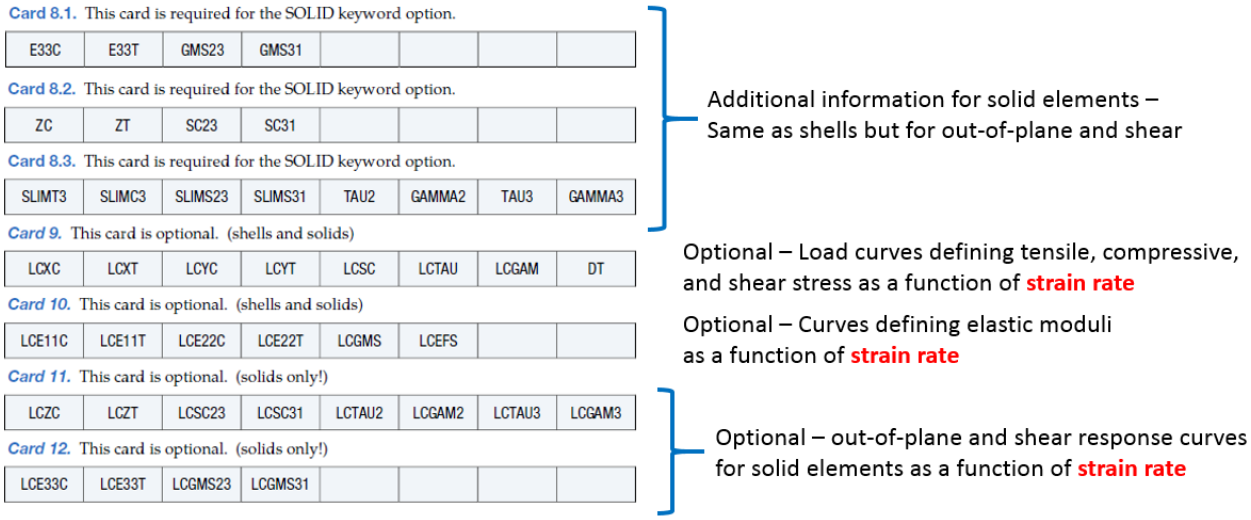

Figure B.41.—Additional input parameters for solid elements and optional strain-rate response curves in MAT58.

B.6.2 Flat Crush Coupon Test and Analysis Comparisons

Figure B.42 to Figure B.44 report both force–displacement history and cumulative energy absorption during crushing in comparison with repeated test results.

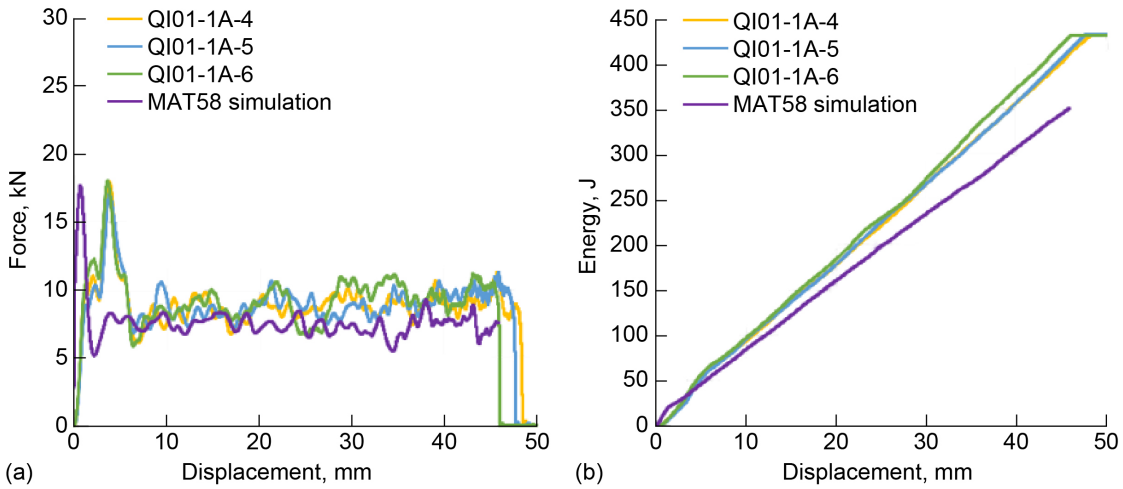

Figure B.42.—Comparison of test and MAT58 simulation for quasi-isotropic layup. (a) Force–displacement. (b) Energy–displacement.

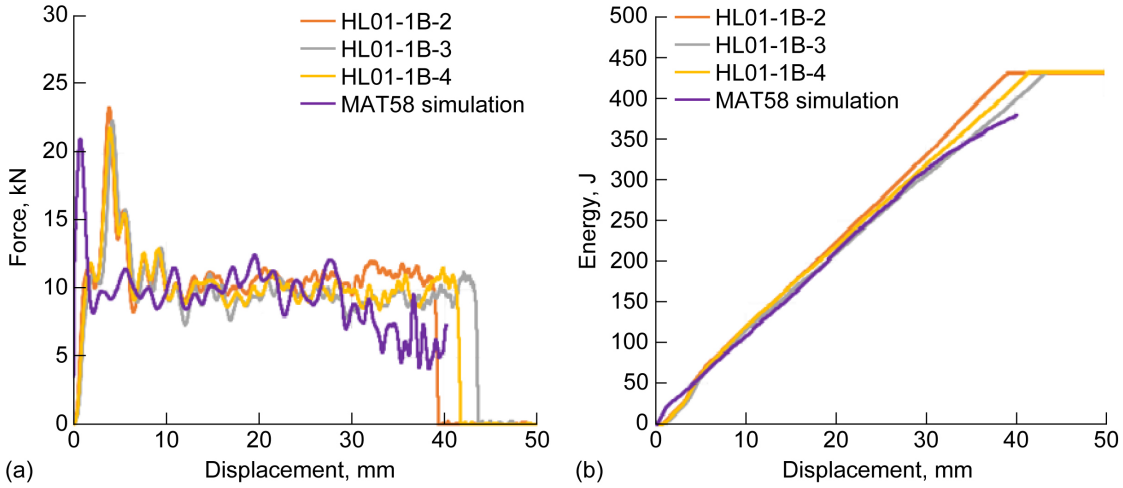

Figure B.43.—Comparison of test and MAT58 simulation for HL01. (a) Force–displacement. (b) Energy–displacement.

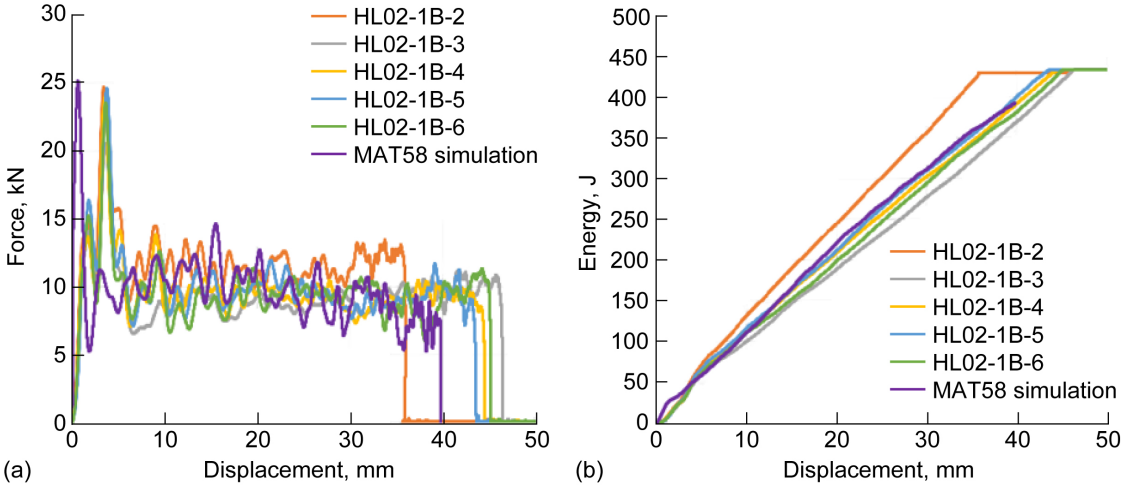

Figure B.44.—Comparison of test and MAT58 simulation for HL02. (a) Force–displacement. (b) Energy–displacement.

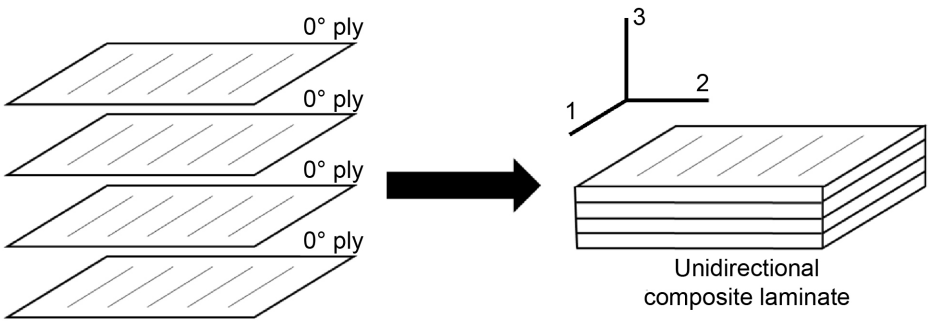

Figure B.45.—Four-ply unidirectional composite laminate showing principal material directions.

B.7 LS–DYNA® MAT213 Material Model in Round Robin 3

This section provides additional information about the simulations discussed in Section 4.3.

B.7.1 Deformation Model

As shown in Figure B.45, the principal material directions that define unidirectional composites follow traditional nomenclature, where the 1-direction is parallel to the fibers, the 2-direction is transverse to the fibers in the plane of the plies, and the 3-direction is orthogonal to the ply planes.

The nonlinear deformation response of the material is formulated using an orthotropic plasticity model (Ref. 1). In this model, the commonly used Tsai–Wu (Ref. 55) failure model (Eqs. (B.19) and (B.20)) is generalized and extended to a strain-hardening model with a quadratic yield function f (with additional linear terms) and a nonassociative flow rule function h (Eq. (B.21)).

$$\sigma_i = \{\sigma_1\ \sigma_2\ \sigma_3\ \sigma_4\ \sigma_5\ \sigma_6\} = \{\sigma_{11}\ \sigma_{22}\ \sigma_{33}\ \sigma_{12}\ \sigma_{23}\ \sigma_{13}\} \tag{B.19}$$

$$f = -1 + F_i\sigma_i + F_{ij}\sigma_i\sigma_j$$

where

$$F_i = \{F_1\ F_2\ F_3\ 0\ 0\ 0\} \text{ and } F_{ij} = \begin{bmatrix} F_{11} & F_{12} & F_{13} & 0 & 0 & 0 \\ F_{12} & F_{22} & F_{23} & 0 & 0 & 0 \\ F_{13} & F_{23} & F_{33} & 0 & 0 & 0 \\ 0 & 0 & 0 & F_{44} & 0 & 0 \\ 0 & 0 & 0 & 0 & F_{55} & 0 \\ 0 & 0 & 0 & 0 & 0 & F_{66} \end{bmatrix} \tag{B.20}$$

where f is the quadratic yield function and F_i and F_{ij} are the yield function coefficients.

$$h^2 = \begin{Bmatrix} \sigma_1 \\ \sigma_2 \\ \sigma_3 \\ \sigma_4 \\ \sigma_5 \\ \sigma_6 \end{Bmatrix}^T \begin{bmatrix} H_{11} & H_{12} & H_{13} & 0 & 0 & 0 \\ H_{12} & H_{22} & H_{23} & 0 & 0 & 0 \\ H_{13} & H_{23} & H_{33} & 0 & 0 & 0 \\ 0 & 0 & 0 & H_{44} & 0 & 0 \\ 0 & 0 & 0 & 0 & H_{55} & 0 \\ 0 & 0 & 0 & 0 & 0 & H_{66} \end{bmatrix} \begin{Bmatrix} \sigma_1 \\ \sigma_2 \\ \sigma_3 \\ \sigma_4 \\ \sigma_5 \\ \sigma_6 \end{Bmatrix} \tag{B.21}$$

where the flow rule coefficients are represented by H_{ij}.

Including the linear terms in the yield function allows the tension and compression response to be defined independently. In reality, the nonlinear deformation response of composite materials is most likely due to a combination of the plasticity and viscoelasticity of the polymer matrix in combination with local damage mechanisms such as matrix microcracking. However, in MAT213, the nonlinear deformation response of the composite is simulated using the orthotropic plasticity model.

The coefficients of the Tsai–Wu-based yield function of the deformation model (F_i and F_{ij}) are calculated using the current values of the yield stresses in the various coordinate directions (e.g., 1-direction tension, 2-direction compression, shear in 1–3 plane, etc.). By allowing the coefficients to vary, the yield surface evolution and hardening in each of the material directions can be precisely defined. Equation (B.22) shows the calculations to obtain the yield function coefficients where the superscripted letters denote tension (T) or compression (C), and the hyphenated superscripts for the off-diagonal terms denote the plane of rotation for the yield stress of an off-axis (OA) tension (or compression) test.

$$
\begin{aligned}
F_1 &= \frac{1}{\sigma_1^T} - \frac{1}{\sigma_1^C} \quad F_{11} = \frac{1}{\sigma_1^T \sigma_1^C} \quad F_{44} = \frac{1}{\sigma_4^2} \\
F_2 &= \frac{1}{\sigma_2^T} - \frac{1}{\sigma_2^C} \quad F_{22} = \frac{1}{\sigma_2^T \sigma_2^C} \quad F_{55} = \frac{1}{\sigma_5^2} \\
F_3 &= \frac{1}{\sigma_3^T} - \frac{1}{\sigma_3^C} \quad F_{33} = \frac{1}{\sigma_3^T \sigma_3^C} \quad F_{66} = \frac{1}{\sigma_6^2} \\
F_{12} &= \frac{2}{\left(\sigma_{OA45_y}^{1-2}\right)^2} - \frac{F_1 + F_2}{\sigma_{OA45_y}^{1-2}} - \frac{1}{2}\left(F_{11} + F_{22} + F_{44}\right) \\
F_{23} &= \frac{2}{\left(\sigma_{OA45_y}^{2-3}\right)^2} - \frac{F_2 + F_3}{\sigma_{OA45_y}^{2-3}} - \frac{1}{2}\left(F_{22} + F_{33} + F_{55}\right) \\
F_{13} &= \frac{2}{\left(\sigma_{OA45_y}^{1-3}\right)^2} - \frac{F_1 + F_3}{\sigma_{OA45_y}^{1-3}} - \frac{1}{2}\left(F_{11} + F_{33} + F_{66}\right)
\end{aligned}
\tag{B.22}
$$

To compute the current value of the yield stresses needed for the yield function, the common practice in plasticity constitutive equations is to use analytical functions to define the evolution of the stresses as a function of the components of plastic strain (or the effective plastic strain). Alternatively, in the developed model, tabulated stress–strain curves (Section 5.2.3) are used to track the yield stress evolution. The constitutive equation for MAT213 is given in Equation (B.23), where C_{ij} is the stiffness matrix, $\dot{\varepsilon}_j$ is strain rate, $\dot{\varepsilon}_j^{EL}$ is the elastic strain rate, and $\dot{\varepsilon}_j^{PL}$ is the plastic strain rate.

$$
\dot{\sigma}_i = C_{ij}\dot{\varepsilon}_j^{EL} = C_{ij}\left(\dot{\varepsilon}_j - \dot{\varepsilon}_j^{PL}\right) \tag{B.23}
$$

The user is required to input 12 stress–strain curves for each principal material direction in a tabulated, discretized form, and these curves are converted to stress versus plastic strain curves internally. The required curves include uniaxial tension curves in each of the normal directions (1, 2, and 3), uniaxial compression curves in each of the normal directions (1, 2, and 3), shear stress–strain curves in each of the shear directions (1–2, 2–3, and 3–1), and 45° off-axis compression curves in each of the 1–2, 2–3, and 3–1 planes. Single-element representations of the three 45° off-axis orientations are shown in Figure B.46. The 45° curves are required in order to calculate the off-diagonal terms (F_{12}, F_{23}, and F_{13}) in the yield

function. By utilizing tabulated stress–strain curves to track the evolution of the deformation response, the experimental stress–strain response of the material can be captured to a much higher degree of accuracy than would be possible by using an analytical function and the relevant failure stresses (and strains) to approximate the stress–strain curves. Additionally, the user is required to input a table of yield strain values, which the model uses to internally compute yield stress using the user-input stress–strain curves. These values are typically selected based on defining the strain where nonlinearity is first detected in each principal material direction.

The required stress–strain data can be obtained either from actual experimental test results based on ASTM test standards (Section 5.2.3) or by appropriate numerical experiments utilizing stand-alone codes. An important point to note is that due to experimental or numerical variability, or alternatively, simply due to the fundamental behavior of the material, the computed off-diagonal terms of the yield function may result in a yield function that is not convex, as shown in Figure B.47. As a result, to satisfy the requirements of the chosen yield function, the off-diagonal terms may need to be adjusted (i.e., convex correction applied) based on the values of the other coefficients in the yield function to ensure convexity of the yield surface (Ref. 1), as required by plasticity theory.

A quadratic nonassociative flow rule, shown in Equation (B.21), is used to compute the evolution of the components of plastic strain. The values of the flow rule coefficients H_{ij} can be determined through the use of plastic Poisson's ratios or an optimization procedure (Refs. 1 and 20).

The plastic potential function (Eq. (B.24)) is used in combination with the usual normality assumptions of classical plasticity to compute the evolution of the components of plastic strain, where λ is a scalar plastic multiplier.

$$\dot{\varepsilon}_j^{PL} = \dot{\lambda}\frac{\partial h}{\partial \sigma_i} \tag{B.24}$$

By utilizing the principle of the equivalence of plastic work, the flow rule function (h) can be defined as the effective stress, and $\dot{\lambda}$ can be defined as the effective plastic strain rate (Eq. (B.25)).

$$\dot{W}^{PL} = \sigma_i \dot{\varepsilon}_i^{PL} = h\dot{\lambda} \tag{B.25}$$

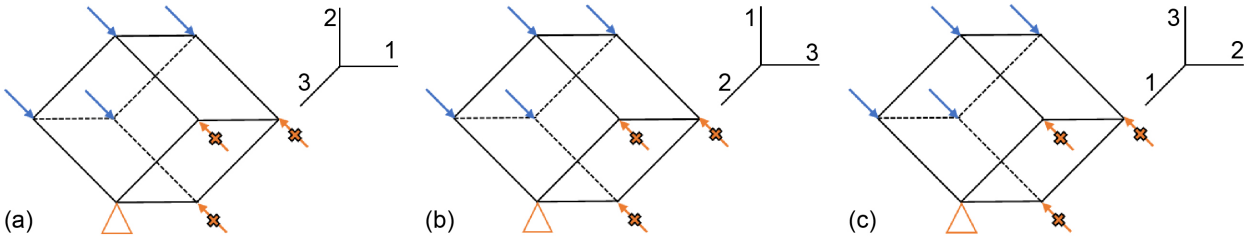

Figure B.46.—Applied loads and boundary conditions for single-element representations of three 45° off-axis compression orientations with principal material directions labeled. (a) 1–2 orientation. (b) 3–1 orientation. (b) 2–3 orientation.

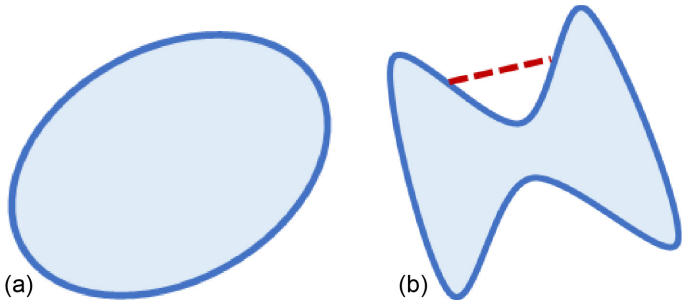

Figure B.47.—Examples of convex and nonconvex surfaces. (a) Convex. (b) Nonconvex; red dashed line indicates breach of convexity condition.

To track the evolution of the deformation response along each of the stress–strain curves, the effective plastic strain is chosen to be the tracking parameter. Using a numerical procedure based on the radial return method (Ref. 95) in combination with an iterative approach, the effective plastic strain is computed for each time/load step. The stresses for each of the tabulated input curves corresponding to the current value of the effective plastic strain are then used to compute the yield function coefficients. More information regarding the MAT213 deformation model can be found in Reference 1.

Additional features have been added to the original deformation model. Strain-rate effects have been incorporated by allowing users to define different stress–strain curves at various strain rates (Ref. 20). Similarly, users may also define different stress–strain curves at various temperatures. The local temperature rises that can occur during a dynamic event due to adiabatic heating can be calculated using the Taylor–Quinney coefficient (Refs. 21 and 22). Additionally, stochastic variation is now included, which allows users to vary input properties with user-defined probabilistic criteria (Ref. 22). However, these additional features of MAT213 were not incorporated in the current crash simulations.

B.7.2 Damage Model

The damage model in MAT213 enables the simulation of the prepeak stress stiffness reduction of composites as well as postpeak stress degradation. Simulating the prepeak stiffness reduction allows for the simulation of the nonlinear unloading (including a reduction in the average unloading modulus) observed in composites. The postpeak stress degradation allows for a gradual reduction in stresses following the maximum stress until a specified maximum strain is obtained. Prior experience has indicated that assuming composites fail in a brittle fashion immediately once the maximum stress is reached underpredicts the maximum strains that actually occur in a dynamic event. As shown in Figure B.48, the prepeak damage allows the user to effectively adjust the average stiffness of the unloading/reloading response. Conversely, incorporating postpeak damage allows the user to add strain-softening behavior after the peak load.

In the damage law formulation, strain equivalence is assumed, in which for every time step, the total, elastic, and plastic strains in the actual and effective (equivalent undamaged) stress spaces are the same. The utilization of strain equivalence permits the plasticity and damage calculations to be uncoupled, as all of the plasticity computations can take place in the effective stress space. To maintain a one-to-one relationship between the effective stresses and the actual stresses (i.e., to ensure that a uniaxial load in the actual stress space does not result in a multiaxial load in the effective stress space), a diagonal damage tensor is defined to relate the stresses in actual and effective stress spaces (Ref. 23).

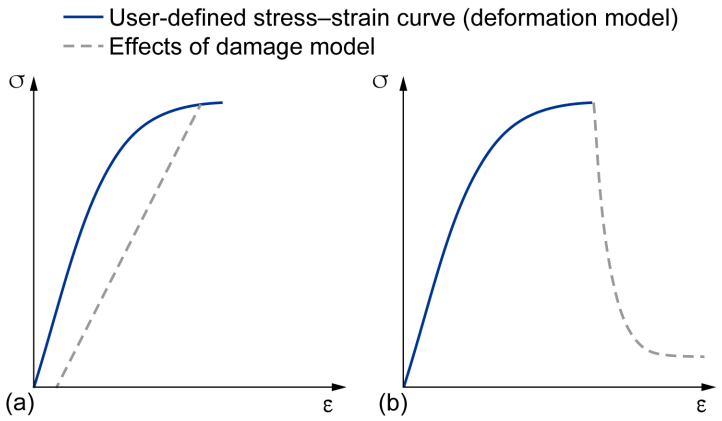

Figure B.48.—Effects of prepeak and postpeak damage; solid line indicates user-defined stress–strain curve (deformation model); dashed line shows effects of damage model. (a) Prepeak damage. (b) Postpeak damage.

The diagonal damage tensor is shown in Equation (B.26), where the M_{ij} terms are the diagonal damage terms and $0 \leq M_{ij} \leq 1$.

$$\begin{pmatrix} \sigma_1 \\ \sigma_2 \\ \sigma_3 \\ \sigma_4 \\ \sigma_5 \\ \sigma_6 \end{pmatrix} = \begin{bmatrix} M_{11} & 0 & 0 & 0 & 0 & 0 \\ 0 & M_{22} & 0 & 0 & 0 & 0 \\ 0 & 0 & M_{33} & 0 & 0 & 0 \\ 0 & 0 & 0 & M_{44} & 0 & 0 \\ 0 & 0 & 0 & 0 & M_{55} & 0 \\ 0 & 0 & 0 & 0 & 0 & M_{66} \end{bmatrix} \begin{pmatrix} \sigma_1 \\ \sigma_2 \\ \sigma_3 \\ \sigma_4 \\ \sigma_5 \\ \sigma_6 \end{pmatrix}_{eff} \tag{B.26}$$

An implication of a diagonal damage tensor is that loading the composite in a particular coordinate direction leads only to a stiffness reduction in the direction of the load due to the formation of matrix cracks perpendicular to the direction of the load. However, in actual composites, particularly those with complex fiber architectures, a load in one coordinate direction can lead to stiffness reductions in multiple coordinate directions. Furthermore, loading a composite in tension and/or compression can lead to a corresponding stiffness reduction in compression and/or tension. To maintain a diagonal damage tensor while still allowing for the damage interaction in at least a semicoupled sense, each term in the diagonal damage matrix should be a function of the total and plastic strains in each of the normal and shear coordinate directions. Note that total and plastic strains are chosen as the tracking parameters because, within the context of the developed formulation, the material nonlinearity during loading is simulated by use of a plasticity-based model (Ref. 23). The strains, therefore, track the current state of load and deformation in the material. As an example of how the M_{ij} terms are calculated, the expanded form of M_{11} (for plane stress) is shown in Equation (B.27):

$$M_{11} = \left(1 - d_1^1\left(\varepsilon_1^{PL}\right)\right)\left(1 - d_2^1\left(\varepsilon_1^{PL}\right)\right)\left(1 - d_4^1\left(\varepsilon_1^{PL}\right)\right) \tag{B.27}$$

The user-defined damage parameters (d), which are given by the user as tabulated values alongside strain values, are used in this calculation where the subscript indicates the load direction and the superscript defines the principal material direction affected by the damage (Ref. 23). As the computed strains in each of the coordinate directions evolve, the current values of the damage model parameters are

adjusted based on the strains. The input parameters and tables for the damage model are characterized through the use of a series of load/unload tests that are performed on the composite. Further information on the damage model can be found in References 22, 23, and 96.

B.7.3 Failure Model

The failure model determines when an element is eroded from the mesh. In the current implementation of MAT213, there are three failure models available: the Tsai–Wu model (Ref. 55), the Puck model (Ref. 97), and a generalized tabulated failure model (Refs. 98 and 99). The former models are based on well-established failure models commonly used for polymer composites. For the tabulated failure model, an approach is utilized in which a stress- or strain-based invariant is specified as a function of the location of the current stress state in stress space to define the initiation of failure (Ref. 98). This allows the geometrical failure surface to be reinterpreted as a single-valued analytical function, which can be implemented in a tabular fashion. The advantage of this approach is that failure surfaces can be defined with any arbitrary shape, unlike traditional failure models (e.g., Tsai–Wu and Puck) where the mathematical functions used to define the failure surface impose a specific shape on the failure surface.

B.7.4 MAT213 Material Card Parameters Description

A screenshot of the material card parameters used in the MAT213 card for the 0° plies is shown in Figure B.49. Although elastic properties are defined in the first two rows of the material card, these values are only used in the determination of the default time step. The constitutive behavior is defined as tabular data, which are referenced in the LT1 to LT12 curve inputs.

1	MID	RO	EA	EB	EC	PRBA	PRCA	PRCB
	1	1.473e-04	2.199e+07	1.370e+06	1.370e+06	0.0240000	0.0240000	0.4000000
2	GAB	GBC	GCA	KFAIL	AOPT	MACF		
	6.600e+05	3.672e+05	6.600e+05	1.000e-06	2.0000000	1		
3	XP	YP	ZP	A1	A2	A3		
	0.0	0.0	0.0	0.0	1.0000000	0.0		
4	V1	V2	V3	D1	D2	D3	BETA	
	0.0	0.0	0.0	-1.0000000	0.0	0.0	0.0	
5	H11	H22	H33	H12	H23	H13	H44	H55
	0.0100000	1.0000000	0.0	0.0	0.0	0.0	11.800000	0.0
6	H66	LT1	LT2	LT3	LT4	LT5	LT6	LT7
	0.0	1001	1002	0	1004	1005	0	1007
7	LT8	LT9	LT10	LT11	LT12	YSC	TEMP	DC
	0	0	1010	0	0	100	1.0000000	50
8	FTYPE	PFAIL	FV1	FV2	FV3	FV4	FV5	FV6
	3	100.000000	0.0	9013.0000	0.0	0.0	0.0	0.0
9	FV7	FV8	FV9	FV10	FV11	FV12		
	0.0	0.0	0.0	0.0	0.0	0.0		

Figure B.49.—MAT213 material card parameters for 0° plies.

Several other parameters in the material card are specific to MAT213. The YSC input points to a user-input table that lists the yield strains in each principal material direction, which defines the yield surface described in Equation (B.20). The H11 to H66 inputs define the nonassociated flow rule parameters described in Equation (B.21). The DC curve points to a user-input table that defines the damage parameters. The FTYPE parameter selects the failure model that controls element erosion, and FTYPE = 3 defines the strain-based generalized tabulated failure criterion (GTFC) model in MAT213. For shell elements, only FV2 is required for the GTFC model.

The stress–strain curves for the five principal material directions are shown in Figure B.50. These curves include information from the deformation, damage, and failure models of MAT213. For this model, only postpeak damage is utilized, so the deformation model determines the material behavior from zero load to peak stress. The GTFC failure strain was set to 0.24 in all directions for this model, which was selected based on calibration with experimental data.

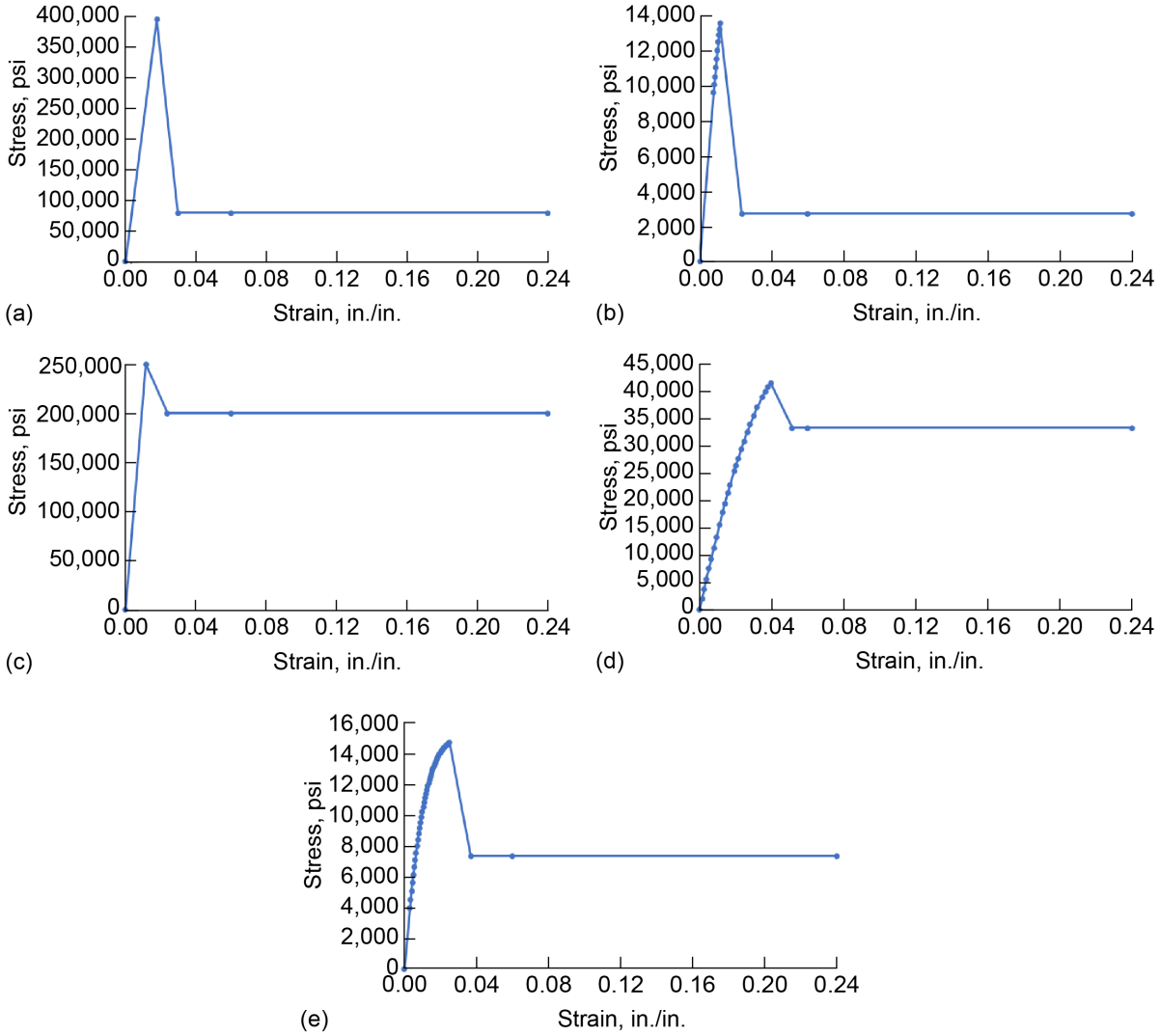

Figure B.50.—MAT213 stress–strain input curves including postpeak damage for shell elements. (a) 1-direction tension. (b) 2-direction tension. (c) 1-direction compression. (d) 2-direction compression. (e) 1–2 plane shear.

B.7.5 Predictive Simulation of Flat-Plate Specimen Model Using Laminate HL02

After the calibration of the flat-plate specimen model using laminate HL01, a second simulation was completed using the HL02 stacking sequence: $[90/45/0_2/90/-45/0_2]_S$. This simulation was considered predictive because the exact same model was used as the calibration case except that the stacking sequence of the plies was altered. The simulated force–displacement curve, as shown in Figure B.51, falls within the experimental scatter. The agreement found between the flat-plate simulations and the flat-plate crush experiments signified the conclusion of the calibration steps.

B.7.6 Drop Tower Simulation of C-Channel Specimen Using Laminate HL01

The simulated force–displacement curve of the C-channel simulation is shown in Figure B.52. The force–displacement curve does not have a discernible peak, which is probably related to the unrefined mesh in the trigger region. The mesh of the trigger region in the calibrated flat-plate models was refined and produced a notable peak force; however, the mesh was not refined for the C-channel models to reduce run times. The stable crushing region has a mean stable crushing force near 5,000 lbf. The simulation was stopped at a crush displacement of 1.6 in. to conserve computational resources for future runs.

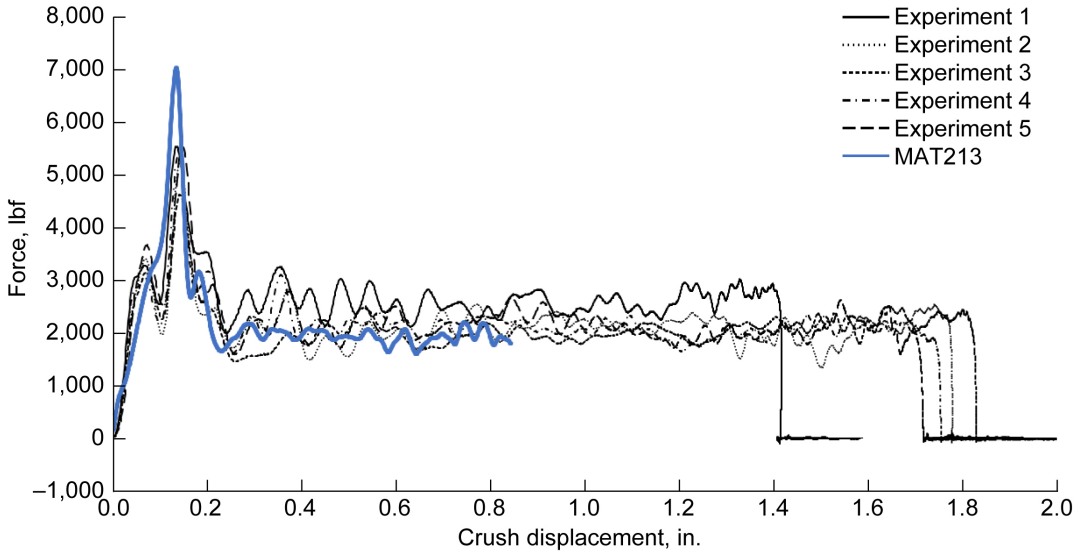

Figure B.51.—Force–displacement curve for MAT213 flat-plate crush simulation of HL02 filtered with low-pass Butterworth filter with cutoff frequency of 2,500 Hz. Five experimental replicates plotted for comparison.

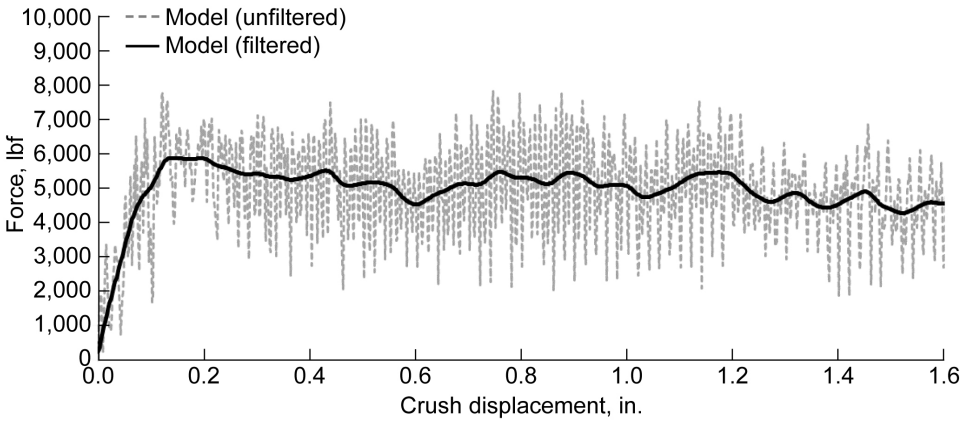

Figure B.52.—Simulated force–displacement curve for C-channel drop tower test.

B.8 LS–DYNA® MAT219 Material Model in Round Robin 3

This section contains supplementary information related to MAT219 material model formulation, simulation results of progressive fracture tests, and crushing simulation of C-channel composite structures subjected to impact loading conditions identical to those used for the crushing of flat coupons. This information supplements the Section 4.4 discussion of the MAT219 material model.

B.8.1 LS–DYNA® MAT219 Material Model Constitutive Equations

The current version of CODAM2, implemented as MAT219 in LS–DYNA®, is a physically based and yet simple continuum damage mechanics (CDM) approach that describes progressive damage evolution in fiber-reinforced composite laminates, as illustrated in Equations (B.28) to (B.33). Detailed descriptions and applications can be found in Reference 100. Damage is governed by equivalent strain functions. The longitudinal (fiber) equivalent strain ε_1^{eq} is taken to be equal to the longitudinal normal strain ε_{11}:

$$\varepsilon_1^{eq} = |\varepsilon_{11}| \tag{B.28}$$

while the transverse (matrix) equivalent strain ε_2^{eq} accounts for the interaction of transverse tensile and shear strains ε_{22} and γ_{12}, respectively, such that

$$\varepsilon_2^{eq} = \text{sign}(\varepsilon_{22})\sqrt{(\varepsilon_{22})^2 + \left(\frac{\gamma_{12}}{2}\right)^2} \tag{B.29}$$

Damage evolution is described by the damage variable ω_α for longitudinal ($\alpha = 1$) and transverse ($\alpha = 2$) directions. These damage variables describe linear softening and are functions of predefined damage initiation strains ε_α^i and damage saturation strains ε_α^s ($\alpha = 1,2$) such that

$$\omega_\alpha = \left(\frac{\left|\varepsilon_\alpha^{eq}\right| - \varepsilon_\alpha^i}{\varepsilon_\alpha^s - \varepsilon_\alpha^i}\right)\left(\frac{\varepsilon_\alpha^s}{\varepsilon_\alpha^{eq}}\right) \text{ for } \left(\left|\varepsilon_\alpha^{eq}\right| - \varepsilon_\alpha^i\right) > 0 \tag{B.30}$$

Stiffness reduction factors R_1 and R_2 in longitudinal and transverse directions, respectively, are defined as

$$R_\alpha = (1 - \omega_\alpha), \alpha = 1,2 \tag{B.31}$$

Applied to a laminate consisting of n sublaminates (layers), the constitutive behavior of each layer k is described by the effective in-plane secant stiffness matrix $\mathbf{Q}_k$ in the kth layer as

$$\mathbf{Q}_k = \frac{1}{D}\cdot\begin{bmatrix} R_1E_1 & R_1R_2\nu_{12}E_2 & 0 \\ & R_2E_2 & 0 \\ sym & & DR_2G_{12} \end{bmatrix} \tag{B.32}$$

where $D = 1 - (R_1R_2\nu_{12}\nu_{21})$ and E_1, E_2, and G_{12} are the elastic longitudinal, elastic transverse, and shear moduli, respectively, and ν_{12} is the major Poisson's ratio. The overall in-plane secant stiffness $\mathbf{A}$ of the laminate (consisting of n layers) is then given by

$$\mathbf{A} = \sum_{k=1}^{n} \mathbf{T}_k^T \mathbf{Q}_k \mathbf{T}_k t_k \tag{B.33}$$

with t_k being the thickness of the kth layer and $\mathbf{T}_k$ the corresponding transformation matrix to rotate the strain vector from principal material directions into global coordinates.

CODAM2 results in bilinear stress–strain responses in longitudinal (fiber) and transverse (matrix) directions, respectively. The area under each stress–strain curve is defined as the fracture energy density $g_{f^\alpha} = G_{f^\alpha}/l^*$, which relates to the ply-based fracture energy G_{f^α} and characteristic element length l^* according to Bazant's crack band method (Ref. 101).

B.8.2 Simulation Results of Progressive Fracture Tests

It is assumed that the influence of the material version (which results in different ply thicknesses) on the fiber fracture energies is negligible. The validity of this assumption will be verified when the full set of over-height compact tension (OCT) and compact compression (CC) test results for similar laminates made up of the thicker-plied material system becomes available. The dimensions and numerical models of OCT and CC specimens are shown in Figure 93. The force versus pin opening displacement curves of OCT and CC simulations are shown in Figure B.53. Based on these curves, the laminate fracture energy, G_f, can be calculated according to Equation (B.34):

$$G_f = \frac{\Delta W - \Delta U}{t\Delta a} \tag{B.34}$$

where W is total dissipated energy, U is elastic strain energy, t is laminate thickness (here, $t = 4$ mm), and Δa is the crack length measured at a specific instant of pin opening displacement. With the help of these simulations and experimental data, the ply-based fiber fracture energies in tension and compression, used as input data for the simulation model, were calibrated. It was found that $G^t_{f1} = 120$ kJ/m^2 and $G^c_{f1} = 80$ kJ/m^2 yield satisfactory correlations between simulations and experiments. The calibration process for OCT tests is presented in detail in Reference 30.

As shown in Figure B.53, CODAM2 does not include any plastic effects, which results in linear unloading without permanent deformation. This leads to lower energy evaluations ($\Delta W - \Delta U$) and hence lower dissipated energies compared to experiments where the force response shows nonlinear unloading.

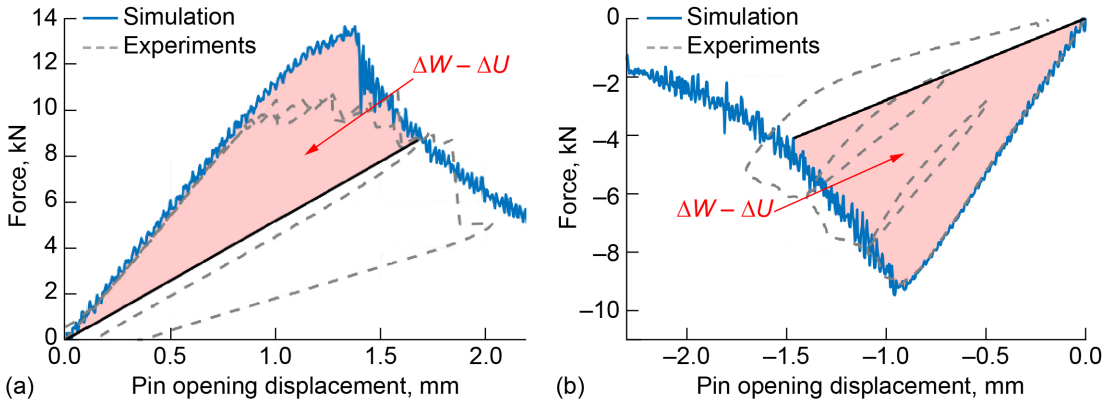

Figure B.53.—Comparison of experimentally measured and numerically predicted force versus pin opening displacement curves of OCT and CC fracture tests. (a) OCT fracture tests. (b) CC fracture tests.

B.8.3 Simulation Results of Progressive Crushing of C-Channel

Figure B.54 shows the unfiltered force versus displacement response for the quasistatic and two dynamic load cases with different initial velocities applied to the impact plate. The required quantities for crush characterization are listed in Table B.10. It can be seen that the higher initial velocity of 7.62 m/s (300 in./s) leads to a crush distance of 67.1 mm, which is 4 times higher than the crush distance predicted by the simulation with initial velocity of 3.81 m/s (150 in./s). Average crush forces and hence Stable SEA values are consistent in all three load cases. The predicted Stable SEA value is 36.0 kJ/kg, which is 18 percent lower compared to values obtained from the flat coupon analysis for the hard laminates. The load cases differ in predicting peak forces.

The quasistatic load case and that of the low initial velocity (3.81 m/s) yield a peak force of 79 kN, whereas the higher initial velocity (7.62 m/s) results in a lower peak force of 61 kN. Therefore, the crush efficiency of 0.30 is higher in this case compared with the quasistatic and low-initial-velocity simulations. Peak force values (and hence crush efficiency) highly depend on the configuration of the crush trigger. The predicted force response for the three cases is shown in Figure B.54.

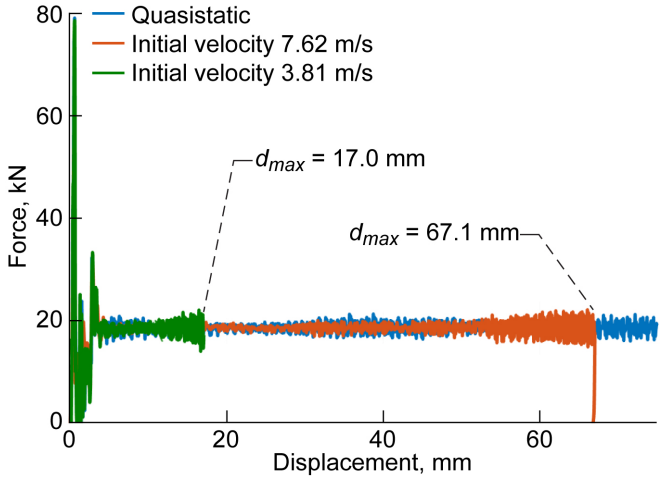

Figure B.54.—Simulation results of C-channel crushing response of hard laminates subjected to one quasistatic and two dynamic load cases. Maximum displacement, d_{max}.

TABLE B.10.—SUMMARY OF PREDICTIONS FROM CRUSH SIMULATION OF C-CHANNEL STRUCTURES

	Quasistatic simulation with constant velocity of 3.81 m/s	Drop-test simulation with initial velocity of 3.81 m/s	Drop-test simulation with initial velocity of 7.62 m/s
Crush distance, mm	----	17.0	67.1
Peak crush force, kN, unfiltered	79.1	78.5	61.5
Avg. crush force, kN	18.6 (5 mm ≤ d ≤ 70 mm)	18.6 (5 mm ≤ d ≤ 15 mm)	18.6 (5 mm ≤ d ≤ 60 mm)
Stable SEA, kJ/kg	36.0	36.0	36.0
Crush efficiency	0.23	0.23	0.30

Predictions of the C-channel crushing show similar trends compared to results from flat coupon crush simulations with respect to SEA. Therefore, we believe that the predicted Stable SEA values for the C-channel crushing of hard laminates are reasonable yet conservative. The relatively low Stable SEA values lead to the prediction of crush distances that are likely to be higher than experimentally measured values. Moreover, consistent results are obtained throughout all levels of the building block. This indicates that intralaminar material properties could be validated virtually by means of simple and computationally efficient single-element analyses.

B.9 LS–DYNA® MAT261 Material Model in Round Robin 3: Material Card

Section 4.5 describes the use of MAT261 for composite crush and crashworthiness simulations. The MAT261 material card is shown in Figure B.55, where LCSS 109 is a nonlinear shear stress–strain load curve from typical in-plane shear tensile load tests. The AOPT material axis is set to define the local fiber x-axis in the z-direction, as the coupon is oriented for edge-on crushing in the z-direction.

B.10 LS–DYNA® MAT297 Material Model in Round Robin 3

This section supplements the Section 4.6 discussion of the MAT297 material model.

B.10.1 Input Material Properties for LS–DYNA® MAT297

Table B.11 gives mechanical properties for orthotropic materials, and Table B.12 gives common parameters for crash simulation composite models. Table B.13 gives parameters for the prefailure submodel of the Ladevèze model.

```
$---------------------------------------------------------------------------
$ 0 Degree
*MAT_LAMINATED_FRACTURE_DAIMLER_PINHO
$      MID        RO         EA         EB         EC       PRBA       PRCA       PRCB
       101  1.45E-04  21990000.   1370000.   1370000.      0.024      0.024      0.400
$      GAB        GBC        GCA       AOPT        DAF        DKF        DMF        EFS
    660000.    367200.    660000.        2.0        0.0        0.0        0.0     -0.050
$       XP         YP         ZP         A1         A2         A3
                                         0.0        0.0        1.0
$       V1         V2         V3         D1         D2         D3       BETA
       0.0       0.00   1.000000        0.0        1.0        0.0        0.0
$   ENKINK        ENA        ENB        ENT        ENL
     348.0     1170.0      1.850      4.440      4.440
$       XC         XT         YC         YT         SL
    249940.    362690.    41590.     13640.    14155.0
$      FIO        SIGY       LCSS       BETA        PFL       PUCK       SOFT
       53.        8875.        109        0.0        70.        1.0       0.50
$---------------------------------------------------------------------------
```

Figure B.55.—MAT261 material card used in flat coupon crush simulations.

TABLE B.11.—MECHANICAL PROPERTIES
FOR ORTHOTROPIC MATERIALS

Density, RO, g/cm^3	1.57
Longitudinal tensile modulus, E1T, GPa	184.2
Longitudinal compressive modulus, E1C, GPa	152.6
Transverse direction tensile modulus, E2T, GPa	8.9
Transverse direction compressive modulus, E2C, GPa	10.0
Shear modulus: 12-plane, G12, GPa	4.69
Shear modulus: 23-plane, G23, GPa	5.03
Shear modulus: 13-plane, G13, GPa	5.03
Poisson's ratio: 12-plane, PR12	0.27
Poisson's ratio: 23-plane, PR23	0.013
Poisson's ratio: 13-plane, PR13	0.013
Longitudinal tensile strength, X1T, GPa	2.50
Longitudinal compressive strength, X1C, GPa	1.714
Transverse tensile strength, X2T, GPa	0.064
Transverse compressive strength, X2C, GPa	0.285
Shear strength, 12-plane, XS, GPa	0.110

TABLE B.12.—PARAMETERS COMMON IN
COMPOSITE MODELS FOR CRASH SIMULATION

Strain at longitudinal tensile strength, E1TPK	0.016
Strain at longitudinal compressive strength, E1CPK	0.011
Strain at transverse tensile strength, E2TPK	0.013
Strain at transverse compressive strength, E2CPK	0.029
Strain at shear strength, 12-plane, ESPK	0.3
Residual longitudinal tensile strength, RES1T, GPa	0.12 (5%)
Residual longitudinal compressive strength, RES1C, GPa	0.852 (50%)
Residual transverse tensile strength, RES2T, GPa	0.006 (5%)
Residual transverse compressive strength, RES2C, GPa	0.142 (50%)
Residual shear strength, 12-plane, RESS, GPa	0.11 (100%)
Softening reduction factor for strength in the crush front, SOFT	0.9
Softening for fiber tensile strength after compressive failure, FBRT	1.0
Value of equivalent strain at element erosion, EPSMAX	Not available
Value of strain component ε_1 at element erosion, ElDELE	0.5
Value of strain component ε_2 at element erosion, E2DELE	0.9
Value of strain component γ at element erosion, E4DELE	0.9
Ratio of reversible strain to total strain for ε_1, RATIO1	0.2
Ratio of reversible strain to total strain for ε_2, RATIO2	0.2
Ratio of reversible strain to total strain for γ, RATIO1	0.5

TABLE B.13.—PARAMETERS FOR PREFAILURE SUBMODEL OF LADEVÈZE MODEL

Damage initiation point under longitudinal tensile load, Y1O, $\sqrt{\text{GPa}}$	0.117
Ending point of Ladevèze model under longitudinal tensile load, Y1C, $\sqrt{\text{GPa}}$	0.651
Damage initiation point under longitudinal compressive load, Y1OC, $\sqrt{\text{GPa}}$	0.088
Ending point of Ladevèze model under longitudinal compressive load, Y1CC, $\sqrt{\text{GPa}}$	0.392
Damage initiation point under transverse tensile load, Y2O, $\sqrt{\text{GPa}}$	0.013
Ending point of Ladevèze model under transverse tensile load, Y2C, $\sqrt{\text{GPa}}$	0.076
Damage initiation point under transverse compressive load, Y2OC, $\sqrt{\text{GPa}}$	0.031
Ending point of Ladevèze model under transverse compressive load, Y2CC, $\sqrt{\text{GPa}}$	0.256
Damage initiation point under shear load, Y12O, $\sqrt{\text{GPa}}$	0.01
Ending point of Ladevèze model under shear load, Y12C, $\sqrt{\text{GPa}}$	0.32
Plasticity parameters, threshold stress, R0, GPa	0.03
Plasticity parameters, exponent in strain hardening law, M	0.49
Plasticity parameters, index in strain hardening law, BETA1, GPa	0.25

B.10.2 Damage Parameter Definitions for LS–DYNA® MAT297

Damage parameters for MAT297 are defined in Equations (B.35) and (B.36). Damage variable d is related to damage force Y by the following expression:

$$d = \frac{Y - Y_0}{Y_c} \tag{B.35}$$

where Y can be determined from experimentally measured strength σ,

$$Y = \frac{\sigma}{(1-d)(2E)^{1/2}} \tag{B.36}$$

and Y_0 and Y_c are material parameters to be determined from experiments as detailed in Reference 12. Following the same approach, the damage laws in MAT297 are written as

$$d_1 = \frac{\langle Y_1 - Y_{10T/C} \rangle +}{Y_{1cT/C}} \text{ if } d_1 < 1 \tag{B.37}$$

$$d_2 = \frac{\langle Y_2 - Y_{20T/C} \rangle +}{Y_{2cT/C}} \text{ if } d_2 < 1 \tag{B.38}$$

$$d_{12} = \frac{\langle Y_{12} - Y_{120} \rangle +}{Y_{12c}} \text{ if } d_{12} < 1 \tag{B.39}$$

where subscript *T/C* denotes separate values for tension and compression.

The irreversible strain is only considered in the shear direction through a strain-hardening plasticity law

$$R = R_0 + \beta_1 (\varepsilon_p)^m \tag{B.40}$$

where R_0 is the threshold stress for plasticity, β_1 and m are the strain hardening parameters. In the postfailure submodel, the damage evolution law follows an exponential expression as

$$d = 1 + \left(d_f - 1\right) e^{\frac{1}{m}\left(1 - \left(\frac{\varepsilon}{\varepsilon_f}\right)^m\right)} \tag{B.41}$$

where d_f and ε_f are the damage and strain at the peak load, respectively; m is computed internally. The irreversible strain is considered in the postfailure submodel through a user-defined ratio $eratio_i = d\varepsilon_{i\_\text{reversible}} / d\varepsilon_{i\_\text{total}}$.

MAT297 employs a set of simplified Hashin criteria, similar to the criteria used by Matzenmiller et al. (Ref. 102), as the initial failure criteria:

Longitudinal direction:

$$\left(\frac{\sigma_1}{X_{1t,1c}}\right)^2 - 1 \begin{cases} \geq 0 & \text{Failure} \\ \leq 0 \end{cases} \tag{B.42}$$

Transverse and shear direction:

$$\left(\frac{\sigma_2}{X_{2t,2c}}\right)^2 + \left(\frac{\tau}{X_s}\right)^2 - 1 \begin{cases} \geq 0 & \text{Failure} \\ \leq 0 \end{cases} \tag{B.43}$$

MAT297 has two options for element deletion. Elements are eroded when one of the following two conditions is met:

$$\varepsilon_1 = E1DELE, \text{ or } \left(\frac{\varepsilon_2}{E2DELE}\right)^2 + \left(\frac{\gamma}{E4DELE}\right)^2 = 1 \tag{B.44}$$

$$\sqrt{\frac{2}{3}\left[\left(\frac{\varepsilon_1}{E1DELE}\right)^2 + \left(\frac{\varepsilon_2}{E2DELE}\right)^2 + \left(\frac{\gamma}{E4DELE}\right)^2\right]} = EPSMAX \tag{B.45}$$

B.10.3 C-Channel Crush Simulation Force–Displacement Results

The force–displacement curves are presented in Figure B.56. For the two cases with an initial velocity, the simulation was terminated after the platen had rebounded. Figure B.57 shows the case of v_0 = 7.62 m/s (300 in./s). The crush distance increased, and the velocity decreased over time. The velocity reached zero at time = 8.8 ms. A maximum crush distance of 29.5 mm occurred at this instant. The value then reduced slightly. The mean crush force and the SAE were determined between 10 mm and the maximum crush distance (or a crush distance of 30 mm). For v_0 = 3.81 m/s (150 in./s), the crush distance was 7.7 mm, which is less than 10 mm, and therefore the mean crush force and the SAE were not calculated.

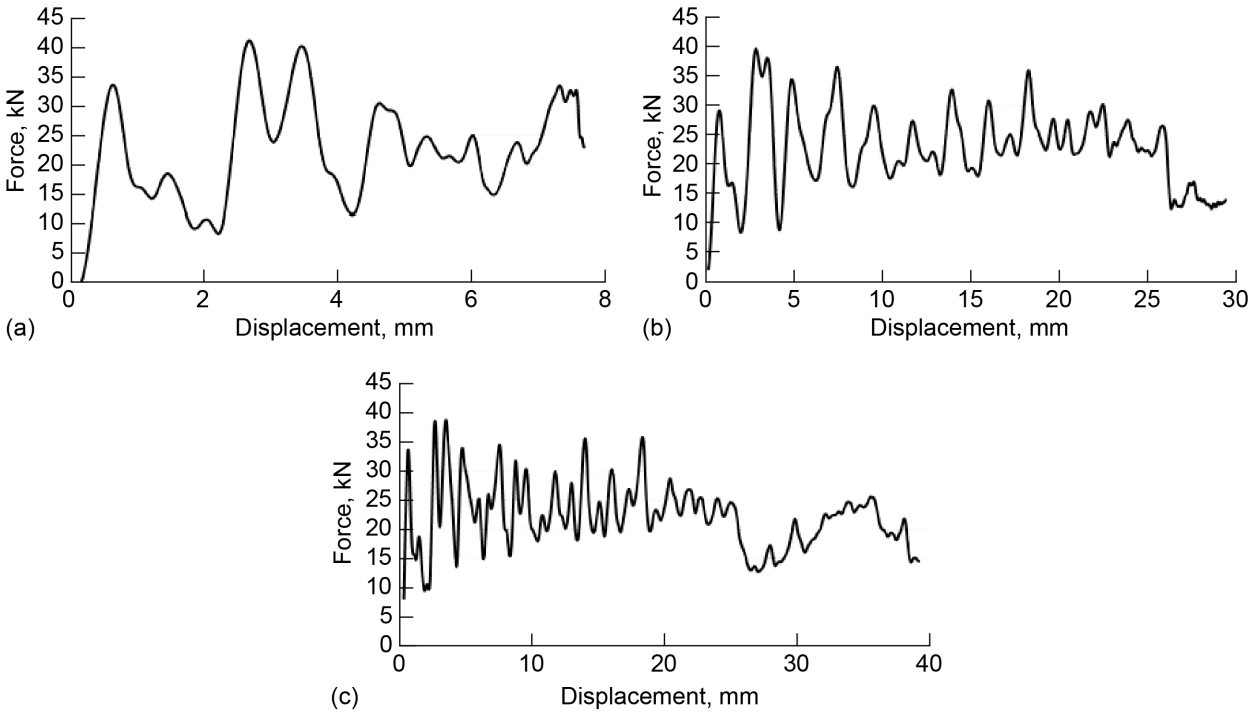

Figure B.56.—Force–displacement curves of C-channel crush at various velocities obtained by simulations, filtered with SAE 3000. (a) Initial velocity v_0 = 3.81 m/s (150 in./s). (b) Initial velocity v_0 = 7.62 m/s (300 in./s). (c) Initial velocity v_0 = 3.81 m/s (150 in./s).

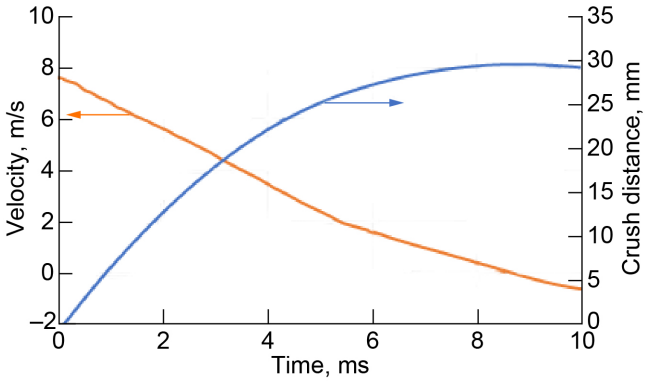

Figure B.57.—C-channel crush at initial velocity v_0 of 7.62 m/s (300 in./s).

B.11 LS–DYNA® Modified Ladevèze Material Model in Round Robin 3

This section supplements the Section 4.7 discussion of the modified Ladevèze mesomodel. Following the works of Allix and Ladevèze (Ref. 103), a bilinear interface model, modified Ladevèze (as documented by Rajaneesh et al. (Ref. 36)), was coded in LS–DYNA®. The interface damage (d_I) was governed by equivalent thermodynamic force ($Y_{EQ,I}$) as shown in Figure B.58 to achieve a bilinear traction–separation law. Delamination between the plies was modeled using cohesive interface elements. Interface failure strengths were regularized using the methodology proposed by Turon et al. (Ref. 104). Determination of deformation-gradient-based element erosion criteria was used. The effect of interface angle was accounted for by varying interface fracture toughness values in mode II. Interface fracture toughness values and their dependency on the interface angle as reported in References 78, 79, 82, and 83 were used. This led to a

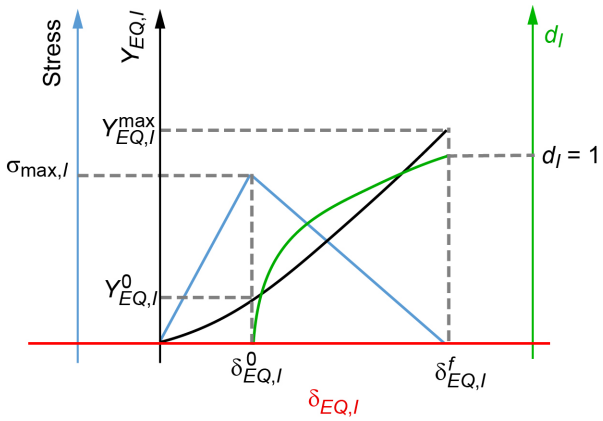

Figure B.58.—Bilinear interface model.

fracture toughness in mode I G_{Ic} of 0.22 kJ/m^2, as provided in Section 5.3.1, and was reported to be independent of interface angle. However, mode II fracture toughness G_{IIc} was reported to strongly depend on the interface angle.

B.12 ABAQUS® Ladevèze: ABQ_DLR_UD Material Model in Round Robin 3

This section supplements the Section 4.8 discussion of the DLR material model ABQ_DLR_UD.

B.12.1 Material Model Description

The DLR material model ABQ_DLR_UD is implemented as user material in ABAQUS®/Explicit (VUMAT subroutine). ABQ_DLR_UD is a mesoscale, plane-stress ply damage model in the CDM framework that captures the intralaminar damage and failure in unidirectional-fiber-reinforced polymers. Stiffness degradation and energy dissipated during the damaging process are captured by damage variables and damage evolution laws. The material model is based on a lamina-level modeling approach for stiffness and strength and uses intralaminar fracture toughness test data for damage propagation in the fiber direction as well as cyclic coupon test data for plasticity and damage propagation in the transverse and shear directions.

The elementary ply is assumed to be homogeneous and orthotropic and is represented by its two basic constituents: fiber and matrix. Fiber damage is based on fracture mechanics where tensile and compressive loading is assumed to be linear elastic until a maximum stress criterion is reached and damage initiates. The fiber damage threshold is defined as

$$F_i = \frac{\sigma_{11}}{X_{T/C}} \tag{B.46}$$

Damage evolution is described using an exponential softening law considering the fiber fracture energies in tension and compression. The scalar damage parameter is defined as

$$d_1 = 1 - \frac{\varepsilon_1^i \exp\left(\Phi\left(\varepsilon_1^i - \varepsilon_{11}\right)\right)}{\varepsilon_{11}} \text{ with } \Phi = \frac{2(1-k)}{\frac{2g_1^f}{X_{T/C}} - \varepsilon_1^i} \tag{B.47}$$

where $\varepsilon_1^i = E_1^{T/C} \big/ X_1^{T/C}$ is the damage initiation strain and $g_1^f = G_1^{T/C} \big/ l^*$ is the fracture energy density that relates the fiber fracture energy $G_1^{T/C}$ to the characteristic length l^* of the FEs.

Additional fiber softening options based on fiber fracture energies are implemented in the material model. Those options contain linear softening, the transition from exponential or linear softening into a constant residual stress plateau, as well as brittle failure after reaching maximum stress with subsequent constant residual stress plateau. In the scope of this work, the exponential softening law from Equation (B.47) is used.

Matrix damage under transverse tension and shear loading, as well as plasticity, are based on the theories originally defined by Ladevèze and LeDantec (Ref. 12) and slightly modified by Schueler et al. (Ref. 105). Transverse tension and in-plane shear damage are governed by energy release rate functions Y_2 and Y_{12}, respectively, such that

$$Y_2 = \frac{\langle \sigma_{22} \rangle^2}{2E_2 (1 - d_2)^2} \tag{B.48}$$

$$Y_{12} = \frac{\tau_{12}^2}{2G_{12} (1 - d_{12})^2} \tag{B.49}$$

The evolution of damage due to matrix microcracking and fiber/matrix debonding is based on experimental findings in which Ladevèze and LeDantec introduced the quantities $\underline{Y}$ and $\underline{Y}_2$ as

$$\underline{Y} = \sup_{\tau \le t} \left(\sqrt{Y_{12}(\tau) + b Y_2(\tau)} \right) \tag{B.50}$$

$$\underline{Y}_2 = \sup_{\tau \le t} \left(\sqrt{Y_2(\tau)} \right) \tag{B.51}$$

where the parameter b couples transverse tension and shear loading. The evolution laws for transverse tension and shear damage are then defined as

$$d_2 = \begin{cases} \dfrac{\langle \underline{Y} - Y_{20} \rangle}{Y_{2c}}, \; d_2 < d_{2\max}, \underline{Y} < Y_{12s}, \text{and } \underline{Y}_2 < Y_{2s} \\ d_{2\max}, \text{else} \end{cases} \tag{B.52}$$

and

$$d_{12} = \begin{cases} \dfrac{\langle \underline{Y} - Y_{120} \rangle}{Y_{12c}}, \; d_{12} < d_{12\max}, \; \underline{Y} < Y_{12s}, \text{ and } \underline{Y}_2 < Y_{2s} \\ d_{12\max}, \text{else} \end{cases} \tag{B.53}$$

The failure threshold parameters Y_{2s} and Y_{12s} control brittle failure of the matrix/fiber interface whereas progressive damage propagation is governed by Y_{20}, Y_{2c}, Y_{120}, and Y_{12c}.

Matrix damage under transverse compressive loading is not included in the formulations of Ladevèze and LeDantec (Ref. 12). In the ABQ_DLR_UD model, a maximum stress criterion for transverse compressive loading with subsequent failure is implemented with the failure transverse compressive threshold defined as

$$F_2 = \frac{\sigma_{22}}{Y_c} \tag{B.54}$$

To model plasticity due to internal friction of permanent transverse and shear strains, a plasticity law, also based on the work of Ladevèze and LeDantec (Ref. 12), is introduced in ABQ_DLR_UD with an elastic domain function f and the hardening law $R(p)$ such that

$$f = \sqrt{\tilde{\tau}_{12}^2 + \alpha^2 \tilde{\sigma}_{22}^2} - R(p) - R_0 \text{ with } R(p) = \beta p^{\mu} \tag{B.55}$$

with $\tilde{\tau}_{12}$, $\tilde{\sigma}_{22}$ (both tensile and compressive) being the effective stresses, α the material-dependent plasticity coupling parameter, and R_0 the yield stress. The isotropic hardening law, $R(p)$, is a function of the effective plastic strain p, a scaling factor β, and the exponent μ.

B.12.2 Simulation of Progressive Crushing: C-Channel Crush Test Analysis

The analysis teams were tasked to simulate the C-channel crush response for two hard laminates selected from the set of layups previously tested with the flat crush coupons:

- Layup 1 with the stacking sequence $[90_2/0_2/\pm45/0_2]_S$
- Layup 2 with the stacking sequence $[90/45/0_2/90/-45/0_2]_S$

The two stacking sequences correspond to the layups HL01 and HL02 of the previously presented flat coupon simulations. The C-channel specimens were tested quasistatically, as well as in drop tests with different initial velocities of 3.81 m/s (150 in./s) and 7.62 m/s (300 in./s) using a drop mass of 39.92 kg (88 lb).[21] With the platen mass for the C-channel test assumed identical to that of the flat coupon crush test, we can analytically compare the crush energy absorption behavior of the two specimen geometries at a given impact energy level. In addition to a drop mass of 39.92 kg applied in the simulations for both initial velocities, a separate simulation was performed applying a constant impact plate velocity of 3.81 m/s. The following properties were identified as responses of the C-channel simulation models:

- Crush distance
- Peak crush force
- Average crush force
- Stable SEA
- Crush force efficiency

B.12.2.1 Simulation of C-Channel Crush Test for HL01 $[90_2/0_2/\pm45/0_2]_S$

The simulation results for HL01 with stacking sequence $[90_2/0_2/\pm45/0_2]_S$ for different initial impact plate velocities are shown in Figure B.59. The results are presented in terms of contact force versus displacement of the impact plate. The simulation results were filtered using a Butterworth low-pass filter with a cutoff frequency of 20 kHz without filtering out significant information in the force–displacement curve.

The peak crush forces for the three loading conditions are given in Table B.14. The peak force is highly influenced by setup-specific details and applied filtering measures. In the simulation with constant velocity, the maximum crush distance was selected to be 65 mm. In the drop test simulations, the crush distance was reached when the initial kinetic energy of the impact plate was entirely absorbed. The crush distances are given in Table B.15.

[21]As noted in Section 4.0, impactor mass for the C-channel crush test was incorrectly assumed to match that of the flat coupon; see Table 21 for correct values.

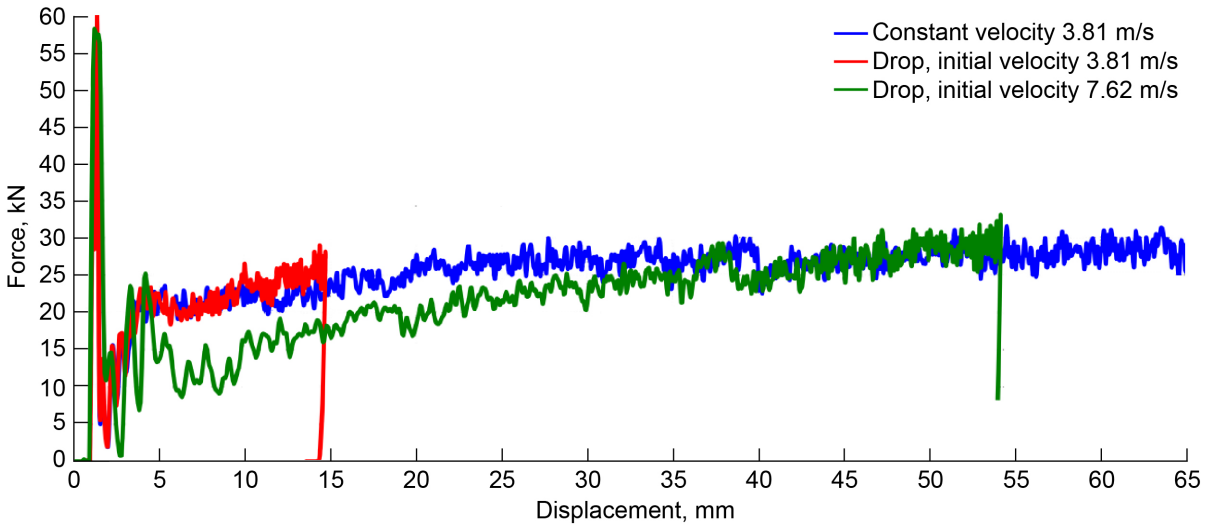

Figure B.59.—Force–displacement predictions for C-channel HL01 $[90_2/0_2/\pm45/0_2]_S$ crush simulations filtered with low-pass Butterworth filter with cutoff frequency of 20 kHz.

TABLE B.14.—SUMMARY RESULTS OF C-CHANNEL CRUSHING SIMULATION FOR HL01 $[90_2/0_2/\pm45/0_2]_S$

	Constant velocity of 3.81 m/s	Drop test with initial velocity of 3.81 m/s (drop mass 39.92 kg)	Drop test with initial velocity of 7.62 m/s (drop mass 39.92 kg)
Crush distance, mm	65	14.7	53.4
Peak crush force, kN	60	63	58
Average crush force, kN	26 (δ_f = 65 mm)	23 (δ_f = 14 mm)	18 (δ_f = 50 mm)
Stable SEA, kJ/kg (δ_i = 5 mm)	43 (δ_f = 25 mm) 46.5 (δ_f = 50 mm) 48.1 (δ_f = 65 mm)	38.4 (δ_f = 10 mm) 40.9 (δ_f = 14 mm)	25.6 (δ_f = 25 mm) 39.5 (δ_f = 50 mm)
Crush force efficiency	0.44	0.37	0.4

In Figure B.59, the three force–displacement curves show differences mainly between the two loading rates of 3.81 m/s (150 in./s) and 7.62 m/s (300 in./s). This behavior results in different average crush forces for the loading conditions, as seen in Table B.14. The average crush force is defined here as the mean force between 5 mm (δ_i) and the maximum displacement (δ_f). The Stable SEA, here based on δ_i = 5 mm, determined with the average crush force at maximum crush distance is 48.1 kJ/kg for the constant velocity, 40.9 kJ/kg for 3.81 m/s initial velocity, and 39.5 kJ/kg for 7.62 m/s initial velocity. Additional Stable SEA values based on crush distances smaller than the maximum displacement are given in Table B.14. The crush force efficiency is defined as the ratio of the average crush force to peak crush force and varies between 0.37 and 0.44, as shown in Table B.14.

To demonstrate the differences in force–displacement characteristics between the impact velocities, contour plots of the simulations are shown in Figure B.60, where ABAQUS® solution-dependent variable 6 (SDV6) indicates matrix damage. The contour plots show matrix damage at two states, directly after reaching the peak force and at a crush displacement of 14.7 and 14.5 mm, respectively. With an impact velocity of 3.81 m/s, a local damage zone develops after the initial impact. After crushing down this initial damage region and full development of the crush zone, at d_{crush} = 14.7 mm, the contour plot shows very localized damage, which can be identified as fragmentation crush mode. With 7.62 m/s initial velocity and hence a higher initial impact impulse, the initial cohesive interface failure is more distinct resulting in larger delamination.

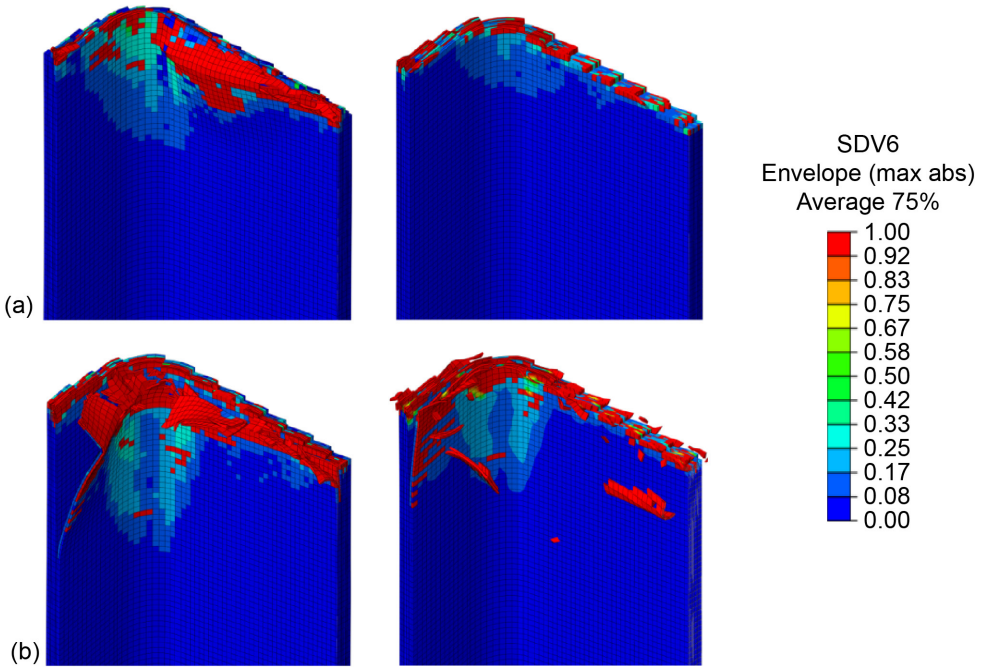

Figure B.60.—C-channel HL01 $[90_2/0_2/\pm45/0_2]_S$ crush simulations. SDV6 is ABAQUS® solution-dependent variable 6, matrix damage. Envelope plot of all plies showing absolute maximum value (max abs). (a) Impact velocity 3.81 m/s; directly after reaching peak force at 1.9 mm (left) and at crush displacement of 14.7 mm (right). (b) Impact velocity 7.62 m/s; directly after reaching peak force at 1.9 mm (left) and at crush displacement of 14.5 mm (right).

The delamination results in splaying of the shell layers and, consequently, in a lower force level compared to the simulation with 3.81 m/s impact velocity. Because the initial spread of delamination is not propagating farther, the crush failure mode continuously changes from splaying into fragmentation, reaching steady-state crushing at approximately 35 mm displacement and, with that, the same force level as obtained with 3.81 m/s impact velocity.

B.12.2.2 Simulations of C-Channel Crush Test for HL02 $[90/45/0_2/90/-45/0_2]_S$

The second investigated layup, HL02, has a stacking sequence of $[90/45/0_2/90/–45/0_2]_S$. The simulation results for different loading conditions are shown in Figure B.61. The force–displacement curves show trends similar to those obtained for the HL01 simulations. However, the crush force for the 7.62 m/s initial velocity remains below the force level for 3.81 m/s initial velocity for the entire crush distance. The prediction results for HL02 are summarized in Table B.15.

Contour plots of matrix damage in Figure B.62 show similar effects as identified for HL01. For HL02, the contour plot of the simulation with 7.62 m/s initial velocity shows more distinct initial delamination damage, which further grows in longitudinal direction and results in a larger extent of splaying compared to the simulation with HL01. This effect may explain that for HL02, the force level for 7.62 m/s initial velocity remains below the one for 3.81 m/s initial velocity for the entire crush distance.

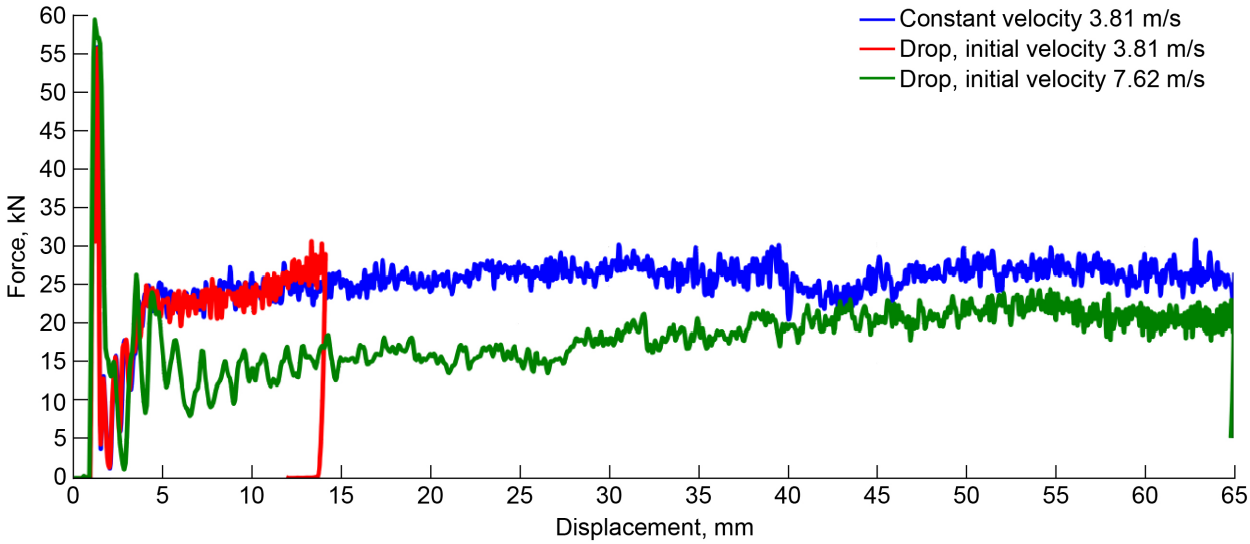

Figure B.61.—Force–displacement prediction for C-channel HL02 [90/45/0_2/90/–45/0_2]s crush simulations filtered with low-pass Butterworth filter with cutoff frequency of 20 kHz.

TABLE B.15.—SUMMARY RESULTS OF C-CHANNEL CRUSHING SIMULATION FOR HL02 [90/45/0_2/90/–45/0_2]s

	Constant velocity of 3.81 m/s	Drop test with initial velocity of 3.81 m/s (drop mass 39.92 kg)	Drop test with initial velocity of 7.62 m/s (drop mass 39.92 kg)
Crush distance, mm	65	14.1	65
Peak crush force, kN	56	56	59
Average crush force, kN	26 (δ_f = 65 mm)	25 (δ_f = 14 mm)	19 (δ_f = 60 mm)
Stable SEA, kJ/kg δ_i = 5 mm	45.7 (δ_f = 25 mm) 46.9 (δ_f = 50 mm) 47.7 (δ_f = 65 mm)	41.8 (δ_f = 10 mm) 44.0 (δ_f = 14 mm)	27.2 (δ_f = 25 mm) 33.0 (δ_f = 60 mm)
Crush efficiency	0.47	0.45	0.32

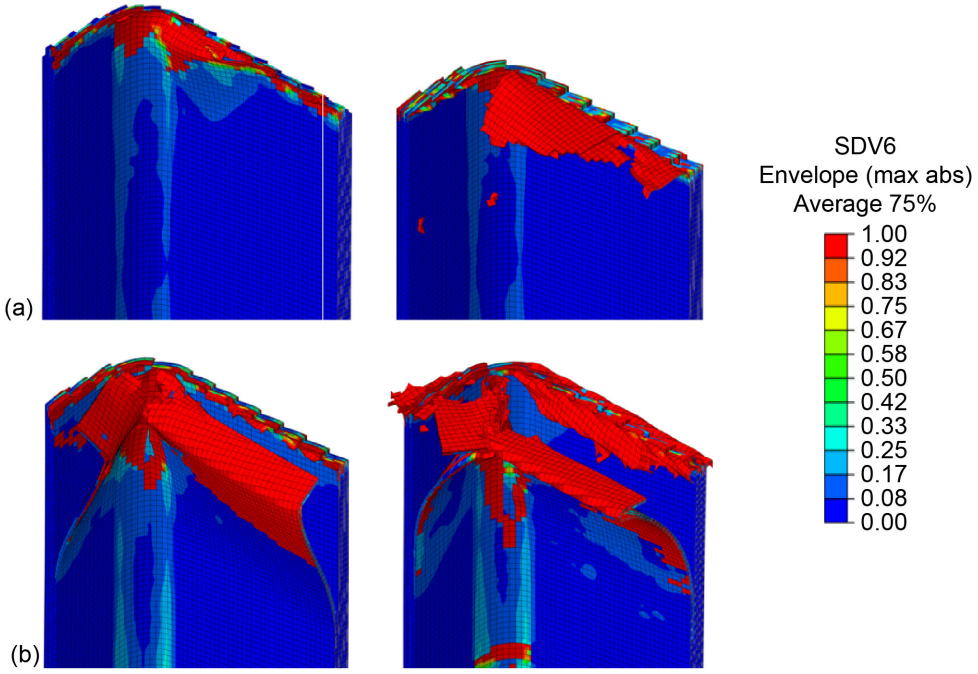

Figure B.62.—C-channel HL02 [90/45/0_2/90/–45/0_2]$_S$ crush simulations. (a) Impact velocity 3.81 m/s; results at crush displacements of 1.9 mm (left) and 12.9 mm (right). (b) Impact velocity 7.62 m/s; results at crush displacement of 3.8 mm (left) and 12.8 mm (right).

B.13 ABAQUS® CZone Analysis Method in Round Robin 3

This section supplements the Section 4.9 discussion of the ABAQUS®/Explicit CZone add-on.

B.13.1 Damping Properties

To acquire the damping properties for the IM7/8552 carbon/epoxy material, dynamic mechanical analysis (DMA) tests were performed at frequencies ranging from 0 to 200 Hz. The shear storage and shear loss modulus were measured as a function of frequency, as shown in Table B.16.

B.13.2 Shear Degradation Properties

Table B.17 presents the results and values implemented into the CZone material card (see Section 4.9.2).

B.13.3 Fracture Energy Release Rate Properties

To define the resistance of a composite material to crack propagation, Engenuity Ltd. uses compact tension (CT) and compact compression (CC) tests to define the fracture energy release rate (FERR) perpendicular to the fiber (translaminar) and parallel to the fiber, respectively. These values are then implemented into the VUMAT-defined user-material card, where the CZone code adjusts the total FERR proportionately to the crack direction and the laminate stacking sequence. Because crack propagation is dependent on the laminate stacking sequence, the direction of the crack growth, and the loading conditions, four different tests were performed to determine FERR values: a CT test parallel to the fiber (FERR T90), a CT test perpendicular to the fiber (FERR T0), a CC test perpendicular to the fiber (FERR C0), and a CC test parallel to the fiber (FERR C90). The results of the FERR testing are presented in Table B.18. Note, however, that for the analyses presented in this report, in order for the CZone model to run stably, the T0 value was increased to 11.73 lbf·in/in^2.

TABLE B.16.—IM7/8552 DAMPING PROPERTIES FROM DYNAMIC MECHANICAL ANALYSIS TESTING (REF. 47)

Frequency, Hz	Storage modulus, ksi	Loss modulus, ksi
0.10	1,303.2	31.3
0.16	1,305.6	27.9
0.25	1,309.6	26.4
0.40	1,314.1	25.5
0.63	1,319.7	24.5
1.00	1,324.7	23.9
1.60	1,329.4	23.6
2.50	1,333.8	23.4
3.00	1,336.3	23.3
6.30	1,342.0	23.1
10.00	1,346.6	23.2
15.80	1,350.7	23.6
25.00	1,354.4	25.3
39.80	1,356.9	26.2
63.00	1,357.5	28.3
100.00	1,347.4	31.5
158.00	1,243.2	48.3
200.00	1,453.2	180.6

TABLE B.17.—SHEAR PLASTICITY INPUT PARAMETERS FOR IM7/8552 USED IN CZONE INPUT

Shear stress at damage onset, ksi	5.96
Shear damage parameter	0.292
Maximum shear damage	1
Coefficient in hardening equation	567
Power term in hardening equation	0.402

TABLE B.18.—FRACTURE ENERGY RELEASE RATE (FERR) VALUES OF IM7/8552 USED IN CZONE INPUT (REF. 47)

	T90	T0	C0	C90
FERR, $(lbf \cdot in)/in^2$	1,268.62	4.05	324.63	283.64

B.13.4 CZone Simulation Validation

Figure B.63 compares the average crush force obtained from crush testing with the predictions from CZone simulations for both the unsupported (free) and pin-supported flat coupons. Average crush force results were nearly identical, which was expected, given that the CZone simulations used the average crush stress acquired from the experimental results as an input property.

Figure B.64 compares the calculated SEA obtained from crush testing with the predictions for the CZone simulation for both the unsupported and pin-supported flat coupons. Figure B.63 and Figure B.64 have nearly identical results because the SEA is proportionally related to the average crush force. The CZone simulation predicted a 51.6 kJ/kg SEA for the unsupported (free) coupon tests and a 51.7 kJ/kg SEA for the pin-supported coupon tests. The C-channel result shown in Figure B.65 was anticipated, as the C-channel is designed to crush rather than undergo catastrophic failure.

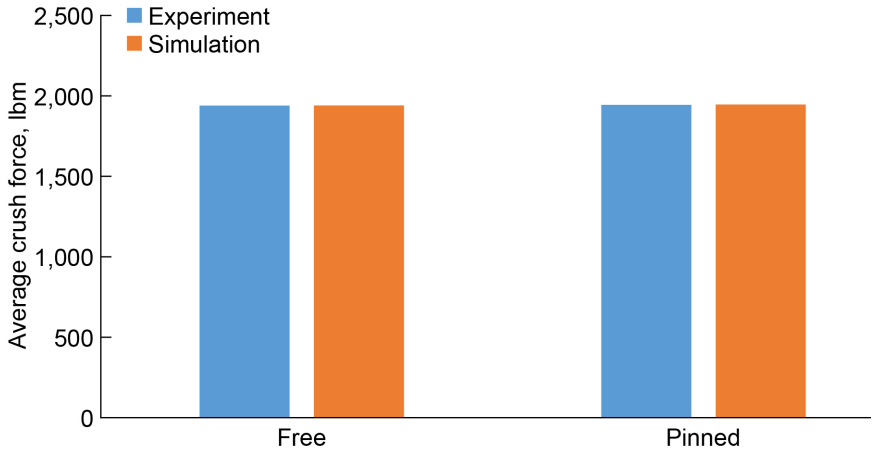

Figure B.63.—Comparison of average crush stress for flat coupon crush tests and CZone simulations.

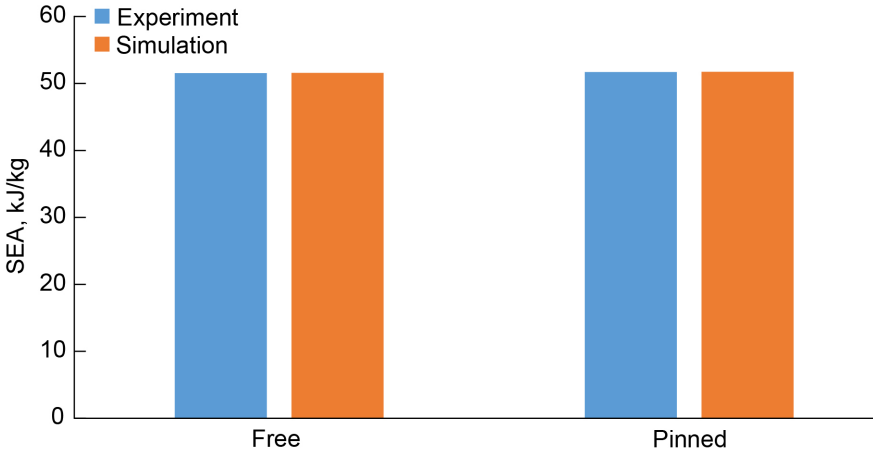

Figure B.64.—Comparison of SEA for flat coupon crush tests and CZone simulations.

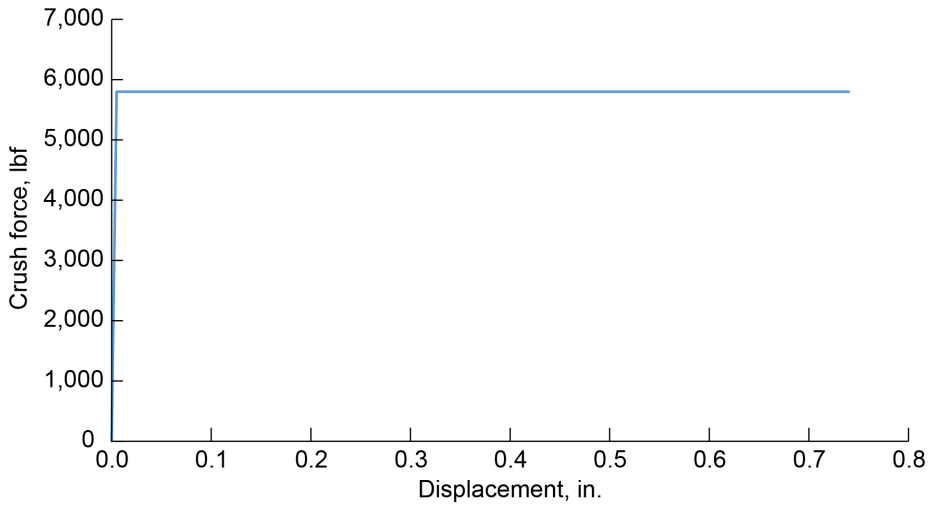

Figure B.65.—Simulated C-channel force–displacement response.

B.14 ESI VPS Waas–Pineda Implementation in Round Robin 3

This section provides a detailed description of the Waas–Pineda (WP) damage model discussed in Section 4.10. Additional details can be found in References 49 and 50.

B.14.1 Description of Numerical Model

In the WP damage model, the transition from the continuum state to the cohesive state is triggered by a quadratic failure criterion derived from experiments and defined by five threshold levels:

Fiber tensile:
$$\left(\frac{\sigma_{11}}{X_t}\right)^2 \geq 1 \text{ for } \sigma_{11} > 0 \tag{B.56}$$

Fiber compressive:
$$\left(\frac{\sigma_{11}}{X_c}\right)^2 \geq 1 \text{ for } \sigma_{11} < 0 \tag{B.57}$$

Matrix tensile:
$$\left(\frac{\sigma_{22}}{Y_t}\right)^2 + \left(\frac{\sigma_{12}}{Z}\right)^2 \geq 1 \text{ for } \sigma_{22} > 0 \tag{B.58}$$

Matrix compressive:
$$\left(\frac{\sigma_{22}}{Y_c}\right)^2 + \left(\frac{\sigma_{12}}{Z}\right)^2 \geq 1 \text{ for } \sigma_{22} < 0 \tag{B.59}$$

where X_t, X_c, Y_t, Y_c, and Z are the failure initiation stresses for the respective load directions.

In the cohesive state, the continuum equations are replaced using internal bilinear traction–separation formulations, allowing effective negative tangent stiffness in the damaging elements. Several damage modes are modeled individually using specific fracture energy quantities. The effects represented numerically include fiber rupture under tension and kinking under compression, matrix cracking and fiber–matrix debonding under tension, and matrix cracking under transverse compression and shear. In this stage, the virtual crack face separations are obtained from the element lengths along the directions of orthotropy:

$$\begin{cases} \delta_{11} = l_f \varepsilon_{11} \\ \delta_{22} = l_m \left(\varepsilon_{22} - \varepsilon_{22}^p \right) \\ \delta_{12} = 2 l_m \left(\varepsilon_{12} - \varepsilon_{12}^p \right) \end{cases} \tag{B.60}$$

where l_f and l_m are the projections of the element lengths along the two main axes of orthotropy. Tractions at the virtual crack faces are calculated using the cohesive stiffness $K_{ij} = \sigma_{ij}/\delta_{ij}$ and the damage is then governed by two internal scalars, for fiber and matrix cracks respectively:

$$\begin{cases} \sigma_{11} = (1 - D_1) K_{11} \delta_{11} \\ \sigma_{22} = (1 - D_2) K_{22} \delta_{22} \\ \sigma_{12} = (1 - D_2) K_{12} \delta_{12} \end{cases} \tag{B.61}$$

The evolution of damage is the conventional cohesive linear form between two limits:

$$D_1 = \frac{\delta_{11}^f \left(\delta_{11}^{\max} - \delta_{11}^0 \right)}{\delta_{11}^{\max} \left(\delta_{11}^f - \delta_{11}^0 \right)} \tag{B.62}$$

$$D_2 = \frac{\delta_m^f \left(\delta_m^{\max} - \delta_m^0 \right)}{\delta_m^{\max} \left(\delta_m^f - \delta_m^0 \right)} \tag{B.63}$$

Here, the matrix crack opening is defined as $\delta_m = \sqrt{(\delta_{22})^2 + (\delta_{12})^2}$, and the "max" superscripts indicate the maximum separation reached over time. The initial separation δ^0 is that found at the time of transition to cohesive state, while the final separation $\delta^f = 2G_c/\sigma^{\max}$ derives from the specified modal fracture energy.

Coupling between shear and transverse deformation requires the definition of one additional parameter, η, which is introduced in the definition of the mixed-mode transverse fracture energy and represents the Benzeggagh–Kenane exponent for mixed-mode formulation:

$$G_{cm} = G_{22c} + (G_{12c} - G_{22c}) \left(\frac{G_{12}}{G_{22} + G_{12}} \right)^{\eta} \tag{B.64}$$

Finally, note that both mode I and mode II fracture energies can be defined separately under tension and compression. Once the maximum prescribed degradation is reached, the elements enter a post-damage state to ensure a limitation in transferable stresses. The prescribed critical value $D_{\max} = (1 - \sigma_{ij}/\sigma^{\max})$ is unique and prescribed for all damage modes and it differs from the internal damage scalars used in the cohesive state.

B.14.2 Modeling Strategies and Ply Data

Table B.19 provides a summary of the IM7/8552 unidirectional material parameters described in Section 4.10.2, highlighting the description of each input as well as derivation methodology. Figure B.66 shows these data as they appear in the software material card. Cells highlighted in gray are unused or nonphysical inputs.

TABLE B.19.—MATERIAL PARAMETER DERIVATION CHART FOR IM7/8552 PLY 1 CARD AND WAAS–PINEDA DAMAGE

Parameter	Value	Property	Type	Measurement
E0t1	154.6 GPa	Axial tensile modulus	Experimental (CMH–17)	$[0]_N$ tension
E0t2	9 GPa	Transverse modulus	Experimental (CMH–17)	$[90]_N$ tension
E0t3	9 GPa	Out-of-plane modulus	Assumption	Equal to E0t2 modulus
E0c1	138.2 GPa	Axial compressive modulus	Experimental (NCAMP)	$[0]_N$ compression
NU12	0.316	Major Poisson's ratio 12	Experimental (CMH–17)	$[0]_N$ tension
NU23	0.3	Major Poisson's ratio 23	Assumption	NA
NU13	0.316	Major Poisson's ratio 13	Assumption	Equal to NU12
G012	4.7 GPa	In-plane shear modulus	Experimental (CMH–17)	$[+45/–45]_{NS}$ tension
G023	4 GPa	Transverse shear modulus	Assumption	NA
G013	4.7 GPa	Transverse shear modulus	Assumption	Equal to G012
R0	0.0325 GPa	Matrix shear yield stress	Experimental (DLR)	$[+45/–45]_{NS}$ tension
BETA	0.68 GPa	Plasticity multiplier	Experimental (DLR)	$[+45/–45]_{NS}$ tension
m	0.45	Plasticity power index	Experimental (DLR)	$[+45/–45]_{NS}$ tension
A	0.563	Plasticity transverse–shear coupling	Experimental (DLR)	$[+67.5/–67.5]_{NS}$ tension
VAR11	2.238 GPa	Axial tensile strength	Experimental (NCAMP)	$[0/90]_{2S}$ tension
VAR11C	1.716 GPa	Axial compressive strength	Experimental (NCAMP)	$[90/0/90]_S$ compression
VAR22	0.084 GPa	Transverse tensile strength	Experimental (NCAMP)	$[90]_N$ tension[a]
VAR22C	0.286 GPa	Transverse compressive strength	Experimental (NCAMP)	$[90]_N$ compression[a]
VAR12	0.118 GPa	In-plane shear strength	Experimental (NCAMP)	Short beam strength
ETA	3	Mixed-mode coupling	Assumption	From interlaminar tests
EFR11t	0.092 J/mm^2	Axial tensile fracture energy	Calibrated (UBC, NCAMP)	OCT, OHT tests
EFR11c	0.15 J/mm^2	Axial compressive fracture energy	Calibrated (UBC, NCAMP)	CC, OHC tests
EFR22t	0.015 J/mm^2	Transverse tensile fracture energy	Calibrated (UBC, NCAMP)	OCT, OHT tests[a]
EFR22c	0.03 J/mm^2	Transverse compressive fracture energy	Calibrated (UBC, NCAMP)	CC, OHC tests[a]
EFR12	0.03 J/mm^2	Shear fracture energy	Calibrated (UBC, NCAMP)	OHT, OHC, OCT, CC tests[a]
Dmax	0.7	Post-damage cutoff stress	Calibrated (UBC, NCAMP)	OCT, CC tests
EPSIslim	0.15	Elimination equivalent shear strain	Calibrated	NA

[a]Require additional calibration for numerical stability.

	PLY ITYP 1	-	Unidirectional composite global ply model					
1	IDPLY	ITYP	RHO	FAILINP				
	IM7/8552	1	1.55E-6	*1*				
2	E0t1	E0t2	E0t3	NU23	NU13			
	154.6	9	9	0.3	0.316			
3	G012	G023	G013	NU12	KAPPA23	KAPPA13	ISHD	ITRD
	4.7	4.	4.7	0.316				
4	Yc	Y0	Ycp	Y0p	b	Ysp	Yr	Dmax
5	EPSIfti	EPSIftu	Dftu	Dsat1	Dsat2	Ycpc	Y0pc	Yspc
6	IFUNd1	IFUNd2	IFUNd2c	Dsat2c				
7	E0c1	GAMMA	EPSIfci	EPSIfcu	Dfcu	IBUCK		
	138.2							
8	R0	BETA	m	A				
	0.0325	0.68	0.45	0.563				
11	FAILDAM	FAILTYP						
	1	11						
12	IFL11	VAR11	VAR11C	IFL22	VAR22	VAR22C	VAR12	ETA
	0	2.5	1.716	*0*	0.064	0.286	0.095	3
13	EFR11t	EFR11c	EFR22t	EFR22c	EFR12	Dmax	EPSIslim	Ifelim
	0.092	0.15	0.015	0.03	0.015	0.7	0.15	*1*

Figure B.66.—PLY 1 material card implemented for IM7/8552 unidirectional ply (VPS2020).

TABLE B.20.—MATERIAL PARAMETER DERIVATION CHART FOR IM7/8552 DELAMINATION INTERFACE FOR MAT303

Parameter	Value	Property	Type	Measurement
hcont	–0.01	Height for kinematics	Calibrated	DCB, ENF tests
E0	9 GPa	Modulus for mode I cohesive stiffness	Assumption	From transverse tensile test
G0	4.7 GPa	Modulus for mode II cohesive stiffness	Assumption	From in-plane shear test
ETA	3	Benzeggagh–Kenane mixed-mode exponent	Experimental[a]	MMB tests
SIGMApr	0.064 GPa	Mode I propagation stress	Calibrated	Matrix tensile failure
GAMMApr	0.095 GPa	Mode II propagation stress	Calibrated	Matrix shear failure
EFRAC1	0.00028 J/mm^2	Mode I fracture toughness	Experimental (CMH–17)	DCB tests
EFRAC2	0.00078 J/mm^3	Mode II fracture toughness	Experimental (CMH–17)	ENF tests
SIGMAst	0.064 GPa	Mode I initiation stress	Calibrated	Numerical stability
GAMMAst	0.095 GPa	Mode II initiation stress	Calibrated	Numerical stability

[a]Reference 85.

B.14.3 Modeling Strategies and Interface Data

A summary of interface material properties, highlighting the description of each input and derivation, is shown in Table B.20. These data are then reported in Figure B.67 as they appear in the software's MAT303 card.

	MAT 303	-	TIED LINK				
1	IDMAT	**MATYP**	RHO	ISINT	ISTRAT		
	8552	**303**	1.55E-6				
2	KSI	SLFACm	IDEABEN	IDELBEND	DAMRATE	TLSTIF	
3	I3DOF	IDELA					
	1	*1*					
4	hcont	E0	G0	STRAT1	STRAT2	Nfilt	ETA
	-0.01	9.	4.7				3
5	SIGMApr	GAMMApr	EFRAC1	EFRAC2	SIGMAst	GAMMAst	NFEQD
	0.064	0.095	0.00028	0.00078	0.064	0.095	
6	Ncycle	IFUNGcont					
	1000						

Figure B.67.—MAT303 material card implemented for IM7/8552 unidirectional ply interface (VPS2020); gray shading indicates unused or nonphysical (logical/numerical) inputs.

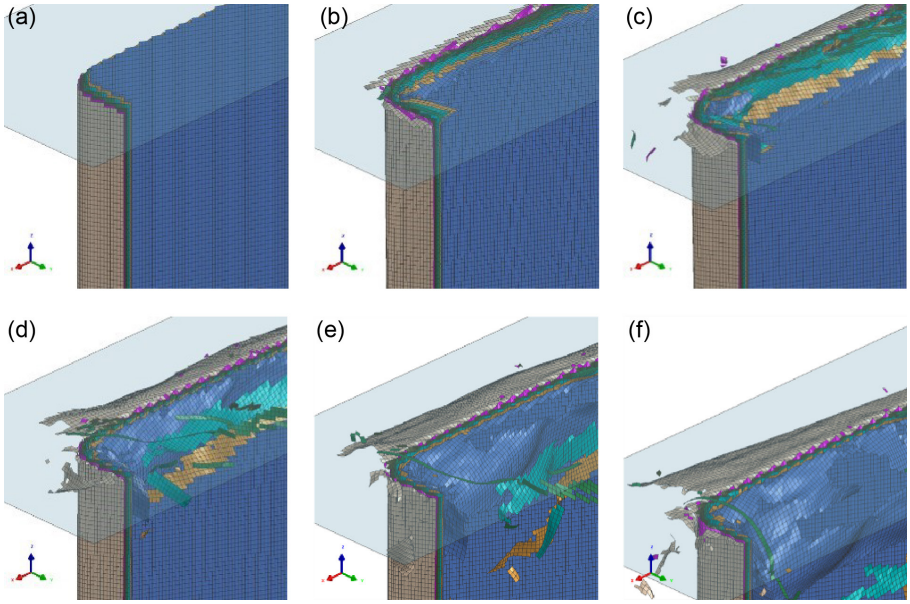

Figure B.68.—Pretest displacement predictions for C-channel model HL01. (a) 0 mm. (b) 5 mm. (c) 10 mm. (d) 15 mm. (e) 20 mm. (f) 30 mm.

B.14.4 C-Channel Crush Simulation Results

In Section 4.10.5, Figure 112 and Figure 113 show the C-channel simulation load–displacement curves for laminates HL01 $[90_2/0_2/\pm45/0_2]_S$ and HL02 $[90/+45/0_2/90/-45/0_2]_S$. Figure 113 shows the summary of calculated SEA values for two hard laminates and differing loading conditions. The results of the C-channel pretest predictions are shown in Figure B.68 to Figure B.71. In Figure B.69 and Figure B.70, the result at the imposed crush plate velocity is indicated with $v = 4$ m/s. The other two results are indicated with their respective impact mass[22] and initial velocity: 144 kg mass and 150 in./s (3.81 m/s), and 113 kg mass and 300 in./s (7.62 m/s). Figure B.71 shows a comparison of the numerical total and steady-state SEA values for the two stacking sequences and the three different test conditions. A summary of numerical simulation results for C-channel geometry is provided in Table B.21.

[22]The mass values in the models reflect the flat coupon and C-channel impact tests defined in Table 21 of Section 4.0.

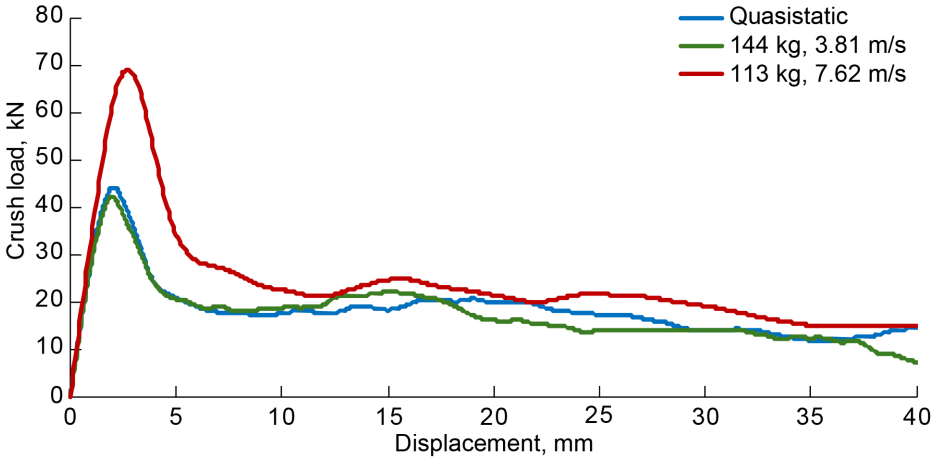

Figure B.69.—CFC1000-filtered load–displacement curves for C-channel HL01 simulations. Imposed 4 m/s velocity (blue), initial velocity of 150 in./s (3.81 m/s) and impact mass of 144 kg (green), and initial velocity of 300 in./s (7.62 m/s) and impact mass of 113 kg (red).

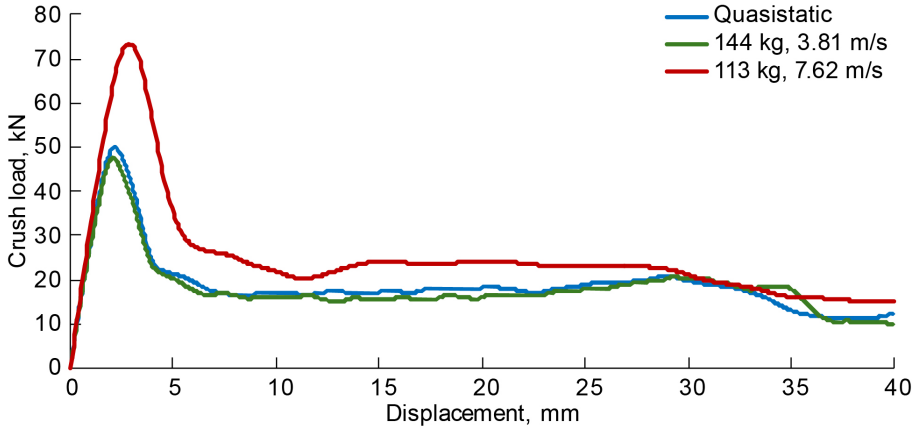

Figure B.70.—CFC1000-filtered load–displacement curves for C-channel HL02 simulations. Imposed 4 m/s velocity (blue), initial velocity of 150 in./s (3.81 m/s) and impact mass of 144 kg (green), and 300 in./s (7.62 m/s) and impact mass of 113 kg (red).

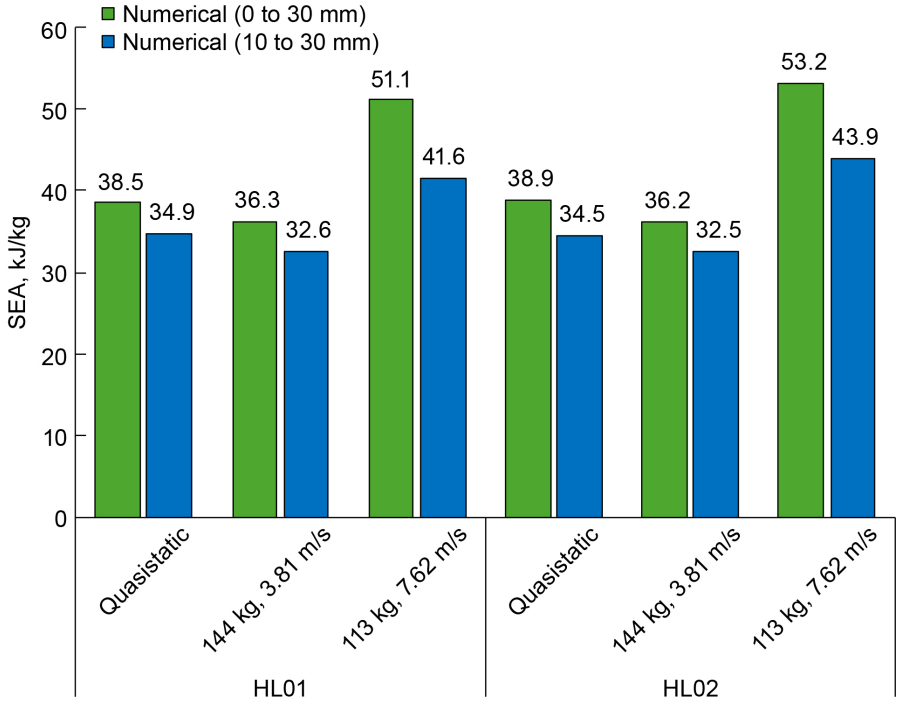

Figure B.71.—C-channel simulation summary of calculated SEA values for two hard laminates and differing loading conditions.

TABLE B.21.—SUMMARY OF NUMERICAL SIMULATED RESULTS FOR C-CHANNEL GEOMETRY

	Initial conditions	Numerical SEA, 0 to 30 mm, J/g	Numerical SEA, 10 to 30 mm, J/g	Peak force, kN	Initial slope, kN/mm
HL01 $[90_2/0_2/\pm45/0_2]_S$	v = 4 m/s	38.5	34.9	49.0	25.5
	144 kg, 3.8 m/s	36.3	32.6	46.6	24.8
	113 kg, 7.6 m/s	51.1	41.6	73.8	22.3
HL02 $[90/+45/0_2/90/-45/0_2]_S$	v = 4 m/s	38.9	34.5	55.0	26.0
	144 kg, 3.8 m/s	36.2	32.5	53.4	26.3
	113 kg, 7.6 m/s	53.2	43.9	82.1	25.9

B.15 Altair® RADIOSS® Material Model in Round Robin 3

This section supplements the Section 4.11 discussion of the Altair® RADIOSS® material model.

B.15.1 RADIOSS® Material Model Description

The orthotropic composite material law proposed in Altair® RADIOSS® software is LAW25 (Ref. 54), based on a visco-elasto-plastic modeling of composites' nonlinear and strain-rate-dependent behaviors. This material law is already implemented in the commercial FE code Altair® RADIOSS®. The plastic flow threshold $F(\sigma)$ is formulated as a Tsai–Wu (Ref. 55) quadratic function of the stress tensor following Equation (B.65):

$$F\left(W_p\right)=\sum_{i=1}^{2}F_i\left(W_p\right)\sigma_i+\sum_{i=1}^{2}F_{ii}\left(W_p\right)\sigma_i^2+2F_{12}\left(W_p\right)\sigma_1\sigma_2+F_{44}\sigma_{12}^2 \tag{B.65}$$

where F values less than 1 mean the material behavior is elastic, and for $F = 1$, the material enters the plastic phase. The F_i, F_{ij}, and F_{ii} coefficients describing the elastic to plastic transition envelope are dependent on the global plastic work W_p according to the following relationships:

$$F_i\left(W_p\right)=-\frac{1}{\sigma_{iy}^{c}\left(W_p\right)}+\frac{1}{\sigma_{iy}^{t}\left(W_p\right)} \tag{B.66}$$

$$F_{ii}\left(W_p\right)=\frac{1}{\sigma_{1y}^{t}\left(W_p\right)\sigma_{1y}^{c}\left(W_p\right)} \tag{B.67}$$

$$F_{12}\left(W_p\right)=-\frac{\alpha}{2}\sqrt{F_{11}\left(W_p\right)F_{22}\left(W_p\right)} \tag{B.68}$$

$$F_{44}\left(W_p\right)=\frac{1}{\sigma_{12y}^{t}\left(W_p\right)\sigma_{12y}^{c}\left(W_p\right)} \tag{B.69}$$

where W_p is $W_p(\varepsilon_i)=\int\sigma_i\varepsilon_i\cdot d\varepsilon_i-W\varepsilon_i(\varepsilon_i)$ and σ_{iy}^{c} and σ_{iy}^{t} are compression and tension yield stresses in direction i (i = 1,2). The plastic surface can grow and rotate during loading, allowing for different plastic behavior depending on the directions (1, 2, and shear) as shown in Figure B.72.

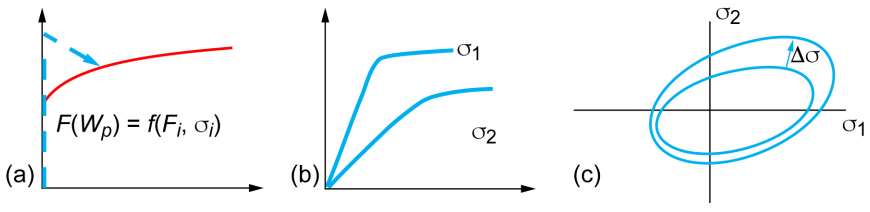

Figure B.72.—Plastic threshold evolution during loading. (a) 1-direction. (b) 2-direction. (c) Shear.

Stress components are computed as follows:

$$\sigma_{iy}^{t}\left(W_{ip}^{c*},\dot{\varepsilon}\right)=\sigma_{iy}^{t0}\left(1+b_i^t\left(W_{ip}^{t*}\right)^{n_i^t}\right)\left(1+c_i^t\ln\left(\frac{\dot{\varepsilon}}{\dot{\varepsilon}_0}\right)\right) \tag{B.70}$$

$$\sigma_{12y}\left(W_{ip}^{c*},\dot{\varepsilon}\right)=\sigma_{12y}\left(1+b_{12}\left(W_{12}^{*}\right)^{n_i}\right)\left(1+c_{12}\ln\left(\frac{\dot{\varepsilon}}{\dot{\varepsilon}_0}\right)\right) \tag{B.71}$$

$$\sigma_{iy}^{c}\left(W_{ip}^{c*},\dot{\varepsilon}\right)=\sigma_{iy}^{c0}\left(1+b_i^t\left(W_{ip}^{t*}\right)^{n_i^c}\right)\left(1+c_i^c\ln\left(\frac{\dot{\varepsilon}}{\dot{\varepsilon}_0}\right)\right) \tag{B.72}$$

In Equations (B.70) to (B.72), σ_{iy}^{t0} and σ_{iy}^{c0} are the initial tension and compression yield stresses in direction i (i = 1, 2), b is the plastic hardening parameter, n is the plastic hardening exponent, and c is the strain-rate coefficient for plastic work criteria. These parameters must be identified from tensile testing (according to standards ASTM D3039–95 (tension), SACMA SRM 1–94 (compression), and ASTM D2344–95 (shear)). The first terms, depending on the plastic work W_p, describe the nonlinear static behaviors according to parameters b_i^t, b_i^c, n_i^t, and n_i^c, respectively, in tension and compression.

The second terms describe strain-rate dependency as a function of strain rate and reference strain rates. That means there is no strain-rate effect in the elastic behavior; the strain rate will affect only the yield stress by offsetting the plastic curve.

Figure B.73 depicts the CRASURV parameters for nonlinear behavior (Ref. 106).

Damage and rupture can be modeled in two different ways: inside the LAW25 material law or using a failure model combined with the material law.

If we consider only LAW25, we can distinguish two ways of failure modeling: tensile damage and post-rupture softening behavior. Tensile damage can be activated only by tensile loads in both directions (1 and 2). As shown in Equation (B.73), the stiffness related to the damaged directions is reduced by a damage factor d:

$$\sigma_i^{\text{reduced}}=\sigma_i\left(1-d_i\right)d_i=\max\left(\frac{\varepsilon_i-\varepsilon_{ti}}{\varepsilon_{mi}-\varepsilon_{ti}},d_{\max}\right) \tag{B.73}$$

Three strain values are needed to define this damage behavior: ε_{ti} (damage initiation), ε_{mi} (strain at maximum damage), and ε_{fi} (element deletion strain). The first two values can be set up using the critical strain energy release rate G_c for directions 1 and 2. Element deletion strain can be set up as $1.25\cdot\varepsilon_{mi}$. This practice ensures a stable rupture process. This tensile failure can be activated in the elastic region or the plastic region, as shown in Figure B.74.

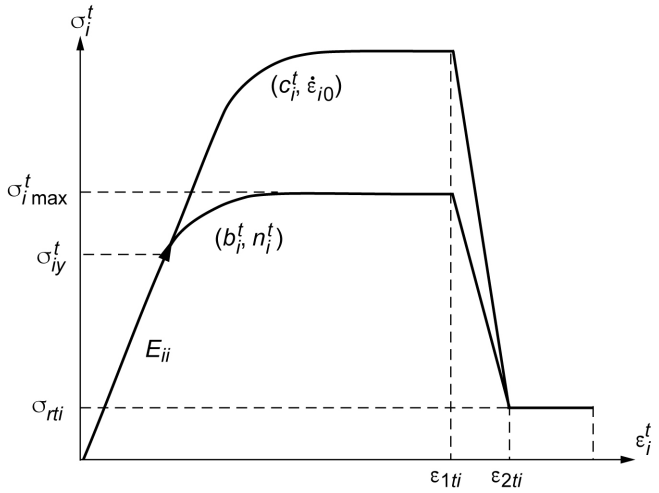

Figure B.73.—CRASURV parameters for nonlinear behavior. Reference strain rate, $\dot{\varepsilon}_0$; global strain-rate coefficient for plastic work criteria, *c*; softening parameter in tension for direction *i*, σ_{rti}.

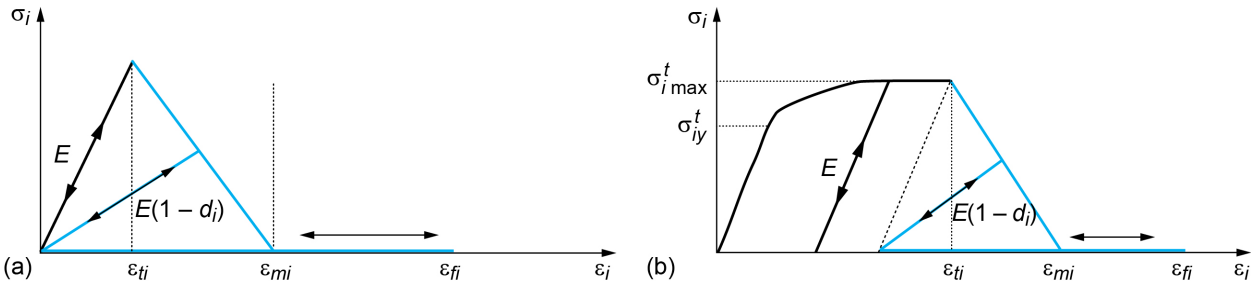

Figure B.74.—Tensile-strain-based failure in LAW25. (a) Brittle failure. (b) Ductile failure.

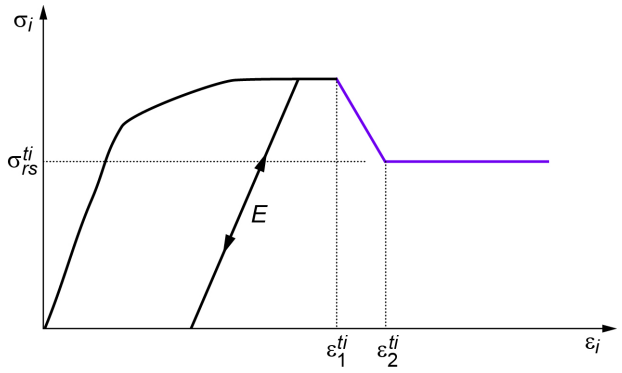

Figure B.75.—Tensile-strain-based failure in LAW25 with failure behavior modeled by softening.

Post rupture and softening use only plasticity to reduce the maximum plastic stress. The material will flow with less effort. This method is very useful to represent all the complex phenomena involved in composite failure under compression. Figure B.75 shows the behavior modeled by the softening.

Three parameters are needed to define the softening: ε_{ic}^{1}, ε_{ic}^{2}, and σ_{ires}. The first strain value represents the softening initiation, the second defines softening end, and σ_{ires} is the residual stress after softening. Element deletion will be controlled by W_p value. This limit can be global or specific for each direction (tension and compression). Some failure criteria outside the material LAW25 are

- Hashin
- Puck
- Orthstrain

/FAIL/ORTHSTRAIN works very well combined with LAW25. This is an orthotropic strain-based failure criterion with strain-rate dependency and mesh size regularization. Composite behavior with softening will be driven by LAW25, and final failure (element deletion) will be driven by the failure criterion.

B.15.2 Single-Element Simulation Results for Model Verification

Figure B.76 shows stress–strain characteristics of single-element simulations of longitudinal tensile loading (Figure B.76(a)), longitudinal compressive loading (Figure B.76(b)), transverse tensile loading (Figure B.76(c)), and shear tensile loading (Figure B.76(e)).

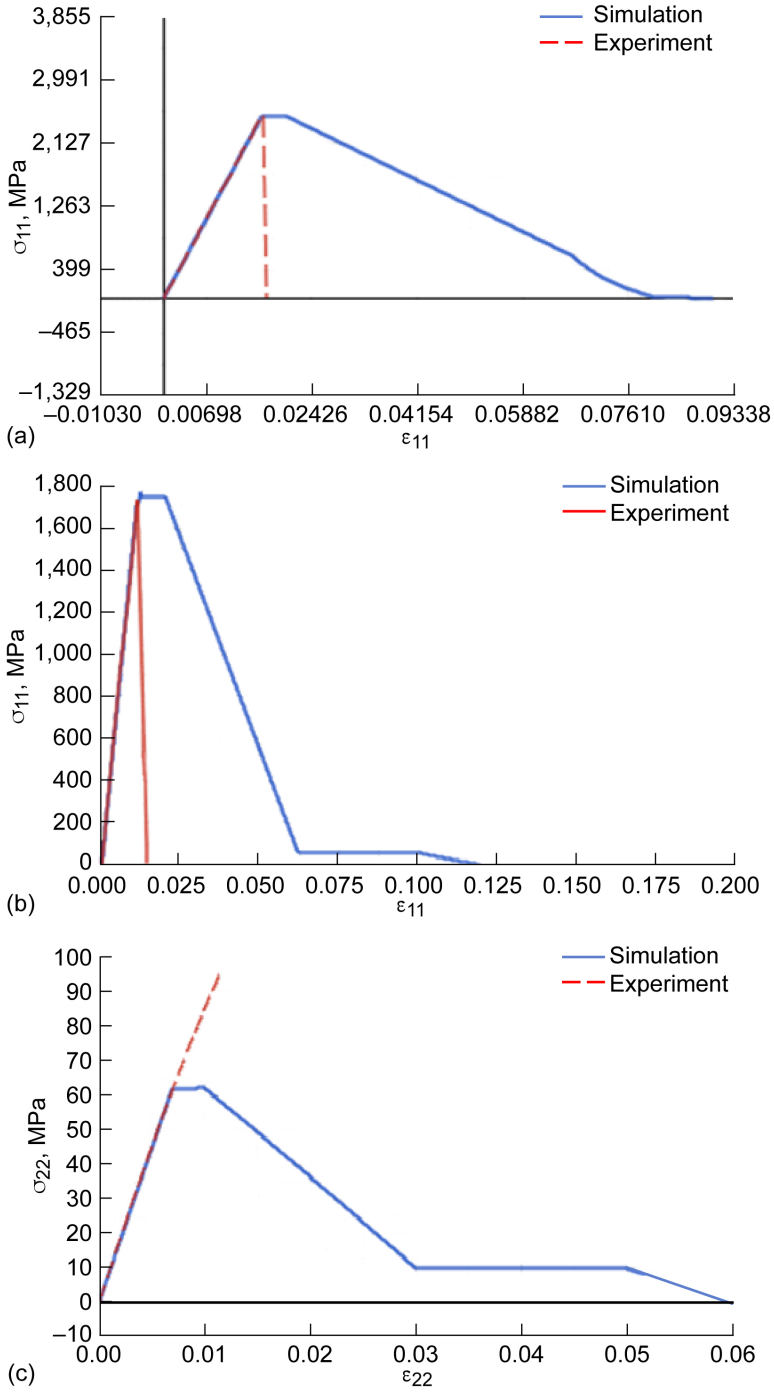

Figure B.76.—Stress–strain characteristics of single-element simulations compared with experiment results. (a) Longitudinal tension. (b) Longitudinal compression. (c) Transverse tension. (d) Transverse compression. (e) Shear tension 45° loading.

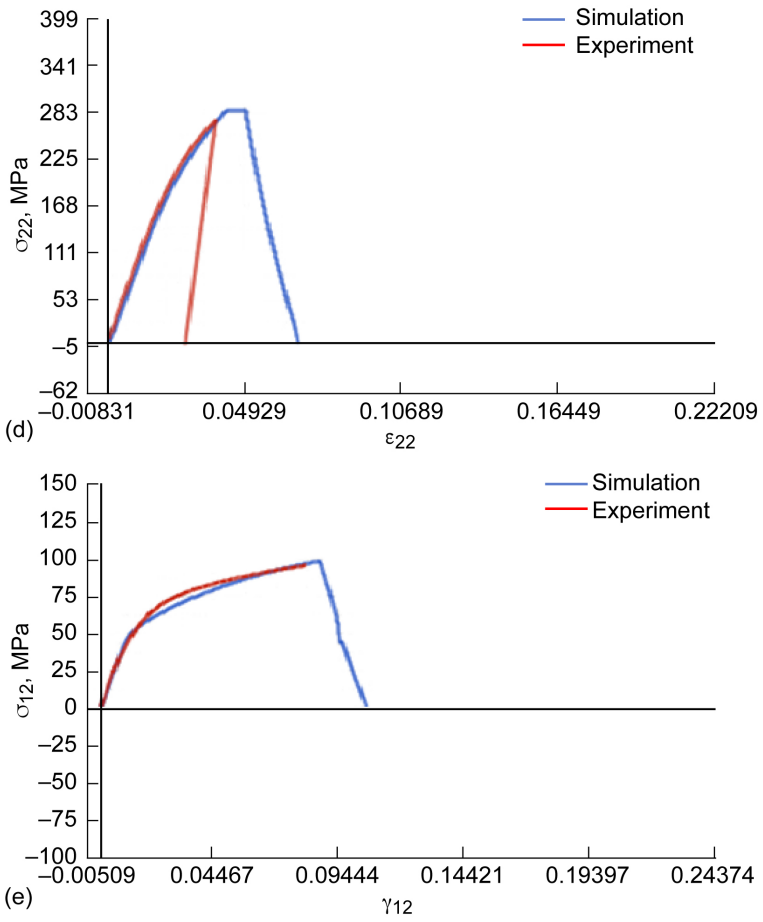

Figure B.76.—Concluded.

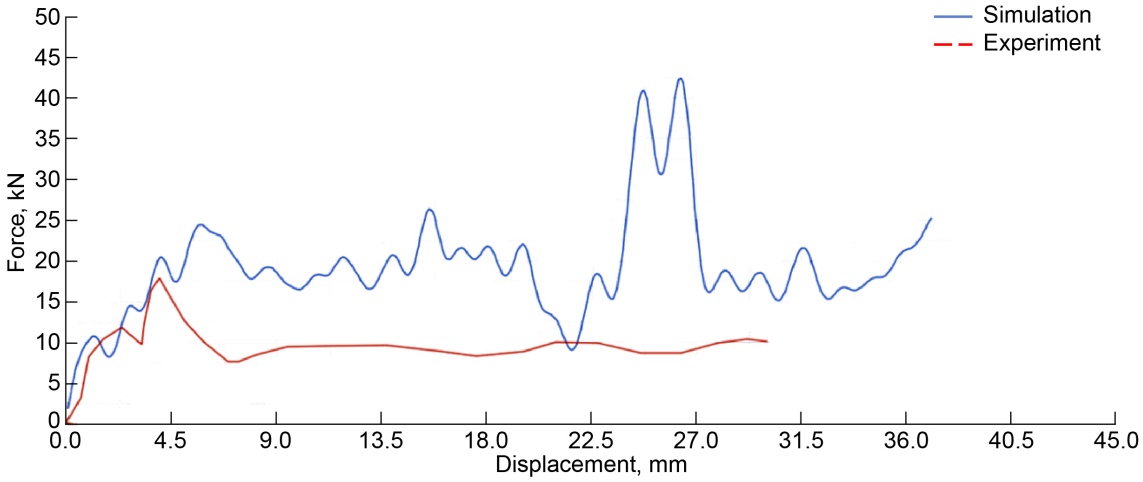

Figure B.77.—Force–displacement characteristics of flat coupon laminate QI01 $[90/\pm45/0]_{2S}$ simulation using single-shell model versus experimental results.

B.15.3 Flat Coupon and C-Channel Crush Test Simulations Results

Force–displacement results are shown in Figure B.77 to Figure B.79 for simulations using a single-shell model. Figure B.77 gives results for a quasi-isotropic flat coupon laminate simulation; Figure B.78 and Figure B.79 give results for various quasi-isotropic and hard laminate simulations.

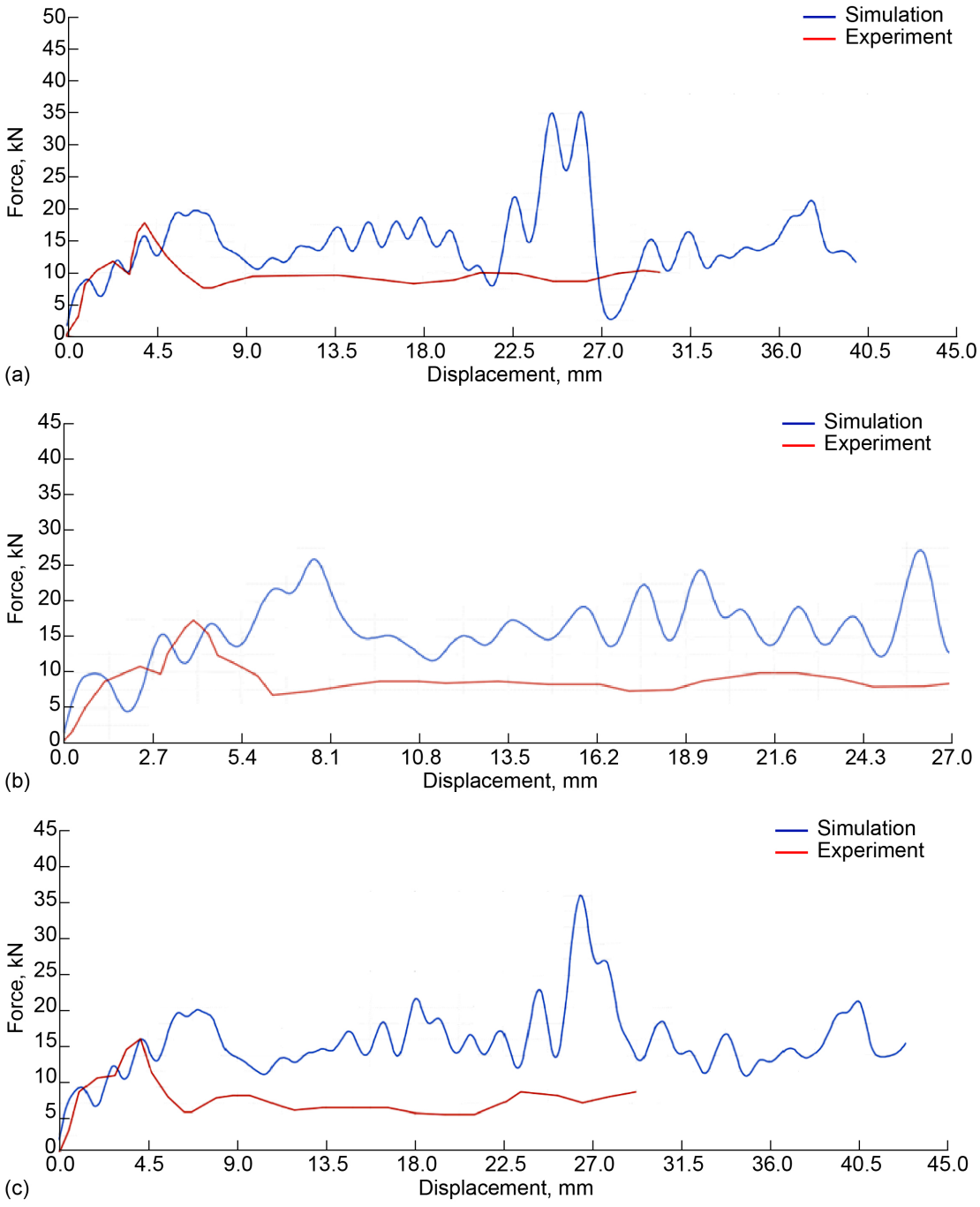

Figure B.78.—Force–displacement characteristics of various quasi-isotropic and hard laminate simulations using single-shell model compared with experimental results. (a) $[90/\pm45/0]_{2S}$. (b) $[\pm45/90/0]_{2S}$. (c) $[(\pm45)_2/90_2/0_2]_S$.

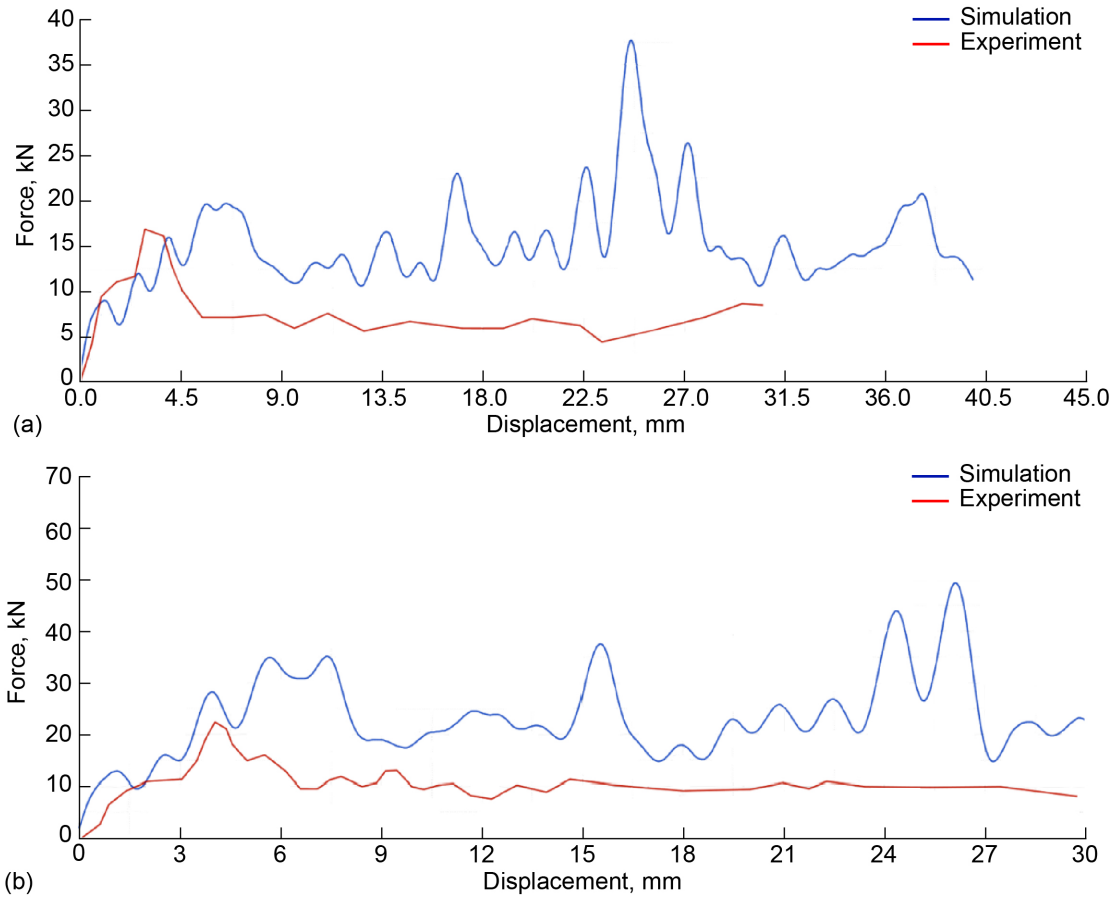

Figure B.79.—Force–displacement characteristics of various quasi-isotropic and hard laminate simulations using single-shell model compared with experimental results. (a) $[90_2/(\pm45)_2/0_2]_S$. (b) $[90_2/0_2/(\pm45_2)/0_2]_S$.

B.15.4 C-Channel Crush Simulation for HL01 $[90_2/0_2/\pm45/0_2]_S$

The simulation results for laminate HL01 with stacking sequence $[90_2/0_2/\pm45/0_2]_S$ for differing initial velocities of the impact plate are shown in Figure B.80. The results are presented in terms of contact force versus displacement of the impact plate.

The peak crush forces for the three loading conditions are given in Table B.22. The peak force, which is highly influenced by setup-specific details and applied filtering measures. The SEA and crush distances are given in Table B.22 for imposed velocity, 150 and 300 in./s cases.

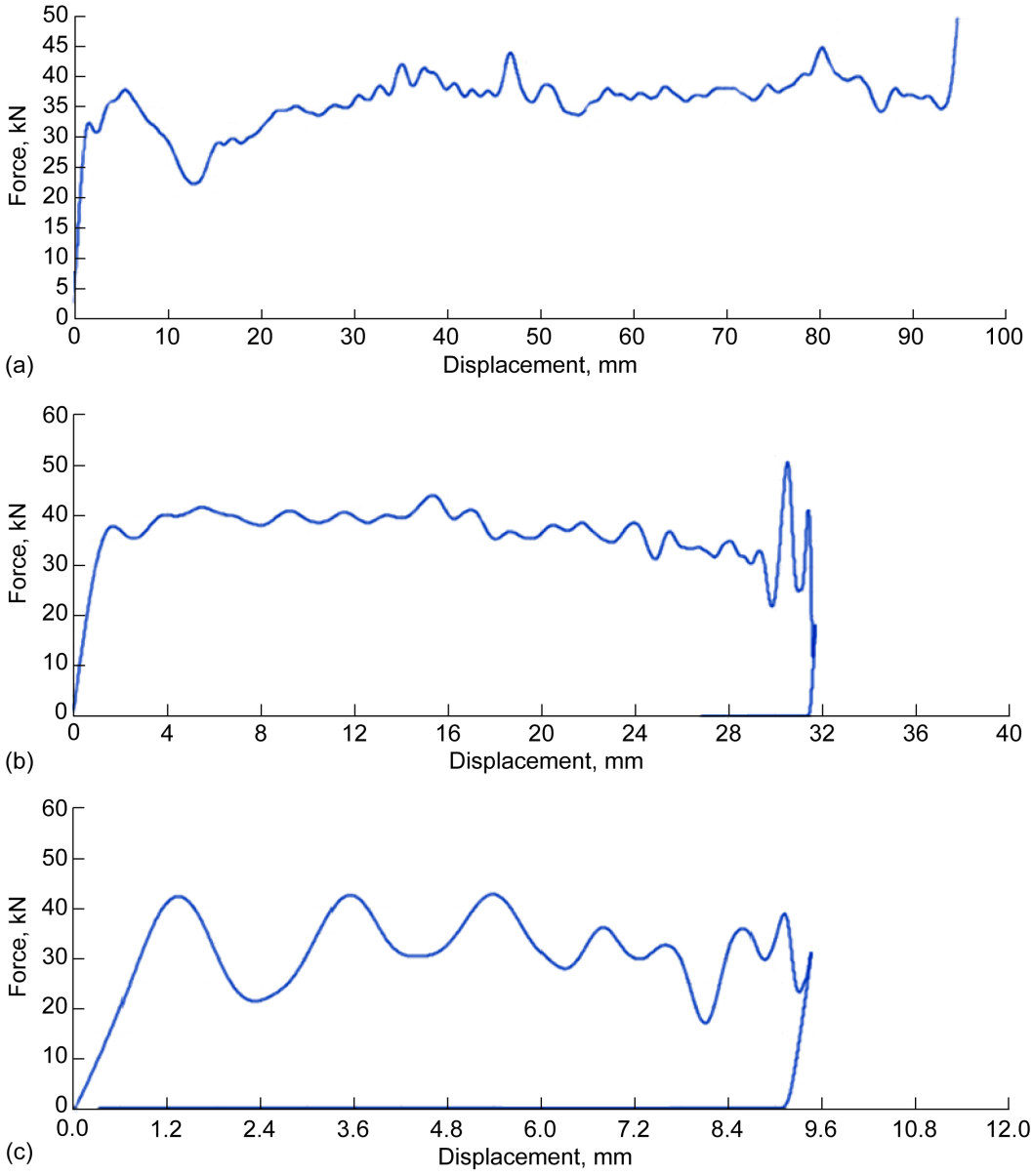

Figure B.80.—Force–displacement simulation results for C-channel HL01 $[90_2/0_2/\pm45/0_2]_S$ crush simulations at various velocities. (a) Quasistatic. (b) 300 in./s. (c) 150 in./s.

TABLE B.22.—SUMMARY OF C-CHANNEL CRUSHING SIMULATION RESULTS FOR HL01 $[90_2/0_2/\pm45/0_2]_S$

HL01	QS	150 in./s	300 in./s
Crush distance, mm	NA	9.4	31.7
Peak crush force, kN	45	44	45
Average crush force, kN	35.8	35	37.8
SEA, kJ/kg	71.72	70.12	75.73

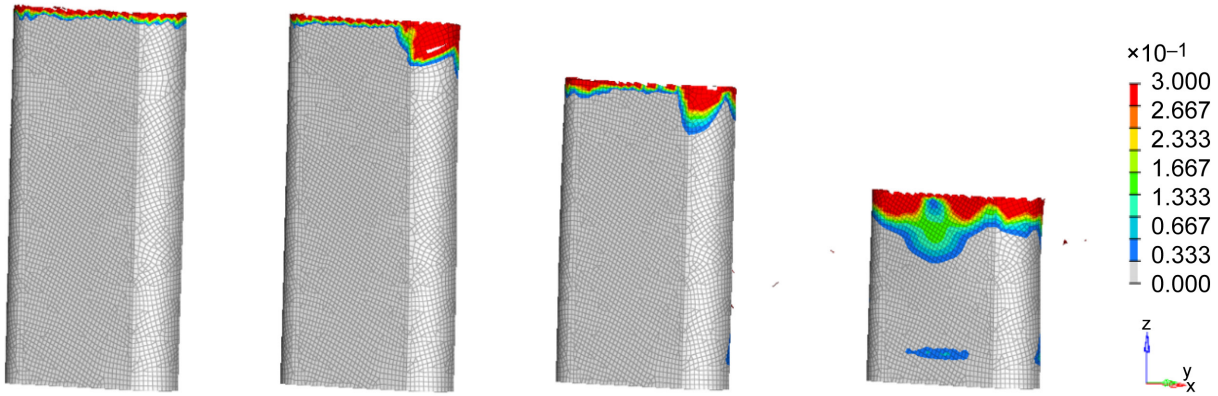

Figure B.81.—Plastic work (dimensionless) of C-channel QS crushing for HL01 $[90_2/0_2/\pm45/0_2]_S$.

Figure B.81 shows the maximum dimensionless plastic work for QS analysis for HL01. This figure helps in understanding the force drop in the curve between 10 and 20 mm. In fact, a crack perpendicular to the load direction appears in the C-channel edge and propagates inside. After this, the coupon enters into a steady crushing.

B.15.5 C-Channel Crush Simulation for HL02 $[90/45/0_2/90/-45/0_2]_S$

The second investigated layup, HL02, has a stacking sequence of $[90/45/0_2/90/-45/0_2]_S$. Results for the three different loads are shown in Figure B.82. A more stable crushing is observed for this laminate compared with HL01 curves. SEA and crushing distance simulation results for HL02 are shown in Table B.23.

Maximum plastic work contour plots are shown in Figure B.83 for four different simulation times. No massive plastic work is observed outside the crushing zone, which confirms what can be observed in the force versus displacement curve: the crushing is highly stable.

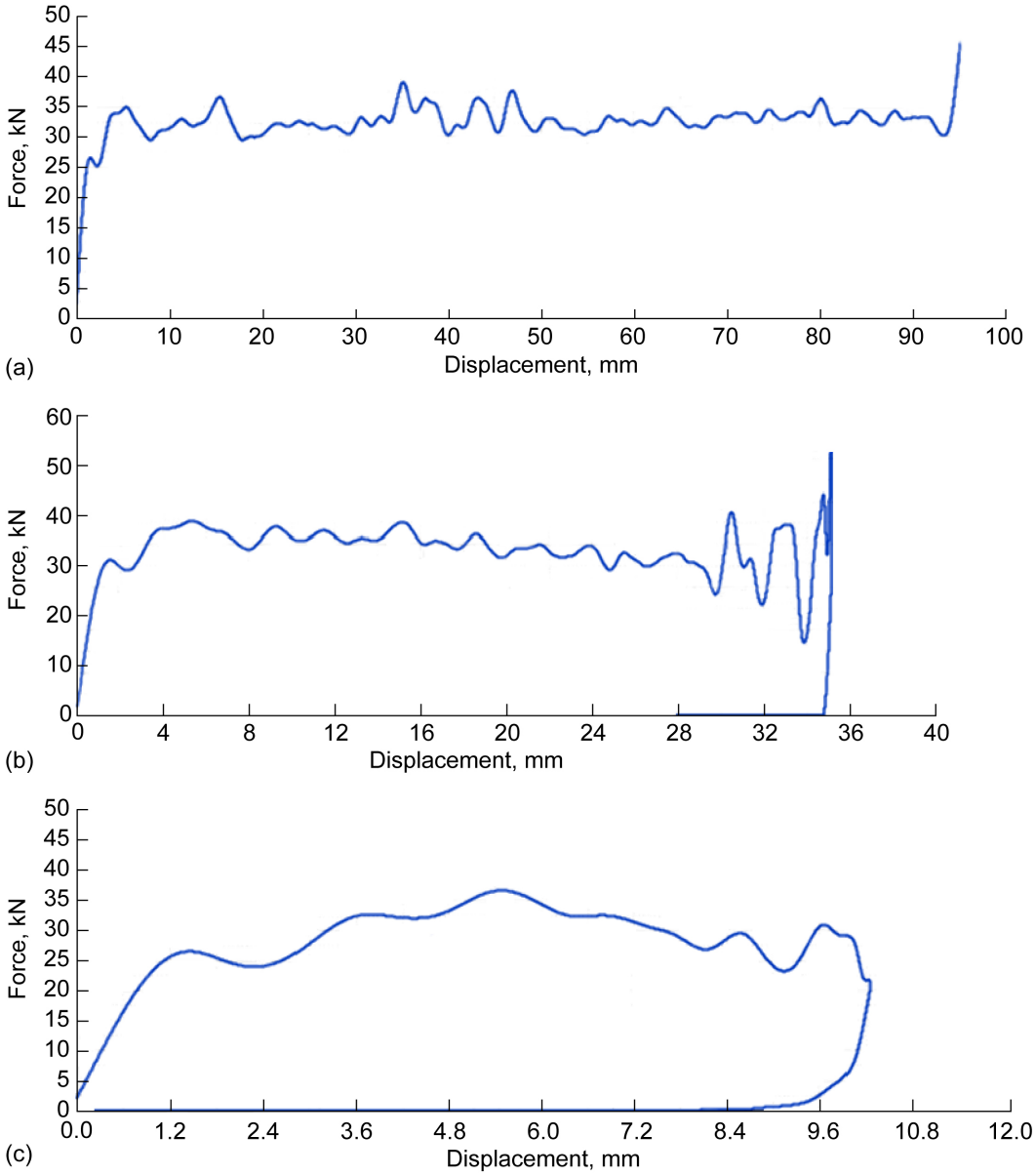

Figure B.82.—Force–displacement simulation results for C-channel HL02 $[90/45/0_2/90/-45/0_2]_S$ crush simulations with different impact velocities. (a) Quasistatic. (b) 300 in./s. (c) 150 in./s.

TABLE B.23.—SUMMARY OF C-CHANNEL CRUSHING SIMULATION RESULTS FOR HL02 [90/45/0_2/90/-45/0_2]$_S$

	QS	150 in./s	300 in./s
Crush distance, mm	NA	10.23	35.19
Peak crush force, kN	38.77	36.65	38.88
Average crush force, kN	32.62	29.74	34.28
SEA, kJ/kg	65.35	59.58	68.68

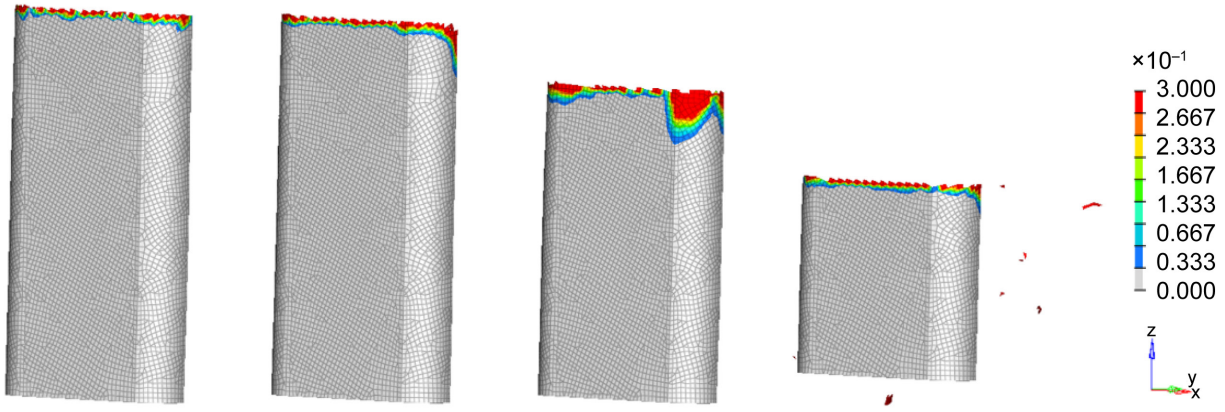

Figure B.83.—Plastic work of C-channel QS crushing for HL02 [90/45/0_2/90/–45/0_2]$_S$.

Appendix C.—Supplementary Testing Information: ABQ_DLR_UD Material Model Nonstandard Characterization Tests

This section presents supplementary information on the ABAQUS® Ladevèze ABQ_DLR_UD material model nonstandard characterization tests.

C.1 Shear Damage and Plasticity Parameters ($[\pm 45]_{4S}$ Tests)

The $[\pm 45]_{4S}$ tests were used to determine the shear damage and plasticity parameters. The specimens were cyclically loaded and unloaded in a combination of force and piston displacement control with increased force amplitude. Details of the loading/unloading cycles are listed in Table C.1.

The shear stress for each load/unload point was determined with the longitudinal stress of the specimen at each load/unload point σ_{Li}:

$$\tau_{12i} = \frac{\sigma_{Li}}{2} \tag{C.1}$$

The corresponding shear strain (γ_{12i}) was determined with the specimen longitudinal (ε_{Li}) and transverse (ε_{Ti}) strains determined from the biaxial strain gauges as

$$\gamma_{12i} = \varepsilon_{Li} - \varepsilon_{Ti} \tag{C.2}$$

From this, the shear modulus for each load/unload cycle was calculated using

$$G_{12_i} = \frac{\tau_{12i}}{\gamma_{12,el}} \tag{C.3}$$

where τ_{12i} is the peak shear stress of the i^{th} cycle and $\gamma_{12,el}$ is the elastic part of the corresponding total strain as shown in Figure C.1. The plastic strain of each cycle, $\gamma_{12,pl}$ was determined from the point where the straight line through the i^{th} load/unload point intersects the shear strain axis.

The initial undamaged shear modulus G_{12}^0 was determined from the initial slope between 5 and 20 MPa shear stress. The shear damage variable d_{12i} was then calculated as

$$d_{12i} = 1 - \frac{G_{12i}}{G_{12}^0} \tag{C.4}$$

TABLE C.1.—DETAILS OF LOADING/UNLOADING CYCLES FOR $[\pm 45]_{4S}$ TESTS

Cycle	1	2	3	4	5	6	7	8
Load	5,000 N	7,500 N	10,000 N	12,500 N	7.5 mm	12.5 mm	17.5 mm	22.5 mm
Unload	1,000 N	1,000 N	1,000 N	1,000 N	1,000 N	1,000 N	1,000 N	1,000 N

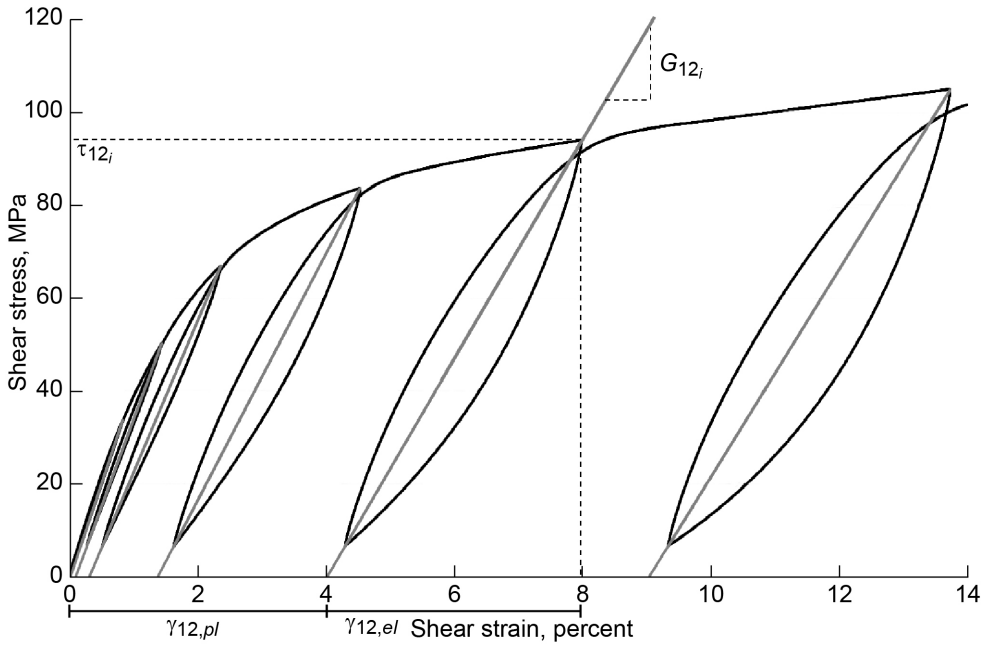

Figure C.1.—Cyclic tensile test on $[\pm 45]_{4s}$ specimen for measuring shear damage and plastic strain.

From the procedure outlined by Ladevèze and LeDantec (Ref. 12), the damage evolution law $\underline{Y}_i$ was calculated as

$$\underline{Y}_i = \sqrt{Y_{12i}} = \frac{\tau_{12i}}{(1-d_{12i})\sqrt{2G_{12}^0}} \tag{C.5}$$

Having calculated d_{12i} and $\underline{Y}_i$ for each cycle of all repeats, the shear damage master curve for the material IM7/8552 is plotted in Figure C.2. In this plot, it is clear that good repeatability was obtained between each test. The $\underline{Y}_i - d_{12}$ behavior is approximately linear up to a damage value of $d_{12} \sim 0.45$. This linear relationship in Figure C.2 can also be expressed according to Ladevèze and LeDantec as

$$d_{12} = \frac{\underline{Y} - Y_{120}}{Y_{12c}} \tag{C.6}$$

This linear relationship is plotted in Figure C.2. The initial shear damage threshold parameter Y_{120} is the point at which d_{12} becomes zero, and the shear damage evolution parameter Y_{12c} is the inverse of the slope.

Additionally, to the procedure proposed by Ladevèze and LeDantec (Ref. 12), Schueler et al. (Ref. 105) introduced the shear failure threshold Y_{12s} and the transverse damage failure threshold Y_{2s}, which are used in VUMAT ABQ_DLR_UD to control brittle failure of the matrix/fiber interface. From the linear relationship, the value of Y_{12s} was determined to be $Y_{12s} = 183\sqrt{\text{MPa}}$, which corresponds to the point where the shear damage master curve becomes nonlinear in Figure C.2.

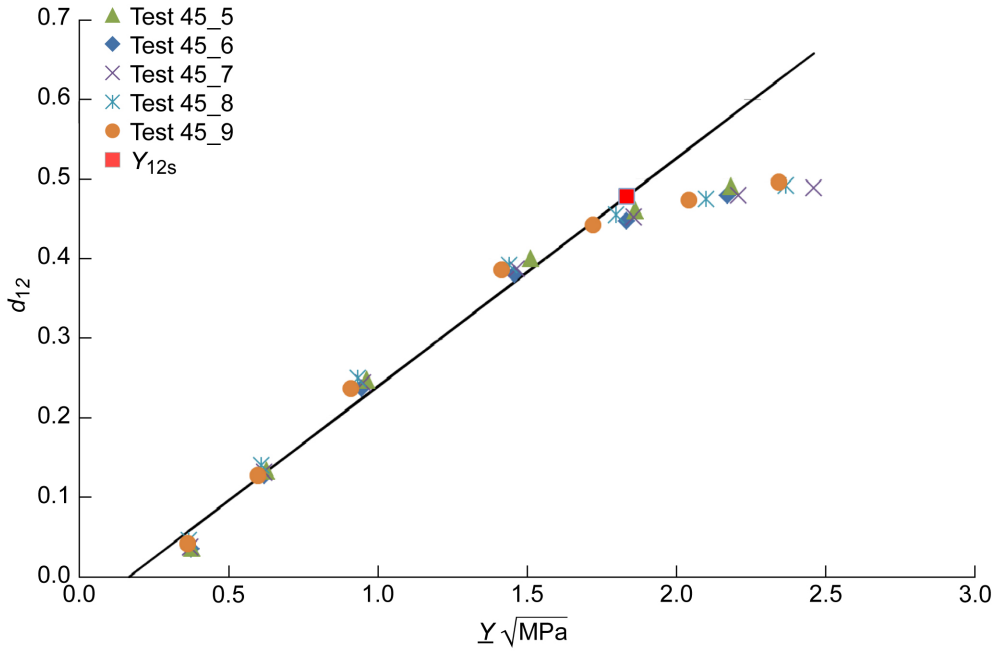

Figure C.2.—Shear damage master curve for IM7/8552.

The model plasticity development law parameters were also determined from $[\pm 45]_{4S}$ tests. According to Ladevèze and LeDantec (Ref. 12), the plasticity threshold value, the sum of the yield stress R_0 and the plasticity development law parameter R_i at the i^{th} cycle, were calculated as

$$R_i + R_0 = \frac{\tau_{12i}}{(1 - d_{12i})} \tag{C.7}$$

The accumulated plastic strain $\tilde{p}$ was calculated from Ladevèze and LeDantec as

$$\tilde{p} = \int_0^{\gamma_{12,pl}} (1 - d_{12i})\, d\gamma \tag{C.8}$$

The $\tilde{p}$ value can be determined by plotting the plastic strain $\gamma_{12,pl}$ at the i^{th} cycle against $(1 - d_{12i})$ as shown in Figure C.3 for test specimen CST_IM7_8552_45_5. By calculating the area under the curve in Figure C.3 between each interval, A_i, the accumulated plastic strain up to each n^{th} cycle is calculated as

$$\tilde{p}_n = \sum_0^{i=n} A_i \tag{C.9}$$

With $R_i + R_0$ and $\tilde{p}$, the shear plasticity master curve for IM7/8552 is plotted in Figure C.4. A curve is fitted to the master curve using the power law

$$R(\tilde{p}) = \beta \tilde{p}^{\mu} \tag{C.10}$$

where β is the plastic hardening law coefficient and μ the plastic hardening law exponent. The values for IM7/8552 determined from cyclic $[\pm 45]_{4S}$ tests are listed in Table C.2.

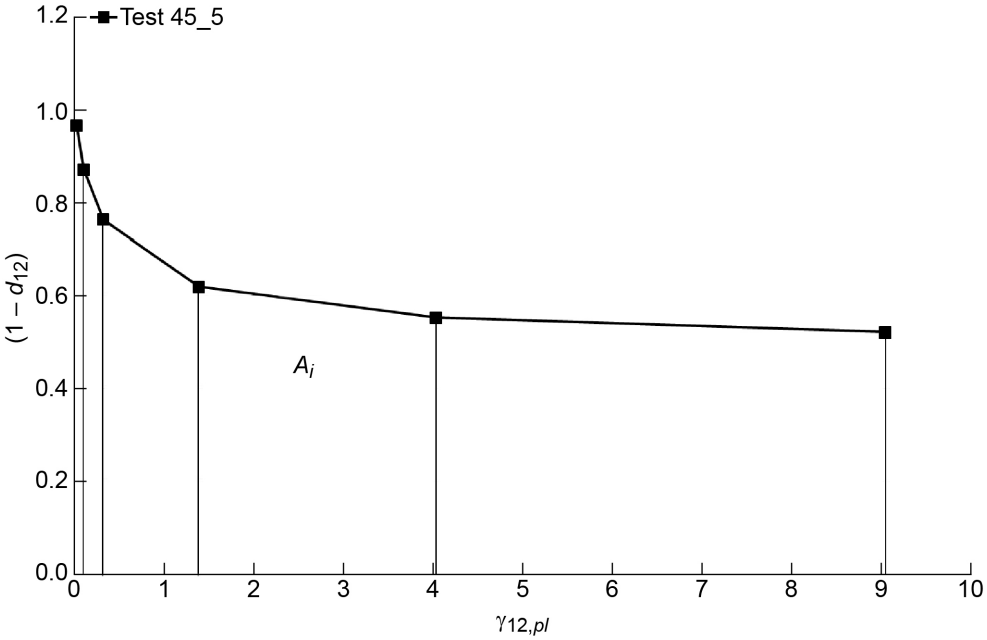

Figure C.3.—Development of accumulated plastic strain of IM7/8552.

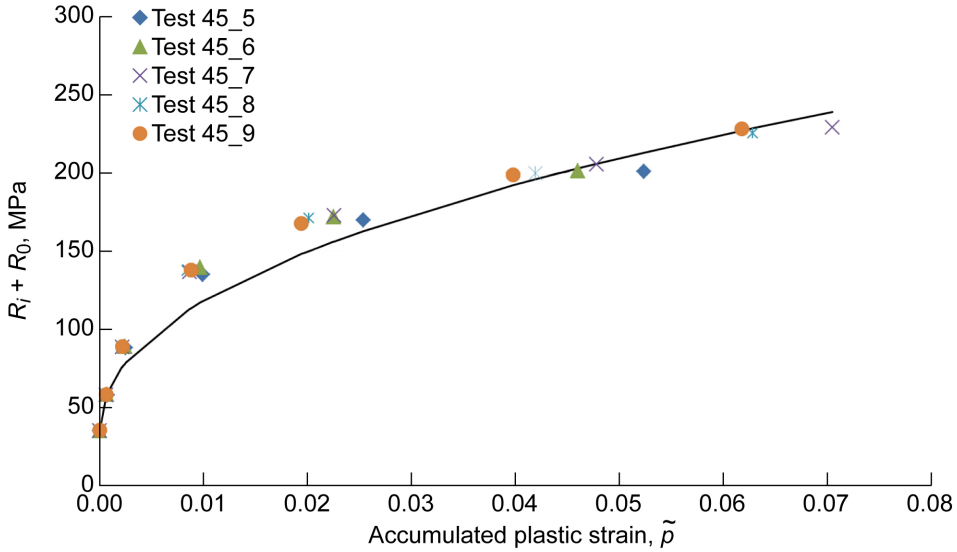

Figure C.4.—Shear plasticity master curve for IM7/8552.

TABLE C.2.—SHEAR DAMAGE AND PLASTICITY PARAMETERS FOR MATERIAL SYSTEM IM7/8552.

Test	Y_{120}, $\sqrt{\text{MPa}}$	Y_{12c}, $\sqrt{\text{MPa}}$	Y_{12s}, $\sqrt{\text{MPa}}$	R_0, MPa	β, MPa	μ
$[\pm 45]_{4S}$	0.168	3.48	1.83	32.5	680	0.45

C.2 Transverse Damage and Coupling Parameters

The $[\pm 67.5]_{4S}$ tests were used to determine transverse damage parameters and the shear–transverse damage and plasticity coupling parameters. The specimens were cyclically loaded and unloaded in force control with increased force amplitude for the loading cycles. Details are listed in Table C.3.

To determine the shear–transverse damage and coupling parameters, the shear and transverse strains were calculated using classical lamination theory as described in Reference 76:

$$\sigma_{22i} = (1 - B)\sigma_{Li} \tag{C.11}$$

$$\tau_{12i} = \frac{-1}{2mn}\left(B\left(1 - 2m^2\right) + m^2\right)\sigma_{Li} \tag{C.12}$$

with

$$B = \left[\frac{m^2\left(2m^2 - 1\right) + 4m^2n^2\dfrac{G_{12}^0}{E_{22}^0}\left(\dfrac{E_{22}^0}{E_{11}}\nu_{12} + 1\right)}{4m^2n^2\dfrac{G_{12}^0}{E_{22}^0}\left(\dfrac{E_{22}^0}{E_{11}} + 2\dfrac{E_{22}^0}{E_{11}}\nu_{12} + 1\right) + \left(2m^2 - 1\right)\left(m^2 - n^2\right)}\right] \tag{C.13}$$

where $m = \cos(67.5)$, $n = \sin(67.5)$. The scalar value of constitutive material constant B was calculated with the elastic material properties of IM7/8552. With $E_{11} = 154.58$ GPa, $E_{22} = 8.96$ GPa, $G_{12} = 4.69$ GPa, $\nu_{12} = 0.316$, B is equal to 0.207 for $[\pm 67.5]_{4S}$ laminates of material IM7/8552.

The principal lamina strains are

$$\varepsilon_{22i} = n^2\varepsilon_{Li} + m^2 + \varepsilon_{Ti} \tag{C.14}$$

$$\gamma_{12i} = -2mn\left(\varepsilon_{Li} - \varepsilon_{Ti}\right) \tag{C.15}$$

From this, the cyclic behavior of the $[\pm 67.5]_{4S}$ specimens can be plotted in terms of transverse stress–strain and shear stress–strain behavior, as shown in Figure C.5(a) and Figure C.5(b), respectively.

TABLE C.3.—DETAILS OF LOADING/UNLOADING CYCLES FOR [±67.5]4S TESTS

Cycle	1	2	3	4	5	6	7	8	9	10
Load	1,250 N	2,000 N	3,000 N	3,500 N	4,000 N	4,500 N	4,800 N	5,000 N	5,500 N	6,000 N
Unload	100 N	100 N	100 N	100 N	100 N	100 N	100 N	100 N	100 N	100 N

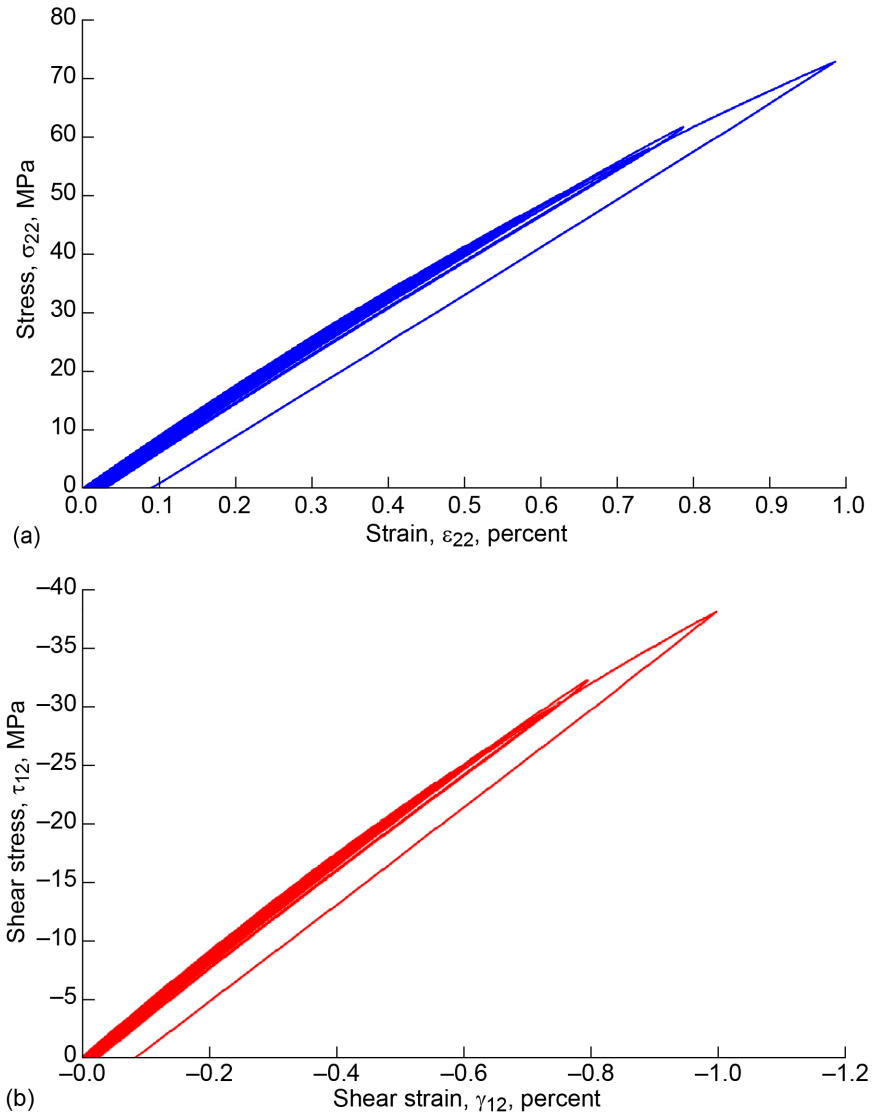

Figure C.5.—Cyclic tensile test on $[\pm 67.5]_{4S}$ specimen for measuring transverse damage and shear–transverse damage and plasticity coupling parameters. (a) Transverse stress–strain response. (b) Shear stress–strain response.

For each cycle plotted in Figure C.5, the transverse moduli E_{22i}, shear moduli G_{12i}, and shear damage variables d_{12i} were determined in the same method described previously. The transverse damage variables for each cycle were calculated as

$$d_{2i} = 1 - \left(\frac{E_{22i}}{E_{22}^{0}} \right) \tag{C.16}$$

where E_{22i} is the transverse modulus in the principal material coordinate system for the i^{th} cycle and E_{22}^{0} is the initial undamaged transverse modulus, which was calculated for the initial, linear slope between 1 and 4 MPa initial transverse stress for each tested specimen. The initial shear modulus G_{12}^{0} was determined for the initial, linear slope between 1 and 2 MPa initial shear stress.

With d_{2i} and d_{12i}, the transverse and shear damage functions Y_{2i} and Y_{12i} were calculated following the procedure outlined by Ladevèze and LeDantec (Ref. 12):

$$Y_{2i} = \frac{1}{2}\frac{\sigma_{22i}^2}{E_{22}^0 (1-d_{2i})^2} \tag{C.17}$$

$$Y_{12i} = \frac{1}{2}\frac{\tau_{12i}^2}{G_{12}^0 (1-d_{12i})^2} \tag{C.18}$$

From these variables, the shear–transverse damage coupling parameter b was calculated as

$$b = \frac{(Y_{12c}d_{12i} + Y_{120})^2 - Y_{12i}}{Y_{2i}} \tag{C.19}$$

with Y_{12c} and Y_{120} as determined previously and listed in Table C.2. As b is assumed to be a constant for material system IM7/8552, it can be found by plotting Y_{2i} against $(Y_{12c}d_{12i} + Y_{120})^2 - Y_{12i}$ for all tested specimens and applying a linear fit where the value of b is the slope. This is shown in Figure C.6. From this, the value of b was determined for the material IM7/8552 to be $b = 0.465$.

With the shear–transverse coupling factor b, the transverse damage development law can be determined thus:

$$\underline{Y}_i = \sqrt{(Y_{12i} + bY_{2i})} \tag{C.20}$$

and the master curve of the transverse damage for the material IM7/8552 can be plotted as illustrated in Figure C.7. It is shown that good repeatability of the results could be achieved.

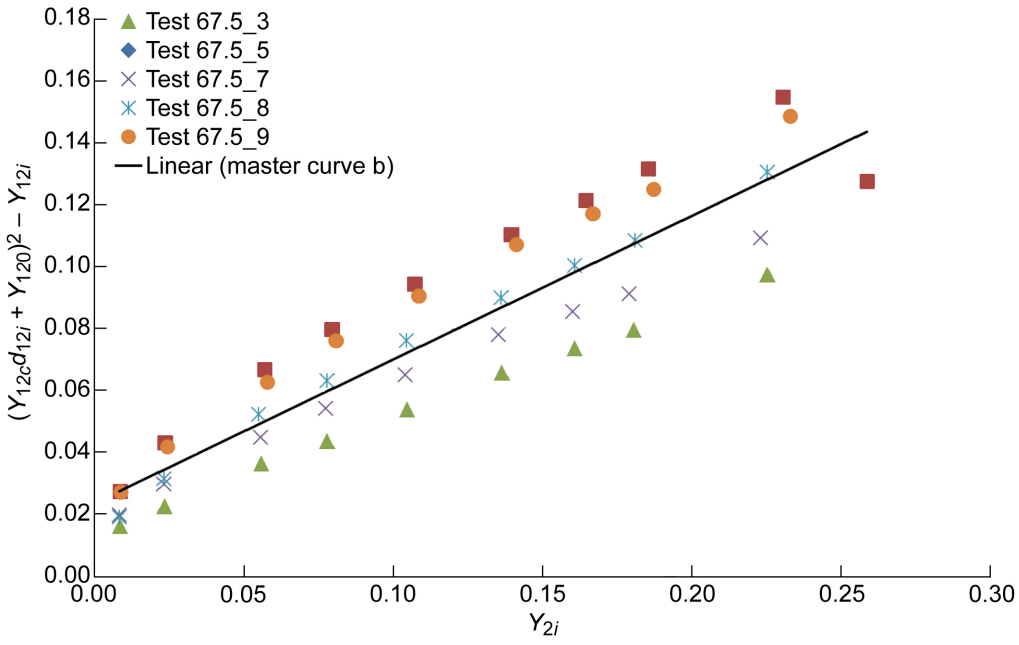

Figure C.6.—Determination of shear–transverse coupling parameter b from $[\pm 67.5]_{4s}$ tests.

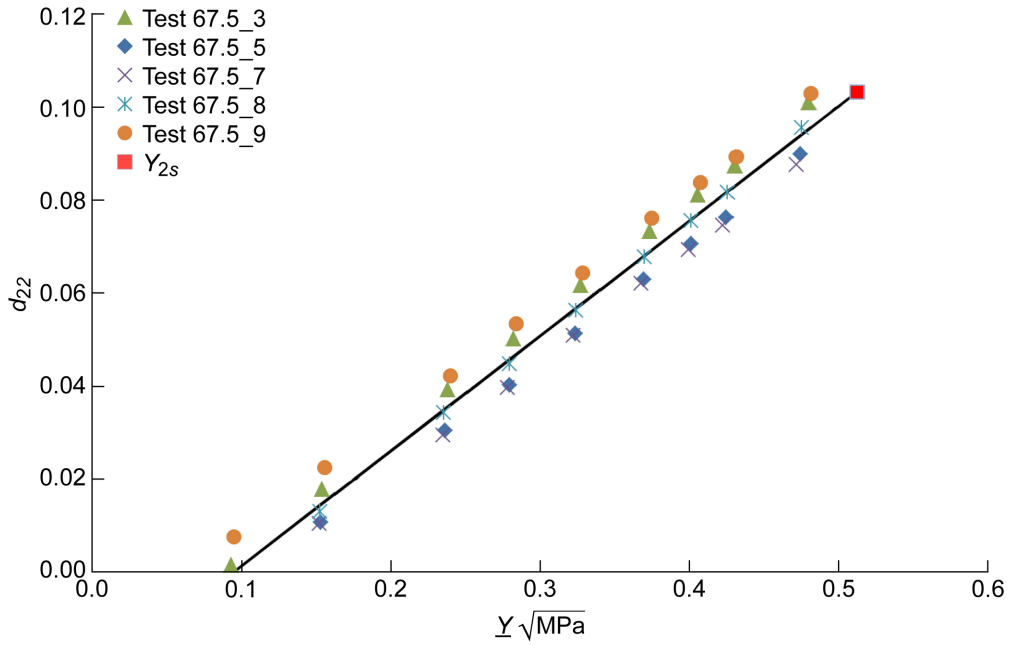

Figure C.7.—Transverse damage master curve for IM7/8552 from $[\pm 67.5]_{4S}$ tests.

As outlined by Ladevèze and LeDantec (Ref. 12), the linear transverse damage master curve can also be expressed as

$$d_{22i} = \frac{Y - Y_{20}}{Y_{2c}} \tag{C.21}$$

The transverse damage threshold parameter Y_{20} is the point at which d_{22} becomes zero, and the transverse damage evolution parameter Y_{2c} is the inverse of the slope of the linear plot in Figure C.8. The transverse failure threshold, Y_{2s}, as introduced by Schueler et al. (Ref. 105), was determined as $Y_{2s} = 0.512$ $\sqrt{\text{MPa}}$, which corresponds to the highest damage values seen in the tests.

The shear–transverse plasticity coupling parameter α^2 was calculated following the procedure outlined in References 12 and 75:

$$\alpha_i^2 = \frac{\varepsilon_{22\,pl,i}\,(1-d_{2i})^2\,\tau_{12i}}{\gamma_{12\,pl,i}\,(1-d_{12i})^2\,\sigma_{22i}} \tag{C.22}$$

It is assumed that α^2 is a constant and can be determined by plotting $\gamma_{12pl,i}(1 - d_{12i})^2\,\sigma_{22i}$ against $\varepsilon_{22pl,i}(1 - d_{2i})^2\,\tau_{12i}$ for all tested specimens and applying a linear fit. The value of α^2 is the slope and was found to be $\alpha^2 = 0.563$. However, for material input of VUMAT ABQ_DLR_UD, a value of $\alpha = \sqrt{0.563} = 0.75$ is used.

The values for IM7/8552 determined from cyclic $[\pm 67.5]_{4S}$ tests are listed in Table C.4.

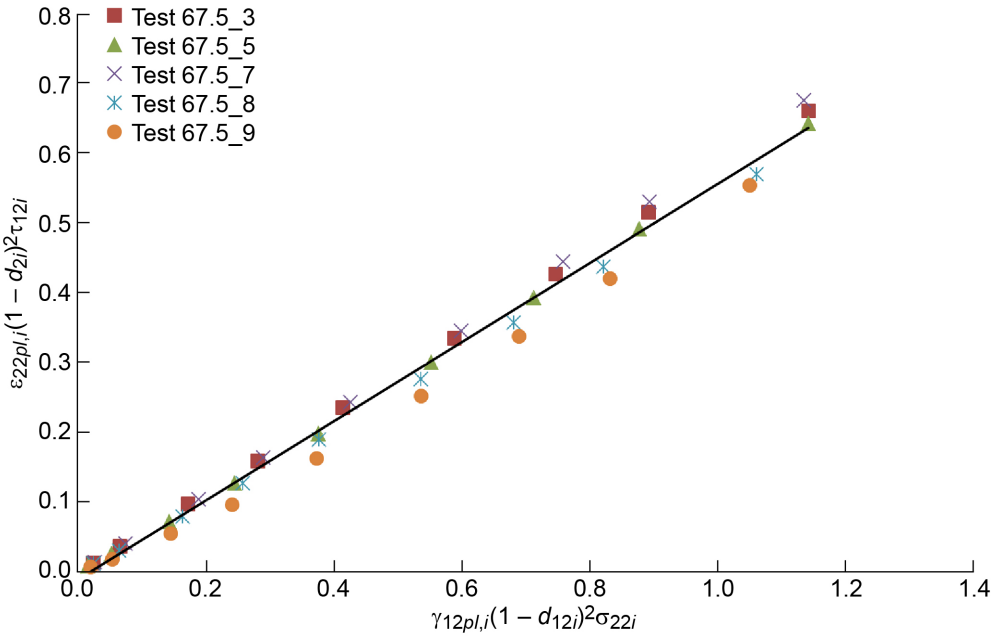

Figure C.8.—Determination of shear–transverse plasticity coupling parameter α^2 from $[\pm 67.5]_{4S}$ tests.

TABLE C.4.—TRANSVERSE DAMAGE AND COUPLING PARAMETERS FOR MATERIAL SYSTEM IM7/8552

Test	Y_{20}, $\left(\sqrt{\text{MPa}}\right)$	Y_{2c}, $\left(\sqrt{\text{MPa}}\right)$	Y_{2s}, $\left(\sqrt{\text{MPa}}\right)$	b	α
$[\pm 67.5]_{4S}$	0.094	4.05	0.512	0.465	0.75

References

1. Goldberg, Robert K., et al.: Development of an Orthotropic Elasto-Plastic Generalized Composite Material Model Suitable for Impact Problems. J. Aerosp. Eng., vol. 29, no. 4, 2016.
2. Hoffarth, Canio, et al.: Development of a Tabulated Material Model for Composite Material Failure, MAT213. Part 1: Theory, Implementation, Verification and Validation. DOT/FAA/TC-19/50, P1, 2020.
3. SAE International: Composite Materials Handbook. Polymer Matrix Composites: Materials Usage, Design, and Analysis, Vol. 3, CMH–17–3H, To be published.
4. Federal Aviation Administration: Special Conditions: Boeing Model 787–8 Airplane; Crashworthiness. 72 FR 54531, 2007.
5. Byar, Alan: Crashworthiness Study of a Boeing 737 Fuselage Section. Ph.D. Thesis, Drexel University, 2003.
6. Schatrow, P., et al.: Method Development for Full Aircraft Crash Simulation at Different Levels of Modeling Detail. The Ninth Triennial International Aircraft Fire and Cabin Safety Research Conference, Atlantic City, NJ, 2019.
7. Hashin, Z.: Failure Criteria for Unidirectional Fiber Composites. J. Appl. Mech., vol. 47, no. 2, 1980, pp. 329–334.
8. Chang, Fu-Kuo; and Chang, Kuo-Yen: A Progressive Damage Model for Laminated Composites Containing Stress Concentrations. J. Compos. Mater., vol. 21, no. 9, 1987, pp. 834–855.
9. Matzenmiller, Anton; and Schweizerhof, Karl: Crashworthiness Simulations of Composite Structures—A First Step With Explicit Time Integration. Nonlinear Computational Mechanics. A State of the Art, P. Wriggers and W. Wagner, eds., Springer, Berlin, 1991.
10. Engineering Systems International: Pam-Crash FE Code. Rungis-Cedex, France.
11. Johnson, A.F.: Modelling Impact Damage in Composite Structural Elements. Multi-Scale Modelling of Composite Material Systems, C. Soutis and P.W.R. Beaumont, eds. Woodhead Publishing, Cambridge, 2005, pp. 401–429.
12. Ladeveze, P.; and LeDantec, E.: Damage Modelling of the Elementary Ply for Laminated Composites. Compos. Sci. Technol., vol. 43, no. 3, 1992, pp. 257–267.
13. Johnson, A.F.; Pickett, A.K.; and Rozycki, P.: Computational Methods for Predicting Impact Damage in Composite Structures. Compos. Sci. Technol., vol. 61, no. 15, 2001, pp. 2183–2192.
14. Greve, L.; and Pickett, A.K.: Delamination Testing and Modelling for Composite Crash Simulation. Compos. Sci. Technol., vol. 66, no. 6, 2006, pp. 816–826.
15. Johnson, Alastair F.; and David, Matthew: Failure Mechanisms in Energy-Absorbing Composite Structures. Philos. Mag., vol. 90, no. 31–32, 2010, pp. 4245–4261.
16. Livermore Software Technology Corporation: LS-DYNA® Keyword User's Manual. Vol. II: Material Models, LS-DYNA R11, 2/18/19 (r:10850), 2019.
17. Deleo, Francesco, et al.: Crashworthiness of Composite Structures: Experiment and Simulation. Joint Advanced Materials & Structures Center of Excellence (JAMS), 2010.
18. Wade, Bonnie; and Feraboli, Paolo: Crushing Behavior of Laminated Composite Structural Elements: Experiment and LS-DYNA Simulation. DOT/FAA/TC-15/25, 2016.
19. Livermore Software Technology Corporation: LS-DYNA® Keyword User's Manual. Vol. I, LS-DYNA R10.0, 10/16/17 (r:9023), 2017.
20. Hoffarth, Canio, et al.: Implementation and Validation of a Three-Dimensional Plasticity-Based Deformation Model for Orthotropic Composites. Compos. Part A Appl. Sci. Manuf., vol. 91, no. 1, 2016, pp. 336–350.

21. Taylor, Geoffrey Ingram; and Quinney, H.: The Latent Energy Remaining in a Metal After Cold Working. Proc. R. Soc. Lond. A, vol. 143, no. 849, 1934, pp. 307–326.
22. Achstetter, Tobias: Development of a Composite Material Shell-Element Model for Impact Applications. Ph.D. Dissertation, George Mason University, 2019.
23. Goldberg, Robert K., et al.: Analysis and Characterization of Damage Utilizing a Generalized Composite Material Model Suitable for Impact Problems. J. Aerosp. Eng., vol. 31, no. 4, 2018.
24. Dong, Sheng, et al.: Analysis of Crush-Damaged Carbon-Fiber-Reinforced-Polymer (CFRP) Composites With Optimization-Assisted Post-Peak-Stress Modeling. J. Compos. Mater., vol. 55, no. 6, 2021, pp. 759–774.
25. Justusson, Brian P., et al.: Overview of Coupon Testing of an IM7/8552 Composite Required to Characterize High-Energy Impact Dynamic Material Models. NASA/TM—2020-220498, 2020. https://ntrs.nasa.gov
26. Reiner, Johannes, et al.: Prediction of Damage Progression in Notched Tensile Specimens: Comparison Between Two Intralaminar Damage Models. VI ECCOMAS Thematic Conference on the Mechanical Response of Composites, Eindhoven, Netherlands, 2017.
27. Feser, Thomas, et al.: Simulation of Dynamic Crushing of Composite Structures Using Two Intra-Laminar Damage Models Implemented in LS-DYNA and ABAQUS/Explicit. Aerospace Structural Impact and Dynamics International Conference (ASIDIC), Wichita, KS, 2017.
28. Feser, Thomas, et al.: Simulation of Axial Crushing of Flat Coupon Specimens Using Two Intra-Laminar Damage Models Implemented in LS-Dyna and Abaqus/Explicit. 13th World Congress in Computational Mechanics, New York, NY, 2018.
29. Feser, Thomas, et al.: A Study on Crashworthiness of CFRP Laminates: Comparison of Two Finite Element Models in LS-DYNA and ABAQUS/Explicit. Aerospace Structural Impact and Dynamics International Conference (ASIDIC), Madrid, Spain, 2019.
30. Reiner, Johannes, et al.: Comparison of Two Progressive Damage Models for Studying the Notched Behavior of Composite Laminates Under Tension. Compos. Struct., vol. 207, 2019, pp. 385–396.
31. Zobeiry, N.; Vaziri, R.; and Poursartip, A.: Characterization of Strain-Softening Behavior and Failure Mechanisms of Composites Under Tension and Compression. Compos. Part A Appl. Sci. Manuf., vol. 68, 2015, pp. 29–41.
32. Reiner, Johannes, et al.: Axial Crush Simulation of Composites Using Continuum Damage Mechanics: FE Software and Material Model Independent Considerations. Compos. B Eng., vol. 225, no. 109284, 2021.
33. SAE International: Composite Materials Handbook. Polymer Matrix Composites: Guidelines for Characterization of Structural Materials, Vol. 1, CMH–17–1H, 2022.
34. Shi, Danghe; and Xiao, Xinran: An Enhanced Continuum Damage Mechanics Model for Crash Simulation of Composites. Compos. Struct., vol. 185, 2018, pp. 774–785.
35. Shi, Danghe; and Xiao, Xinran: A New Shell-Beam Element Modeling Method and Its Use in Crash Simulation of Triaxial Braided Composites. Compos. Struct., vol. 160, 2017, pp. 792–803.
36. Rajaneesh, A.; and Bruyneel, M.: Finite Element Simulation of Axial Crushing of Flat and C-Channel Composite Coupons Using a Modified Mesomodel. Int. J. Impact Eng., vol. 189, no. 104932, 2024.
37. Abisset, E.; Daghia, F.; and Ladeveze, P.: On the Validation of a Damage Mesomodel for Laminated Composites by Means of Open-Hole Tensile Tests on Quasi-Isotropic Laminates. Compos. Part A Appl. Sci. Manuf., vol. 42, no. 10, 2011, pp. 1515–1524.

38. Pinho, S.T.; Robinson, P.; and Iannucci, L.: Fracture Toughness of the Tensile and Compressive Fibre Failure Modes in Laminated Composites. Compos. Sci. Technol., vol. 66, no. 13, 2006, pp. 2069–2079.
39. Laffan, M.J., et al.: Translaminar Fracture Toughness Testing of Composites: A Review. Polym. Test., vol. 31, no. 3, 2012, pp. 481–489.
40. Catalanotti, G., et al.: Measurement of Resistance Curves in the Longitudinal Failure of Composites Using Digital Image Correlation. Compos. Sci. Technol., vol. 70, no. 13, 2010, pp. 1986–1993.
41. Camanho, P.P.; Maimi, P.; and. Davila, C.G.: Prediction of Size Effects in Notched Laminates Using Continuum Damage Mechanics. Compos. Sci. Technol., vol. 67, no. 13, 2007, pp. 2715–2727.
42. Livermore Software Technology Corporation: LS-DYNA Aerospace Working Group Modeling Guidelines Document. 2019.
43. Garijo, Diego, et al.: Multiscale FE Modelling and Design of Composite Laminates Under Impact. Comprehensive Composite Materials II, Carl Zweben and Peter Beaumont, eds., Elsevier, Amsterdam, Netherlands, 2017.
44. Waimer, M.; Siemann, M.H.; and Feser, T.: Simulation of CFRP Components Subjected to Dynamic Crash Loads. Int. J. Impact Eng., vol. 101, 2017, pp. 115–131.
45. David, Matthew; and Johnson, Alastair F.: Effect of Strain Rate on the Failure Mechanisms and Energy Absorption in Polymer Composite Elements Under Axial Loading. Compos. Struct., vol. 122, 2015, pp. 430–439.
46. David, Matthew; Johnson, Alastair F.; and Voggenreiter, H.: Analysis of Crushing Response of Composite Crashworthy Structures. Appl. Compos. Mater., vol. 20, 2013, pp. 773–787.
47. Blessing, E.A.: Numerical Analysis of Carbon/Epoxy Crush Structures Using ABAQUS/EXPLICIT With CZONE. M.S. Thesis, University of Utah, 2023.
48. ESI Group: Virtual Performance Solution 2020.0: Solver Reference Manual. ESI Group 8, 2008.
49. Pineda, Evan J.; and Waas, Anthony M.: Numerical Implementation of a Multiple-ISV Thermodynamically-Based Work Potential Theory for Modeling Progressive Damage and Failure in Fiber-Reinforced Laminates. Int. J. Fract., vol. 182, 2013, pp. 93–122.
50. Pineda, Evan Jorge: A Novel Multiscale Physics-Based Progressive Damage and Failure Modeling Tool for Advanced Composite Structures. Ph.D. Thesis, University of Michigan, 2012.
51. Rondina, Francesco; and Donati, Lorenzo: Comparison and Validation of Computational Methods for the Prediction of the Compressive Crush Energy Absorption of CFRP Structures. Compos. Struct., vol. 254, no. 112848, 2020.
52. Rondina F., et al.: Numerical Simulation of the Compression Crushing Energy of Carbon Fiber-Epoxy Woven Composite Structures. Compos. Struct., vol. 303, no. 116300, 2023.
53. National Institute for Aviation Research: Hexcel 8552 IM7 Unidirectional Prepreg 190 gsm & 35%RC Qualification Material Property Data Report. NCAMP Test Report CAM–RP–2009–015, Rev. A, 2011.
54. Altair Engineering Inc.: Altair Radioss 2020 Reference Guide. 2020.
55. Tsai, Stephen W.; and Wu, Edward M.: A General Theory of Strength for Anisotropic Materials. J. Compos. Mater., vol. 5, no. 1, 1971, pp. 58–80.
56. Justusson, Brian, et al.: An Overview of the NASA Advanced Composites Consortium High Energy Dynamic Impact Phase II Technical Path. AIAA 2019–2052, 2019.
57. Hunziker, Kenneth J., et al.: NASA ACC High Energy Dynamic Impact Methodology and Outcomes. AIAA 2018–1700, 2018.

58. Livermore Software Technology Corporation: LS-DYNA® Keyword User's Manual. Vol. II, LS-DYNA R9.0, 8/31/16 (r:7893), 2016.
59. Cuenca, Fernando, et al.: Determination of Ballistic Limit of Skin-Stringer Panels Using Nonlinear, Strain-Rate Dependent Peridynamics. AIAA 2019–2057, 2019.
60. Hexcel Corporation: HexPly® 8552 Product Data Sheet. https://www.hexcel.com/Resources/DataSheets/Prepreg. Accessed Feb. 13, 2024.
61. Haluza, R.T.: Measurement and Explicit Finite Element Modeling of Dynamic Crush Behavior of Carbon Fiber Reinforced Polymer Composites. Ph.D. Dissertation, The Pennsylvania State University, 2022.
62. ASTM D7136/D7136M–15: Standard Test Method for Measuring the Damage Resistance of a Fiber-Reinforced Polymer Matrix Composite to a Drop-Weight Impact. ASTM International, West Conshohocken, PA, 2020.
63. Thorsson, Solver I., et al.: Prediction of Low-Velocity Face-On Impact Response of Composite Laminates Using High-Fidelity Finite Element Modeling Techniques. AIAA 2016–2184, 2016.
64. Ji, Wooseok, et al.: Face-On and Edge-On Impact Response of Composite Laminates. AIAA 2015–0956, 2015.
65. Gama, Bazle A., et al.: Punch Shear Behavior of Thick-Section Composites Under Quasi-Static, Low Velocity, and Ballistic Impact Loading. 50th International SAMPE Symposium & Exhibition, Long Beach, CA, 2005.
66. Gama, B.Z.: A Short Course on Progressive Composite Damage Modeling in LS–DYNA Using MAT162. University of Delaware Center for Composite Materials, Newark, DE, 2015.
67. Xiao, J.R.; Gama, B.A.; and Gillespie, J.W.: Progressive Damage and Delamination in Plain Weave S-2 Glass/SC-15 Composites Under Quasi-Static Punch-Shear Loading. Compos. Struct., vol. 78, no. 2, 2007, pp. 182–196.
68. Hoffarth, Canio: A Generalized Orthotropic Elasto-Plastic Material Model for Impact Analysis. Doctoral Dissertation, Arizona State University, 2016.
69. Khaled, Bilal: Experimental Characterization and Finite Element Modeling of Composites to Support a Generalized Orthotropic Elasto-Plastic Damage Material Model for Impact Analysis. Doctoral Dissertation, Arizona State University, 2019.
70. ASTM D3039/D3039M–17: Standard Test Method for Tensile Properties of Polymer Matrix Composites Materials. ASTM International, West Conshohocken, PA, 2017.
71. ASTM D7291/D7291M–15: Standard Test Method for Through-Thickness "Flatwise" Tensile Strength and Elastic Modulus of a Fiber-Reinforced Polymer Matrix Composite Material. ASTM International, West Conshohocken, PA, 2022.
72. ASTM D3410/D3410M–16: Standard Test Method for Compressive Properties of Polymer Matrix Composite Materials With Unsupported Gage Section by Shear Loading. ASTM International, West Conshohocken, PA, 2021.
73. ASTM D5379/D5379M–12: Standard Test Method for Shear Properties of Composite Materials by the V-notched Beam Method. ASTM International, West Conshohocken, PA, 2019.
74. Haluza, Rudy T., et al.: Out-of-Plane Shear Properties of IM7/8552 Carbon/Epoxy by V-Notched Shear Testing. AIAA 2020–1212, 2020.
75. O'Higgins, R.M.; McCarthy, C.T.; and McCarthy, M.A.: Identification of Damage and Plasticity Parameters for Continuum Damage Mechanics Modelling of Carbon and Glass Fibre-Reinforced Composite Materials. Strain, vol. 47, no. 1, 2011, pp. 105–115.

76. ASTM D3518/D3518M–18: Standard Test Method for In-Plane Shear Response of Polymer Matrix Composite Materials by Tensile Test of a ±45° Laminate. ASTM International, West Conshohocken, PA, 2018.
77. Martin, R.H.; Elms, T.; and Bowron, S.: Characterisation of Mode II Delamination Using the 4ENF. 4th European Conference on Composites: Testing and Standardisation, Lisbon, Portugal, 1998, pp. 161–170.
78. Schon, Joakim, et al.: A Numerical and Experimental Investigation of Delamination Behaviour in the DCB Specimen. Compos. Sci. Technol., vol. 60, no. 2, 2000, pp. 173–184.
79. Schon, Joakim, et al.: Numerical and Experimental Investigation of a Composite ENF-Specimen. Eng. Fract. Mech., vol. 65, no. 4, 2000, pp. 405–433.
80. European Structural Integrity Society, Polymer and Composite Task Force. Protocol for interlarninar fracture testing Nos. 1 and 2, March 1992.
81. ASTM D5528/D5528M–21: Standard Test Method for Mode I Interlaminar Fracture Toughness of Unidirectional Fiber-Reinforced Polymer Matrix Composites. ASTM International, West Conshohocken, PA, 2022.
82. Andersons, J.; and Konig, M.: Dependence of Fracture Toughness of Composite Laminates on Interface Ply Orientations and Delamination Growth Direction. Compos. Sci. Technol., vol. 64, nos. 13–14, 2004, pp. 2139–2152.
83. Hiley, M.J.: Delamination Between Multi-Directional Ply Interfaces in Carbon-Epoxy Composites Under Static and Fatigue Loading. ESIS, vol. 27, 2000, pp. 61–72.
84. Kinloch, A.J., et al.: The Mixed-Mode Delamination of Fibre Composite Materials. Compos. Sci. Technol., vol. 47, no. 3, 1993, pp. 225–237.
85. Hansen, Peter; and Martin, Rod: DCB, 4ENF and MMB Delamination Characterisation of S2/8552 and IM7/8552. Materials Engineering Research Laboratory Ltd. Final Technical Report ERO/2, Contract N68171–98–M–5177, 1999.
86. ASTM D7905/D7905M–19e: Standard Test Method for Determination of the Mode II Interlaminar Fracture Toughness of Unidirectional Fiber-Reinforced Polymer Matrix Composites. ASTM International, West Conshohocken, PA, 2019.
87. Ravindran, Suraj, et al.: Mode-I Behavior of Adhesively Bonded Composite Joints at High Loading Rates. Compos. Sci. Technol., vol. 198, no. 108310, 2020.
88. The Boeing Company, Wichita State University, and NIAR: 2C19—High Energy Dynamic Impact (HEDI) Fastener Joints Fabrication & Test Plan—ACC Phase II Deliverable Item 4.9.2. Feb. 9, 2018. Internal Report.
89. The Boeing Company, Wichita State University, and NIAR: 2C19—High Energy Dynamic Impact (HEDI) Fastener Joints Test Report—ACC Phase II Deliverable Item 4.9.3. Apr. 30, 2018. Internal Report.
90. Kona Ravi, A., et al.: High Rate Testing of Composite Fastener Joints With and Without Clamp-Up. American Society for Composites 2018 Thirty-Third Technical Conference, Anthony Waas, ed., Seattle, WA, 2018.
91. Hobbs, James Mark: Effects of Laminate Design on the Crashworthiness of Carbon/Epoxy Composite Materials. Ph.D. Dissertation, University of Utah, 2019.
92. Ostler, D.W.: Characterization of Carbon/Epoxy C-Channels for Crashworthiness Applications. Doctoral Dissertation, University of Utah, 2021.
93. Haluza, R.T., et al.: Novel Crash Sled With a Translating Support Mass. Exp. Mech., vol. 62, 2022, pp. 715–728.

94. Wade, Bonnie; and Feraboli, Paolo: CMH-17 Crashworthiness WG Numerical Round Robin. Composite Damage Material Modeling for Crash Simulation: MAT54 & the Efforts of the CMH-17 Numerical Round Robin, Joint Advanced Materials & Structures Center of Excellence, Mostafa Rassaian, ed., Technical Review, 2014, p. 7.
95. Khan, Akhtar S.; and Huang, Sujian: Continuum Theory of Plasticity. John Wiley & Sons, New York, NY, 1995.
96. Khaled, Bilal, et al.: Development of a Tabulated Material Model for Composite Material Failure, MAT213. Part 2: Experimental Tests to Characterize the Behavior and Properties of T800-F3900 Toray Composite. DOT/FAA/TC–19/50, P2, 2020.
97. Puck, A.; and Schurmann, H.: Failure Analysis of FRP Laminates by Means of Physically Based Phenomenological Models. Failure Criteria in Fibre-Reinforced-Polymer Composites, 2004, Elsevier, London, pp. 832–876.
98. Goldberg, R.K., et al.: Implementation of a Tabulated Failure Model Into a Generalized Composite Material Model. J. Compos. Mater., vol. 52, no. 25, 2018, pp. 3445–3460.
99. Shyamsunder, Loukham, et al.: Implementing Deformation, Damage, and Failure in an Orthotropic Plastic Material Model. J. Compos. Mater., vol. 54, no. 4, 2020, pp. 463–484.
100. Forghani, Alireza; Poursartip, Anoush; and Vaziri, Reza: An Orthotropic Non-Local Approach to Modeling Intra-Laminar Damage Progression in Laminated Composites. Int. J. Solids Struct., vols. 180–181, 2019, pp. 160–175.
101. Bazant, Zdenek P.; and Oh, B.H.: Crack Band Theory for Fracture of Concrete. Mater. Construct., vol. 16, 1983, pp. 155–177.
102. Matzenmiller, A.; Lubliner, J.; and Taylor, R.L.: A Constitutive Model for Anisotropic Damage in Fiber Composites. Mech. Mater., vol. 20, 1995, pp. 125–152.
103. Allix, O.; and Ladeveze, P.: Interlaminar Interface Modelling for the Prediction of Delamination. Compos. Struct., vol. 22, no. 4, 1992, pp. 235–242.
104. Turon, A., et al.: An Engineering Solution for Mesh Size Effects in the Simulation of Delamination Using Cohesive Zone Models. Eng. Fract. Mech., vol. 74, no. 10, 2007, pp. 1665–1682.
105. Schueler, Dominik; Toso-Pentecote, Natalie; and Voggenreiter, Heinz: Simulation of High Velocity Impact on Composite Structures—Model Implementation and Validation. Appl. Compos. Mater., vol. 23, no. 4, 2016, pp. 857–878.
106. Delsart, David, et al.: Evaluation of Finite Element Modelling Methodologies for the Design of Crashworthy Composite Commercial Aircraft Fuselage. 24th International Congress of the Aeronautical Sciences, Yokohama, Japan, 2004.